

Lecture Notes in Mechanical Engineering

Banh Tien Long · Kozo Ishizaki ·  
Hyung Sun Kim · Yun-Hea Kim ·  
Nguyen Duc Toan ·  
Nguyen Thi Hong Minh ·  
Pham Duc An *Editors*

# Proceedings of the 3rd Annual International Conference on Material, Machines and Methods for Sustainable Development (MMMS2022)


Volume 1: Advanced Materials  
and Manufacturing Technologies

 Springer

# Lecture Notes in Mechanical Engineering


## Series Editors

Fakher Chaari, National School of Engineers, University of Sfax, Sfax, Tunisia

Francesco Gherardini , Dipartimento di Ingegneria “Enzo Ferrari”, Università di Modena e Reggio Emilia, Modena, Italy

Vitalii Ivanov, Department of Manufacturing Engineering, Machines and Tools, Sumy State University, Sumy, Ukraine

## Editorial Board

Francisco Cavas-Martínez , Departamento de Estructuras, Construcción y Expresión Gráfica Universidad Politécnica de Cartagena, Cartagena, Murcia, Spain

Francesca di Mare, Institute of Energy Technology, Ruhr-Universität Bochum, Bochum, Nordrhein-Westfalen, Germany

Mohamed Haddar, National School of Engineers of Sfax (ENIS), Sfax, Tunisia

Young W. Kwon, Department of Manufacturing Engineering and Aerospace Engineering, Graduate School of Engineering and Applied Science, Monterey, CA, USA

Justyna Trojanowska, Poznan University of Technology, Poznan, Poland

Jinyang Xu, School of Mechanical Engineering, Shanghai Jiao Tong University, Shanghai, China

**Lecture Notes in Mechanical Engineering (LNME)** publishes the latest developments in Mechanical Engineering—quickly, informally and with high quality. Original research reported in proceedings and post-proceedings represents the core of LNME. Volumes published in LNME embrace all aspects, subfields and new challenges of mechanical engineering.

To submit a proposal or request further information, please contact the Springer Editor of your location:

**Europe, USA, Africa:** Leontina Di Cecco at [Leontina.dicecco@springer.com](mailto:Leontina.dicecco@springer.com)

**China:** Ella Zhang at [ella.zhang@springer.com](mailto:ella.zhang@springer.com)

**India:** Priya Vyas at [priya.vyas@springer.com](mailto:priya.vyas@springer.com)

**Rest of Asia, Australia, New Zealand:** Swati Meherishi at [swati.meherishi@springer.com](mailto:swati.meherishi@springer.com)

Topics in the series include:

- Engineering Design
- Machinery and Machine Elements
- Mechanical Structures and Stress Analysis
- Automotive Engineering
- Engine Technology
- Aerospace Technology and Astronautics
- Nanotechnology and Microengineering
- Control, Robotics, Mechatronics
- MEMS
- Theoretical and Applied Mechanics
- Dynamical Systems, Control
- Fluid Mechanics
- Engineering Thermodynamics, Heat and Mass Transfer
- Manufacturing
- Precision Engineering, Instrumentation, Measurement
- Materials Engineering
- Tribology and Surface Technology

**Indexed by SCOPUS, EI Compendex, and INSPEC.**

All books published in the series are evaluated by Web of Science for the Conference Proceedings Citation Index (CPCI).

To submit a proposal for a monograph, please check our Springer Tracts in Mechanical Engineering at <https://link.springer.com/bookseries/11693>.

Banh Tien Long · Kozo Ishizaki · Hyung Sun Kim ·  
Yun-Hea Kim · Nguyen Duc Toan ·  
Nguyen Thi Hong Minh · Pham Duc An  
Editors

# Proceedings of the 3rd Annual International Conference on Material, Machines and Methods for Sustainable Development (MMMS2022)

Volume 1: Advanced Materials  
and Manufacturing Technologies

 Springer



*Editors*

Banh Tien Long  
Vietnam Association for Science Editing  
Hanoi University of Science  
and Technology  
Hanoi, Vietnam

Hyung Sun Kim  
Department of Materials Science  
and Engineering  
Inha University  
Nam-gu, Korea (Republic of)

Nguyen Duc Toan  
School of Mechanical Engineering  
Hanoi University of Science  
and Technology  
Hanoi, Vietnam

Pham Duc An  
Hanoi University of Science  
and Technology  
Hanoi, Vietnam

Kozo Ishizaki  
Nagaoka University of Technology  
Nagaoka, Japan

Yun-Hea Kim  
Department of Ocean Advanced Materials  
Convergence Engineering  
Korea Maritime and Ocean University  
Busan, Korea (Republic of)

Nguyen Thi Hong Minh  
Hanoi University of Science  
and Technology  
Hanoi, Vietnam

ISSN 2195-4356

ISSN 2195-4364 (electronic)

Lecture Notes in Mechanical Engineering

ISBN 978-3-031-31823-8

ISBN 978-3-031-31824-5 (eBook)

<https://doi.org/10.1007/978-3-031-31824-5>

© The Editor(s) (if applicable) and The Author(s), under exclusive license to Springer Nature Switzerland AG 2023

This work is subject to copyright. All rights are solely and exclusively licensed by the Publisher, whether the whole or part of the material is concerned, specifically the rights of translation, reprinting, reuse of illustrations, recitation, broadcasting, reproduction on microfilms or in any other physical way, and transmission or information storage and retrieval, electronic adaptation, computer software, or by similar or dissimilar methodology now known or hereafter developed.

The use of general descriptive names, registered names, trademarks, service marks, etc. in this publication does not imply, even in the absence of a specific statement, that such names are exempt from the relevant protective laws and regulations and therefore free for general use.

The publisher, the authors, and the editors are safe to assume that the advice and information in this book are believed to be true and accurate at the date of publication. Neither the publisher nor the authors or the editors give a warranty, expressed or implied, with respect to the material contained herein or for any errors or omissions that may have been made. The publisher remains neutral with regard to jurisdictional claims in published maps and institutional affiliations.

This Springer imprint is published by the registered company Springer Nature Switzerland AG  
The registered company address is: Gewerbestrasse 11, 6330 Cham, Switzerland

# Organizing Committee

## Conference Chairs

Prof. Sci. Dr. Banh Tien Long, Vietnam Association for Science Editing, Vietnam;  
Hanoi University of Science and Technology

Prof. Yun-Hea Kim, Professor in Ocean Advanced Materials Convergence Engineering; Ex-Acting President of KMOU; Visiting Professor, Naval Postgraduate School (NPS), USA; Vice President of the Korean Society for Composite Materials; Editor-in-Chief of *Nano Hybrids Composites*

Prof. Hyung Sun Kim, Inha University

Prof. Kozo Ishizaki, Nagaoka University of Technology, Japan

## Conference Co-chairs

Prof. Le Anh Tuan, Hanoi University of Science and Technology, Vietnam, e-mail: [Tuan.LeAnh@hust.edu.vn](mailto:Tuan.LeAnh@hust.edu.vn)

Prof. Nguyen Duc Toan, Hanoi University of Science and Technology, Vietnam, e-mail: [Toan.NguyenDuc@hust.edu.vn](mailto:Toan.NguyenDuc@hust.edu.vn)

Prof. Dinh Van Chien, Vietnam Association for Science Editing, Vietnam, e-mail: [vanchien.dinh@gmail.com](mailto:vanchien.dinh@gmail.com)

Assoc. Prof. Nguyen Thi Hong Minh, Vietnam Association for Science Editing, Vietnam; Hanoi University of Science and Technology, e-mail: [Minh.NguyenThiHong@hust.edu.vn](mailto:Minh.NguyenThiHong@hust.edu.vn)

Dr. Ho Xuan Nang, Phenikaa University, e-mail: [nangvicostone@gmail.com](mailto:nangvicostone@gmail.com)

Dr. Nguyen Tien Dung, Nam Can Tho University

Prof. Kim Kyuman, Kyungpook National University, Korea

Prof. S.-H. Chang, National Kaohsiung University of Science and Technology, Taiwan, ROC

## Contact Persons

Dr. Phan Van Hieu, Hanoi University of Science and Technology, Vietnam, e-mail: [hieu.phanvan@hust.edu.vn](mailto:hieu.phanvan@hust.edu.vn)

Dr. Pham Duc An, Hanoi University of Science and Technology, Vietnam, e-mail: [An.PhamDuc@hust.edu.vn](mailto:An.PhamDuc@hust.edu.vn)

Dr. Hoang Van Quy, Hai Phong University, e-mail: [Quyhv@dhhp.edu.vn](mailto:Quyhv@dhhp.edu.vn)

## Science Secretaries

Dr. Pham Duc An, Hanoi University of Science and Technology, Vietnam, e-mail: [An.PhamDuc@hust.edu.vn](mailto:An.PhamDuc@hust.edu.vn)

Dr. Phan Van Hieu, Hanoi University of Science and Technology, Vietnam, e-mail: [hieu.phanvan@hust.edu.vn](mailto:hieu.phanvan@hust.edu.vn)

Dr. Mac Thi Thoa, Hanoi University of Science and Technology, Vietnam, e-mail: [Thoa.MacThi@hust.edu.vn](mailto:Thoa.MacThi@hust.edu.vn)

## International Organizing Committee

Banh Tien Long, Vietnam Association for Science Editing, Vietnam

Bui The Duy, Ministry of Science and Technology, Vietnam

Hoang Minh Son, Ministry of Education and Training, Vietnam

Nguyen Van Phuc, Ministry of Education and Training, Vietnam

Phan Xuan Dung, Vietnam Union of Science and Technology Associations, Vietnam

Dinh Van Phong, Hanoi University of Science and Technology, Vietnam

Huynh Dang Chinh, Hanoi University of Science and Technology, Vietnam

Hyungsun Kim, Council of Asian Science Editors, Korea

Kim Kyuman, Kyungpook National University, Korea

Kim Youngsuk, Kyungpook National University, Korea

Kozo Ishizaki, Nagaoka University of Technology, Japan

I. A. Parinov, Southern Federal University, Russia

S.-H. Chang, National Kaohsiung University of Science and Technology, Taiwan

Nobuhiko Azuma, Nagaoka University of Technology, Japan

Nguyen Tien Dung, Nam Can Tho University, Vietnam

Nguyen Van Quang, Nam Can Tho University, Vietnam

Vu Ngoc Pi, Thai Nguyen University, Vietnam

Truong Hoanh Son, Hanoi University of Science and Technology, Vietnam

## **International Advisory Committee**

Chinda Charoenphonphanich, King Mongkut's Institute of Technology Ladkrabang, Thailand

Nguyen Duc Chien, Hanoi University of Science and Technology, Vietnam

Kim Kyuman, Kyungpook National University, Korea

Nguyen Duc Toan, Hanoi University of Science and Technology, Vietnam

Heidy Visbal, Kyoto University, Japan

Holger Kohl, Fraunhofer IPK Berlin, Germany

Hyungsun Kim, Inha University, Korea

Jong Kyu Ha, Seoul National University, Korea

Jung-II Jin, Korea University, Korea

Kozo Ishizaki, Nagaoka University of Technology, Japan

Makoto Nanko, Nagoya Institute of Technology, Japan

Nobumasa Sekishita, Toyohashi University of Technology, Japan

Nobutaka Ito, Chiang Mai University, Thailand

Ralph J. Hexter, UC Davis, USA

Ramanathan Subramaniam, National Institute of Education, Singapore

Ramesh S. Kanwar, University of Hawaii, USA

Seung-Han Yang, Kyungpook National University, Korea

Soo Wahn Lee, Professor, Sun Moon University, Korea

Takashi Shirai, Kyoto Institute of Technology, Japan

Tetsuro Majima, Osaka University, Japan

Wim Dewulf, Katholieke Universiteit Leuven, Belgium

Worachart Sirawaraporn, Mahidol University, Thailand

Yoshiki Mikami, Nagaoka University of Technology, Japan

Yukari Matsuo, Hosei University, Japan

Bui Van Ga, Da Nang University, Vietnam

Le Anh Tuan, Hanoi University of Science and Technology, Vietnam

Tran Van Nam, Da Nang University, Vietnam

Nguyen Thanh Nam, Ho Chi Minh City University of Technology (HCMUT), Vietnam

Nguyen Hay, Nong Lam University, Vietnam

Nguyen Dinh Tung, Research Institute of Agricultural Machinery, Vietnam

Tran Duc Quy, Hanoi University of Industry, Vietnam

Bui Trung Thanh, Hung Yen University of Technology and Education, Vietnam

Vu Ngoc Pi, Thai Nguyen University, Vietnam

Cao Hung Phi, Vinh Long University of Technology Education, Vietnam

Pham Xuan Duong, Vietnam Maritime University, Vietnam

Nguyen Quoc Hung, Vietnamese-German University, Vietnam

Huynh Trung Hai, Hanoi University of Science and Technology, Vietnam

Truong Hoanh Son, Hanoi University of Science and Technology, Vietnam

Luong Cong Nho, Vietnam Maritime University, Vietnam

Tran Van-Nghia, Ministry of Science and Technology, Vietnam

V. K. Gupta, PDPM-Indian Institute of Information Technology, Design and Manufacturing Jabalpur, India  
 R. Hastijanti, University of 17 Agustus 1945 Surabaya, Indonesia  
 K. Hasyim, University of Darul Ulum, Jombang, Indonesia  
 H. -C. Huang, National Kaohsiung University of Science and Technology, Taiwan, ROC  
 M. A. Jani, University of 17 Agustus 1945 Surabaya, Indonesia  
 V. V. Kalinchuk, Southern Scientific Center of Russian Academy of Sciences, Russia  
 P. K. Kankar, Indian Institute of Technology Indore, India  
 C.-T. Lin, National Kaohsiung University of Science and Technology, Taiwan, ROC  
 M. B. Manuilov, Southern Federal University, Russia  
 A. V. Metelitsa, Southern Federal University, Russia  
 V. I. Minkin, Southern Federal University, Russia  
 E. L. Mukhanov, Southern Federal University, Russia  
 M. Musta'in, University of Darul Ulum, Jombang, Indonesia  
 T. Nakayama, Nagaoka University of Technology, Japan  
 M. Nanko, Nagaoka University of Technology, Japan  
 Nurmawati, University of 45 Surabaya, Indonesia  
 I. Prasetyawan, Lloyd's Register Asia, Malaysia  
 M. A. Rahim, University of 17 Agustus 1945 Surabaya, Indonesia  
 Sajjo, University of 17 Agustus 1945 Surabaya, Indonesia  
 T. Sekino, Osaka University, Japan  
 A. N. Soloviev, Don State Technical University, Russia  
 I. A. Verbenko, Southern Federal University, Russia  
 J.-K. Wu, National Kaohsiung University of Science and Technology, Taiwan, ROC  
 M.-C. Wu, National Tsing Hua University, Taiwan, ROC

## **Local Organizing Committee**

Banh Tien Long, Vietnam Association for Science Editing, Vietnam  
 Dinh Van Chien, Vietnam Association for Science Editing, Vietnam  
 Nguyen Thi Hong Minh, Vietnam Association for Science Editing, Vietnam  
 Nguyen Duc Toan, Vietnam Association for Science Editing, Vietnam  
 Phan Van Hieu, Vietnam Association for Science Editing, Vietnam  
 Mac Thi Thoa, Hanoi University of Science and Technology, Vietnam  
 Pham Duc An, Hanoi University of Science and Technology, Vietnam  
 Nguyen Huu Quang, Vietnam Association for Science Editing, Vietnam  
 Hoang Van Quy, Vietnam Association for Science Editing, Vietnam  
 Bui Van Bien, Haiphong University  
 Hoang Long, Vietnam Association for Science Editing, Vietnam  
 Bui Long Vinh, Hanoi University of Science and Technology, Vietnam  
 Dinh Van Phong, Hanoi University of Science and Technology, Vietnam

Le Anh Tuan, Hanoi University of Science and Technology, Vietnam  
 Nguyen Minh Hong, Ministry of Information and Telecommunications, Vietnam  
 Bui Trung Thanh, Hung Yen University of Technology and Education, Vietnam  
 Tran The Van, Hung Yen University of Technology and Education, Vietnam  
 Do Anh Tuan, Hung Yen University of Technology and Education, Vietnam  
 Nguyen Tien Dung, Nam Can Tho University, Vietnam  
 Nguyen Van Quang, Nam Can Tho University, Vietnam  
 Quach Hoai Nam, Nha Trang University, Vietnam  
 Tran Hung Tra, Nha Trang University, Vietnam  
 Nguyen Van Tuong, Nha Trang University, Vietnam

## Scientific Committee

Banh Tien Long, Hanoi University of Science and Technology, Vietnam  
 Bui Van Ga, Da Nang University, Vietnam  
 Le Anh Tuan, Hanoi University of Science and Technology, Vietnam  
 Tran Van Nam, Da Nang University, Vietnam  
 Nguyen Thanh Nam, Ho Chi Minh City University of Technology (HCMUT), Vietnam  
 Nguyen Hay, Nong Lam University, Vietnam  
 Chu Van Dat, Military Technical Institute, Vietnam  
 Nguyen Lac Hong, Le Quy Don University, Vietnam  
 Luong Cong Nho, Vietnam Maritime University, Vietnam  
 Nguyen Tien Dung, Nam Can Tho University, Vietnam  
 Nguyen Van Quang, Nam Can Tho University, Vietnam  
 Nguyen Duc Toan, Hanoi University of Science and Technology, Vietnam  
 Chinda Charoenphonphanich, King Mongkut's Institute of Technology Ladkrabang, Thailand  
 Dao Hong Bach, Hanoi University of Science and Technology, Vietnam  
 Tran Hung Tra, Nha Trang University, Vietnam  
 Dang Xuan Phuong, Nha Trang University, Vietnam  
 Bui Anh Hoa, Hanoi University of Science and Technology, Vietnam  
 Dinh Van Hai, Hanoi University of Science and Technology, Vietnam  
 Truong Hoanh Son, Hanoi University of Science and Technology, Vietnam  
 Phan Van Hieu, Hanoi University of Science and Technology, Vietnam  
 Hoang Hong Hai, Hanoi University of Science and Technology, Vietnam  
 Nguyen Dinh Tung, Research Institute of Agricultural Machinery, RIAM, Vietnam  
 Truong Viet Anh, Hanoi University of Science and Technology, Vietnam  
 Nguyen Phong Dien, Hanoi University of Science and Technology, Vietnam  
 Nguyen Ngoc Trung, Hanoi University of Science and Technology, Vietnam  
 Nguyen Huy Bich, Nong Lam University, Vietnam  
 Erik Bohez, Asian Institute of Technology, Thailand  
 Gyu Man Kim, Kyungpook National University, Korea

Jung-Il Jin, Korea University, Korea  
Le Quang, Hanoi University of Science and Technology, Vietnam  
Nobuhiko Azuma, Nagaoka University of Technology, Japan  
Nobumasa Sekishita, Toyohashi University of Technology, Japan  
Nghiem Trung Dung, Hanoi University of Science and Technology, Vietnam  
Nguyen Dang Binh, Viet Bac University, Vietnam  
Nguyen Hong Lanh, Military Technical Institute, Vietnam  
Nguyen The Mich, Hanoi University of Science and Technology, Vietnam  
Nguyen Thi Thu Hien, Hanoi University of Science and Technology, Vietnam  
Nguyen Viet Dung, Hanoi University of Science and Technology, Vietnam  
Pham Minh Tuan, Hanoi University of Science and Technology, Vietnam  
Pham Thanh Huy, Hanoi University of Science and Technology, Vietnam  
Pham Van Hung, Hanoi University of Science and Technology, Vietnam  
Seung-Han Yang, Kyungpook National University, Korea  
Soo Wahn Lee, Professor, Sun Moon University, Korea  
Tran Van Dich, Hanoi University of Science and Technology, Vietnam  
Truong Ngoc Than, Hanoi University of Science and Technology, Vietnam  
Vu Duc Lap, Military Technical Institute, Vietnam  
Vu Quoc Huy, Hanoi University of Science and Technology, Vietnam  
Wim Dewulf, Katholieke Universiteit Leuven, Belgium  
Heidy Visbal, Kyoto University, Japan  
Holger Kohl, Fraunhofer IPK Berlin, Germany  
Hyungsun Kim, Inha University, Korea  
Jong Kyu Ha, Seoul National University, Korea  
Kozo Ishizaki, Nagaoka University of Technology, Japan  
Makoto Nanko, Nagoya Institute of Technology, Japan  
Nobutaka Ito, Chang Mai University, Thailand  
Ralph J. Hexter, UC Davis, USA  
Ramanathan Subramaniam, National Institute of Education, Singapore  
Ramesh S. Kanwar, University of Hawaii, USA  
Takashi Shirai, Kyoto Institute of Technology, Japan  
Tetsuro Majima, Osaka University, Japan  
Worachart Sirawaraporn, Mahidol University, Thailand  
Yoshiki Mikami, Nagaoka University of Technology, Japan  
Yukari Matsuo, Hosei University, Japan  
Nguyen Huy Bich, Nong Lam University, Vietnam  
Nguyen Van Tuong, Nha Trang University, Vietnam  
Pham Dinh Tung, Le Quy Don University, Vietnam  
Tran The Van, Hung Yen University of Technology and Education, Vietnam  
Do Anh Tuan, Hung Yen University of Technology and Education, Vietnam  
Nguyen Khac Tuan, Thai Nguyen University, Vietnam  
Vu Dinh Quy, Hanoi University of Science and Technology, Vietnam  
Nguyen Duc Nam, Ho Chi Minh University of Industry, Vietnam  
Ngo Van He, Hanoi University of Science and Technology, Vietnam

Nguyen Van-Thien, Hanoi University of Industry, Vietnam

Nguyen Tuan Linh, Hanoi University of Industry, Vietnam

Nguyen Tien-Han, Hanoi University of Industry, Vietnam



# Welcome Message

On behalf of the Organizing Committee, we are pleased to present the volume of *Lecture Notes in Mechanical Engineering*, which contains a selection of papers from The Third International Conference on Material, Machines, and Methods for Sustainable Development (MMMS2022) held from November 10–13, 2022, in Can Tho, Vietnam. Since 2018, MMMS has been focused on extending overall Sustainable Development Engineering to engage more researchers from different areas and various fields. Building on the success of the 2018 conference in Nalod, Danang, Vietnam, and the 2020 conference in Nha Trang, MMMS2022 aimed to evolve into one of the leading academic conferences in the field of Sustainable Development Engineering, underpinned by insightful lectures and presentations to attract even more attendees.

MMMS2022 is an international symposium hosted by the Vietnam Association of Science Editing (VASE) in collaboration with prestigious institutions such as Hanoi University of Science and Technology (HUST), Nam Can Tho University (NTU), Phenikaa University (PKA), Thai Nguyen University (TNU), Kyungpook National University (KNU-Korea), Nagaoka University of Technology (NUT Japan), Vietnam Federation of Mechanical Engineering Associations (VFMEA), and Council of Asian Science Editors (CASE). The event covers a wide range of topics related to engineering and sustainable manufacturing for the benefit of a global society. Researchers, policymakers, industry professionals, practitioners, and students from all countries are invited to submit papers and participate in various sessions, keynotes, and workshops.

The main objective of the conference is to explore critical aspects of sustainable development, particularly in the areas of materials, machines, and methods. Through interactive sessions, policymakers, researchers, and industry professionals can exchange feedback and inputs on the topics to ensure local technological development toward sustainable development in a global context. Furthermore, networking is promoted between participants through special sessions organized by VASE, including those focusing on improving writing for publishing in advanced international journals, presented by Prof. Hyusun Kim, Former President of the Council of Asian Science Editors (CASE).

The purpose of this volume of *Lecture Notes in Mechanical Engineering* is to explore and ensure an understanding of the critical aspects that contribute to sustainable development, particularly materials, machines, and methods. The conference aims to assist policymakers, industries, and researchers at various levels to position local technological development toward sustainable development in the global context and to promote decision-making toward a greener approach, especially for materials, machines, and methods.

We would like to express our gratitude to the members of the International Organizing and Academic Committees of the Conference for their hardwork and advice, which helped to maintain the high level of the conference. We also thank Springer Nature Switzerland AG 2020 for publishing the selected papers in the *Lecture Notes in Mechanical Engineering*. We hope that all the papers will provide valuable information for academics, researchers, engineers, and students.

Prof. Banh Tien Long  
Vietnam Association for Science Editing (VASE)  
Hanoi University of Science and Technology  
Hanoi, Vietnam

Prof. Nguyen Duc Toan  
Hanoi University of Science and Technology  
Hanoi, Vietnam

## Keynote Speakers



**Prof. Yun-Hae Kim**

**Affiliation:** Korea Maritime and Ocean University, Republic of Korea.

**Bio Statement:**

Professor Yun-Hae Kim graduated from the Department of Marine Engineering, Korea Maritime and Ocean University in 1983 and received Ph.D. degree from Kyushu University in Mechanical Engineering, Japan. He worked at NIST, USA, as a visiting professor from 1997 to 1998, and his studies focused on the fabrication and evaluation of composite materials. He worked as a research assistant, 1985–1987, at Korea Maritime and Ocean University. He published over 150 papers in international and national journals; He joined over 60 conferences and symposia at international and national levels as a general speaker, invited speaker, or keynote speaker. He founded two international conferences, namely Asian Conference on Engineering Education (ACEE, 2009) and Asian Conference on Campus Sustainability (ACCS, 2015). He was the president of the Korea Association of Green Campus Initiatives

(KAGCI). He was the ex-Acting president of Korea Maritime and Ocean University, ex-Dean of Student Affairs, and ex-Dean of Academic Affairs from 2014 to 2016. He was a conference chair of the Advanced Materials Development and Performance (AMDP 2014). At that time, over 400 delegates participated in this conference. He was the editor of SCI journal, *International Journal of Modern Physics B*. Now, he is working as the Editors-in-Chief of the *Journal of Ocean Engineering and Technology* for 9 years and *Nano Hybrids Composites*. In particular, he joined in the last five years (2013 and 2017) over 20 conferences as Keynote Speaker and Conference Co-Chairs. He is working as Director of Idea Factory Center at KMOU. He received many awards, Ministry of Science and Technology (Jang Young Sil Best Award, Korea), Ministry of Science and Technology, Korea, Distinguished Professor Award, The Korean Society of Engineering Education, Distinguished Service Medal, The Korean Society of Engineering Education, Ministry of Education, Science and Technology (Ministry Award) (Engineering Education Innovation Field), Ministry of Education, Science and Technology, Korea, Best Paper Award, ICPNS, Seattle, USA. His research interests include R&D of novel materials and composites based on polymer materials (in particular, environmental characteristics, fracture mechanics and strength evaluations, ocean applications of advanced materials and composites.

Yun-Hae Kim was chairman and co-chairman of the following International Conferences:

- (i) 1st Asian Conference on Engineering Education (ACEE), ACEE 2009 (October 28–30, 2009, Busan, Korea)
- (ii) Advanced Materials Development and Performance (AMDP), AMDP 2014 (July 17–20, 2014, Busan, Korea)
- (iii) Asian Conference on Campus Sustainability 2015, ACCS 2015 (November 10–11, 2015, Busan, Korea)
- (iv) 6th International Joint Symposium on Engineering Education (IJSEE), IJSEE 2016 (December 23, 2016, Busan, Korea)
- (v) 7th Advanced Materials Development and Performance (AMDP), AMDP 2017 (July 11–15, 2017, Pune, India).

**Gyu Man Kim**

Professor, School of Mechanical Engineering

Kyungpook National University

Micro-System and Nano-Engineering (MSNE) Research Group

<http://msne.knu.ac.kr/>

1370, Sankyuk-Dong, Daegu, Republic of Korea, 702-701

Tel: 82-53-950-7570 Fax: 82-53-950-6550 Cp: 82-10-9902-6755

e-mail: [gyuman.kim@knu.ac.kr](mailto:gyuman.kim@knu.ac.kr)

**Research Interests**

- Research on micro-/nanoscale fabrication
  - microelectromechanical system (MEMS)
  - Micro-/nano-stencil (shadowmask) technology for micro-/nanoscale patterning
  - Soft lithography
  - Self-assembled monolayer for surface modification.
- Research on microtechnology for life science
  - Micropatterned cell culture
  - Preparation of mono-dispersed biopolymer microparticles
  - Lab-on-a-chip (LOC) and bio-sensors.
- Research on precision manufacturing for miniaturized mechanical systems
  - Micro-electro-discharge machining (MEDM)
  - Micro-electro-chemical machining (MECM).

Gyu Man Kim received the B.S., M.S., and Ph.D. degrees in mechanical design and production engineering from the Seoul National University, Seoul, Korea, in 1993, 1995, and 1999, respectively.

Currently, he is an professor at School of Mechanical Engineering, Kyungpook National University, Korea. He has been a postdoctoral research fellow at MESA+ Research Institute, Twente University, the Netherlands, and at Microsystems Laboratory, Ecole Polytechnique Federale de Lausanne (EPFL).

His recent research works include the formation of hydrogel microdroplet and particles in a microfluidic device, microfabrication using nano- and microstencil, soft lithography, and hybrid technologies of MEMS and precision manufacturing processes. His recent research project includes “Laboratory on microfabrication of enzymatic biofuel cell,” “Fabrication of micro/mesoscale hybrid structures based on porous biopolymer,” “Micropatterned cell culture for stem cell for therapeutic strategies in neurodegenerative disease,” “Inkjetting of biopolymer for Biomedical applications,” and “Nanoparticle and cell-laden microparticle fabrication and its bio application.” He has published over 100 peer-reviewed scientific publications. His research includes micro-/nano-scale fabrication, microfluidics, and miniaturized mechanical systems to be applied to the field of life science, industry, and energy. He is also co-inventor of over 20 patents.

He is member of the KSME, KSPE, and KSMPE. He is an Editor-in-Chief of *International Journal of Precision Engineering and Manufacturing-Green Technology*.

### **Awards**

- Gaheon Award, Gaheon-Sindoh Foundation, 2021
- Best Paper Award, Korean Society for Precision Engineering, 2017
- IJPEM Highly Commended Paper Award, Korean Society for Precision Engineering, 2016
- Best Poster Award, International Symposium on Green Manufacturing and Applications, 2015
- Baek-Am Award, Korean Society for Precision Engineering, 2015
- Best Paper Award, JCK MEMS/NEMS with Nano Korea, 2014
- Best Paper Award, International Symposium on Green Manufacturing and Applications, 2012
- Best Poster Prize, International Conference for Micro- and Nanotechnologies for the Biosciences.

### **Professional Association Activities**

- Editor/Editor-in-Chief *International Journal of Precision Engineering and Manufacturing-Green Technology (IJPEM-GT)*, 2014~
- Editorial committee member/Editor, *International Journal of Precision Engineering and Manufacturing (IJPEM)*, 2009~2017
- Editorial Director, *Korean Society for Precision Engineering (KSPE)*, 2012~
- Member, *Korean Society for Mechanical Engineers (KSME)*, 2003~
- Member, *Korean Society for Precision Engineering (KSPE)*, 2003~

**Makoto Nanko**

Professor, the Department of Mechanical Engineering  
Nagaoka University of Technology  
1603-1, Kamitomioka, Nagaoka, Niigata 940-2188, Japan

**Education**

Bachelor of Engineering, Nagaoka University of Technology, Japan, 1990  
Master of Engineering, Nagaoka University of Technology, Japan, 1992  
Doctor of Engineering, Nagaoka University of Technology, Japan, 1995

**Works**

Assistant Professor, Tokyo Institute of Technology, 1995–2001  
Associate Professor, Nagaoka University of Technology, 2001–2016  
Professor, Nagaoka University of Technology, 2016–Current  
Presidential Aide, 2021–Current

**Major**

Materials Science and Engineering, in particular, High-temperature Physical Chemistry

**Publications**

Nine books, 96 journal papers, 32 reviews, 39 proceedings papers, and eight patents

**Awards**

Young Research Award, Japan Institute of Metals (2000)  
The Commendation for Science and Technology by the Minister of Education, Culture, Sports, Science and Technology (April 2014)

**Prof. Quang-Cherng Hsu**

Department of Mechanical Engineering

National Kaohsiung University of Science and Technology (NKUST), Taiwan

e-mail: [hsuqc@nkust.edu.tw](mailto:hsuqc@nkust.edu.tw)

**Brief Introduction of Professor Quang-Cherng Hsu**

Dr. Quang-Cherng Hsu currently is a professor of Mechanical Engineering, National Kaohsiung University of Science and Technology (NKUST), Taiwan. He earned his Ph.D. degree in Mechanical Engineering, National Cheng-Kung University in 1981. After two-year service in military, he joined Metal Industries Research and Development Center, a government fund non-profit research organization, in Kaohsiung as a research engineer about two years. Then, he joined the current university. In 2003~2004, he visited Ohio State University, USA, as a visiting scholar for one year. During September 12–30, 2016, he visited Aachen University, German, to study Industry 4.0. From March 3 to 26, 2017, he visited Hung Yen University of Technology and Education, and Hai-Phone University, Vietnam, and gave intensive speeches. Research interests of his include image processing and machine vision, metal forming (forging, extrusion, sheet metal forming), nanoimprint lithography applications, molecular dynamics simulation. He has published 61 referred journal papers, has obtained 14 invention patents, and has attended 77 international conferences among 13 countries to present his research results. He also likes to organize student's handy-team to attend domestic professional competitions including industrial robot competition, computer-aided measurement and verification competition, mold and die industrial application and innovation competition, image servo and precision measurement competition, optical-electronic inspection instrument competition, and precision machinery competition.





**Prof. Chyi-Yeu Lin**

Department of Mechanical Engineering and the founding director of the University Research Center: Center for Intelligent Robotics in National Taiwan University of Science and Technology, Taiwan.

Chyi-Yeu Lin is a distinguished professor in the Department of Mechanical Engineering and the founding director of the university research center: Center for Intelligent Robotics in National Taiwan University of Science and Technology, Taiwan. He was elected as a corresponding member of Russian International Academy of Engineering since 2011. Since 2018, he served as the vice-director of the Center for Cyber-physical System Innovation (CPSi), from the Featured Areas Research Center Program within the framework of the Higher Education Sprout Project by the Ministry of Education (MOE) in Taiwan. The CPSi center is the only center funded by MOE in the area of robotics.

He received his Ph.D. degree from the University of Florida in 1991. His research interests and extensive scientific contributions cover from structural optimization and evolutionary methods before 2005, and since 2005 mostly on intelligent robotics and intelligent manufacturing.

He led a research team to debut the world-first robot theater performance with male and female bipedal androids with facial expression capability and two dual-wheeled robots at NTUST campus theater in December 27, 2008. The performed programs included hand puppet show, real-time music note reading and singing, real-time face portrait painting, the Phantom of the Opera show, and harmonic dance and singing. He made many innovative robots in different application domains.

He published about 100 SCI journal papers and 150 conference papers. He participated in near 80 research projects from government and industry with a total budget of more than 8 million USD.

He also founded a robotics and automation company in Taiwan, providing cutting-edge technologies and systems to industries. He loved to invent and had generated more than 50 invention patents globally.

# Contents

<b>Advanced Materials Towards Sustainability</b>	
<b>Influences of Various Bracing on the Buckling Behavior of Steel Frames</b> .....	3
Huy-Phuoc Nguyen and Phu-Cuong Nguyen	
<b>Structural Optimization via 3D Printing Technology Using NPR Materials</b> .....	11
Tran-Trung Nguyen, Phu-Cuong Nguyen, Thanh-Tuan Tran, and Nguyen Van Thuan	
<b>Improving the Accuracy of ACI 318-08 Design Standard for Predicting Strength of CFST Columns Using Machine Learning</b> ....	19
Tran-Trung Nguyen and Phu-Cuong Nguyen	
<b>The Recognition Accuracy in the SSD Model</b> .....	27
Van-Nam Nguyen	
<b>Research and Fabrication of Metal Powder Dispersing Equipment for 3D Printing Technology</b> .....	37
Doan Van Phuc, Vu Van Quang, and Vu Toan Thang	
<b>Cutting Methods in the Single Point Diamond Turning and Surface Roughness of the Ultra-Precision Products—A Brief Review</b> .....	45
Pham Van Tuan, Duong Xuan Bien, Pham Quoc Hoang, Do Tien Lap, and Le Thanh Binh	
<b>Defects Classification on Garment Fabrics and Application of Artificial Intelligence to Detect Defects During Fabric Inspection</b> ....	51
Nguyen Thi Thuy Ngoc, Nguyen Thi Ngoc Lan, and Nguyen Minh Hieu	
<b>Behavior Analysis for One-Way Wide Module Joist Concrete Floor System</b> .....	61
Nhu-Thao Thi Nguyen and Phu-Cuong Nguyen	

<b>Research on the Hydromechanical Forming for the Conical Products by Numerical Simulation</b> .....	69
Thu Nguyen Thi and Trung Nguyen Dac	
<b>Numerical Study on Unwelded Pair of Sheets in Hydrostatic Forming</b> .....	77
Thu Nguyen Thi	
<b>A Parametric Study on Product Quality During Forward-Reverse Extrusion Process</b> .....	83
Thu Nguyen Thi, Minh-Quan Nguyen, and Nguyen Thi Hong Minh	
<b>Calculating the Inherent Strain in 3D Printed Part Based on the Heat Affected Zone</b> .....	91
Ngoc-Hien Tran and Thai-Son Nguyen	
<b>Numerical Investigation of Heat Transfer Characteristics of Ribs with Trenches in Gas Turbine Internal Cooling Channel</b> .....	99
Tuong-Linh Nha, Khanh-Duy Cong Do, Van-Thuc Tran, Viet-Dung Duong, Sung-Goon Park, and Cong-Truong Dinh	
<b>Aerodynamic Performance of Single-Stage Transonic Axial Compressor with Multi-Bleed Airflow</b> .....	109
Tuong-Linh Nha, Van-Hoang Nguyen, Xuan-Truong Le, and Cong-Truong Dinh	
<b>Developing and Improving the Finished Product Warehouse in the Footwear Manufacturing Company Using Logic Simulation</b> .....	117
Thi Tuyet Mai Tran, Minh Tai Le, Cao Tien Dat Tran, and Ngoc Minh Nguyen	
<b>Application of Magnetorheological Elastomer (MRE) for Smart Vibration Systems</b> .....	127
Quang Du Nguyen, Cung Le, and Xuan Bao Nguyen	
<b>Study on Predict Spring-Back in V-Bending of SS400 Steel Plate and Select Bending Parameters by Finite Element Method</b> .....	135
Vuong Gia Hai, Hoang Van Quy, Nguyen Thi Hong Minh, and Nguyen Duc Toan	
<b>Modeling Thrust and Torque of the Propeller on Ship Container Fortune Navigator</b> .....	145
Ngo D. Vuong, Do D. Luu, Lai H. Thien, Hoang Q. Dong, Do V. Doan, Pham X. Duong, Pham V. Ngoc, Bui M. Tuan, and Nguyen X. Tru	

**Forecast Working Regime of the Main Propulsion Plant Using Marine Diesel Engine by Shaft-Line Power Signal** ..... 155  
 Nguyen Xuan Tru, Do Duc Luu, Pham Van Ngoc, Cao Duc Hanh, Luong Cong Nho, Lai Huy Thien, Do Van Doan, Hoang Van Si, and Le Van Vang

**Torsional Resonance Vibrations on the Main Propulsion System Using Two-Stroke Diesel Engine** ..... 163  
 Bui Minh Tuan, Do Duc Luu, Cao Duc Hanh, Dong Xuan Thin, Do Van Doan, Nguyen Xuan Tru, Hoang Van Si, Le Van Vang, and Nguyen Quang Vinh

**Effect of Hot-Pressing Mold Design on Uniformity of Dome-Shaped Products from Infrared Optical Ceramics** ..... 173  
 Nguyen Tuan Hieu, Le Minh Thai, Nguyen Thai Dung, Do Van Thom, and Phung Van Minh

**On the Free Vibration Analysis of Micro FG Beams Considering the Initial Geometrical Imperfection** ..... 181  
 Le Minh Thai, Nguyen Tuan Hieu, Nguyen Thai Dung, Ta Duc Tam, and Phung Van Minh

**Experimental Study on the Dynamic Response of a First-Generation Bump-Foil Bearing** ..... 189  
 Minh-Quan Nguyen and Minh-Hai Pham

**Free Vibration Response of Micro FG Beams Taking the Initial Geometrical Imperfection into Consideration** ..... 197  
 Nguyen Van Dung, Le Minh Thai, Nguyen Thai Dung, and Phung Van Minh

**Assessing the Impact of Heat-Assisted and High Speed Machining on the Performance of Different Cutting Tools During Heat-Treated SKD61 Steel Milling** ..... 205  
 Tran Phap Dong and Nguyen Duc Toan

**Material Application for Sustainable Development**

**Comparative Confined Compressive Strengths of Normal Concrete and HPCFR in Experiment and Model** ..... 213  
 H. T. Tai Nguyen, Duy-Liem Nguyen, My Ngoc-Tra Lam, and Tri Nhat Minh Nguyen

**A Proposed Model for DDMRP Implementation and Application in a Plastic Manufacturing Company** ..... 221  
 Truong Thi Phuc and Phan Thi Mai Ha

**A Study on the Effect of Gas Ratio  $N_2/C_2H_2$  on Some Properties of Hard Thin Films TiAlCN on SKD61 Steel** ..... 229  
Luan Duc Nguyen, Dinh Quang Nguyen, and Cuong Duc Pham

**Studying the Efficiency of Car Brake Force Distribution by a Three-Dimensional Dynamics Model** ..... 237  
Nguyen Thanh Tung and Luong Van Van

**The Effects of the Ratio of Grip to the Ratio of Slip When Braking the Semi-Trailer at 60 kmph** ..... 245  
Nguyen Thanh Tung and Luong Van Van

**Combustion Characteristics of DA465QE Engine Fueled with HHO Enriched Biogas** ..... 253  
Anh Vu Vo, Thi Minh Tu Bui, Tan Tien Huynh, and Thong Ngo Tan

**Electromagnetic Induction Generator by Harvesting Vibration Energy** ..... 263  
Hoa Thi Truong and Dung Hoang

**Reaction Kinetics of the Extraction of Magnesium from Dolomite via the Silicothermic Reduction Process** ..... 269  
Vu Viet Quyen, Vu Thi Thu Trang, and Nguyen Duong Nam

**Optimizing the Structure of the Axle Housing Multi-purpose Forest Fire Fighting Vehicle by Finite Element Method** ..... 277  
Luong Van Van, Nguyen Thanh Tung, Nguyen Thai Van, and Mai Phuoc Trai

**Design and Experimental Test of Magneto-Rheological Seal** ..... 285  
Le Hai Zy Zy, Diep Bao Tri, Do Qui Duyen, Vo Van Cuong, and Quoc Hung Nguyen

**Study the Effects of Geometry and Materials on Modal Characteristics of Honeycomb Composite** ..... 293  
Le Thi Tuyet Nhung, Tran Minh Duy Dat, and Vu Dinh Quy

**An Active Seismic Isolation Two-Layer Floor Based on Hedge Algebra Control** ..... 303  
Thanh-Lam Bui and Xuan-Thuan Nguyen

**Optimization of High Temperature Technology Parameters for 42CrMo Steel** ..... 313  
Le Hong Ky

**Study on Recycling of Chrome-Tanned Leather and Agriculture Waste for Insole Towards Sustainable Development** ..... 323  
Vu Dinh Giap

**Influence of Recrystallization Annealing on the Microstructure and Ductility of Al–Zn–Mg–Cu Alloy Added La, Ce** ..... 333  
 Bùi Thi Ngoc Mai

**A New Design of a Three-Speed Gearbox Provides Continuously Variable Torque During Gear Shifting in Electric Cars** ..... 341  
 Nguyen Hoang Viet, Nguyen Thanh Trung, and Nguyen Hong Thai

**Research Design and Manufacture Eccentric Elliptical Gear Pair with an Improved Cycloid Profile** ..... 349  
 Nguyen Hong Thai, Nguyen Thanh Trung, and Phung Van Thom

**Studying the Influence of Geometric Design Coefficient on Flow and Pressure of Lobe Blower by Numerical Method** ..... 359  
 Nguyen Hong Thai, Trinh Dong Tinh, and Nguyen Thanh Trung

**Dynamic Simulation of Differential-Driven Mobile Robot Taking into Account the Friction Between the Wheel and the Road Surface** .... 367  
 Trinh Thi Khanh Ly, Hoang Thien, Dam Khac Nhan, and Nguyen Hong Thai

**Research on the Vibration of Passenger Car Using Magnetorheological Fluid Damper** ..... 377  
 Nguyen Anh Ngoc, Le Hong Quan, Vu Hai Quan, Nguyen Minh Tien, and Nguyen Ngoc Anh

**Design and Durability Test of the Main Assemblies of Active Anti-roll bar** ..... 385  
 Nguyen Anh Ngoc, Tran Phuc Hoa, Vu Hai Quan, Nguyen Minh Tien, and Kieu Huu Bang

**Determination of Magnetorheological Brake Characteristics by Experiment on the Test Rig** ..... 395  
 Tuan-Hoang Quang, Hoang-Trinh Minh, Ngoc-Nguyen Anh, and Tung-Tran Thanh

**A Short Review of Renewable Energy Generation: Sustainable Development, Successful Lessons from Leading Countries** ..... 403  
 V. L. Trinh, C. K. Chung, X. C. Nguyen, Q. T. Nguyen, and T. S. Nguyen

**Research Automotive Line Performance Increasing by Using Modular Assembly** ..... 411  
 Nguyen Thanh Quang

**Aerodynamic Characteristics of Multi-door Thrust Reverser Using Fan Flow in High Bypass-Ratio Turbofan Engine** ..... 419  
 Anh-Tuan Nguyen, Van-Hiep Nguyen, Van-Hoang Nguyen, Tuong-Linh Nha, Van-Thuc Tran, The-Mich Nguyen, Cong-Thanh Nguyen, Cong-Truong Dinh, and Xuan-Truong Le

**Study on Selecting the Appropriate Process Parameters When CNC Cylindrical Grinding Heat-Treated Alloy Steel** ..... 427  
Ngoc Tuyen Bui and Trong Nghia Hoang

**Analysis of Vehicle Structural Performance During Side Impact Using Computer Model** ..... 437  
Van Hieu Phan and Luu Phu Thuong Nguyen

**Investigation on TiAgN Thin Film Formation Employing Co-Sputtering Method Toward Applying for Medical Instruments** ..... 447  
Dinh Quang Nguyen, Luan Duc Nguyen, Viet Quoc Dang, and Cuong Duc Pham

**Estimating the Uncertainty of the Torque Standard Machine at Vietnam Metrology Institute** ..... 455  
Vu Van Duy, Pham Thanh Ha, Ta Thi Thuy Huong, and Vu Toan Thang

**Using of Composite Materials for the Rear Axle Housing** ..... 465  
Nguyen Thanh Quang, Nguyen Quang Thai, Pham Viet Thanh, and Le Dinh Manh

**FEM Simulation and Experimental Study on Improving the Forming Ability in Stamping SS400 Sheet Material with a Variable Blank Profile** ..... 475  
The-Thanh Luyen, Duc-Toan Nguyen, Van-Nam Nguyen, and Thi-Hoa Pham

**Researching the Effect of High-Velocity Oxygen Fuel Spraying Parameters on Porosity of WC-12Co Coating on Inner Cylinder** ..... 485  
Thanh-Phu Nguyen, Van-Chien Dinh, Van-Thoai Le, Khac-Khanh Bui, and Thanh-Hoa Doan

**Research on Effects of Welding Amperage, Velocity and Voltage on Tensile Strength of Joint Welding Metal on Narrow Gap Welding SAW** ..... 493  
Khac-Khanh Bui, Van-Thoai Le, Thanh-Phu Nguyen, and Van-Nhat Nguyen

**Study the Design Automation of Two-Plate Plastic Injection Molds** ..... 501  
Truong Duc Phuc and Pham Vu Hung

**Study Effects of Cutting Parameters on Surface Quality in High Speed Milling of CuZn40Pb1 Brass Alloy** ..... 513  
Truong Duc Phuc, Pham Hong Phuc, Nguyen Thanh Trung, Hoang Tien Dung, and Hoang Trung Kien

**A Study on Integrated Flexible Manufacturing Systems** ..... 527  
Vuong Gia Hai, Le Thi Lan, Do Thi Thu Thuy, Dinh Van Hien, and Hoang Van Quy

**Accuracy Evaluation of Slump and Slump-Flow Test for 3D Concrete Printing with the Kinect v1** ..... 535  
Van-Bien Bui, Thi-Loan Pham, Duc An Pham, and Thi Thu Thuy Do

**Comparative Analysis of Simulated and Experimental Results for SUS-304 Sheet Material in Incremental Sheet Metal Forming Process** ..... 545  
Nguyen Duc Toan and Hoang Trung Kien



# **Advanced Materials Towards Sustainability**

# Influences of Various Bracing on the Buckling Behavior of Steel Frames



Huy-Phuoc Nguyen and Phu-Cuong Nguyen

**Abstract** Bracing systems are effective secondary structures. They are used commonly to increase the stability of structures, especially steel structures. Many types of braces are used in steel structures such as diagonal bracing, portal bracing, inverted V-bracing, X-bracing, K-bracing, etc. They will make structures to obtain the various buckling behaviors. This paper makes clear the influences of various bracing on the buckling behavior of steel frames. Structures of bracing systems must be paid attention to in steel structural design because structural stability is the one of significant criteria. The authors used a commercial software package SAP2000 to simulate the buckling behavior of multi-story planar steel frames by various bracing parameters to clarify this problem. Results of this study will help structural engineers to understand more clearly these influences, therefore they can choose suitable bracing types for steel frames to ensure technical, economic, and aesthetic factors for practical design.

**Keywords** Bracing · Stability · Steel frames · Buckling factor · Buckling load

## 1 Introduction

Steel is one of the types of material that is used commonly in all types of structures because of its strength and ductility. Besides, its all members can be connected conveniently by welding or bolting and it is not very difficult to create various structural shapes as architectural requirements. Steel structures are used to construct very tall buildings because of their less weight, high strength, and easier constructability compared to reinforcement structures.

---

H.-P. Nguyen · P.-C. Nguyen (✉)

Advanced Structural Engineering Laboratory, Department of Structural Engineering, Faculty of Civil Engineering, Ho Chi Minh City Open University, Ho Chi Minh City, Vietnam  
e-mail: [cuong.pn@ou.edu.vn](mailto:cuong.pn@ou.edu.vn); [henycuong@gmail.com](mailto:henycuong@gmail.com)

Most members of steel structures usually have small sections. This reduces the stiffness and stability of steel structures. Therefore, stability is one of the major concerns in studies of steel structures. There are several studies about the actual behavior of steel structures [1–11]. With various geometrical, material, and connection nonlinearity models and different analysis methods under dynamic and static loads [1–5], these studies determined stress–strain relationships to likely predict the second-order inelastic behavior of planar, 3D steel frames that include the effects of lateral-torsional buckling [6], residual stresses and shear deformation [7], and geometry imperfections, and so on. Nguyen et al. [8] analyzed the nonlinear buckling behavior of steel frames under earthquakes. Tran et al. [9] investigated the nonlinear behavior of offshore wind turbines using the distributed plasticity method. Tran et al. [10, 11] examined the seismic behavior of electric devices in the nuclear power plant using seismic fragility analysis. Although these studies do not refer to the methods of stabilizing the steel frame, they clarified the instability problem in steel structures. From this, many methods can be carried out to stabilize steel structures. In this paper, the bracing system is one of them.

A bracing system is an efficient solution to this problem. It not only increases the stiffness and stability of steel structures but also reduces lateral displacements significantly [12].

Compared to knee-braced frames (KBFs) and eccentrically braced frames (EBFs), concentrically braced frames (CBFs) are the most popularly used because of their practical and economical advantages for normal structures [13]. Three popular brace configurations that are often used in actual construction are Diagonal, X, and V (or inverted V) bracing. These brace configurations belong to CBFs. In this study, the concerned problem is to influences of Diagonal, X, and Inverted V bracing on steel frames through buckling loads.

The value of load in service or an experimental loading test that makes a compressed element, member, or frame change suddenly shape and collapse is the buckling load [14]. To determine the buckling load, we have to find out the buckling factor. The formula used to calculate the buckling load is given as follows:

Buckling Load = Applied Load  $\times$  Buckling Factor [15].

SAP2000 [16] is used to execute the buckling analysis of planar steel frames without bracing and with various types of bracing systems to find out buckling factors and compare them to each other.

## 2 Investigated Configuration of Steel Frames

In this research, 16 planar steel frames were divided into 4 groups: 5 storeys, 10 storeys, 15 storeys and 20 storeys. They are simulated with various bracing. Their geometry, dimension, section, and loading are shown in Table 1. Structural steel frames are simulated in 2 cases: A. Steel frames without any bracing. B. Steel

frames with different types of braces. Steel frames considered for the examination are displayed in Figs. 1, 2, 3, and 4.

**Table 1** Geometry and loading of steel frames are simulated in this study

Parameter	Type/value
Number of storeys	5, 10, 15, 20—storey
Typical storey height	3.8 m
Number of bays	4
Bay width	5 m
Beam size	ISBM550
Column size	ISBM300
Brace size	ISBM100
Load	60 KN/m

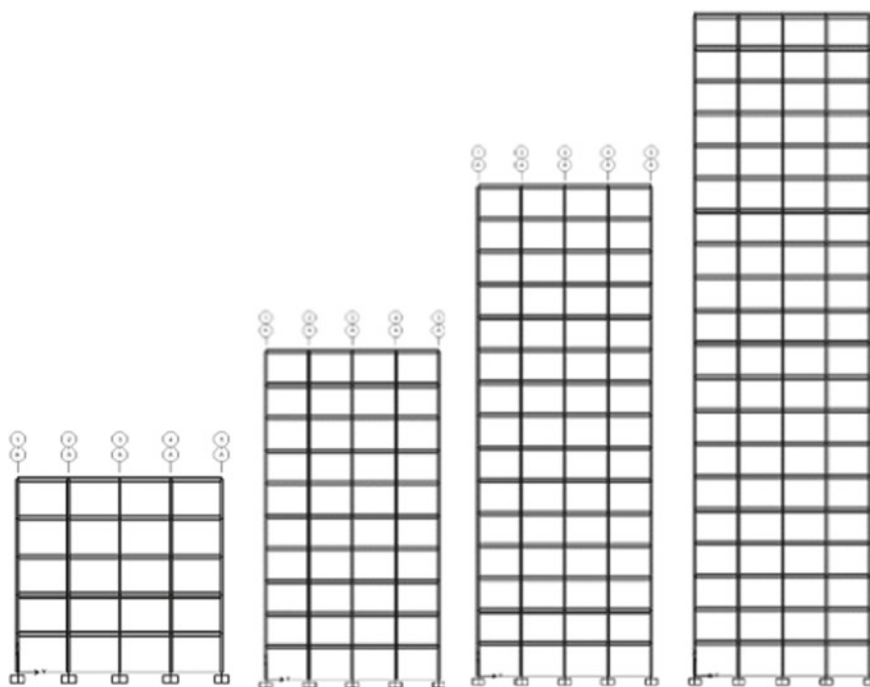


**Fig. 1** Steel frames without bracing

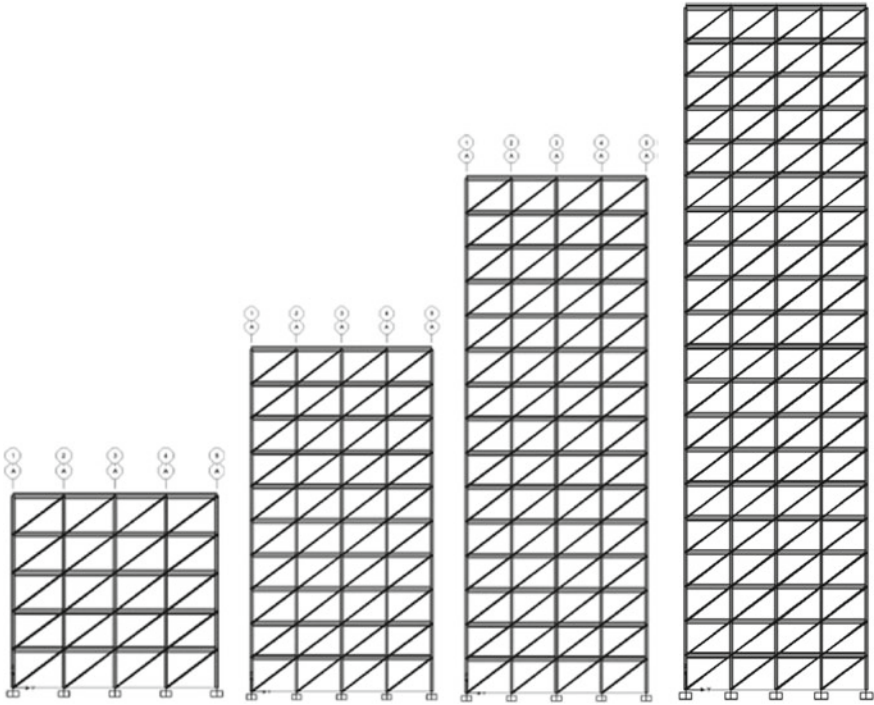


Fig. 2 Steel frames have been installed diagonal bracing

### 3 Results and Discussions

Table 2 displays the values of buckling factors that are obtained from analyses. The buckling factors increase from left to right in all cases of the number of storeys. The diagonal Bracing’s buckling factor is the minimum and the X- Bracing’s buckling factor is the maximum.

Table 3 displays the ratios between every buckling factor of the braced frame and bare frame. These ratios help us know how effective the bracing systems are. This explains why bracing systems have been used to increase stiffness and stability in steel structures widely.

Figure 5 displays the relationships between the number of storeys and buckling factors in cases without bracing and with every type of bracing as above, respectively. These relationships are nonlinear. The buckling factors increase significantly in braced steel frames compared to those without braced steel frames. In addition,

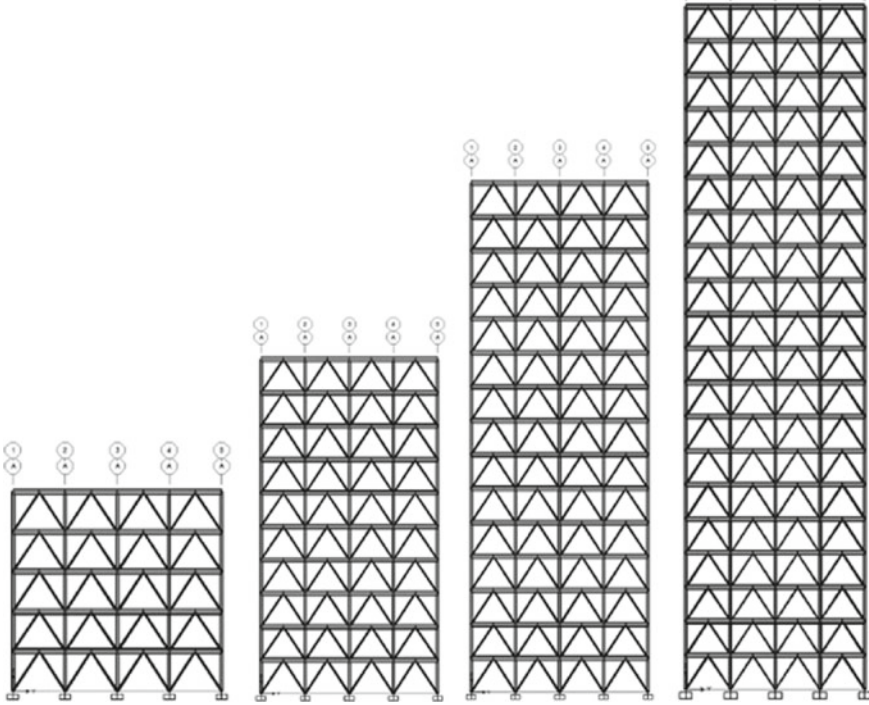


**Fig. 3** Steel frames have been installed inverted V-bracing

the difference of buckling factors among these three braces is not considerable in 20 storeys case, especially Inverted V-bracing and X-bracing. This is against 5 storeys case.

From these results, we can realize easily that the buckling factor decreases when the slenderness of steel frames increases and vice versa. The variation of buckling factors corresponding with the change of the slenderness in the case of X-bracing is the clearest. The difference between buckling factors of X-bracing and inverted V-bracing can be not significant as the slenderness of steel frames reaches some value or steel frames is higher than 15 storeys in this case.

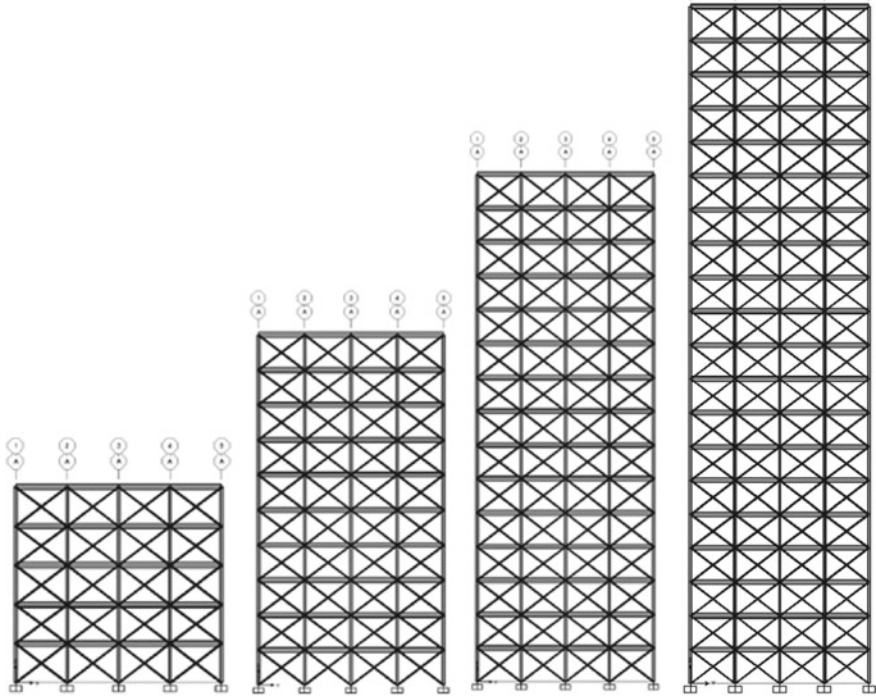


**Fig. 4** Steel frames have been installed X-bracing

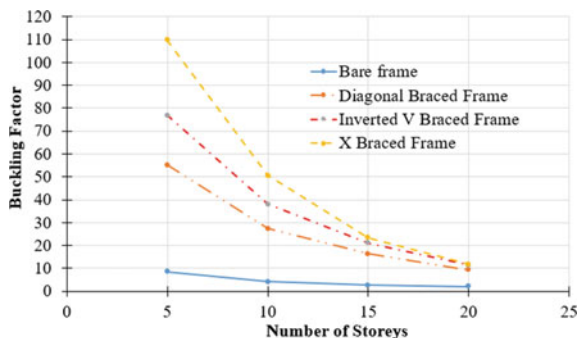
**Table 2** Values of buckling factors with various types of braces

No. storeys	Bare frame	Diagonal braced frame	Inverted V-braced frame	X-braced frame
5	8.63	55.24	76.83	109.69
10	4.23	27.43	38.01	50.69
15	2.77	16.34	21.08	23.36
20	2.04	9.40	11.34	11.85

**Table 3** The ratios between every buckling factor of the braced frame and bare frame

No. storeys	Bare frame	Diagonal braced frame	Inverted V-braced frame	X-braced frame
5	1	6.40	8.90	12.71
10	1	6.48	8.99	11.98
15	1	5.90	7.61	8.43
20	1	4.61	5.56	5.81

**Fig. 5** Variation of buckling factors with various types of bracing



## 4 Conclusion

The results of these analyses show that the increasing of buckling factor is significant after the installation of bracing systems when compared to steel frames without bracing. Amongst all number of storeys cases, the buckling factor gained in the X-bracing system is maximum when compared to diagonal and inverted V-bracing systems.

From this, we withdraw some conclusions as follows:

To strengthen steel structures, the bracing system is one of the efficient solutions.

The slenderness of steel frames plays a very important role in their stability.

Compared to the others, the X-bracing makes the buckling factor increase in the best superior way.

Moreover, the advantages of the bracing system in stabilizing steel structures are illustrated by numerical examples. It can be concluded that understanding the influence of bracing on the buckling behavior of steel structures and choosing suitable bracing types for steel structures are very necessary and significant for practical design engineers.

**Acknowledgements** This research is funded by the Ministry of Education and Training (MOET), Vietnam, under the grant number B2023–MBS–03.

## References

1. Nguyen P-C, Doan NTN, Ngo-Huu C, Kim S-E (2014) Nonlinear inelastic response history analysis of steel frame structures using plastic-zone method. *Thin-Walled Struct* 85:220–233
2. Nguyen P-C, Kim S-E (2014) Distributed plasticity approach for time-history analysis of steel frames including nonlinear connections. *J Constr Steel Res* 100:36–49
3. Nguyen P-C, Kim S-E (2015) Second-order spread-of-plasticity approach for nonlinear time-history analysis of space semi-rigid steel frames. *Finite Element Anal Des* 105:1–15
4. Nguyen P-C, Kim S-E (2016) Advanced analysis for planar steel frames with semi-rigid connections using plastic-zone method. *Steel Compos Struct* 21:1121–1144



5. Nguyen P-C, Kim S-E (2017) Investigating effects of various base restraints on the nonlinear inelastic static and seismic responses of steel frames. *Int J Non-Linear Mech* 89:151–167
6. Nguyen P-C, Kim S-E (2018) A new improved fiber plastic hinge method accounting for lateral-torsional buckling of 3D steel frames. *Thin-Walled Struct* 127:666–675
7. Nguyen P-C, Tran TD (2021) Impacts of residual stress and shear deformation on 2D steel frames using fiber plastic hinge element: nonlinear behavior and strength. *SN Appl Sci* 3. <https://doi.org/10.1007/s42452-021-04638-w>
8. Nguyen PC, Tran TT, Nghia-Nguyen T (2021) Nonlinear time-history earthquake analysis for steel frames. *Heliyon* 7:e068321
9. Tran T-T, Hussan M, Kim D, Nguyen P-C (2020) Distributed plasticity approach for the nonlinear structural assessment of offshore wind turbine. *Int J Naval Architect Ocean Eng* 12:743–754
10. Tran T-T, Nguyen P-C, So G, Kim D (2020) Seismic behavior of steel cabinets considering nonlinear connections and site-response effects. *Steel Compos Struct* 36:17–29
11. Tran T-T et al (2021) Probabilistic seismic demand model and seismic fragility analysis of NPP equipment subjected to high- and low-frequency earthquakes. *Nucl Sci Eng* 195:1327–1346
12. Zasiah T, Shovona K (2013) Structural behavior of steel building with concentric and eccentric bracing: a comparative study. *Int J Civil Struct Eng* 4. <https://doi.org/10.6088/ijcser.201304010002>
13. Yu X, Ji T, Zheng T (2015) Relationships between internal forces, bracing patterns and lateral stiffness of a simple frame. *Eng Struct* 89:147–161
14. Ziemian RD (2010) *Guide to stability design criteria for metal structures*. Wiley
15. Vidyasagar P, Kiran K (2017) Buckling analysis of multi-storey steel building with and without bracing under different soil conditions. *IOSR J Mech Civil Eng* 14:20–33
16. SAP2000 v22, *CSI Analysis Reference Manual*, Computer and Structures, Inc. Berkeley, California, USA

# Structural Optimization via 3D Printing Technology Using NPR Materials



Tran-Trung Nguyen, Phu-Cuong Nguyen, Thanh-Tuan Tran,  
and Nguyen Van Thuan

**Abstract** 3D printing technology is now the trendiest term in engineering in general and advanced structural design engineering in particular. Finding structures with optimum geometry and materials that fit the technologies above is difficult. This study presents an approach to creating a hybrid structure by combining Rhino Grasshopper and Karamba3D to replace the hybrid structure reinforced with hard particles presented in Ref. (Tee in *Jom* 72:1105–1117, 2020 [3]). The proposed hybrid structure is improved from the honeycomb structure by the Galapagos optimization algorithm, one of Rhino Grasshopper's optimization plugins. It considers the properties of materials with a Negative Poisson Ratio (NPR). These material properties were established based on the formulas presented in Sect. 3 using the Karamba3D parametric design tool. The tensile stress–strain curve demonstrates the optimal hybrid structure efficiency compared with the sample without the reinforcement and the two samples with the reinforced hard grain with different printing orientations in 3D printing technology. This demonstration was established using ABAQUS finite element software with the Arruda-Boyce material model for polymer materials.

**Keywords** 3D printing · Negative Poisson ratio materials · Galapagos algorithm · Karamba3d · Rhino grasshopper · Structural optimization

---

T.-T. Nguyen

Department of Architectural Engineering, Faculty of Architecture, Van Lang University, Ho Chi Minh City, Vietnam

P.-C. Nguyen (✉) · T.-T. Tran · N. Van Thuan

Advanced Structural Engineering Laboratory, Department of Structural Engineering, Faculty of Civil Engineering, Ho Chi Minh City Open University, Ho Chi Minh City, Vietnam

e-mail: [cuong.pn@ou.edu.vn](mailto:cuong.pn@ou.edu.vn); [henycuong@gmail.com](mailto:henycuong@gmail.com)

N. Van Thuan

Department of Transportation Engineering, Nha Trang University, Nha Trang, Vietnam

## 1 Introduction

Additive manufacturing (AM), often known as 3D printing, enables lighter, stronger components and systems in industrial production. Communications, photography, architecture, and engineering have undergone digital revolutions. AM improves digital flexibility and efficiency in industrial operations.

AM adds material to an item. Creating an item by hand sometimes requires milling, machining, carving, sculpting, or other material removal methods.

Polymer-based composites are one of the most widely used and robust materials in 3D printing technology that Bekas et al. [1] have done with an overview of this material. The material determines 3D printing. Homogenization and local function multi-functionality is required for these materials. However, everyday objects have complicated forms and materials. Therefore, Toursangsaraki [2] demonstrated that developing a structure with various materials is efficient when subjected to loads with a significant weight reduction. The combination also alters AM manufacturing from multi-stage to single-process.

Furthermore, the work of Tee et al. [3] is interesting in using polymer-based composites. The rigid-rubbery polymeric material was used in PolyJet tensile testing. These tensile samples have two parts: VeroMagentaV polymer for rigidity and Agilus30 polymer for flexibility. His study examined these materials' mechanical characteristics and interactions utilizing 3D-printed composite stiff reinforcement particles.

Negative Poisson Ratio (NPR) is another Poisson ratio-related material property. Material and structure have this characteristic. The study by Lakes [4] demonstrated an overview of the advantages of materials and structures with NPR. NPR structures like honeycombs, diamond crystals, and Voronoi have parallels with nature. The characteristics of these structures are sustainability, considered in the field of engineering in general and the construction industry in particular, presented in the awe-inspiring study of Nazir et al. [5].

ABAQUS simulated a tensile test in this investigation. Based on the research [3]; the sample is made of two materials: rigid VeroMagentaV polymer and flexible Agilus30 polymer with a honeycomb structure. We optimize the honeycomb structure using NPR materials using Rhino Grasshopper's Galapagos algorithm plugin. Through stress-strain relationship curves, the post-optimized structure has better tensile strength than the study's constructions [3].

## 2 Effective Combination of Powerful Tools Rhino Grasshopper

Rhino precedes Grasshopper. This software's 3D rendering is unmatched. Rhino's Render image processing technologies help create clean, vibrant results. Rhino software is used by major companies for industrial design, pattern design, reliefs,

footwear design, jewellery design, mechanical engineering (ships, cars, etc.), and more. McNeel also improves RhinoBIM solutions.

Rhino's Add-ons, like other major solutions, include Grasshopper. It provides a "clear history" of the model and improves rendering in 3DMax and Maya. Rhino created "Clear History" to tackle user difficulties in the model creation process, allowing updated modeling to backtrack. Grasshopper explains this.

Optimized add-ons, notably Galapagos, are Grasshopper's best feature. Rutten [6] created the first Rhino Grasshopper optimization algorithm [6]. Rhino plugins like LadyBug and HoneyBee for form blending, Pufferfish for multi-objective optimization, and Octopus for energy design are popular. Structural engineering analysis mentions Karamba3D.

### 3 Structural Optimization Process

As stated in the Introduction, this work builds on interesting concepts from studies [3] and [5], particularly [3]. The HoneyComb structure was used to optimize structural optimization with the Poisson ratio as a parameter. Pham et al. [7] and [8] examined the efficiency of this honeycomb construction. Auxetic honeycomb sandwich plates and nanoplates were studied for free vibration.

As illustrated in Fig. 1, this optimization approach only considers the flexible region of the tensile sample studied [3].

The structure's material is this study's biggest optimization issue. The Karamba3D plugin's settings changed the issue of the material's Negative Poisson Ratio. These parameters are calculated from the proposed formulas of Kováčik [9].

Poisson's ratio has been re-calculated to develop a new correlation between Poisson's ratio and the porosity in materials Eq. (1), showing the relationship among  $\nu$ ,  $E$ , and  $G$ .

$$\nu = \frac{E}{2G} - 1 \quad (1)$$

where  $E$  and  $G$  are defined based on the percolation model.  $E$  and  $G$  parameters have to consider the effect of porosity on parameters  $p$  and  $p_c$  according to Eqs. (2) and (3).

$$E = E_o \left( \frac{p_c - p}{p_c} \right)^{f_E} \quad \text{for } p \leq p_c \quad (2)$$

$$G = G_o \left( \frac{p_c - p}{p_c} \right)^{f_G} \quad \text{for } p \leq p_c \quad (3)$$

where  $E_o$  and  $G_o$  are respectively Young's modulus and shear modulus of the solid material,  $p_c$  is the percolation threshold with Young modulus and shear modulus

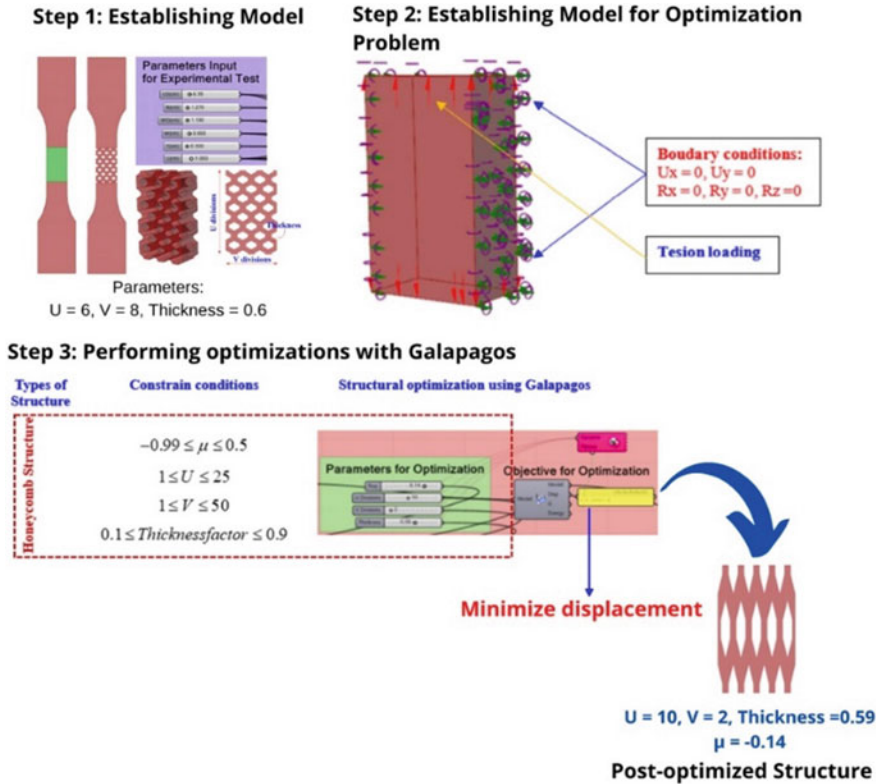


Fig. 1 Structural optimization process

being fixed at zeros,  $f_E$  and  $f_G$  are the characteristic exponents for the elastic and shear modulus of the porous material, respectively.

From Eqs. (1), (2), and (3), Poisson’s ratio can be calculated as follows:

$$v = \frac{E_o}{2G_o} \left( \frac{p_c - p}{p_c} \right)^{f_E - f_G} - 1 \text{ with } p \leq p_c \tag{4}$$

It can be noted that in Eq. (4),  $\frac{E_o}{2G_o}$  is equal to  $v_o + 1$ , and Poisson’s ratio can be rewritten as:

$$v = (v_o + 1) \left( \frac{p_c - p}{p_c} \right)^{f_v} - 1 \text{ with } p - p_c \leq 0 \tag{5}$$

Where  $f_v = f_E - f_G$ . Equation (5) provides a new percolation model for Poisson’s ratio. The porosity of porous material depends on homogeneous and isotropic characteristics.

Step 3 of Fig. 1 illustrates this paper's optimization challenge. This graphic shows how to use Galapagos. The slider's features enable it to constrain optimization difficulties. Minimize displacement ( $d$ ) is the objective function. Tension load ( $F$ ) causes this displacement:

$$\text{Min}(d) \text{ where } d \text{ is defined by } d = \sum_{i=1}^j D_i \quad (6)$$

where  $D_i$  is the displacement at the  $i$ th element. Moreover,  $j$  is the total number of structural elements. The displacement is given by:

$$D = \frac{F}{K'} \quad (7)$$

where  $F$  is the tension load, and  $K'$  is the bending stiffness of the structure calculated in Karamba3D.

## 4 Verification with FEM

The structure must be validated. We may use third-party technologies to verify the optimized design. This numerical verification analyzes using ABAQUS. Pre- and post-processing includes analysis.

Pre-processing builds models. This study imports a Rhino model into ABAQUS. Import \*.igs or \*.iges formatted models.

The next stage is defining the material, a vital portion of the simulation. The material Hybrid VMVmA30p is mentioned in the Introduction section [3]. It comprises a flexible polymer, Agilus30 (A30), and a rigid polymer, VeroMagentaV (VMV). Equation (8) Arruda et al. [10] shows that the Arruda-Boyce model explains the A30 material, which is ideal for hyperelastic materials.

$$\begin{aligned} U = \mu \left\{ \frac{1}{2} (\bar{I}_1 - 3) + \frac{1}{20\lambda_m^2} (\bar{I}_1^2 - 9) + \frac{11}{1050\lambda_m^4} (\bar{I}_1^3 - 27) \right. \\ \left. + \frac{19}{7000\lambda_m^6} (\bar{I}_1^4 - 81) + \frac{519}{673750\lambda_m^8} (\bar{I}_1^5 - 243) \right\} \\ + \frac{1}{D} \left( \frac{J_{el}^2 - 1}{2} - \ln J_{el} \right) \quad (8) \end{aligned}$$

The initial shear modulus ( $\mu$ ) and the locking stretch ( $\lambda_m$ ) are the model coefficients added in ABAQUS. Typical values of  $\mu$  and  $\lambda_m$  are presented in Fig. 2a from the study in [3]. The VMV material has an elastic-plastic mechanical characteristic. The elastic modulus ( $E_s$ ) and yield strength ( $f_y$ ) are the essential parameters, and

**Fig. 2** The following material properties and conditions have been given to modeling: **a** Material properties, **b** Interaction conditions, **c** Boundary conditions, and **d** Tension loading

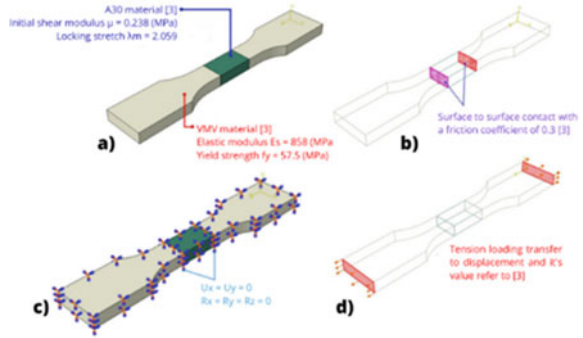
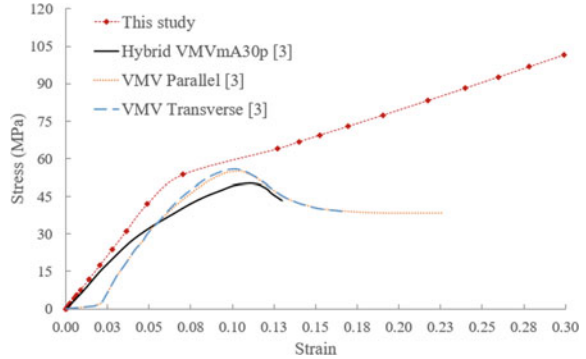


**Fig. 3** The stress–strain curves obtained from the research [3] and the current work



their values are taken from the work in [3], as shown in Fig. 2a. The boundary and contact criteria are imposed in the next phase. It is necessary to define the interaction between the contact surfaces. The requirements are depicted in Fig. 2b, c. As illustrated in Fig. 3d, the hybrid construction is solely exposed to tension stress. The research [3] refers to typical load values. The elements utilized in the model for the end parts of the specimen are 8-node cubic C3D8R elements. The honeycomb structures were created by using C3D8H elements in the middle part. The stress–strain curves are obtained from the analytical findings in the post-processing stage. The following section contains a summary of all findings.

## 5 Results and Discussion

In Fig. 3, stress–strain curves of the optimized structure are compared to those of the Hybrid VMVmA30p specimen test, which was subjected to similar tensile loading [3]. The red dashed-line curve shows the optimized structure’s significant influence in the middle part. The Arruda-Boyce model’s flexible polymer material describes hybrid architectures’ behavior.

## 6 Conclusion

This research shows how Rhino Grasshopper and Karamba3D can build stronger hybrid structures. Karamba3D contains a subroutine for negative Poisson's ratio porous materials. Better mechanical properties than the Honeycomb structure. Finite element analysis characterizes advanced constructions' stress-strain curves. The Arruda-Boyce model makes advanced structures behave like hyperelastic materials.

This study's behavior curves motivate polymer model development and further analysis and creation of novel hybrid structures with parameters. This simplifies structural characteristic data collection. Machine learning is one optimization model in data sciences.

**Acknowledgements** The authors gratefully acknowledge the financial support from the Scientific Research Fund of Van Lang University, Vietnam.

## References

1. Bekas DG et al (2019) 3D printing to enable multifunctionality in polymer-based composites: a review. *Compos B Eng* 179:107–540
2. Toursangsaraki M (2018) A review of multi-material and composite parts production by modified additive manufacturing methods. arXiv preprint [arXiv:1808.01861](https://arxiv.org/abs/1808.01861)
3. Tee YL et al (2020) PolyJet 3D printing of composite materials: experimental and modelling approach. *Jom* 72(3):1105–1117
4. Lakes RS (2017) Negative-Poisson's-ratio materials: auxetic solids. *Annu Rev Mater Res* 47:63–81
5. Nazir A et al (2019) A state-of-the-art review on types, design, optimization, and additive manufacturing of cellular structures. *Int J Adv Manuf Technol* 104(9):3489–3510
6. Rutten D (2013) Galapagos: on the logic and limitations of generic solvers. *Archit Des* 83(2):132–135
7. Pham Q-H et al (2021) Free vibration analysis of nanoplates with auxetic honeycomb core using a new third-order finite element method and nonlocal elasticity theory. *Eng Comput* 1–19
8. Pham Q-H et al (2022) Free vibration response of auxetic honeycomb sandwich plates using an improved higher-order ES-MITC3 element and artificial neural network. *Thin-Walled Struct* 175:109203
9. Kováčik J (2006) Correlation between Poisson's ratio and porosity in porous materials. *J Mater Sci* 41(4):1247–1249
10. Arruda EM et al (1993) A three-dimensional constitutive model for the large stretch behavior of rubber elastic materials. *J Mech Phys Solids* 41(2):389–412



# Improving the Accuracy of ACI 318-08 Design Standard for Predicting Strength of CFST Columns Using Machine Learning



Tran-Trung Nguyen and Phu-Cuong Nguyen

**Abstract** This study proposes a new modified ACI 318-08 formula based on machine learning (ML) to forecast better the compressive strength of Concrete-Filled Steel Tube (CFST) columns. The prediction ML model is established from 663 experimental samples. CFST columns' ultimate compressive strength results show differences when comparing experiments with the current calculation formulas using the Linear Regression algorithm to modify the original ACI 318-08 formula by determining the regression coefficient or slope coefficient and the required intercept value. The prediction model with the updated ACI 318-08 formula yields a more reliable CFST column ultimate compressive strength.

**Keywords** ACI 318-08 · CFST columns · Linear regression · Machine learning · Ultimate compressive strength · Structural design

## 1 Introduction

The finest Civil Engineering structures are circular Concrete-Filled Steel Tube (CFST) columns. Steel sheets, W-section steel, or tubes may support a steel–concrete composite structure. Concrete-filled or concrete-coated steel structures are linked to work.

Several studies have examined CFST columns' advanced behavior. ACI 318-08 [1] is the most frequent country-specific standard for CFST column strength. Recently,

---

T.-T. Nguyen · P.-C. Nguyen (✉)

Advanced Structural Engineering Laboratory, Department of Structural Engineering, Faculty of Civil Engineering, Ho Chi Minh City Open University, Ho Chi Minh City, Vietnam  
e-mail: [cuong.pn@ou.edu.vn](mailto:cuong.pn@ou.edu.vn); [henycuong@gmail.com](mailto:henycuong@gmail.com)

T.-T. Nguyen

Department of Architectural Engineering, Faculty of Architecture, Van Lang University, Ho Chi Minh City, Vietnam

numerous research employing ABAQUS simulation analysis software presented improved equations to compute compressed circular CFST columns, such as Nguyen et al. [2], Pham et al. [3–6] found that regular and high-strength concrete affects CFST column axial compression. Nguyen and Pham’s FEM-ABAQUS nonlinear behavior study of CFST columns yields reliable findings. Nguyen et al. [7] showed finite element software’s power in parameter characteristics utilizing Ansys DesignXplorer, an integrated Ansys Workbench program. In Nguyen et al. [8] study, parametric design is used to build steel sections with strength and beauty. Industry and offshore use circular CFST columns. Tran et al. [9] analyzed an offshore wind turbine using plasticity. Kim et al. [10] built a concrete-filled double-skin steel tube column using two concentric steel pipes of various diameters (CFDST). Concrete grades and diameter/thickness ratios were evaluated. Concrete double-layer steel tube (CFDST) columns function better with an adequate inner steel tube profile ratio. Nguyen et al. [11] employed a unique fiber plastic hinge technique to examine how residual load and shear deformation affect the nonlinear inelastic behavior of 2D steel frames. These approaches are accurate and numerically stable. However, they can only be utilized for one data; hence the planned formula modification has not been done yet. Lack of coverage factor (big data fields) leads to high accuracy. With such obstacles, modern approaches have been studied. Thai [12] reviews machine learning. Jayalekshmi et al. [13] and Zarringol et al. [14] found this useful for time factor data issues with multiple mathematical models. Le et al. [15] employed several machine-learning methods to predict the CFST column’s axial compressive load capability.

This research shows that linear regression can predict CFST circular column strength. ACI 318-08 formula increases the axial compressive strength of 663 circular CFST column experimental samples. [2]. The model shows a substantial disparity between observed axial compressive strength and ACI 318-08’s formula. The loop and intercept coefficients are needed to modify the original formula ACI 318-08 to produce more reliable results for CFST columns’ ultimate compressive strength.

## 2 ACI 318-08 Standard

The following formula determines the strength of axial compression of CFST according to the ACI 318-08 standard [1]:

$$N = 0.85A_c f_{co}' + A_s f_y^s + A_{tube} f_y^{tube} \quad (1)$$

where  $A_c$ ,  $A_s$ , and  $A_{tube}$  are the cross-sectional areas of concrete, reinforced steel, and steel tube, respectively;  $f_{co}'$  is the cylindrical compressive concrete strength;  $f_y^s$  is the reinforced steel yielding stress; and  $f_y^{tube}$  is the steel tube yielding stress.

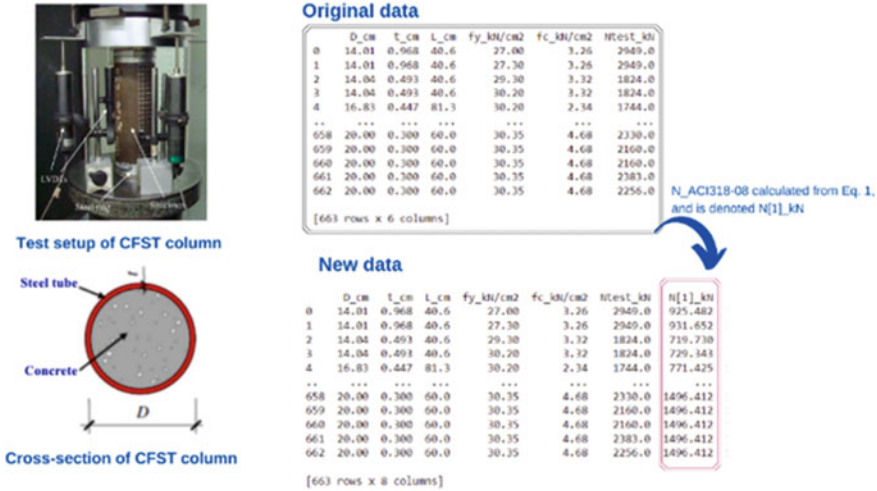


Fig. 1 Test setup of CFST columns (Su et al. [16]) and data reconstruction

### 3 Establish a Prediction Model

#### 3.1 Create and Review Data

The input data is the geometrical dimensions and material strength of 663 samples [2] a. CFST column compressive strength is output. Figure 1 shows a new dataset with one column of axial compressive strength obtained from Eq. (1).

The new data label in Fig. 1 shows the difference in the CFST column axial compressive strength. This research must also address this. This dataset has no noise components when summarizing the data and checking for missing data.

Next, we created prediction models using the cross-sectional geometric dimensions, concrete and steel tube strengths, and CFST columns’ axial compression capacity.

#### 3.2 Prediction Model

Section 3.1 prepares the prediction model. Cross-sectional shape and steel and concrete tube strength are inputs. The experiments and formula ACI 318-08 [1] (Ntest and N[1]) provide the CFST columns’ axial compressive strength values.

The prediction model is unchanged. The original dataset is split into 20% testing and 80% training. Figure 2 shows the axial compression strength of 663 samples after analysis from the study of Nguyen et al. [17].

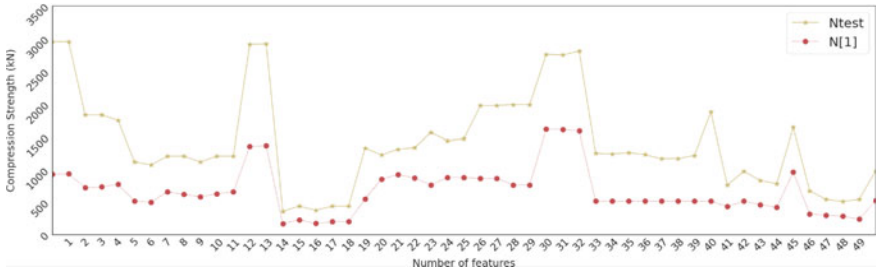


**Fig. 2** Compare the value of axial compressive strength  $N$  (kN) of CFST Columns as determined by actual test ( $N_{test}$ ) and standard ACI 318-08 [1] ( $N[1]$ )

**Fig. 3** Procedure using a linear regression model to calibrate formulas to determine the axial compressive strength of 663 CFST column samples [5]

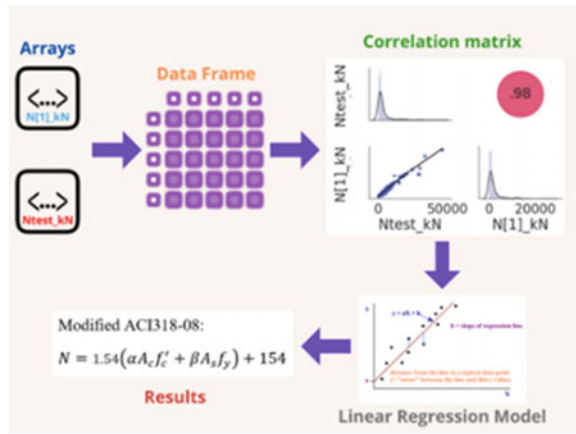
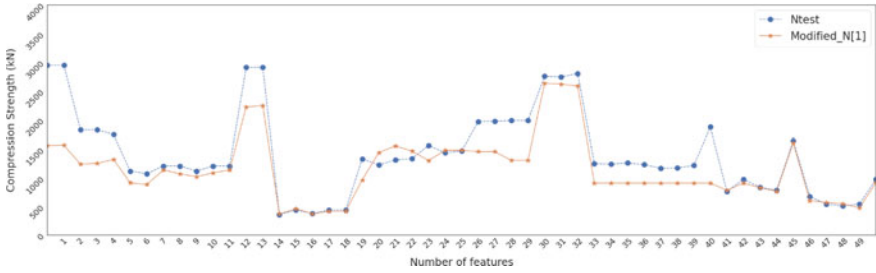


Figure 2 shows a considerable discrepancy, requiring model change.  $N[1]$  is the ultimate strength predicted by ACI 318-08 [1] using input parameters, and  $N_{test}$  is the compression strength from testing. Figure 3 illustrates calibration.

Figure 3 depicts the new ACI 318-08 formula technique. The linear regression error is high when predicting the experimental findings for CFST column ultimate strength ( $N_{test}$  kN) and Eq. (1) ( $N[1]$  kN). Thus, the correlation matrix with a coefficient of 0.98 indicates that  $N_{test}$  kN and  $N[1]$  kN must be considered together. Linear regression is used to create the new ACI 318-08 formula  $N$ , displayed in Fig. 3 and Eq. (2). Slope multiplies  $N[1]$  kN. The intercept coefficient is applied to minimize  $N[1]$  kN and  $N_{test}$  kN error.



**Fig. 4** Correcting CFST columns’ axial compressive strength using ACI 318-08 [1] fitting with experimental data

### 4 Results and Discussions

This effort shows again that machine learning can solve engineering problems by utilizing massive volumes of data. It helps [1] estimates match experimental data. Equation (1) becomes Eq. (2). The CFST column axial compression strength curve in Fig. 4 is closer to the Ntest curve than the previous one in Fig. 2.

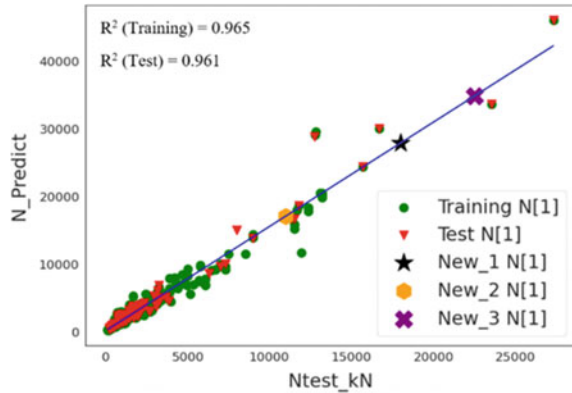
The new formula based on ACI 318-08 [1] is proposed as follows:

$$N = 1.54(\alpha A_c f_c' + \beta A_s f_y) + 154 \tag{2}$$

Some experimental specimens show contradictory projected outcomes. Unprocessed data may cause this issue. We utilize all experimental data without prejudice to demonstrate machine learning algorithms’ capability. This study’s simplistic Linear Regression technique may reduce prediction accuracy.

The modified ACI 318-08 formula [Eq. (2)] is obtained by using the Linear Regression method to 663 circular CFST columns’ ultimate strength based on the previous formula and experimental testing. Figure 5 shows that the anticipated (0.965) and observed (0.961) axial compressive strength models have virtually relative standard deviation R2. The circular CFST column ultimate compressive strength prediction model is trustworthy since the standard deviation R2 for training and test data is more significant than 95%. In real structural engineering, we require dependable and accurate experimental data sets to use Machine Learning algorithms to enhance the accuracy and dependability of existing design standard formulae.

**Fig. 5** The circular CFST columns' compressive strength



## 5 Conclusion

We use circular CFST columns to demonstrate that, using massive data, machine learning (ML) can anticipate structural behavior. Machine learning verifies the present formula ACI 318-08. A natural raw dataset of 663 circular CFST columns predicts their eventual strength. CFST columns' ultimate compressive strength is inaccurately calculated using the ACI 318-08 formula. The Linear Regression technique readily innovates the ACI 318-08 formula, producing Eq. (2) with more excellent reliability [1]. Accurate prediction requires reliable specimen testing. Random Forest Regression, Support Vector Regression, K-nearest Neighbor Regression, and Artificial Neural Network may solve this prediction problem.

**Acknowledgements** The authors gratefully acknowledge the financial support from the Scientific Research Fund of Van Lang University, Vietnam. This research is also funded by the Ministry of Education and Training (MOET), Vietnam, under the grant number B2023-MBS-03.

## References

1. ACI 318-08: Building code requirements for structural concrete: ACI Farmington Hills, MI, USA (2014)
2. Nguyen P-C, Pham D, Tran T, Nghia-Nguyen T (2021) Modified numerical modeling of axially loaded concrete-filled steel circular-tube columns. *Eng Technol Appl Sci Res* 11(3):7094–7099
3. Pham D-D, Nguyen P-C, Nguyen D-L, Le H-A (2020) Simulation of concrete-filled steel box columns. In: *ICSCEA 2019*, Springer, pp 359–366
4. Pham D-D, Nguyen P-C (2020) Finite element modelling for axially loaded concrete-filled steel circular tubes. In: *CIGOS 2019, innovation for sustainable infrastructure*. Springer, pp 75–80
5. Behavior analysis and design of concrete-filled steel circular-tube short columns subjected to axial compression. *arXiv preprint arXiv:2107.06488* (2021)

6. Pham D, Nguyen P, Le H (2019) Normal and high strength concrete-filled steel box columns under axial compression. In: Proceedings of the 17th international symposium on tubular structures, ISTS2019
7. Nguyen T-T, Nguyen P-C, Tran VT, Pham DD, Benabou L (2021) Reliability analysis of concrete-filled steel tube columns under axial compression. In: AIP conference proceedings. AIP Publishing LLC
8. Nguyen T-T, Nguyen P-C, Nguyen HTP (2023) Golden ratio application in the optimization of cold-formed steel sections. In: ICSCEA 2021. Springer, pp 837–845
9. Tran T-T, Hussan M, Kim D, Nguyen P-C (2020) Distributed plasticity approach for the nonlinear structural assessment of offshore wind turbine. *Int J Naval Archit Ocean Eng* 12:743–754
10. Kim S-E, Papazafeiropoulos G, Truong V-H, Nguyen P-C, Kong Z, Duong N-T, Pham V-T, Vu Q-V (2021) Finite element simulation of normal-strength CFST members with shear connectors under bending loading. *Eng Struct* 238:112011
11. Nguyen P-C, Tran T (2021) Impacts of residual stress and shear deformation on 2D steel frames using fiber plastic hinge element: nonlinear behavior and strength. *SN Appl Sci* 3(7):1–22
12. Thai H-T (2022) Machine learning for structural engineering: a state-of-the-art review. *Structures* 38:448–491
13. Jayalekshmi S, Jegadesh J, Goel A (2018) Empirical approach for determining axial strength of circular concrete filled steel tubular columns. *J Inst Eng (India): Series A* 99(2):257–268
14. Zarringol M, Thai H-T, Thai S, Patel V (2020) Application of ANN to the design of CFST columns. *Structures* 28:2203–2220
15. Le T-T, Asteris PG, Lemonis ME (2021) Prediction of axial load capacity of rectangular concrete-filled steel tube columns using machine learning techniques. *Eng Comput* 1–34
16. Su M, Cai Y, Chen X, Young B (2020) Behaviour of concrete-filled cold-formed high strength steel circular stub columns. *Thin-Walled Struct* 157:107078
17. Nguyen T-T, Nguyen P-C (2023) K-fold cross-validation technique for predicting ultimate compressive strength of circular CFST columns, ICSCEA 2021. Springer, pp 867–874

# The Recognition Accuracy in the SSD Model



Van-Nam Nguyen

**Abstract** The Single Shot Multibox Detector (SSD) technique is currently among the fastest and most accurate detection algorithms available. However, the majority of research on the accuracy of this approach has focused on noiseless objects. Thus, this study evaluates the algorithm's accuracy with both noisy and noiseless objects. To that goal, the algorithm is trained to recognize ten different flower species. Experiments are then carried out on photographs in four different scenarios: the item is totally lighted, 1/3 of the object is darkened, 1/2 of the object is darkened, and the object is fully darkened. The performance of the algorithm is then evaluated using SPSS 20.0 software and the analysis of variance (ANOVA) and least significant difference (LSD). The experimental results reveal that the algorithm accuracy is strongly dependent on the noise level. The detection accuracy is 100%, 81.3%, 44.7%, and 62%, respectively, when the item is fully lighted, 1/3, 1/2 size of the object is darkened, and the object is fully darkened.

**Keywords** Artificial intelligence · Computer vision · Deep learning · Identifying the object · Image processing

## 1 Introduction

Many scientists have been interested in the implementation of Deep Learning models in practice in recent years, particularly the Single Shot MultiBox Detector (SSD) model [1, 2]. SSD is a well-known algorithm for dealing with issues including large data processing, input noise management, and online processing. In addition, the Faster region-based convolutional neural networks (Faster R-CNN) model is also one of the best models available today [3, 4].

---

V.-N. Nguyen (✉)

The University of Danang—University of Technology and Education, Da Nang, Vietnam  
e-mail: [nvnam@ute.udn.vn](mailto:nvnam@ute.udn.vn)



**Table 1** Data collection and labeling for flowers [7]

System	VOC2007 test mAP	FPS (Titan X)	Number of Boxes	Input Resolution
Faster R-CNN (VGG16)	73.2	7	~6000	~1000 × 600
SSD300* (VGG16)	77.2	46	8732	300 × 300
YOLO (customized)	63.4	45	98	448 × 448
SSD512*(VGG16)	79.8	19	24,564	512 × 512

SSD is intended for real-time object detection [5, 6]. Faster R-CNN creates boundary boxes using a region proposal network and then uses those boxes to classify objects [3]. While it is called cutting-edge inaccurate, the entire process runs at 7 frames per second, which is much below what real-time processing requires. By eliminating the requirement for the region proposal network, SSD speeds up the procedure. SSD uses a few innovations, such as multi-scale features and default boxes [2], to compensate for the decline in accuracy. These enhancements allow SSD to match the accuracy of the Faster R-CNN utilizing lower quality pictures, increasing the speed even further. Table 1 shows that it reaches real-time processing speed and even outperforms the accuracy of the Faster R-CNN [7].

SSD does not employ a delegated region proposal network. Instead, it boils down to a really simple operation. Both the location and class scores are calculated using small convolution filters. SSD predicts using three convolution filters for each cell after extracting the feature maps. These filters produce the same results as traditional CNN filters.

Recognition accuracy is an essential factor of the model when applied in practice. When the input is noisy (noise: the image is in a dark environment, it's raining or the image is partially obscured...), how does it affect the identification process? In this study, the influence of input noise on the accuracy of recognition will be shown.

## 2 Research Deployment

It is critical to create a data collection in order to train learning models. Because it has an impact on the trained model's output. The data for training learning models include 10 different flower species that were collected from internet sources.

**Table 2** Data collection and labeling for flowers

No.	Name	Total number	Number train	Number test	Label name
1	Apr <sup>1</sup>	50	40	10	Apricot blossom
2	Chr <sup>2</sup>	50	40	10	Chrysanthemum
3	Ger <sup>3</sup>	50	40	10	Gerbera
4	Hyd <sup>4</sup>	50	40	10	Hydrangeas
5	Lil <sup>5</sup>	50	40	10	Lily
6	Lot <sup>6</sup>	50	40	10	Lotus
7	Nar <sup>7</sup>	50	40	10	Narcissus
8	Por <sup>8</sup>	50	40	10	Porcelain flower
9	Ros <sup>9</sup>	50	40	10	Rose
10	Sun <sup>10</sup>	50	40	10	Sun flower
Sum		500	400	100	10 (flowers)

## 2.1 Data Collection and Flower Labeling

A total of 500 photos of objects were gathered for the training of geometric models [8]. The objects (flowers) are labeled and divided into two data sets: one data model was trained to account for 80% of the total item recorded, while the test data set was trained to account for 20%. Data sets for teaching and testing are chosen at random.

The LabelImg software is used to label the objects during the picture preprocessing stage. Table 2 details the number of photos of each object that was gathered and tagged.

## 2.2 Operating Model Environment

Experimental author on PC Intel: CPU core i7 9700F, Memory (RAM) 32 GB, Hard Drive (SSD) 128 GB, Graphics card (VGA) 1050TI.

## 2.3 Model of Training for Learning

SSD architecture based on VGG with 256 output channels,  $3 \times 3$  kernel,  $2 \times 2$  stride, and pad  $1 \times 1$  (Fig. 1).

The author model's training was halted during the training phase due to a tensorboard graph and a histogram of loss over time. As demonstrated in Fig. 2, the loss in training ranges from 0 to 1.5 in step 12,000. As a result, after the model has been trained to this step limit, learning can be stopped. At step 18,000, the author

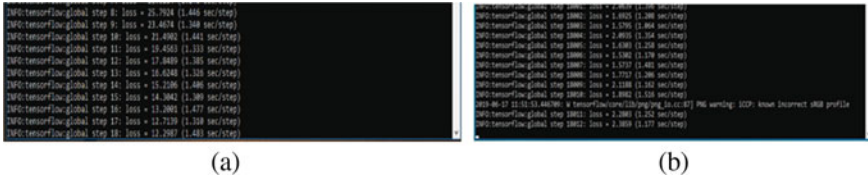
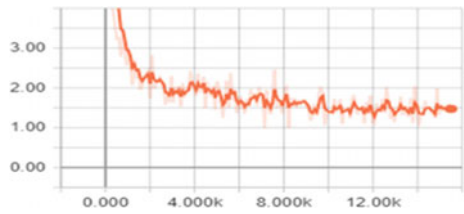


**Fig. 1** **a** The procedure for beginning model data training; **b** the procedure of terminating model data training

**Fig. 2** Loss chart over time of the model



finished training the model and received a value of 1.5, which reflects the training loss (Fig. 1b). One step takes an average of 1.300 s to train.

### 2.4 The Real Model Operation

With 15 samples (pictures) for each flower and an identification process for four distinct environmental variables, the author created a real-life identification model for recognizing 10 species of flowers. The photos were acquired from a Google video source and were inspired by reality. A total of 600 (images) were collected for the identification model [9]. The findings of the author’s photo identification have been preserved in reference [10].

### 2.5 The Performance of the Algorithm

The performance of the recognition process is based on the number of correctly recognized sample images divided by the total number of recognized model sample images.

$$A(\%) = \frac{S}{TS} 100;$$

where:A: Accuracy of the algorithm;

**Table 3** The findings of item identification are fully lightened

		These are the flowers that the model identified										
		Apr	Chr	Ger	Hyd	Lil	Lot	Nar	Por	Ros	Sun	Total
Identification results	Wrong identification	0	0	0	0	0	0	0	0	0	0	0
	Correct identification	15	15	15	15	15	15	15	15	15	15	<b>150</b>
	No identification	0	0	0	0	0	0	0	0	0	0	0
	Total	15	15	15	15	15	15	15	15	15	15	<b>150</b>
	Accuracy (%)	100	100	100	100	100	100	100	100	100	100	100

S: Number of the correctly identified sample images;  
 TS: Total number of the identified model sample images.

### 3 Actual Model Performance

Identification result conventions: A verified input sample produces the correct identification result; the effect of poor identification with the validated input sample produces a false identification result. An unidentified result is one that does not identify any species or recognizes more than one species.

#### 3.1 The Results of Identification with the Object Is Fully Lightened

Table 3 illustrates the outcomes of model recognition when the image is not shaded. Table 3 shows a total of 150 input control samples in the red box, and the number of samples defined by the model in the blue box. The findings revealed that all samples were correctly recognized. In this scenario, the model accurately recognizes and the accuracy rate is 100%.

#### 3.2 The Results of Identification with the 1/3 Size of the Object is Darkened

Similarly, Table 4 shows that the model recognized 122 objects out of 150 input samples, resulting in an identification rate of 81.3%. There were four objects in

**Table 4** The results of identification with the 1/3 size of the object is darkened

		These are the flowers that the model identified										
		Apr	Chr	Ger	Hyd	Lil	Lot	Nar	Por	Ros	Sun	Total
Identification results	Wrong identification		1				2		6			6
	Correct identification	11	12	15	15	9	11	11	8	15	15	<b>122</b>
	No identification	4	2			6	2	4	1			22
	Total	15	15	15	15	15	15	15	15	15	15	<b>150</b>
	Accuracy (%)	73.3	80	100	100	60	73.3	73.3	53.3	100	100	81.3

this scenario that had a 100% identification rate. The model correctly recognized 3 samples, 1 sample was not detected, and 6 samples were incorrectly identified. Porcelain flowers had the lowest recognition rate, with a ratio of 53.3%. There are 22 unidentified objects and 6 false positives in this environment.

### 3.3 *The Results of Identification with the 1/2 Size of the Object is Darkened*

Table 5 shows that we have 150 objects, with the model identifying 67 of them. The identification rate for this scenario is 44.7%, and no object has a 100% identification rate. With an accuracy score of 86.7%, the rose specie has the best identification accuracy, while the apricot blossoms specie has the worst with a rate of 20%. Using 15 objects samples as input The model detected three samples, whereas ten samples were not identified and two samples were incorrectly identified. There were 51 correctly recognized objects in total, with 7 incorrectly identified objects. Moreover, half of the model objects were not detected when the object was occluded 1/2.

### 3.4 *The Results of Identification with the Object is Fully Darkened*

Table 6 reveals that a total of 93 objects samples were accurately recognized. With 15 input samples, the model correctly identified one sample, four samples were incorrectly identified (Lily: three samples; Apricot Blossom: one sample), and ten samples were not identified. There were 28 unidentified samples and four incorrectly recognized samples in the case of the objects in the dark.

**Table 5** The results of identification with the 1/2 size of the object is darkened

		These are the flowers that the model identified													
		Apr	Chr	Ger	Hyd	Lil	Lot	Nar	Por	Ros	Sun	Total			
Identification results	Wrong identification	2	2	4	0		2				1	11			
	Correct identification	3	9	9	6	4	9	4	5	13	5	<b>67</b>			
	No identification	10	4	2	9	11	4	11	10	2	9	72			
	Total	15	15	15	15	15	15	15	15	15	15	15	<b>150</b>		
	Accuracy (%)	20	60	60	40	26.7	60	26.7	33.3	86.7	33.3	44.7			

**Table 6** The results of identification with the object is fully darkened

		These are the flowers that the model identified											Total
		Apr	Chr	Ger	Hyd	Lil	Lot	Nar	Por	Ros	Sun	Total	
Identification results	Correct identification	15	15	8	11	7	5	8	1	8	15	<b>93</b>	
	Wrong identification			6		1		1	10			18	
	No identification			1	4	7	10	6	4	7		39	
	Total	15	15	15	15	15	15	15	15	15	15	<b>150</b>	
	Accuracy (%)	100	100	53.3	73.3	46.7	33.3	53.3	6.7	53.3	100	62	

**Table 7** The effect of the shade on the model recognition

	State of the object				Level of significance (P)	LSD <sub>0,05</sub>
	Object fully lightened	1/3 object is darkened	1/2 object is darkened	Object fully darkened		
A (%)	100.0 ± 0.0 <sup>a</sup>	81.3 ± 17.7 <sup>a</sup>	44.7 ± 21.1 <sup>b</sup>	62.0 ± 31.3 <sup>b</sup>	0.000	18.9

*Note* Values followed by the same letter are not significantly different based on LSD Test with  $\alpha = 5\%$

### 3.5 Comparison of the Effect of the Shade on the Model Recognition

To test whether the noise affects the model recognition, we compared the accuracy of the model recognition corresponding to different part shades.

The results showed that the accuracy of the model recognition when the object is fully lightened, 1/3 size of the object is darkened, then 1/2 size of the object is darkened and the object is fully darkened is 100.0 (%), 81.3(%), 44.7(%) and 62.0 (%), respectively (Table 7). The results of the analysis of variance (ANOVA) illustrated a significant difference ( $p < 0.05$ ) in the accuracy of the model recognition from different part shades. The accuracy of the model recognition was significantly higher in the case of the object being fully lightened and 1/3 size of the object being darkened than in the case of 1/3 of the size of the object being darkened and the object being fully darkened ( $p < 0.05$ , Least Significant Difference Test). However, there were no significant differences were found between the object being fully lightened and 1/3 size of the object being darkened ( $p > 0.05$ , Least Significant Difference Test). A similar tendency was detected also for 1/2 size of the object is darkened and the object is fully darkened ( $p < 0.05$ , Least Significant Difference Test).

## 4 Conclusions

In this paper, we have proposed an experimental method for the SSD model to detect objects in normal states and noisy states. The algorithm has been shown to be able to detect objects under poor conditions, such as changes in illumination, 1/3, 1/2 size of the object is darkened. The results showed that the detection accuracy decreases when the subject is placed under poorer conditions. The proposed algorithm achieves modern detection accuracy of 100.0% and 62.0%, the object is fully lightened and the object is fully darkened, respectively. The accuracy rate of the model is also reduced in the case of 1/3 and 1/2 of the objects being obscured, to 81.3% and 44.7%, respectively. This research result will certainly bring offer much value to the application of the SSD model in practice. In our future works, we will aim to



improve the recognition accuracy of the model when the object is placed under poor conditions.

## References

1. Liu W et al (2016) SSD: single shot multibox detector. *Lect Notes Comput Sci (including Subser Lect Notes Artif Intell Lect Notes Bioinformatics)* 9905:21–37
2. Shuai Q, Wu X (2020) Object detection system based on SSD algorithm. *Proc 2020 Int Conf Cult Sci Technol ICCST 2020*, 141–144
3. Abbas SM, Singh SN (2018) Region-based object detection and classification using faster R-CNN. *Int Conf Computational Intell Commun Technol CICT 2018*, pp 1–6
4. Liu B, Zhao W, Sun Q (2017) Study of object detection based on Faster R-CNN. *Proc 2017 Chinese Autom Congr CAC 2017*, 6233–6236
5. Kanimozhi S, Gayathri G, Mala T (2019) Multiple real-time object identification using single shot multi-box detection. *ICCIDS 2019—2nd Int Conf Comput Intell Data Sci Proc*, pp 1–5
6. Kang HJ (2019) Real-time object detection on  $640 \times 480$  image with VGG16+SSD. *Proc 2019 Int Conf Field-Programmable Technol ICFPT 2019*, 419–422
7. Hui J (2018) SSD object detection: single shot multibox detector for real-time processing [Online]. Available: <https://jonathan-hui.medium.com/ssd-object-detection-single-shot-multibox-detector-for-real-time-processing-9bd8deac0e06>
8. Drive G (2022) Training image for learning model [Online]. Available: <https://drive.google.com/file/d/1FRzMiQQsOQ9uHsJSDkxCRCELoHuPFp-d/view?usp=sharing>
9. Drive G (2022) Image included into identification [Online]. Available: [https://drive.google.com/file/d/1ugIOpvn9G9ad-aNn0rjLio\\_FFT7ELNI5/view?usp=sharing](https://drive.google.com/file/d/1ugIOpvn9G9ad-aNn0rjLio_FFT7ELNI5/view?usp=sharing)
10. Drive G (2022) Image is identified by the model [Online]. Available: <https://drive.google.com/file/d/1cz58OjMJSp8MwcZjObODEzCc20l0jdsG/view?usp=sharing>

# Research and Fabrication of Metal Powder Dispersing Equipment for 3D Printing Technology



Doan Van Phuc, Vu Van Quang, and Vu Toan Thang

**Abstract** Liquid alloy dispersion is considered to be the most popular manufacturing technology of 3D printing metal powder fabrication technology nowadays. This paper presents some research results, design and fabrication of 3D printing metal powder dispersing equipment based on liquid alloy dispersion technology using centrifugal atomization and an inert gas at high pressure. The survey results have determined a set of geometrical parameters and basic specifications for the metal powder dispersing equipment; accordingly, metal powder has been successfully manufactured with the properties that meet the requirements for 3D printing metal technology.

**Keywords** Metal powder · 3D printing powder · Liquid alloy dispersion · Dispersion chamber · Gas nozzle

## 1 Introduction

The development of science and technology frequently leads to more stringent input materials requirements. A prominent example of this is metal 3D printing based on Selective Laser Sintering (SLS). Currently, a significant obstacle to the widespread implementation of the technology in production is the very high cost of metal powders—the input materials for 3D printing, due to having to meet very strict requirements for particle size, morphological structure and chemical composition

---

D. Van Phuc

Military Institute of Science and Technology of Vietnam, Hanoi 10000, Vietnam

V. Van Quang (✉) · V. T. Thang (✉)

Hanoi University of Science and Technology, Hai Ba Trung District, No. 1 Dai Co Viet Street, Hanoi 10000, Vietnam

e-mail: [quang.vuvan1@hust.edu.vn](mailto:quang.vuvan1@hust.edu.vn)

V. T. Thang

e-mail: [thang.vutoan@hust.edu.vn](mailto:thang.vutoan@hust.edu.vn)

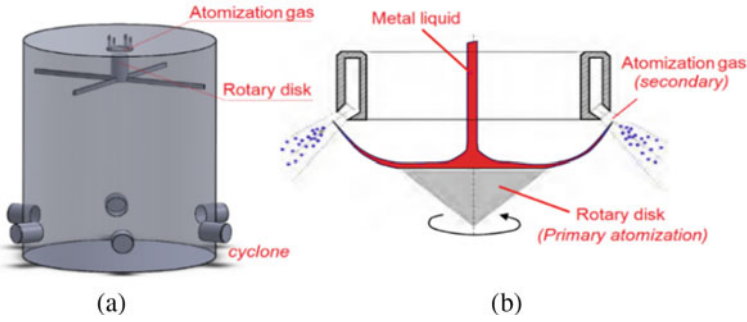


**Fig. 1** Diagram of the hybrid atomizer by centrifugal and inert gas: **a** diagram of the device; **b** centrifugal and high-pressure gas injector

[1, 2]. The solution to this problem is none other than mastering the fabrication technology of metal 3D printing powder.

Today, several well-known methods for fabricating metal powders can be listed as mechanical grinding, ore reduction, electrolysis, an electric explosion of wires, liquid alloy dispersion via centrifugation (centrifugal atomization), liquid alloy dispersion by high-pressure gas/liquid flow (pneumatic atomization), or combination of the mentioned methods. Among them, over 90% of metal powders for 3D printing purposes are fabricated based on the last two methods [1, 3]. In this study, the method of fabrication of metal powder using a combination of centrifugation and high-pressure gas will be taken into consideration. It is the most universal and synthetic metal powder fabrication method that is able to achieve powders of various materials, including those with high viscosity, low surface tension or low density, such as aluminum alloy [4]. The working principle of the method is illustrated in Fig. 1 [4].

The essence of this method is to use a centrifugal rotating disc to create primary atomization for the liquid metal in order to increase their specific surface energy. The liquid metal stream at the end of the primary atomization will move due to its inertia to the area where the atomized gas velocity has a large value  $W_{min}$  (which is temporarily called the minimum required velocity) and is further atomized by high-pressure gas streams (secondary dispersion).

Although molten alloy atomization technology has been used in metal powder production since the 60s of the last century, the study of the movement and dispersion of metal streams at high temperatures is still a challenge today. The urgency of the problem is evidenced by a large number of patents as well as scientific publications related to metal powder dispersion equipment and processes. At the same time, the relationship between the geometrical parameters of the fabrication equipment, the technological process parameters and the properties of the powdered material still has not been fully studied. The objective of the research is to design and fabricate equipment for metal powder dispersion using a combination of centrifugal and high-pressure gas, oriented for application in SLS 3D printing technology. Thus, the research objects are listed as bellow: Dynamic process and dispersion process of

AlSi<sub>10</sub>Mg liquid alloy under the effect of centrifugal force and high-pressure gas flow; Fabrication of AlSi<sub>10</sub>Mg metal powder.

## 2 Numerical Simulation Study

### 2.1 Determine the Minimum Required Velocity of the Atomized Gas

A prerequisite for the formation of liquid metal droplets of diameter  $d_k$  is that the kinetic energy of the dispersed gas stream must be greater than the viscous force and surface tension of the liquid metal [1, 5].

$$\frac{\rho_G \cdot W^2}{2} \geq \frac{We \cdot \sigma_m}{2c_f \cdot d_K} \quad (1)$$

where:  $W$ —dispersion gas velocity at the vicinity of the liquid alloy droplet surface, m/s;  $\rho_{Ar}$ —density of dispersed gas Ar. In the dispersion condition, the density of Ar gas has an average value of  $\rho_{Ar} = 1,85 \text{ kg/m}^3$ ;  $We$ —Weber coefficient;  $\sigma_m$ —the surface tension of the liquid alloy (for aluminum alloys at temperatures from 850 to 900 °C,  $\sigma_m = 520 \cdot 10^{-3} \text{ N/m}$  [6]);  $d_k$ —diameter of liquid metal droplet formed;  $c_f$ —front aerodynamic drag coefficient;  $c_f = 1$  [1, 5]. Due to inequality (1), the minimum velocity of the dispersed gas flow to obtain a drop of liquid metal of diameter  $d_k$  can be determined:

$$W_{\min} = \sqrt{\frac{We \cdot \sigma_m}{\rho_G \cdot d_K}} \quad (2)$$

The minimum gas velocity required to obtain a liquid metal droplet of diameter  $d_k = 50 \text{ }\mu\text{m}$  is  $W_{\min}^{50} = 300 \text{ m/s}$ .

### 2.2 Determine the Necessary Gas Pressure $p_{PT}$ for the Atomized Gas Velocity to Reach the Required Minimum Value $W_{\min}^{50}$

The simulation was performed on a representative nozzle (Fig. 2). The simulation results are shown in Fig. 3. Conduct a survey on the particle size distribution of the metal powder group with the above spherical shape. It can be seen that the particle size distribution of AlSi<sub>10</sub>Mg metal powder follows Gauss's law, has the particle size is very concentrated with the average size (*Median size*)  $d_{50} = 31.11 \text{ }\mu\text{m}$ . Based on

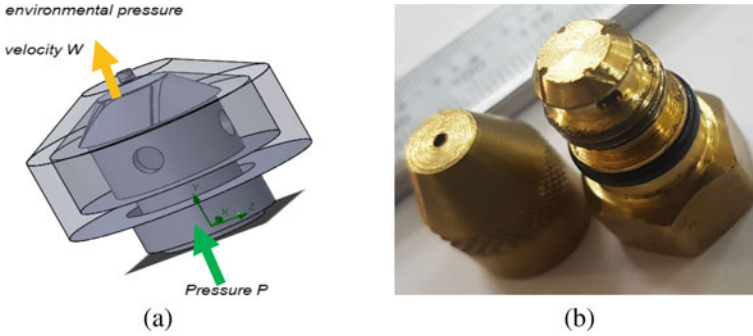


Fig. 2 Distributed gas nozzle model with loading conditions (a) and actual nozzle pictures (b)

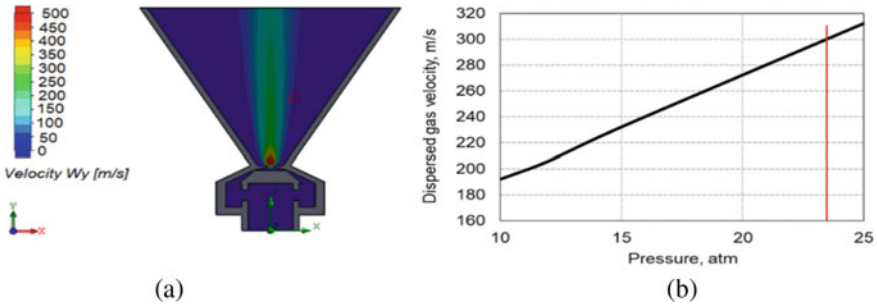


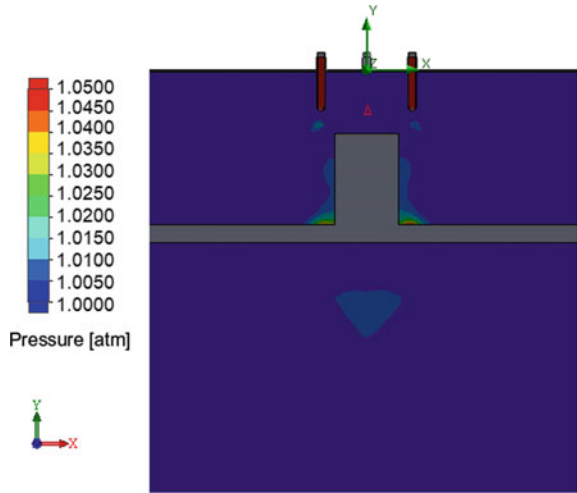
Fig. 3 Velocity field (a) and graph depicting the dependence of the dispersed gas velocity on pressure (b)

the graph describing the dependence of the dispersed gas velocity on the pressure in Fig. 3b, it is possible to determine the necessary gas pressure for the gas velocity at the injector  $W_{min}^{50} = 300 \text{ m/s}$  to be  $p_{PT} = 24 \text{ atm}$ .

### 2.3 Distribution of Residual Pressure in the Dispersion Chamber

The residual pressure is investigated with different ratios of inlet gas cross-sections  $S_{inlet}$  and  $S_{outlet}$  gas cross-sections. The Distribution of residual pressure in the dispersion chamber is shown in Fig. 4. The result also shows that with the inlet gas pressure  $p_{inlet} = 24 \text{ atm}$ , the outlet pressure  $p_{outlet} = 1 \text{ atm}$ , the residual gas pressure in the dispersion chamber reaches the smallest value when the ratio  $S_{outlet} / S_{inlet} \geq 76$ .

**Fig. 4** Residual pressure distribution in the dispersion chamber with the ratio of inlet and outlet gas cross-sections  $S_{outlet} / S_{inlet} = 76$

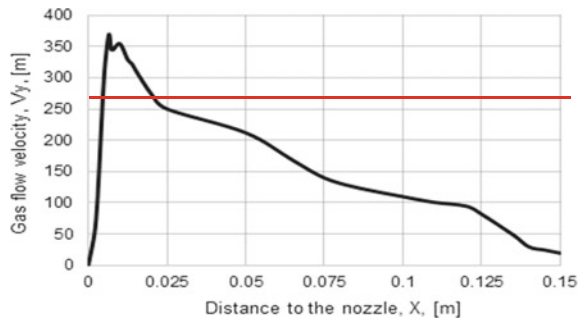


**2.4 Determine the Area Where Atomized Gas Flow with Maximum Kinetic Energy, Giving the Best Atomization Effect**

Based on the graph describing the change of gas flow velocity when exiting the nozzle, shown in Fig. 5, the best atomization effect, it can be seen that the gas flow has the maximum velocity at the position from 1,0 to 1.5 cm to the nozzle.

Based on the distribution of dispersed gas velocity, for the best dispersion effect it can be determined that at a distance of 1.5 cm from the nozzle outlet, the region of space where the dispersed gas velocity has a value above 300 m/s is in the circular sector with the radius 1.5 cm and the chord about 1.8 cm.

**Fig. 5** Change of gas flow velocity along the nozzle axis



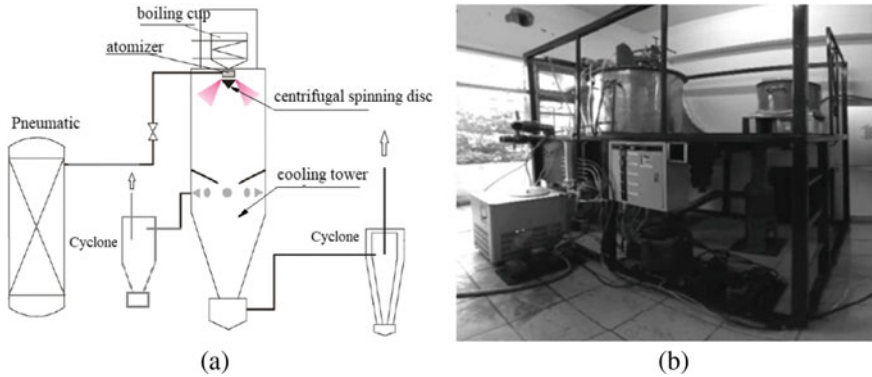


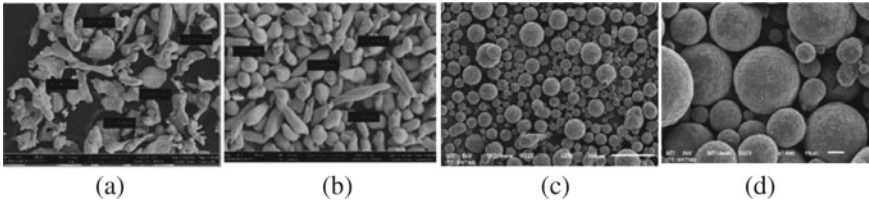
**Fig. 6** Technological scheme (a) and actual picture of metal powder fabrication equipment using a combination of centrifugal and compressed gas (b)

### 3 Experiment of Fabricating Metal Powder

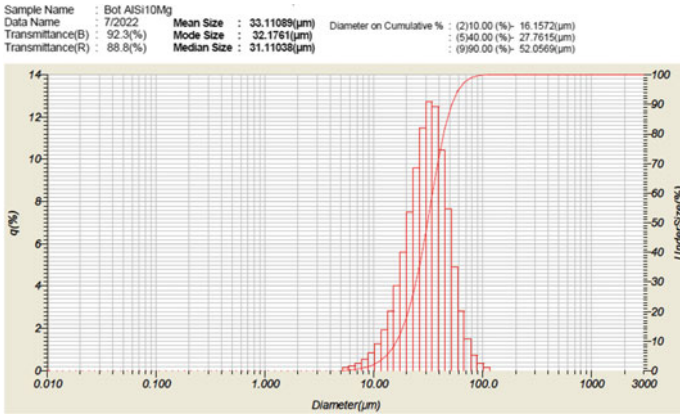
Based on the numerical simulation results, the optimal set of parameters for metal powder fabrication equipment has been determined. Those parameters will be used in order to construct the metal powder dispersion device. The production process of AlSi10Mg aluminum powder is carried out on equipment with the following main settings: AlSi10Mg aluminum alloy is completely melted at 900 °C in the period of about 20 min; speed of the motor (attached to the centrifugal disc) is set at about 10 000 rpm; the valves at the outlet of the cyclones are opened while increasing the flow of inert gas into the dispersion chamber; the inert gas flow rate is about 60 m<sup>3</sup>/hr. Under the action of gravity, the liquid metal flows along the conduit down to the dispersion chamber. Liquid metal flows with a velocity of about 30 kg/hour (Fig. 6).

Figure 7 shows the SEM images of metal powder fabricated by the research team with different particle sizes. The imaging results of obtained metal powder SEM show that the powder group with a size of less than 63 μm has a standard spherical shape (Fig. 7c). The content of metal powder in this group accounts for about 8% of the total volume of fabricated metal powder. Those metal particles with a double sphere shape (Fig. 7b) and rod-shaped (Fig. 7a) will be separated and used as smelting materials for subsequent dispersions.

The survey results are presented in the graph in Fig. 8. It can be seen that the particle size distribution of AlSi<sub>10</sub>Mg metal powder follows Gauss's law, has the particle size is very concentrated with the average size (*Median size*)  $d_{50} = 31.11 \mu\text{m}$ .



**Fig. 7** SEM image of fabricated AlSi10Mg metal powder with different particle sizes: **a**  $d_K > 125 \mu\text{m}$ ; **b**  $63 \mu\text{m} < d_K \leq 125 \mu\text{m}$ ; **c**  $d_K \leq 63 \mu\text{m}$  ( $\times 250$ ); **d**  $d_K \leq 63 \mu\text{m}$  ( $\times 1000$ )



**Fig. 8** Grain size distribution of AlSi<sub>10</sub>Mg metal powder produced by the project team

## 4 Conclusion

In this work, an atomizer using a combination of inert gas and centrifugation has been studied and fabricated. By calculations based on similarity theory and dynamic simulation, the minimum gas velocity to obtain a metal powder with average particle size  $d_{50} = 50 \mu\text{m}$  has been determined  $W_{\min}^{50} = 300 \text{ m/s}$ ; The required dispersive gas pressure is  $p_{PT} = 24 \text{ atm}$ . The simulation results also investigated the residual pressure distribution in the dispersion chamber with different geometrical parameters and, at the same time, determined the area of dispersed gas flow with maximum kinetic energy for good atomization efficiency. On the basis of those calculations and simulation results, an atomizer has been designed and fabricated. The results of experimental production of AlSi<sub>10</sub>Mg aluminum powder on the device gave a good performance, and the fabricated AlSi<sub>10</sub>Mg aluminum powder has a spherical morphological structure with a relatively smooth surface and high concentration of particles with size average particle size  $d_{50} = 31.11 \mu\text{m}$ .

**Acknowledgments** All individuals agree to acknowledge.



**Funding** This research was funded by Military Institute of Science and Technology of Vietnam with the project code 152/2021.

**Institutional Review Board Statement:** Not applicable.

**Informed Consent Statement:** Not applicable.

**Data Availability Statement:** Not applicable.

**Conflicts of Interest:** The authors declare no conflict of interest.

## References

1. Oglesneva SA, Smetkin AA, Mitin VI, Kalinin KV (2017) Influence of melt atomization parameters on technological characteristics of 12Kh18N10T powder. *Mech Eng, Mat Sci* 19b(4):122–138. 10.155-93/2224-9877/2017.4.09
2. Sentyurina A (2016) Fabricating spherical powders from alloys based on nickel aluminide NiAl for additive technologies. Dissertation for the degree of candidate of technical sciences
3. Czisch C, Lohner H, Fritsching U, Bauckhage K, Edlinger A. In: Bauckhage K, Fritsching U, Ziesenis J, Uhlenwinkel A, Leatham A (Eds.) *Proc Spray Deposition and Melt Atomization Conference SDMA 2003*. University of Bremen, Bremen, June 22–25
4. Fritsching U, Uhlenwinke V (2012) Hybrid gas atomization for powder production. *Powder Metall.* <https://doi.org/10.5772/35807>
5. Nechiporenko OS (1980) *Atomized metal powders*, Nechiporenko OS, Naida YI, Medvedovsky AB. Science. Dumka, Kyiv, 240
6. Nizhenko VI, Floka LI (1981) *Surface tension of liquid metals and alloys (one- and two-component systems): Handbook*. Metallurgy, .208

# Cutting Methods in the Single Point Diamond Turning and Surface Roughness of the Ultra-Precision Products—A Brief Review



Pham Van Tuan, Duong Xuan Bien, Pham Quoc Hoang, Do Tien Lap, and Le Thanh Binh

**Abstract** The single point diamond turning (SPDT) method is an ultra-precise machining (UPM) method and holds the unique position in the field of material removal mechanical machining such as turning, milling, drilling, and more. The surface quality produced by the SPDT method is typically characterized by a surface shape tolerance of a micrometer fraction and a nanometer scale surface roughness (RS). Achieving such fine surfaces requires good assessment and control of factors affecting surface quality ultra-precision (UP) products. This paper focuses on surveying the influence of cutting methods (CM) in the SPDT on surface quality in general and surface roughness in particular. The main CM mentioned include Slow Tool Servo (STS) and Fast Tool Servo (FTS). The related research results in the SPDT method and some comments are presented in order to contribute to improving the products surface quality in the SPDT method.

**Keywords** Diamond turning machining · Cutting methods · Slow tool servo · Fast tool servo

## 1 Introduction

Precision and UPM has developed rapidly thanks to the advent and continuous development of CNC machines, high-speed machining, the controllers with nanoscale precision and accompanying auxiliary systems. The UPM technology is also supported based on advances in techniques and measuring equipment for the inspection and products quality evaluation with the accuracy that seems “unattainable” [1]. The SPDT method was researched and developed quite early in the US, UK, Japan,

---

P. Van Tuan · D. X. Bien (✉) · P. Q. Hoang · D. T. Lap · L. T. Binh  
Le Quy Don Technical University, Hanoi, Vietnam  
e-mail: [duongxuanbien@lqdtu.edu.vn](mailto:duongxuanbien@lqdtu.edu.vn)

**Table 1** Studies related to SR in the SPDT and UPM method

Related contents	Publications
Machine tools, kinematics and dynamics machine and CM	[1, 5]
<b>STS method</b>	[1, 5, 8–10, 16–18, 23]
<b>FTS method</b>	[1, 5, 7, 12–15, 23–25]
Fly cutting, Raster Milling	[5, 6]
Cutting parameters, toolpaths, and CM	[1, 10, 19, 22]
Workpiece materials, tool materials, vibration and CM	[1, 5]

China [2] from the 1980s onwards. The comparison between different the UPM methods with the SPDT through the criterion of the SR and material removal rate is described in detail in [3]. Some of the UPM methods with diamond cutting tools can be mentioned as the SPDT, Raster Milling (RT), Fly Cutting (FC), Ultra-precision grinding (UPG), Ultra-Precision Polishing (UPP) [4–6]. Among them, the SPDT method has emerged as a perfect and comprehensive super-precision machining method. This method is used to machine the UP products for applications in key fields such as the aerospace, defense industry and biomedical field [1, 8]. Some typical papers relating to CM and SR in the SPDT are briefly listed in Table 1.

This paper focuses on surveying the recent research about the influence of FTS and STS cutting methods in the SPDT on surface quality, especially surface roughness.

## 2 Effect of Cutting Methods on the Surface Roughness

Synchronizing the motion of axes for machining asymmetrical surfaces can be accomplished by the main methods of the STS or Slow Slide Servo (SSS) and the FTS method [1, 7]. The STS method is determined based on the synchronization of the spindle rotation and Z-axis linear motion available on the SPDT machine. The STS method is often applied to machining free surfaces with high slopes or large deflections [10, 11]. The FTS method is defined based on the addition of an extra reciprocating motion on top existing linear motion of the SPDT machine. The sampling and interpolation strategies of each CM have a great influence on the surface quality of the products [1].

### Influence of the STS and FTS methods on SR

An overview of the FTS method for machining optically free surfaces is presented in [7]. Some challenges when applying FTS are also pointed out. The FTS method applied with large size range surface is also reviewed and presented in [12]. The displacement of the cutting tool reaches 2 mm. The surface roughness of the product reaches 20-30 nm in Ra units. The FTS method was applied in [13] for machining

non-coaxial symmetric surfaces. The research results show that, if the FTS drive system has high rigidity and small mass, it can achieve vibration frequencies higher than 2 kHz. The off-axis parabolic faces were machined by FTS method in study [14] with 1 mm motion range, 50 Hz minimum bandwidth and 25 nm resolution. The machined surfaces are used to fabricate the Keck telescope. A design of a SPDT machine using rotational FTS method to fabricate ophthalmic surfaces is described in [15]. The nanoscale microstructures introduced in [8] with the application of the STS cutting method allow to create many new applications in the fields of telecommunications, security monitoring equipment and display systems with high definition. STS technology is also applied in [9] to fabricate glass arrays for use in microscopes and other optical devices. The off-axis conic-shaped aspherical surface described in [16] was also studied and fabricated by the STS method. The freeform surface prism array for 3D microscopy studied and fabricated using STS technology is also presented in [17]. The workpiece material is aluminum alloy. Yi in [18] describes the problem of designing and manufacturing optical glass arrays based on STS size  $5 \times 5$ .

### **Influence of the toolpaths and control algorithms in STS and FTS on SR**

An overview study of different types of toolpaths in UPM in general and SPDT in particular is presented in detail in [19]. The linear interpolation problem for toolpaths is difficult to generate surfaces with nanometer level of accuracy and roughness [20]. The newly proposed spline interpolation method in [21] can satisfy the perfect coordination of motion between axes in FTS and STS cutting method. The general spiral toolpath proposed in [18, 22] for machining freeform surfaces using the FTS method shows higher efficiency and surface quality than with traditional toolpaths. The toolpath compensation technique in the STS method is described in [10].

Regarding control in SPDT machining, the sliding mode control algorithm is applied to the FTS toolpath in [23]. The movement frequency resonance between the FTS drive, the spindle and the heat dissipation are the main problems that need to be solved. The work [24] studies on FTS control method with extremely low feed rate in UPM. An adaptive controller developed to control the trajectory of the CT in FTS machining during free optical surface fabrication was developed in [25]. Similarly, the adaptive control system in [26] is also developed to further improve the accuracy and SR for freeform optical surfaces.

## **3 Conclusions**

In SPDT method, in addition to applying conventional CM such as traditional lathe machining to fabricate spherical surfaces, FTS and STS methods have been developed to be able to fabricate diffraction surfaces and freeform surfaces. These CM require a coordinated and synchronized movement of the cutting tool with two rotations of the spindle. The problem of calculating the mathematical constraints to generate a suitable toolpath is very complex. Among the many factors that affect surface quality,

the choice of FTS or STS machining method is also significantly influenced because it is related to the generation of the toolpath and the corresponding tool compensation techniques. Motion characteristics such as position interpolation, velocity and acceleration of the cutting tool can all affect vibrations, cutting heat and cutting forces during the machining process, directly affecting SR.

Based on the analysis of the above research results on the influence of cutting methods on SR, some comments can be shown as follows.

- For most optical surface types, rotary tool machining methods such as FC, Raster milling give lower surface quality than FTS and STS methods. The SR level achieved by non-SPDT cutting methods is in sub-micron level. In SPDT, the SR values can be achieved at nanometer level. The SR response for STS and FTS methods can reach from 1 to 20 nm, the surface shape error is less than 1  $\mu\text{m}$ . Conventional SPDT method can give even higher surface quality.
- The FC method is an intermittent cutting process, the machining efficiency is low, the relative motion of the tool-workpiece is not continuous, the geometry shape of the tool is deeply imprinted on the machined surface. For array optical surfaces, the STS method gives higher surface quality than other methods. The FTS method of machining takes the least amount of time.
- The STS method has the advantage of being able to process curved surfaces with large slopes. However, the main drawback is the low cutting speed, the low input/output tool frequency, so the spindle speed is also low. This also greatly affects the surface quality when considering the selection of cutting parameters.
- The FTS method has the opportunity to grow stronger than other methods because of the flexibility of the structure and the number of degrees of freedom that this method can generate. From there, it is possible to expand the scope and machining capabilities of the machine system. On the other hand, FTS can be combined with FC method more easily than STS method.
- The choice of FTS or STS machining method will largely determine the cutting force, cutting heat, vibration and cut marks on the machined surface, thereby greatly affecting the SR. Therefore, studying the relationship between these factors associated with surface quality is always a very necessary issue and needs to be analyzed more specifically.
- It should be remembered that the machining time of ultra-precise optical surfaces in general and freeform surfaces in particular is very large. Similar automatic tool change system on CNC machines in most SPDT machines (including FTS, STS) is currently not integrated in order to reduce the cost of machining time, setting time, and adjustment. Accordingly, the algorithm of motion control, tool-path generation, and tool compensation will be greatly complicated problems. However, this trend is expected to develop in the near future.
- The problems of toolpath optimization, energy consumption optimization, machining costs, and environmental issues are still open and need to be considered and studied more in the future.
- It should be recalled that, for freeform optical surfaces and complex profiles, the choosing the cutting method and choosing the right toolpath interpolation method

problems are always the biggest challenge. They will determine the size of the machining data set, directly affecting the working efficiency of the control system and the machining time. Continuity and smoothness of the toolpath is also a huge issue.

- Many studies have shown that, despite choosing the suitable cutting method, the role of the building the corresponding manufacturing process, mounting, measuring equipment, monitoring and feedback mechanisms is extremely important. They are all challenges that need to be thoroughly addressed for SPDT machining in order to achieve sub-micrometer accuracy and nanometer level surface roughness.

## References

1. Balasubramaniam R, Sarepaka RV, Subbiah S (2017) *Diamond turn machining: theory and practice*. CRC Press. Taylor & Francis Group, USA
2. Li S, Zhang Y (2016) Application of single point diamond turning in infrared optics. In: 2016 International Symposium on Advances in Electrical, Electronics and Computer Engineering (ISAEECE 2016), 12–19
3. Stower IF, Komanduri R, Baird ED (1988) Review of precision surface generating processes and their potential applications to the fabrication of large optical components. *SPIE* 966:62–73
4. Tohme YE, Lowe JA (2004) Machining of freeform optical surfaces by slow slide servo method. In: *Proceedings of the American Society for Precision Engineering (ASPE) Annual Meeting*
5. Lucca DA, Klopstein MJ, Riemer O (2020) Ultra-precision machining: cutting with diamond tools. *J Manuf Sci Eng* 142
6. Zhang SJ, To S, Zhu ZW, Zhang GQ (2016) A review of fly cutting applied to surface generation in ultra-precision machining. *Int J Mach Tools Manuf.* <https://doi.org/10.1016/j.ijmactools.2016.01.001>
7. Zhu L, Li Z, Fang F et al (2017) Review on fast tool servo machining of optical freeform surfaces. *Int J Mach Tools Manuf.* <https://doi.org/10.1007/s00170-017-1271-4>
8. Jiang W (2009) Diamond turning microstructure optical components. In: 4th International Symposium on Advanced Optical Manufacturing and Testing Technologies: Design, Manufacturing, and Testing of Micro- and Nano-Optical Devices and Systems. <https://doi.org/10.1117/12.832062>
9. Li L, Yi A (2010) Design and fabrication of a freeform prism array for 3D microscopy. *Opt Soc Am* 27:2613–2620
10. Mishra V, Burada DR, Pant KK et al (2019) Form error compensation in the slow tool servo machining of freeform optics. *Int J Adv Manuf Tech.* <https://doi.org/10.1007/s00170-019-04359-w>
11. Wang X, Fu X, Li C, Kang M (2015) Tool path generation for slow tool servo turning of complex optical surfaces. *Int J Adv Manuf Technol.* <https://doi.org/10.1007/s00170-015-6846-3>
12. Stefan R, Cuttino JF (2009) Design and testing of a long-range, precision fast tool servo system for diamond turning. *Prec Eng* 33:18–25
13. Thomas AD, Miller MH, Falter PJ (1991) Application of a fast tool servo for diamond turning of non-rotationally symmetric surfaces. *Precis Eng* 13:243–250
14. Moorefield GM, Thomas AD, Falter KJ, Paul R (1993) Long range fast tool servo. Final Report. North Carolina State University, Raleigh. Precision Engineering Center
15. Stephen JL, Chargin DA, Calzaretta JA, Trumper DL (1999) Design of a rotary fast tool servo for ophthalmic lens fabrication. *Precis Eng* 23:253–259

16. Dai YF, Guan CL, Yin ZQ, Tie GP, Chen HF, Wang JM (2011) Tool decentration effect in slow tool servo diamond turning off-axis conic aspheric surface. In: 5th International Symposium on Advanced Optical Manufacturing and Testing Technologies: Advanced Optical Manufacturing Technologies. <https://doi.org/10.1117/12.867694>
17. Li L, Collin SA, Yi A (2010) Optical effects of surface finish by ultraprecision single point diamond machining. *J Manuf Sci Eng* 132
18. Yi AY, Li L (2005) Design and fabrication of a micro-lens array by use of a slow tool servo. *Opt Lett*, 1707–1709
19. Gong H, Ao S, Huang K, Wang Y, Yan C (2019) Tool path generation of ultra-precision diamond turning: a state-of-the-art review. *Nanotech Prec Eng* 2:118–124
20. . Lee YC, Yang J (2012) Three-axis tool-path B-spline fitting based on preprocessing, least square approximation and energy minimization and its quality evaluation. *MM Sci J*, 351–358
21. Sebastian S, Allen YY, Andreas G (2011) Freeform manufacturing of a microoptical lens array on a steep curved substrate by use of a voice coil fast tool servo. *Opt Express* 19:23938–23951
22. Gong H, Wang Y, Song L, Fang FZ (2015) Spiral tool path generation for diamond turning optical freeform surfaces of quasi-revolution. *Comput Aided Des* 59:15–22
23. Hector MG, Ro PI (1998) Sliding-mode control of a nonlinear-input system: application to a magnetically levitated fast-tool servo. *IEEE Trans Industr Electron* 45:921–927
24. Ku SS, Larsen G, Cetinkunt S (1998) Fast tool servo control for ultra-precision machining at extremely low feed rates. *Mech* 8:381–393
25. Zhou X, Hu L (2010) An improved adaptive feedforward cancellation for tool trajectory tracking in diamond turning of freeform optics, School of Mechanical Science and Engineering Jilin University Changchun, JL 130022, China. IEEE ISBN: 978-1-4244-7739-5
26. Zhu Z, To S (2015) Adaptive tool servo diamond turning for enhancing machining efficiency and surface quality of freeform optics. *Opt Exp* 23. <https://doi.org/10.1364/OE.23.020234>

# Defects Classification on Garment Fabrics and Application of Artificial Intelligence to Detect Defects During Fabric Inspection



Nguyen Thi Thuy Ngoc, Nguyen Thi Ngoc Lan, and Nguyen Minh Hieu

**Abstract** This report presents the study results of defects classification that often appear on garment fabrics and a defects identification model made by artificial intelligence. The classification system of fabric defects is created for the artificial intelligence recognition model to ensure a comprehensive and general overview in many aspects: the type of garment fabric, the stage and causes of the defects, objects and the degree of defects. The recognition model for identification of fabric defects is built on the experimental method using the YOLO algorithm version 5. The data for model training and testing are selected and made by the algorithm's requirements, including 261 samples of fabric defect on 2D images of fabrics that have different characteristics such as weaves, textures, thicknesses, weights, yarn densities, and compositions. The testing results show that the model achieves an average of over 65% accuracy depending on the difficulty of the detected defect types. This model is the initial basis for designing an automatic detection system of the defects for many different types of fabrics.

**Keywords** Fabric inspection · Fabric defects · Artificial intelligence · Convolutional neural network

## 1 Introduction

The fabric inspection process plays an extremely important role, one of the decisive steps to the quality of the garment. Actual fabric inspection is the process of determining the location, type and size of irregularities present in the fabric. Human quality inspection of fabric to detect fabric defects to prevent unnecessary damage

---

N. T. T. Ngoc (✉) · N. T. N. Lan · N. M. Hieu  
Hanoi University of Science and Technology, Hanoi, Vietnam  
e-mail: [ngoc.nguyenthithuy@hust.edu.vn](mailto:ngoc.nguyenthithuy@hust.edu.vn)



later. However, Vietnamese garment enterprises have been implementing superficially, not methodically and not paying attention to the necessity of pre-production fabric inspection (especially in small and medium enterprises). In fact, at present, there is only one study in the world on the model of fabric inspection, automatic fault detection and the application of automatic fabric inspection machine to detect fabric defects, which is only applicable to fabrics without textures. Therefore, it is necessary to study, classification, and systematize errors that frequently appear on fabrics in the process of industrialization, modernization and economic integration requires a high level of competition today. It will be the basis for building and designing a system that can check and identify fabric defects automatically.

This paper presents the method and results to build a fabric fault classification system and an automatic fabric defect identification model using the YOLO algorithm version 5 by identifying defects on the fabric surface by image processing techniques.

## **2 Contents and Methods**

### ***2.1 Build a Category of Fabric Defects***

Based on analyzing the characteristics of the origin, shape and characteristics of types of defects appearing on the fabric as a basis for the study of the automatic fault identification model, it is necessary to ensure that the list of fabric defects must be comprehensive, generalized, comprehensive based on all causes of them. The construction of a list of fabric defects should be based on the required characteristics of the generality of all types of defects. A type of defects can occur in one feature or occur simultaneously on many features or all features. The aspects to be considered when classifying fabric defects include: according to the type of fabric, the production and the reason for defects, the object on the fabric, the severity of defects.

The category of fabric defects used for classification and as a basis should satisfy the following requirements: (1) Comprehensive data in all defects cases. (2) Defect characteristics must be related closely correlated with each other, one feature is the basis for evaluating the other. (3) From this category, businesses can easily classify defects into specific groups from which to accurately assess the defect condition and provide methods to remedy the damage caused by fabric defects.

### ***2.2 Data Structure and Fabric Error Detection Problem Based on Artificial Intelligence Application***

Whole types of defects meet the requirements in the list of fabric defects mentioned in Sect. 2.1. The dataset is created on plain, textured, and plaid fabrics—fabric surface effects, these are very common in production. The fabric structure is woven and

knitted fabric. Fabrics with special surface structures such as velvet, fur, leather, felt, etc. will not be used as data. The color variation defects haven't been mentioned in this study yet.

The input data in the form of fabric defect images is extracted through Feature map to transform the function of the data through Pooling layer layers. Data regions with different characteristics on the fabric are processed through Fully connected layer. The results of the defect detection are presented through the image of the detected defect, the results table showing the effectiveness of the study and the chart comparing the effectiveness of using CNN compared to other networks. Convolutional neural networks are used to detect errors on fabrics such as Deep Convolutional Neural Networks (DCNN) [3], Faster regions with CNN features (Faster-RCNN) [2] and so on. The framework using CNN for data processing used in the study is YOLO v5 (You only look once—version 5). Not only powerful, but also one of the models with the fastest object detection speed and it is one of currently the fastest of all object detection models. It is the best choice for this research. YOLO can detect many different objects in an image instead of just classifying a single label for an image.

The implementation sequence to build a fabric fault identification model applying artificial intelligence includes 4 main steps, which are: data preparation, data labeling, model training and validation, model testing.

### 2.2.1 Data Preparation

The data prepared for the fabric defect detection model consists of 261 real images collected from the fabrics mentioned above (Table 1). Sampling rules for the model will be divided: 60% of samples for training, 20% of samples for validation and 20% of samples for testing. The data prepared for YOLO with the normal model, the more samples, the more accurate the results obtained (according to the theory of convolutional neural networks). However, the accuracy of the model not only depends on the number of input samples but also depends on the nature and characteristics of the data set. The feature of the data set for the automatic detection of fabric defects is a variety of textures and surface features, so when the number of samples increases, the fabric surface effect also increases. This effects the obtained results and then, the model's results cannot be concluded with absolute accuracy or not.

Requirements for the fabric samples used: (a) The specimen has no stains or colors that differ from the fabric surface in adjacent areas; (b) The fabric should be smooth, flat, and free of wrinkles, no crease marks or folds compared to the original structure of the fabric; (c) The size of the fabric samples are different. However, the size of the fabric sample should not be less than 10 × 10 cm. If it is smaller than this specified size, the input data will be unreliable because the shooting distance is not guaranteed.

Fabric sample photography diagram is arranged in accordance with the fabric inspection model currently being implemented in reality as Fig. 1.

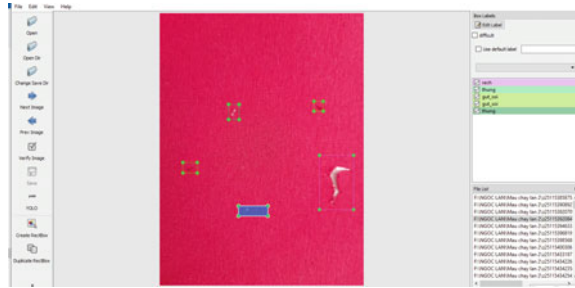
**Table 1** The number of fabric samples used for model training, validation and testing

Test times	Training			Validation			Testing		
	Solid fabric	Textured fabric	Plaid fabric	Solid fabric	Textured fabric	Plaid fabric	Solid fabric	Textured fabric	Plaid fabric
1	23	28	12	6	9	5	7	10	4
2	71	59	26	24	20	9	24	20	8

**Fig. 1** Fabric sample photography diagram



**Fig. 2** Labeled fabrics



**2.2.2 Data Labeling**

Implementation steps: (1) Encode the fabric defect type name as a serial number, (2) Image selection, (3) Labeling fabric defects.

The result obtained after the labeling process is a system of errors coded and located by the coordinates of the point around the fabric error called the coordinates of the base frame (Fig. 2).

**2.2.3 Model Training and Validation**

Training and validating the model through 2 experiments. The resulting prediction histogram after training is predicted by the cells forming the blue diagonal. The training and validation results are better the darker the diagonal (Fig. 3).

Indicators to evaluate the effectiveness of the model are: Object is recognized correctly:  $IoU > 0.5$  (True positive: TP); Falsely is recognized object:  $IoU < 0.5$  (False positive: FP); Object is not recognized (False negative: FN); Prediction accuracy P; Rcall R; mean Average Precision mAP.

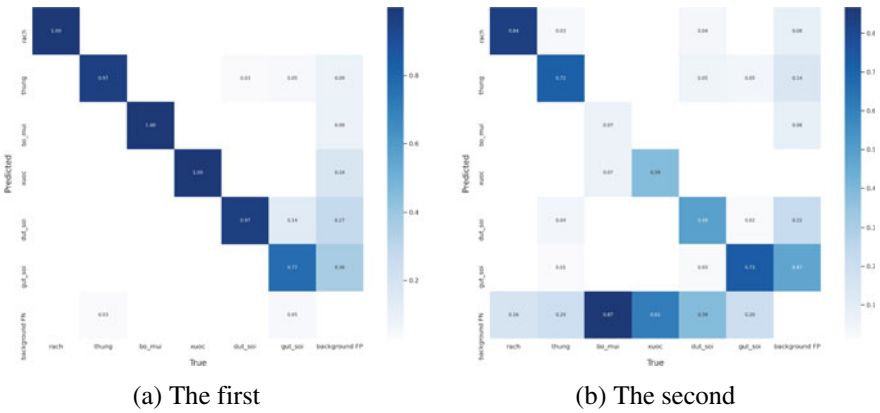


Fig. 3 Object detection prediction graph of the first and the second experiment

### 3 Results and Discussion

#### 3.1 The Fabric Defects Category

The category of fabric defects is classified according to the diagrams in Figs. 4 and 5.

Six common types of fabric defects in the textile industry are selected, including: hole, tear, scratch, yarn, break yarn, machine stop weaving. The selected errors are not related to color defects and meet the requirements in Sect. 2.1 outlined.

Fig. 4 Diagram of classification according to the objects in fabrics

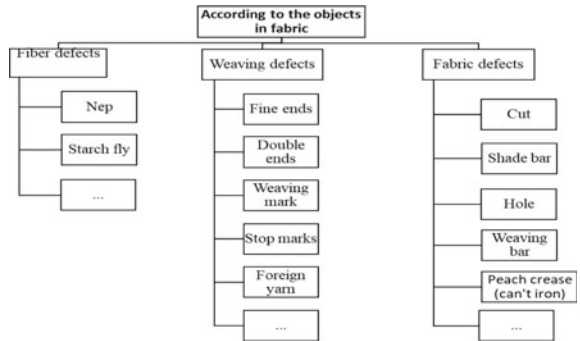
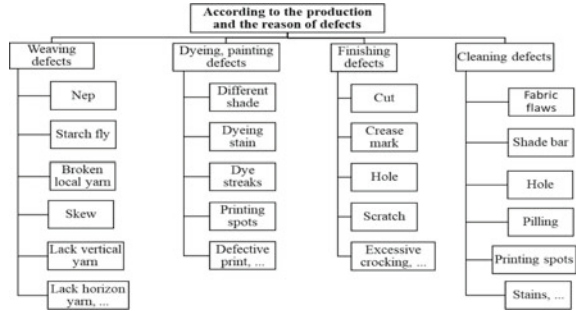


**Fig. 5** Diagram of classification according to the production and the reason of defects



### 3.2 The Identification Model of Fabric Defects Applying Artificial Intelligence

Fabric defects image data collection model is established in accordance with the fabric testing conditions in actual production. After training, validating and testing the model, the results are as shown in Fig. 6.

Based on these figures:

P (Precision): in the first experiment, the average value was higher than the second experiment and there was a larger difference between the number of learning times than in the second experiment.

R (Recall), mAP@0.5, mAP@0.5:0.95: in the first experiment were all higher than those in the second experiment. It can be seen that the training and validation results of the first experiment were better than the second experiment.

To have a more objective and accurate assessment, we need to evaluate the effectiveness of the model based on the test results in the form of data (Table 2).

Thus, it can be seen that the second test results showed that hole, tear, and stop weaving were lower than that of the first time due to the influence of the variety of fabric surface effects. There are 3 types of defects that have a much better level of recognition: scratch, yarn knot, broken yarn. Easy-to-recognize fabric defect samples are:

- Hole: recognizable and fairly accurate due to the large number of samples and easily identifiable surface features.
- Tear: recognizable and quite accurate, similar to the puncture defect, although the sample is not large, but due to the surface of the error, it is easy to detect.
- Yarn knot and broken yarn: although the level of error recognition is average, the ability to correctly identify it is high. This type of defect is small in size, difficult to detect, and the result is noisy by surrounding textures.
- Scratch: low level of recognition and through 2 experiments, the ability to recognize is average. This type of defects is both small and affects the detection results by the fabric surface.

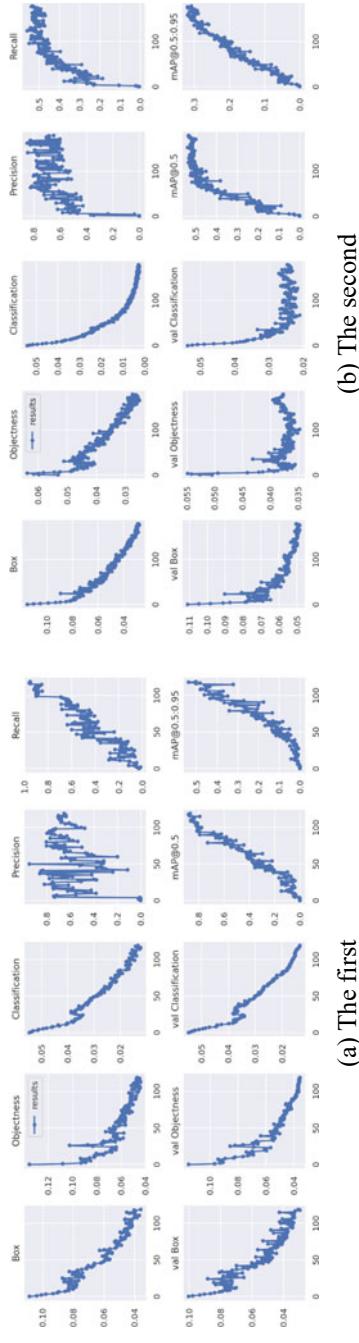


Fig. 6 Results of the first and second training and validation in the form of histogram

**Table 2** Test results of the first time and second time

Type of defects	Test results of the first time				Test results of the second time					
	Label	P	R	mAP@0.5	mAP@0.5:0.95	Label	P	R	mAP@0.5	mAP@0.5:0.95
All	114	0.654	0.952	0.867	0.504	264	0.649	0.533	0.535	0.308
Tear	17	0.874	1	0.995	0.659	38	0.74	0.842	0.821	0.546
Hole	34	0.778	0.912	0.929	0.515	74	0.761	0.689	0.718	0.405
Stop weaving	1	0.999	1	0.995	0.597	15	0.369	0.0667	0.821	0.0543
Scratch	7	0.388	0.939	0.728	0.417	18	0.636	0.388	0.368	0.227
Broken yarn	33	0.513	0.864	0.832	0.494	75	0.764	0.507	0.556	0.331
Yarn knot	22	0.369	0.864	0.72	0.34	44	0.625	0.705	0.662	0.286



- Stop weaving is the type of defect with the lowest level of recognition. The reason as well as the scratch error.

In fact, the experimental results show that the recognition ability of the YOLO v5 fabric test model is closely correlated with the fabric surface effect and error size. This is quite similar to the current human-powered fabric inspection, but the possibility of inspection uniformity is much higher.

## 4 Conclusion

The defect classification data system is very necessary in industrial garment production, helping to properly assess the defects condition that the fabric is experiencing and is the basis for building an automatic fabric inspection model applying artificial intelligence. Easy-to-recognize fabric defect samples are hole, tear, yarn knot and broken yarn, scratch, stop weaving. The types of hole and tear defect are recognizable and fairly accurate. Yarn knot and broken yarn defects are although the level of error recognition is average, the ability to correctly identify it is high. The types of scratch and stop weaving defect is with low level of recognition. Although the results are not really good, this is the initial basis for building a more advanced automatic fabric checking model to save labor, time, and costs, to improve production quality.

## References

1. Thi Ngoc Lan N (2021) Understanding the types of fabric defects and applying artificial intelligence to detect during fabric inspection. Hanoi University of Science and Technology: Engineering graduation thesis
2. Wei B, Hao K, Tang XS, Ren L (2018) Fabric defect detection based on faster RCNN. In: Proceedings of the artificial intelligence on fashion and textiles conference, Hong Kong, pp 45–51
3. Lv Y, Yue X, Chen Q, Wang M (2018) Fabric defect detection with cartoon–texture decomposition. In: Proceedings of the artificial intelligence on fashion and textiles conference, Hong Kong, pp 277–283
4. Gao C, Zhou J, Wong WK, Gao T (2018) Woven fabric defect detection based on convolutional neural network for binary classification. In: Proceedings of the artificial intelligence on fashion and textiles conference, Hong Kong, pp 307–313

# Behavior Analysis for One-Way Wide Module Joist Concrete Floor System



Nhu-Thao Thi Nguyen and Phu-Cuong Nguyen

**Abstract** In this study, the behavior of the One-Way Wide Module Joist Concrete Floor System (OWWMJCFs) is researched by using two methods: hand calculation and the Finite Element Method (FEM) employing SAP2000. For the hand calculation method, the internal forces of the floor are predicted by using the practical parameter tables. With the finite element method employing SAP2000, we simulate the whole of the one-way wide module joist concrete floor system by using a three-dimensional space FEM modeling for predicting accurately the behavior of the OWWMJCFs. Obtained results show that the finite element method employing SAP2000 is much different from the hand calculation method. This study gives some useful advices for practical design engineers.

**Keywords** Reinforced concrete floor · Finite element method · Hand calculation · Internal forces · SAP2000

## 1 Introduction

Construction is one of the first fields that apply soon information technology in design, construction, and quality management. The introduction of many structural calculation software packages based on the finite element method (FEM) resolved very difficult and challenging structural problems. The slab is one indispensable structure of construction, one of the slab structures owning the large load-carrying capability, high stiffness, durability, and simple calculation is a one-way wide module joist concrete floor system (OWWMJCFs). The popular method for designing is

---

N.-T. T. Nguyen · P.-C. Nguyen (✉)

Advanced Structural Engineering Laboratory, Department of Structural Engineering, Faculty of Civil Engineering, Ho Chi Minh City Open University, Ho Chi Minh City, Vietnam  
e-mail: [cuong.pn@ou.edu.vn](mailto:cuong.pn@ou.edu.vn); [henycuong@gmail.com](mailto:henycuong@gmail.com)

the traditional hand-calculation method [1–3]. However, there are still many limitations to using the traditional hand-calculation method because reality constructions are complicated. Today, several commercial software packages were developed and invented to support design calculation for engineers. The finite element method is more accurate than the traditional hand-calculation method. Recently, several complicated structural problems have been solved using finite element methods [4–10]. The work of [9] stated that two-dimensional models can not predict all eigenmodes, and torsional, flexural horizontal, and distortional phenomena accurately. Particularly, FEM can solve nonlinear behavior in addition to linear elastic analysis [10]. So we raised the question, “How are the differences between the FEM software and the traditional hand-calculation method?”. Therefore, this study will compare the differences between the FEM software and the traditional hand-calculation method.

## 2 Research Method

In the research, we perform behavior calculation of the structural slab of one industrial building with a length of main beams of 12 m, the length of extra beams of 7.6 m, and load-bearing walls around the slab system. Figure 1 shows a studied plan of a one-way wide module joist concrete floor system. Materials use concrete B25 and steel AII, AI as Vietnam’s design standard [11].

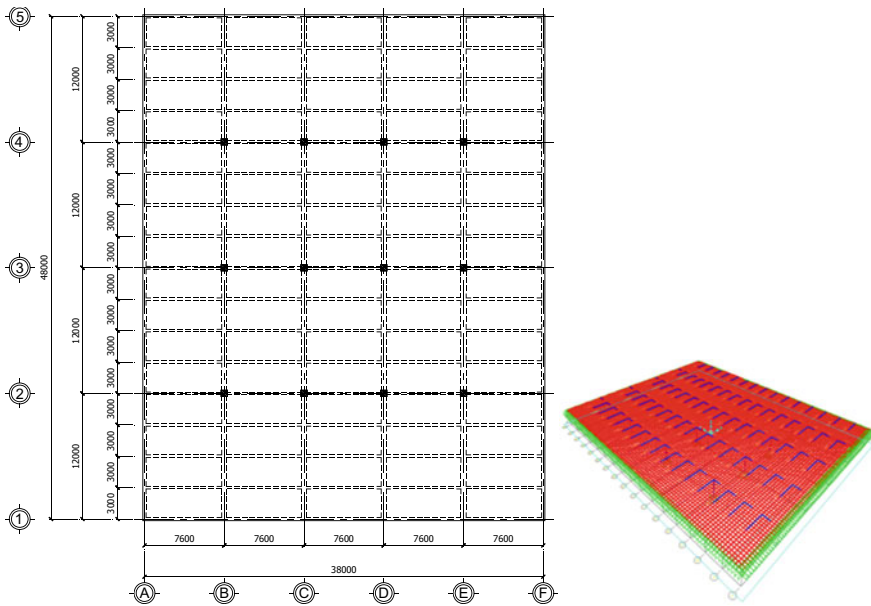


Fig. 1 The floor plan and three-dimensional slab is modelled using SAP2000

- +The wall width at the main beams is 0.200 m.
- +The wall width at extra beams (axis 2, 3, and 4) is 0.3 m.
- +The exterior wall width is 0.3 m.
- +The story height is 3.6 m.
- +Live load:  $P = 8 \text{ kN/m}^2$ .

### 2.1 Traditional Hand-Calculation Method

This section presents a structural analysis of construction based on the traditional hand-calculation method. The traditional hand-calculation method is used to analyze the behavior of a one-way wide module joist concrete floor system (OWWMJCFs) as shown in Fig. 1. The structural slab is separated into main beams, extra beams, and sub-slabs modeled the calculation as the elastic diagram and the plasticity diagram referred from [1–3]. Internal forces in sub-slabs, main beams, and extra beams are estimated by formula and table diagrams. However, this method still meets difficult problems when construction structures are complex geometry and architecture. Formula and lookup tables just apply for simple shape structures.

### 2.2 Finite Element Method Employing SAP2000

The research also uses the finite element method employing SAP2000 v22 [12] software for modeling 3D construction as shown in Fig. 1 describing approximately as reality. In this study, we set 11 load cases including one Dead Load (DL), and 10 cases of Live Load (Live load =  $10.44 \text{ kN/m}^2$ ) for the slab as shown in Fig. 2.

All load combinations are set as follows:

Combo 1: DL + LL1. Combo 2: DL + LL2. Combo 3: DL + LL3. Combo 4: DL + LL4. Combo 5: DL + LL5. Combo 6: DL + LL6. Combo 7: DL + LL7. Combo 8: DL + LL8. Combo 9: DL + LL9. Combo 10: DL + LL10. Combo ENV: Envelop all Combo 1, Combo 2, ... to Combo 10.

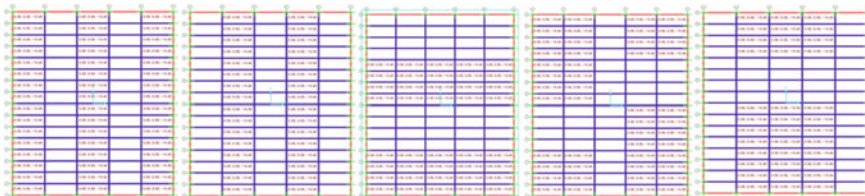
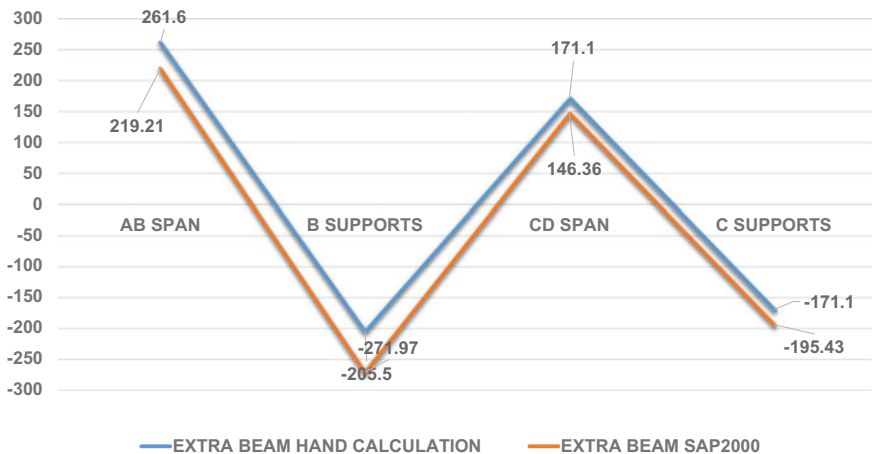


Fig. 2 Ten important cases of applied live load for the slab using SAP2000

### 3 Results and Discussions

After calculating with two methods, it can be found that in the extra beam, the internal bending moment values at spans generated by the finite element software SAP2000 v22 [12] are smaller than the hand calculation method as illustrated in Fig. 3, the differences compared to the value of the software method are 19.3% at the AB span and 16.9% at interior spans (BC, CD, etc.) as shown in Fig. 5. While at the support positions, the internal bending moment values generated by the hand calculation method are smaller than the FE software method as illustrated in Fig. 3, the differences are 24.4% at the B support and 12.4% at the C support as shown in Fig. 5. Using the results of the hand-calculation method for designing the extra beam at the support position is not safe for buildings. This obvious difference depends greatly on the working principle of the structure together, the reason why in the hand calculation method, there is a more harmonious change because in this method, the extra beam is separated into small elements and they depend on the change of the coefficient  $\beta$  according to the fixed internal force ratio [1–3]; while in the finite element method using SAP2000 [12] software, it is considered that the extra beam works in the whole structural system, so the behavior of the extra beam does not only depend on the size and load of the beam but also depends on the simultaneous operation of the floor, main beams and columns.

The internal moment values for main beams calculated by the finite element software SAP2000 [12] and the traditional hand-calculation method are presented in Fig. 4. It can be seen that the results generated by using SAP2000 are smaller than the hand calculation in all locations. In this case, using the results of the hand calculation method is safe for designing but it is not economic. Deviation percentages of the finite element software SAP2000 [12] and the hand-calculation method are



**Fig. 3** Bending moment diagram values (kN m) for extra beams using hand calculation and SAP2000

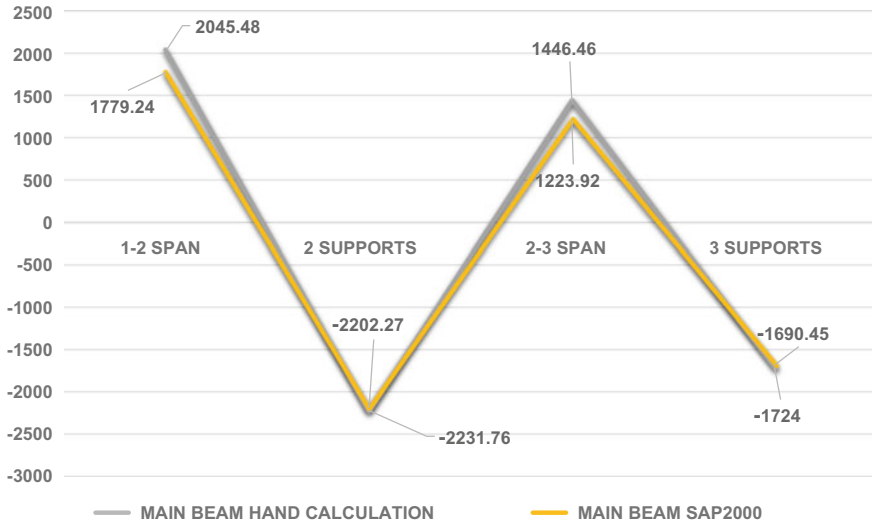


**Fig. 4** Bending moment diagram values (kN m) for main beams using hand calculation and SAP2000

shown in Fig. 5. Errors of support moments are small (1.3%, 2%), but they are still large in spans (15%, 18.2%). This is due to that loadings transferring from extra beams to the main beam assigned equivalently as concentrated forces at points using the hand-calculation method lead to larger moments. But the reality, the main beam does not suffer the concentrated forces which are distributed on the area of extra beams, walls, and slabs. The finite element software SAP2000 [12] can model nearly the structural slab as reality.

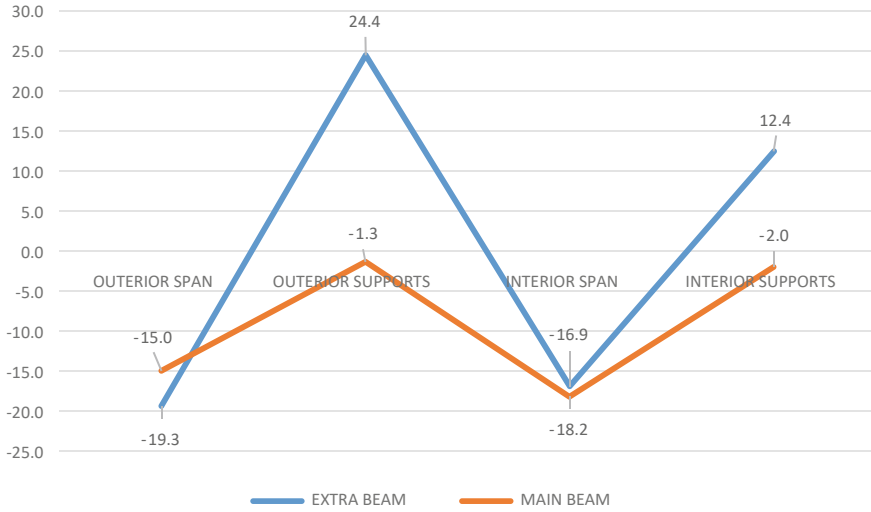


**Fig. 5** Errors (%) of moment values on the extra and main beams between hand calculation and SAP2000

### 4 Conclusion

The purpose of this study is to present and show differences between the two methods: the traditional hand-calculation and the finite element method using SAP2000 v22 software to analyze the behavior of a one-way wide module joist concrete floor system. This study is a good reference document for structural design engineers. As a result, the research proved that the finite element method is accurate, reliable, convenient, fast, and reduces a lot of work, and is safer than using the traditional hand calculation. The hand-calculation method exits many inconvenient problems: (1) just calculating for simple geometry of buildings, (2) lookup tables are not full and inaccurate. We can conclude that the finite element method should be used for structural design instead of the traditional hand-calculation method.

**Acknowledgements** This research is funded by the Ministry of Education and Training (MOET), Vietnam, under the grant number B2023–MBS–03.

### References

1. Vo BT, Ho DD (2011) Project: one-way wide module joist concrete floor system. Construction Publishing, Hanoi, Vietnam
2. Phan QM, Ngo TP, Nguyen ĐC (2006) Reinforced concrete structures: basic components. Technology and Science Publishing House, Hanoi, Vietnam

3. Vo BT (2020) Reinforced concrete structures: building structures. Ho Chi Minh city, Vietnam: National University Press
4. Schladitz F, Frenzel M, Ehlig D, Curbach M (2012) Bending load capacity of reinforced concrete slabs strengthened with textile reinforced concrete. *Eng Struct* 40:317–326
5. Ruggieri S, Porco F, Uva G (2018) A numerical procedure for modeling the floor deformability in seismic analysis of existing RC buildings. *J Build Eng* 19:273–284
6. Khajehdehi R, Panahshahi N (2016) Effect of openings on in-plane structural behavior of reinforced concrete floor slabs. *J Build Eng* 7:1–11
7. Hassan NZ, Sherif AG, Zamarawy AH (2017) Finite element analysis of reinforced concrete beams with opening strengthened using FRP. *Ain Shams Eng J* 8(4):531–537
8. Hekal GM, Salama MI, Elsamak G, Almaadawy AH (2022) Shear behavior of RC beams strengthened with ultra-high-performance fiber-reinforced concrete using finite-element analysis. *Asian J Civ Eng*
9. Abramowicz M, Berczyński S, Wróblewski T (2020) Modelling and parameter identification of steel–concrete composite beams in 3D rigid finite element method. *Arch Civ Mech Eng* 20:103
10. Hu HT, Schnobrich WC (1991) Nonlinear finite element analysis of reinforced concrete plates and shells under monotonic loading. *Comput Struct* 38(5–6):637–651
11. TCVN 5574:2018 (2018) Design of concrete and reinforced concrete structures. Ministry of Construction, Vietnam
12. SAP2000 v22 (2022) CSI analysis reference manual, computer and structures, Inc. Berkeley, California, USA



# Research on the Hydromechanical Forming for the Conical Products by Numerical Simulation



Thu Nguyen Thi  and Trung Nguyen Dac

**Abstract** Hydromechanical forming has been an impressive technology in manufacturing thin-shell products. Under the support of high-pressure liquid, the product can achieve many outstanding advantages such as increasing the level of deformation, reducing thinning, and improving surface quality. Especially, this technology is suitable for specific parts requiring great depth, or complex profiles that are difficult to shape by conventional methods, and one type of them is conical part. There are many factors affecting the product quality, especially the liquid pressure and blank holder force. In order to clarify this issue, in the article, a parametric study on the impact of liquid pressure and blank holder force on the quality of the average conical product is presented using numerical simulation method. The results demonstrate the impact of key technological parameters on product quality, namely the radius at the top of the product and on the thinning of the product. Moreover, the optimal set of parameters to achieve high efficiency in the forming process is also proposed. The investigation is meaningful in predicting the shaping process to give an appropriate control plan.

**Keywords** Hydromechanical forming · Conical product · Numerical simulation

## 1 Introduction

In recent years, hydromechanical forming technology has been widely applied into shaping thin-shell parts because of its special properties. In the technology, the metal is hugged tightly to the punch under supporting of high-pressure liquid. Various studies have shown that fluid pressure is one of the most important technological parameters of hydromechanical forming. Fluid pressure is the main factor that

---

T. N. Thi (✉) · T. N. Dac  
Hanoi University of Science and Technology, Hanoi, Vietnam  
e-mail: [thu.nguyenthi@hust.edu.vn](mailto:thu.nguyenthi@hust.edu.vn)

creates a state of compressive stress on the workpiece for supporting the workpiece to conform to the punch profile and reducing the relative displacement between the workpiece and the punch [1–4]. In the studies, Lang et al. [5] used numerical simulation combined with experiment to stamp cylindrical cup details from Al1050-H0 aluminum and Al-Mg-Si alloy. Besides, blank holder force (BHF) is an important factor affecting the phenomenon of wrinkling, thinning, and cracking of products [6].

However, the previous studies have mainly focused on low cylindrical or conical details. For details that are difficult to shape, such as medium or high conical products, there have not been any published investigations. Therefore, in order to clarify the influence of technological parameters including blank holder force and forming fluid pressure, this paper shows research on hydromechanical forming for medium conical details. Numerical simulation was employed in the study for low carbon steel DC04. Optimal data sets of key technological parameters were also found to satisfy precise product shaping.

## 2 Research Object and Objective

In hydromechanical forming technology, under the support of liquid pressure in the die cavity, the workpiece is pressed closely to the punch. Thus, the product quality is better. Based on that, the research object of this paper is the conical detail as shown in Fig. 1.

This is a conical part with a narrow rim. The material used is DC04 steel—a specialized material in the technology of forming sheet details. The workpiece is 100 mm in diameter and 1.0 mm in thickness.

The objective of this study is to determine the influence of BHF and liquid pressure on the quality of conical products in hydromechanical forming technology, namely the radius at the corner between rim (top radius—shown in Fig. 2) and wall and the degree of largest thinning of the product.

The research method used in the paper is numerical simulation via Dynaform® software. Investigated values of the parameters of BHF and fluid pressure are  $(80 \div$

Fig. 1 Conical detail

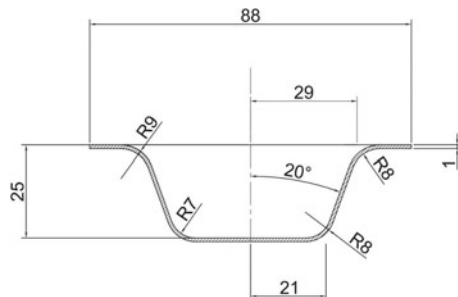
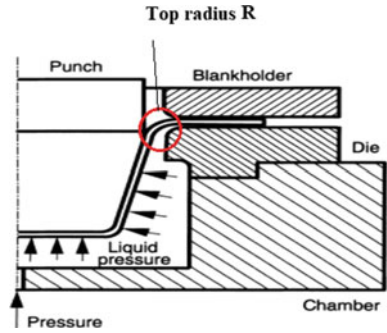


**Fig. 2** Schematic illustration of the hydromechanical drawing system [7]



180) kN and (14 ÷ 32) MPa respectively. The given parameters include stamping speed of 20 mm/s, coefficient of friction of 0.125, gap between punch and die of 1.0 mm.

### 3 Discussions

#### 3.1 Effect of BHF on Product Forming Ability

##### a. Effect of BHF on the top radius R

In order to determine the effect of BHF on the top radius R, simulation was conducted with the following input parameter including the liquid pressure of 24 MPa, Clearance of punch and die at the first stage of 1 mm. The blank holder force changes from 80 to 180 kN with a step of 10 kN. The simulation results are summarized and built in the form of a graph in Fig. 3.

**Fig. 3** Change of radius value according to the BHF

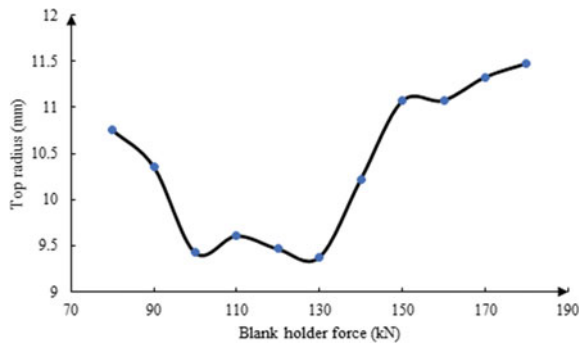


**Fig. 4** The influence of the BHF on the largest thinning ratio

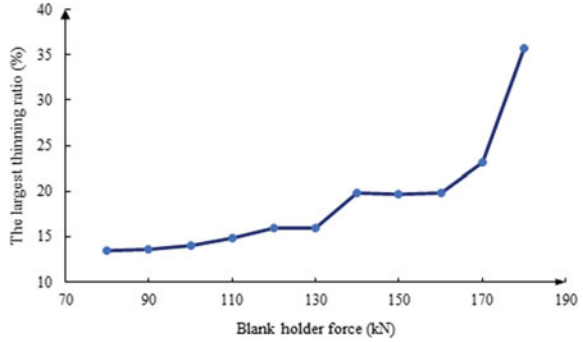


Figure 3 shows the relationship between the corner radius at the mouth of the product and the BHF in a non-linear way. The BHF is in the range of 100–130 kN, which is optimal because the top radius is closest to the required value.

**b. Effect of BHF on the thinning of the product**

With the fixed parameters of fluid pressure in the inside of the die and the gap between the punch and die, the change of the BHF also significantly affects the degree of thinning of the product. The largest thinning ratio  $\epsilon_{max}$  is defined by Eq. (1)

$$\epsilon_{max} = \frac{s_0 - s_{min}}{s_0} * 100 \tag{1}$$

In which,  $s_0$  is the original workpiece thickness;  $s_{min}$  is the thickness at the thinnest part of the product.

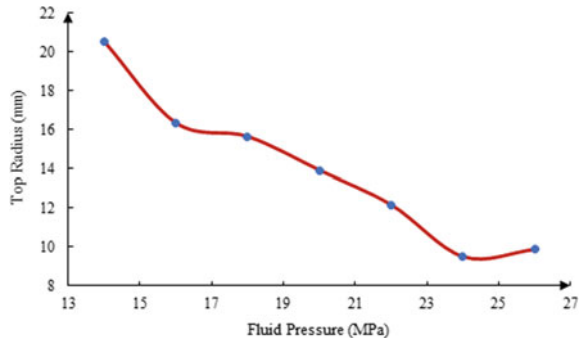
Graph showing the dependence of the largest thinning ratio increase on the BHF is established in Fig. 4. According to the simulation results, when the BHF increases gradually from 140 to 180 kN, it is harder for the workpiece to be pulled into the inside of the die, causing the ratio to gradually increase from about 19.9–37.5%, exceeding the allowable degree of thinning. This can be considered as a dangerous interval. Surveying with BHF of 120 and 130 kN, both thinning ratio and the top radius are quite similar in value. However, according to the simulation results, the thinning distributed in the bottom corner radius at the BHF of 130 kN is more dangerous.

From the simulations and analysis of the forming ability and the degree of thinning, the optimal BHF when hydromechanical forming of conical parts is 120 kN. This value can ensure that the formability as well as the ratio thinning do not exceed the allowable level.

**3.2 Effect of Liquid Pressure on the Product Quality**

To determine the effect of liquid pressure on the product quality in the process of hydromechanical forming of the cone by simulation, the given input parameters

**Fig. 5** The effect of fluid pressure on the top radius



include the gap between punch and die of 1.0 mm, the blank holder force of 120 kN. The fluid pressure changes from 14 to 32 MPa with a step of 2 MPa.

**a. Effect of liquid pressure on the top radius**

When the pressure is raised too high, the initial bulging becomes more pronounced. The punch goes down to shape, making the liquid pressure in the die increase. Consequently, this part of the radius is inflated beyond the required amount, causing damage to the product. In fact, too high pressure can destroy the product even before the punch has reached its full stroke. In addition, if the sealing is not guaranteed, the liquid will overflow.

The graph in Fig. 5 shows that as the fluid pressure increases, the radius of the corner is lowered. According to the simulation results, at the pressure of 14 MPa, the initial bulging is little or trivial, thus reducing the deformation level of the part somewhat. This is also the reason to explain the onset of tearing at the radius of the punch. When the pressure is low, it is not enough to press the workpiece on the punch, making the wall part not really close to the punch, causing a lot of wrinkles.

As the pressure gradually increases in the range of (16 ÷ 24) MPa, the wall of the detail is gradually pressed close to the punch. At this pressure range, an initial bulging occurs, raising deformation of the material. Therefore, at dangerous sections, tearing is reduced due to limiting radial stress. The wall of the product under the action of suitable pressure is pressed against the punch, so the product is precisely shaped.

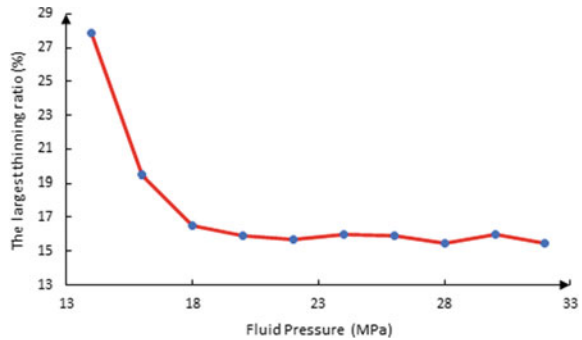
In the liquid pressure range from (26 ÷ 32) MPa, when the pressure increases too high, the initial bulging occurs more clearly. The punch moves to the cavity of the die to shape the material and the pressure increases at the same time, causing the top radius to swell too much, making product damage.

Thus, the liquid pressure in the range of (24 ÷ 26) MPa can form products with a suitable radius as required.

**b. Effect of liquid pressure on the thinning of the product**

When varying the fluid pressure, the measured largest thinning ratios are illustrated in Fig. 6.

**Fig. 6** Effect of liquid pressure on the degree of thinning



The graph in Fig. 6 demonstrates the dependence of the largest thinning ratio on the forming pressure. This dependence is quite evident when the pressure increases from 14 to 24 MPa. Then the percentage of the largest thinning ratio reduced from 27.9% to only 16%.

In summary, from the simulations and analysis of the forming ability and the degree of thinning, the optimal pressure when hydromechanical forming of the conical detail is 24 MPa. This is the reasonable pressure to ensure the shaping ability as well as the thinning does not exceed the allowable level.

## 4 Conclusions

The article presents the influence of the BHF and the liquid pressure on the product quality in the process of hydromechanical forming for conical product. Some of the contributions from this study are:

- If the BHF is too low, the product rim will be wrinkled. In the contrary, if the BHF is too large, the workpiece cannot be pulled into the cavity of the die; the wall becomes thin, causing tearing of the product.
- The fluid pressure has a great influence on accuracy in product shaping according to the profile of the punch. When the pressure is too low, the workpiece is not pressed against the punch, causing wrinkles to the product. When the pressure is too high, it can even cause tearing of the product in the early stages of the forming process.

The research results found the optimal values of the BHF (120 kN) and the liquid pressure (24 MPa). The results allow us to evaluate the influence trend of technological factors in the product shaping process.

**Acknowledgements** This research was funded by Hanoi University of Science and Technology (HUST) under project number T2022-PC-019.

## References

1. Assempour A, Taghipour E (2011) The effect of normal stress on hydro-mechanical deep drawing process. *Int J Mech Sci* 53:407–416
2. Meng B, Wan M, Yuan S, Xu X, Liu J, Huang Z (2013) Influence of cavity pressure on hydro-dynamic deep drawing of aluminum alloy rectangular box with wide flange. *Int J Mechanical Sci* 77:217–226
3. Bakhshi-Jooybari M, Gorji A, Elyasi M, Developments in sheet hydroforming for complex industrial parts. <https://doi.org/10.5772/48142>
4. Lang LH, Wang YM, Xie YS, Yang XY, Xu YQ (2012) Pre-bulging effect during sheet hydro-forming process of aluminum alloy box with unequal height and flat bottom. *Trans Nonferrous Metals Soc China* 22:s302–308
5. Lang L, Danckert J, Nielsen KB (2004) Investigation into the effect of pre-bulging during hydromechanical deep drawing with uniform pressure onto the blank. *Int J Mach Tools Manuf* 44(6):649–657
6. Kumar RU, Reddy PR, SitaRamaraju AV (2012) Determination of blank holder pressure in hydroforming deep drawing process. *Int J Mech Eng Robot Res* 1:242–249
7. Zhang SH, Nielsen KB, Danckert J, Kang DC, Lang LH (2000) Finite element analysis of the hydromechanical deep-drawing process of tapered rectangular boxes. *J Mater Process Technol* 102(1–3):1–8

# Numerical Study on Unwelded Pair of Sheets in Hydrostatic Forming



Thu Nguyen Thi 

**Abstract** In recent years, high-pressure liquid forming technology has been widely applied into the manufacture of thin shell and tubular parts. In addition to superiorities including surface quality guarantee and operation reduction, this technology can also improve productivity and product diversity in one forming step by punching pairs of sheet metal. The generated pair of sheets can be symmetrical or asymmetrical. However, assessing the impact of technological parameters on the forming ability of the pair is difficult, especially the products stamped from a pair of unwelded sheet metal. Therefore, in the paper, the effects of blank holder force on cylindrical cup from unwelded pairs of sheets are investigated. Numerical simulation method was selected for study in this issue. The results give an important assessment of the impact of the factor on the shaping ability of the product. Based on these results, controlling stability of the forming process will be more convenient.

**Keywords** High fluid pressure · Unwelded pair of sheets · Blank holder force · Numerical simulation

## 1 Introduction

Today, products made from single-layer and double-layer metallic materials (also known as Bimetal) have been widely applied in various industries such as electricity, electronics, automatic control, medical equipment, aerospace, machine part manufacturing, etc. Especially, for double-layer materials made by pushing tightly together through laminating, pressing, welding, or gluing, technicians can exploit advantages of each material suitably for different purposes, such as improving deformation, heat conduction, wear resistance, impact resistance, vibration reduction, etc. [1–3]. It can

---

T. N. Thi (✉)

Hanoi University of Science and Technology, Hanoi, Vietnam

e-mail: [thu.nguyenthi@hust.edu.vn](mailto:thu.nguyenthi@hust.edu.vn)



be seen from the literature that the potential for application of double-layer materials is very large.

One of the advanced forming methods to produce double-layer thin shell products with complex shapes and high geometrical accuracy is the high liquid forming method. Compared with the conventional forming, this method has many advantages such as being more suitable for complex forming, minimizing residual stress due to deformation, better surface quality, uniformity in product quality [4–6]. Under the direct impact of high-pressure liquid, the material layers are pressed together tighter so that the details can have contact in a large surface, enabling the deformation between the material layers to be more uniform. However, this technology also has major disadvantages that make it difficult for the forming process, such as lower productivity than traditional stamping technology and difficulty in ensuring tightness to keep high pressure in the process. Therefore, this technology has currently only been applicable to specific products where conventional methods are difficult or impossible to shape. Realizing the high potential of application and development, this paper presents high-pressure liquid stamping technology on two layers of sheet metal through a numerical simulation. Research results show the relationship between blank holder force and deformation of 2-layer products.

## 2 Research Object and Experiments

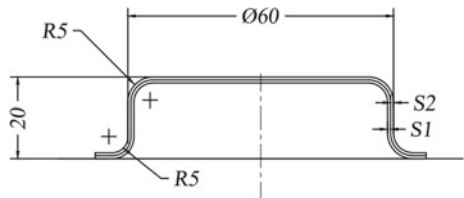
### 2.1 Research Object

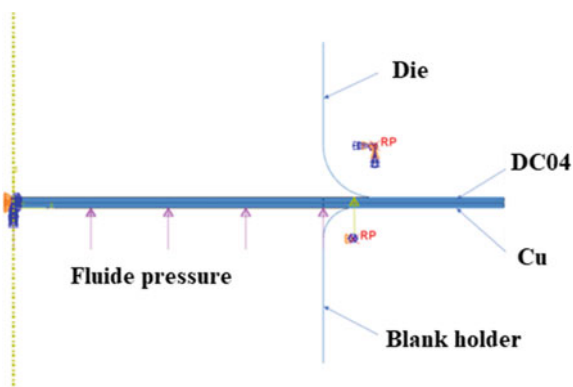
Cylindrical product is a typical part of deep stamping technology (Fig. 1). Therefore, it is selected as a research detail in this paper.

Materials used in the paper are steel (DC04) and copper (Cu). The thickness of each workpiece is 0.5 mm, and the initial diameter of the workpiece is 95 mm. The depth of the die is 20 mm, and the diameter of the die is 60 mm.

The purpose of the study is to investigate the finishing stage in the hydrostatic forming for two layers of different materials by numerical simulation method via Abaqus software.

Fig. 1 Research detail



**Fig. 2** Geometrical model**Table 1** The geometric values of the die

Inner diameter of die, $d$	$d_c = 60$ mm
Depth of die, $h_i$	$h_i = 20$ mm
Radius at the mouth of die, $R_{mc}$	$R_{mc} = 5$ mm
Radius at bottom die, $R_{dc}$	$R_{dc} = 5$ mm

## 2.2 Simulation

A geometrical model is shown in Fig. 2.

The forming tools including die and blank holder (BH) are modeled as rigid parts. Two samples of DC04 and Cu are modeled as deformable parts.

Contact conditions: The coefficients of friction between the workpiece and the surface of the die, the workpiece and the blank holder were selected as 0.1.

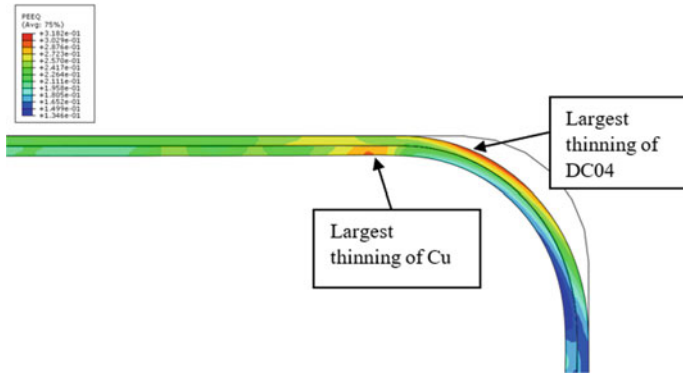
The geometric values of the die are given in Table 1.

## 3 Discussions

To investigate the effect of the BH force on product quality, the fluid pressure was fixed in all cases as 80 MPa. In this study, the product quality is considered in terms of two factors: the largest thinning on the product and the bottom radius of the product.

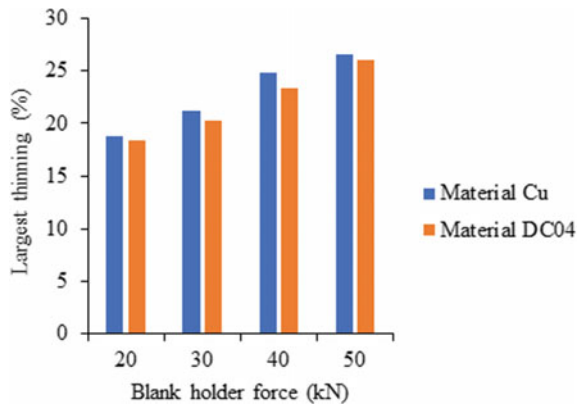
The simulation results illustrate that when the BH force grows up, the workpiece is more difficult to move into the die and the thickness of the workpiece is also thinner. Specifically, the positions of the largest thinning of DC04 steel, and Cu are shown in Fig. 3.

Figure 4 illustrates the ratio of thinning of each material with different values of BH forces. The higher the blank holder force is, the thinner the sheet is. Comparing the maximum thinness of the two layers of Cu and DC04 materials, it can be inferred that the Cu material is slightly thinner.



**Fig. 3** Largest thinning position

**Fig.4** Largest thinning of each material at different values of BH force



As the BH force increases, the radius of the bottom of the product also grows up as shown in Figs. 5 and 6. The increase in the radius of the bottom of the product means that the workpiece is more difficult to get close to the die's profile, thus the accuracy of the product decreases. The reason is that due to the increased resistance on the workpiece rim during the forming process, it is difficult for the workpiece to be pulled to fill the concave corners of the die.

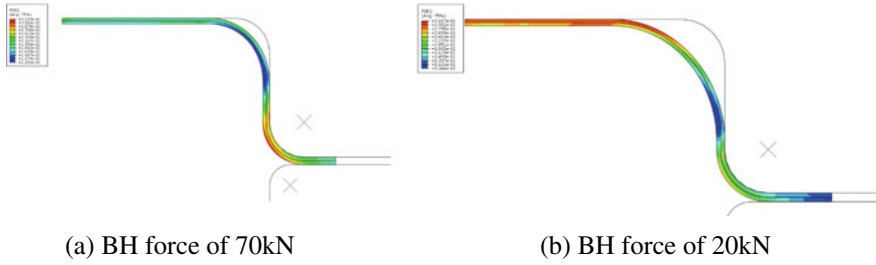
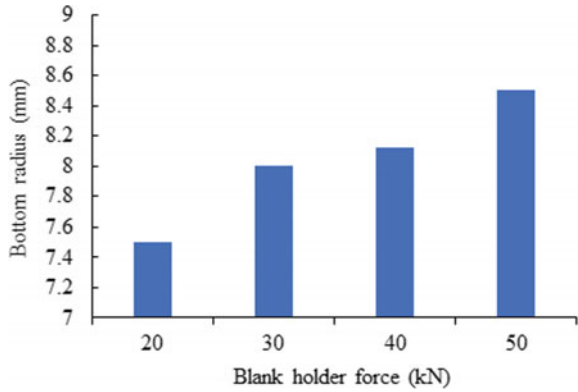


Fig. 5 Bottom radius R of product in simulation

Fig. 6 Bottom radius of each product at different values of BH force



### 4 Conclusions

This paper presents the effect of BH force on the forming ability of 2-layer products in hydrostatic forming technology. The results show that the BH force plays an important role during forming. It directly affects the degree of thinning and the corner radius of the product, specifically:

- When the BH force increases, the material becomes thinner. Comparing the two materials, copper is thinner than steel in all the cases considered. The thinnest region, also known as the most dangerous zone, is at the corner radius of the product.
- The larger the BH force, the bigger the radius of the product created. When the BH force is too large, the product will be torn in a dangerous position.

**Acknowledgements** This research was funded by Hanoi University of Science and Technology (HUST) under project number T2022-PC-019.

## References

1. Habibi Parsa M, Yamaguchi K, Takakura N (2001) Redrawing analysis of aluminum-stainless-steel laminated sheet using FEM simulations and experiments. *Int J Mech Sci* 43:2331–2347
2. Bagherzadeh S, Mollaei-Darianib B, Malekzadeh K (2012). Theoretical study on hydro-mechanical deep drawing process of bimetallic sheets and experimental observations. *J Mater Process Technol* 212:1840–1849. <https://doi.org/10.1016/j.jmatprotec.2012.04.002>
3. Bagherzadeh S, Mirnia MJ, Dariani BM (2015) Numerical and experimental investigations of hydro-mechanical deep drawing process of laminated aluminum/steel sheets. *J Manuf Process* 18:131–140
4. Taye FF, Digavalli RK (2019) Enhancement of drawability of cryo-rolled AA5083 alloy sheets by hydroforming. *J Market Res* 8:411–423. <https://doi.org/10.1016/j.jmrt.2018.02.012>
5. Olayinka A, Emblom WJ, Pasacreta TC, Wagner SW (2017) The effect of hydraulic bulge process on the surface topography of annealed AISI 304 stainless steel. *Procedia Manuf* 10:243–252. <https://doi.org/10.1016/j.promfg.2017.07.052>
6. Zahedi SA, Shamsi-Sarband A, Bakhshi-Jouybari M, Hossinipour SJ, Banabic D (2012) Optimizitation of the pressure path in sheet metal hydroforming. *Proc Romanian Acad* 13:351–359

# A Parametric Study on Product Quality During Forward-Reverse Extrusion Process



Thu Nguyen Thi , Minh-Quan Nguyen, and Nguyen Thi Hong Minh

**Abstract** Forward-reverse extrusion is a common method in the manufacture of transmission components that require high strength and rigidity. This is a method that helps the metal to deform in two directions: forward and reverse directions compared to the punch movement. However, there are many factors affecting product quality that need to be investigated such as pressing speed, friction, temperature, pressing amount, etc. Therefore, in this paper, the forward-reverse extrusion process of H-shaped products is investigated to clearly evaluate the influence of some essential factors including pressing speed, pressing depth and friction. Numerical simulation method with advantages of convenience, time reduction and high reliability was applied in this study. Research results are meaningful in deforming prediction and the design of extrusion dies later.

**Keywords** Hydromechanical forming · Conical product · Numerical simulation

## 1 Introduction

Extrusion is a method of manufacturing a product by pressing an object with enough force so that the material can flow through the hole into the shape of the die. In this process, the metal is plastically deformed in the cavity of the extrusion die, but there is only one preferred direction of deformation to form the part. Material types can be metal, plastic, rubber in block or powder form. Extrusion is used to produce solid or hollow cylindrical parts, rods, and tubes which have been widely used in industry and civil production. In addition, this technology is also applied to prepare workpieces for the processes of forging, stamping, or forming other complex products.

---

T. N. Thi (✉) · M.-Q. Nguyen · N. T. H. Minh  
Hanoi University of Science and Technology, Hanoi, Vietnam  
e-mail: [thu.nguyenthi@hust.edu.vn](mailto:thu.nguyenthi@hust.edu.vn)

Because of its good forming ability and high practical application, this technology has been studied extensively, with various topics including friction [1], temperature during extruding [2], shape and structure of die [3]. Specifically, Lechner et al. [4] indicates that in addition to withstanding severe process loads, die must be designed with the aim of producing good profiles (free from defects, with high mechanical properties, within required tolerances) and ensuring the required level of productivity. In the study, four tool materials (hot work tool steel 1.2367 and CS1, Ni-based alloy 718, Co-Cr Stellite 1 alloy) were compared to conclude that Ni-based alloys are suitable consolidation for specific applications. New method of rotating backward extrusion (RBE) has been proposed by Qiang Wang [5]. The research shows that with this extrusion method, the force required to manufacture the product is 20% less than the conventional backward force.

In general, the above studies focus on optimizing the die structure as well as technological parameters. However, there have not been many studies on the reversible extrusion process for metals. Therefore, in this paper, a study on determining the relationships between forming force and parameters including coefficient of friction, pressing depth, and pressing speed for lead materials is presented. The results show the impact of each parameter on product quality in the reversible extruding process. A comparison of simulation and experiment is made to indicate the similarity of research results.

## 2 Research Objects and Objectives

The object studied is a cylindrical part with holes at both ends as shown in Fig. 1. Due to the limitation of hot forming test conditions, the material selected for use in this study is lead.

According to the working principle and extrusion theory studied above, the mold and the workpiece are assembled as shown in Fig. 2.

The workpiece material used is lead. Lead is a bright blue metal with a face-centered cubic lattice pattern. Lead belongs to the group of heavy non-ferrous metals, atomic mass of 207.19; density of 11.34 g/cm<sup>3</sup>. The melting point is low (327.4 °C) while the boiling point is high (1740 °C).

Pressing force is one of the main technological parameters in metal forming technology. This parameter determines the shape and accuracy of the product. Therefore, the objective of this study is to determine the relationship between parameters such as coefficient of friction, pressing speed, roll angle in the mold, pressing stroke and pressing force.

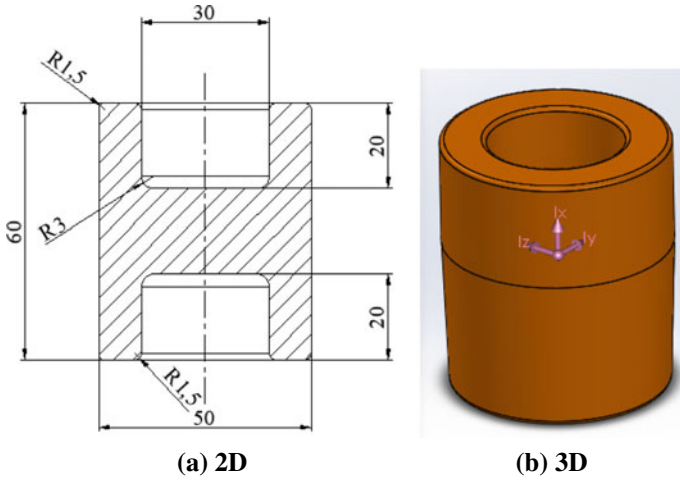
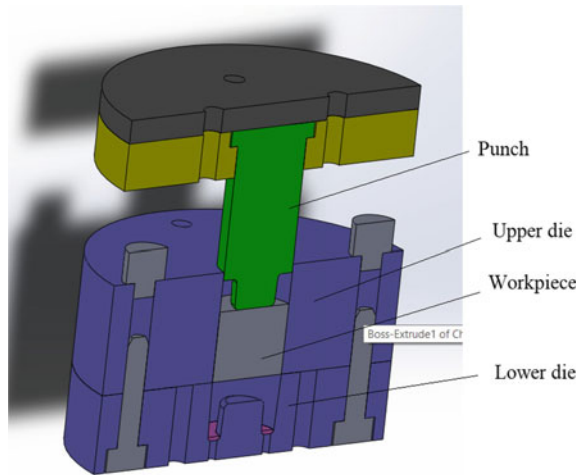


Fig. 1 Research product

Fig. 2. 3D model of the die

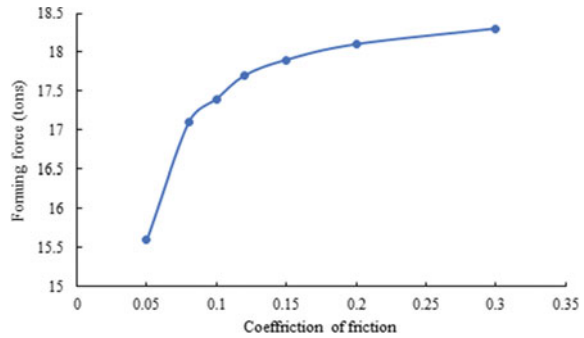


### 3 Results and Discussion

The software used in investigating impacts of various factors on the forming force that greatly affects the quality of the product is the specialized software Deform.



**Fig. 3** Diagram of dependence of forming force on coefficient of friction



### ***3.1 Effect of Coefficient of Friction on Forming Force***

To investigate the influence of friction on forming force, the given input parameters include pressing speed of 8 mm/s, workpiece temperature of 20 °C and pressing depth of 20 mm. The coefficient of friction is changed respectively of (0.05; 0.08; 0.1; 0.12; 0.15; 0.2; 0.3).

The results of the study on the influence of the coefficient of friction in the H-cup extrusion process are shown in Fig. 3.

The metal deforms according to the principle of minimal resistance. According to this principle, when the resistance caused by friction increases, it will hinder the deformation of the workpiece. From the graph, when the friction increases (from 0.05 to 0.3), the forming force also raises significantly. This is consistent with the theory plastic forming.

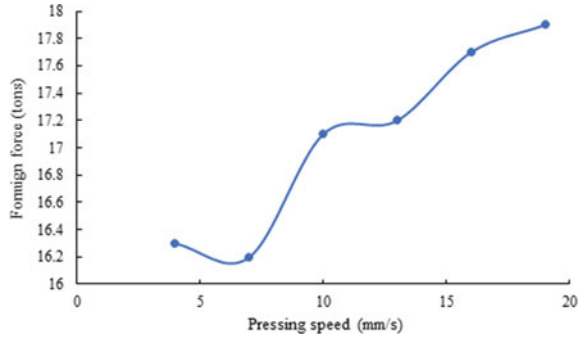
### ***3.2 Effect of Pressing Speed on Forming Force***

Based on the equipment that can be tested later, the pressing speed is changed respectively of (4; 7; 10; 13; 16; 19) mm/s. The input parameters of the survey include workpiece temperature of 20 °C, pressing depth of 20 mm, and coefficient of friction of 0.08.

Pressing speed is also an important factor affecting the calculation and selection of the machine. Large pressing speed will result in a large strain rate. The results of the study on the effect of pressing speed in the H-cup extrusion process are presented in Fig. 4.

The obtained simulation results agree with the initial assumptions. Figure 4 shows that the force changed significantly, from 16.3 to 17.9 tons when changing the pressing speed from 4 to 19 mm/s.

**Fig. 4** Effect of pressing speed on forming force



### 3.3 Effect of Pressing Depth on Forming Force

Pressing depth indicates the deformation ability of the material, from which the pressing stroke can be designed, and the forming force can be calculated. The given input parameters include workpiece temperature of 20 °C, pressing speed of 8 mm/s, coefficient of friction of 0.08. The surveyed pressing depth is (15; 18; 21; 24; 27; 30) mm/s respectively.

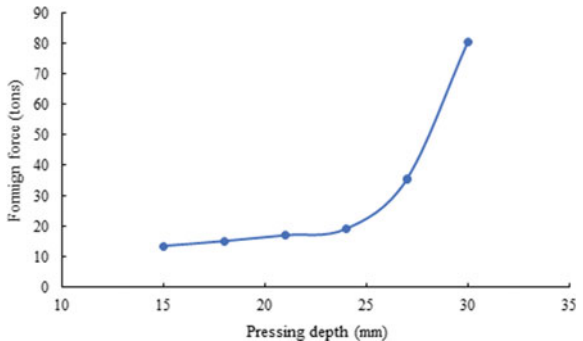
The results of studying the effect of pressing depth in the H-cup extrusion process are shown in Fig. 5.

Figure 5 shows that the larger the stroke is, the greater the force is. Especially, when the amount of pressing depth reaches a large value, the pressure suddenly increases (up to 80.5 tons at a depth of 30 mm). This shows that it is not possible to press the workpiece with too much depth because it will affect the die structure as well as the machine’s ability to generate loads.

After investigating some factors affecting the forming force, the values of the optimal set of parameters are set as follows: pressing speed is 8 mm/s, pressing depth is 20 mm, the coefficient of friction is 0.08.

The simulation results with the optimal set of input parameters are shown in Fig. 6.

**Fig. 5** Effect of pressing depth on forming force



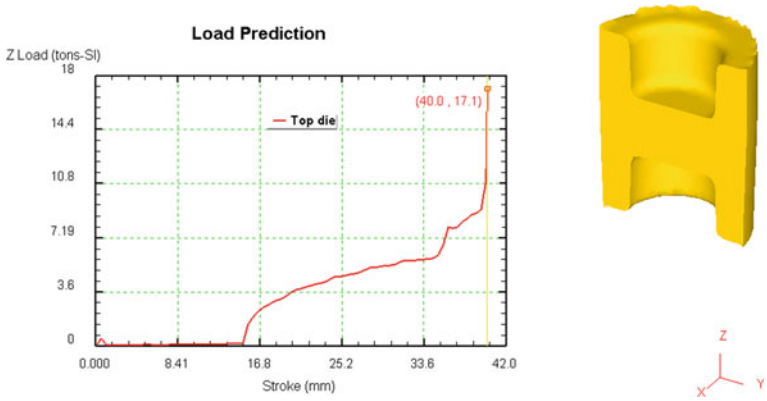


Fig. 6 Force diagram in the process of extrusion a cup H



Fig. 7 The experimental results

Experimenting with the optimal set of parameters found by numerical simulation, the results show a high similarity with the simulation results as shown in Fig. 7.

Experimental results show that the reverse extrusion is easier to shape than the forward-flow extrusion. On one hand, the reason is that the mold does not have a gas outlet below, so it is more difficult for the workpiece to flow in the forward direction. On the other hand, there is a gap between the punch and the die in the opposite direction, so the workpiece is easier to shape up.

## 4 Conclusions

This paper presents the study on the reversible pressing process of H cup with the lead material. The study achieves the following main results:

- Evaluate the influence of parameters including coefficient of friction, pressing speed, pressing depth on the extrusion pressing process by simulation method. Build a graph of the relationship of each surveyed parameter to the forming force.

- Find the optimal set of technological parameters to facilitate the experimental process.
- Experimental results have a high similarity with simulation results.

The research results are meaningful in evaluating the extrusion process and in designing the mold, to achieve the optimal product. However, to accurately evaluate and stabilize the forming process, further studies on other geometrical and technological parameters need conducting.

**Acknowledgements** This research was funded by Hanoi University of Science and Technology (HUST) under project number T2022-PC-019.

## References

1. Kačmarčík I, Movrin D, Ivanišević A (2011) One contribution to the friction investigation in bulk metal forming. *J Technol Plasticity* 36(1):35–48. <https://doi.org/10.2478/v10211-011-0001-4>
2. Dewang Y, Sharma V (2021) Effect of process parameters on thermo-mechanical behavior of extrusion of aluminum alloy. *Iranian J Mater Sci Eng* 18(1). <https://doi.org/10.22068/ijmse.18.1.3>
3. Choi B-J, Moon IY, Oh Y-S, Kang S-H, Kim S-J, Jung J, Kim J-H, Kim D-K, Lee HW (2021) Die design for extrusion process of titanium seamless tube using finite element analysis. *Metals* 11:1338. <https://doi.org/10.3390/met11091338>
4. Lechner S, Nitschke R, Muller S (2021) Numerical analysis of plastic die deformation during high temperature copper extrusion. In: *ESAFORM 2021: proceedings of the 24th international conference on material forming MS03*. <https://doi.org/10.25518/ESAFORM21.4785>
5. Wang Q, Zhang Z, Yu J, Xue Y (2017) A novel backward extrusion process through rotating die and open punch. *Procedia Eng* 207:383–388. <https://doi.org/10.1016/j.proeng.2017.10.792>

# Calculating the Inherent Strain in 3D Printed Part Based on the Heat Affected Zone



Ngoc-Hien Tran and Thai-Son Nguyen

**Abstract** Today, 3D printing technology has been applied in industrial applications. However, improving the quality of printed products is still an issue that needs to be studied for this technology to be used more widely. This research proposes the calculation of the inherent strain (IS) value based on the heat affected zone (HAZ). Then, the IS values are used for calculating the deformation of the printed part. HAZ depends on the printing process parameters and material properties. This paper presents method to calculate the HAZ in different plans according to the printing process parameters for printing Ti6Al4V with selective laser melting (SLM) printing method.

**Keywords** Additive manufacturing · Metal printing · Inherent strain · Heat affected zone · Deformation

## 1 Introduction

3D printing is used widely in the manufacturing industry because of its advantage. It is applied in aerospace, biomedical, automotive, etc. The 3D printing process can be divided into two groups such as powder spreading and powder spraying method. Selective laser melting (SLM) is a powder spreading method using a laser source to melt a thin powder layer. SLM is developed in 1995 by German scientists [1].

---

N.-H. Tran (✉)

Faculty of Mechanical Engineering, University of Transport and Communications, Hanoi, Vietnam

e-mail: [tranhien.tkm@utc.edu.vn](mailto:tranhien.tkm@utc.edu.vn)

T.-S. Nguyen

Center for Transport Science and Technology, University of Transport and Communications, Hanoi, Vietnam

**Fig. 1** Model of SLM printing process

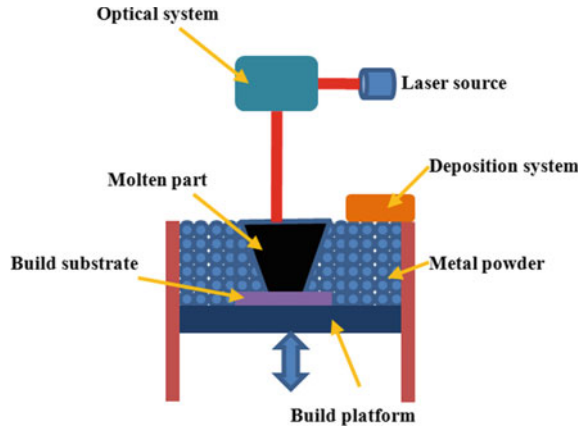


Figure 1 shows the SLM process. During the SLM process, a product is formed by selectively melting layers of powder using a laser beam. The powder is heated and melted to form a liquid pool. Then the molten pool solidifies and cools down and starts to form the product. The building platform is lowered by the amount of layer thickness and a new layer is deposited. The process is repeated until the product is made. Because of its ability to heat and cool rapidly, the SLM is used commonly. However, several defects usually exist in an SLM part, such as part distortion and cracks. The printed parts are affected by key influence factors such as powder properties, printing process parameters, and machine characteristics.

To obtain the best quality in a printed part, key influence factors must be considered. However, during the SLM process, large thermal gradients and fast cooling exist that cause residual stress, which leads to a loss of part shape and other failures of the SLM part. The failure quality of parts results in manufacturing costs, as well as waste and scrap [2]. Therefore, all requirements and predictions for the process need to be fulfilled at the design stage to reduce failure and increase accuracy. To predict the quality at the design stage, a computational simulation is the best choice.

According to the previous research on this, the current methods to reduce deformation include [1, 2]:

- Experiment: Achieve printing experiments to resolve the relationship between the printing parameters and deformation.
- Simulation: Analysis to complete the residual stress and then predict the deformation.

The contribution of this research is to suggest the deformation calculation based on the inherent strain (IS) value. The IS values in x, y, z directions are determined by the heat-affected zone (HAZ). HAZ depends on the printing process parameters and material properties. This paper presents a method to calculate the HAZ in different plans according to various printing process parameters using Ti6Al4V alloy material with selective laser melting (SLM) printing method.

## 2 Calculation of Inherent Strain

Inherent strain resulting from welding is a combination of thermal strains  $\varepsilon_{thermal}$ , phase transfer strain  $\varepsilon_{phase}$ , plastic strains  $\varepsilon_{plastic}$  and creep strain  $\varepsilon_{creep}$  [3, 4].

In SLM printing process, the total strain is calculated as follows:

$$\varepsilon_{total} = \varepsilon_{elastic} + \varepsilon^* \quad (1)$$

in which  $\varepsilon_{elastic}$  is the elastic strain;  $\varepsilon^*$  is the inherent strain.

The  $\varepsilon^*$  value is calculated by considering other strains as follows:

$$\varepsilon^* = \varepsilon_{thermal} + \varepsilon_{plastic} + \varepsilon_{phase} + \varepsilon_{creep} \quad (2)$$

During heating and cooling process, at the plastic stage the IS value in x, y, z directions can be defined as follows [5]:

$$\varepsilon_x^* = \frac{W_x}{F_x}; \varepsilon_y^* = \frac{W_y}{F_y}; \varepsilon_z^* = \frac{W_z}{F_z} \quad (3)$$

In which  $F_x$ ,  $F_y$ , and  $F_z$  are the heat effected zone (HAZ) areas where  $W_x$ ,  $W_y$ , and  $W_z$ , respectively, are distributed.  $W_x$ ,  $W_y$ , and  $W_z$  are calculated as follows:

$$W_x = \xi \cdot q_v; W_y = W_z = K \cdot q_v \quad (4)$$

In which  $q_v$  is the linear energy density (J/mm) [6]:

$$q_v = \frac{Q_{heatsource}}{u} \quad (5)$$

$\xi$  and  $K$  (mm/J) values are used from the welding process due to the same heating and cooling process.

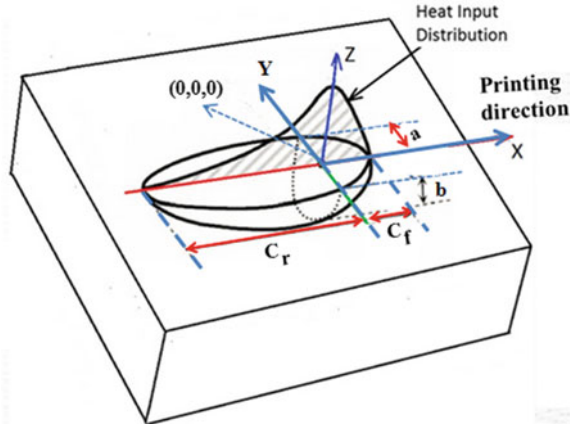
## 3 Numerical Model for SLM Process

For determining the temperature distribution during SLM process, the mathematical model of the heat transfer is as follows [7]:

$$\rho C \frac{\partial T}{\partial t} + \rho C u \nabla T = \nabla(k \nabla T) + Q_{heatsource} \quad (6)$$

in which  $T$  is temperature;  $\rho$ ,  $C$ ,  $k$ , and  $u$  are density, thermal capacity, thermal conductivity factor and laser velocity, respectively.  $Q$  is defined as follows:

**Fig. 2** The Goldak’s heat source model



$$Q_{heatsource} = Q_{requiredpower} + Q_{conduction} \tag{7}$$

$$Q_{requiredpower} = Q_{deliveredlaser} - Q_{convection} - Q_{radiation} - Q_{conduction}$$

$$Q_{deliveredlaser} = Q \frac{6\sqrt{3}}{ab\pi\sqrt{\pi}} e^{\left[\frac{-3z^2}{a^2} + \frac{-3y^2}{b^2}\right]} \left[ \frac{f_f}{C_f} e^{\frac{-3x^2}{c_f^2}} + \frac{f_r}{C_r} e^{\frac{-3x^2}{c_r^2}} \right]$$

The power distribution is given by the moving Goldak’s double-ellipsoid heat source model as shown in Fig. 2 [8]. The model parameters are explained in Table 1.

### 4 Results and Discussion

To determine the HAZ during the SLM process, we use the data from Table 1 as the input data using Comsol tool. Figures 3, 4 and 5 show the method to calculate the HAZ in F<sub>x</sub>, F<sub>y</sub>, F<sub>z</sub> plans.

$$F_x = (x + e).d - e.c \tag{8}$$

With  $d = 0.153$  mm;  $c = 0.09$  mm;  $e = 1.97$  mm; and  $x = 2.34$  mm, we have  $F_x = 0.482$  mm<sup>2</sup>. With  $\xi = 1.57 \cdot 10^{-3}$  mm<sup>3</sup>/J;  $q_v/h^2 = 104.52$  J/mm<sup>3</sup> for Ti6Al4V and  $h = 0.045$  mm, we have:

$$\varepsilon_{inh-x} = -0.000937$$

$$F_y = 2(x + e).(a + b) - 2a.e \tag{9}$$



**Table 1** SLM process parameters for Ti6Al4V material

Name	Description	Value
$x_0$	X-start coordinate	0 (mm)
$y_0$	Y-start coordinate	0 (mm)
$Q$	Laser power from machine	140 (W)
$a$	Ellipsoid length in y axis	0.4205 (mm)
$b$	Ellipsoid length in z axis	0.1682 (mm)
$c_f$	Front ellipsoid length in x axis	0.4205 (mm)
$c_r$	Rear ellipsoid length in x axis	0.84 (mm)
$f_f$	Coefficient of heat source in the front ellipsoid	2/3
$f_r$	Coefficient of heat source in the rear ellipsoid	4/3
$u$	Printing speed	1300 (mm/s)
$C$	Thermal capacity	$500 \times 10^{-3}$ (J/(g.K))
$\lambda$	Thermal conductivity factor	$19.4 \times 10^{-3}$ [W/(mm.K)]
$T_a$	Ambient temperature	293 (K)
$h_c$	Convective and (W/mm <sup>2</sup> .K)	186.3 [W/(mm <sup>2</sup> .K)]
$h_r$	Radiant heat transfer coefficient	4.4 [W/(mm <sup>2</sup> .K)]
$h$	Layer thickness	0.045 (mm)
$Ha$	Hatch distance	0.07 (mm)

**Fig. 3** Calculation of the HAZ in Fx plane

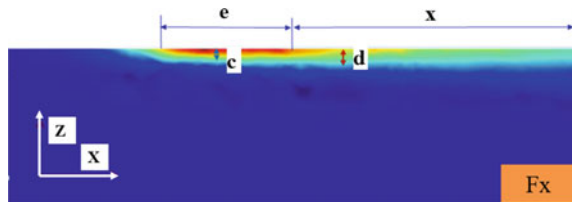
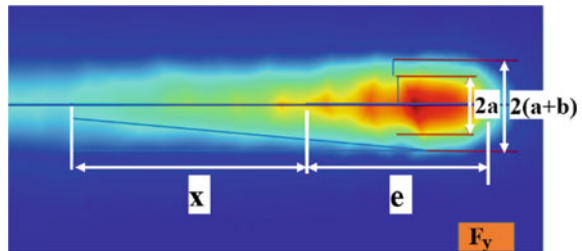


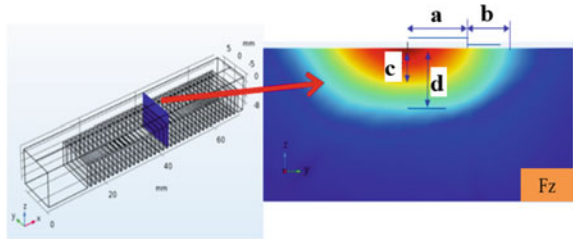
**Fig. 4** Calculation of the HAZ in Fy plane



With  $a = 0.19$  mm;  $b = 0.102$  mm;  $e = 1.97$  mm; and  $x = 2.34$  mm, we have  $F_y = 1.275$  mm<sup>2</sup>.

With  $K = 0.58 \cdot 10^{-3}$  mm<sup>3</sup>/J;  $q_v/h^2 = 104.52$  J/mm<sup>3</sup> for Ti6Al4V and  $h = 0.045$  mm, we have:

**Fig. 5** Calculation of the HAZ in Fz plane



$$\varepsilon_{inh-y} = -0.0000963$$

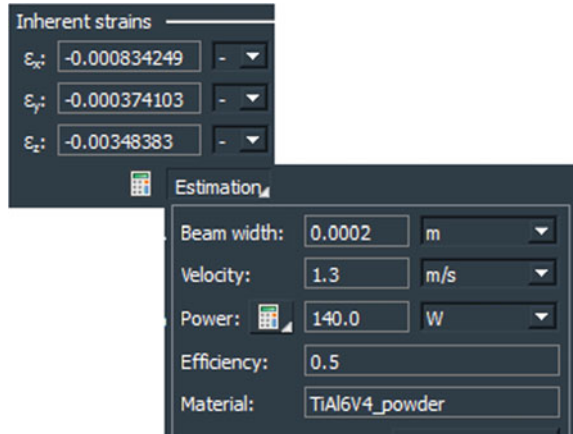
$$F_z = 2[(a + b).d - a.c] \tag{10}$$

$a = 0.19$  mm;  $b = 0.106$  mm;  $d = 0.153$  mm; and  $c = 0.09$  mm, we have  $F_z = 0.0564$  mm<sup>2</sup>. With  $K = 0.58 \cdot 10^{-3}$  mm<sup>3</sup>/J;  $q_v/h^2 = 104.52$  J/mm<sup>3</sup> for Ti6Al4V and  $h = 0.045$  mm, we have:

$$\varepsilon_{inh-z} = -0.00217$$

With the same processing parameters such as the beam width, velocity, power, and material, we used Simufact™ tool for predicting the inherent strain. The predicted results are shown in Fig. 6. In comparison with the proposed method, the biggest IS value is in the Z direction, this is correct for both simulation and experiment [2, 7].

**Fig. 6** Calculation of the inherent strain by using Simufact



## 5 Conclusions

In this study, we propose to calculate IS value based on printing process parameters and HAZ area. To calculate the HAZ area during SLM printing process, the heat transfer equation was established. Then, Comsol™ was used to determine the temperature distribution in the printed part. From the temperature distribution, the HAZ surfaces were calculated. The IS values are used to calculate the deformation of the printed part in all directions. From that, the reasonable printing process parameters are determined to reduce distortion when carrying out the actual printing process. The proposed IS calculation results are reliable when compared with the IS values calculated by Simufact™ software under the same conditions and printing method.

## References

1. Schoinochoritis B, Chantzis D, Salonitis K (2015) Simulation of metallic powder bed additive manufacturing processes with the finite element method: a critical review. *Proc IMechE Part B: J Eng Manuf* 231:96–117
2. Setien I, Chiumenti M, Veen S, Sebastian MS, Garcíandía F, Echeverría A (2019) Empirical methodology to determine inherent strains in additive manufacturing. *Comput Math Appl* 78:2282–2295
3. Shokrieh MM, Jalili SM, Kamangar MA (2018) An eigen-strain approach on the estimation of non-uniform residual stress distribution using incremental hole-drilling and slitting techniques. *Int J Mech Sci* 148:383–392
4. Wang J, Ma N, Murakawa H (2015) An efficient FE computation for predicting welding induced buckling in production of ship panel structure. *Mar Struct* 41:20–52
5. Chen J, Lu H, Wang J, Chen W, Hao D (2000) Prediction of welding deformation with inherent strain method based on FEM, Shanghai Huizhong Automotive Manufacturing Co. LTD report
6. Donik Č, Kraner J, Paulin I, Godec M (2020) Influence of the energy density for selective laser melting on the microstructure and mechanical properties of stainless steel. *Metals* 10:919
7. Roberts IA (2012) Investigation of residual stresses in the laser melting of metal powders in additive layer manufacturing. Dissertation, University of Wolverhampton
8. Samad Z, Nor NM, Fauzi ERI (2019) Thermo-mechanical simulation of temperature distribution and prediction of heat-affected zone size in MIG welding process on aluminium alloy EN AW 6082-T6. *IOP Conf Ser: Mater Sci Eng* 530

# Numerical Investigation of Heat Transfer Characteristics of Ribs with Trenches in Gas Turbine Internal Cooling Channel



Tuong-Linh Nha, Khanh-Duy Cong Do, Van-Thuc Tran, Viet-Dung Duong, Sung-Goon Park, and Cong-Truong Dinh

**Abstract** In this work, several trenches are placed in the ribs to reduce disadvantages of square ribs. These configurations open up some small extra passages for the coolant to remove the local vortices. Furthermore, the remained square pillars of the ribs act like pin-fins which promote horseshoe vortices. These vortices significantly enhance the heat transfer capability in the junction of pillars and endwall. To investigate the effect of trenches number and shape on the heat transfer capacity of the channel and flow characteristics, a parametric study of ribs with trenches is performed using RANS equations with the SST turbulence model. Furthermore, the staggered and in-line arrangements of ditches are studied. It is concluded that the staggered trenches show a higher Nusselt number than the in-line arrangement, but it comes with a higher friction factor. The parametric study resulted in a higher heat transfer efficiency index (HTEI) of the new designs than the square ribs. At  $Re = 26,500$ , the Nusselt number of 3 trenches with staggered arrangement increases by 41.9%. Moreover, a slight increase in friction factor combines with that to form a 31.9% increase in the overall Heat transfer efficiency index. The designs of 3 trenches with in-line arrangement come with a slight increase of 13.7% in Nusselt number; a decrease in friction factor of this design forms a 16.4% increase in Heat transfer efficiency index compared to the case of the original ribs.

---

T.-L. Nha (✉) · K.-D. C. Do · V.-T. Tran · C.-T. Dinh  
Ha Noi University of Science and Technology, No. 1, Dai Co Viet Road, Hai Ba Trung District,  
Hanoi 10000, Vietnam  
e-mail: [linh.nhatuong@hust.edu.vn](mailto:linh.nhatuong@hust.edu.vn)

V.-D. Duong  
School of Aerospace Engineering, Vietnam National University, University of Engineering and  
Technology, Hanoi City, Vietnam

S.-G. Park  
Department of Mechanical Engineering and Automotive Engineering, Seoul National University  
of Science and Technology, No 232 Gongreung-Ro, Nowon-Gu, Seoul, Korea

**Keywords** Heat transfer characteristics · Ribs with trenches · RANS analysis · Internal cooling

## 1 Introduction

By avoiding the blending of cooling air and hot gas coming from the combustor, the internal cooling method, which includes three main forms, i.e., impinging jet cooling, rib turbulators cooling [1], and pin-fins cooling, provides a more reliable turbine's aerodynamic performance. The rib turbulators, which can enhance local turbulence due to flow separation and confluence in turbine blade serpentine channels, are the subject of research in this paper. Pham et al. [2] studied the influence of rib profiles on the HTEI and the obtained results showed that the HTEI changed significantly when changing the rib profiles. Another study by Dinh et al. [3] investigated a clearance height of 20% compared to the height of the ribs yields the highest HTEI. For cooling channel, the different cooling gases produce different heat transfer characteristics. Shi et al. [4] studied experimentally the differences between steam and air used in a cooling channel with different angled ribs. They found that when steam is used as a coolant of gas turbine internal cooling passage, heat transfer is enhanced significantly.

Besides ribs, pin-fin is another type of structure that promotes turbulence in the cooling cascade of the channel. Do et al. [5] studied the effect of endwall on enlarging the size of high heat transfer region and reducing the low heat transfer regions in channel with pin-fins. Won et al. [6] studied the distribution of heat transfer coefficient in a cooling channel with multiple rows of pin-fins. Based on the results of Shi et al. [4] of the channel with 90° ribs, this work investigated the effects of trenches on the heat transfer characteristics of channels.

## 2 Numerical Methodology

### 2.1 Description of Geometry

The computational domain was constructed based on the experimental model of Shi et al. [4] as shown in Fig. 1. The testing sample of Shi et al. [4] consists of three channels: the development, the heated, and the output, where 12 ribs are attached to the heated channel. The height and sample width of the tested channel are  $W = 80$  mm and  $H_s = 20$  mm, respectively, and the top surface of the channel is specified as symmetry to simplify the channel. Hence, the real height of the total channel is  $H = 40$  mm. The cross-section of the computed domain is a rectangle with the aspect ratio  $AR = W/H = 80/40 = 2$ . The equivalent diameter of the channel,  $D_h = 2HW/(H + W)$  is 53.3 mm. The direction of the flow corresponds to the direction of the x-axis. The detailed dimensions of the design model are given in Table 1. The total length

of the calculated domain is  $L_t = 600$  mm. Table 1 describes the design variables of the tested channel.

The number of trenches varies from three to five with in-line and staggered arrangements. The trenches were distributed evenly on the y-direction of ribs in the channel, spread from the middle of the channel for the opposition. The number of trenches will vary from 3 to 5 trenches a rib. Figure 2 illustrates specifically the overview of ribs with trenches of in-line and staggered arrangements.

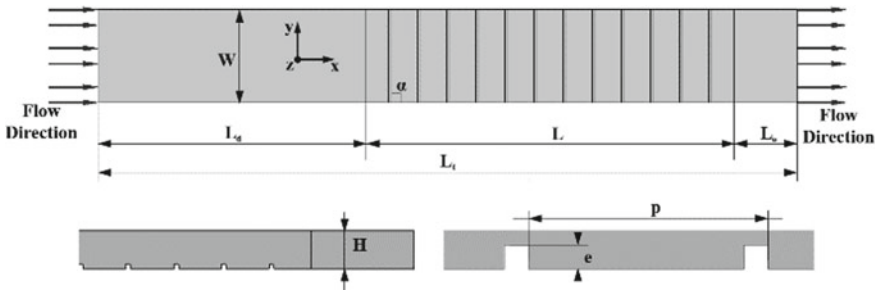


Fig. 1 Schematic diagram of geometric configurations

Table 1 Variables of geometric configurations

Variable	Value	Variable	Value
$W$ (mm) $\times$ $H_s$ (mm)	$80 \times 20$	$\alpha$	$90^\circ$
$e$ (mm)	2.5	$L_d$ (mm)	230
$p$ (mm)	25	$L$ (mm)	316
$D_h$ (mm)	53.33	$L_o$ (mm)	54

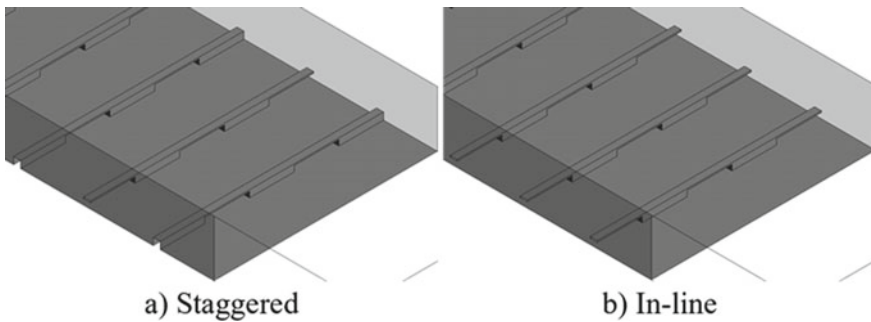


Fig. 2 Sample of design arrangements for trenches

## 2.2 Data Reduction

The Reynolds number (Re) of the channel is defined as:

$$Re = \frac{\rho u D_h}{\mu} \quad (1)$$

where  $u$  is the inlet velocity of the channel;  $\rho$  is the air density,  $D_h$  and  $\mu$  are the channel hydraulic diameter and dynamic viscosity of the coolant, respectively.

The local heat transfer coefficient ( $h$ ) of the heated surfaces is determined by:

$$h = \frac{q}{T_w - T_b} \quad (2)$$

where  $q$  is the heat flux of the heated wall,  $T_w$  is wall temperature, and  $T_b$  is the bulk temperature of the fluid.

The local Nusselt number (Nu) is used to represent the local heat transfer capacity, which can be written as:

$$Nu = \frac{h D_h}{\lambda} \quad (3)$$

where  $\lambda$  is the thermal conductivity of coolant fluid.

According to the correlation formula of Dittus-Boelter [7], the Nusselt number ( $Nu_0$ ) and friction factor for fully developed turbulent flow in a smooth channel of a rectangular cross-section is defined as:

$$Nu_0 = 0.023 \cdot Re^{0.8} Pr^{0.4} \quad (4)$$

$$f_0 = [1.58 \ln(Re) - 3.28]^{-2} \quad (5)$$

The friction factor which represents the pressure loss of the channel is defined as:

$$f = \frac{\Delta P D_h}{2 \rho \Delta L u^2} \quad (6)$$

The heat transfer efficiency index ( $\eta$ ) is defined as:

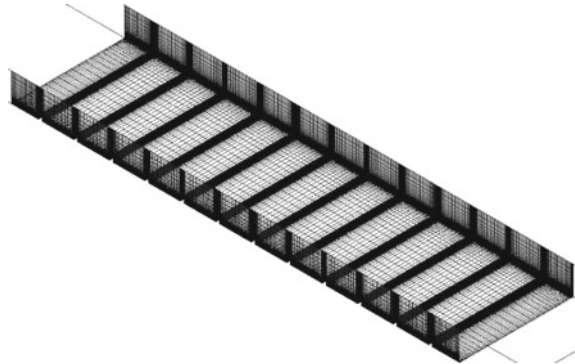
$$\eta = \left( \frac{Nu}{Nu_0} \right) / \left( \frac{f}{f_0} \right)^{1/3} \quad (7)$$

### 2.3 Numerical Analysis

In the present study, the governing differential equations are solved numerically to study the flow characteristics and heat transfer in the channel with pin-fins using the commercial software Ansys CFX<sup>®</sup> 19.1 [8]. The SST turbulence model is used for all the simulations throughout the work. This work uses the structured grid divided in ANSYS-ICEM<sup>®</sup> software. The elements adjacent to the wall and the pin-fins are specified with a height of  $5 \times 10^{-6}$  (m) to satisfy a  $y^+$  value less than 1 for the entire Reynolds number range, to fit the criteria of the turbulence model. The structural grid shown in Fig. 3 is created using hexahedral elements. The test grid will be used for Reynolds 53,648, and the number of grids will vary from 1.0 million to 11.5 million.

The boundary conditions adopted here are used the same as the Ref. [4] as shown in Fig. 4. The fluid was set as steam (IAPWS-97). The walls both in the entrance and in the outlet section are specified as adiabatic. A uniform heat flux of  $5000 \text{ W/m}^2$  is allocated at the ribbed surfaces and the two sides of smooth walls. The reference pressure of the computational domain and the inlet temperature of steam flow was 0.3 MPa and 447 K, respectively. The outlet was subject to static pressure of 0 Pa. The mass flow rate was given at the inlet according to the corresponding Reynolds numbers ranging from 9098 to 53,648. A turbulence intensity of 5% was given at the inlet. The walls of the channels were applied as the no-slip boundary condition.

**Fig. 3** Sample of mesh structure





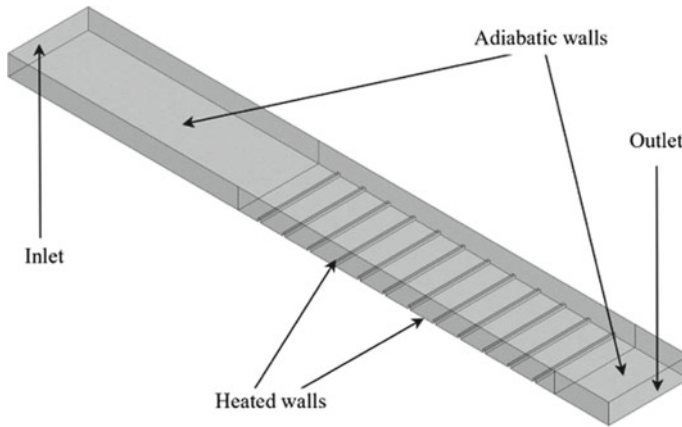


Fig. 4 Boundary conditions

### 3 Results and Discussion

#### 3.1 Grid Independence Test and Validation of Numerical Results

A grid independence test has been conducted by using the SST  $k-\omega$  model at  $Re = 53,648$  with mesh numbers ranging from 1 to 11.5 million. The grid convergence index (GCI) based on the Richardson extrapolation method was analyzed to evaluate the convergence of the grid system used in this study. Table 2 lists the results of the GCI analysis for the channel with ribs. In Fig. 5, the Nusselt number increase when decreasing the normalized grid spacing. It is shown that the Nusselt number is converging to the value of extrapolation by Richardson's method. Grid 2 was selected for further computation.

In order to validate the SST  $k-\omega$  model, a comparison of numerical and experimental results of averaged Nusselt number distribution on the heated walls for three Reynolds numbers (9098, 26,587, 53,648) is shown in Fig. 6, where the boundary conditions are also in accordance with the experimental investigations [4]. The averaged Nu numbers on the heated walls for  $Re = 9098$ , 26,587, and 53,648 are 0.03%, 3.09%, and 8.09% higher than that of experimental data. This is partly because the uncertainty of 8.5% exists in the experimental system. Therefore, the numerical deviations are acceptable.

**Fig. 5** Comparison of investigated mesh with Richardson extrapolation

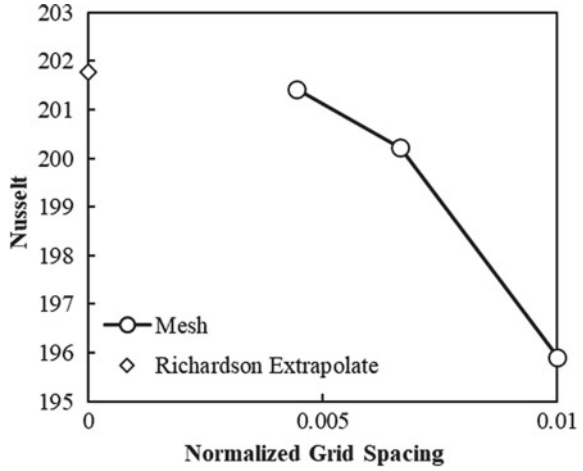


**Fig. 6** Comparison of experimental and numerical data with  $Re = 53,648$

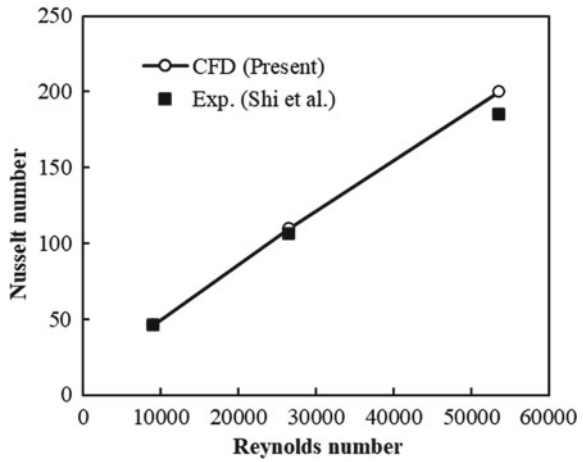


**Table 2** Results of analysis of grid convergence

Parameter	Symbol	Value
Numbers of elements (milliin cells)	Grid 1/Grid 2/Grid 3	11.5/3.4/1.0
Grid refinements factors	$r_{21}/r_{32}$	1.50/1.50
Normalized grid spacing	$h_1/h_2/h_3$	0.0100/0.0067/0.0044
Nusselt number corresponding to Grid 1/Grid 2/Grid 3	$Nu_1/Nu_2/Nu_3$	201.429/200.223/195.912
Apparent order	$p$	3.12
Extrapolated value	$\phi_{ext}^{21}$	201.9023
Approximated relative error	$e_a^{21}$	0.60%
Extrapolated relative error	$e_{ext}^{21}$	0.23
Grid convergence index	$GCI_{fine}^{21}$	0.29

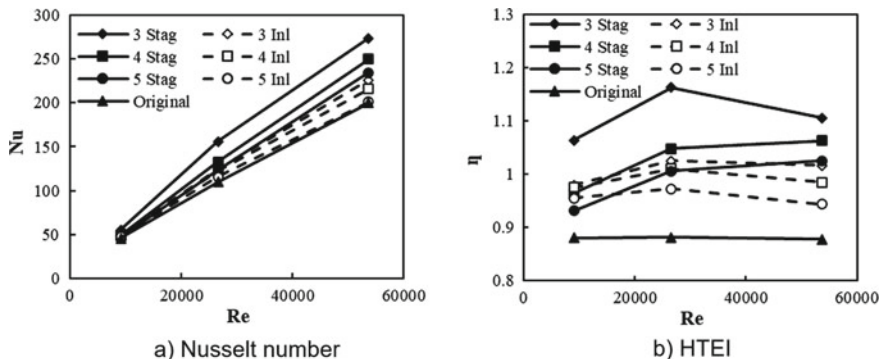


Fig. 8 Comparisons of Nu and  $\eta$  with all cases

### 3.2 Effect of Ribs with Trenches on Convective Heat Transfer

Figure 8 shows the comparison of Nu, and  $\eta$  with the cases of 3, 4, and 5 trenches with both arrangements. It is discovered that the staggered arrangements induce a higher Nusselt number for all cases compared to the in-line arrangements but accompany by a higher friction factor. The Nusselt number is increased by about 20.1%, 41.9%, and 36.5% for three Re of 9098, 26,587, and 53,648 for the case of 3 trenches with the staggered arrangement and it is increased by 7.9%, 13.7%, and 12.9% for in-line arrangement. Overall, the HTEI of staggered designs is increased by 20.8%, 31.9%, and 26.0% and that of in-line designs show an increase by 11.3%, 16.4%, and 15.8% for all Reynolds number.

## 4 Conclusion

The results show that the trenches open up some extra passages for the flow to destruct the stagnant vortices in front of and behind the ribs and increase the heat transfer characteristics in the heated walls and the ribs. Besides, the staggered arrangement induces a higher Nusselt number than the in-line cases and hence, creates a higher friction factor. However, the increase in Nusselt number is higher than the increase in friction factor and the overall HTEI is increased. The HTEI of staggered designs is increased by 20.8%, 31.9%, and 26.0% compared to the original design for Re = 9098, 26,587, and 53,648, respectively. Besides, the in-line arrangement comes with a maximum increase of 13.7% in the Nusselt number for Re = 26,587. It combines with a decrease of 9.3% in friction factor to form an increase of 16.4% in HTEI.

**Acknowledgements** This study is funded by Hanoi University of Science and Technology (HUST) under grant number T2022-PC-018.

## References

1. Moon MA, Kim KY (2016) Exergetic analysis for optimization of a rotating equilateral triangular cooling channel with staggered square ribs. *Int J Fluid Mach Syst* 9(03):229–236. <https://doi.org/10.5293/IJFMS.2016.9.3.229>
2. Pham KQ, Nguyen QH, Vu TD, Dinh CT (2020) Effects of boot-shaped rib on heat transfer characteristics of internal cooling turbine blades. *J Heat Transf* 142(10):102106. <https://doi.org/10.1115/1.4047490>
3. Dinh CT, Nguyen TM, Vu TD, Park SG, Nguyen QH (2021) Numerical investigation of truncated-root rib on heat transfer performance of internal cooling turbine blades. *Phys Fluids* 33(7). <https://doi.org/10.1063/5.0054149>
4. Shi X, Gao J, Xu L, Li F (2013) Heat transfer efficiency index comparison of steam and air in gas turbine cooling channels with different rib angles. *Heat Mass Transf* 49(11):1577–1586. <https://doi.org/10.1007/s00231-013-1171-6>
5. Do KD, Chung DH, Tran DQ, Dinh CT, Nguyen QH, Kim KY (2022) Numerical investigation of heat transfer characteristics of pin-fins with roughed endwalls in gas turbine blade internal cooling channels. *Int J Heat Mass Transfer* 195:123125. <https://doi.org/10.1016/j.ijheatmasstransfer.2022.123.125>
6. Won SY, Mahmood GI, Ligrani PM (2004) Spatially-resolved heat transfer and flow structure in a rectangular channel with pin fins. *Int J Heat Mass Transf* 47(8–9):1731–1743. <https://doi.org/10.1016/j.ijheatmasstransfer.2003.10.007>
7. Dittus FW, Boelter LMK (1985) Heat transfer in automobile radiators of the tubular type. *Int Commun Heat Mass Transfer* 12(1):3–22. [https://doi.org/10.1016/0735-1933\(85\)90003-x](https://doi.org/10.1016/0735-1933(85)90003-x)
8. ANSYS CFX 19.1 (2018) ANSYS CFX-solver theory guide, ANSYS Inc

# Aerodynamic Performance of Single-Stage Transonic Axial Compressor with Multi-Bleed Airflow



Tuong-Linh Nha, Van-Hoang Nguyen, Xuan-Truong Le,  
and Cong-Truong Dinh

**Abstract** Bleeding air in the axial compressor is a well-known method to take air for cooling treatment in the turbine and provide an atmosphere in the cabin. A most common bleed system which is used in gas turbine engine frequently reduce the efficiency and stall margin of the compressor. This study proposes a new bleed air method, the multi-bleed air method, which is enhanced the efficiency and stall margin of the compressor. The multi-bleed air method contains 36 bleed air channels on the rotor domain's shroud surface. The bleeding system is studied using three different bleed types: single-bleed, double-bleed, and triple-bleed in a single-stage transonic axial compressor, NASA Stage 37. The numerical results demonstrated that the aerodynamic performance of a single-stage transonic axial compressor was improved with the multi-bleed method, including total pressure ratio, adiabatic efficiency, and stall margin compared to the smooth casing case. In addition, the adiabatic efficiency and stall margin increase more in the double-bleed case than in single-bleed and triple-bleed cases.

**Keywords** Single-stage transonic axial compressor · Multi-bleed · 3D-RANS

## 1 Introduction

The tip leakage vortices and their airflow trajectories are the primary sources of aerodynamic performance reduction in axial compressors. Many experimental and numerical studies have been performed to reduce compressor performance reduction. As for the bleeding airflow, a new casing configuration is investigated by Koch and Smith [1], where the airflow is bled from the shroud surface of an axial compressor

---

T.-L. Nha (✉) · V.-H. Nguyen · X.-T. Le · C.-T. Dinh  
School of Mechanical Engineering, Hanoi University of Science and Technology, Hanoi 11615,  
Vietnam  
e-mail: [linh.nhatuong@hust.edu.vn](mailto:linh.nhatuong@hust.edu.vn)

rotor with a  $30^\circ$  bleeding angle of the flow direction to improve the stall range as compared to the smooth casing by reducing the accumulation of endwall blockage. A passive control method of endwall blockage was investigated by Hathaway [2], and the best bleeding positions were between the start of tip leakage flow (40% of rotor chord length) and further blockage aft of leakage (80% of rotor chord length). The effects of axisymmetric bleed slot position on rotor and stator shroud surface in a single-stage subsonic axial compressor were presented by Wellborn and Michael [3], in which the rotor tip bleed position was most effective near the leading and trailing edges. A bleeding air system on a shroud surface downstream of a rotor in a multistage axial compressor of a gas turbine engine was investigated by Ress et al. [4]. The bleedin]g air system with a 3% bleed rate reduced the separated region near the suction surface of the rotor to increase by 1% in efficiency and 5% in stall margin. Dinh et al. [5, 6] presented the effects and optimization of rotor bleeding airflow on aerodynamic performances of a single-stage transonic axial compressor.

In this work, multi-bleed airflow from the rotor shroud surface through 36 bleed air channels and its geometrical design were performed to determine the effect of bleeding airflow on the aerodynamic performance and stability.

## 2 Numerical Analysis

### 2.1 Description of Geometry

To investigate the influences of multi-bleed casing treatments on the aerodynamic performance of the high-speed axial compressor, the transonic axial compressor, NASA Stage 37, was used in this study. The design values of the overall parameters and detailed specifications for NASA Stage 37 were performed by Reid and Moore [7].

Figure 1 illustrates the designs and position of multi-bleed casing treatment in NASA Stage 37. Three different types of bleeding channels along the shroud surface of the rotor domain are presented as “Single-Bleed”, “Double-Bleed”, and “Triple-Bleed”, as shown in Fig. 1c.

### 2.2 Numerical Method

For the aerodynamic analysis, ANSYS CFX 19.1<sup>®</sup> [8] was employed to solve the three-dimensional (3D) RANS equations. As illustrated in Fig. 2, the grid systems contain three regions: rotor, stator, and Multi-Bleed. For steady-state simulation, the boundary condition of the stator outlet was defined as an average static pressure. At the rotor inlet boundary, the turbulence intensity and static frame total temperature were set at 5% and 288.15 K, respectively. No-slip wall, smooth wall, and adiabatic

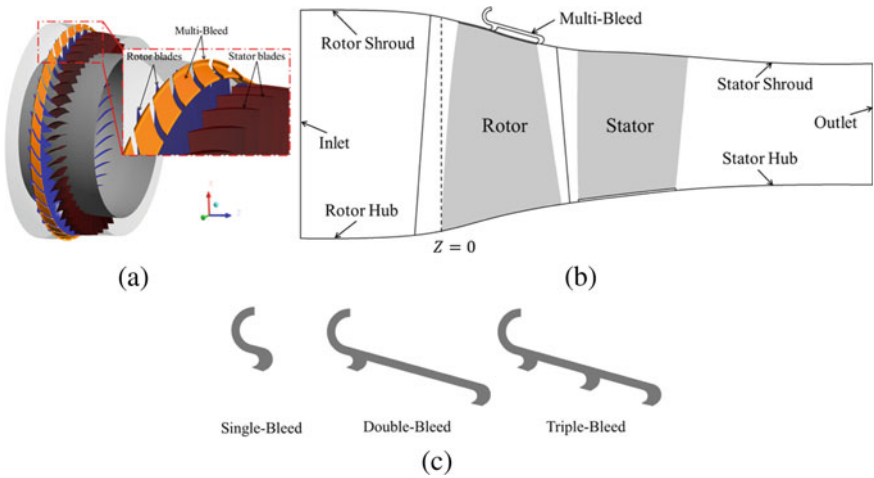


**Fig. 1** Geometry of NASA stage 37 with the multi-bleed: **a** 3D view, **b** meridional view, **c** different types of bleeding channels

were applied to the wall surfaces. For the analysis of the stability and performance of the transonic axial compressor: total pressure ratio (PR), adiabatic efficiency ( $\eta$ ), stall margin (SM), and stable range extension (SRE) [5, 6] were used to evaluate.

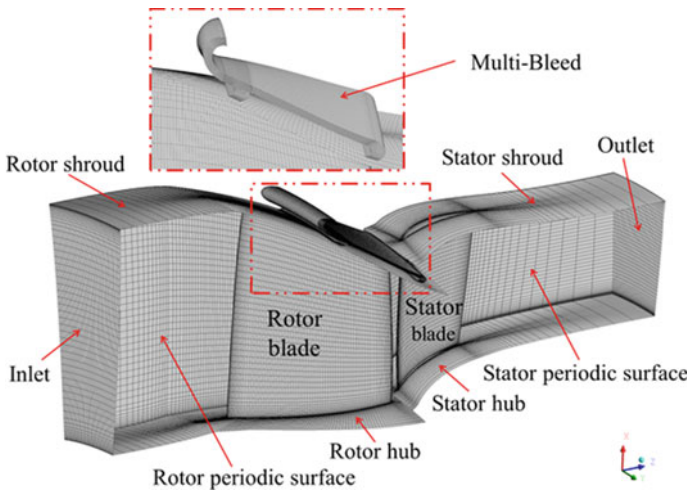


**Fig. 2** Computational domain and mesh structure

**Table 1** Grid dependency test of NASA Stage 37

	Mesh 1	Mesh 2	Mesh 3
Grid number ( $\times 10^6$ )	0.34	0.59	0.91
SM	9.30	9.95	9.99
Deviation of SM (%)	6.99	0.40	–
$\dot{m}_{choke}$	20.96	20.98	20.99
Deviation of $\dot{m}_{choke}$ (%)	0.10	0.05	–
$PR_{dc}$	2.064	2.076	2.077
Deviation $PR_{dc}$ (%)	0.54	0.07	–
$\eta_{dc}$	81.34	82.35	82.50
Deviation of $\eta_{dc}$ (%)	1.24	0.18	–

### 3 Results and Discussion

#### 3.1 Grid Dependency Test and Validation

A grid dependency result of NASA Stage 37 (smooth casing case) is shown in Table 1. The results indicated that the deviation of mass flow rate at choking condition, total pressure ratio, and adiabatic efficiency at design condition are less than 0.2% when the mesh density reaches 0.59–0.91 million nodes. To reduce the computation time as well as increase the accuracy of the results, mesh 2 with 0.59 million nodes was selected for validation and further calculations. In Fig. 3, the numerical model of NASA Stage 37 was validated by comparing with the experiment data [10]. The numerical results presented a good agreement with the experiment data of total pressure ratio and adiabatic efficiency.

#### 3.2 Effect of Multi-Bleed Casing Treatments on Tip Clearance Flow

Figure 4a demonstrates the effects of the Single-Bleed (SB), Double-Bleed (DB), and Triple-Bleed (TB) on the aerodynamic performance of NASA Stage 37, in comparison with the SC case. The results showed that the stall inception was delayed by the operating range enhancement from 0.9385 to 0.9298. In addition, the adiabatic efficiency increased marginally, and the total pressure ratio was slightly reduced. Figure 4b clarifies the operation range extension by comparing the stability and performance of the compressor among four cases: SC, SB, DB, and TB. Additionally, Fig. 4c indicates the gain in adiabatic efficiency are marginal, while the reduction of total pressure ratio is unremarkable in SB, DB, and TB cases. Consequently, the Multi-Bleed in the DB and TB cases improved the stability and aerodynamic performance of the compressor more than the SB.



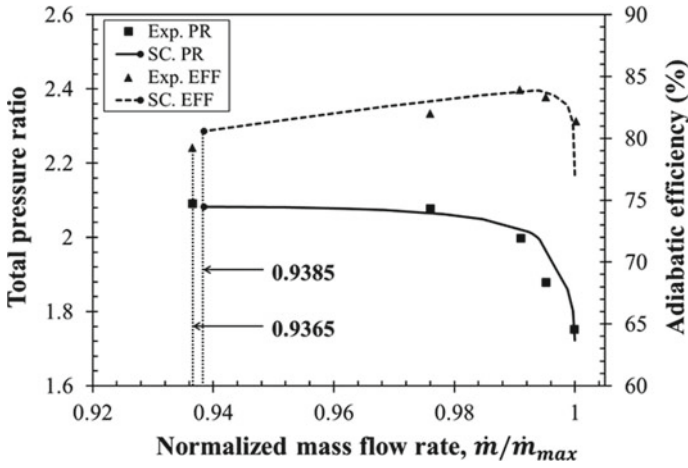


Fig. 3 Numerical validation of NASA Stage 37

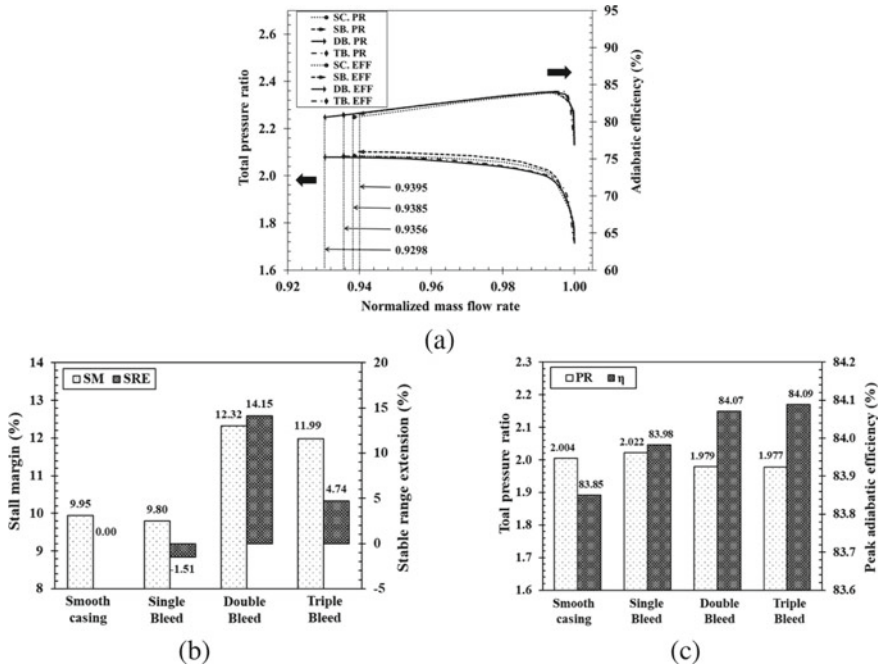
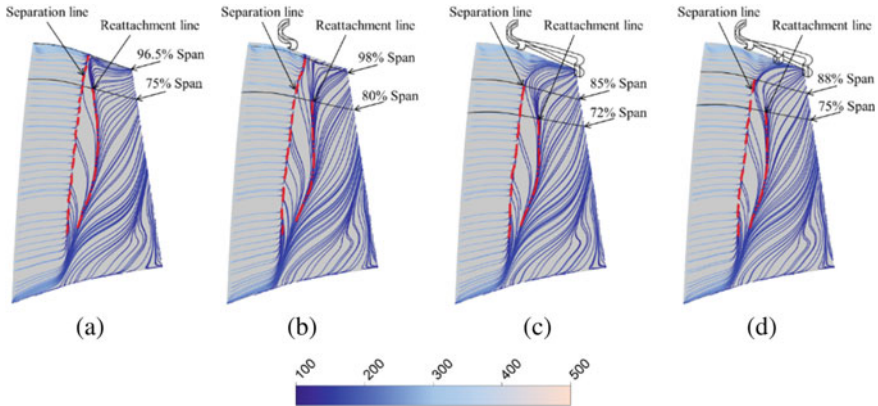


Fig. 4 Influence of multi-bleed casing treatment types on aerodynamic performance in NASA Stage 37: **a** performance curves, **b** SM and SRE, **c** PR and  $\eta$



**Fig. 5** Streamlines near rotor suction surface at near-stall condition: **a** SC, **b** SB, **c** DB, **d** TB

Figure 5 illustrates the streamlines near the suction surface of the rotor at the near-stall condition for the four cases: SC, SB, DB, and TB. As shown in Fig. 5a, the separation line near the mid-chord is pushed backward by the recirculation flow, which appears in the DB and TB cases as shown in Fig. 5c and d, respectively. Moreover, the length of the separation and reattachment line was reduced significantly by 85% and 72% with the DB case, respectively, 88% and 75% with the TB case, respectively, compared with 85% in the SC case. In contrast, the length of the separation and reattachment line reduced slightly (98% and 80%, respectively) compared with the SC case.

Figure 6 shows the relative Mach number contours at 95% span at the near-stall condition for four cases. The low-speed zones are indicated by regions with a Mach number value under 0.6. The low Mach number regions near mid-pitch and around both the pressure side and suction side of the downstream of the blade reduce considerably with applying the SB, DB and TB (Fig. 6b, c, d) compared to SC (Fig. 6a). In addition, the separation after mid-chord occurs on the suction side of the rotor in the SC and SB cases, while the separation is reduced remarkably in the DB and TB cases.

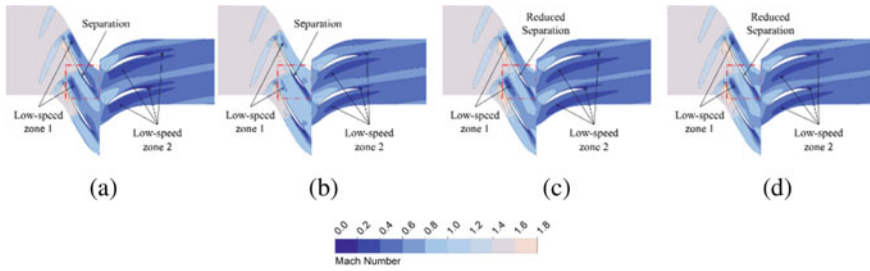


**Fig. 6** Relative Mach number on 95% blade span at near-stall condition in NASA Stage 37: **a** SC, **b** SB, **c** DB, **d** TB

## 4 Conclusion

Aiming to increase the stability of a transonic axial compressor, NASA Stage 37, multi-bleed casing treatments, was numerically investigated using 3D RANS analysis. It was confirmed that the DB and TB cases increased the SM, SRE and efficiency, but slightly decreased the total pressure ratio compared to those of the SC. When compared to SC, the increasement of SM was 2.37% and 2.04%, respectively, and the rise of SRE 14.15% and 4.74%, respectively. With the multi-bleeding channels, the low momentum air would still be reduced significantly from the tip clearance region. Thus, the performance of the compressor was enhanced greatly. Based on this study's results, the geometry of multi-Bleed will be optimized using the multi-objective optimization technique to maximize aerodynamic performances of NASA Stage 37.

**Acknowledgements** This study is funded by Hanoi University of Science and Technology (HUST) under grant number T2022-PC-032. The authors are also grateful to the cooperation between Viettel Aerospace Institute (Vietnam) and Hanoi University of Science and Technology for the support during this research.

## References

1. Koch CC, Smith LH Jr (1968) Experimental evaluation of outer casing blowing or bleeding of single stage axial flow compressor, Part IV—performance of bleed insert configuration no. 3, NASA CR-54590
2. Hathaway MD (2002) Self-recirculating casing treatment concept for enhanced compressor performance. In: Proceedings of the ASME turbo expo 2002, Amsterdam, Netherlands, GT2002-30368
3. Wellborn SR, Michael LK (2002) Bleed flow interactions with an axial-flow compressor power-stream. In: 38th AIAA/ASME/SAE/ASEE joint propulsion conference & exhibit, Indianapolis, Indiana, USA, AIAA Paper 2002-4057
4. Ress RA, Carmel Jr, Hansen JL (2002) Compressor endwall bleed system. U.S. Patent 6,428,271 B1

5. Dinh CT, Vu DQ, Kim KY (2020) Effects of rotor-bleeding airflow on aerodynamic and structural performances of a single-stage transonic axial compressor. *Int J Aeronaut Space Sci* 21(3):599–611
6. Tran DQ, Le XT, Nguyen VH, Dinh CT, Vu TS (2022) Aerodynamic performance optimization of a single-stage axial compressor using circumferential bleeding airflow. *J Aeronaut Astronaut Aviat* 54(4):451–465. ISSN: 1990-7710
7. Reid L, Moore RD (1978) Design and overall performance of four highly loaded, high-speed inlet stages for an advanced high-pressure-ratio core compressor. NASA Technical Paper 1337, Lewis Research Center, National Aeronautics and Space Administration, Cleveland, Ohio 44135
8. ANSYS CFX 19.1 (2018) ANSYS CFX-solver theory guide. ANSYS Inc.

# Developing and Improving the Finished Product Warehouse in the Footwear Manufacturing Company Using Logic Simulation



Thi Tuyet Mai Tran, Minh Tai Le, Cao Tien Dat Tran,  
and Ngoc Minh Nguyen

**Abstract** Warehouse management helps businesses easily capture timely information about goods, supplies, raw materials, and products. Accordingly, business managers can make right plans and decisions, reduce costs, increase competitiveness, and improve production and business results. Warehouse management is one of the indispensable steps in the production and business process. Effective warehouse management helps businesses capture information about products, materials, suppliers, and items simply and quickly. For Vietnamese, small and medium-sized private enterprises, whose issue is even more necessary and should be paid attention to in the current context. This article will study the finished product warehouse of the footwear factory, thereby giving the most objective assessment. The Flexsim tool was used to simulate and analyze the current status of the finished goods warehouse. The results was used to evaluate problems in warehouse management and clarify the operation of this department. Then, come up with solutions to the issues that cause difficulties and greatly affect warehouse operations.

**Keywords** FlexSim · Warehouse · Layout · Footwear company

---

T. T. M. Tran · M. T. Le (✉) · C. T. D. Tran · N. M. Nguyen  
Department of Industrial Systems Engineering, University of Technology and Education, Ho Chi Minh City, Vietnam  
e-mail: [tailm@hcmute.edu.vn](mailto:tailm@hcmute.edu.vn)

T. T. M. Tran  
e-mail: [19104024@student.hcmute.edu.vn](mailto:19104024@student.hcmute.edu.vn)

C. T. D. Tran  
e-mail: [19104006@student.hcmute.edu.vn](mailto:19104006@student.hcmute.edu.vn)

N. M. Nguyen  
e-mail: [19104025@student.hcmute.edu.vn](mailto:19104025@student.hcmute.edu.vn)

## 1 Introduction

Inventory is one of the most important components of Profit and Loss (trading) account as well as the current asset of Balance Sheet [1, 2]. High inventory causes many disadvantages for businesses such as stagnant capital, maintenance costs, ... Solutions to improve the quality of warehouse management are always focused on research and implementation. Production and business efficiency is always the top goal, determining the success or failure of enterprises. Although some corporations have used the bookkeeping methodology, this method is inefficient since the records of such warehouses are paper-based in nature, and these papers are highly significant because they include crucial data of many types of items that reside in the warehouse [3]. Therefore, the tools in the warehouse become obsolete, cannot support employees, reduce quality, and do not improve productivity. On the other hand, manufacturers' warehouses frequently encounter problems such as challenges with tracking inventory and consulting as they move to a warehouse or distribution center, identifying problems through information about each type of item in stock, from location, quantity, expiration date.... A warehouse management system is a part of a supply chain that is intended to keep the movement and storage of materials under control within the warehouse and to process associated transactions, including shipping, receiving, delivery and pick up [4]. In factory and warehouse planning a wide range of decisions must be made [5]. Improving the efficiency of inventory management really brings many good effects to reducing costs and improving profits for production and business activities. Focus of warehousing logistics optimization is the storage location assignment, optimization and material distribution two seemingly unlikely related problems integrate together and optimizes them at the same time [6].

Industry 4.0 technologies allow warehouse facilities to adapt to changes in their processes [7]. In the last decades, there has been an increasing amount of published research in the field of the Automatic Simulation Model Generation [8]. Automation and robotics are today ways to reduce costs is to collect multiple orders simultaneously, as well as avoid unnecessary travel of operators [9]. The introduction of sophisticated automation, robotics and advanced software systems into warehouse operations can potentially influence logistics operations comparable to the introduction of the wheel millennia ago. Simulation modeling provides users with the ability to test operational schemes and their parameters as well as the impact of alternatives without testing in a real environment because it is too expensive or impossible to carry out [10]. Simulation modeling is one of the most effective approaches to functional analysis of LWs [11]. Modelers can quickly change the model in a variety of ways thanks to FlexSim. The smart supply chain presents unprecedented opportunities to reduce cost and improve efficiency [12].

Users may easily change model inputs and parameters for staffing, order release, capacity, picking speeds, and other criteria while conducting warehouse simulations .... The simulation technique can show the specific state and find bottlenecks and idle resources of the system, giving a detailed description of the process and actual

information of the simulated system. By using the FlexSim tool, the authors developed a warehouse management system for a shoe manufacturing company to find out the causes of bottlenecks. In a shoe company's warehouse system, a management system was designed and guaranteed to allow users to track inventory and product supplies more efficiently as they move through the warehouse or distribution center.

## **2 Method**

### ***2.1 Build a Current Model***

After studying in-depth about the finished goods warehouse of the Binh Tien consumer goods manufacturing company (Biti's) with the purpose of simulating and improving the efficiency of this warehouse, the authors collected, and analyzed standard information, and came up with solutions for the most appropriate warehouse design.

Using FlexSim software, the authors simulated the warehouse according to areas. From the left to the right, the warehouse has four spaces: an area used to receive goods into the warehouse; an area used to receive goods onto the 2nd floor; a storage area by type; a delivery area from the 2nd floor and a remaining area used to deliver goods from the warehouse.

With the Operator object, we implemented scheduling for workers in loading and unloading positions. In the current model, 10 employees will be employed in the warehouse. In the FlexSim simulation, employees in the model will affect several parameters such as: Staytime, employees' working time distribution, and placement of employees.

The Source object and Sink object installed the location of delivery and receiving gates as shown in Figs. 1 and 2. Then, Queue object was set up for storage items.

To complete simulation as well as create movement and distribution of goods for moving and stationary tools, we must perform A—connects and S—connects links. (Fig. 3) is the image of the warehouse after being simulated with full links.

### ***2.2 Setting Parameters for the Current Finished Product Warehouse Simulation***

Using the Maximum Content option, we set the maximum quantity of stock at storage locations to 1000. The boxes will be transported by the staff, and this will be set up in the Flow and the Use Transport section. With a warehouse length of 34 m, we can calculate the speed of the person who can pick up 5 boxes each time working in the warehouse is 0.3 m/s.

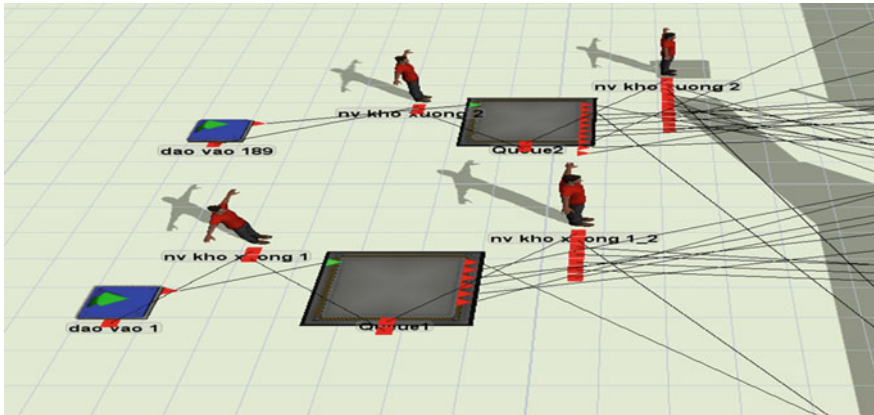


Fig. 1 Location of receiving

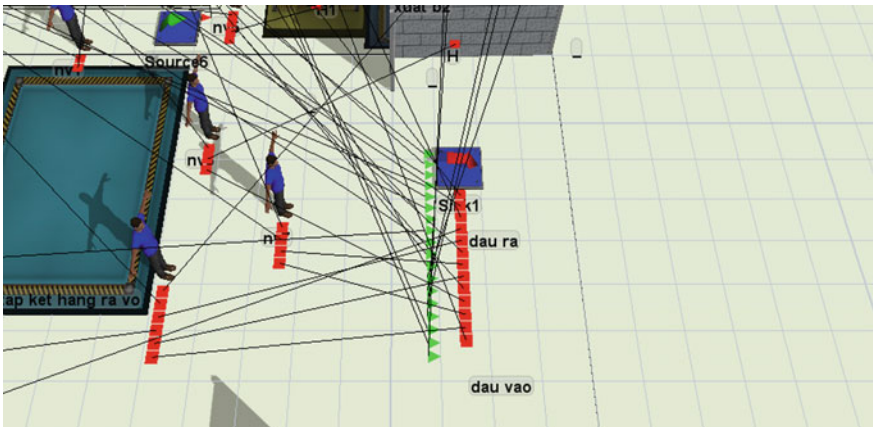


Fig. 2 Location of delivering

With the TimeTable object, the time for AGVs and Operators was set up, and the highlighted periods in red will be the periods when the employee is inactive.

### 2.3 Improvemens

#### *Implement the Automated Guided Vehicles (AGVs) system*

AGVs were used to replace 5 people working with the same workload in a day and the load in the AGV system can reach 100 kg.



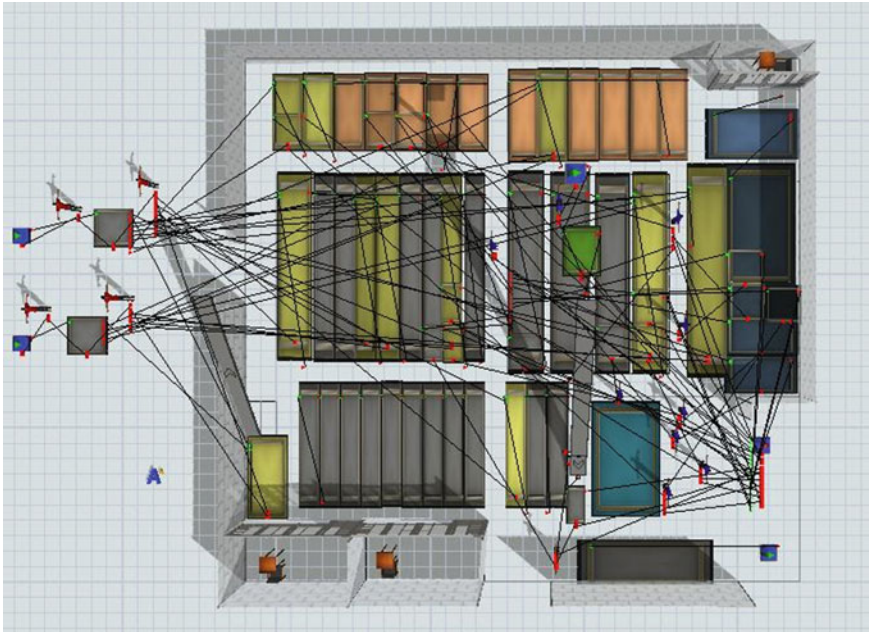


**Fig. 3** Overall layout

Before improvement: Employees have worked for 8 h a day. With 10 people, the corresponding workload is 80 h per day, showing that the company’s progress in paying people to work is very large.

After improvement:

- Reduce the cost of daily wages for employees.
- Allocate time better and reduce pressure on employees.
- Support the coordination of human resources in the company’s warehouses.
- Reduce the risk in the process of work for both employees and businesses.
- Ensure accuracy and easy integration with the production management system.

Besides, Straight Path and Control Point were established for the travel route and pick-up location for the AGV (Fig. 4).

*Improving 2nd floor delivery location*

The actual survey shows that the location of the 2nd floor slide to bring the goods to the 1st floor takes a lot of time and the distance to move the goods is up to 6 m (Fig. 5). To solve this problem, re-positioning the slide towards the delivery gate will facilitate transportation, in addition, it will optimize the transport distance from 6 to 1 m (Fig. 6).

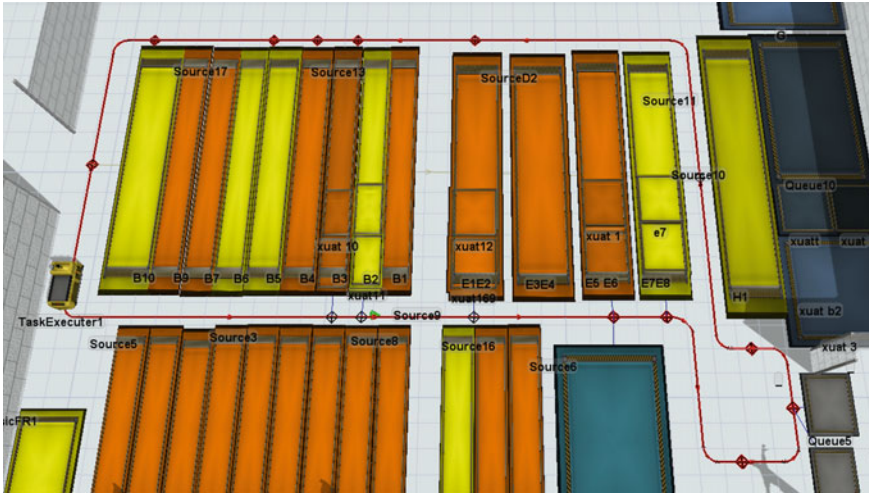


Fig. 4 Setting up a route for the AGVs

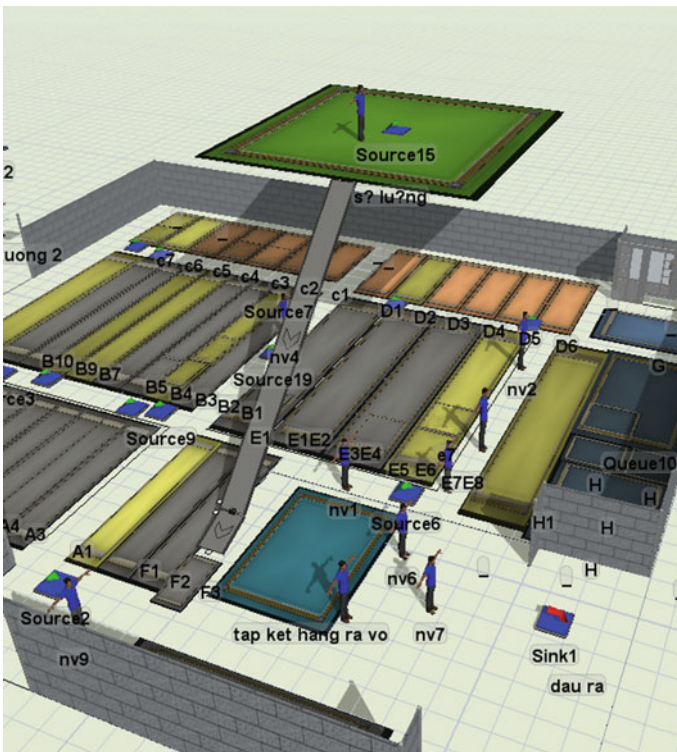


Fig. 5 Current slide

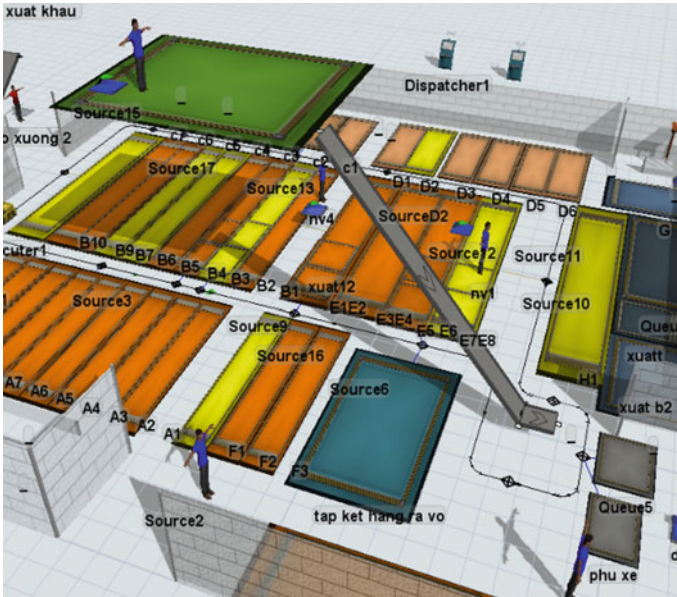


Fig. 6 Innovative slide

The Dispatcher object was also used to control the location of operators and AGVs. One Dispatcher for staff and AGVs on the 1st floor and another one for controlling the delivery staff on the 2nd floor.

### 3 Results and Discussions

The average travel time of employees in the finished goods warehouse is currently 330.68(s), 5 times higher than after the improvement. This is the reason for installing the automatic transportation system AGV to support workers, helping to optimize the time and distance of employees to travel and deliver goods (Fig. 7).

Figure 8 shows that the delivery time allocation of employees in the improved warehouse decreased by 9% compared to the original warehouse. With the same workload of the day, warehouse workers have reduced work pressure from 54 to 45%. This allows employees to do other tasks in the warehouse, aiding in allocating resources within the company’s warehouse, and getting the day’s work done more efficiently.

Figure 9 shows one of the improvements that can help reduce work pressure and optimize workflow. With the current 531 finished products, shipping takes about 120 min and there are 6 employees working in this position. On the other hand, by optimizing the initial shipping distance from 6 to 1 m and shortening the delivery

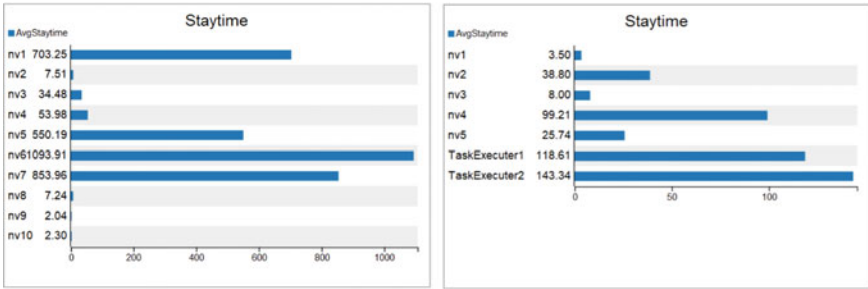


Fig. 7 Staytime—average travel time in finished goods warehouse

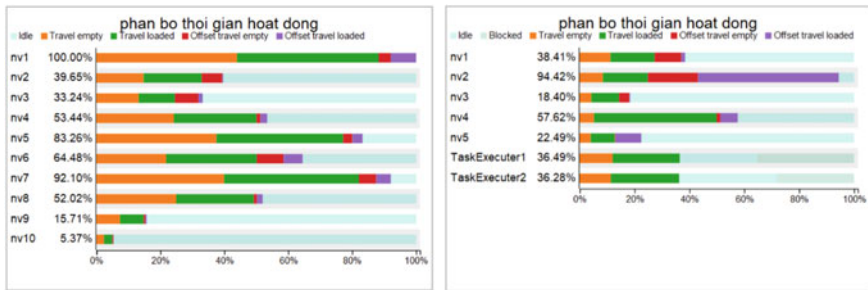


Fig. 8 Distribution of working time of staff and machines in the warehouse

time, the upgraded-finished goods warehouse in this area takes only 100 min to transport and the number of employees is reduced to 2 people.

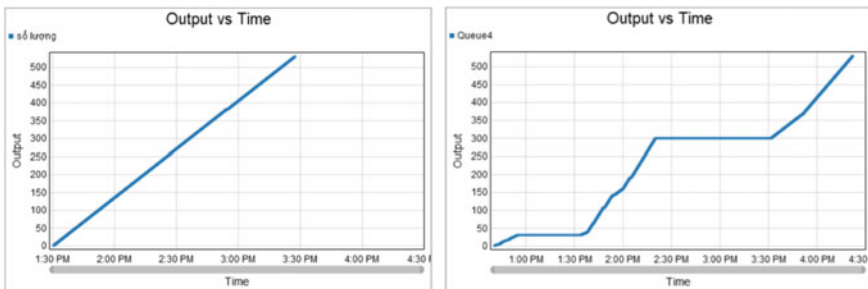


Fig. 9 Flow of the quantity of goods out of floor 2

## 4 Conclusion

The simulation results show an overview of the improvement between the existing finished goods warehouse and the improved finished product warehouse. Staytime before improvement averaged 330.68(s) and after improvement dropped to a mean of 35.05(s). The distribution of working time for an export process for one working day with the same export volume, a pre-improvement warehouse is 54% and post-improvement is 45%. The AGV system with a load of up to 100 kg was installed with the price only 300 million, reduced the cost of one year for 5 employees is 450 million (excluding salary and bonus). This decision saved the company 150 million Vietnamese dong per year. In the future, the authors will continue to establish a standard fixed import and export process for all warehouses in the company to serve a warehouse management process of shoes manufacturing companies for sustainable purposes. Developing and improving the entire warehouse in the company will bring back the most complete and superior system.

## References

1. Khan AK, Faisal SM, Aboud OA (2016) An analysis of optimal inventory accounting models—pros and cons. *Eur J Acc Audit Fin Res* 6(3):65–77
2. Bychkov I, Oparin G, Tchernykh A, Feoktistov A, Bogdanova V, Dyadkin Y, Andrukhova V, Basharina O (2017) Simulation modeling in heterogeneous distributed computing environments to support decisions making in warehouse logistics. In: 3rd international conference “information technology and nanotechnology”, pp 524–533
3. Aimufua GI, Muhammad UA, Auwal M (2022) Development of computerized warehouse management system. *Quest J J Softw Eng Simul* 8(2):5–10
4. Pekel E, Kara S (2013) Warehouse management with a simulation programme, researchgate
5. Kallat F, Pfrommer J, Bessai J, Rehof J, Meyer A (2021) Automatic building of a repository for component-based synthesis of warehouse simulation models. In: 54th CIRP conference on manufacturing systems, pp 1440–1445
6. Yafei L, Qingming W, Peng G (2018) Research on simulation and optimization of warehouse logistics based on flexsim-take C company as an example. In: 7th International conference on industrial technology and management (ICITM)
7. Lototsky V, Sabitov R, Smirnova G, Sirazetdinov B, Elizarova N, Sabitov S (2019) Model of the automated warehouse management and forecasting system in the conditions of transition to industry 4.0. *IFAC PapersOnLine*, pp 78–82
8. Reinhardt H, Weber M, Putz M (2019) A survey on automatic model generation for material flow simulation in discrete manufacturing. *Procedia CIRP* 81:121–126
9. Hmidach, S., El Kihel, Y., Amegouz, D., El Kihel, B., & Regad, Y., Optimizing warehouse logistics flows by integrating new technologies: Case study of an agri-food industry, 2020 IEEE 2nd International Conference on Electronics, Control, Optimization and Computer Science (ICECOCS), 2020.
10. Bychkov I, Oparina G, Tchernykh A, Feoktistov A, Bogdanova V, Dyadkin Y, Andrukhova V, Basharina O (2017) Simulation modeling in heterogeneous distributed computing environments to support decisions making in warehouse logistics. In: 3rd International conference “information technology and nanotechnology

11. Taha HA (2016) *Operations research: an introduction*. Pearson, Cambridge
12. Wu L, Yue X, Jin A, Yen DC (2016) Smart supply chain management: a review and implications for future research. *Int J Logist Manage* 27(2):395–417

# Application of Magnetorheological Elastomer (MRE) for Smart Vibration Systems



Quang Du Nguyen, Cung Le, and Xuan Bao Nguyen

**Abstract** Magnetorheological elastomers are intelligent materials in which many scientists have recently been interested in innovative vibration systems. MRE is made by embedding micro-sized iron particles into an elastomer such as natural rubber. MRE has overcome the disadvantages of magnetorheological fluids (MRF), such as deposition problems, leak problems, and response only under velocity. MRE-based devices have many outstanding advantages in intelligent vibration systems, such as MRE-based isolators, absorbers, and MRE sensors. Mechanical properties, especially the modulus, change remarkably when a magnetic field is applied. MRE-based devices combine with a semi-active controller so that the system can avoid resonance, isolate excitation vibrations, or absorb existing vibrations. These systems can be remarkably effective in car suspension, construction sites, and mechanical systems. This paper aims to provide a comprehensive overview of MRE application aspects, including fabrication methods, properties of MREs, modeling, and applications of MREs in vibration systems.

**Keywords** Magnetorheological elastomer · Vibration control system · Semi-active control

---

Q. Du Nguyen (✉) · X. B. Nguyen  
The University of Danang, University of Technology and Education, 48 Cao Thang, Danang,  
Vietnam  
e-mail: [nqdu@ute.udn.vn](mailto:nqdu@ute.udn.vn)

X. B. Nguyen  
e-mail: [nxbao@ute.udn.vn](mailto:nxbao@ute.udn.vn)

C. Le  
The University of Danang, University of Science and Technology, 54 Nguyen Luong Bang,  
Danang, Vietnam  
e-mail: [lcung@dut.udn.vn](mailto:lcung@dut.udn.vn)



## 1 Introduction

Magnetorheological (MR) materials have become important intelligent materials in industrial potential [1]. MR materials can adjust dynamic modulus and viscosity under an external magnetic field. MR materials include MR—Foam (MR foam), MR—Gel (MRG), MR—Fluid (MRF), and MR—Elastomer (MRE). MRE is an intelligent material consisting of micrometer-sized magnetic particles dispersed in a polymer elastomer. Among them, natural rubber has excellent mechanical properties and other comprehensive properties that are the ideal base material for the preparation of MRE. MRE has many advantages, such as fast response, good reversibility, and controllability. Therefore, the application of MRE in suspension systems and integrated semi-active controllers has great research value and potential for application in engineering.

The MRE's viscoelastic properties significantly depend on the magnetic field strength [2]. Therefore, modeling the MRE characteristics is a major challenge, especially in the design of semi-active controllers. Many researchers have proposed different models such as The Kelvin-Voigt, the Dahl, the LuGre friction, the Bouc-Wen, smooth Coulomb friction models [3–5].

The semi-active suspension system can adjust the stiffness and operating mechanism of the system. A system using an MRE-based device needs to integrate a semi-active controller. There are many control methods [6–10], such as optimized control methods, self-adaptive control methods, fuzzy logic control methods, sky-hook, PID, Fuzzy, Clip-optimal, Bang-bang, Lyapunov, adaptive algorithms, and neural network control methods. This study presents problems related to magnetorheological elastomers, including fabrication methods, MRE properties, modeling, and applications. A single degree of freedom system was simulated to evaluate the effectiveness of the material.

## 2 MRE Material Overview: Fabrication, Properties, and Modeling

### 2.1 Fabrication of MRE Materials

The fabrication of MRE is almost the same as that of the curing of rubber. The material composition includes silicon rubber, silicon oil, and iron particles (10  $\mu\text{m}$ ) with a ratio of 60%:2%:38%, respectively. The material was mixed into a homogeneous mixture using a centrifugal mixer for 10 min. After mixing, the mixture is placed in a low-pressure chamber to remove air bubbles inside the material for about 20 min. Then the mixture is then poured into a plastic mold and cured at room temperature for 24 h. The mixture is placed in a magnetic field of strength 0.5 T to form an anisotropic material during curing. MRE samples has been fabricated (Fig. 1).



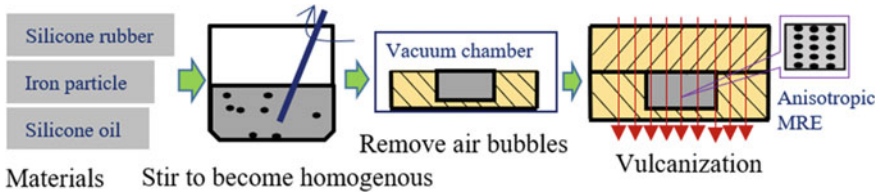


**Fig. 1** The MRE fabrication process

## 2.2 Experiment Set up

In this study, the MRE property measurement system is used to test the dynamics properties of the MRE, as shown in Fig. 2. The system consists of a fixed iron core mounted with a force sensor. The movable core with the integrated coil is attached to the vibrating table to perform harmonic oscillation. The coil with a diameter of 1 mm is wound 650 turns to create an electromagnet in the movable iron core. The movable core is attached to the vibration table, while the stationary core is connected to a force sensor to measure the strain response force of the material (Piezoelectronic PCB, Model: 208C02). Two samples of MRE material are placed between two electromagnet cores. Direct current (DC) power supplies current to the coil to change the strength of the magnetic field passing through the material. A laser sensor for measuring table displacement (laser displacement sensor KEYENCE LB-02). The force and displacement sensors are connected to the oscilloscope to measure the force–displacement responses. A servo motor drives an eccentric wheel. In this study, we used two eccentric wheels with deviations of 0.4 and 0.8 mm, respectively. Eccentricity is the amplitude of the vibration. The table is heavy enough to ensure that the table is always in contact with the eccentric wheel. The servo motor’s speed is also the table’s vibration frequency and can be adjusted. To further investigate the influence of the magnetic field on the mobility characteristics of the MRE, in this study, the frequency excitation is performed from 1 to 30 Hz, and the magnetic field from 0 to 350 mT corresponds to the voltage current. Use from 0 to 5 A. The oscillation amplitude is 0.4 to 0.8 mm, corresponding to the shear strain of 4 to 14%.

## 2.3 Numerical Model and Properties of MRE

It is necessary to develop a numerical model to represent the dynamic characteristics of the MRE to design systems using the MRE. Many researchers in recent years have exploited numerical models for MRE materials. In this study, the Bouc-wen model is used to represent the behaviors of MREs as shown in Fig. 2. The model consists of two parts: the linear stiffness associated with damping that represents the viscoelastic properties and the Bouc-Wen component that describes the hysteresis behavior of the material. The response force of the model is expressed as,

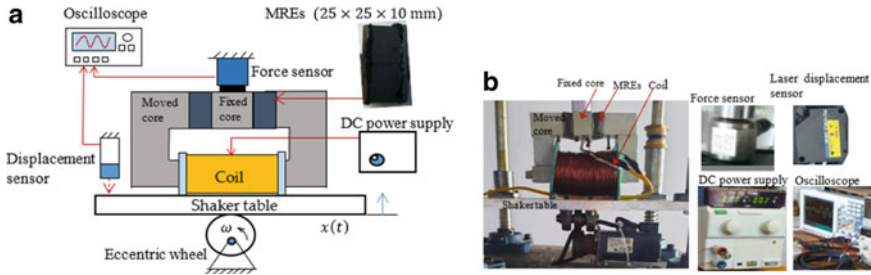


**Fig. 2** Experiment set up to measure the properties of the MRE in the shear state: **a** schematic **b** photo of devices

$$F_{\text{MRE}} = \alpha k_0 x + c_0 \dot{x} + (1 - \alpha) k_0 h, \quad (1)$$

$$\dot{h} = A \dot{x} - \beta |\dot{x}| |h|^{n-1} z - \gamma \dot{x} |h|^n, \quad (2)$$

where the linear stiffness force and a purely hysteretic force are  $\alpha k_0 x$  and  $(1 - \alpha) k_0 h$ , respectively. The coefficient,  $\alpha \in (0, 1)$ , represents the linearity level of the loop. The parameters  $A$ ,  $n$ ,  $\beta$ , and  $\gamma$  represent the shape and size of the hysteresis loop as shown in the Eq. (2). Where  $A$  is related to the amplitude of the hysteresis loop,  $\beta$  and  $\gamma$  represent the shape of the delay, and  $n$  is the nonlinear order of the hysteresis.

The variables model are approximated under input current as follow,

$$\begin{aligned} k_0 &= k_{0a} + k_{0b} I, \quad c_0 = c_{0a} + c_{0b} I, \\ \alpha &= \alpha_a + a_b I, \quad A = A_a + A_b I, \\ \beta &= \beta_a + \beta_b I, \quad \text{and } \gamma = \gamma_a + \gamma_b I. \end{aligned}$$

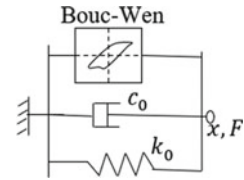
The least squares method is used to determine the parameters of the model. A data set is used to update the parameter so that the least mean square error is within the allowed range. This method is easy to use and highly effective in determining the parameters of nonlinear models. The parameter values of the model are listed in Table 1 (Fig. 3).

Comparison of force–displacement response between model and experimental results under different levels of applied current with excitation amplitude  $x_0 = 0.75$  mm: (a)  $f = 1$  Hz, (b) 15 Hz, as shown in Fig. 4. When performed at a low

**Table 1** Parameter values of MRE-based absorber using Bouc–Wen model

$k_{0a}$	$c_{0a}$	$\alpha_a$	$A_a$	$\beta_a$	$\gamma_a$	$k_{0b}$	$c_{0b}$	$a_b$	$A_b$	$\beta_b$	$\gamma_b$
25	0.06	0.6	2	3.8	-1	12	0.01	0.05	0.2	0.2	0.3

Fig. 3 Bouc-Wen model



frequency (1 Hz), the viscosity of the material is negligible; we see that the amplitude of the force response increases significantly with increasing current. However, the loop width increases significantly with increasing current. This demonstrates that the magnetic field affects the hysteresis properties of the material. When the amplitude of oscillation changes, the angle of inclination of the loop also changes. As the oscillation frequency increases to 15 Hz, the loop becomes more elliptical due to the influence of viscous. Figure 5 shows the change in the stiffness under the applied current (magnetic field) levels. In this experiment, the stiffness is defined as  $k = F_0/x_0$ , where  $k$  is the stiffness,  $F_0$  is the amplitude force of the shear force, and  $x_0$  is the amplitude displacement of the shear strain. The stiffness increases significantly when the material is placed in the magnetic field. From the figures, we see that the model represents the properties of the MRE well. This model can be used for the design of vibration systems.

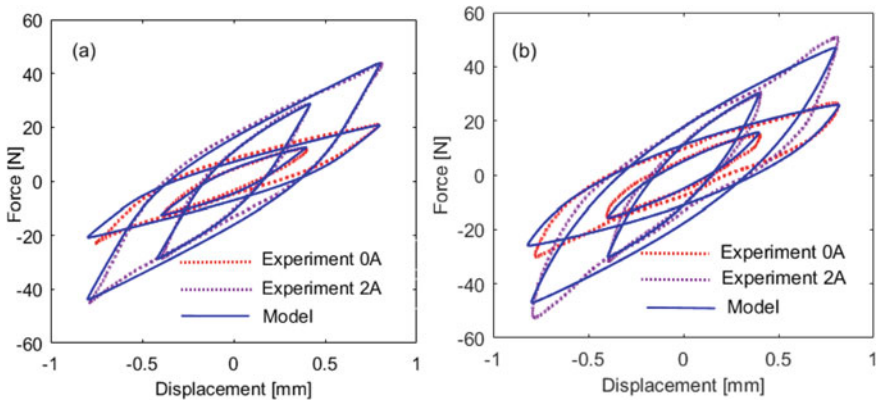
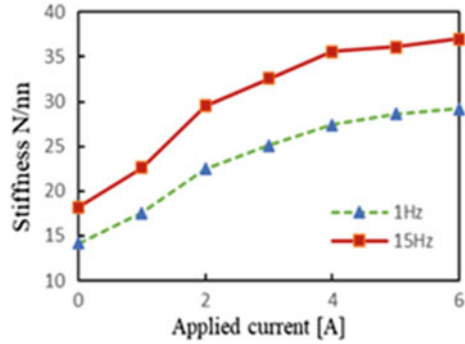


Fig. 4 Comparison between model and experimental

**Fig. 5** Stiffness response of MRE



### 3 Application of Magnetorheological Elastomer (MRE) in Vibration Systems

The one-degree-of-freedom oscillation system is investigated, as shown in Fig. 6, to analyze the damping effect using MRE. The MRE is the system’s elastomer, where the stiffness is adjustable. Assuming the system uses the material sample as investigated above, the minimum stiffness (no current applied) is  $k_1 = 13 \text{ N/mm}$ , the maximum stiffness (4 A) is  $= 30 \text{ N/mm}$ , mass  $m = 1.5 \text{ kg}$ , and the damping coefficient  $c = 1 \text{ Ns/mm}$ . The dynamic equation of the system is described in the time domain as,

$$m\ddot{y} + c\dot{y} + ky = c\dot{z} + kz. \tag{3}$$

Equation (3),  $m$  is the mass,  $z$  the displacement of the ground base,  $c$  the MRE damping coefficient,  $y$  the displacement of mass,  $k$  is the variable stiffness parameter of the MRE,  $k$  stiffness value is adjustable from  $k_1$  to  $k_2$ .

Use the Laplace transform for Eq. (3) and the ratio of the output to the input is determined

$$L(s) = \frac{Y(s)}{Z(s)} = \frac{\frac{c}{k}s + 1}{\frac{m}{k}s^2 + \frac{c}{k}s + 1}, \tag{4}$$

where  $Z(s)$  is the Laplace transform function of  $z(t)$ , and  $Y(s)$  the transform of  $y(t)$ .

**Fig. 6** 1DOF vibration system using MRE

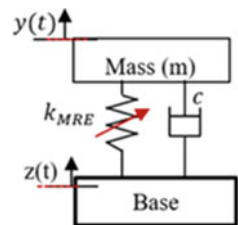
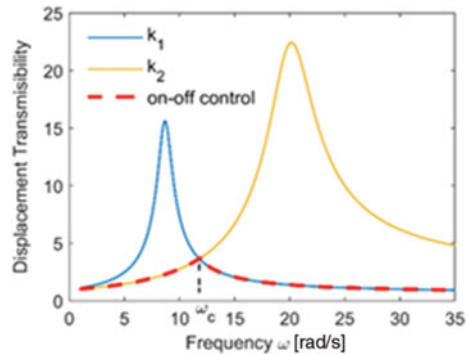


**Fig. 7** The transmissibility of mass response in frequency domain



By replacing  $s$  with  $j\omega$  in function  $L(s)$ , displacement transmissibility  $T_R(\omega)$  of the system  $L(j\omega)$  is further defined in frequency domain as

$$T_R(\omega) = |L(j\omega)| = \sqrt{\frac{1 + (\omega\eta)^2}{(1 - \omega/\omega_0)^2 + \eta^2}} \quad (5)$$

where  $\omega_0 = \sqrt{k/m}$  is the tunable natural frequency of the system

The switching control algorithm was used to optimize the response in the frequency domain,

$$k = \begin{cases} k = k_1(k_{\min}, I = 0 \text{ A}), & \text{if } \omega \leq \omega_c \\ k = k_2(k_{\max}, I = 4 \text{ A}), & \text{if } \omega > \omega_c \end{cases}, \quad (6)$$

where  $\omega$  is the base excitation frequency,  $I$  is the applied current to the coil,  $\omega_c$  is the switching frequency value that is the characteristic frequency of the system and determined as shown in Fig. 7.

The response of the system is shown in Fig. 7. The figure shows that the system's natural frequency can be adjusted from 8 to 22 rad/s. The transmissibility of the system is greatly reduced when using the on-off algorithm. From the investigation of the 1-DOF system using MRE, it is found that the system is efficient and avoids resonance for the vibration system.

## 4 Conclusion

This study introduces magnetorheological elastomer (MRE) in the field of vibration, including fabrication methods, mechanical properties, models, and applications. The MRE properties are non-linear functions of the magnetic field density, displacement amplitude, and excitation frequency. A dynamic elastic model of an isolator based

on the MRE has been presented. Models are also introduced to represent the MRE properties, in which the Bouc-Wen model has described the MRE's dynamic properties well. Vibration systems using the MRE were also introduced. One-degree-of-freedom vibration system has been investigated; the results show that the response is significantly reduced when the system is combined with a control algorithm.

## References

1. Jolly MR, Carlson JD, Muñoz BC, Bullions TA (1996) The magnetoviscoelastic response of elastomer composites consisting of ferrous particles embedded in a polymer matrix. *J Intell Mater Syst Struct* 7(6):613–622
2. Nguyen XB, Komatsuzaki T, Iwata Y, Asanuma H (2017) Fuzzy semiactive vibration control of structures using magnetorheological elastomer. *Shock Vibr (Hindawi)* 2017:3651057-1-3651057-15
3. Lewandowski D (2019) Modeling of magnetorheological elastomers using the elastic-plastic model with kinematic hardening. *Materials* 12(6):892. <https://doi.org/10.3390/ma12060892>
4. Nguyen XB, Komatsuzaki T, Truong HT (2020) Novel semiactive suspension using a magnetorheological elastomer (MRE)-based absorber and adaptive neural network controller for systems with input constraints. *Mech Sci* 11:465–479. <https://doi.org/10.5194/ms-11-465-2020>
5. Nguyen XB, Komatsuzaki T, Zhang N (2020) A nonlinear magnetorheological elastomer model based on fractional viscoelasticity, magnetic dipole interactions, and adaptive smooth Coulomb friction. *Mech Syst Signal Process* Volume 141:106438
6. Truong HT, Nguyen XB, Bui CM (2022) Singularity-free adaptive controller for uncertain hysteresis suspension using magnetorheological elastomer-based absorber. *Shock Vibr (Hindawi)* 2022:2007022-1–2007022-17. <https://doi.org/10.1155/2022/2007022>
7. Liao GJ, Gong X-L, Xuan SH, Kang CJ, Zong LH (2012) Development of a real-time tunable stiffness and damping vibration isolator based on magnetorheological elastomer. *J Intell Mater Syst Struct* 23(1):25–33. <https://doi.org/10.1177/1045389X11429853>
8. Nguyen XB, Komatsuzaki T, Truong HT (2022) Adaptive parameter identification of Bouc-wen hysteresis model for a vibration system using magnetorheological elastomer. *Int J Mech Sci* 213:106848. ISSN 0020-7403. <https://doi.org/10.1016/j.ijmecsci.2021.106848>
9. Jansen LM, Dyke SJ (2000) Semiactive control strategies for MR dampers: comparative study. *J Eng Mech (ASCE)* 126(8):795–803
10. Nguyen XB, Komatsuzaki T, Iwata Y, Asanuma H (2018) Modeling and semi-active fuzzy control of magnetorheological elastomer-based isolator for seismic response reduction. *Mech Syst Signal Process* 101:449–466

# Study on Predict Spring-Back in V-Bending of SS400 Steel Plate and Select Bending Parameters by Finite Element Method



Vuong Gia Hai, Hoang Van Quy, Nguyen Thi Hong Minh,  
and Nguyen Duc Toan

**Abstract** In this study, SS400 steel plate was used to bend the V-shaped parts with different corner radii and bending angles. Based on the desired angle value, punch radius and bend angle (punch stroke) must be selected to get the correct shape. The combined kinematic/isotropic hardening law was used and shown more accurately than other laws. When comparing with corresponding experiment data was used to predict spring back in V-bending. To decide the punch radius and bend angle (punch stroke) for the desired shape, some values of the punch radius and bend angle (punch stroke) of the V-bending process were first changed to simulate and investigate the corner radius and forming angle of the part after spring-back. A Minitab 17 software tool was used to determine corner radius and forming angle after elastic deformation as functions of punch radius and bend angle. Thereby as a basis for the correct selection of punch radius and bending angle when bending to achieve the value of corner radius and bending angle in later experiments.

**Keywords** SS400 steel plate · FEM · Spring-back · V-bending

## 1 Introduction

Nowadays, the steel sheet has been widely used in the processing of to make products in many different fields such as: shipbuilding, automobile, aviation, space, ... Among of the products made from steel sheet, the parts machined by bending technology account for a large of proportion. In the process of forming sheet metal by bending

---

V. G. Hai · H. V. Quy (✉)  
Hai Phong University, Hai Phong, Vietnam  
e-mail: [quyhv@dhpu.edu.vn](mailto:quyhv@dhpu.edu.vn)

N. T. H. Minh · N. D. Toan  
Hanoi University of Science and Technology, Ha Noi, Vietnam

technology, the spring-back after forming deformation is a factor that greatly affects the accuracy of the product. The spring-back after deformation to shape the parts processed by bending method is often greatly influenced by technological parameters such as: punch radius, bending angle, material, part thickness, punching speed, heating temperature when bending, ... The determining a suitable set of technological parameters is essential, it can help manufacturers save maximum production costs while still bringing high economic efficiency. Among the technological parameters affecting the spring-back after forming deformation, the bending angle and the punch radius are also parameters that have a great influence, many studies [1–4] have shown that that the bending angle and radius of the punch change, the spring-back after forming deformation is greatly affected. These studies also used simulation and experimental methods to evaluate the influence of temperature on the spring-back after forming deformation.

In this study, in order to more accurately predict the spring-back after V-bending, tensile test pieces are first cut from the metal sheet parallel to the rolling direction and a single tensile test is carried out a axis. The Voce's model has been proposed for SS400 sheet metal, which is a hot rolled steel material used in the automotive and shipbuilding industry. The tensile test pieces are first cut from sheet metal in a direction parallel to the rolling direction and uniaxial tensile tests are carried out. To describe the test data through the material continuity equations, the stress–strain curve is hardened according to Voce's law [5]. The material constants of the yield function are then determined through the Excel calculation tool based on the experimental data and the least squares fit method. The ABAQUS finite element analysis software had use to describes the SS400 sheet metal tensile/compression process, making predictions of stress–strain curves based on the object hardening model that has a good fit compared to that of the steel plate with experimental data. The ABAQUS finite element analysis software is also used to simulate the bending of V-shaped details with the change of two technological parameters as punch radius and bending angles to determine elastic deformation angle and the radius of the part after the bending process. From the results of finite element analysis, the relationship equation between elastic angle, detail radius with bending angle and radius of bending punch can be built. This result is the basis for making the selection of punch radius and bending angle when you want to perform detailed radius bending.

## 2 Material Hardening Model

In this study, we use Voce's hardening law [5] to express the relationship between stress and strain as Eq. (1).

$$\bar{\sigma} = \sigma_y + A(1 - \exp(-B\varepsilon_{eq}^p)) \quad (1)$$



**Table 1** Chemical composition of SS400 steel sheet

C	Si	Mn	P	S	Cr
0.19–0.21	0.05–0.17	0.4–0.6	0.04	0.05	≤ 0.3

where A and B are the plastic coefficients  $\bar{\sigma}$ ,  $\varepsilon_{eq}^{pl}$ , and  $\sigma_y$  are the equivalent stress, equivalent strain, and tension yield stress, respectively.

## 2.1 Materials and Experimental Setup

### 2.1.1 Materials

The material used in this study is SS400 steel sheet, according to JISG 3101 [6] with a chemical composition as Table 1.

The tensile test pieces are cut on a wire cutting CNC machine, the tensile specimens were cut from the sheet in parallel to the rolling direction with 6 mm thickness in order to carry out uni-axial tensile tests. After that, the tensile specimens are honed smoothly with a armor paper. The shapes and dimensions of the specimens were prepared in accordance with TCVN 197-85 (197-2000) [7], as show in Fig. 1.

The experiment tensile tests pieces are carried out on the Hung Ta H-200 kN compressor as shown in Fig. 2.

The experimental results of tensile tests are shown in Fig. 3.

The material attribute parameters used to finite element analysis determined by tensile test data are presented in Table 2.

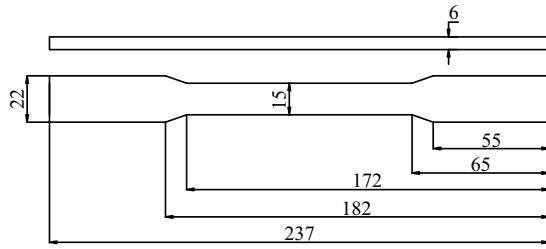
### 2.1.2 Experimental Setup

The experimental tensile/compression test was also performed using the Hung Ta H-200 kN tensile/compression machine Fig. 3. The tensile/compression results were automatically obtained through the machine's control software.

## 2.2 Determination of the Material Parameters

When Voce's hardening law is used to simulate predictive stress–strain curves in uniaxial tensile/compression then it is only necessary to specify the parameters  $\sigma_y$ , A and B in Eq. (1) as the input data for the simulation. By using Eq. (1) in combination with the experimental data in Fig. 3 and using advantage of the least squares method of Excel software tool, the corresponding values of  $\sigma_y$ , A, and B can be determined, respectively are 348 (MPa), 188.86 (MPa) and 28.3293.

**Fig. 1** Tensile test coupon and dimensions. **a** Dimensions and **b** wire cutting CNC machine **c** test coupons



(a)



(b)



(c)



**Fig. 2** Tensile and bending test machine

**Fig. 3** Comparison of Voce's laws with experimental data

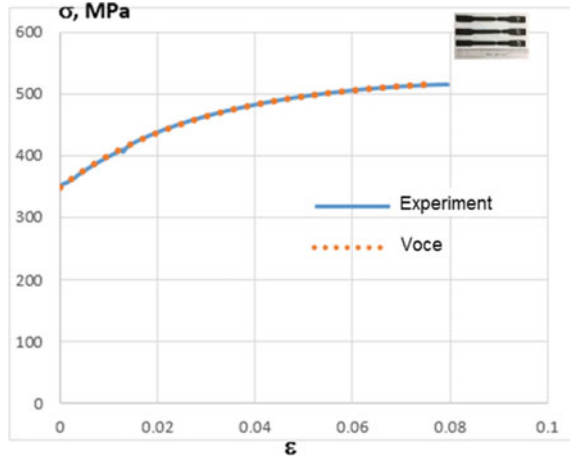


**Table 2** Material attribute parameters for numerical simulation

Parameters	Levels
Bending speed (mm/s)	1
Thickness sheet (mm)	6
Poisson's ratio	0.3
Young's modulus (MPa)	213,000

### 3 Simulation for V-Bending with Variable Punch Radius and Bending Angle by Abaqus Analysis Software

In this study, to Spring-back prediction when bending SS400 plate using Voce's model, the data collected from the test results and the calculation are using Abaqus/Explicit and then imported the deformed results into Abaqus/Standard, 3D Experience® 2016 HF2 (2016 HF2, Dassault Systemes Simulia Corp., Providence, RI, USA, 2016). This software can provide elastic-plastic and rigid-plastic simulations of metal forming for a case of large deformation, significantly reducing the cost and time involved in tool and die design.

#### 3.1 Finite Element Model and Simulation Method of V-Bending

The V-bending models are depicted in Fig. 4. Specifically, reduced-integration eight-node linear brick elements (C3D8R) are utilized for the blank. The die/tool and clamping parts are assigned as the rigid body. The size of the element for all parts corresponds to approximately 6 × 55 × 160 mm (Thickness × width × length). The

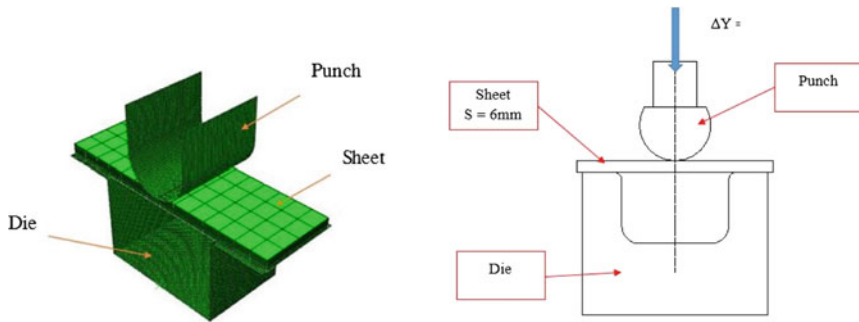


**Fig. 4** V-bending models

boundary conditions in the model are as follows: a die part—ENCASTRE condition; a punch part: vertical movement; a sheet part: symmetrical boundary condition with respect to the center of the sheet. In order to determine spring-back angle and bending radius through simulation, the bending part deformation of V-shaped part is done by moving the punch down vertically  $\Delta Y$  (5 levels).

### 3.2 Spring-Back Predictions When V-Bending

To predict the spring-back of hardening laws, isotropic hardening law was used to simulate the V-bending process. 5 values of RPunch punch size include: 42 mm; 44 mm; 46 mm; 48 mm; 50 mm and 5 values of bending angle  $\alpha$  include: 1250; 1300; 1350; 1400; 1450 is used for simulation. Figure 5 shows simulation procedures to predict spring-back after deformation.

Here, forming process was first performed with Abaqus/Explicit (Fig. 5), after designing punches, dies and sheet in Abaqus/standard. Based on the law of hardening, the elasticity and residual stress state Von-mises are calculated and predictions are made according to the isotropic hardening law. The deformation shape, bending angle and detailed radius of the sheet cross-section are measured by scanning and importing the image into Autocad Fig. 6.

### 3.3 Die Radius and Bending Angle Selections

To Spring-back prediction after bending the V-shaped part, this study uses FE simulation results to verify the effect of changing parameters such as: punch radius and bending angle, effect on the part radius ( $R_{SP}$ ) and bending angle ( $\theta_{SP}$ ) of the product after spring-back. Table 3 lists the level selected for the two parameters defined in Fig. 5. When simulating FE using a five-level factor with two parameters, the full

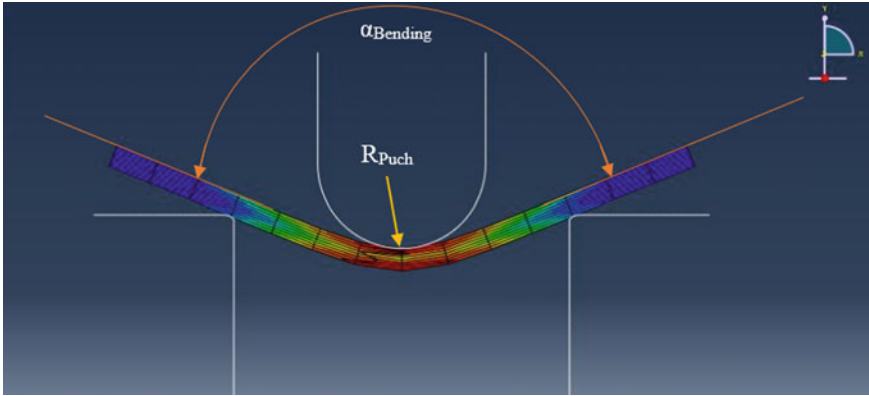


**Fig. 5** Deformed shape in FE simulations for V-bending process with abaqus/explicit

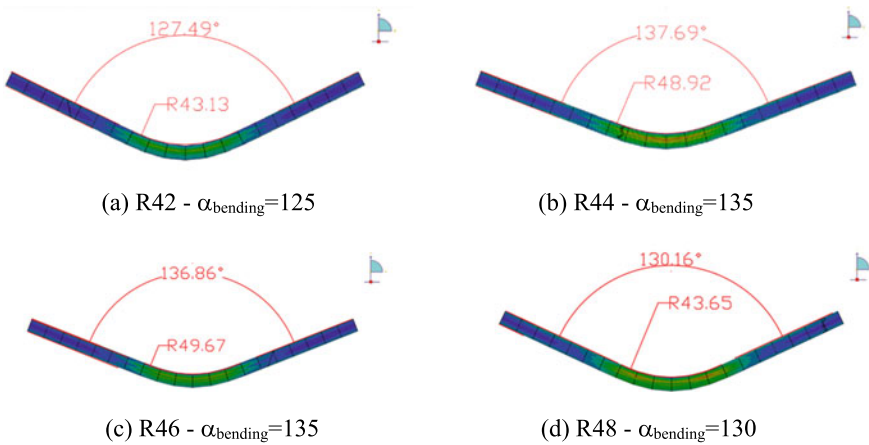


**Fig. 6** Simulation result of V-bending

factorial design is 25 trials. Tables 4 and 5 show the FEM simulation results of the detail radius and bending angle of the plate after elastic deformation based on different levels of the punch radius parameter and the corresponding bending angle.

**Table 3** Factors and their levels in FE simulations

Level					
Factors	1	2	3	4	5
$R_{Punch}$ (mm)	42	44	46	48	50
$\alpha_{bending}$ (degree)	125	130	135	140	145

**Table 4** Detail radius  $R_{SP}$  (mm) after spring-back based on punch radius and bending-angle

Bending angle $\alpha_{bending}$ (degree)	Punch radius $R_{Punch}$ (mm)				
	42	44	46	48	50
125	43.13	42.58	43.13	43.76	45.29
130	45.96	43.87	45.68	43.65	45.1
135	48.8	48.92	49.67	48.88	48.76
140	54.77	55.42	51.6	50.75	54.83
145	61.49	57.91	57.72	62.45	60.88

**Table 5** Bending angle  $\theta_{sp}$  (degree) after spring-back based on punch radius and bending-angle

Bending angle $\theta_{bending}$ (degree)	Punch radius $R_{Punch}$ (mm)				
	42	44	46	48	50
125	127.49	126.34	123.54	121.45	119.87
130	132.94	131.88	131.44	130.16	128.23
135	138.72	137.69	136.86	136.52	135.94
140	143.26	143.32	142.38	141.88	141.33
145	147.52	147.49	146.93	147.46	146.24

To select the punch radius and bend angle for the desired shape, we first use the relationship between the output (part radius and part forming angle after spring-back) and the input data (radius of punch and bend angle) as shown in Tables 2 and 3.

$$R_{SP} = f(R_{Punch}, \alpha_{bending}) \quad (2)$$

$$\theta_{qSP} = f(R_{Punch}, \alpha_{bending}) \quad (3)$$

Two polynomials of order 2 [Eqs. (2) and (3)] describe the relationship between part radius and detail angle after spring-back with punch radius and bending angle built using the Fitting tool Regression of Minitab 17 software is shown in Eqs. (4) and (5).

$$R_{SP} = 644 - 7.R_{Punch} - 7.33.\alpha_{bending} - 0.007.R_{Punch}.\alpha_{bending} + 0.0865.(R_{Punch})^2 + 0.03142.(\alpha_{bending})^2 \quad (4)$$

$$\theta_{SP} = -79.2 - 4.86.R_{Punch} + 3.853.\alpha_{bending} + 0.04092.R_{Punch}.\alpha_{bending} - 0.0122.(R_{Punch})^2 - 0.01693.(\alpha_{bending})^2 \quad (5)$$

Table 5 shows the results in calculation for die radii ( $R_{punch}$ ) and bending angles ( $\theta_{bending}$ ) from Eqs. (4) and (5) for five validated cases of desired corner (R) radius

**Table 6** Die radii ( $R_{\text{Punch}}$ ) and bending angles ( $\alpha_{\text{bending}}$ ) calculations based on desired shapes ( $R_{\text{SP}}$ ,  $\theta_{\text{SP}}$ ) and the simulation measurements of corner radius ( $R_{\text{simulation}}$ ) and bending angle ( $\theta_{\text{simulation}}$ )

$R_{\text{Punch}}$ (mm)	$\alpha_{\text{bending}}$ (degree)	$R_{\text{SP}}$ (mm)	$\theta_{\text{SP}}$ (degree)	$R_{\text{simulation}}$ (mm)	$\theta_{\text{simulation}}$ (degree)
42	125	44,27	127,08	43,13	127,49
44	125	43,40	125,49	42,58	126,34
46	125	43,22	123,81	43,13	123,54
48	125	43,73	122,02	43,76	121,45
50	125	44,94	120,14	45,29	119,87

and bending angle ( $\theta$ ). Those values are then used to simulate and verify spring-back predictions by measuring corner radius ( $R_{\text{simulation}}$ ) and wall angles ( $\theta_{\text{simulation}}$ ) after spring-back as shown in Table 6. The simulation results were in good agreement with the selections of die radius and bending angle which were calculated by our proposed method.

## 4 Conclusion

In this study, to simulate and predict the amount of spring-back after V-bending with different radius and angles, an isotropic hardening model was used. In order to determine the parameters of the isotropic strength model, a uniaxial tensile test was performed, thereby serving as a basis to find the coefficients of the model and use as input data for the process. Simulating the V-bending process by ABAQUS software.

The different punch radius and bend angle were changed to determine the bending part angles and radius after spring-back. The radius and detail angle after V-bending are then constructed as a polynomial of order 2 of the radius of the punch and the angle of the bend. The equations found can help determine the part radius and desired part angle by varying the radius of the punch and the bending angle.

## References

1. Stachowicz F, Trzepieciński T, Pieja T (2010) Warm forming of stainless steel sheet. Arch Civ Mech Eng 10(4):85–94. [https://doi.org/10.1016/s1644-9665\(12\)60034-x](https://doi.org/10.1016/s1644-9665(12)60034-x)
2. Nguyen DT, Kim YS, Jung DW (2012) Flow stress equations of Ti-6Al-4V titanium alloy sheet at elevated temperatures. Int J Precis Eng Manuf 13(5):747–751. <https://doi.org/10.1007/s12541-012-0097-0>
3. Bruni C, Forcellese A, Gabrielli F, Simoncini M (2006) Air bending of AZ31 magnesium alloy in warm and hot forming conditions. J Mater Process Technol 177(1–3):373–376. <https://doi.org/10.1016/j.jmatprotec.2006.03.222>
4. Wang A et al (2017) Springback analysis of AA5754 after hot stamping: experiments and FE modelling. Int J Adv Manuf Technol 89(5–8):1339–1352. <https://doi.org/10.1007/s00170-016-9166-3>

5. Voce E (1948) The relationship between stress and strain for homogeneous deformation. *J Inst Met*
6. G. Jis and G. Jis, "JIS G3101 SS400 steel plate / sheet for general purpose structural steels," p. 86011881.
7. M. M.-T. T. P. 1-2. (2002) TCVN 197



# Modeling Thrust and Torque of the Propeller on Ship Container Fortune Navigator



Ngo D. Vuong, Do D. Luu, Lai H. Thien, Hoang Q. Dong, Do V. Doan,  
Pham X. Duong, Pham V. Ngoc, Bui M. Tuan, and Nguyen X. Tru

**Abstract** This paper proposes a method and results of modeling the thrust force (F) and torque (M) generated by the propeller working behind the hull in water environment for the container vessel Fortune Navigator (CV. FN), that belongs to the Vietnam Ocean Shipping Joint Stock Company. The input data for modeling consists of periodic-changing signal pairs (F, M) that are obtained by authors from the hull–propeller numerical simulations for CV. FN using CFD method and commercial software STAR/CMM+. The input database is obtained based on design of experiments (DoE) for CV. FN with: Draft varies from ballast to full load; the draught difference ( $\text{Trim} = T_A - T_F$ ), considered as a disturbance (where:  $T_A$ —draft of the aft,  $T_F$ —draft of the forward) and the changing propeller speed. The propeller’s excited force/torque are transformed from the time domain to the frequency domain by the FFT method after re-sampling twice the input data. This implementation method ensures that the data is sampled in a constant time step, and the sample number of the extracted data vectors (T and M) is applied to the exact FFT-algorithm. The database obtained from processing F and M signals in the frequency domain is the input for regression modeling to determine force and moment components according to the impact factors. Research on signal processing and modeling the forces and moments are carried out on the LabView (NI, USA Company).

**Keywords** Propeller’s thrust and moment · Resampling and FFT · Regression modeling

---

N. D. Vuong · D. D. Luu (✉) · L. H. Thien · H. Q. Dong · D. V. Doan · P. X. Duong · P. V. Ngoc ·  
B. M. Tuan · N. X. Tru  
Vietnam Maritime University, 484-Lach Tray, Hai Phong City, Vietnam  
e-mail: [luudd@vimaru.edu.vn](mailto:luudd@vimaru.edu.vn)

N. D. Vuong · B. M. Tuan · N. X. Tru  
Naval Technical Institute, Hai Phong City, Vietnam

## 1 Introduction

The propeller torque and thrust when the propeller works behind the hull in the water environment are variable parameters and changes following the propeller working cycle. The mean torques of the engine and the propeller are used to evaluate the power of the main propulsion plant (MPP) at steady-state rotation. The average power, torque, and rotational speed are used to determine the operating (static) mode of the engine-propeller system. Similarly, the mean propeller's thrust is equal the average hull resistance when the ship works in the water. This feature is combined with the ship's speed set at the average propeller's rotary revolution give an estimation of the hull and propeller powers, and working efficiencies.

The periodic-variable components of the excited torque  $M$  (or Thrust,  $F$ ) generated by the propeller affects the excited torsional vibrations (the axial vibrations) on the MPP. The excited torsional moment and axial force (ETM, EAF) of the propeller are expressed as harmonic functions, which is a multiple of the number of propeller blade  $z_p$ . It is necessary to pay attention to the amplitudes orders 1, 2, and 3, or harmonic degree:  $k = z_p, 2z_p, \text{ and } 3z_p$ .

The study of vibrations (torsional and axial) on the MPP needs to determine the exciting forces/moments with harmonics of 1st, 2nd, or 3rd orders of the propeller's blade number ( $z_p$ ) because the propeller can lead to some resonance states.

The American Bureau of Shipping (ABS) [1] provides the results of more 20 real ship studies of the propeller's torque and axial force. In the reference [1], there are not shown any specific boundary condition and research using method. In other aspects, the results show that the amplitudes of the torque harmonics  $AM$  ( $k = z_p, 2z_p, \text{ and } 3z_p$ ) are expressed through the mean torque  $M_0$  (same for the axial force  $F_0$ ). In [2], Yuriy Batrak also pointed out that there is not any information about the force/torque calculation used by the CFD method. That raises the study problem to determine ETM and EAF by CFD method in this paper.

The commercial professional software STAR-CCM+, developed by SIEMENS, is adapted in the hull-propeller working investigations in water environment. In order to ensure accurate calculation results, the finite elements number of the calculated area surrounding the hull is selected according to detailed instructions of the company [7]. In addition, the hydrodynamic calculation method (CFD) is usually used as RANSE (Reynolds Averaged Navies-Stokes Equations) to ensure real-time results [3].

## 2 Materials and Methods

### 2.1 Making Torque and Thrust Signals from Hull-Propeller Simulation by CFD

Using CFD method and STAR-CCM+ software the two digital array signals in real-time are obtained moment  $M(t)$  and force  $F(t)$ . Under the received convergence data we choose some  $N_c$  cycles (about  $3 \div 5$ ) for noise processing later. In the last  $N_c$  cycles, often the time step is different  $dt(m) = k \cdot dt_{\min}$ ,  $k = 1, 2$ , we re-sample with step  $dt_0 = dt_{\min} = 1$  (ms) as the smallest step [see Eq. (1)].

From Eq. (1), the outputs are two steady periodic signals  $M(t)$  and force  $F(t)$ , with the same  $dt = 1$  ms. Proposing the propeller speed  $n_p$  (rpm), one revolution will be extracted  $N_{1c}$  samples (calculated by Eq. (2), the integer part of the rounded number).

$$\begin{aligned} M(m+i) &= M(m) + i \cdot dM(m); \quad dM(m) = k \cdot dt_0; \quad i = 1 \dots k \\ dM(m) &= M(m+1) - M(m); \\ F(m+i) &= F(m) + i \cdot dF(m); \quad dF(m) = k \cdot dt_0; \quad i = 1 \dots k \\ dF(m) &= F(m+1) - F(m); \end{aligned} \quad (1)$$

And, a chunk of data with  $N_s = N_c \cdot N_{1c}$  samples, where  $N_c$  is the number of cycles to be sampled  $N_c = 3, 4$  or  $N_c = 5$ .

$$N_{1c} = [60/n_p/0.001] = [60000/n_p]; \quad N_s = N_c \cdot N_{1c} \quad (2)$$

[.]—The integer part is rounded of the sample numbers.

The transformation of the signal is done by the FFT algorithm, where the number of samples in  $NFFT = 2^k = 512$ , for example,  $k = 9$ ,  $NFFT = 512$ . Resampling by “spline” approximation method, we can use the module included in LabView to build signal processing software (VI). The average propeller thrust and torque vectors for one cycle from  $N_c$  cycles were resampled ( $M_{RS}$ ) with resampling in the  $N_{RS} = 512$  samples. The FFT transform, coded in LabView with the  $FFT(.)$  statement, is an example of a filtered signal of torque ( $X_M$ ).

$$\begin{aligned} X_M(k) &= \frac{1}{N_c} \sum_{i=1}^{N_c} M_{RS}(i, k); \quad k = 1 \dots 512 \\ X_F(k) &= \frac{1}{N_c} \sum_{i=1}^{N_c} F_{RS}(i, k); \quad k = 1 \dots 512 \end{aligned} \quad (3)$$

$$FFT(X_M) \Rightarrow \{M_0, AM_1, AM_2, \dots; \zeta_1, \zeta_2 \dots\}$$

$$\begin{aligned}
M(t) &= M_0 + \sum_{k=1}^{M_p} AM_k \sin(k\omega t + \zeta_k) \\
M(t) &= AM_1 \sin(\omega t + \zeta_1) + M_{Z_p} \sin(Z_p \omega t + \zeta_{Z_p}) \\
&\quad + AM_{2.Z_p} \sin(2Z_p \omega t + \zeta_{2Z_p})
\end{aligned} \tag{4}$$

where:  $\omega$ ,  $Z_p$ —angular velocity, number of blades of propeller;  $M_0$ —average value of torque;  $AM$ ,  $\zeta$ —amplitude and phase of the harmonics.

Formula (4) represents the signal according to all harmonics from 1 to  $M_p$ , but only focuses on two harmonics that have practice:  $k = 1, Z_p, 2Z_p$ .

## 2.2 Building Signal Processing Module on LabView

Simulating with CCM+, the input signal is large for one experiment (about 5000 samples) and saved in \*.csv format. Therefore, it is necessary to code in high-level code programming to read \*.csv recorded data files. The authors create a subVI that reads \*.csv, relatively in LabView.

Resample for signal torque ( $\mathbf{M}$ ) of 1 cycle with  $N_{1c}$  samples, to get a new array of the same cycle with 512 samples, we create two sequences of variables  $x_1$  and  $x_2$  and follow the command:

In MathScripts some statements are used for research:

$$\begin{aligned}
dx_1 &= 1/N_{1c}; dx_2 = 1/512; x_1 = 1 : N_{1c}; \\
x_1 &= x_1 * dx_1; x_2 = 1 : 512; x_2 = x_2 * dx_2; \\
\mathbf{M}_2 &= \text{interpolate1d}(x_1, \mathbf{M}, x_2, 'spline');
\end{aligned} \tag{5}$$

The FFT for the resampled vector  $\mathbf{M}_2$ , obtain the amplitude ( $\mathbf{R}$ ) and phase ( $\mathbf{ph}$ ) values of the complex number harmonics ( $z$ ) by the corresponding command:

$$z = \text{fft}(\mathbf{M}_2, 512)/258; \mathbf{R} = \text{abs}(z); \mathbf{ph} = \text{angle}(z); \tag{6}$$

## 2.3 Simulation Plan for MV.FN

MV.FN is a container ship of VOSCO as the studied object of the article. The basic parameters of the MV main propulsion system. The FN in the normal regime when the ship is newly built, at the sea-trial tests, is significant in the torque/force simulation (shown in Tables 1 and 2 [8]).

Checking the reliability of the simulation model with real data of MV.FN at the sea-trial regimes shows the difference in power  $\delta P = [P_w(\text{sea-trial}) - P_w(\text{CFD})]/$

**Table 1** Informations about MV. FN and Sea-Trial tests

ME		Propeller		Sea-trial tests
Type	B&W 8L35 MC HITACHI ZOSEN	Propeller Blade number $Z_p$	1 4	Data: 27th of May 1998 Place: off the coast of Yuge Island (Japan)
MCR	Maximum cont. rate—210 (RPM)	Diameter, m Pitch (m) (0.7R)	4.05 2.5	Drafts(m)-Fore/Middle/Aft: <b>3.537/4.444/5.349</b>
Output: 4657 kW at M.C.R		Pitch ratio 7(0.7R)	0.61	Sea condition: <b>Slight.</b> <b>Weather: Blue-sky</b>

**Table 2** Results of the FV. FN Sea-Trial and CFD simulation

No.	ME LI	MV speed	ME rev	Torque	Power (CFD)	Power (sea-trial)	$\delta P$
	%	knot	$\omega, \text{rad}^{-1}$	M, kN	$P_{WkW}$	kW	%
1	50	13.33	17.51	124.7	2184	2491	12.38
2	75	15.22	20.01	156.7	3137	3478	9.81
3	90	16.02	21.29	179.8	3829	4196	8.75
4	100	16.39	21.97	195.5	4295	4681	8.25

$P_w(\text{sea-trials}) < 13\%$  (Table 2) between the two methods are acceptable in practice. Since then, continue to use 3-D model using CFD for the design of experiments (DoE).

From the actual operation data of the MPP of CV.FV, we consider the following: the ship usually operates with an engine rotation of about 173.5 (rpm), or:  $n_t\% = 82.5$  (M.C.R), load LI = 56.4% when loading (Load Cargo Index)  $LCI\% = 100$ , corresponding to mean draft:  $D_m = 7.8 \div 8.8$  (m). The mode of the train running without cargo, (ballast) at the average draft is about  $D_{mb} = 4.4$  m. Therefore, the authors simulated in different loading regimes corresponding to draft from ballast to full mode, different trims (cause of noise), as shown in Table 3.

### 2.4 Mathematical Model of $F_m(\text{Draft})$ and $M_m(\text{Draft})$

The results of the average thrust  $F_m$  and average torque  $M_m$  generated by the propeller at each cargo-loading— $D_m$  (Draft, m) need to be set. To get a suitable model, we draw the whole graph in the form of  $Y(D_m)$ . And from there, we can select each variation segment of the D-axis and build the corresponding regression model. Analyzing the representation with the results of the regression model for the entire Draft  $D_m = [4.4, 9.5]$  (m), we find that both thrust and torque cannot follow a common model. From there, it is necessary to divide each segment to perform modeling to ensure the accuracy and reliability of the tree according to the corresponding Fisher statistical criteria.

**Table 3** DoE and CFD results for mean force and moment of propeller

No.	D	V	n	Tm	Mm	No	D	V	n	Tm	Mm
Unit	m	knots	rpm	kN	kNm	Unit	m	knots	rpm	kN	kNm
1	4.38	14.15	160.20	214.00	94.80	23	7.30	12.30	173.46	330.30	138.70
2	4.39	14.08	166.50	365.10	158.60	24	7.63	11.60	173.46	343.70	144.60
3	4.40	14.00	155.65	355.90	153.10	25	7.70	11.60	173.46	337.70	142.50
4	4.41	14.10	160.20	374.60	158.40	26	7.75	11.70	173.45	337.70	142.40
5	4.42	14.20	160.20	212.80	95.30	27	7.95	11.30	173.45	353.80	148.40
6	5.35	13.60	172.14	276.90	121.80	28	8.00	11.30	173.47	354.00	149.00
7	5.46	13.80	173.30	281.60	123.70	29	8.09	11.30	174.03	353.50	150.20
8	5.53	13.60	173.02	285.70	124.70	30	8.10	11.32	173.52	352.70	147.20
9	5.61	13.82	173.12	287.90	125.70	31	8.13	11.30	172.37	346.60	146.50
10	5.65	13.70	173.50	283.60	122.70	32	8.14	11.31	173.40	352.60	149.00
11	6.10	13.40	173.47	290.20	123.20	33	8.15	11.20	173.45	353.40	148.10
12	6.25	13.30	173.47	294.30	124.90	34	8.40	11.03	173.60	357.90	150.50
13	6.35	13.25	173.47	298.70	125.10	35	8.50	11.00	173.60	361.20	150.60
14	6.43	13.15	173.12	303.60	133.10	36	8.60	10.63	173.60	365.30	153.70
15	6.52	13.30	173.51	308.80	135.90	37	8.70	10.60	173.60	365.90	154.00
16	6.55	13.22	173.48	308.00	135.00	38	8.80	10.50	173.60	365.20	153.30
17	6.65	13.22	173.46	306.20	132.80	39	8.90	10.40	173.60	368.90	156.00
18	6.85	12.80	173.46	307.00	130.40	40	9.00	10.36	174.50	367.70	155.80
19	6.90	12.60	173.30	315.60	132.70	41	9.10	10.36	174.50	367.50	154.90
20	6.95	12.60	173.50	318.30	134.10	42	9.20	10.34	174.50	370.40	155.00
21	7.06	12.50	173.46	322.60	135.10	43	9.30	10.30	174.50	370.10	155.80
22	7.10	12.40	173.45	321.1	134.00	44	9.40	10.10	174.50	374.70	158.30

## 2.5 Harmonic Amplitudes of the Force $AF(T_m, k_p)$ and Torque $AM(M_m, k_p)$

At each mode of average draft  $D_m(m)$ , we have determined the average thrust and moment through the regression functions mentioned in (2.3) corresponding to the using rotation speed (n, rpm). To calculate the axial and torsional vibrations of the shaft system, we need to determine the excited harmonics by the propeller. According to the recommendations of the ABS registry (USA), as well as the experience of Prof. D.D.Luu, only need to determine two or three harmonic degrees of the propeller. This is also consistent with the investigation of the total  $M_h$  harmonics for diesel engines:  $M_h = 12$  for two-stroke engines, and  $M_h = 25$  - for four-stroke engines. The first, second or third order ( $k_{p1}, k_{p2}, k_{p3}$ ) for the forcing forces/moments will be respectively:  $k_{p1} = z_p, k_{p2} = 2z_p, k_{p3} = 3z_p$ . The amplitude of the force/moment is expressed through the corresponding force/moment mean values [1].

### 3 Results and Discussion

#### 3.1 Accuracy of 3-D Model for Simulation by CFD for VT-CV

The first requirement is that the 3-D model must be suitable for the object calculated by CFP. The methodology for testing the confidence of the 3-D model is that the CFD results compared with the actual ship results tested at the same boundary conditions are similar. The results are shown in Table 2 with an error of 13% of propeller powers between the sea-trial tests and the CFD simulation, allowing a reliable 3-D model to continue the simulation in the future.

#### 3.2 Synthesizing Simulation Results $F_m(D_m)$ and $M_m(D_m)$

In Table 4 are shown the regressive models of the thrust  $F_m(D_m)$  and torque  $M_m(D_m)$ . For example, in the  $D_m = [6.85 \ 9.54]$  (m), the  $F_m$  and  $M_m$  are calculated:

$$T_m = [-283.18 \ 133.0 \ -6.73] * [1 \ D_m(D_m)]^T$$

$$= -283.18 + 133.0 * D_m - 6.73] * (D_m)^2$$

and  $M_m = [-111.07 \ 53.87 \ -2.70] * [1 \ D_m(D_m)]^T$  with the confidence 99%.

**Table 4** Regressive models  $F_m(D_m)$  and  $M_m(D_m)$

$D_m$ , m	Reg. models: $F_m(D_m)$	Confidence	Reg. models: $M_m(D_m)$	Confidence
[4.42 5.61]	[-37.23 187.80 -12.27]	377.2 >> 12.06 = $F_{It}$ (0.99, 3, 5)	[-18.43 93.53 - 6.70]	220.5 >> 12.06 = $F_{It}$ (0.99, 3, 5)
[5.61 5.65]	[-107.25 889.56]—level 1	100%	[-75.0 546.45]—level 1	100%
[5.65 6.25]	[622.87 -129.92 12.37]	384.2 >> 215.7 = $F_{It}$ (0.95, 3, 1)	[158.23 -15.04 1.55]	1460 >> 215.7 = $F_{It}$ (0.95, 3, 1)
[6.25 6.35]	[44.40 16.80]—level 1	100%	[2.00 112.4]—level 1	100%
[6.35 6.52]	[-714.16 257.42 -15.42]	189,970 >> 5403 = $F_{It}$ (0.99, 3, 1)	[-14602 4516.74 -346.05]	459.5 >> 215.71 = $F_{It}$ (0.95, 3, 1)
[6.52 6.85]	[3067.7 -824.29 61.29]	18.7 >> 9.28 = $F_{It}$ (0.95, 3, 3)	[157526 -415.49 29.86]	348.6 >> 29.46 = $F_{It}$ (0.99, 3, 3)
[6.85 9.40]	[-283.18 133.0 -6.73]	5.5 >> 4.76 = $F_{It}$ (0.99, 3, 23)	[-111.07 53.87 -2.70]	5.4 >> 4.76 = $F_{It}$ (0.99, 3, 23)

**Table 5** Amplitudes of MV.FN propeller force and moment at  $k = 1, 4, 8$  harmonics

No. Exp	$D_m$ , m	$M_m$ , kNm	MAH1	MAH4	MAH8	$F_m$ , kN	FAH1	FAH4	FAH8
15	6.52	1359	0.010309	0.052673	0.004945	308.8	0.001311	0.009935	0.002096
20	6.95	1341	0.005200	0.052100	0.004200	318.3	0.000630	0.006989	0.001047
25	7.70	142.5	0.007000	0.043500	0.006500	337.7	0.000783	0.007161	0.001923
30	8.10	147.2	0.011415	0.037169	0.004869	352.7	0.000307	0.006544	0.001401
35	8.50	150.6'	0.019570	0.033049	0.006642	361.2	0.000909	0.007185	0.001815

### 3.3 Harmonic Amplitudes of Propeller Thrust Force and Torque

After the FFT, the amplitudes are expressed on a relative scale dividing by the parameter's mean value. Table 5 shows the results obtained in some experiments of simulating the propeller force/torque harmonics according to the experimental order.

## 4 Conclusion

The database of the propeller's thrust and torque via the draft is built by the CFD method using software STAR/CMM+. The article has built a DoE to verify the 3-D model of MV.FN used with CFD in accordance with test data at sea-trial. The test results show that the difference in propeller powers between simulation and experiment is less than 13%. The 3-D model was built for the MV.FN propeller hull-propeller is reliable enough for simulations with the CFD method in other experiments of the offered simulation DoE. The simulation DoE (Table 3) simulated on CCM+ with draft from ballast to full cargo loading. The obtained from simulation data were twice-resampled and processed in real-time and in frequency domain, summarizing the force/torque results we received regressive models  $F_m$  and  $M_m$  via draft. The obtained database allows for determining the harmonics amplitudes of the propeller force and torque.

## References

1. ABS (2018) Guidance notes on ship vibration.
2. Batrak Y (2022) Torsional vibration calculation issues with propulsion system. <http://www.shaftdesigner.com/>. Accessed from 15 Mar 2022
3. Luu DD et al (2020) Numerical study on the influence of longitudinal position of centre of buoyancy on ship resistance using RANSE method. *Nav Eng J* 132(4):151–160



4. Molland AF (2017) Ship resistance and propulsion: practical estimation of ship propulsive power. Cambridge University Press. Online ISBN: 9781316494196; <https://doi.org/10.1017/9781316494196>
5. Ngoc PV, Luu DD (2022) Calculating torsional moment of propeller in simulation of marine vessel hull-propeller by the CFD method. *J Giao thong Van tai (Viet Nam)* 7. ISSN: 1859-316X
6. Ngoc PV, Luu DD (2022) Processing thrust of numeric simulation results for marine vessel hull-propeller using STAR-CCM+ software. *JMST (Vimaru, Viet Nam)* 70:59–63. ISSN: 2354-0818
7. Siemens (2020) STAR-CCM+ user guide.
8. VOSCO, Technical documents of container vesel (CV.) fortunier navigator

# Forecast Working Regime of the Main Propulsion Plant Using Marine Diesel Engine by Shaft-Line Power Signal



Nguyen Xuan Tru, Do Duc Luu, Pham Van Ngoc, Cao Duc Hanh, Luong Cong Nho, Lai Huy Thien, Do Van Doan, Hoang Van Si, and Le Van Vang

**Abstract** Working regime (WR) of the main propulsion plant (MPP) with marine diesel engine (MDE) is the established parameter set of: MDE's power; rotary speed of propeller (or engine); ship's speed ( $P_w$ -n-V), [kW—rpm—knot], so that the MPP's major components are not subjected to mechanical and thermal overload. The WOR is established in accordance with the followings: Real operation conditions of hull and propeller; uniform working cycles of the MDE's cylinders; fuel consumption characteristics of the MDE. The selecting WOR was carried out on the base of: digital databases constructed during the design and construction phase of the ship MPP; result of predicting misfire states of cylinders and an established optimal functional. The instantaneous power signal is calculated by product signals of the instantaneous torque and average rotary speed. The WOR forecasts were verified for the MPP of the MV.HR34000DWT using the simulation software programmed on LabView, at the normal working sea-conditions.

**Keywords** Main propulsion plant · Working operation regime · Instantaneous power signal · Instantaneous torque signal · Misfiring diagnostics of diesel cylinders

---

N. X. Tru · D. D. Luu (✉) · P. V. Ngoc · C. D. Hanh · L. C. Nho · L. H. Thien · D. V. Doan  
Vietnam Maritime University, 484-Lach Tray, Hai Phong City, Vietnam  
e-mail: [luudd@vimaru.edu.vn](mailto:luudd@vimaru.edu.vn)

N. X. Tru  
Naval Technical Institute, Hai Phong City, Vietnam

H. V. Si · L. V. Vang  
Transport University of HCM City, Ho Chi Minh City, Vietnam

## 1 Introduction

In MPP operation, the officer selects a speed ( $n$ , rpm) corresponding to the fuel rack position ( $h_p$ ). Therefore, the engine's and propeller's power  $P_w$  (kW) could produce the propulsive force  $F$  (kN) overcome the total hull resistance  $R$  (kN), push the ship forward with speed  $V$  (knot).

Theoretically, we have to determine the three most important parameters ( $P_w$ ,  $n$ ,  $V$ ) while exploiting MPP. There are: consuming propeller power or engine power  $P_w$  (kW); the working revolution regime  $n$  (rpm) and the ship speed  $V$  (knot). In addition, we need to collect the temperature and pressure's information about the auxiliary systems for main engine: Cooling, lubrication, high-pressure air supplied systems. Addition, we need to have the curve of the S.F.O.C (g/kWh) via speed  $n$ .

In operation, non-combustion may occur in one or several cylinders. It's not desirable breakdown but is a potential problem in reality. As a result, the new dangerous resonance of torsional vibration may happen. This is not allowed to be added in the exploitation zone, outside the barred zone ( $BZ_1$ ) that is set in the regime of all cylinders working normally [6]. In these incident cases, the first task is to diagnose, identify which cylinder the fault occurs in. Then take the speed jumping out of the additional resonance region and determine the new safety working mode on the universal characteristics  $P_w$ - $n$ - $V$ , called the improved universal graph. Timely non-combustion diagnosis can be identified using the instantaneous torque signal  $M(t)$  with the diagnostic signal vector being the maximum values  $VA$ , or the vector of the minimum values  $VB$  of the torsional moment  $M(t)$ , that is measured on the shaft-line [4, 5]. In this paper, the authors will use the instantaneous power signal (output) of the main engine to select a reasonable operation regime for MPP.

## 2 Materials and Methods

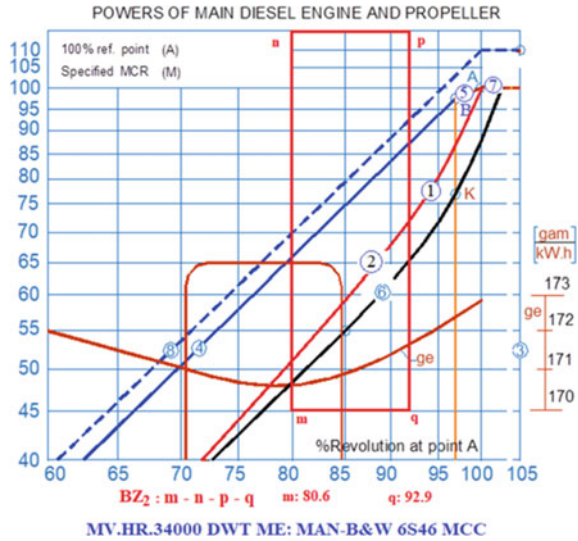
### 2.1 Drawing Safety Working Zone for the MPP Without Any Barred Zone

The safety operation zone is shown on the  $P_w(n)$ : power—rotary speed curves, developed from the engine manufacturer's database, sea-trail testing result, and is complemented with data from TVs researching on the MPP (Fig. 1).

Research TV, set up barred zone 1 ( $BZ_1$ ) in the regime of all cylinders operating normally as well as barred zone 2 ( $BZ_2$ ) when one cylinder does not burn, and the remaining cylinders burn normally. Using the TV calculation (TVC) for measuring TV (TVM) during the sea-trial tests, then the TVC is corrected in accordance with the TVM results. The final TVC result is put into a digital (electronic) record to automatically select the exploiting regime later.

The  $BZ_1$  is normally placed outside the operation zone when all of the cylinders work normally. It is set up to quickly pass through this  $BZ_1$  during transitions. The

**Fig. 1** Draw the safety effective regime ME of the MV.HR 34,000 DWT. Line 1—propeller curve through point A; Line 2—propeller curve, heavy running, recommended limit for fouled hull at calm weather condition; Line 3—speed limit; Line 4—torque/speed limit; Line 5—mean effective pressure limit; Line 6—propeller curve, light running (rang 2.5–5.0%) for clean hull and calm weather condition; Line 7—power limit for continuous running; Line 8—overload limit



BZ<sub>2</sub> lies in the regular exploitation if there're no incident. However, when an incident occurs, MDE couldn't be operated in BZ<sub>2</sub> since it can lead to a break down the shaft-line (mechanical overload: Torsional stress). The solution is not only quickly to switch the regime out of the BZ<sub>2</sub>, but before having to timely identify and diagnose the misfiring status in one of the cylinders.

## 2.2 Power Signals for the Selecting the Suitable Regime of the MPP

The average power value is calculated and used for drawing the P<sub>w</sub>(n) graphs (see Fig. 1). The instantaneous power signals (IPS) will be used for diagnosing the firing/misfiring states of the cylinders. The engine output (power) is considered equal to the propeller power (ignoring mechanical losses). The power P<sub>w</sub>(t) is a product of the torque M(t) and the angle speed ω(t). The average power is calculated as:

$$\bar{P}_w = \bar{M} \cdot \bar{\omega}; \bar{M} = \frac{1}{T} \int_0^T M(t) dt; \bar{\omega} = \frac{1}{T} \int_0^T \omega(t) dt; \bar{P}_w = \frac{1}{T} \int_0^T M(t) \cdot \omega(t) dt; \tag{1}$$

The real time signal P<sub>w</sub>(t) is used to diagnose firing condition in the cylinders. In diagnostic principle, when we can diagnose by the torque signal M(t), then using the signal k.M(t) can also diagnose according to the same built algorithm, where parameter k is unchanged. In that way, with the diagnostic regime at constant speed

$\omega_d = \text{const}$ , using the power signal in real time domain, determined by the formula:

$$P_w(t) = \omega_d \cdot M(t) \quad (2)$$

We diagnose and identify the class of normal/misfire state of the MDE's cylinder in accordance to the methods, algorithms and software built by  $M(t)$  [3, 4].

### 2.2.1 Express Classification Fire/ Misfire States of Every MDE Cylinder

In technical operation of MPP, it's necessary to determine the **IPS** using suitable devices. In principle, **IPS** is specified by measured instantaneous moment signal (**IMS**) and angle speed (measured average speed,  $\omega_d$  ( $s^{-1}$ )): **IPS** = **IMS** $\times\omega_d$ .

The IMS is measured by the torsional vibration measurement device. The TV stress on the surface of shaft is measures by a strain gauge. The device measures the average rotational speed  $n_d$ (rpm) made by optical sensor. The optical sensor, such as Omron, senses one pulse per one rotary cycle through a reflective piece. Defining the sample numbers  $N_s$  between the two rising (or descending) edges of the two consecutive square—pulses and using the sample frequency  $F_s$  of the DAQ, we estimate the average speed  $n = [60F_s/N_s]$  (rpm). The system of measuring and processing the torsional vibration signal (from which the power will be calculated) has been mentioned in the works of Luu et al. [7].

The results of the torsional vibration calculation (TVC) is improved by the results of the torsional measurement on the sea-trial. In the TVC there are defined the freedom frequencies of the mode-1 and mode-2:  $\omega_{0j}$  ( $s^{-1}$ ) or  $n_{0j}$  (cpm);  $n_{0j} = 30\omega_{0j}/\pi$ ;  $j = 1, 2$ . After that are defined the resonance revolutions in the operation speed zone.

Diagnostic revolution regime (DRR) is a speed range with an average  $n_d$  (rpm) and error  $\pm 5\%$ :  $DRR = [0.95 \ 1.05]n_d$ . DRR is selected so that it doesn't contain any resonant speed to eliminate diagnostic error from resonant phenomenon.

Suppose that DRR has  $m_R$  speed values, which is seen as repeat times, we conduct diagnosis process based on power signal. For each speed, we extract a specific number of cycles, for example 50 cycles. Thus, one state  $D_k$ ,  $k = 0, 1, \dots, z$  (total  $R = z + 1$  status), we specify  $N_k = 50 \cdot m_R$  real-time signals (cycles). According to the diagnosis algorithm based on vector of diagnostic sign VA (or VB, the power extreme values) we collect a matrix contains  $N_k$  rows and  $z$  columns: MA (or MB) corresponds to VA (or VB). This input database for diagnosis MA (or MB) is processed to the mean vector  $\mu_k$  and covariance matrix  $K_k$ , respectively [see Eq. (1)].

Reference database (RDB) for classifying the **R** technical states are called standard diagnostic characteristics (SDC) for every class  $D_k \{\mu_k, K_k, N_k\}$ . For the current state  $D_x$  in the same way we also construct the characteristic:  $D_x \{\mu_x, K_x, N_x\}$ . Normally,  $N_x = N_k = \text{const} = N$ .

$$\begin{aligned} \boldsymbol{\mu}_k &= [\mu_k(1), \mu_k(2), \dots, \mu_k(z)]; \mu_k(i) = \frac{1}{N_k} \sum_{j=1}^{N_k} V_k(i,j) \\ \mathbf{K}_k &= \text{cov}(\mathbf{V}_k); \boldsymbol{\mu}_k = \text{mean}(\mathbf{V}_k); \end{aligned} \quad (3)$$

The Mahalanobis distance between the two classes  $D_x$  and  $D_k$  is calculated:

$$d_{xk} = (\boldsymbol{\mu}_k - \boldsymbol{\mu}_x) \mathbf{K}_{xk}^{-1} (\boldsymbol{\mu}_k - \boldsymbol{\mu}_x)^T \quad (4)$$

$$\mathbf{K}_{xk} = \frac{m_x \mathbf{K}_x + m_k \mathbf{K}_k}{m_x + m_k} \quad (5)$$

The current state  $D_x$  is classified in to the  $D_m$  (referenced) class, if:

$$D_x \cong D_m : d_{xm} = \min\{d_{xk}; k = 1 \dots R\} \quad (6)$$

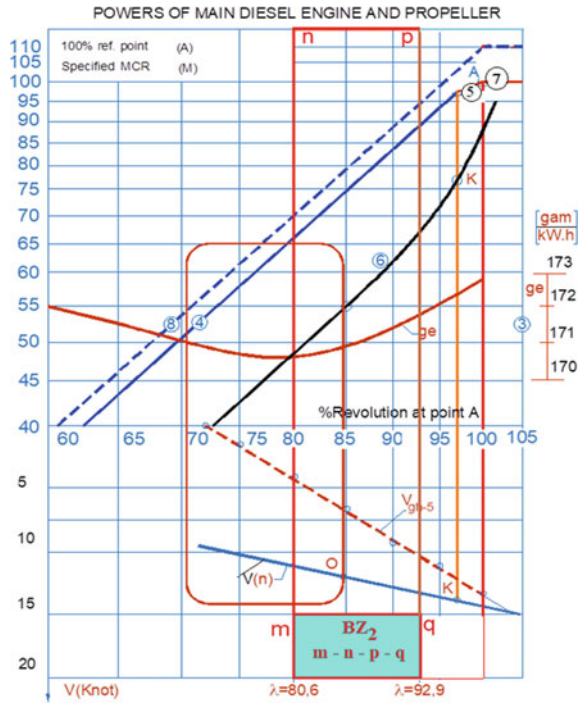
### 2.2.2 Draw $P_w - N$ Characteristic of the Propeller and $V_s - N$ of the Hull

After ensuring the operation speed safety for MDE, that to be free from mechanical and thermal overload, corresponding to  $g_e(n)$  characteristic, there are two possible cases could be happened with the predicted MDE: (1) All of the cylinders are fired normally; (2) One of these cylinders is misfired (abnormal). The first case allows diagnosing on any working revolution of engine as in Fig. 1:  $n = [63 \ 130]$  (rpm). The propeller characteristic line is forecasted based on the mean power values and the working revolution  $n$  of this propeller, because we consider the power value and revolution of both MDE and propeller are equal. In the case 2, the exploitation mode of MPP must be in the new established range (item 3), in which the working speed is analyzed with error rate  $\pm 5\%$  (see Fig. 2).

The propeller curve  $P_w(n)$  and hull characteristic  $V_s(n)$  are predicted based on the hull-propeller database and specific exploitation conditions of the ship. The propeller's characteristics depend on the operation revolution, average draft (cargo), sea conditions in which the ship is operating (normal or special operation regimes). For the new building ship, the prediction of the hull's and propeller's characteristics are executed on the base of the built (made): Hull and propeller database; algorithm and software. After years of operating, the prediction of the hull's and propeller's characteristics are executed on the base of the built: Daily acquisition database; suitable algorithm and software. The power prediction is conducted with devices and measuring methods based on the average power on the shaft-line.

For making hull and propeller's database it's need to build 3-D line ship-shaped line of the hull-propeller when operating in the normal operation regime, with water-line draft ( $D, m$ ) from smallest to largest (from the ballast to full cargo load). On the

**Fig. 2** Draw the suitable working regime of the MV.HR 34,000 DWT



basis of 3-D model, build a mathematical model to determine all hydrostatic parameters  $X_k$  according to draft:  $X_k(D)$ . The hydrostatic parameters are typical parameters for the hull, propeller used in the design and calculation of hull & propeller characteristics. Using the ITTC approximation method to calculate the total hull resistance at different draft  $D$ :  $R_T(D)$ . As a result, we can build hull's and propeller's database when cargo ships with different draft  $D$  (m) and pair selection ( $V_s$ - $n$ ) according to regression model set up with propeller characteristics ( $P_w(n)$ ) [9].

### 2.3 Predicting Characteristics of the MV's MPP During at Sea Operation

In MPP operation of the marine ship, we monitor the power, revolution and speed parameters under specific boundary conditions. The data is collected every month. Based on this collected database, we conduct analysis, synthesize and build regression model to forecast the characteristics of MPP via the operation time [2].

### 3 Results and Discussion

The paper verifies for MPP of MV.HR.34000 DWT. The results of TVC and TVM [10] defined values of mode-1 and mode-2:  $\omega_{0j}$  ( $s^{-1}$ ),  $n_{0j}$  (rpm);  $n_{0j} = 30\omega_{0j} / \pi$ ;  $j = 1, 2$ . On Fig. 3 are shown:  $n_{01} = 337.16$ ;  $n_{02} = 1436.02$ .

- Major resonance:  $n_{r1} = 56$  with  $k = 6$ .
- Minor resonances:  $n_{r2} \approx 67$ ,  $k = 5$ ;  $n_{r3} \approx 85$ ,  $k = 4$ ;  $n_{r3} \approx 112$  with  $k = 3$ .

There are selected 2 DRRs:  $DRR_1 = [94.2 \ 104.1]$ ;  $DRR_2 = [70 \ 77.4]$  (rpm).

Figure 2 displays graph of safe operation characteristics of MPP on MV.HR34000 DWT, using ME type MAN-B&W 6S46MC-C7,  $n_{MCR} = 129$  (rpm). Researching TV helps to figure out the dangerous resonant revolution and establish two barred zones  $BZ_1 = [51, 64]$  and  $BZ_2 = [104, 119.9]$  [6].

Using related speed  $\lambda = n/n_{MCR}$ :  $BZ_1 = [39.5, 49.6]\%$ ;  $BZ_2 = [80.6, 92.9]\%$ .

The  $BZ_1$  barred zone is normally outside of the exploiting rotation, when all cylinders work NORMAL, set to pass quickly through this zone during transitions.

The  $BZ_2$  zone is within the regular exploiting zone if there are no incidents. However, when there is a fault, it is impossible for MDE to operate in this area because it will lead to shaft fracture (overload—torsional stress).  $BZ_2$ : m-n-p-q in Fig. 2:  $BZ_2 = [80.6, 92.9]\%$ —the area corresponding to the relative speed  $\lambda$ .

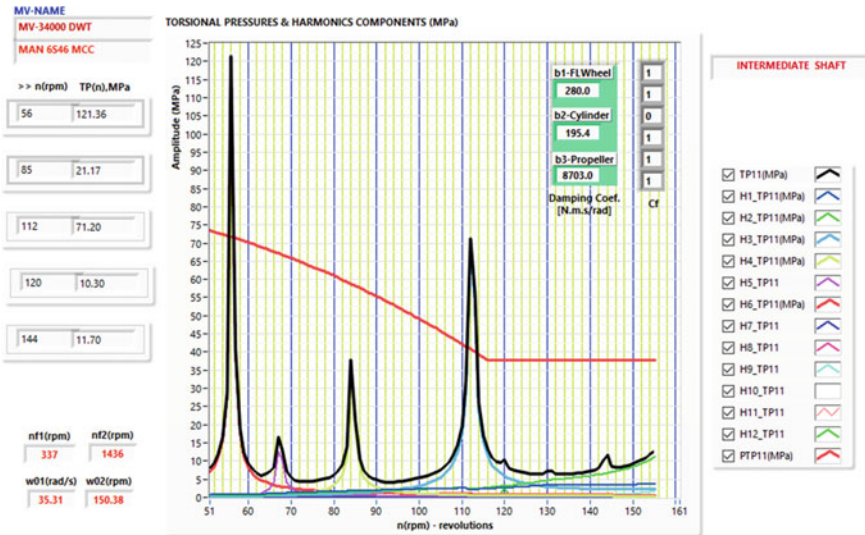


Fig. 3 Result of TVC of the MV.HR.34000 DWT, Misfire in third cylinder



## 4 Conclusion

Applying the technology to increase safety and efficient exploitation of the marine vessel MPP by: Measurement and continuously monitoring instantaneous power signals of the ship's MPP; use the digital hull's and propeller's databases in the design and construction of new ships. Thanks to this new technology, the ship's management officers (Chief Engineers) receive advice and experts to choose a safe and economic operating regime. In the fault situations with misfiring cylinders: timely diagnose the fault and thereby forecast a reasonable and safe operation regime in forecasted abnormal conditions.

## References

1. Luu DD (2009) Dynamics and vibro-diagnostics of marine diesel engines. Publisher "Transport", Ha Noi
2. Luu DD (2005) Predicting working regime of the MPP in the changed hull-propeller's technical state. *Trans J* 8:44–46, 71
3. Luu DD (2005) Predicting working regime of the MPP in the changed draft of the working cargo load. *Trans J* 9:59–63
4. Luu DD, Duong PX, Hanh CD, Ngoc PV, Tru NX (2021) Creating standard diagnostic characteristics for misfiring diagnostics of main diesel engine by torsional vibrations. *NEJ* 133(2):111–120. ISSN: 0028-1425. SCIE IF = 0.232. <https://www.ingentaconnect.com/contentone/asne/nej/2021/00000133/00000002/art00025>
5. Luu DD, Hanh CD, Ngoc PV, Tru NX (2021) Smart diagnostics for marine diesel engines using torsional vibrations signals on the ship propulsion shaft—line. *NEJ* 133(1):143–153. ISSN: 0028-1425. SCIE IF = 0.232. <https://www.ingentaconnect.com/contentone/asne/nej/2021/00000133/00000001/art0002>
6. Luu DD, Hanh CD (2020) Automatic calculation of torsional vibrations on marine propulsion plant using marine two-stroke diesel engine: algorithms and software. *J Inst Eng (India) Ser C* 102(1):51–58. <https://doi.org/10.1007/s40032-020-00626-y>. ISSN: 2250-0553; 2250-0545
7. Luu DD, Nho LC, Tu TN (2016) Modeling reasonable operation regimes of the MPP: MDE—propeller—hull on the general cargo ship. In: *Proceedings of the 17th AGA IAMU*, pp 360–365. ISBN 978-604-937-120-2
8. Luu DD et al (2017) Research and build a multi-channel VMS for dynamic studying of the MPP. In: *Proceedings of the 18th AGA IAMU*, pp 283–292. ISBN 978-954-8991
9. Nho LC, Luu DD, et al (2019) Researching, building simulation of main propulsion plant and main switch-board on the marine cargo ship. National Independent Project on Science and Technology with ID.DTDL.CN-14/15 carrying out in Vietnam Maritime University, Viet Nam, 2015–2019
10. Pha Rung shipyard. MV 34000 DWT. Technical documents (MV 34000 DWT. Results of the sea-trial tests; TV calculation; ME: MAN-B&W 6S46MCC7 documents

# Torsional Resonance Vibrations on the Main Propulsion System Using Two-Stroke Diesel Engine



**Bui Minh Tuan, Do Duc Luu, Cao Duc Hanh, Dong Xuan Thin, Do Van Doan, Nguyen Xuan Tru, Hoang Van Si, Le Van Vang, and Nguyen Quang Vinh**

**Abstract** This paper studied the resonance regimes of the torsional vibrations on the Main Propulsion Plant (MPP) using the two-stroke marine diesel engine (MDE) type MAN-B&W 6G70ME-C9.2, measured on the sea-trial test before the handover. The new physical phenomenon was gotten: turbulences, unfocused the phases in cycles of the first mode resonance. The requirement was to model the relationship and impact between the torsional vibration and the burning process in each of the engine cylinders. The authors investigated the indicator diagram  $p(\varphi)$  inside the cylinder when changing the phase of fuel distribution, in order to explain the physical nature of turbulence of torque in the resonance mode. The authors proposed the mathematical model with the small parameter for the torsional vibration system in the propulsion system of the MDE at the risk resonance mode.

**Keywords** Torsional resonance vibrations · Relationship between torsional vibrations and firing in cylinders · Mathematical model with the small parameter for torsional vibration

---

B. M. Tuan · D. D. Luu (✉) · C. D. Hanh · D. X. Thin · D. Van Doan · N. X. Tru  
Vietnam Maritime University, 484-Lach Tray, Hai Phong City, Vietnam  
e-mail: [luudd@vimaru.edu.vn](mailto:luudd@vimaru.edu.vn)

B. M. Tuan · N. X. Tru  
Naval Technical Institute, Hai Phong City, Vietnam

H. Van Si · L. Van Vang  
Transport University of HCM City, Ho Chi Minh City, Vietnam

N. Q. Vinh  
Naval Technical College, Ho Chi Minh City, Vietnam

## 1 Introduction

Torsional vibrations (TVs) on the shaft-line are very dangerous, therefore, in the designing and building a new or renew sea-going ship, the torsional vibration calculation (TVC) of the main propulsion plant (MPP) is compulsory. In addition, we measure TVs during the sea-trial test for the checking calculation results [1, 2]. Some maritime registration organizations approve the TVC and TVM results. The Rules for Classification and Construction of Sea-going Ships [2] recommend a method for TVC and the TVC's speeds need to be covered the ability to operate in the real-working scripts of MPP. To carry out the TVC, the MPP is modeled by the system with  $n$ -lumped masses with the constant inertial moments of masses, which are connected by the massless coefficients of the torsional weightless stiffness (torsional spring). These systems usually are linear systems with constant coefficients. Based on the integration of methods: Linear system with multi-degree freedom, Fast Fourier Transform (FFT) of the forced torque. Prof. Do Duc Luu proposed a combination of methods to solve equations with modern numerical theory: Harmonic balance in complex numbers; super-position; matrix algebra and main axes method (MAM). He proposed and built software for automatic TVs calculation (SATVC) coding in LabView platform [3]. The results calculated by these methods and SATVC software have high accuracy and similar to the previous results. This methodology and SATVC software have an outstanding advantage that the calculation process is fully automatic after preparing suitable input data provided by engine manufacturers and shaft system designers.

In the experimental TV's study on MPP on ship, Prof D.D. Luu (Maritime Research Institute of Vietnam Maritime University) cooperated with experts in Korea. Based on TVs measurements and analysis at MV\_XXX-XXX-XXX, using main engine MAN-B&W 6G70 ME-C9.2, the research group find out that TVs were not stable and high oscillation amplitude at the engine speed  $n = 36$  rpm. The research group has analyzed and separated TVs signals to each of cycle by the phase—square pulse signals for finding out the sample extraction time. Each square pulse represents one rotation. The fast processing results of 10 TVs cycles showed as in Fig. 1.

In the resonance  $n = 36$  rpm, the TVs are big and unstable. In contrast, on the near-resonance,  $n = 34$  rpm, the TVs are not so big, and stable. Therefore, the problem needs to be clarified which is the physical nature of the resonance phenomenon and modeling more accuracy this phenomenon by the mathematical model, which was solved in this research.

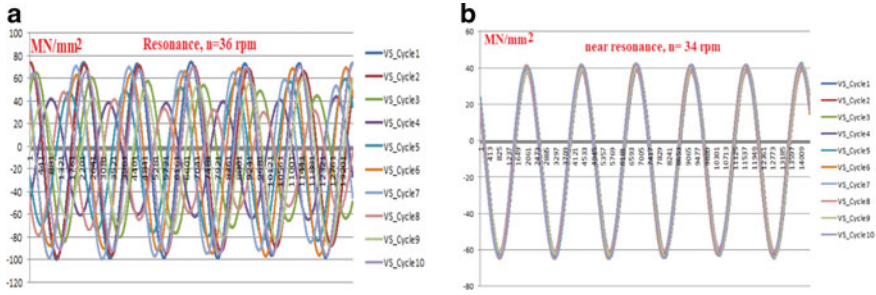


**Fig. 1** **a** Measured resonance TVs at  $n = 36$  rpm on the Intermediate shaft of an MV using MAN-B&W 6G70ME-C9.2, NORMAL. **b** Measured TVs at  $n = 34$  rpm on the Intermediate shaft of an MV using MAN-B&W 6G70ME-C9.2, NORMAL

## 2 Materials and Methods

### 2.1 Improve the Mathematical Model of Resonance TVs of the MPP with MDE

The mathematical model for TVC is presented as in Eq. (1).

$$J\ddot{\varphi} + B\dot{\varphi} + C\varphi = M(t) \tag{1}$$

where:  $\mathbf{J} = \text{diag}(J_1, J_2, \dots, J_n)$ —Diagonal matrix of inertial moments;  $\mathbf{C}$ —Stiffness matrix;  $\varphi$ —TV state vector,  $\varphi = [\varphi_1 \dots \varphi_n]^T$ ;  $n$ —number of system (1).  $\mathbf{M}$ —vector of excited torsional moments (ETM), [Nm].

The moments in the right side of the Eq. (2), ETM of  $i$ —cylinder,  $M_i(t)$  contains gas component and equivalent moment of the rotary—translational movement of connection—rod—crosshead—piston set. The first moment component of one cylinder is defined by:

$$M(\varphi) = [p(\varphi) + m\ddot{x}(\varphi)] \cdot \text{TF}(\varphi); \tag{2}$$

$$\text{TF}(\varphi) \approx \frac{\pi D^2}{4} \left( \sin\varphi + \frac{\lambda}{2} \sin 2\varphi \right)$$

where, the value  $p(\varphi)$  of current state cylinder pressure  $p$ , (MPa, Bar);  $\lambda = 0.5$  S/L and  $D$ —parameters of the diesel ( $L, D, S$ —connection rod, diameter of the cylinder, length stroke respectively), that are given in the MDE technical document.

$$\varphi = \varphi_s + \varphi_d = (\varphi_0 + \omega t) + \varphi_d \tag{3}$$

$$M(\varphi) \approx M(\omega t) + M_\varphi \varphi_d;$$

$$M_\varphi = \frac{\partial M}{\partial \varphi} \quad (4)$$

$$M(\omega t) = M_0 + \sum_{k=1}^{Mh} A_k \sin(k\omega t) + \sum_{k=1}^{Mh} B_k \cos(k\omega t) \quad (5)$$

$$\begin{aligned} M_\varphi(\omega t) &= \sum_{k=1}^{Mh} k A_k \cos(k\omega t) \\ &+ \sum_{k=1}^{Mh} -k B_k \sin(k\omega t) \\ &= \sum_{k=1}^{Mh} A_{\varphi.k} \sin(k\omega t - \pi/2) \\ &+ \sum_{k=1}^{Mh} B_{\varphi.k} \cos(k\omega t - \pi/2); \end{aligned} \quad (6)$$

$$A_{\varphi.k} = k A_k; \quad B_{\varphi.k} = k B_k$$

$$\begin{aligned} M(\varphi) \approx & M_0 + \sum_{k=1}^{Mh} A_k \sin(k\omega t) + \sum_{k=1}^{Mh} B_k \cos(k\omega t) \\ & + \left[ \sum_{k=1}^{Mh} A_{\varphi.k} \sin(k\omega t - \pi/2) + \sum_{k=1}^{Mh} B_{\varphi.k} \cos(k\omega t - \pi/2) \right] \cdot \varphi_d \end{aligned} \quad (7)$$

The formulas (2) ÷ (7) are used for every cylinder, in that  $\varphi_0$  is defined by the firing order of the MDE. The cylinder crank-shaft angle  $\varphi$  is the sum of the static and dynamic parts (3). Equation (7) is a mathematical model to calculate the excited torsional moment (ETM) while considering the TV effect on to the ETM.

At the resonance speed  $n = 36$  rpm with the Fig. 1a, we consider that TVs are very chaotic. The real cause of the turbulent scene of the TVs (torsional vibration stresses) is the unstable firing processes in every cylinder (see Eq. (2)) and we would study a little more about the firing process in a cylinder, when we change the starting combustion point (SCP) via the crank-shaft angle.

In Fig. 2 we show the results of the simulation in MatLab the pressure  $p(\varphi)$  inside the combustion chamber, when SCP are changed relatively 3, 6 and 8 degree after TDC when  $n = 76$  rpm.

$$J\ddot{\varphi} + B\dot{\varphi} + C\varphi = \mathbf{M}(\omega t) + \mathbf{M}_\varphi(\omega t)\varphi \quad (8)$$

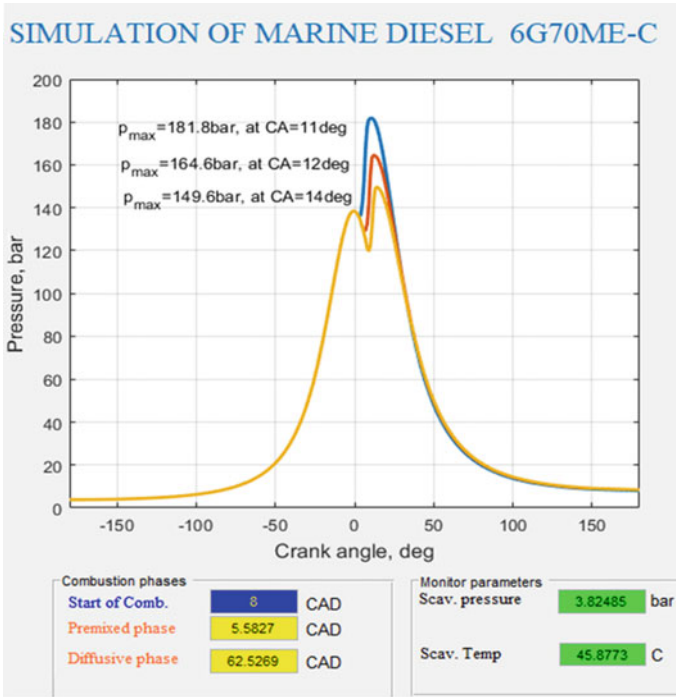


**Fig. 2** Indicator diagrams of cylinder when angle of SCP are 3, 6 and 8 degrees after TDC, at  $n=76$  rpm

The comparison of the new model with the traditional one for the 1-mode resonance TVC is focused in the right side of the equation. The forced moment was estimated with an additional moment part due to the affection of the torsional vibration angle (the dynamic factor) in Eq. (8).

Considering the maximal torsional angle is smaller than  $3^\circ$ , or 0.05 rad ([4], page: 30), we could propose that  $\mathbf{M}_\varphi(\omega t)\varphi \ll \mathbf{M}(\omega t)$  and the Eq. (8) would be in the small parameter form ([1], page: 112)

$$J\ddot{\varphi} + B\dot{\varphi} + C\varphi = \mathbf{M}(\omega t) + \mu\mathbf{H}(\omega t); \tag{9}$$

$\mu$  – small parameter

The small parameter method to solve the Eq. (9) could be found in the monograph ([1], page: 119–120).

## 2.2 Verified Studying TVs on the MPP, Using MAN-B&W 6G70ME-C9.2

The particulars of the HYUNDAI-MAN B&W 6G70ME-C9.2 are written in Tables 1 and 2.

The MPP on MV.XXX-XXX-XXX using a DME MAN-B&W6G70 MEC-9.2 [5]. The MV was built in South Korea (Because of copyright reasons, the authors couldn't provide the specific name of the ship).

**Table 1** Technical parameters of the MDE 6G70 MEC 9.2

Nº	Parameter	Value	Unit
1	Engine type: HYUNDAI-MAN B&W 6G70ME-C9.2		
2	Output at MCR	15,980	kW
3	MCR	76	rpm
4	Cylinder diameter	700	mm
5	Piston stroke	3,256	mm
6	Number of cylinders	6	
7	MIP	17.8	bar
8	Engine ratio	0.5	
9	Crosshead mass	9,686	kg/cyl
10	Gas harmonic	T248079	
11	Firing order	1-5-3-4-2-6	

**Table 2** Model for TVC of the MPP using 6G70ME-C9.2

Nº	Mass name	Moment of inertia, kgm <sup>2</sup>	Stiffness MNm/rad	Abs. damp %	Relative damp % or Nms/rad
1	D290.OUT	16,800.00		0.00	
2	D.IN + FLG + M	6789.00	9.00	0.00	200,000.0
3	CYLINDER 1	42,716.00	3717.47	- 0.85	0.00
4	CYLINDER 2	42,716.00	3205.13	- 0.85	- 1.00
5	CYLINDER 3	42,716.00	3236.25	- 0.85	- 1.00
6	CYLINDER 4	42,716.00	3154.57	- 0.85	- 1.00
7	CYLINDER 5	42,716.00	3225.81	- 0.85	- 1.00
8	CYLINDER 6	42,716.00	3344.48	- 0.85	- 1.00
9	CH.DRIVER + M	13,322.00	4444.44	0.00	- 1.00
10	TURN.WHEEL	15,608.14	6666.67	- 0.50	0.00
11	FLANGE	962.79	90.87	0.00	0.00
12	PROPELLER	177,442.75	190.60	- 4.96	0.00

Sign ' - ' damping coefficient in %.

### 3 Results and Discussion

The TVC and results of the torsional vibration measurements (TVM) at the sea-trial tests are obtained and shown in Table 3.

The TVC gives the barred speed ranges:

- Barred speed zone-1 (BSZ1):  $[31 \div 40]$  (rpm)
- Additional BSZ2 (Misfire in a cylinder):  $[64 \div 77]$  (rpm).

Simulating indicator diagram of the 6G70ME-C9.2 in the resonance speed  $n = 36 \pm 2$  (rpm),  $t.m\ n = \{34,36,38\}$  and starting combustion point  $\{1,3,5\}$  deg. After TDC, using software coded in LabView by authors [6] results of the simulation are shown in Fig. 3.

The excited torsional moment at the resonance  $n = 36$  rpm is calculated and transformed in the frequency domain with FFT algorithm. The simulation is coded in LabView platform. The studied results are shown in Fig. 4.

**Table 3** Freedom TVs study of the MPP using the ME: 6G70ME-C9.2

<b>TVC</b>	$n_{01} = 205.7$ rpm; $k = 6$ , $n_r = 34.2$ rpm	Selected $J_p = 177,443$ kgm <sup>2</sup>
<b>TVM</b>	$n_r = 36$ rpm; $k = 6$ ; $n_{01} = 216$ rpm	–
<b>TVC</b>	$n_{01} = 215.7$ rpm; $n_r = 35.95$ rpm $n_{02} = 251$ rpm; $k = 6$ , $n_r = 41.83$ rpm	Corrected $J_p = 150,375$ kgm <sup>2</sup> , the repetition calculates the TVs

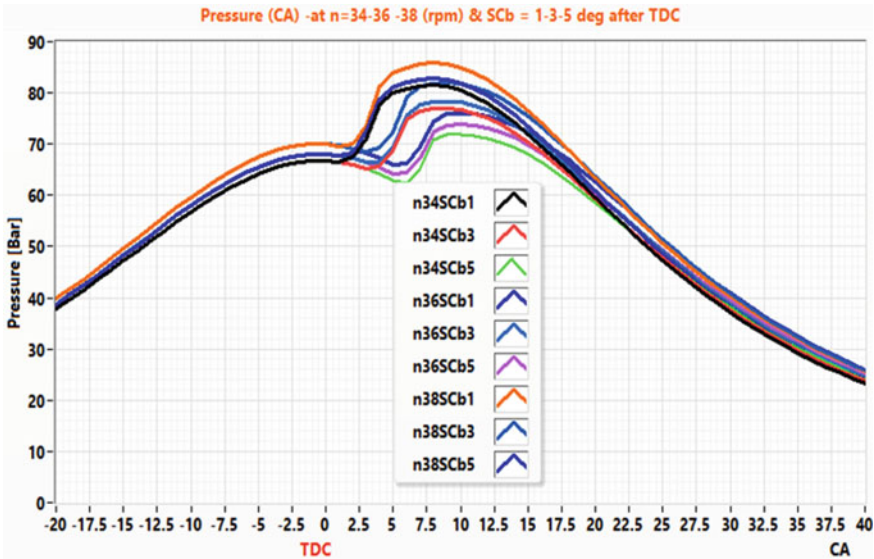


**Fig. 3** Simulating torsional influence to unstable firing in cylinders at resonance speed  $n = 36$  rpm with the SCP: 1–3–5 deg. after TDC



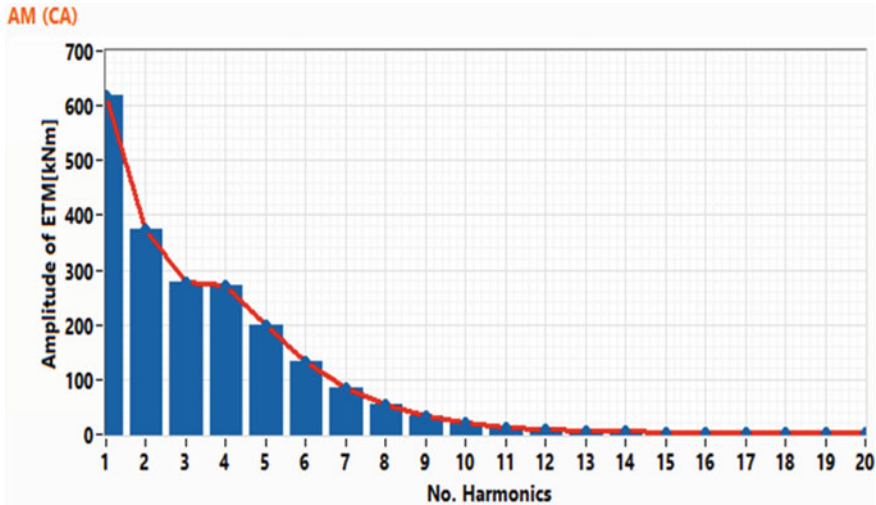


Fig. 4 Harmonic amplitude of cylinder ETM at the speed  $n = 36$  rpm with the SCP: 3 deg. after TDC, using FFT and coding in LabView

The firing process in the working cycle is depended on the speed and starting combustion point. At the resonance mode  $n = 36$  rpm appeared big torsional vibrations of the speed and angle forms, that lead to vibrations of the speed regime and the SCP. Figure 3 illustrates the relationship between the TV resonances with the working process that means the essential causes of the new physical phenomenon (in Fig. 1).

## 4 Conclusion

This paper presented the serious torsional vibration on the main shaft system using 2-stroke marine diesel engine MAN—B&W 6G70MEC9.2, based on the integral research TVC and TVM according to the document of the sea-trial tests on the ship. The key reasons for new physical phenomena along with TVs at resonance mode  $n = 36$  rpm are the effects among TVs, fuel supply process, and fuel combustion stages. At this great resonance mode, a series of dynamic affection occurred: TVs, fuel injection, burning, expansion, and power process distort strongly (Figs. 1 and 3). The paper also proposed a procedure for TV calculation at the resonance mode according to the small parameter method.

## References

1. Luu DD (2009) Dynamics and vibro-diagnostics of marine diesel engines. Publisher “Transport”, Ha Noi (in Vietnamese)
2. Russian Maritime Register of Shipping Edit (2014) Rules for classification and construction of sea-going ships. Saint Petersburg, Russian Federation
3. Luu DD, Hanh CD (2020) Automatic calculation of torsional vibrations on MPP using marine two-stroke diesel engine: algorithms and software. *J Inst Eng (India) Ser C*. 102(1):51–58. <https://doi.org/10.1007/s40032-020-00626-y>. ISSN: 2250–0553; 2250–0545
4. Minchev ND (1983) Dynamics of marine machines. Publisher “Army”, Sophia (in Bulgarian)
5. MAN–B&W. CEAS engine calculations. Retrieved from <https://www.man-es.com/marine/products/planning-tools-and-downloads/ceas-engine-calculations>. Accessed on Sep 2021
6. Luu DD, Quang VN (2021) Affections of turbine nozzle cross-sectional area to the marine diesel engine working. <https://doi.org/10.17818/NM/2021/2.1> *Our Sea (NASE MORE)* ISSN: 0469-6255. 68(2):65–73

# Effect of Hot-Pressing Mold Design on Uniformity of Dome-Shaped Products from Infrared Optical Ceramics



Nguyen Tuan Hieu, Le Minh Thai, Nguyen Thai Dung, Do Van Thom, and Phung Van Minh

**Abstract** This article explores the effects of structural characteristics on the quality of dome-shaped hot-pressed products made from infrared optical ceramic materials. The research simulated the effect of the coefficient of friction between the mold cavity and the injection mold material on the pressed product's uniformity. Simultaneously, practical experiments are used to validate the simulation findings.

**Keywords** Hot-pressing mold · Mold structure · Infrared optical ceramic friction · Magnesium fluoride

## 1 Introduction

MgF<sub>2</sub>, CaF<sub>2</sub>, ZnS, ZnSe, and other infrared optical ceramic materials are frequently employed in the manufacture of optical components [1–4]. Polycrystalline materials have superior physical and mechanical qualities, which is why they are often used for fabricating infrared optical components [5–7]. Homogeneity of hot-pressed products is defined as the similarity in quality amongst dome heat pressed products used in diverse applications [8, 9]. To guarantee the quality of the dome hot-pressed product, the density difference between the top and bottom of the dome must be as little as possible [10, 11]. The works [12, 13], and [14] explored the influence of hot-pressing pressure on the quality of hot-pressed products made from Magnesium Fluoride optical ceramics. Chang and Hon [15] investigated the effect of pressed product

---

N. T. Hieu  
Hanoi Institute of Technology, Hanoi City, Vietnam

L. M. Thai (✉) · N. T. Dung  
Faculty of Special Equipment, Le Quy Don Technical University, Hanoi City, Vietnam  
e-mail: [thaileminh@lqdtu.edu.vn](mailto:thaileminh@lqdtu.edu.vn)

D. Van Thom · P. Van Minh  
Faculty of Mechanical Engineering, Le Quy Don Technical University, Hanoi City, Vietnam

structure on the quality of pressed products. In certain studies, such as Krell and Klimke [16], they simply emphasized particle coordination homogeneity in green bodies. The purpose of this work is to present the findings of a study on the effect of structural parameters on the uniformity of infrared optical ceramic products.

## 2 Process of Experimentation

In this study, the ABAQUS software is employed. The effect of mold cavity opening angle  $\alpha$ , as specified in Fig. 1, was explored.

A normal value of  $150^\circ$  and  $180^\circ$  are taken to analyze the impact of mold opening angle. Then, to perform hot-pressing of the dome-shaped  $\text{MgF}_2$  optical ceramic sample with a dome edge diameter of 70 mm, a hot-pressing mold was built with an opening angle of the mold cavity of  $150^\circ$ . The resultant hot-pressed product is processed to create nine flat samples with a minimum dimension of  $10 \times 10$  mm in nine places, as illustrated in Fig. 2. One needs a condition: parallelism between two working surfaces is less than 0.005;  $R_a < 0.05$ ; and surface cleanliness is class IV [17].

The density of these nine flat samples was determined using a hydrostatic density balance, and the transmittance at  $4.5 \mu\text{m}$  (the wavelength at which  $\text{MgF}_2$  optical ceramics transmit the most infrared light) was determined using a single beam infrared spectrometer with Michelson interferometer [18]. Equation (1) was used to calculate the density homogeneity and transmittance uniformity, respectively.

**Fig. 1** Structure of hot-pressing mold (1–pestle; 2–mortar; 3–shell; 4–pressed material;  $\alpha$ –opening angle of the mold cavity)

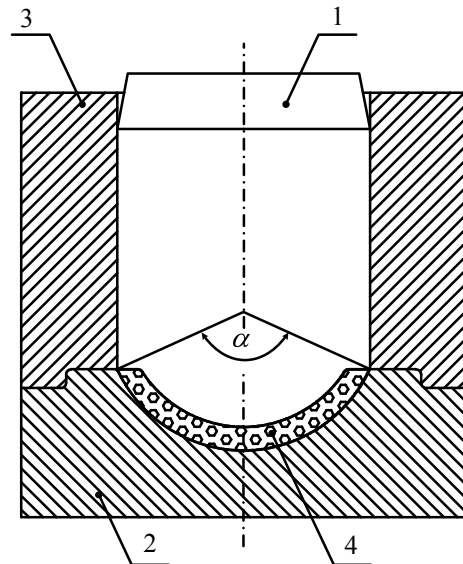
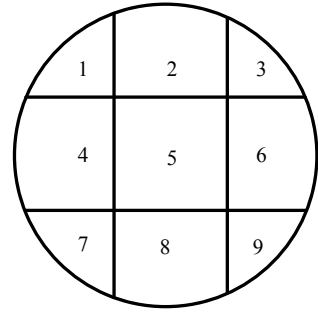


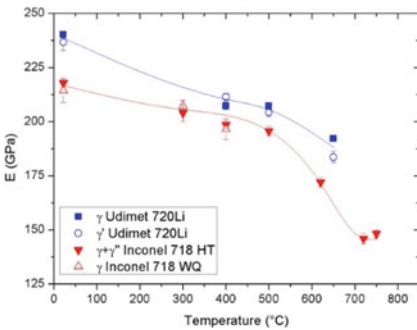
**Fig. 2** Areas for determining the homogeneity of hot-pressed products



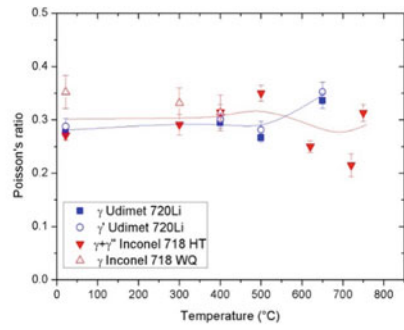
$$\Delta_{\rho} = \frac{\delta_{\max} - \delta_{\min}}{\delta_{\max}} \tag{1}$$

$$\Delta_T = \frac{T_{\max} - T_{\min}}{T_{\max}} \tag{2}$$

where  $\Delta_{\rho}$  and  $\Delta_T$  denote the homogeneity of density and transmittance, respectively;  $\delta_{\max}$  and  $\delta_{\min}$  are the maximum and lowest densities of the nine flat samples taken at nine different positions on the pressed product;  $T_{\max}$  and  $T_{\min}$  represent the maximum and lowest transmittance values at  $4.5 \mu\text{m}$  for the nine flat samples taken at nine different positions on the pressed product. Inconel alloy 718 (see Fig. 3) is a high-strength, corrosion-resistant nickel–chromium alloy that is used for high-pressure machine components operating between  $-253^{\circ}\text{C}$  and  $+700^{\circ}\text{C}$  [19, 20].



(a)



(b)

**Fig. 3** The temperature-dependent mechanical properties of Inconel 718 steel; **a** Young’s modulus; **b** Poisson’s ratio

### 3 Results and Discussions

#### 3.1 The Effect of the Friction Coefficient Between the Mold and the Pressed Material on the Product's Quality After Pressing

When the program is simulated with two coefficients of friction,  $f_{fr1} = 0.25$  and  $f_{fr2} = 0.4$ , the following results are obtained (Fig. 4).

For  $f_{fr} = 0.25$ , the maximum and minimum densities are respectively  $3.526 \text{ kg/cm}^3$  and  $2.701 \text{ kg/cm}^3$ . And when  $f_{fr} = 0.4$ , the maximum density is  $4.048 \text{ kg/cm}^3$ , whereas the minimum density is  $2.475 \text{ kg/cm}^3$ . When pressing in practice, if the mold cavity is not sufficiently polished, the friction between the mold cavity and the pressed material is excessive, resulting in the pressed product failing (Fig. 5). Additionally, when the mold cavity is meticulously polished to a gloss  $R_a = 0.16$ , the friction between the mold cavity and the pressed material is minimal, resulting in a very high-quality pressed product (Fig. 6).

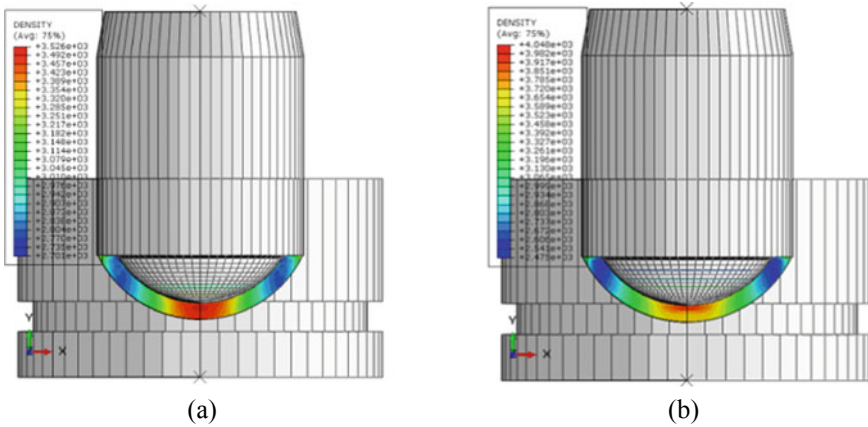
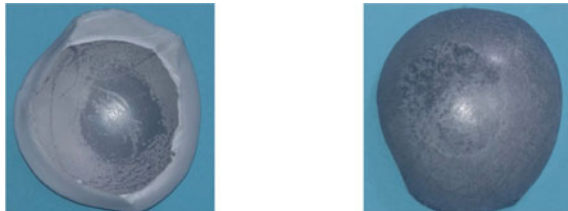
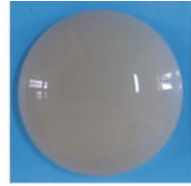
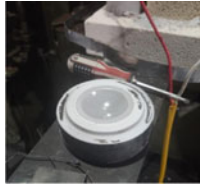


Fig. 4 Effect of coefficient of friction **a**  $f_{fr1} = 0.25$ ; **b**  $f_{fr2} = 0.4$

Fig. 5 The failure of a material sample pressed on a high-friction mold surface



**Fig. 6** MgF<sub>2</sub> optical ceramic products when pressed against the mold surface have small friction



### 3.2 The Effect of the Injection Mold Profile

- (a) Shape change of product during pressing

The simulation results can be seen in Fig. 7.

As can be observed, there is a region with the lowest density throughout the pressing process (blue).

- (b) Change the selection of the suitable working profile for the injection mold

By using two structures with an angle of 150° and 180°, respectively, we run simulations to acquire the findings illustrated in Figs. 8 and 9.

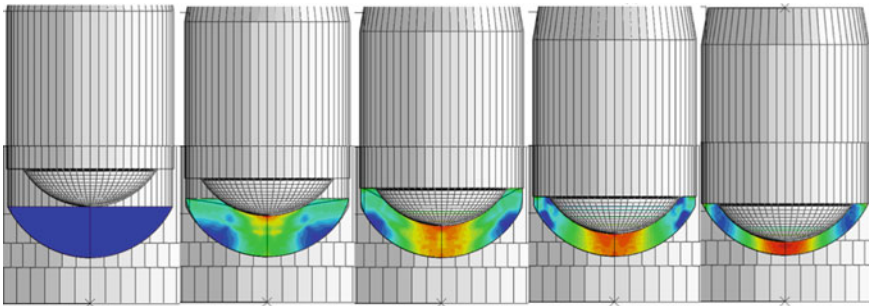


**Fig. 7** Density distribution on workpiece during pressing

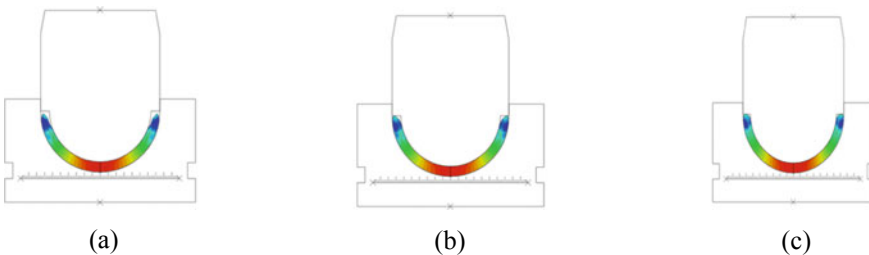


**Fig. 8** Simulation results with  $\alpha = 180^\circ$ ; **a**  $h = 21$  mm; **b**  $h = 24$  mm; **c**  $h = 27$  mm

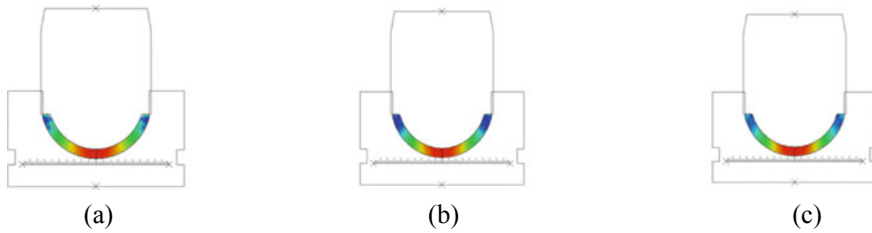


**Fig. 9** Simulation results with  $\alpha = 150^\circ$ ; **a**  $h = 21$  mm; **b**  $h = 24$  mm; **c**  $h = 27$  mm

The findings indicate that when pressing at an angle of  $180^\circ$ , the low-density zone is located farther away from the product’s top than when pressing at an angle of  $150^\circ$ . Table 1 shows the maximum and lowest densities at various angles and heights  $h$ .

Tables 2 and 3 provide the experimental results of measuring the homogeneity of hot-pressed products at an angle of  $150^\circ\text{C}$ .

From the results in Tables 2 and 3, the density uniformity and transmittance homogeneity can be determined as follows:

Homogeneity according to density:

$$\Delta_\rho = \frac{\delta_{\max} - \delta_{\min}}{\delta_{\max}} = \frac{3.177 - 3.170}{3.177} = 0.0022$$

**Table 1** The maximum and minimum densities at different angles  $\alpha$  and height  $h$

$\alpha$	$h = 21$ (mm)		$h = 24$ (mm)		$h = 27$ (mm)	
	$\rho_{\max}$ ( $\text{kg/m}^3$ )	$\rho_{\min}$ ( $\text{kg/m}^3$ )	$\rho_{\max}$ ( $\text{kg/m}^3$ )	$\rho_{\min}$ ( $\text{kg/m}^3$ )	$\rho_{\max}$ ( $\text{kg/m}^3$ )	$\rho_{\min}$ ( $\text{kg/m}^3$ )
$150^\circ$	2902	962.4	3259	1772	3710	2224
$180^\circ$	2000	555	3227	695.2	3617	943.0

**Table 2** The density of nine samples corresponds to nine hot-pressed  $\text{MgF}_2$  optical ceramics product locations

N <sup>o</sup>	1	2	3	4	5	6	7	8	9
( $\rho$ )	3.171	3.177	3.172	3.176	3.177	3.176	3.171	3.174	3.170

**Table 3** The transmittance of nine samples corresponds to nine positions on the hot-pressed  $\text{MgF}_2$  optical ceramic product

N <sup>o</sup>	1	2	3	4	5	6	7	8	9
(T)	89.58	93.90	88.71	93.10	94.43	91.46	88.09	92.80	87.28



Homogeneity according to transmittance:

$$\Delta_T = \frac{T_{\max} - T_{\min}}{T_{\max}} = \frac{94.43 - 87.28}{94.43} = 0.076$$

## 4 Conclusion

In this study, the influence of the friction coefficient of the mold cavity and the molding profile on the quality of the wind tip product was simulated when hot-pressing and sintering with  $\text{MgF}_2$  powder. The simulation results are compared with the experimental one. Both simulation and experimental results have shown that low product density and easy-to-fracture regions are concentrated around the edge of a component.

## References

1. Weber MJ (2018) Handbook of optical materials
2. Caniou J (1999) Materials for infrared and optical filters. In: Passive infrared detection, pp 288–324
3. Li Y (2019) A study on the consolidation of sulfide-based infrared optical ceramics
4. Newswander T, Paquin RA (2017) Materials for optical systems
5. Rius G, Baldi A, Ziaie B, Atashbar MZ (2017) Introduction to micro-/nanofabrication
6. Zhang H, Kim ES (1995) Dome-shaped diaphragm microtransducers. Proc IEEE Micro Electro Mech Syst, pp 256–260. <https://doi.org/10.1109/memsys.1995.472570>
7. Harris DC (2017) Weibull analysis and area scaling for infrared windows. Wind Dome Technol Mater XV 10179:1017909. <https://doi.org/10.1117/12.2258537>
8. Krell A, Hutzler T, Klimke J (2009) Transmission physics and consequences for materials selection, manufacturing, and applications. J Eur Ceram Soc 29(2):207–221. <https://doi.org/10.1016/j.jeurceramsoc.2008.03.025>
9. David SP, Sarkar D (2019) Transparent ceramics
10. Wang SF et al (2013) Transparent ceramics: processing, materials and applications. Prog Solid State Chem 41(1–2):20–54. <https://doi.org/10.1016/j.progsolidstchem.2012.12.002>
11. Roy WR (1990) Ceramic processing: an overview. AIChE J 36(4):481–510
12. Shivaee HA (2010) Effects of pressure sintering parameters on IR transmittance of  $\text{MgF}_2$  optical ceramics. J Mater Sci 2(1):28–35
13. Hieu NT, Do VT, Thai ND, Long TD, Van Minh P (2020) Enhancing the quality of the characteristic transmittance curve in the infrared region of range 2.5–7  $\mu\text{m}$  of the optical magnesium fluoride ( $\text{MgF}_2$ ) ceramic using the hot-pressing technique in a vacuum environment. Adv Mater Sci Eng 2020:7258431-1–7258431-8. <https://doi.org/10.1155/2020/7258431>
14. Yang SJ, Chang CS, Hon MH (1990) Effects of calcination and hot-pressing temperatures of magnesium fluoride powder on its optical property. Jpn J Appl Phys 29(12R):2751–2754. <https://doi.org/10.1143/JJAP.29.2751>
15. Chang CS, Hon MH (2003) Texture effect of hot-pressed magnesium fluoride on optical transmittance. Mater Chem Phys 81(1):27–32. [https://doi.org/10.1016/S0254-0584\(02\)00460-1](https://doi.org/10.1016/S0254-0584(02)00460-1)

16. Krell A, Klimke J (2006) Effects of the homogeneity of particle coordination on solid-state sintering of transparent alumina. *J Am Ceram Soc* 89(6):1985–1992. <https://doi.org/10.1111/j.1551-2916.2006.00985.x>
17. Gavrishchuk EM, Timofeev OV, Pogorelko AA, Suchkov AI (2004) Effect of polishing conditions on the optical properties of zinc selenide surfaces. *Inorg Mater* 40(3):217–220. <https://doi.org/10.1023/B:INMA.0000020517.39272.16>
18. Ikram M, Hussain G (1999) Michelson interferometer for precision angle measurement. *Appl Opt* 38(1):113. <https://doi.org/10.1364/ao.38.000113>
19. Patel S, DeBarbadillo J, Coryell S (2018) Superalloy 718: evolution of the alloy from high to low temperature application. *Miner Met Mater Ser*, pp 23–49. [https://doi.org/10.1007/978-3-319-89480-5\\_2](https://doi.org/10.1007/978-3-319-89480-5_2)
20. Aba-Perea PE, Pirling T, Withers PJ, Kelleher J, Kabra S, Preuss M (2016) Determination of the high temperature elastic properties and diffraction elastic constants of Ni-base superalloys. *Mater Des* 89:856–863. <https://doi.org/10.1016/j.matdes.2015.09.152>

# On the Free Vibration Analysis of Micro FG Beams Considering the Initial Geometrical Imperfection



Le Minh Thai, Nguyen Tuan Hieu, Nguyen Thai Dung, Ta Duc Tam,  
and Phung Van Minh

**Abstract** This work examines the free oscillation characteristics of FG microbeams supported by an elastic medium while accounting for a geometric flaw. The finite element formulations are developed using the FEM, high-order shear strain theory, and modified coupling stress. This hypothesis does away with reduced integrals and shear correction factors.

**Keywords** Finite element method · FGM beam · Free vibration · Rotation · Imperfection

## 1 Introduction

This is the new effort, and the outcomes are of considerable use to the designers and users previously mentioned. The Cosserat brothers introduced the pair stress hypothesis, sometimes known as the Cosserat theory, in 1909 [1]. Following their contributions, it garnered little notice. Using a single length-scale parameter, Yang et al. [2] offered a improved pair stress hypothesis. In the years that followed [3–5], the modified pair stress theory was employed to explore the size impact of FG microstructures. Tuan and his colleagues [6] explored non-stationary dynamics in composite structures using the Cosserat model. Dehrouyeh-Semnani and coworkers [7] investigated oscillation of functionally graded microbeams. Shafiei and colleagues [8] used GDQM to address the size-dependent nonlinear oscillation of tapered AFG microbeams.

---

L. M. Thai · N. T. Dung

Faculty of Special Equipment, Le Quy Don Technical University, Hanoi City, Vietnam

N. T. Hieu (✉)

Hanoi Institute of Technology, Hanoi City, Vietnam

e-mail: [hieuhtip@gmail.com](mailto:hieuhtip@gmail.com)

T. D. Tam · P. Van Minh

Faculty of Mechanical Engineering, Le Quy Don Technical University, Hanoi City, Vietnam

Simşek et al. [9] used Newmark’s approach to address the bending response and oscillation of a flawed functionally graded construction. Attia [10] devised a elasticity model for functionally graded nanobeam size dependence. Shanab et al. [11] demonstrated the nonlinear bending response of functionally graded nanobeams, which included surface energy. The temperature dependency of the free vibration of FG microbeams was examined by Babaei et al. [12]. Civalek and Akgoz [13] examined natural frequencies for functionally graded thick microbeams. These related works [14–34] may be of interest to readers.

## 2 Finite Element Formulations

This study will focus on the oscillation analysis of the spinning FM microbeam as illustrated in Fig. 1. The geometric parameters are  $L$  in length,  $b$  in breadth, and  $h$  in thickness.

The functionally graded microbeam, made of metal and ceramic, has the following physical characteristics [27–29]:

$$E = (E_c - E_m)V_c + E_m; \rho = (\rho_c - \rho_m)V_c + \rho_m; \nu = (\nu_c - \nu_m)V_c + \nu_m \quad (1)$$

in which  $E$ ,  $\rho$ , and  $\nu$  depend on  $z$  coordinate.  $V_m$  and  $V_c$  are the material volumes of metal and ceramic.

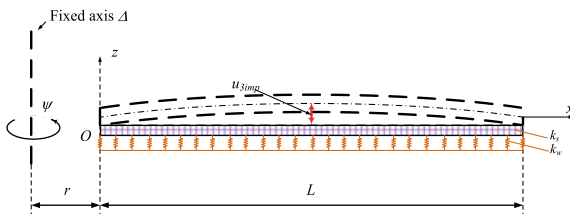
$$V_m + V_c = 1 \quad (2)$$

in which  $V_c = (z/h + 1/2)^n$ ,  $n \geq 0$ , and  $-h/2 \leq z \leq h/2$ .

The modified coupling stress assumption asserts that strain energy be contingent on strain tensor (coupled with the stress tensor) and curvature one. The isotropic linear elastic bodies in volume  $V$  have strain energy [2].

$$H^E = 0.5 \times \int_V (\boldsymbol{\sigma} : \boldsymbol{\varepsilon} + \mathbf{m} : \boldsymbol{\theta}) dV \quad (3)$$

**Fig. 1** A spinning FGM beam



in which  $\mathbf{m}$ ,  $\sigma$ , and  $\epsilon$  are couple stress, stress, and strain tensors, and  $\theta$  is a symmetrical curvature one. The bellow equation expresses these tensors:

$$\begin{aligned} \sigma &= \mu_1 \text{tr}(\epsilon) \mathbf{I} + 2\mu_2 \epsilon; \mathbf{m} = 2l^2 \mu_2 \theta; \\ \epsilon &= 0.5 \times [\nabla \mathbf{u} + (\nabla \mathbf{u})^T]; \theta = 0.5 \times [\nabla \delta + (\nabla \delta)^T] \end{aligned} \tag{4}$$

in which  $\mathbf{u}$  is the vector of displacement,  $\mu_1$  and  $\mu_2$  are Láme invariables,  $l$  is the length-scale coefficient, and  $\delta$  is rotational vector.

$$\delta = 0.5 \times \text{curl } \mathbf{u} \tag{5}$$

This work uses the TSDT to correctly evaluate mechanical responses of FG microbeam. The components of displacement  $u_1$ , and  $u_3$  in  $x$ - and  $z$ -courses are shown as:

$$\begin{aligned} u_1(x, z) &= u_{01}(x, 0) + \frac{1}{4} \left( 5\varphi_x + \frac{\partial w_0}{\partial x} \right) z - \frac{5}{3h^2} \left( \varphi_x + \frac{\partial w_0}{\partial x} \right) z^3 \\ u_3(x, z) &= u_{03}(x, 0) + u_{3imp}(x) \end{aligned} \tag{6}$$

Finally, one gets the equation for determining the fundamental frequency and oscillation mode shape of the rotating FGM micro beam:

$$\left\{ \sum_e (\mathbf{K}_e^E + \mathbf{K}_e^F + \mathbf{K}_e^\psi) - \omega^2 \sum_e \mathbf{M}_e \right\} \sum_e \mathbf{u}_e = 0 \tag{7}$$

### 3 Numerical Results

Consider a microbeam with geometric parameters: length  $L$ , cross-sectional dimension  $b \times h$ ,  $h = 15 \cdot 10^{-6}$  m,  $E_m = 70$  GPa,  $E_c = 380$  GPa,  $\nu_m = 0.3$ ,  $\nu_c = 0.3$ ,  $\rho_c = 3960$  kg/m<sup>3</sup> and  $\rho_m = 2702$  kg/m<sup>3</sup>. Take note  $u_{3im}(x) = U_{03} \sin(\pi x)$  is the microbeam inadequacy, with  $U_0$  is the magnitude of the failure and  $w_{imp}^{ratio} = \frac{U_{03}}{L}$  is the imperfection ratio. As the distance  $r$  grows, the first natural frequency of the oscillating microbeam increases for each value of the length scale parameter  $l$ , as shown in Fig. 2. Figure 3 reveal that when  $r$  grows, the beam’s rotational speed and first natural frequency increase. Figure 4 indicates that for all values of the volume exponential, increasing  $r$  enhances the natural frequency.

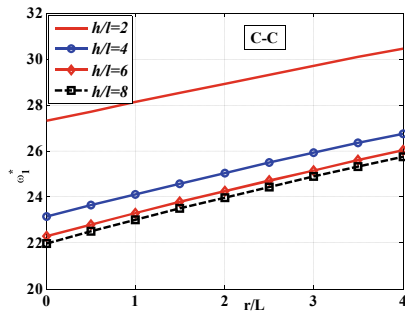
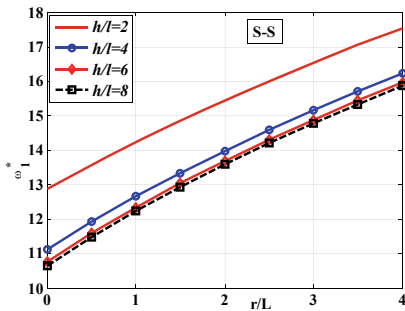


**Fig. 2** The subordination of the first natural frequency of rotating FG microbeams on  $r$  and length scale  $l$ ,  $K_w^* = 10$ ,  $K_s^* = 2$ ,  $\psi^* = 5$ ,  $w_{imp}^{ratio} = 0.001$ ,  $n = 0.5$

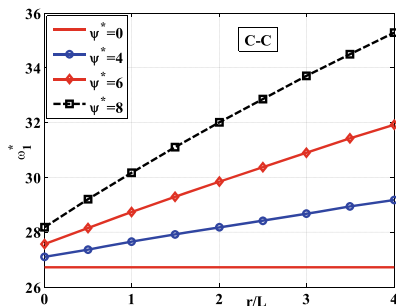
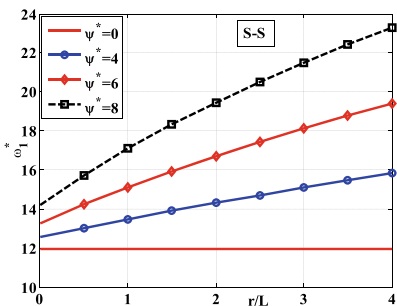


**Fig. 3** The subordination of the first natural frequency of rotating FG microbeams on  $r$  and rotating velocity,  $K_w^* = 10$ ,  $K_s^* = 2$ ,  $h/l = 2$ ,  $w_{imp}^{ratio} = 0.001$ ,  $n = 0.5$

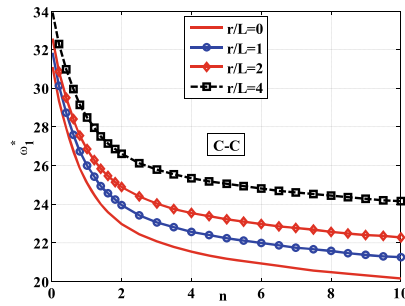
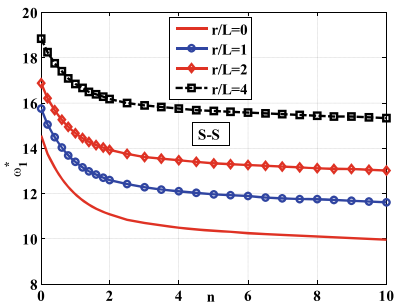


**Fig. 4** The subordination of the first natural frequency of rotating FG microbeams on  $r$  and  $n$ ,  $K_w^* = 10$ ,  $K_s^* = 2$ ,  $h/l = 2$ ,  $w_{imp}^{ratio} = 0.001$ ,  $\psi^* = 8$

## 4 Conclusion

This work blends the high-order strain hypothesis with the improved coupling stress hypothesis for the first time to examine the particular vibrational behavior of a rotating micro GM microbeam on a two-parameter elastic substrate. The evaluation formulae are based on the FE approach for a two-node beam element with four degrees of freedom at each node. The numerical results from this investigation are pretty intriguing to ponder.

## References

1. Cosserat E, Cosserat F (1909) *Théorie des corps déformables*. Hermann, Paris
2. Yang F, Chong ACM, Lam DCC, Tong P (2002) Couple stress based strain gradient theory for elasticity. *Int J Solids Struct* 39(10):2731–2743. [https://doi.org/10.1016/S0020-7683\(02\)00152-X](https://doi.org/10.1016/S0020-7683(02)00152-X)
3. Asghari M, Ahmadian MT, Kahrobaiyan MH, Rahaeifard M (2010) On the size-dependent behavior of functionally graded micro-beams. *Mater Des* 31(5):2324–2329. <https://doi.org/10.1016/j.matdes.2009.12.006>
4. Reddy JN (2011) Microstructure-dependent couple stress theories of functionally graded beams. *J Mech Phys Solids* 59(11):2382–2399. <https://doi.org/10.1016/j.jmps.2011.06.008>
5. Ke LL, Wang YS (2011) Size effect on dynamic stability of functionally graded microbeams based on a modified couple stress theory. *Compos Struct* 93(2):342–350. <https://doi.org/10.1016/j.compstruct.2010.09.008>
6. Tuan LT, Dung NT, Van Thom D, Van Minh P, Zenkour AM (2021) Propagation of non-stationary kinematic disturbances from a spherical cavity in the pseudo-elastic cosserat medium. *Eur Phys J Plus* 136
7. Dehrouyeh-Semnani AM, Mostafaei H, Nikkiah-Bahrami M (2016) Free flexural vibration of geometrically imperfect functionally graded microbeams. *Int J Eng Sci* 105:56–79. <https://doi.org/10.1016/j.ijengsci.2016.05.002>
8. Shafiei N, Kazemi M, Ghadiri M (2016) Nonlinear vibration of axially functionally graded tapered microbeams. *Int J Eng Sci* 102:12–26. <https://doi.org/10.1016/j.ijengsci.2016.02.007>
9. Şimşek M, Aydın M (2017) Size-dependent forced vibration of an imperfect functionally graded (FG) microplate with porosities subjected to a moving load using the modified couple stress theory. *Compos Struct* 160:408–421. <https://doi.org/10.1016/j.compstruct.2016.10.034>
10. Attia MA (2017) On the mechanics of functionally graded nanobeams with the account of surface elasticity. *Int J Eng Sci* 115:73–101. <https://doi.org/10.1016/j.ijengsci.2017.03.011>
11. Shanab RA, Attia MA, Mohamed SA (2017) Nonlinear analysis of functionally graded nanoscale beams incorporating the surface energy and microstructure effects. *Int J Mech Sci* 131–132:908–923. <https://doi.org/10.1016/j.ijmecsci.2017.07.055>
12. Babaei A, Noorani MRS, Ghanbari A (2017) Temperature-dependent free vibration analysis of functionally graded micro-beams based on the modified couple stress theory. *Microsyst Technol* 23(10):4599–4610. <https://doi.org/10.1007/s00542-017-3285-0>
13. Akgöz B, Civalek Ö (2017) Effects of thermal and shear deformation on vibration response of functionally graded thick composite microbeams. *Compos Part B Eng* 129:77–87. <https://doi.org/10.1016/j.compositesb.2017.07.024>
14. Luat DT, Van Thom D, Thanh TT, Van Minh P, Van Ke T, Van Vinh P (2021) Mechanical analysis of bi-functionally graded sandwich nanobeams. *Adv Nano Res* 11(1):55–71. <https://doi.org/10.12989/anr.2021.11.1.055>

15. Nguyen Thai D, Van Minh P, Phan Hoang C, Ta Duc T, Nguyen Thi Cam N, Nguyen Thi D (2021) Bending of symmetric sandwich FGM beams with shear connectors. *Math Probl Eng* 2021. <https://doi.org/10.1155/2021/7596300>
16. Dung NT, Van Minh P, Hung HM, Tien DM (2021) The third-order shear deformation theory for modeling the static bending and dynamic responses of piezoelectric bidirectional functionally graded plates. *Adv Mater Sci Eng* 2021. <https://doi.org/10.1155/2021/5520240>
17. Van Phung M, Nguyen DT, Doan LT, Van Nguyen D, Van Duong T (2022) Numerical investigation on static bending and free vibration responses of two-layer variable thickness plates with shear connectors. *Iran J Sci Technol—Trans Mech Eng*. <https://doi.org/10.1007/s40997-021-00459-9>
18. Duc DH, Van Thom D, Cong PH, Van Minh P, Nguyen NX (2022) Vibration and static buckling behavior of variable thickness flexoelectric nanoplates. *Mech Based Des Struct Mach*. <https://doi.org/10.1080/15397734.2022.2088558>
19. Dung NT, Thai LM, Van Ke T, Huyen TTH, Van Minh P (2022) Nonlinear static bending analysis of microplates resting on imperfect two-parameter elastic foundations using modified couple stress theory. *Comptes Rendus—Mec* 350:121–141. <https://doi.org/10.5802/crmeca.105>
20. Tran TT, Nguyen NH, Van Do T, Van Minh P, Duc ND (2021) Bending and thermal buckling of unsymmetric functionally graded sandwich beams in high-temperature environment based on a new third-order shear deformation theory. *J Sandw Struct Mater* 23(3):906–930. <https://doi.org/10.1177/1099636219849268>
21. Hoa LK, Van Vinh P, Duc ND, Trung NT, Son LT, Van Thom D (2021) Bending and free vibration analyses of functionally graded material nanoplates via a novel nonlocal single variable shear deformation plate theory. *Proc Inst Mech Eng Part C J Mech Eng Sci* 235(18):3641–3653. <https://doi.org/10.1177/0954406220964522>
22. Doan TN et al (2020) Analysis of stress concentration phenomenon of cylinder laminated shells using higher-order shear deformation Quasi-3D theory. *Compos Struct* 232. <https://doi.org/10.1016/j.compstruct.2019.111526>
23. Duc ND, Trinh TD, Van Do T, Doan DH (2018) On the buckling behavior of multi-cracked FGM plates. *Lect Notes Mech Eng Part F3*:29–45. [https://doi.org/10.1007/978-981-10-7149-2\\_3](https://doi.org/10.1007/978-981-10-7149-2_3)
24. Bui TQ, Doan DH, Van Do T, Hirose S, Duc ND (2016) High frequency modes meshfree analysis of Reissner-Mindlin plates. *J Sci Adv Mater Devices* 1(3):400–412. <https://doi.org/10.1016/j.jsamd.2016.08.005>
25. Nam VH, Nam NH, Vinh PV, Khoa DN, Thom DV, Minh PV (2019) A new efficient modified first-order shear model for static bending and vibration behaviors of two-layer composite plate. *Adv Civ Eng* 2019. <https://doi.org/10.1155/2019/6814367>
26. Thai LM, Luat DT, Phung VB, Van Minh P, Van Thom D (2022) Finite element modeling of mechanical behaviors of piezoelectric nanoplates with flexoelectric effects. *Arch Appl Mech* 92(1):163–182. <https://doi.org/10.1007/s00419-021-02048-3>
27. Vu Hoai N, Hong Doan D, Khoa NM, Van Do T, Thi Tran H (2019) Phase-field buckling analysis of cracked stiffened functionally graded plates. *Compos Struct* 217:50–59. <https://doi.org/10.1016/j.compstruct.2019.03.014>
28. Nguyen HN, Tan TC, Luat DT, Phan VD, Van Thom D, Van Minh P (2019) Research on the buckling behavior of functionally graded plates with stiffeners based on the third-order shear deformation theory. *Materials (Basel)* 12(8). <https://doi.org/10.3390/ma12081262>
29. Bui TQ et al (2016) On the high temperature mechanical behaviors analysis of heated functionally graded plates using FEM and a new third-order shear deformation plate theory. *Compos Part B Eng* 92:218–241. <https://doi.org/10.1016/j.compositesb.2016.02.048>
30. Van Minh P, Van Ke T (2022) A comprehensive study on mechanical responses of non-uniform thickness piezoelectric nanoplates taking into account the flexoelectric effect. *Arab J Sci Eng*. <https://doi.org/10.1007/s13369-022-07362-8>
31. Van Minh P, Thai LM, Luat DT, Vu NDA (2022) Static bending analysis of nanoplates on discontinuous elastic foundation with flexoelectric effect. *J Sci Tech* 17(5)



32. Nguyen TCN (2022) Static bending analysis of variable thickness microplates using the finite element method and modified couple stress theory. *J Sci Tech* 17(3). <https://doi.org/10.56651/lqdtu.jst.v17.n03.351>
33. Chi Tho N, Van Thom D, Hong Cong P, Zenkour AM, Hong Doan D, Van Minh P (2023) Finite element modeling of the bending and vibration behavior of three-layer composite plates with a crack in the core layer. *Compos Struct* 305. <https://doi.org/10.1016/j.compstruct.2022.116529>
34. Phung VM (2020) Static bending analysis of symmetrical three-layer FGM beam with shear connectors under static load. *J Sci Tech* 15(3):68–78. <https://doi.org/10.56651/lqdtu.jst.v15.n03.213>

# Experimental Study on the Dynamic Response of a First-Generation Bump-Foil Bearing



Minh-Quan Nguyen and Minh-Hai Pham

**Abstract** With compliant foil structure, bump-foil bearing, one type of foil-air bearing, has been widely applied in high-speed machines thanks to oil-free operation. In this paper, two types of experiment have been implemented to study dynamic behaviour of this foil bearing. Before that, one bump-foil bearing structure was manufactured with two kinds of material: the foil structure made of stainless steel 304 with 0.1-mm thickness and the bearing body made of stainless steel CT3. Static-shaft experiment was deployed to compute the nominal stiffness of the foil structure through load–displacement relationships. The data shows the same tendency with computed results from a mathematical model of foil structure proposed in the previous research. Differences can be reasoned by manufacturing error. Moreover, through rotating-shaft experiment, air thin film is proved to appear inside the bearing, and aerodynamic pressure bears a significant influence from rotating speed. The study demonstrates important meanings in confirming the theoretical model of foil structure and shaft-bearing system.

**Keywords** Bump-foil bearing · Nominal stiffness · Dynamic response

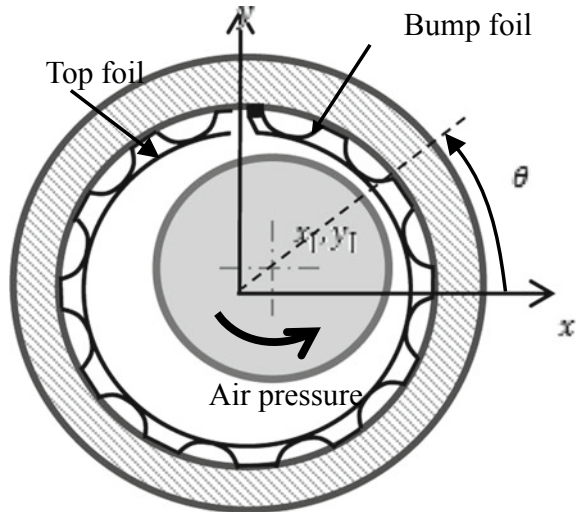
## 1 Introduction

Foil bearing can be described as a type of self-acting bearing with the generation of air pressure inside the bearing during shaft's rotating time. However, unlike conventional air bearing, an outstanding characteristic of the foil bearing is a foil structure inside the bearing. The compliancy of the foil structure enables elastic deflections under the act of air pressure. The deflections are shown to prevent the bearing from being seized on the shaft due to thermal expansion of the shaft. Different foil structures

---

M.-Q. Nguyen (✉) · M.-H. Pham  
Hanoi University of Science and Technology, Hanoi, Vietnam  
e-mail: [quan.nguyenminh@hust.edu.vn](mailto:quan.nguyenminh@hust.edu.vn)

**Fig. 1** Bump-foil bearing structure with shaft



create various types of the foil bearings, but one of the most common types that draw much attention is bump-foil bearing as shown in Fig. 1. In this kind of bearing, the compliant foil structure consists of a bump foil (in corrugation shape) and a top foil (in circular shape). Various works have been done to assess the performance of the bump-foil bearing.

Through a numerical approach, Bonello and Hai Pham introduced a technique of simultaneously solving state equations to analyze both transient response and static equilibrium stability of the system including a turbocharger shaft supported by two bump-foil bearings [1]. The computation indicates that the length-to-radius ratio, the compliance of the foil and nominal radial clearance have significant influence on promoting the stability of static equilibrium. K. Sim et al. proposed an improved foil bearing structure with three metal shims inserted under bump-strip layers [2]. With smaller radial clearance than normal foil bearing, the shimmed bearing demonstrated its ability to significantly lessen the big sub-synchronous motions of rotor arising in the normal bearing. It should be noted that experimental results met a good agreement in a turbocharger test rig and a passenger vehicle diesel engine test bench. Using finite element method [3], J. Yan et al. predicted critical speeds of turbocharger rotor considering bearing stiffness and damping coefficients. Additional experiments also revealed significant effects of nominal radial clearance on the rotor performance. In addition to the clearance, F. Walter et al. conducted a numerical investigation on dynamic performance and stability characteristics as a function of preload [4]. Through stability analysis in transient and steady state, optimal values of preload could be obtained with corresponding clearance. It can be seen from the literature that due to huge effect on the bearing's performance, the foil structure needs to be analyzed thoroughly to investigate dynamic characteristics of the foil and its influences on dynamics response of the shaft-bearing system.

In the previous study, by introducing an enhanced model of the foil structure, the authors investigated impacts of geometrical parameters of the bump foil on the critical speeds of the rotor through variations in foil stiffness [5]. With higher foil stiffness, the rotor was assumed to retain the stable state for a longer time.

In this study, experiments were conducted to verify the theoretical model of the foil structure. One bump-foil bearing with chosen dimensions was manufactured. The static-shaft experiment was conducted with static loads applying onto the shaft and shaft displacement measured by a proximity probe. Load–displacement relationships are illustrated in graphs for different cases, and then, the nominal stiffness of the foil structure was computed and compared with the previous study. This study is believed to make contribution to improving shaft structure design in real applications.

## 2 Experiment System

In the research, experiment were conducted to scrutinize the dynamic response of the bump-foil bearing. Static-shaft experiment was proposed to verify the theoretical nominal stiffness of the foil structure from the foil model. Before experimental procedures, the shaft and the bearing were manufactured, then a measurement system was established.

### 2.1 Shaft and Bearing

Both shaft and bearing body was made of C45 steel. Moreover, the bump foil was manufactured from SUS304 sheet. The top foil was fabricated in the same way but there is not any bump on the top foil.

### 2.2 Measurement System

The composition of the measurement system is shown in Fig. 2. In this study, proximity probe was chosen to conduct non-contact measurement for static and rotating shaft. In both cases, the bump-foil bearing was fixed in the housing; therefore, measurement data are shaft displacements. DASYLab<sup>®</sup> software was installed in the computer to process and display the signals as distances between the probe and the shaft.

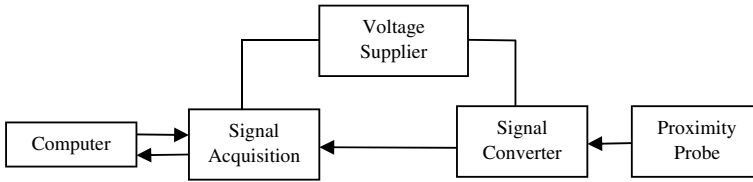


**Fig. 2** Schematic diagram of measurement system

### 3 Experiment Procedures

As can be seen from Fig. 3, vertical loads were put onto one end of the shaft which was assembled with the bump-foil bearing. The proximity probe was mounted above the shaft to measure vertical shaft displacements. Before that, it is essential that the load onto the journal part and the displacement of the journal part should be defined.

To calculate the displacement of the journal part in the bump-foil bearing, force diagram on the shaft was established as shown in Fig. 4, where  $P$  denotes shaft weight,  $S_n$  is the vertical load onto one end of the shaft, and  $Q$  is the load onto the journal part at the bump-foil bearing that needs to be computed.

$Q$  can be calculated as follows:

$$Q = \frac{P \times 83 + S \times 145}{115} \quad (1)$$

The shaft displacement at the bump-foil bearing can also be computed as follows:

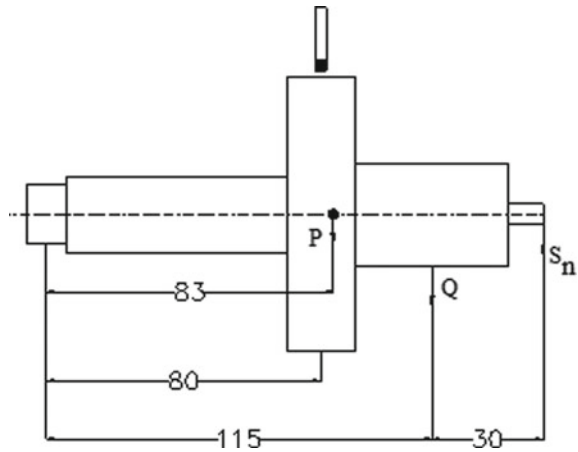
$$\delta = \delta_{do} \cdot \frac{115}{80} \quad (2)$$

where  $\delta_{do}$  denotes displacement at the measured point.

**Fig. 3** Static-shaft experiment



**Fig. 4** Force diagram on the shaft



After experiments with different vertical loads, shaft displacements can be calculated and the relationship between load and displacement can be graphed, then the nominal stiffness of the foil structure can be valued.

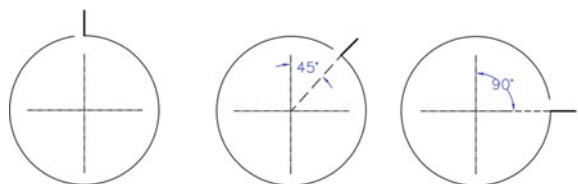
#### 4 Results and Discussions

The static-shaft experiments were implemented for bump-foil bearing with different slot angles as described in Fig. 5.

From load–displacement graphs in Figs. 6, 7 and 8, it can be seen that the loading curves are not similar to the unloading curves. This can be reasoned by appearance of friction between the bump foil and the bearing body. In the unloading process, the bump foil tends to return to initial states after elastic deflection. However, friction forces are assumed to prevent the bump foil so that the radial displacements of the foil structure in unloading process are presumed to be bigger than those in loading process with the same load.

The ratio of load and displacement is evaluated to be around  $7 \times 10^5$  N/m, smaller than the value of  $8 \times 10^6$  N/m in theoretical model. This difference can be argued that the shaping of bump foil is not accurate enough, causing the bump ends to be

**Fig. 5** Three positions of slot



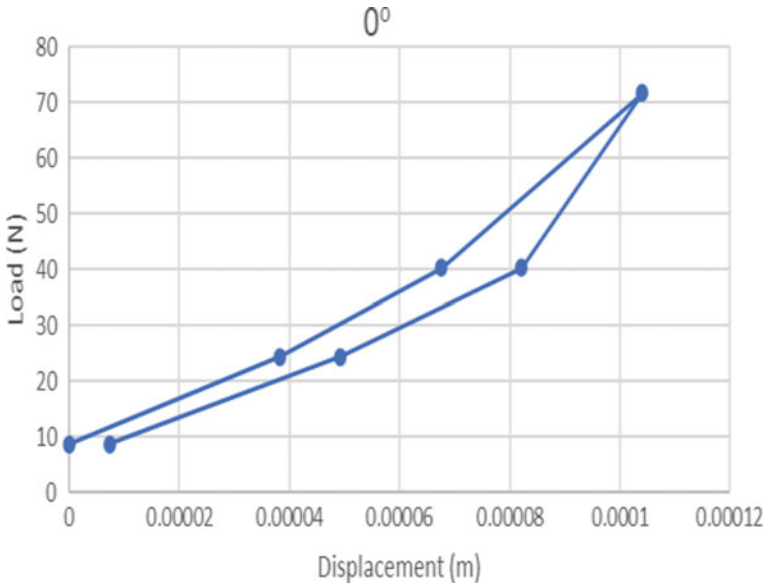


Fig. 6 Load–displacement relationship at slot angle 0°

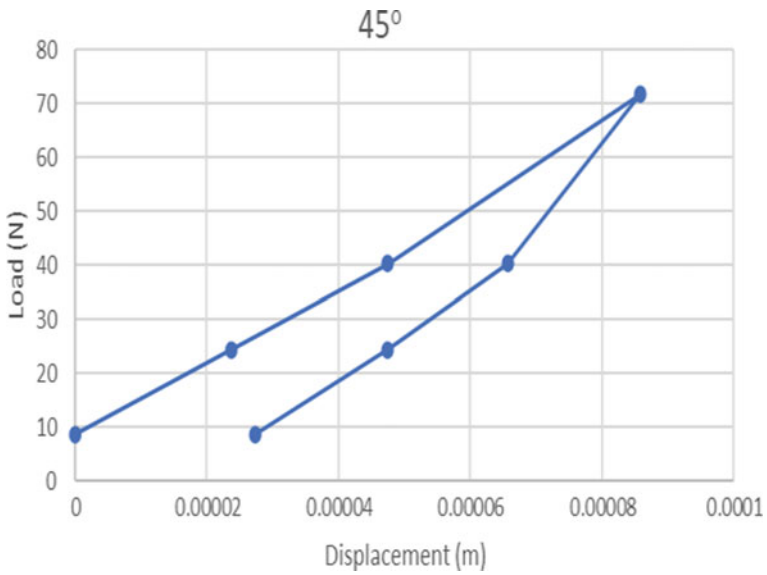


Fig. 7 Load–displacement relationship at slot angle 45°

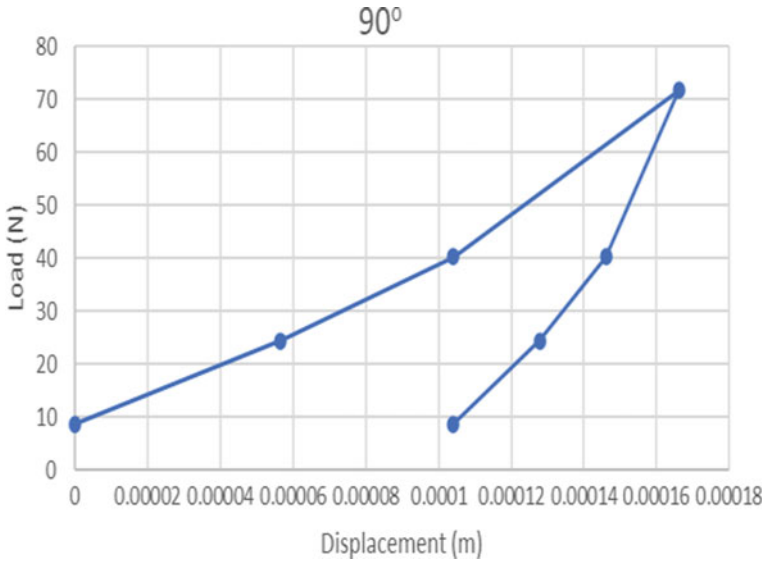


Fig. 8 Load–displacement relationship at slot angle 90°

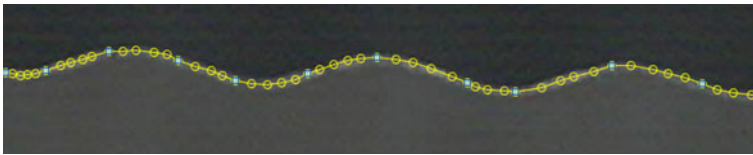


Fig. 9 Bump foil profile rebuilt from image points

flatter gradient as demonstrated in Fig. 9. The real shape of the bump foil is assumed to be softer, leading the smaller nominal stiffness.

## 5 Conclusions

In this study, experiments were conducted to evaluate the dynamic response of the first-generation bump-foil bearing. Domestic technologies have been utilized to manufacture one bump-foil bearing together with the shaft. Measuring system has been also established to acquire data of shaft displacements.

The static-shaft experiment was deployed to verify computation model of bump foil proposed in the previous research. The data indicate a similar tendency of load–displacement relationship in loading and unloading processes. However, the nominal stiffness of the foil structure from experiment is slightly smaller than in computation



model. This difference can be reasoned by the dissimilarity between real bump foil and computation model due to manufacturing error.

## References

1. Bonello P, Hai P (2014) Nonlinear dynamic analysis of a turbocharger on foil-air bearings with focus on stability and self-excited vibration. In: Turbo expo: power for land, sea, and air, American society of mechanical engineers, vol 45776, p V07BT32A003. <https://doi.org/10.1115/GT2014-25176>
2. Sim K, Yong-Bok L, Ho Kim T, Lee J (2012) Rotordynamic performance of shimmed gas foil bearings for oil-free turbochargers. ASME J Tribol 134(3):031102. <https://doi.org/10.1115/1.4005892>
3. Yan J, Liu Z, Zhang G, Yu X, Xu L (2019) Feasibility study of a turbocharger rotor supported by air foil bearings with diameter of 17 mm focusing on rotordynamic performance. Proc Inst Mech Eng, Part D: J Automobile Eng 233(5):1331–1344. <https://doi.org/10.1177/0954407018758134>
4. Walter F, Sinapius M (2021) Influence of aerodynamic preloads and clearance on the dynamic performance and stability characteristic of the bump-type foil air bearing. Machines 9(8):178. <https://doi.org/10.3390/machines9080178>
5. Quan NM, Hai PM, Phong DV (2020) The dynamic response of a rotor supported by two foil-air bearings with an enhanced model of foil structure. Int J Mod Phys B 34(22–24):2040160. <https://doi.org/10.1142/S0217979220401608>

# Free Vibration Response of Micro FG Beams Taking the Initial Geometrical Imperfection into Consideration



Nguyen Van Dung, Le Minh Thai, Nguyen Thai Dung, and Phung Van Minh

**Abstract** This investigation studies the free vibration response of micro FG beams on elastic foundations with geometrical imperfections. Finite element, high-order shear strain, and modified couple stress theories compute formulas. High-order shear deformation theory removes reduced integrals and shear correction factors. Calculation results are essential for designing, manufacturing, and operating beam constructions that revolve around a fixed axis.

**Keywords** Finite element method · FGM beam · Free vibration · Rotation · Imperfection

## 1 Introduction

The Cosserat brothers introduced the pair stress hypothesis, sometimes known as the Cosserat theory, in 1909 [1]. Due to the difficulties in determining their values, Yang et al. [2] introduced a modified pair stress theory using a single material length scale parameter. In the years that followed [3–5], the modified pair stress theory was employed extensively to study the influence of FG microstructure size. Tuan et al. [6] investigated non-stationary dynamics in composite material structures using the Cosserat model. The longitudinal-transverse coupling vibrations of FG microbeams were investigated by Dehrouyeh-Semnani et al. [7]. Shafiei et al. [8] used GDQM to solve the size-dependent nonlinear vibrations of tapered axially functionally graded (AFG) microbeams, which included von Kármán nonlinearity. imşek and Aydın [9] used Newmark's method to address the static bending and forced vibration of a flawed

---

N. Van Dung · L. M. Thai (✉) · N. T. Dung  
Faculty of Special Equipment, Le Quy Don Technical University, Hanoi City, Vietnam  
e-mail: [thaileminh@lqdtu.edu.vn](mailto:thaileminh@lqdtu.edu.vn)

P. Van Minh  
Faculty of Mechanical Engineering, Le Quy Don Technical University, Hanoi City, Vietnam

FG. Attia [10] developed a nonlocal-couple stress-surface elasticity model to examine the size-dependent bending, buckling, and free vibration of FG nanobeams. Shanab et al. [11] demonstrated the nonlinear bending response of FG nanobeams, which included surface energy. The temperature dependency of the free vibration of FG microbeams was examined by Babaei et al. [12]. Akgoz and Civalek [13] computed more accurate natural frequencies for FG thick microbeams. These related works [14–34] may be of interest to readers.

## 2 Finite Element Equations

As illustrated in Fig. 1, the structure is supported by a two-parameter elastic foundation with two parameters  $k_w$  and  $k_s$ . The geometrical dimensions are length  $L$ , width  $b$ , and thickness  $h$ .

The FG microbeam, made of ceramic and metal, has the following physical properties [27–29]:

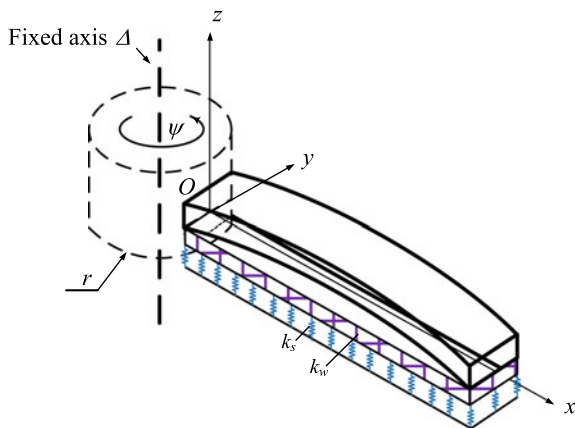
$$\begin{aligned}
 E(z) &= E_m + (E_c - E_m)V_c; \rho(z) = \rho_m + (\rho_c - \rho_m)V_c; \\
 \nu(z) &= \nu_m + (\nu_c - \nu_m)V_c
 \end{aligned}
 \tag{1}$$

in which  $E$  is the modulus of Young,  $\rho$  is the density, and  $\nu$  is the ratio of Poisson.  $V_c$  and  $V_m$  are the volume ratios of the ceramic and metal.

$$V_m + V_c = 1
 \tag{2}$$

where  $V_c = (z/h + 1/2)^n$ , ( $n \geq 0$ ) is the volume fraction index, and  $-h/2 \leq z \leq h/2$ .

**Fig. 1** A spinning FGM beam



The modified couple stress theory asserts that the strain energy density depends on the strain tensor (coupled with the stress tensor) and the curvature tensor (conjugated with couple stress tensor). Deformed isotropic linear elastic bodies in volume  $V$  have strain energy [2].

$$H^E = \frac{1}{2} \int_V (\boldsymbol{\sigma} : \boldsymbol{\varepsilon} + \mathbf{m} : \boldsymbol{\theta}) dV \quad (3)$$

in which  $\boldsymbol{\sigma}$  is the stress tensor,  $\boldsymbol{\varepsilon}$  is the strain tensor,  $\mathbf{m}$  is the deviatoric component of the couple stress tensor, and  $\boldsymbol{\theta}$  is the symmetric curvature tensor. The bellow equation expresses these tensors:

$$\begin{aligned} \boldsymbol{\sigma} &= \mu_1 \text{tr}(\boldsymbol{\varepsilon})\mathbf{I} + 2\mu_2 \boldsymbol{\varepsilon}; \mathbf{m} = 2l^2 \mu_2 \boldsymbol{\theta}; \\ \boldsymbol{\varepsilon} &= 0.5 \times [\nabla \mathbf{u} + (\nabla \mathbf{u})^T]; \boldsymbol{\theta} = 0.5 \times [\nabla \boldsymbol{\delta} + (\nabla \boldsymbol{\delta})^T] \end{aligned} \quad (4)$$

in which  $\mathbf{u}$  is the displacement vector,  $\mu_1$  and  $\mu_2$  are Lámé's invariables,  $l$  is the material length-scale coefficient, and  $\boldsymbol{\delta}$  is the rotation vector.

$$\boldsymbol{\delta} = 0.5 \times \text{curl} \mathbf{u} \quad (5)$$

The displacements  $u_1$ , and  $u_3$  in the  $x$ -, and  $z$ -directions at any point with the coordinate  $(x, z)$  are shown as:

$$\begin{aligned} u_1(x, z) &= u_{01}(x, 0) + \frac{1}{4} \left( 5\varphi_x + \frac{\partial w_0}{\partial x} \right) z - \frac{5}{3h^2} \left( \varphi_x + \frac{\partial w_0}{\partial x} \right) z^3 \\ u_3(x, z) &= u_{03}(x, 0) + u_{3imp}(x) \end{aligned} \quad (6)$$

Finally, one gets the equation for determining the fundamental frequency and oscillation mode shape of the rotating FGM micro beam:

$$\left\{ \sum_e (\mathbf{K}_e^E + \mathbf{K}_e^F + \mathbf{K}_e^\psi) - \omega^2 \sum_e \mathbf{M}_e \right\} \sum_e \mathbf{u}_e = 0 \quad (7)$$

### 3 Numerical Results

Let's suppose the beam's length is  $L$ , and the cross-section is  $b \times h$ ,  $h = 15.10^{-6}$  m,  $E_c = 380$  GPa,  $\nu_c = 0.3$ ,  $\rho_c = 3960$  kg/m<sup>3</sup>,  $E_m = 70$  GPa,  $\nu_m = 0.3$ , and  $\rho_m = 2702$  kg/m<sup>3</sup>. Vibration response of rotating beam with parameters is shown in detail in Figs. 2, 3, 4 and 5.

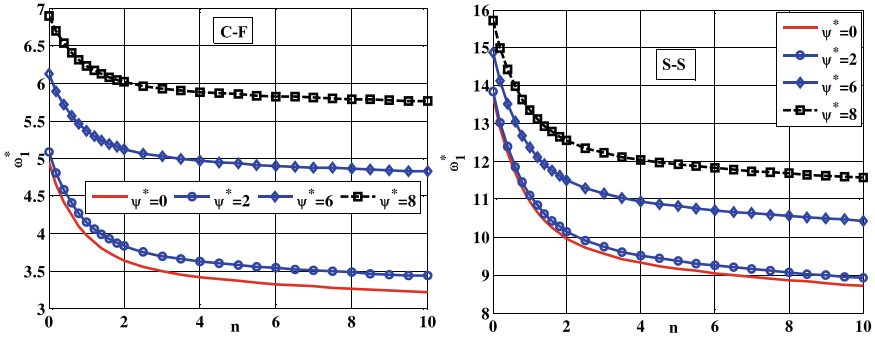


**Fig. 2** The relationship between  $n$  and the rotational speed and the first nondimensional frequency,  $w_{imp}^{ratio} = 0.001$ ,  $K_w^* = 10$ ,  $K_s^* = 2$ ,  $h/l = 2$ ,  $r/L = 0$

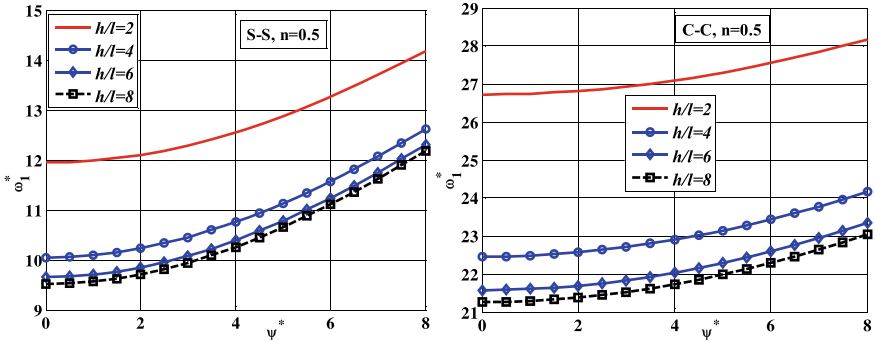


**Fig. 3** The relationship between  $h/l$  ratio and the rotational speed and the first nondimensional frequency,  $w_{imp}^{ratio} = 0.001$ ,  $K_w^* = 10$ ,  $K_s^* = 2$ ,  $r/L = 0$

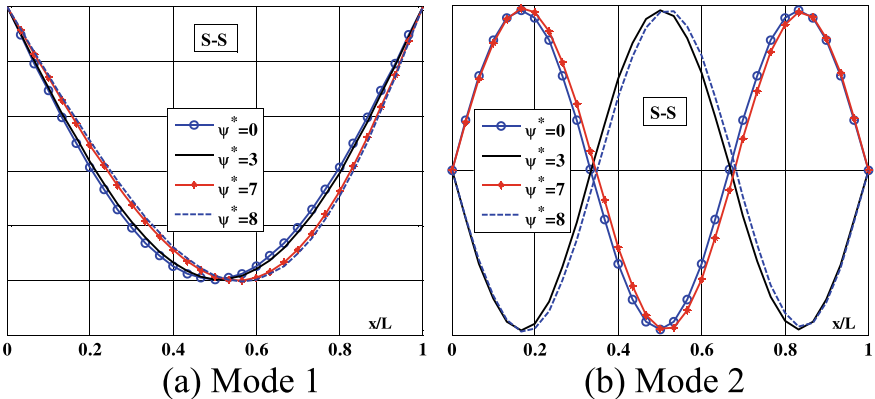


**Fig. 4** The dependence of the first and second vibration mode shapes on the rotational speed, S-S,  $n = 0.5$ ,  $w_{imp}^{ratio} = 0.001$ ,  $K_w^* = 10$ ,  $K_s^* = 2$ ,  $r/L = 2$ ,  $h/l = 8$

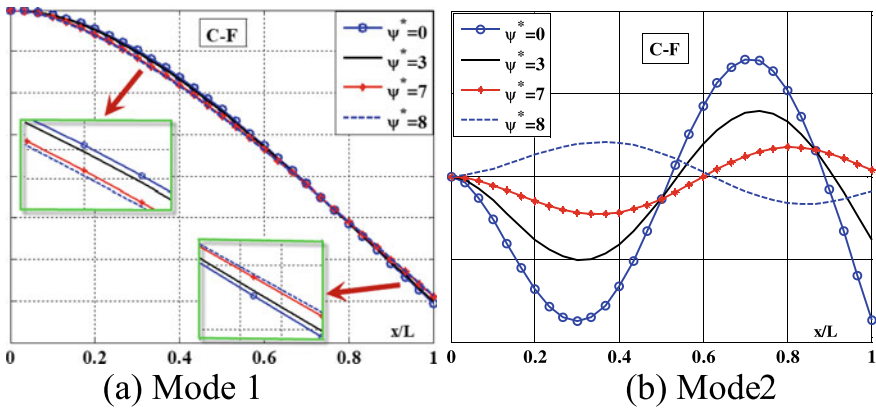


**Fig. 5** The dependence of the first and second vibration mode shapes on the rotational speed, C–F,  $n = 0.5$ ,  $w_{imp}^{ratio} = 0.001$ ,  $K_w^* = 10$ ,  $K_s^* = 2$ ,  $r/L = 2$ ,  $h/l = 8$

The first two vibration mode morphologies of beams exposed to C–F and S–S barriers are shown in Figs. 4 and 5 respectively.

## 4 Conclusion

For the first time, this study combines the high-order deformation theory and the modified couple stress theory to figure out how a rotating micro FGM beam on a two-parameter elastic foundation vibrates. The formulas are based on the finite element method for a two-node beam element with four degrees of freedom at each node. The numbers that came out of this study are very intriguing to consider about.

## References

1. Cosserat E, Cosserat F (1909) *Théorie des corps déformables*. Hermann, Paris
2. Yang F, Chong ACM, Lam DCC, Tong P (2002) Couple stress based strain gradient theory for elasticity. *Int J Solids Struct* 39(10):2731–2743. [https://doi.org/10.1016/S0020-7683\(02\)00152-X](https://doi.org/10.1016/S0020-7683(02)00152-X)
3. Asghari M, Ahmadian MT, Kahrobaiyan MH, Rahaeifard M (2010) On the size-dependent behavior of functionally graded micro-beams. *Mater Des* 31(5):2324–2329. <https://doi.org/10.1016/j.matdes.2009.12.006>
4. Reddy JN (2011) Microstructure-dependent couple stress theories of functionally graded beams. *J Mech Phys Solids* 59(11):2382–2399. <https://doi.org/10.1016/j.jmps.2011.06.008>
5. Ke LL, Wang YS (2011) Size effect on dynamic stability of functionally graded microbeams based on a modified couple stress theory. *Compos Struct* 93(2):342–350. <https://doi.org/10.1016/j.compstruct.2010.09.008>

6. Tuan LT, Dung NT, Van Thom D, Van Minh P, Zenkour AM (2021) Propagation of non-stationary kinematic disturbances from a spherical cavity in the pseudo-elastic cosserat medium. *Eur Phys J Plus* 136
7. Dehrouyeh-Semnani AM, Mostafaei H, Nikkhah-Bahrami M (2016) Free flexural vibration of geometrically imperfect functionally graded microbeams. *Int J Eng Sci* 105:56–79. <https://doi.org/10.1016/j.ijengsci.2016.05.002>
8. Shafiei N, Kazemi M, Ghadiri M (2016) Nonlinear vibration of axially functionally graded tapered microbeams. *Int J Eng Sci* 102:12–26. <https://doi.org/10.1016/j.ijengsci.2016.02.007>
9. Şimşek M, Aydın M (2017) Size-dependent forced vibration of an imperfect functionally graded (FG) microplate with porosities subjected to a moving load using the modified couple stress theory. *Compos Struct* 160:408–421. <https://doi.org/10.1016/j.compstruct.2016.10.034>
10. Attia MA (2017) On the mechanics of functionally graded nanobeams with the account of surface elasticity. *Int J Eng Sci* 115:73–101. <https://doi.org/10.1016/j.ijengsci.2017.03.011>
11. Shanab RA, Attia MA, Mohamed SA (2017) Nonlinear analysis of functionally graded nanoscale beams incorporating the surface energy and microstructure effects. *Int J Mech Sci* 131–132:908–923. <https://doi.org/10.1016/j.ijmecsci.2017.07.055>
12. Babaei A, Noorani MRS, Ghanbari A (2017) Temperature-dependent free vibration analysis of functionally graded micro-beams based on the modified couple stress theory. *Microsyst Technol* 23(10):4599–4610. <https://doi.org/10.1007/s00542-017-3285-0>
13. Akgöz B, Civalek Ö (2017) Effects of thermal and shear deformation on vibration response of functionally graded thick composite microbeams. *Compos Part B Eng* 129:77–87. <https://doi.org/10.1016/j.compositesb.2017.07.024>
14. Luat DT, Van Thom D, Thanh TT, Van Minh P, Van Ke T, Van Vinh P (2021) Mechanical analysis of bi-functionally graded sandwich nanobeams. *Adv Nano Res* 11(1):55–71. <https://doi.org/10.12989/anr.2021.11.1.055>
15. Nguyen Thai D, Van Minh P, Phan Hoang C, Ta Duc T, Nguyen Thi Cam N, Nguyen Thi D (2021) Bending of symmetric sandwich FGM beams with shear connectors. *Math Probl Eng* 2021. <https://doi.org/10.1155/2021/7596300>
16. Dung NT, Van Minh P, Hung HM, Tien DM (2021) The third-order shear deformation theory for modeling the static bending and dynamic responses of piezoelectric bidirectional functionally graded plates. *Adv Mater Sci Eng* 2021. <https://doi.org/10.1155/2021/5520240>
17. Van Phung M, Nguyen DT, Doan LT, Van Duong T, Van Nguyen D, Van Duong T (2022) Numerical investigation on static bending and free vibration responses of two-layer variable thickness plates with shear connectors. *Iran J Sci Technol—Trans Mech Eng* <https://doi.org/10.1007/s40997-021-00459-9>
18. Duc DH, Van Thom D, Cong PH, Van Minh P, Nguyen NX (2022) Vibration and static buckling behavior of variable thickness flexoelectric nanoplates. *Mech Based Des Struct Mach*. <https://doi.org/10.1080/15397734.2022.2088558>
19. Dung NT, Thai LM, Van Ke T, Huyen TTH, Van Minh P (2022) Nonlinear static bending analysis of microplates resting on imperfect two-parameter elastic foundations using modified couple stress theory. *Comptes Rendus—Mec* 350:121–141. <https://doi.org/10.5802/crm.eca.105>
20. Tran TT, Nguyen NH, Van Do T, Van Minh P, Duc ND (2021) Bending and thermal buckling of unsymmetric functionally graded sandwich beams in high-temperature environment based on a new third-order shear deformation theory. *J Sandw Struct Mater* 23(3):906–930. <https://doi.org/10.1177/1099636219849268>
21. Hoa LK, Van Vinh P, Duc ND, Trung NT, Son LT, Van Thom D (2021) Bending and free vibration analyses of functionally graded material nanoplates via a novel nonlocal single variable shear deformation plate theory. *Proc Inst Mech Eng Part C J Mech Eng Sci* 235(18):3641–3653. <https://doi.org/10.1177/0954406220964522>
22. Doan TN et al (2020) Analysis of stress concentration phenomenon of cylinder laminated shells using higher-order shear deformation Quasi-3D theory. *Compos Struct* 232. <https://doi.org/10.1016/j.compstruct.2019.111526>

23. Duc ND, Trinh TD, Van Do T, Doan DH (2018) On the buckling behavior of multi-cracked FGM plates. *Lect Notes Mech Eng Part F3*:29–45. [https://doi.org/10.1007/978-981-10-7149-2\\_3](https://doi.org/10.1007/978-981-10-7149-2_3)
24. Bui TQ, Doan DH, Van Do T, Hirose S, Duc ND (2016) High frequency modes meshfree analysis of Reissner-Mindlin plates. *J Sci Adv Mater Devices* 1(3):400–412. <https://doi.org/10.1016/j.jsamd.2016.08.005>
25. Nam VH, Nam NH, Vinh PV, Khoa DN, Thom DV, Minh PV (2019) A new efficient modified first-order shear model for static bending and vibration behaviors of two-layer composite plate. *Adv Civ Eng* 2019. <https://doi.org/10.1155/2019/6814367>
26. Thai LM, Luat DT, Phung VB, Van Minh P, Van Thom D (2022) Finite element modeling of mechanical behaviors of piezoelectric nanoplates with flexoelectric effects. *Arch Appl Mech* 92(1):163–182. <https://doi.org/10.1007/s00419-021-02048-3>
27. Vu Hoai N, Hong Doan D, Khoa NM, Van Do T, Thi Tran H (2019) Phase-field buckling analysis of cracked stiffened functionally graded plates. *Compos Struct* 217:50–59. <https://doi.org/10.1016/j.compstruct.2019.03.014>
28. Nguyen HN, Tan TC, Luat DT, Phan VD, Van Thom D, Van Minh P (2019) Research on the buckling behavior of functionally graded plates with stiffeners based on the third-order shear deformation theory. *Materials (Basel)* 12(8). <https://doi.org/10.3390/ma12081262>
29. Bui TQ et al (2016) On the high temperature mechanical behaviors analysis of heated functionally graded plates using FEM and a new third-order shear deformation plate theory. *Compos Part B Eng* 92:218–241. <https://doi.org/10.1016/j.compositesb.2016.02.048>
30. Chi Tho N, Van Thom D, Hong Cong P, Zenkour AM, Hong Doan D, Van Minh P (2023) Finite element modeling of the bending and vibration behavior of three-layer composite plates with a crack in the core layer. *Compos Struct* 305. <https://doi.org/10.1016/j.compstruct.2022.116529>
31. Van Minh P, Van Ke T (2022) A comprehensive study on mechanical responses of non-uniform thickness piezoelectric nanoplates taking into account the flexoelectric effect. *Arab J Sci Eng.* <https://doi.org/10.1007/s13369-022-07362-8>
32. Van Minh P, Thai LM, Luat DT, Vu NDA (2022) Static bending analysis of nanoplates on discontinuous elastic foundation with flexoelectric effect. *J Sci Tech* 17(5)
33. Phung VM (2020) Static bending analysis of symmetrical three-layer fgm beam with shear connectors under static load. *J Sci Tech* 15(3):68–78. <https://doi.org/10.56651/lqdtu.jst.v15.n03.213>
34. Nguyen TCN (2022) Static bending analysis of variable thickness microplates using the finite element method and modified couple stress theory. *J Sci Tech* 17(3). <https://doi.org/10.56651/lqdtu.jst.v17.n03.351>



# Assessing the Impact of Heat-Assisted and High Speed Machining on the Performance of Different Cutting Tools During Heat-Treated SKD61 Steel Milling



Tran Phap Dong and Nguyen Duc Toan

**Abstract** This paper presents the preliminary research findings on the influence of high-speed and heat-assisted machining on the performance of cutting tools while milling heat-treated SKD61 steel. The study involved two types of cutting tools, namely uncoated and coated. The results indicated that when finishing milling at 0.15 mm/tooth feed rate and 0.3 mm depth of cut at 300–600 rpm and 500 °C, uncoated cutting tools were not suitable for machining heat-treated SKD61 steel highway strips. However, coated cutting tools with high-speed machining up to 600 rpm could machine the steel with the aid of heat in the range of 200–500 °C, a feed rate of 0.15 mm/tooth, and a depth of cut up to 0.5 mm.

**Keywords** Uncoated · Coated cutting tools · Heat-treated SKD61 steel · Heat-assisted machining · High speed cutting

## 1 Introduction

SKD61 steel is a commonly used chromium tool steel in mold making due to its high shock and wear resistance, achieved through heat treatment [1]. Specifically, the SKD61 steel used in this study has undergone treatment at 1050 °C and tempering at 580 °C, resulting in a hardness range of 50–52HRC and impact toughness of 4.6–4.7 J [2]. High-speed processing of this steel requires consideration of cutting force,

---

T. P. Dong

School of Mechanical Engineering, Vietnam Maritime University, Hai Phong, Vietnam

T. P. Dong · N. D. Toan (✉)

School of Mechanical Engineering, Hanoi University of Science and Technology, 1A–Dai Co Viet Street, Hai Ba Trung District, 100000 Hanoi City, Vietnam

e-mail: [toan.nguyenduc@hust.edu.vn](mailto:toan.nguyenduc@hust.edu.vn)

cutting heat, and energy consumption, as well as wear and durability of cutting tools, machining errors and material removal rate, and roughness and surface quality during machining [3].

Previous researchers [4, 5] have explored various aspects of machining, including wear patterns, durability, and wear mechanisms, and the effects of heating on chip morphology and machinability for materials such as SKD11 alloy and 9CrSi Alloy tool steel. However, no previous studies have investigated high-speed machining with heating support for SKD61 steel after heat treatment, particularly using common and inexpensive cutting tools rather than specialized and costly options.

The current study addresses this gap by examining the effect of high temperature and high speed on the milling of SKD61 steel after heat treatment using two types of cutting tools: uncoated and coated. The survey speed ranges from 300 to 600 rpm, with a feed rate of 0.15 mm/tooth and cutting depth of 0.3–0.5 mm, and heating temperature below 500 °C. Results confirm the feasibility of using inexpensive coated common cutting tools at high cutting speeds with heating support.

## 2 Experimental Procedures

In this study, the test specimen is SKD61 steel that has been quenched at 1050 °C and tempered at 580 °C to achieve a hardness of 50 ~ 52HRC, as shown in Fig. 1a. The steel is cut into a size of 80 × 70 × 30 mm<sup>3</sup>, and the surfaces are milled to remove defects and ensure smoothness, as illustrated in Fig. 1b. The processing machine used is a Taiwan MC500, as depicted in Fig. 2a, with the following main parameters: spindle rotation speed ranging from 100 to 30,000 rpm, spindle power of 15 kW, the movement speed of the table when machining ranging from 1 to 30,000 mm/min, maximum idling speed of 48,000 mm/min, and the journey to move the machine version XzYxZ = 500 × 400 × 300 mm. To support the machining process, a high-frequency electromagnetic induction heating device, as illustrated in Fig. 2b, is used in the study. The cutting tool used is an end mill with a diameter of 50 mm and two types of alloy pieces (coated and uncoated), as shown in Fig. 3. To determine the temperature on the machined surface in the study, a hand-held digital thermometer with contact measurement model 3527A of TSURUGA (Japan) is used, which uses a K-type thermocouple, with a measured temperature range from −99.9 °C to 1299 °C. Additionally, Table 1 presents the chemical composition of SKD61 steel.

The study was performed on a 1 mm thick SUS-304 stainless steel sheet. The chemical composition of the material is presented in Table 1.

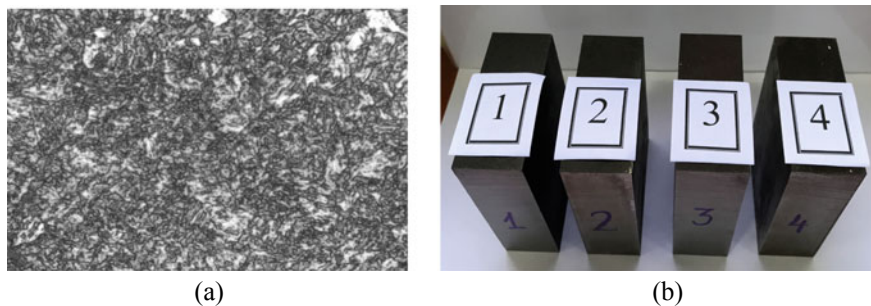


**Fig. 1** After heat treatment: workpiece microstructure **a** and Machined samples **b**



**Fig. 2** CNC machine **a** and induction heating device **b**

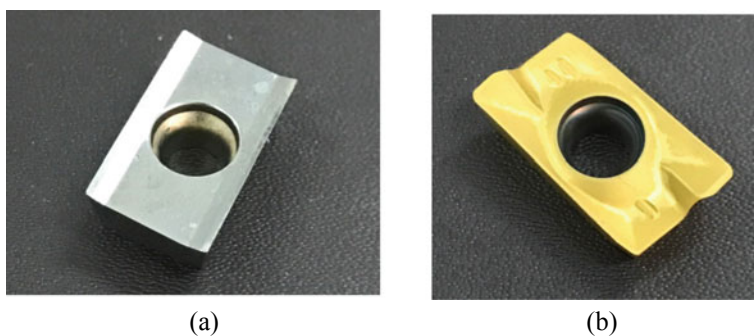


**Fig. 3** Alloy pieces of cutting tool **a** uncoated and **b** coated

**Table 1** Chemical compositions of SKD61

Elements	C	Si	Mn	Cr	P	S	Mo	V
%wt	0.32–0.39	0.8–1.0	< 0.4	4.5–5.15	< 0.03	< 0.03	1.0–1.4	< 1.0

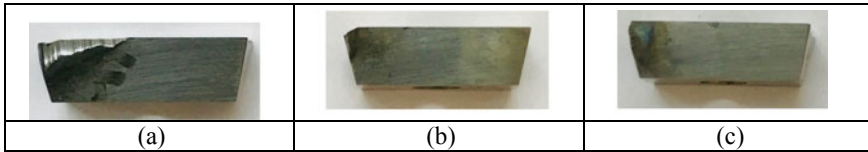


**Fig. 4** Uncoated cutting tool alloy specimens after high-speed machining with heat-assisted method

### 3 Results and Discussion

#### 3.1 Assessment of Uncoated Cutting Tools

The first experiment investigated the highest processing temperature of 500 °C, with a feed rate of 0.15 mm/tooth, a cutting depth of 0.3 mm, and a speed of 600 rpm. However, excessive tool wear occurred (Fig. 4a) and the test was not feasible. The second experiment was still investigated at the highest processing temperature of 500 °C, with a feed rate of 0.15 mm/tooth, a cutting depth of 0.3 mm, but the speed was reduced to 450 rpm. This test was also not possible due to heavy tool wear (Fig. 4b). The third experiment investigated the same parameters as the previous experiments but with a further decrease in speed to 300 rpm. This experiment was also not feasible due to the same tool wear phenomenon (Fig. 4c). Thus, it is not possible to perform high-speed machining with non-coated tools on heat-treated SKD61 steel at the support heating mode of 500 °C, with a feed rate of 0.15 mm/tooth and 0.3 mm cutting depth.

#### 3.2 Evaluation of Coated Cutting Tools

The first experiment investigated the highest processing temperature of 500 °C, with a feed rate of 0.15 mm/tooth, cutting depth of 0.5 mm, and a speed of 1000 rpm. However, heavy tool wear occurred (Fig. 5a), and the test was not feasible. The second experiment investigated the same parameters as the previous experiment but with a decrease in speed to 800 rpm. This experiment was also not feasible due to tool wear (Fig. 5b). The third experiment investigated the same parameters as the previous experiments but with a further decrease in speed to 600 rpm. This test was possible without significant tool wear (Fig. 5c). The fourth experiment investigated the lowest processing temperature of 200 °C, with a feed rate of 0.15 mm/tooth, cutting depth of 0.5 mm, and a speed of 300 rpm. This experiment was possible with no tool wear (Fig. 5d). Hence, it is possible to perform high-speed machining with coated tools on support heating heat-treated SKD61 steel in the heating mode of 200–500 °C, with a feed rate of 0.15 mm/tooth and cutting depth of 0.5 mm, and a cutting speed of 300–600 rpm.

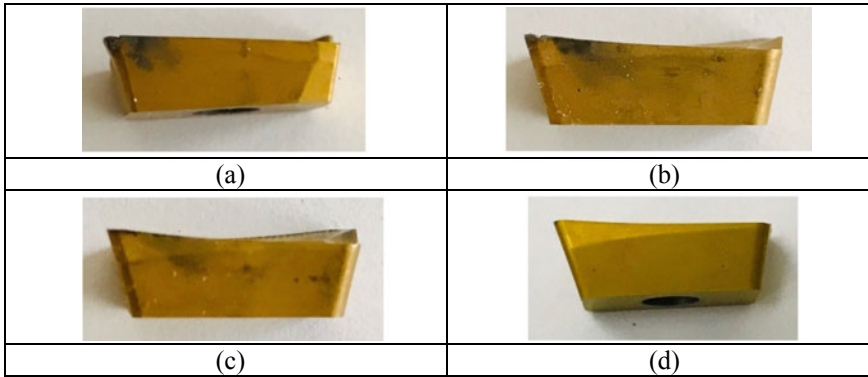


**Fig. 5** Coated cutting tool alloy specimens after high-speed machining with heat-assisted method

## 4 Conclusion

This article investigated the feasibility of high-speed machining with heat-treated SKD61 steel using uncoated and coated cutting tools. The results showed that high-speed machining with an uncoated cutting tool is not feasible at the support heating mode of 500 °C with a feed rate of 0.15 mm/tooth, a cutting depth of 0.3 mm, and speeds of 300–600 rpm due to excessive tool wear. On the other hand, with coated cutting tools, it is possible to perform high-speed machining with heat-assisted heating at a support heating mode of 200 °C–500 °C, a feed rate of 0.15 mm/tooth, and a cutting depth of 0.5 mm at speeds below 600 rpm. This finding suggests that minimal or no tool wear occurs when machining under specified conditions. These results can guide the selection of appropriate machining parameters for high-speed machining with heat-treated SKD61 steel in industrial practice using experimental planning methods.

**Acknowledgements** This work was also supported by Vietnam Ministry of Education and Training (MOET) under grant number B2022-BKA-08.

## References

1. Yeh SH, Chiu LH, Pan YT, Lin SC (2014) Relative dimensional change evaluation of vacuum heat-treated JIS SKD61 hot-work tool steels. *J Mater Eng Perform* 23(6):2075–2082
2. Dong TP, Toan ND (2023) A study on the investigation of the microstructure of SKD61 steel after selected quenching and tempering processes. *Mod Phys Lett B* 2340022. <https://doi.org/10.1142/S0217984923400225>
3. Thi-Bich M, Van-Chien D, Tien-Long B, Duc-Toan N (2018) Cutting force model for thermal-assisted machining of tool steel based on the Taguchi method. *Metals* 8(12):992. <https://doi.org/10.3390/met8120992>

4. Mac TB, Luyen TT, Nguyen DT (2022) A study for improved prediction of the cutting force and chip shrinkage coefficient during the SKD11 alloy steel milling. *Machines* 10(4):229
5. Thanh-Huan N, Duc-Toan N (2021) Experimental researches of turning hardened 9CrSi alloy tool steel with laser-assisted machining. *Arab J Sci Eng.* <https://doi.org/10.1007/s13369-021-05685-6>

# **Material Application for Sustainable Development**

# Comparative Confined Compressive Strengths of Normal Concrete and HPFRC in Experiment and Model



H. T. Tai Nguyen, Duy-Liem Nguyen, My Ngoc-Tra Lam,  
and Tri Nhat Minh Nguyen

**Abstract** This paper comparatively shows the confined compressive strengths of normal concrete (NC) and high-performance fiber-reinforced concrete (HPFRC) in experiment and model. Two types of compressive specimens were designed: no cover and uPVC cover with a 3.2 mm thickness. The applied load was directly applied on the NC/HPFRC core during testing. All NC/HPFRC cores were cylindrical with an identical size as follows: 114 mm in diameter and 600 mm in height. A hybrid fiber system, consisting of 1.0% long hooked and 0.5% short smooth fibers by volume, was used in the HPFRC core. The effect of confinement on axial compressive strength of the NC/HPFRC cores were clear. Besides, the models using Mohr–Coulomb principle and Hoek–Brown principle were also built to forecast the compressive strengths of them.

**Keywords** HPFRC · uPVC tube · Confinement · Mohr–Coulomb criterion · Hoek–Brown criterion

---

H. T. T. Nguyen · D.-L. Nguyen (✉) · M. N.-T. Lam  
Faculty of Civil Engineering, Ho Chi Minh City University of Technology and Education, Ho Chi Minh City, Vietnam  
e-mail: [liemnd@hcmute.edu.vn](mailto:liemnd@hcmute.edu.vn)

H. T. T. Nguyen  
e-mail: [tainht@hcmute.edu.vn](mailto:tainht@hcmute.edu.vn)

M. N.-T. Lam  
e-mail: [mylnt@hcmute.edu.vn](mailto:mylnt@hcmute.edu.vn)

T. N. M. Nguyen  
Campus in Ho Chi Minh City, University of Transport and Communications, Ho Chi Minh City, Vietnam  
e-mail: [trinm\\_ph@utc.edu.vn](mailto:trinm_ph@utc.edu.vn)



## 1 Introduction

Among structural members, columns are popular structures and directly influence on space efficiency and durability of a building. Therefore, enhancing column resistance and minimizing its size are intensively attractive to researchers. The use of uPVC tube covering concrete column is one of the effective solutions to improve resistance of columns. This is because the uPVC cover can limit the lateral deformation of the concrete column under compressive load in addition to play a role as a formwork [1–3], which helps save much construction time. As a concrete core is subjected to an axial load, the lateral uPVC cover will react to core expansion under form of passive pressure. In this paper, the authors employed uPVC cover for compressive specimens with normal concrete (NC) and high-performance fiber-reinforced concrete (HPFRC). The goal of this research is to compare the confined compressive resistance and confinement effect on NC and HPFRC through experimental and modeling work. The useful information from this paper is greatly expected to civil engineer to widen the application of NC/HPFRC column with uPVC cover.

## 2 Experimental Work

### 2.1 *Materials and Specimens Preparation*

The compressive specimens using NC/HPFRC were cylindrical shaped with its diameter  $\times$  height of 114 mm  $\times$  600 mm. Two types of specimens were designed: no cover and uPVC cover 3.2 mm thick. The uPVC making cover had 1.40 g/cm<sup>3</sup> density, 3000 MPa modulus of elasticity, and tensile strength exceeding of 50 MPa. The applied load was directly applied on the NC/HPFRC core during testing. Table 1 provides the compositions of NC and HPFRC regarding weight proportion [4]. The compressive strength of NC was 17.8 MPa while that of HPFRC was 79.6 MPa, measured from cylinder specimens with its diameter  $\times$  height of 114 mm  $\times$  200 mm. Two blended fiber types mixed in HPFRC were macro-hooked fiber with its content of 1.0 vol.% and micro-smooth fiber with its content of 0.5 vol.%. The macro-hooked fiber had length of 35 mm, diameter of 0.5 mm and tensile strength more than 1200 MPa. The micro-smooth fiber had length of 13 mm, diameter of 0.2 mm and tensile strength more than 2500 MPa. All NC/HPFRC specimens were water-cured at a temperature of  $25 \pm 5$  °C. After that, they were taken out of the water and naturally dried under laboratory room condition. Lastly, the experimental test were conducted at the age of 28 days age for all compressive specimens. Detailed information regarding mixing/curing materials can be referred to [4].

**Table 1** NC and HPFRC mortar matrix composition

Concrete	Cement (INSSE PC40)	Silica fume	Silica sand	Fly ash	Superplas-ticizer	Coarse aggregate	Water	Compressive strength (MPa)
NC	1.00	–	2.07	–	–	4.63	0.63	79.6
HPFRC	0.80	0.25	1.10	0.20	0.04	–	0.26	17.8

## 2.2 Experiment Setup

Before testing, all surfaces of the compressive specimens were smoothed carefully. The compressive specimens were tested with a displacement control using MATEST machine system with 300-ton capacity. The speed of displacement control was 1 mm/min during testing and the data collection frequency was 1 Hz. A steel plate was located on the top surface of core and its diameter was exactly equal to inner diameter of cover types for the target of employing compressive load only concrete core. The confined compressive strengths ( $f_{cc}'$ ) of the specimens were computed using the following equation:  $f_{cc}' = 4P_{\max}/\pi D^2$ , where,  $P_{\max}$  and  $D$  are the maximum load and the core diameter, respectively.

## 3 Experiment Result and Discussion

### 3.1 Comparative Resistance of NC/HPFRC Under Passively Confined Compression

Figure 1 displays the comparative resistance of NC/HPFRC under passively confined compression with four series: NC-No cover, NC-uPVC3.2, HPFRC-No cover, HPFRC-uPVC3.2. The resistance of the NC/HPFRC core with respect to cover type was evaluated in terms of compressive strength ( $f_{cc}'$ ), lateral strain capacity ( $\varepsilon_L$ ), axial strain capacity ( $\varepsilon_A$ ). As observed in Fig. 1a, the  $f_{cc}'$  were observed as follows: NC-No cover (15.89 MPa) < NC-uPVC3.2 (23.78 MPa) < HPFRC-No cover (61.43 MPa) < HPFRC-uPVC3.2 (63.49 MPa). Additionally, the  $\varepsilon_L$  were also observed to be same order with the  $f_{cc}'$ , the  $\varepsilon_L$  values shown in Fig. 1b were as follows: NC-No cover (0.13 %) < NC-uPVC3.2 (0.19 %) < HPFRC-No cover (0.34 %) < HPFRC-uPVC3.2 (0.53 %). However, the unclear trend was observed for  $\varepsilon_A$  in Fig. 1c: NC-No cover producing 0.91 %, NC-uPVC3.2 producing 1.79 %, HPFRC-No cover producing 1.58 % and HPFRC-uPVC3.2 producing 1.84 %. The increase of lateral strain capacity was thought to result in the increase of axial strain capacity [4]. The series HPFRC-uPVC3.2 including the highest uPVC thickness and higher strength of score, suitably produced the highest axial strain capacity. The 3.2 mm uPVC cover enhanced 1.50 times and 1.03 times in strength for NC and HPFRC, respectively. The 3.2 mm uPVC cover also contributed to axial strain

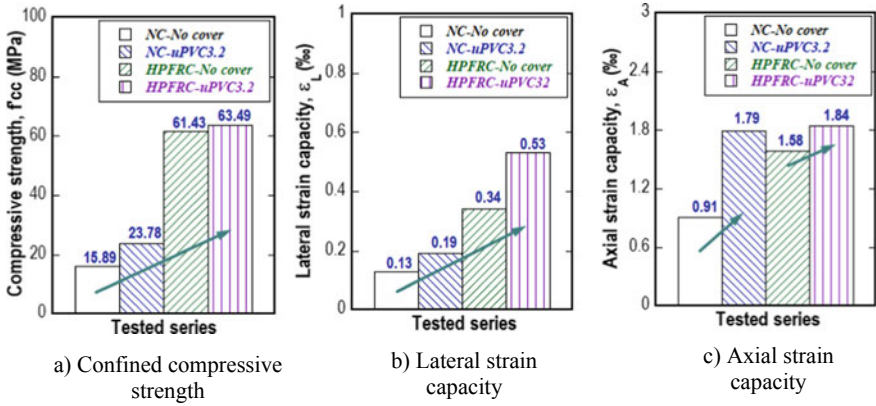


Fig. 1 Comparison of confined compressive parameters of the investigated concretes

capacity: enhancing 1.97 times and 1.16 times for NC and HPFRC, respectively. Generally, the effect of passive confinement by uPVC cover on compressive resistance was clear: significantly enhancing both compressive strength and strain capacity of NC/HPFRC, and, the effect of passive confinement on NC was clearer than that on HPFRC.

### 4 Modeling the Confined NC/HPFRC Core

Figure 2 shows two typical model curves of failure criteria, including Mohr–Coulomb’s and Hoek–Brown’s strength criterion. As displayed in Fig. 2, the Mohr–Coulomb failure criteria is employed in compression only [5], whereas the Hoek–Brown’s failure criteria is covered in both tension and compression [6, 7].

Under triaxial compression, the compressive specimen was exposed to ultimate compressive strength ( $f_{cc}'$ ) along the axial axis and lateral confining strength ( $f_3'$ ). This lateral confining strength was produced by of uPVC. In Fig. 2, the concrete core suffers the triaxial stress, including  $f_3'$  and  $f_{cc}'$  while cover type only exists the  $f_3'$  owing to the increase in the lateral deformation of concrete core under compressive loading at core. Using the equilibrium equations of a half cross section, the value of  $f_3'$  is expressed using the following equation:  $f_3' = 2t\epsilon_L E_L/D$ , where,  $t$  and  $D$  are the cover thickness and core diameter, respectively;  $\epsilon_L$  is the lateral strain; and  $E_L$  is elastic of modulus of uPVC or steel cover.

Based on Mohr–Coulomb failure criterion, the  $f_{cc}'$  is a function of the  $c$ ,  $\phi$  and  $f_3'$  under triaxial compression, which was given using Eq. (1) [5]. In Eq. (1), where  $c$  and  $\phi$  are the cohesive strength and internal friction angle of the compressive specimen, respectively. Under unconfined compression, i.e., the value of  $f_3' = 0$ , the value of  $f_{cc}'$  can be calculated using Eq. (2) [5]. The confinement effectiveness coefficient ( $k$ ) is a terms of  $\phi$ , as shown in Eq. (3) according to Richart et al. [8]. The range of  $k$

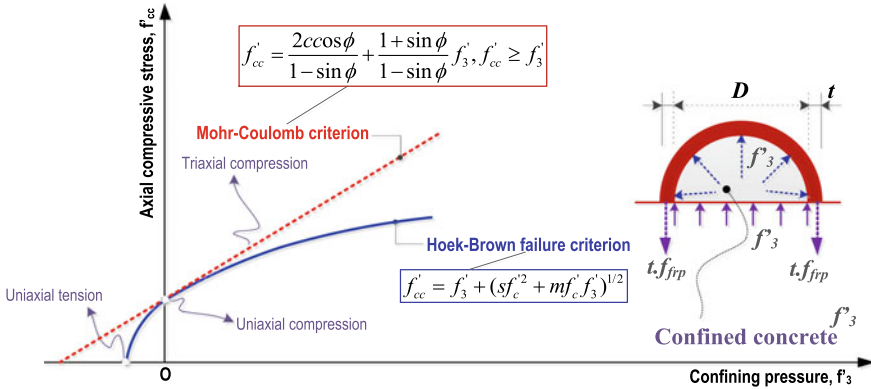


Fig. 2 Strength criterion models and stress states under confined compression

is dependent upon the confinement significance. Hence, the  $f_{cc}'$  value in Eq. (1) can be obtained using Eq. (4).

$$f_{cc}' = \frac{2c \cos \phi}{1 - \sin \phi} + \frac{1 + \sin \phi}{1 - \sin \phi} f_{3}', \quad f_{cc}' \geq f_{3}' \tag{1}$$

$$f_{cc}' = \frac{2c \cos \phi}{1 - \sin \phi}, \quad (f_{3}' = 0) \tag{2}$$

$$k = \frac{1 + \sin \phi}{1 - \sin \phi} \tag{3}$$

$$f_{cc}' = f_c' + k f_{3}' \Leftrightarrow \frac{f_{cc}'}{f_c'} = 1 + k \frac{f_{3}'}{f_c'} \tag{4}$$

According to Hoek–Brown [6], a failure criterion for rock was mathematically expressed using Eq. (5). In Eq. (5), where  $s$  and  $m$  coefficients are the material constants. The  $m$  coefficient depending on the rock type describes the curvature of  $f_{cc}'$  versus  $f_{3}'$  curve. The value of  $s$  illustrates the discontinuities in rocks. The value of  $s$  is 0 and 1 for heavily jointed and intact rocks [6], respectively. In this study, HPFRC core is considered as intact rock material. Hence, the value of  $s$  for HPFRC core is 1. The  $m$  coefficient can be computed in Eq. (6) using from Eq. (5) based on the experimental data.

$$f_{cc}' = f_{3}' + \left( s f_c'^2 + m f_c' f_{3}' \right)^{1/2} \tag{5}$$

$$m = \frac{(f_{cc}' - f_{3}')^2 - s f_c'^2}{f_c' f_{3}'} \tag{6}$$

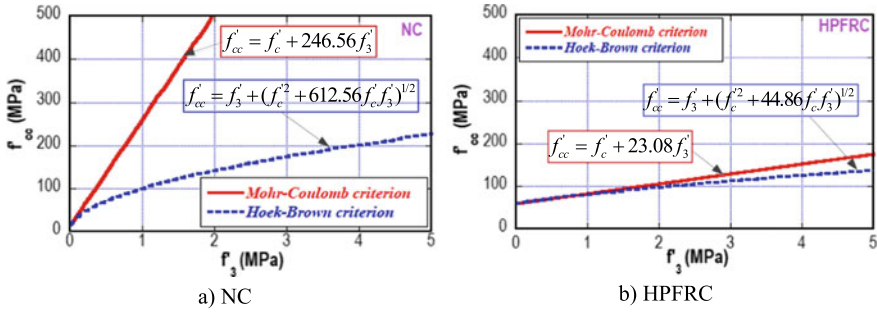


Fig. 3 Relating axial compressive strength and lateral strength

The curves of the obtained equations of the Mohr–Coulomb’s, Hoek–Brown’s criteria were performed in Fig. 3. As shown in Fig. 3a, the obtained  $k$  values from the equation of the Mohr–Coulomb’s criteria were 247.56 for NC and 23.08 for HPFRC. As shown in Fig. 3b, the obtained value of  $m$  coefficient from the equation of Hoek–Brown’s criteria were 612.56 for NC and 44.86 for HPFRC. Additionally, according to observed in Fig. 3, as the lateral confining strength increased, the axial compressive strength also increased. Comparatively, the order of failure criteria under confined compression in term of axial compressive strength as follows: Mohr–Coulomb’s > Hoek–Brown’s criteria. Besides, there was a large difference between two criteria in the case of NC while HPFRC produced a small difference between them.

### 5 Conclusion

The study results of both experiment and model could be concluded from this paper as follows:

- The order of compressive specimen in term of compressive strength and lateral strain capacity was as follows: NC-No cover < NC-uPVC3.2 < HPFRC-No cover < HPFRC-uPVC3.2.
- The effect of passive confinement by uPVC cover on compressive resistance was clear: significantly enhancing both compressive strength and strain capacity of NC/HPFRC. The effect of passive confinement by uPVC cover on NC was clearer than that on HPFRC.
- The relationship between axial compressive strength and lateral confining strength was explored based on Mohr–Coulomb’s and Hoek–Brown’s failure criterion.

## References

1. Woldemariam AM, Oyawa WO, Nyomboi T (2020) Experimental studies on the behavior of concrete-filled uPVC tubular columns under axial compression loads. *Cogent Eng* 7(1):1768649
2. Tue NV, K uchler M, Schenck G, J urgen R (March 2004) Application of UHPC filled tubes in buildings and bridges. In: *Proceeding of international symposium on ultra high performance concrete*. Kassel, Germany, pp 807–817
3. Gupta PK (2013) Confinement of concrete columns with unplasticized Poly-vinyl chloride tubes. *Int J Adv Struct Eng* 5:1–8
4. Nguyen DL, Thai DK, Tran NT, Ngo TT, Le HV (2022) Confined compressive behaviors of high-performance fiber-reinforced concrete and conventional concrete with size effect. *Constr Build Mater* 336:1–23
5. Girgin ZC, Arioglu N, Arioglu E (2007) Evaluation of strength criteria for very-high-strength concretes under triaxial compression. *ACI Struct J* 104:278–284
6. Hoek E, Kaiser PK, Bawden WF (1995) *Support of underground excavations in hard rock*. A.A. Balkema: Rotterdam, Netherlands, p 215
7. Johnston IW (1985) Comparison of two strength criteria for intact rock. *J Geotech Eng Div* 111:1449–1454
8. Richart E, Brandtzaeg A, Brown RL (1929) *Failure of plain and spirally reinforced concrete in compression; bulletin 190*. University of Illinois, Engineering Experimental Station, Champaign, IL, USA

# A Proposed Model for DDMRP Implementation and Application in a Plastic Manufacturing Company



Truong Thi Phuc and Phan Thi Mai Ha

**Abstract** The Demand-Driven Material Requirements Planning (DDMRP) is a new approach that combines the advantages of both push and pull systems. Specifically, DDMRP works based on a combination of principles of core MRP, theory of constraints (TOC) and just-in-time system (JIT). Nevertheless, not many studies have been found in the literature analyzing the implementation of DDMRP in actual production conditions. Besides, the researchers have not yet proposed any method of implementing DDMRP. Therefore, this study aims to propose a model for DDMRP implementation and apply it to a plastic manufacturing company to analyze the possibility of implementing DDMRP in the actual production environment. This study is conducted through two main methods are desk research and case study. The case study selected to collect data is a company operating in the manufacturing sector and has a multi-level material structure. It also proposes opportunities and challenges that should be addressed by future studies.

**Keywords** DDMRP · MRP · MPC · Decoupled lead time · Buffer

## 1 Introduction

In 1975, a breakthrough and effective method introduced by Orlicky changed the production planning and control (MPC) system into a systematic approach known as material requirements planning (MRP) [1]. In the 1980s, with the development of technology, planning was further modified into a more complex system called manufacturing resource planning (MRP II). During the 1990s, further development of technology introduced the Internet, leading to enterprise resource planning (ERP)

---

T. T. Phuc · P. T. M. Ha (✉)

Ho Chi Minh City University of Technology, VNU-HCM, 268 Ly Thuong Kiet, Ward 14, District 10, Ho Chi Minh City, Vietnam

e-mail: [ptmaiha@hcmut.edu.vn](mailto:ptmaiha@hcmut.edu.vn)

approach. Traditional MPC systems are based on a push strategy and have proven unsuitable in a highly flexible manufacturing environment. Since then, the planning systems that follow pull strategy have been introduced in manufacturing companies such as Just-in-Time (JIT) and the theory of constraints (TOC). However, pull-based inventory and materials planning and control methods such as TOC and JIT are also inadequate to implement a demand-driven manufacturing strategy [2].

To solve this problem, a new system that combines the advantages of both push and pull systems is introduced. Demand-driven material requirements planning (DDMRP) was introduced by Ptak and Smith [2] in Orlicky's 3rd edition material requirements planning book. In a systematic review and classification of studies performed on the DDMRP method, Azzamouri et al. [3] concluded that although DDMRP first appeared in 2011, studies on the DDMRP method are still relatively limited, researchers have not yet proposed any method of implementing DDMRP. Therefore, this study aims to propose a model for DDMRP implementation, apply to a plastic manufacturing company and analyze the possibility of implementing DDMRP in the actual production environment.

## 2 Literature Review

MRP is defined as a set of techniques that uses bill of material data, inventory data, and the master production schedule to calculate requirements for materials. However, many authors have analyzed MRP and concluded that it is not the best MPC system to deal with a volatile and changing world [4].

JIT is a manufacturing philosophy based on the plan to eliminate all waste and continuously improve productivity [5, p. 88]. The JIT system is sensitive and susceptible to changes in demand because it works without buffers. This makes the production system more vulnerable and less resilient to fluctuations in demand and supply [2].

TOC is a holistic management philosophy developed by Dr. Eliyahu M. Goldratt that is based on the principle that complex systems exhibit inherent simplicity. The TOC proposes a six-step solution called the theory of supply chain complementary system constraints (TOC SCRS) [6]. However, determining the frequency of replenishment of inventory can be a difficult task, and because it is not combined with the BOM structure, so it may be difficult to manage products with a BOM structure of more than two levels [2].

DDMRP is a multi-level planning and execution approach that promotes and protects the flow of related materials and information through the establishment and management of decoupled strategic inventory points. The buffer is the amount of inventory that will provide and ensure reliable availability to consumers, while allowing the accumulation of demand orders, generating a supply signal more stable, efficient, and practical for the suppliers. DDMRP has five sequential components related to positioning, protection, and pulling (Fig. 1).



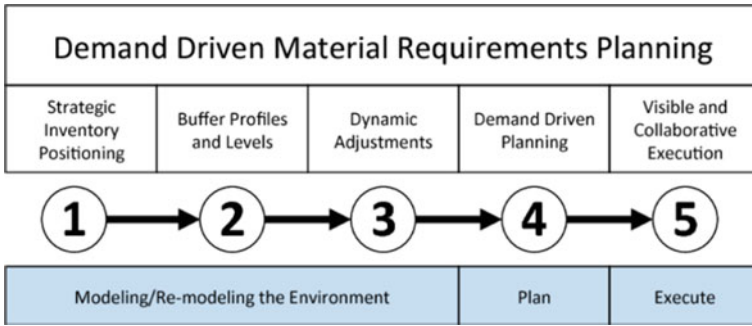


Fig. 1 The 5 components to implement DDMRP [7]

### 3 Methodology

- Research methods and research process

The secondary research method and case study method in qualitative research are used in this study. The research process consists of 4 steps, including (1) Determining the objectives of the study, which are to propose a model for DDMRP implementation; (2) The secondary research method helps to find and synthesize literature to provide a theoretical basis to propose a model for DDMRP implementation; (3) Collect relevant data from a case study and apply the built model; (4) Summarize and conclude on the study, indicate opportunities and challenges that should be addressed by future studies.

- Proposed model for DDMRP implementation

Step 1-Modeling the environment: The entire process to determine what item or component and what data is needed to perform DDMRP is based on DDMRP phase 1 & 2.

Step 2-Plan: The next phase corresponding to the 4th component of the DDMRP approach is demand-driven planning. In step 2, the planner needs to collect the data to prepare sufficient data for the calculation. Once, the data has been sufficiently prepared, the net flow equation is calculated to determine whether new supply orders/ manufactured orders need to be replenished. The full proposed model for DDMRP implementation is shown in Appendix.

## 4 Application of Proposed DDMRP Model—A Case Study

The company is currently one of the leading plastic brands in Vietnam. This study focuses on two key products including BG jar and NS bottle, which belong to group A products and account for more than 50% of the total sales volume of PET product group according to ABC inventory method.

- Strategic Inventory Positioning

First, two product structures showing the respective constitutive materials and supplies for these two product categories are presented. Six positioning factors to position these best buffers positions is applied [7] (Table 1).

After considering and answering to these main factors, the analyzed buffer points are determined. These points are placed into the product structures (Fig. 2).

- Buffer profiles and levels

- Buffer profiles

The buffers are divided into 3 zones: green, yellow and red. To determine the size for each zone, we considered the data characteristics of each component and its own attributes such as decoupled lead time (DLT), average daily usage (ADU) and order quantity minimum (MOQ). Based on the analysis of information and data collected

**Table 1** Answers for decoupling point positioning

Positioning factors	Answers
Customer tolerance time	Usually, these orders are committed to delivery 1 week after the customer places the order. The MLT for finished goods of BG jar is 2 days, and the NS bottle is 1 day
Market potential lead time	In this study, this factor is not applied because in fact, by reducing delivery time, customers are not inclined to pay more or increase their orders
Sales order visibility horizon	The demand for PET products is considered to have a rapid growth rate and is one of the best-selling products. This study considers placing a buffer at the second consumable level is the jar lid and less storage space
External variability	Shikong 5015W plastic beads have a long PLT, (2 months) and almost exclusively used for these two types of products, rarely used for other products
Inventory leverage and flexibility	PP Repol 110MA plastic beads is a common component for both products
Critical operation protection	Shikong 5015W & PP Repol 110MA plastic beads are main materials for blowing preforms of plastic bottles and jars

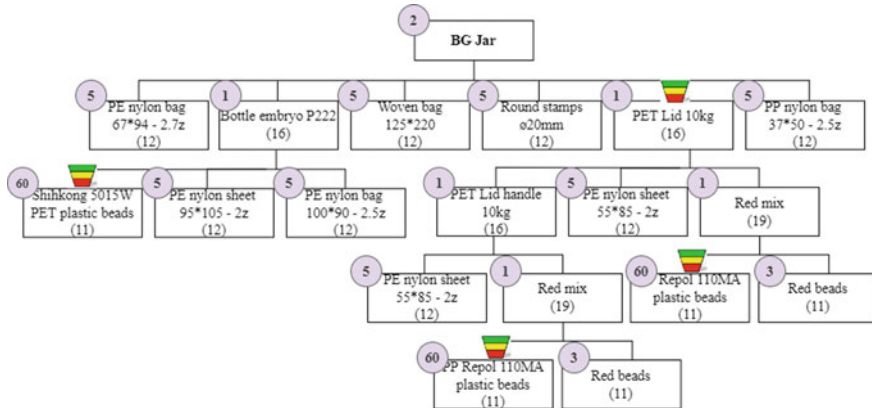


Fig. 2 Product structure tree of BG jar with buffers

from the company, the buffer profiles and individual attributes in this case study are determined.

– Buffer levels

Next, the inventory levels in each zone are reviewed to determine the correct amount of inventory at each level corresponding to each buffer based on detailed data of buffers and individual attributes obtained from the previous step. Table 2 is example of buffer calculation of PET Lid 10 kg.

- Dynamic adjustments

BG jars and NS bottles have seasonal fluctuations in demand. This adjustment period will be made at a time when the fourth quarter is considered the peak season for B2C products to serve the Tet holiday and the first quarter is the time when demand decreases after the increase at the end of last year (Fig. 3).

Table 2 Buffer calculation of PET Lid 10 kg

		PET Lid 10kg		Quantity
ADU	85,000		DLT x ADU x LTF	297,500
Buffer profiles	M, M (0.5), L (0.27)		MOQ	20,000
MOQ	20,000	Green zone	Max {ADU x DLT x LTF; MOQ}	297,500
LT/DLT	7	Yellow zone	ADU x DLT	595,000
		Red zone	Red base + Red safety	377,825
			Red base (DLT x ADU x LTF)	297,500
			Red safety (Red base x FV)	80,325



## 5 Discussion

After applying the proposed DDMRP model to a case study. The author identifies a number of advantages that DDMRP can bring such as: Division of responsibilities within the organization; Faster response to fluctuations; Accurate inventory management.

Besides, there are several challenges that DDMRP may face, including the challenge for buffer location selection because its complexity that increases with the BOM level. At that time, analysis to make important buffer placement decisions will be difficult, it is necessary to develop a tool to assist decision makers in making quick and rational decisions. In addition, the calculation of the buffer structure is influenced by the lead time rate and variation rate. The range of variation is quite wide, which will lead to quite large discrepancies in the results of calculating buffer zones, while DDMRP believes that these coefficients can be estimated empirically by the company.

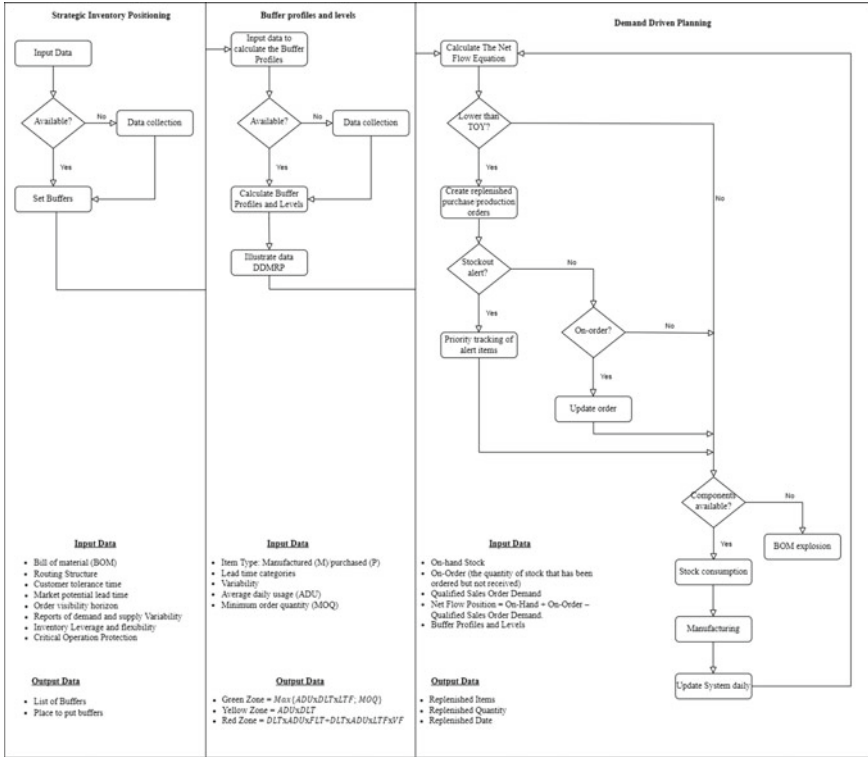
## 6 Conclusion

A model including the implementation steps and the necessary input and output data for the material requirements planning was proposed. The proposed model was built according to the first two phases in three main phases. The author built forms and performed calculations to apply the DDMRP method to material requirements planning for this case study. Finally, the analysis of DDMRP after applying this approach to case study is presented to clarify the advantages, disadvantages and challenges that DDMRP can face when implementing DDMRP in production environment.

In addition, the main limitation of the study is that the research has not measured the benefits obtained from DDMRP when applied in practice compared to the MRP-based planning method that the company is currently using. Future research may focus on recording real-time operational data long enough to measure and compare performance results with the company's current MRP planning methods.

**Acknowledgements** We acknowledge Ho Chi Minh City University of Technology (HCMUT), VNU-HCM for supporting this study.

# Appendix



## References

1. Miclo R, Lauras M, Fontanili F, Lamothe J, Melnyk SA (2019) Demand driven MRP: assessment of a new approach to materials management. *Int J Prod Res* 57:166–181
2. Ptak C, Smith C (2011) Orlicky’s material requirements planning 3/E. McGraw Hill Professional
3. Azzamouri A, Baptiste P, Dessevre G, Pellerin R (2021) Demand driven material requirements planning (DDMRP): a systematic review and classification. *J Ind Eng Manage* 14:439–456
4. Kortabarria A, Apaolaza U, Lizarralde A, Amorrortu I (2018) Material management without forecasting: from MRP to demand-driven MRP. *J Ind Eng Manage* 11:632–650
5. Blackstone JH (2013) APICS dictionary, 14th edn. APICS, Chicago, USA
6. Cox JF, Schleier JG (2010) Theory of constraints handbook. McGraw Hill Professional
7. Ptak C, Smith C (2016) Demand driven material requirements planning (DDMRP). Industrial Press, Inc

# A Study on the Effect of Gas Ratio $N_2/C_2H_2$ on Some Properties of Hard Thin Films TiAlCN on SKD61 Steel



Luan Duc Nguyen, Dinh Quang Nguyen, and Cuong Duc Pham

**Abstract** TiAlCN coating is often used to improve properties of engineering surfaces of a variety of applications such as in the mechanical, medical or decorative fields. In this study, the effect of  $N_2/C_2H_2$  gas ratio static friction and color (through wavelength measurement) of TiAlCN films created by vacuum arc deposition technology was investigated. The TiAlCN coating is fabricated on the surface of SKD61 steel. Using a home-built deposition system, namely HCM-700 (Hard Coating Machine—700 mm in chamber diameter). The static friction of the coated sample is evaluated with that of the uncoated ones. For the color determination, a spectrophotometer was used to analyze the energy present at each wavelength of the coating spectrum. The results show that when the  $N_2/C_2H_2$  gas ratio increases, the static friction of the TiAlCN coating decreases and the color of the coating becomes darker (i.e. increasing wavelength).

**Keywords** Cathode arc · TiAlCN coating · Friction · Color · Wavelength · Gas ratio

## 1 Introduction

Thin hard coatings have become a popular choice for protecting mechanical parts, due to their unique properties. Metal carbides, nitrides, and carbonitrides are some of the most widely used materials for these coatings, as they have high hardness and Young's modulus values. These values are crucial for protecting the softer substrate material. TiAlN and CrAlN are some of the most common materials used, with  $H > 35$  GPa and  $E > 350$  GPa. [1, 2]. Super hard coatings, like nanocomposite Ti-B-N coatings,

---

L. D. Nguyen · D. Q. Nguyen · C. D. Pham (✉)  
Institute of Technology, Ha Noi University Industry, No. 298, Cau Dien Street, Bac Tu Liem District, Hanoi, Vietnam  
e-mail: [phamcuong@hau.edu.vn](mailto:phamcuong@hau.edu.vn)

represent an important step forward in terms of hardness values. These coatings have been found to have  $H$  up to 50 GPa and an  $E$  of up to 500 GPa. These coatings are also notable for their high melting points, which can reach as high as 2950 °C and 3067 °C for refractory nitrides and carbides like TiN and TiC, respectively. The properties of thin hard coatings make them ideal for applications requiring superior surface hardness [3, 4]. Thermal stability is a critical feature for coatings used in cutting applications, as temperatures in the tribological contact can reach high levels. In addition, oxidation resistance is also essential in these applications, as the atmosphere surrounding the contact normally contains oxygen. Examples of coatings that can provide these features include (Ti, Al)N and nano composite TiN-Si<sub>3</sub>N<sub>4</sub> coatings. Both of these coatings have been tested and shown to possess high thermal stability and oxidation resistance. In addition, they are also metastable, meaning they remain stable even at higher temperatures. These properties, coupled with their affordable cost, make them ideal for use in cutting applications. [5–7]. Other aggressive environments demand a high corrosion resistance. TiC<sub>1-x</sub>N<sub>x</sub> coatings have been found to be able to withstand H<sub>3</sub>PO<sub>4</sub> and seawater [8].

TiAl(C,N) coatings have grown in popularity since the 1980s due to their outstanding properties which make them highly desirable for a wide range of applications. These coatings can be produced in a broad composition range, where  $x$  ranges from 0 to 1, and feature a face-centered cubic structure. The combination of titanium nitride (TiN) and titanium carbide (TiC) materials creates a coating that is both hard and tough, making it ideal for applications requiring high levels of wear resistance. TiC<sub>1-x</sub>N<sub>x</sub> coatings can exhibit hardness values up to ~40 GPa, depending on the nitrogen to carbon ratio. Additionally, these coatings are noted for their excellent tribological performance in dry sliding, with low friction at room temperature and in ambient atmosphere [9, 10].

This study presented Ti-Al-C-N hard coatings deposited by arc cathode technique with different N<sub>2</sub>/C<sub>2</sub>H<sub>2</sub> partial pressure ratios. The friction and color properties of these coatings were studied as a function of N<sub>2</sub>/C<sub>2</sub>H<sub>2</sub> partial pressure ratio. It was concluded that the N<sub>2</sub>/C<sub>2</sub>H<sub>2</sub> partial pressure ratio affects the friction and color properties of the coatings, with the presence of carbon providing for the low-friction behavior at room temperature and in ambient air conditions.

## 2 Methods

Friction is an important force in the physical world. It is a resistive force between two surfaces that come in contact with each other. The first law states that the frictional force is proportional to the normal force, or  $F = \mu w$ , where  $\mu$  is the coefficient of friction (COF). The second law states that the frictional force is independent of the apparent area of contact, meaning large and small objects have the same COF. The third law states that the frictional force is independent of the sliding.

The friction force undergoes six stages before reaching a steady-state, as illustrated in Fig. 1.



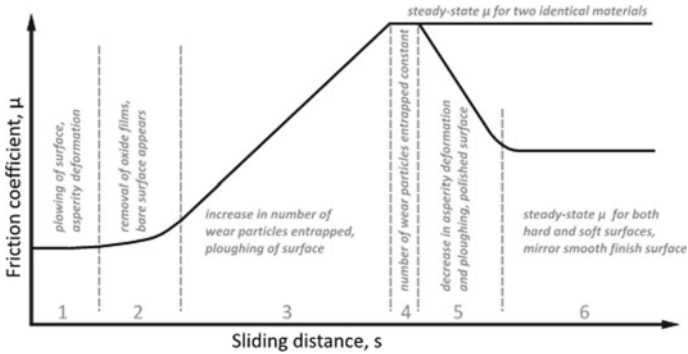


**Fig. 1** The six stages of friction versus sliding distance for steel counterparts, modified after [11]

The CIELAB color system is the universal standard for measuring and quantifying the color of coated objects. It is an objective method of characterizing color, making it a valuable tool for everyone from designers and artists to manufacturers. The CIELAB system is based on three fundamental parameters,  $L^*$ ,  $a^*$ , and  $b^*$ . These parameters measure the lightness, the colorfulness, and the hue of any given color respectively.

$L^*$  is the measurement of the lightness or the darkness of the color. It is measured on a scale from 0 to 100, with 0 being the darkest, and 100 being the brightest.

$a^*$  measures the colorfulness of the color, ranging from a negative value for greenish and bluish colors, to a positive value for reddish and yellowish colors.

$b^*$  measures the hue, or the amount of red, green, and blue in the color, on a scale from  $-128$  to  $+127$ .

The CIELAB color system is a reliable and efficient way to measure, quantify, and compare colors. With its three parameters, it goes beyond the traditional GB system, providing a more comprehensive and accurate way to judge, describe, and compare color (Fig. 2).

The distinction between two hues can be determined by the space between the color points of the two hues.  $\Delta E_{ab}$  measures the color difference between two hues, identified as '1' and '2', that have respective color coordinates of  $L1^*$ ,  $a1^*$ ,  $b1^*$  and

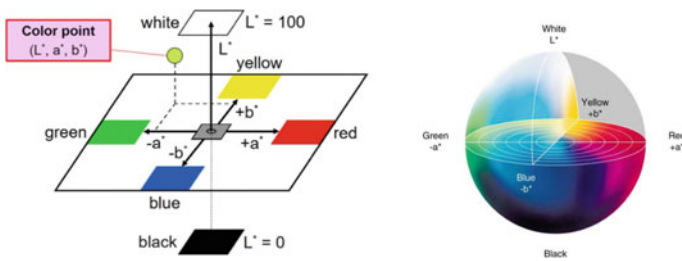


**Fig. 2** The 3-dimensional CIELAB color space (left) and color co-ordinates systems (right) [12]

$L_2^*$ ,  $a_2^*$ ,  $b_2^*$ . If  $\Delta E^*_{ab}$  is small, it means that the two hues are almost identical. The color difference can be determined through the use of the Pythagorean theorem.

$$\Delta E^*_{ab} = \sqrt{(\Delta L)^2 + (\Delta a^*)^2 + (\Delta b^*)^2} = \sqrt{(L_1^* - L_2^*)^2 + (a_1^* - a_2^*)^2 + (b_1^* - b_2^*)^2}$$

The color difference between the batch and the reference is calculated by comparing their color coordinates and finding  $\Delta E_{ab}$ . The acceptable range of color difference can vary, with some industries having a strict limit of  $\Delta E_{ab}$  less than 0.3, while others may have a more relaxed limit of  $\Delta E_{ab}$  less than 1.5. In practical use, the representation of color differences is often simplified as  $\Delta E$  or  $\Delta E$ .

### 3 Experimental Setup

The TiAlCN/TiAlN/TiAl coating was fabricated by arc cathode deposition technique using a hard coating machine HCM-700 (see Fig. 4) that was equipped with four arc sources using a target with a dimension of  $\phi 100 \times 40$  mm. TiAl alloy targets with a ratio of Ti:70/Al:30 and precursor gas  $C_2H_2$  and  $N_2$  were employed for the coating formation.

The SKD61 was chosen as substrates which were cut into pieces of  $\phi 20 \times 5$  mm by wire cutting. The SKD61 samples then were mirror polished to avoid the change of the microstructure of the alloy substrate due to the heat effect zone caused by the wire cutting process. After polishing, the SKD61 samples were sequentially cleaned in acetone, methanol, and deionized water in an ultrasonic bath before drying by blowing nitrogen gas. A turbo-molecular pump backed by a rotary pump was used to achieve a base pressure of  $5 \times 10^{-3}$  Pa before introducing the gases. Once a high vacuum of at least  $5 \times 10^{-3}$  Pa was reached, the sample holder was heated and maintained at 450 °C during the deposition. The targets were then etching cleaned with argon for five minutes. After preparation, the multilayer coating was deposited with the coating parameters and the coating process is detailed in Tables 1 and 2. During the deposition process, the substrate was continuously rotating to give uniform coatings. To determine the color of TiAlCN coating, we use a Ci62 Xrite spectrophotometer, which is used based on measuring the wavelength of the spectrum as shown in the following Fig. 3.

The colorimeter uses a standard light source to illuminate the sample to be measured. Light reflected from the sample is transmitted to the grating which breaks it into its spectral components. This signal falls into the Diode series, and is measured the amount of light at each wavelength. Knowing the spectral data. Spectral data is sent to the microprocessor, and the CIELab X, Y, Z color value is displayed.

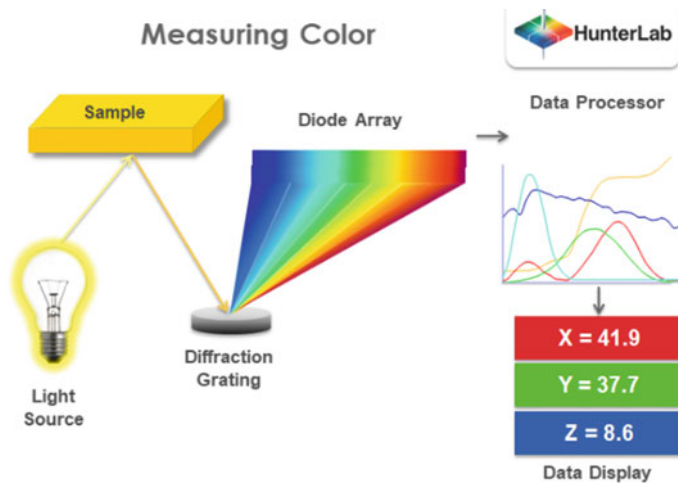
For static friction, we determine through the use of a model, using a flat steel plate, placing the samples on top of the flat plate. Then tilt with different angles to determine when the sample starts to slide, record the value of that angle and the Table 1. From

**Table 1** N<sub>2</sub>/C<sub>2</sub>H<sub>2</sub> ratio used for coating

Sample	N <sub>2</sub> /C <sub>2</sub> H <sub>2</sub>
1 (bare substrate)	Uncoating
2 (TiAlN)	Only N <sub>2</sub>
3 (TiAlCN)	360/40
4 (TiAlCN)	320/80
5 (TiAlCN)	200/200
6 (TiAlC)	Only C <sub>2</sub> H <sub>2</sub>

**Table 2** Step involve fabrication process and coating parameters

No	Step	Time (min)	Temperature (°C)	Arc current (A)	Bias Voltage (V)	Pressure (Pa)
1	Cleaning	5	450	–	–900	$1.2 \times 10^0$
2	Coating TiAl	5	450	80	–900	$5 \times 10^{-3}$
3	Coating TiAlN	10	450	80	–650	$5 \times 10^{-1}$
4	Coating TiAlCN	90	450	80	–100	$5 \times 10^{-1}$
5	Cooling down	80	<150	–	–	–

**Fig. 3** Base instrumentation a spectrophotometer [13]

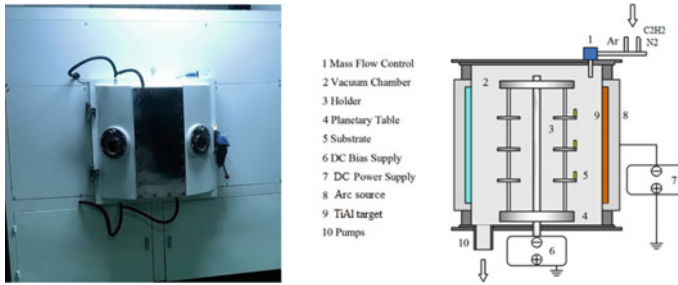


**Fig. 4** The hard coating machine HCM-700 (left) and schematic of the arc cathode deposition (right)

there determine the static friction (increase and decrease) of the samples relative to each other.

The survey was conducted as follows:

Sample 1: Uncoating, Sample 2: 100% N<sub>2</sub>, Sample 3: 90% N<sub>2</sub> and 10% C<sub>2</sub>H<sub>2</sub>, Sample 4: 80% N<sub>2</sub> and 20% C<sub>2</sub>H<sub>2</sub>, Sample 5: 50% N<sub>2</sub> and 50% C<sub>2</sub>H<sub>2</sub>, Sample 6: 100% C<sub>2</sub>H<sub>2</sub>.

## 4 Results and Discussion

The multilayer coating was achieved as shown in Fig. 5. Regarding tribological properties, the friction coefficient show in Table 3.

To compare the static friction of coating samples, the samples were put sequentially on a flat steel sheet with a roughness of 0.85 μm. The sheet then was raised slowly on one end until a sample slipped and then stops at the other end. The tilt angle was recorded. Each experiment was conducted 50 times for each sample. The tilt angle values were averaged as shown in Table 3. It can be seen that samples coated with TiAlC have reduced the static friction by 9.04% compared to the bare surface.

The reduction of static friction can be explained as follows: When the sample is not coated, the metal sample is in a crystalline state with a rather large graininess.

**Table 3** Friction results

Sample	Angle (degree)
1 (bare substrate)	30.5
2 (TiAlN)	30.2
3 (TiAlCN)	29.1
4 (TiAlCN)	28.6
5 (TiAlCN)	28.2
6 (TiAlC)	27.6

**Table 4** CIELAB values of the coating samples

Sample	CIELab	CIELab (reference)	Note
1 (bare substrate)	91	94	Very bright cream color
2 (TiAlN)	86	81	Greyish cream color
3 (TiAlCN)	63	58	Dominant honey color
4 (TiAlCN)	52	47	Dominant brown color
5 (TiAlCN)	40	34	Darken brown color
6 (TiAlC)	89	96	Silver color

Meanwhile, TiAlCN film having a low carbon ratio remained in a crystalline state but the grain size decreased significantly. The increase of carbon ratio results in the change of crystalline state to amorphous state. Therefore, at a large carbon ratio the static friction decrease. The production of a product must follow a strict process to ensure its quality. The color of the TiAlCN layer with varying N<sub>2</sub>/C<sub>2</sub>H<sub>2</sub> ratios was measured and analyzed in the CIELAB color space using a standard D65 light source and a 10 colorimetric observer, as shown in Table 4. The color points are depicted as points in the Lab\* space, with the distance from the center indicating the chroma  $C_{ab}^* = \sqrt{a^{*2} + b^{*2}}$ . Angle between the a\* axis and the color coordinate vector representing the color  $H_{ab} = \arctan \left( \frac{b^*}{a^*} \right)$ . Although color saturation is not formally defined in the CIELAB system, a good sensory correlation for saturation is  $S_{ab} = C_{ab}^*/L^*$ .

The color of TiAlN film will be darker as the carbon ratio increases with the ratio of N<sub>2</sub> and C<sub>2</sub>H<sub>2</sub> as showed in Table 4.

## 5 Conclusions

In this work, TiAlCN coatings synthesized by cathode arc evaporation at different N<sub>2</sub>/C<sub>2</sub>H<sub>2</sub> ratios on SKD61 substrates were investigated. The friction and color properties of the coating were also studied. From the experimental results following conclusions are drawn:

- The static friction of the coating decreases as the N<sub>2</sub>/C<sub>2</sub>H<sub>2</sub> ratio increases. This could be due to when many carbon atoms are added to the TiAlCN film, the film is in an amorphous state, therefore decrease static friction. The static friction of the sample coated with TiAlCN film was reduced by 9.04% at the N<sub>2</sub>/C<sub>2</sub>H<sub>2</sub> ratio of 40/360 SCCM compared to the uncoated sample.

- The color of the characteristic TiAlCN film is yellow copper. That becomes darker when the percentage of carbon atoms increases. But when the carbon ratio increases too high, the color tends to silver.

## References

1. Karlsson L, Hultman L, Johansson MP, Sundgren JE, Ljungcrantz H (2000) *Surf Coat Technol* 126:1–14
2. Forn A, Picas JA, Fuentes GG, Elizalde E (2010) *Int J Refract Met Hard Mater* 19:507–513
3. Andersson J, Erck RA, Erdemir A (2013) *Wear* 254:1070–1075
4. Gomez MA, Romero J, Lousa A, Esteve J (2015) *Surf Coat Technol* 200:1819–1824
5. Derflinger V, Brandle H, Zimmermann H (2019) *Surf Coat Technol* 113:286–292
6. Andersson J, Erck RA, Erdemir A (2013) *Surf Coat Technol* 163–164:535–540
7. Rebelo de Figueiredo M, Neidhardt J, Kaindl R, Reiter A, Tessadri R, Mitterer C (2008) *Wear* 265:525–532
8. Liu Y, Erdemir A, Meletis EI (2016) *Surf Coat Technol* 82:48–56
9. Oliver WC, Pharr GM (2014) *J Mater Res* 7:1564–1580
10. Muratore C, Bultman J, Aouadi SA, Voevodin A (2010) *Wear*. In press
11. Stueber M, Barna P, Simmonds M, Albers U, Leiste H, Ziebert C, Holleck H, Kovács A, Hovsepian P, Gee I (2005) Constitution and microstructure of magnetron sputtered nanocomposite coatings in the system Ti–Al–N–C. *Thin Solid Films* 493(1–2):104–112. <https://doi.org/10.1016/j.tsf.2005.07.290>
12. <https://knowledge.ulprospector.com/10780/pc-the-cielab-lab-system-the-method-to-quantify-colors-of-coatings/>
13. <https://support.hunterlab.com/hc/en-us/articles/209481606-2-Color-Measurement>

# Studying the Efficiency of Car Brake Force Distribution by a Three-Dimensional Dynamics Model



Nguyen Thanh Tung and Luong Van Van

**Abstract** The distribution of car braking force according to the traction conditions of the wheels with different types of roads in order to increase the braking efficiency and the safety of the car's movement. In this paper, the authors have built a three-dimensional dynamics model to investigate the influence of brake force distribution on the braking efficiency of a car. The survey results using Matlab software show that: if a Kia Pride CD5 car is driven on a straight road with a maximum coefficient of longitudinal friction  $\mu_{x\max} = 0.8$  at 90 kph, and then the car is suddenly braked with a braking torque equal to the maximum braking torque; In case the car does not have a mechanical brake force distribution system, the rear wheels are locked and slip completely, causing the car to lose its motion stability; If a car with a mechanical brake force distribution system, the wheels will not be locked, the force generated when braking of the rear wheels will increase by about 25%, the car's braking acceleration will increase by about 15%, the braking efficiency will be satisfactory according to the standards ECE-R13 (The international braking regulation of the UNO-economic commission for Europe in Geneva—ECE-regulation No. 13, ECE-R13, Vehicle Regulations, [1]).

**Keywords** Braking force distribution · Braking efficiency

## 1 Overview

If the car is braked, the longitudinal inertia force is in the same direction as the car's movement, so the load acting on the front wheel increases and the load acting on the rear wheel decreases. The ideal brake force at the wheels is proportional to the load acting on the wheel and the maximum brake force is  $P_{x\max} = P_z \mu_{x\max}$ . If the braking

---

N. T. Tung (✉) · L. Van Van  
Vinh Long University of Technology Education, 73, Nguyen Hue St, Vinh Long City, Vietnam  
e-mail: [tungnt@vlute.edu.vn](mailto:tungnt@vlute.edu.vn)

force  $P_{x_{max}} < P_z \mu_{x_{max}}$ , the braking process has not fully utilized the wheel's grip, so the braking efficiency is low. If the braking force  $P_{x_{max}} > P_z \mu_{x_{max}}$ , the wheel is locked and slips on the road surface, so the braking efficiency is also low. Therefore, in order to increase the braking efficiency of the car, it is necessary to distribute the braking force to match the grip-ability of the wheels. Brake force distribution is done by either a mechanical brake force distribution system or an electronic brake-force distribution system (EBD) [2–4].

## 2 The Dynamics Model

To study the influence of brake force distribution on the braking efficiency of a car, The authors have built a 3D spatial dynamics model of the car by the method of separating the system of many objects as represented in Fig. 1 [4–7].

The authors have established a system of car dynamics equations using Newton's and Euler's equations as follows [8–10]:

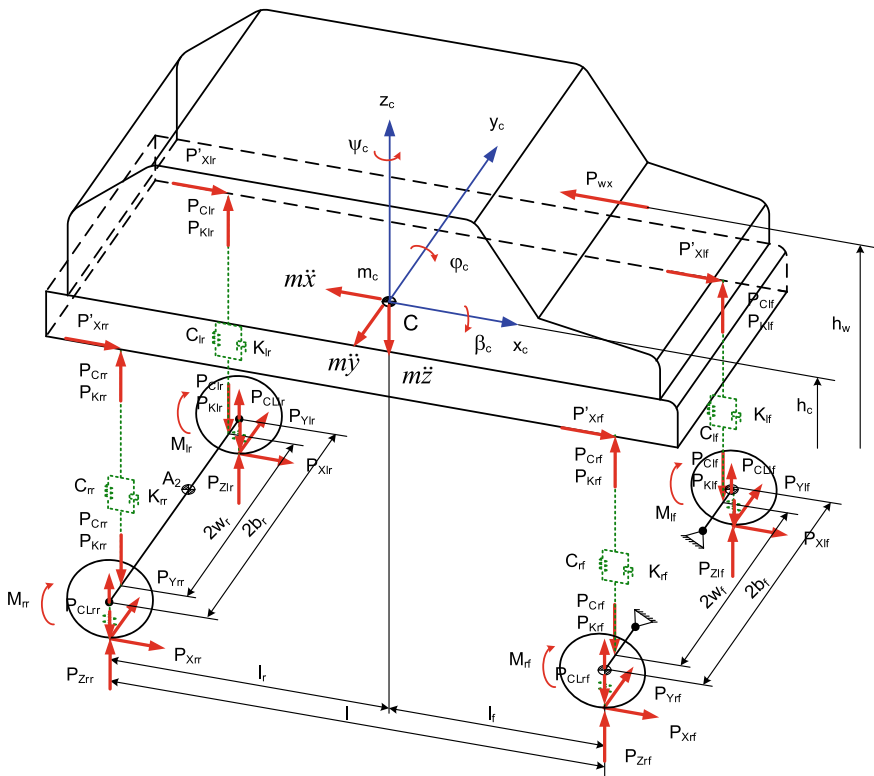


Fig. 1 The 3D spatial dynamics model of the car



$$\begin{aligned} (m_c + m_{Alf} + m_{Arf} + m_{Ar})\ddot{x}_c &= P_{Xlf} \cos \delta_{lf} + P_{Xrf} \cos \delta_{rf} - P_{Ylf} \sin \delta_{lf} \\ &\quad - P_{Yrf} \sin \delta_{rf} + P_{Xlr} + P_{Xrr} \end{aligned} \quad (1)$$

$$\begin{aligned} (m_c + m_{Alf} + m_{Arf} + m_{Ar})\ddot{y}_c &= P_{Xlf} \sin \delta_{lf} + P_{Xrf} \sin \delta_{rf} + P_{Ylf} \cos \delta_{lf} \\ &\quad + P_{Yrf} \cos \delta_{rf} + P_{Ylr} + P_{Yrr} \end{aligned} \quad (2)$$

$$\begin{aligned} J_{zc}\ddot{\psi}_c &= (P_{Xlf} \sin \delta_{lf} + P_{Xrf} \sin \delta_{rf} + P_{Ylf} \cos \delta_{lf} + P_{Yrf} \cos \delta_{rf})l_f \\ &\quad + (P_{Xrr} - P_{Xlr})b_r + (P_{Xrf} \cos \delta_{rf} - P_{Xlf} \cos \delta_{lf} \\ &\quad + P_{Ylf} \sin \delta_{lf} - P_{Yrf} \sin \delta_{rf})b_f - (P_{Yrl} + P_{Yrr})l_r \end{aligned} \quad (3)$$

$$m_c\ddot{z}_c = P_{Clf} + P_{Klf} + P_{Crf} + P_{Krf} \quad (4)$$

$$\begin{aligned} J_{yc}\ddot{\phi}_c &= (P_{Clf} + P_{Klf} + P_{Crf} + P_{Krf})l_f - (P_{Clr} + P_{Klr} + P_{Crr} + P_{Krr})l_r \\ &\quad + M_{lf} + M_{rf} + M_{lr} + M_{rr} \end{aligned} \quad (5)$$

$$J_{xc}\ddot{\beta}_c = (P_{Crf} + P_{Krf} - P_{Clf} - P_{Klf})b_f + (P_{Crr} + P_{Krr} - P_{Clr} - P_{Klr})b_r \quad (6)$$

$$m_{Alf}\ddot{\xi}_{lf} = P_{CLlf} - P_{Clf} - P_{Klf} \quad (7)$$

$$m_{Arf}\ddot{\xi}_{rf} = P_{CLrf} - P_{Crf} - P_{Krf} \quad (8)$$

$$m_{Ar}\ddot{z}_{Ar} = P_{CLlr} + P_{CLrr} - P_{Clr} - P_{Klr} - P_{Crr} - P_{Krr} \quad (9)$$

$$\begin{aligned} J_{Axr}\ddot{\beta}_{Ar} &= (P_{Clr} + P_{Klr} - P_{Crr} - P_{Krr})w_r + (P_{CLrr} + P_{KLrr} - P_{CLlr} - P_{KLlr})b_r \\ &\quad - P_{Ylr}(r_{lr} + \xi_{Alr}) - P_{Yrr}(r_{rr} + \xi_{Arr}) \end{aligned} \quad (10)$$

$$\begin{aligned} J_{Aylf}\ddot{\psi}_{lf} &= M_{Alf} - M_{Blf} - P_{Xlf}r_{dlf} - P_{Zlf}e_{Xlf} \\ &= M_{Alf} - M_{Blf} - (P_{Xlf} - P_{Zlf}f_{lf})r_{dlf} \end{aligned} \quad (11)$$

$$\begin{aligned} J_{Ayrf}\ddot{\psi}_{rf} &= M_{Arf} - M_{Brf} - P_{Xrf}r_{drf} - P_{Zrf}e_{Xrf} \\ &= M_{Arf} - M_{Brf} - (P_{Xrf} - P_{Zrf}f_{rf})r_{drf} \end{aligned} \quad (12)$$

$$\begin{aligned} J_{Aylr}\ddot{\psi}_{lr} &= M_{Alr} - M_{Blr} - P_{Xlr}r_{dlr} - P_{Zlr}e_{Xlr} \\ &= M_{Alr} - M_{Blr} - (P_{Xlr} - P_{Zlr}f_{lr})r_{dlr} \end{aligned} \quad (13)$$

$$\begin{aligned}
 J_{Ayrr}\ddot{\varphi}_{rr} &= M_{Arr} - M_{Brr} - P_{Xrr}r_{drr} - P_{Zrr}e_{Xrr} \\
 &= M_{Arr} - M_{Brr} - (P_{Xrr} - P_{Zrr}f_{rr})r_{drr}
 \end{aligned}
 \tag{14}$$

### 3 Simulation and Commentary

The authors used Matlab-Simulink software to investigate the influence of brake force regulation on car braking efficiency. The authors surveyed under the following conditions: For a Kia Pride CD5 car with a full load, moving straight at  $V_0 = 90$  kph on a road surface with a sinusoidal profile according to ISO 8608:2016 [11]; The survey road is a dry asphalt road with a longitudinal friction coefficient of  $\mu_{x\max} = 0.8$ ;  $\mu_{x\min} = 0.75$ ; When examining the brake with brake torque level  $T_B = T_{B\max} = P_G\mu_{x\max}r_d$ ; Survey in two cases of cars with and without brake force distribution system. The brake torque and transmission torque of the front and rear axle are represented in Fig. 2.

Figure 3 is a graph showing the ratio of slip of the left front wheel  $S_{lf}$  and the ratio of slip of the right front wheel  $S_{rf}$ . The solid red line shows that the car does not have a brake force distribution system (N-No); The blue dotted line represents a car with a brake force distribution system (Y-Yes). Observing the graph, we can see that the slip ratio when braking the left and right front wheels in the two cases of a car with a brake force distribution system and a car without brake force distribution system have the same shape and value are equivalent,  $S_{lf-Y} \approx S_{rf-Y} \approx 5.5\%$  and  $S_{lf-N} \approx S_{rf-N} \approx 6.0\%$ , so the front wheels are working in the stable linear elastic region.

The ratio of slip of the rear wheels is represented in Fig. 4. In case a car is fitted with a mechanical brake force distribution system, the slip ratio of the rear wheels  $S_{lr-Y} \approx S_{rr-Y} \approx 6\%$ , the wheels are working in the stable linear elastic region. In case a car does not have a mechanical brake force distribution system, the slip coefficient of the rear wheels  $S_{lr-N} = S_{rr-N} = 100\%$ , the rear wheels are locked and skid 100% on the road, the braking efficiency is decreased and the car is in unstable motion.

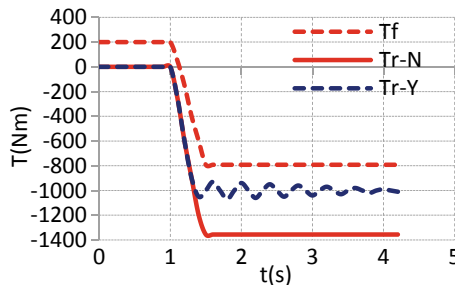


Fig. 2 The brake torque and transmission torque of the front and rear axle

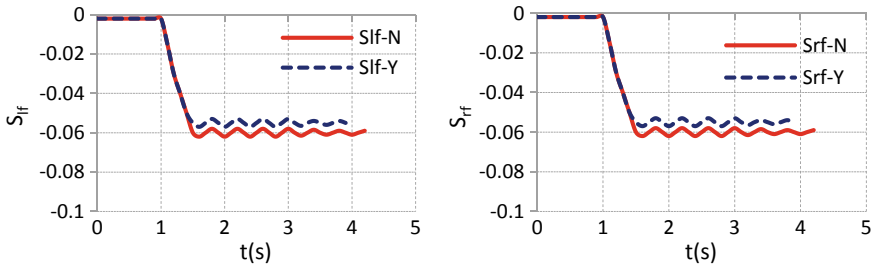


Fig. 3 Slip ratio of the left and right front wheels

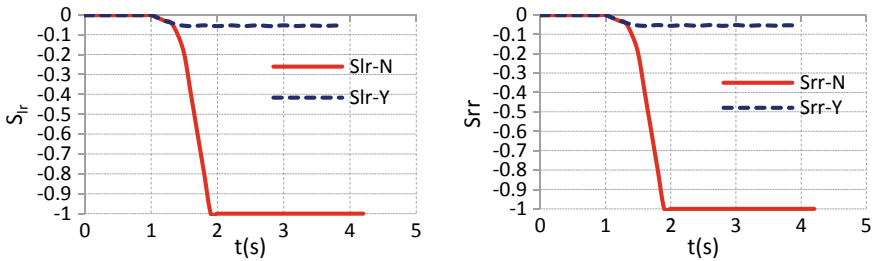


Fig. 4 Slip ratio of the left and right rear wheels

The vertical force on the left and right front wheels is represented in Fig. 5. When braking, the vertical reaction on the front wheels is increased. If a car does not have a mechanical brake force distribution system, the vertical reaction on the front wheels is  $P_{Zlf-N} \approx P_{Zrf-N} \approx 3050N$ , and greater than that of a car with a mechanical brake force distribution system of  $P_{Zlf-Y} \approx P_{Zrf-Y} \approx 2950N$ .

Due to the force of inertia, when braking, the vertical reaction on the rear wheels is decreased. When a car has a mechanical brake force distribution system, the vertical reaction on the rear wheels is  $P_{Zlr-Y} \approx P_{Zrr-Y} \approx 3350N$ , and greater than a car without a mechanical brake force distribution system is  $P_{Zlr-N} \approx P_{Zrr-N} \approx 3250N$ , as Fig. 6.

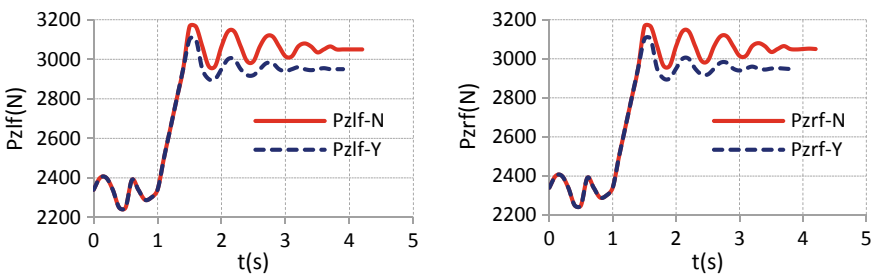


Fig. 5 The vertical force on the left and right front wheels

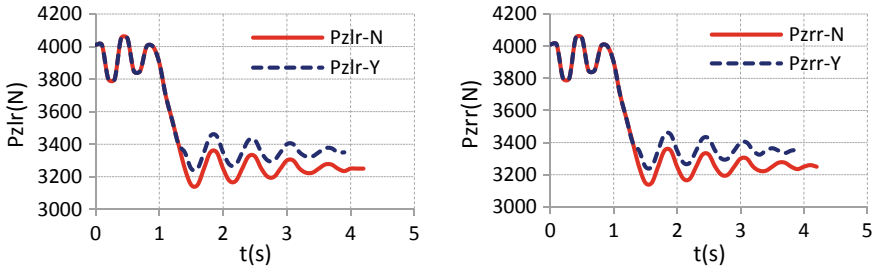


Fig. 6 The vertical force on the left and right rear wheels

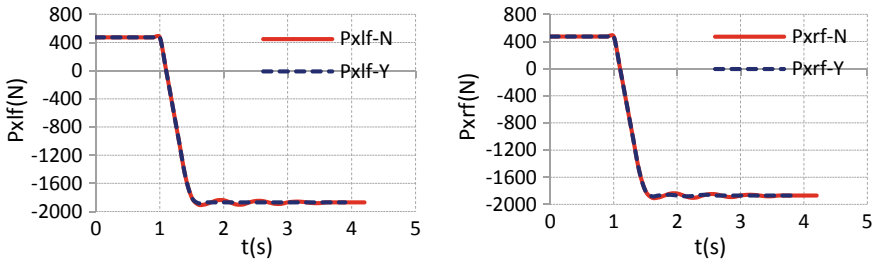


Fig. 7 The brake force of the left and right front tyres

The braking force of the left and right front wheels is represented in Fig. 7. Studying Fig. 7 we see that, the brake force of the left and right front wheels in two cases with and without a mechanical brake force distribution system, have the same shape and value are,  $P_{Xlf-N} \approx P_{Xlf-Y} \approx 1850N$ ;  $P_{Xrf-N} \approx P_{Xrf-Y} \approx 1850N$ .

Figure 8 is a graph of the braking force of the left and right rear tyres. We see that the brake force of the rear tyres in the case of a mechanical brake force distribution system is about 25% greater than the case of a car without a mechanical brake force distribution system. In the case of a car with a mechanical brake force distribution system, the brake force of the left and right rear tyres is  $P_{Xlr-Y} \approx P_{Xrr-Y} \approx 2650N$ . In case the car does not have a mechanical brake force distribution system, the rear tyres are locked and slide 100% on the road surface, so the brake force of the left and right rear tyres is reduced,  $P_{Xlr-N} \approx P_{Xrr-N} \approx 1950N$ .

The braking acceleration of the car and the body rotation angle are represented in Fig. 9. We see that the braking acceleration of a car with a mechanical brake force distribution system is about 15% larger than that of a car without a mechanical brake force distribution system. Braking acceleration of cars with a mechanical brake force distribution system  $a_Y = 7.5 m/s^2$ , the brake performance of the car meets the requirements of the ECE-R13 standard [1]. Braking acceleration of cars without a mechanical brake force distribution system  $a_N = 6.5 m/s^2$ . The body rotation angle of a car has a mechanical brake force distribution system is  $\dot{\psi}_Y \approx 0.2^\circ$  while the body

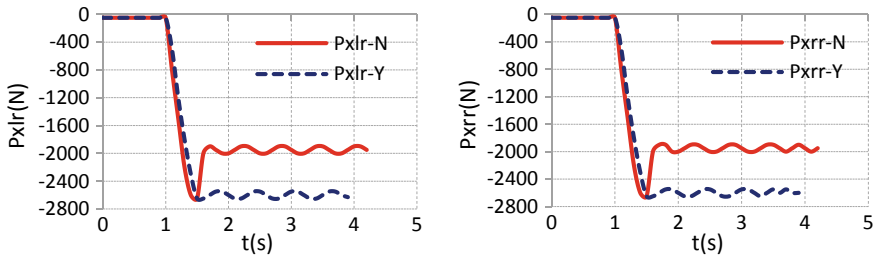


Fig. 8 The brake force of the left and right rear tyres

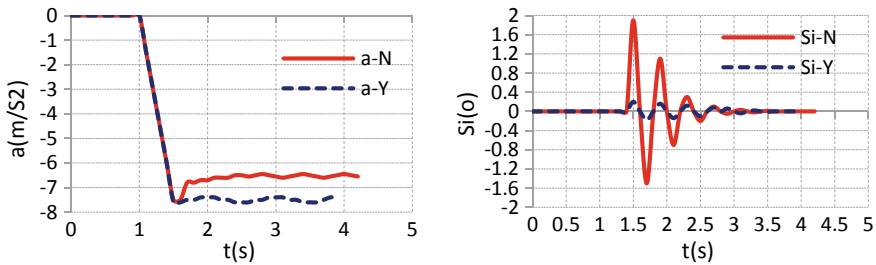


Fig. 9 The braking acceleration and the body rotation angle

rotation angle of a car does not have a mechanical brake force distribution system is  $\ddot{\psi}_N \approx 2^\circ$ .

### 4 Conclusions

When a Kia Pride CD5 car is driven on a straight road with a maximum coefficient of longitudinal friction  $\mu_{xmax} = 0.8$  at 90 kph and then the car is braked with a torque equal to the maximum braking torque, in two cases a car with and without a mechanical brake force distribution system. In the case of a car with a mechanical brake force distribution system, the tyres will not be locked, the brake force of the rear tyres will increase by about 25%, the car’s braking acceleration will increase by about 15%, the braking efficiency will be satisfactory according to the standards ECE-R13 [1]. In case the car does not have a mechanical brake force distribution system, the rear wheels are locked and slip 100%, causing the car to lose its motion stability.

## References

1. The international braking regulation of the UNO-economic commission for Europe in Geneva—ECE-regulation No. 13, ECE-R13, Vehicle Regulations (2004)
2. Jazar RN (2017) *Vehicle dynamics theory and application*. Springer, Switzerland
3. Tung NT, Huong VV, Kiet PT (2020) Experimental research on determining the vertical tyre force of a tractor semi-trailer. *Int J Mod Phys B*. <https://doi.org/10.1142/S0217979220401633>
4. Tung NT (2021) Setting up the braking force measurement system of the tractor semi-trailer. *Eng Solid Mech*. <https://doi.org/10.5267/j.esm.2021.6.001>
5. Tung NT, Van LV, Quang NT (2021) A survey on the effects of bumpy road on the vibration of multi-purpose forest fire fighting vehicle. *Eng Solid Mech*. <https://doi.org/10.5267/j.esm.2021.3.001>
6. Tung NT, Huong VV (2021) Setting up the 3D dynamic model to study the dynamic wheel load of the tractor semi-trailer. *J Phys: Conf Ser (JPCS)*, IOP Publishing, U.K. <https://doi.org/10.1088/1742-6596/2022/1/012025>
7. Tung NT, Huong VV (2020) The effect of the wheel rotation angle on the braking efficiency of the tractor semi-trailer on the wet roundabout route. *Lecture notes in networks and systems*. Springer, Switzerland, pp 798–804. [https://doi.org/10.1007/978-3-030-64719-3\\_87](https://doi.org/10.1007/978-3-030-64719-3_87)
8. Tung NT, Huong VV (2021) Research on the dynamic load of the tractor semi-trailer when braking on the round road. *Lecture notes in mechanical engineering*. Springer, United States, pp 456–461. [https://doi.org/10.1007/978-3-030-69610-8\\_62](https://doi.org/10.1007/978-3-030-69610-8_62)
9. Tung NT, Van LV (2022) A study on the effects of tire vertical stiffness on dynamic load of DVM 2.5 truck. *Lecture notes in mechanical engineering*. [https://doi.org/10.1007/978-3-030-92574-1\\_13](https://doi.org/10.1007/978-3-030-92574-1_13)
10. Tung NT, Van LV (2022) A research on the effects of suspension stiffness on dynamic load on Dongfeng DVM 2.5 truck. *Lecture notes in mechanical engineering*. [https://doi.org/10.1007/978-3-030-99666-6\\_27](https://doi.org/10.1007/978-3-030-99666-6_27)
11. International standard ISO 8608, mechanical vibration—road surface profiles—reporting of measured data (2016)

# The Effects of the Ratio of Grip to the Ratio of Slip When Braking the Semi-Trailer at 60 kmph



Nguyen Thanh Tung and Luong Van Van

**Abstract** This paper shows the results of building a model and simulating the effects of the ratio of grip to the ratio of slip when the semi-trailer is braked at 60 kmph on a straight road. The system of dynamic equations of the semi-trailer is built by the Newton–Euler method. Simulation of the influence of the ratio of grip on the ratio of slip using Matlab software. The results showed that, if the semi-trailer is moved on a straight road with the ratio of grip  $\mu_{x\max} = [0.8:0.1:1.0]$  at 60 kmph, the longitudinal ratio of slip is less than 10%, the brake force reaches the maximum value. If  $\mu_{x\max} = [0.5, 0.6]$ , the ratio of slip of the middle axle, and rear axle reaches the maximum value,  $S = 100\%$ , the wheels are locked and fully slipped, the brake force reaches min value, and the semi-trailer is not safe.

**Keywords** Ratio of grip · Ratio of slip · Braking process

## 1 Introduction

The longitudinal ratio of slip  $S_x$  of the wheels affects the driving, braking, and safety of the semi-trailer,  $S_x < 0$  for driving, and  $S_x > 0$  for braking.  $S_x$  is determined according to the following formula [1]:

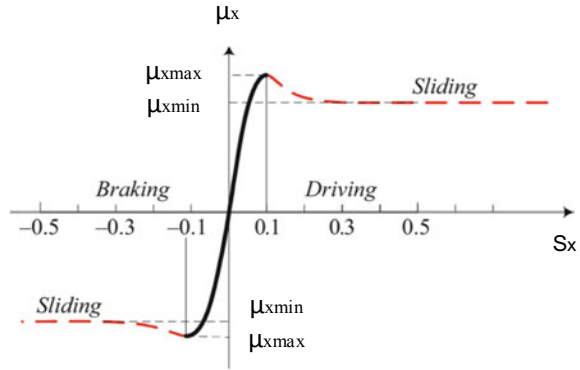
$$S_x = \frac{r_d \omega_w - V_x}{r_d \omega_w}; \quad r_d \omega_w > V_x; \quad -1 < s_x < 0 \quad \text{for driving} \quad (1)$$

$$S_x = \frac{r_d \omega_w - V_x}{V_x}; \quad r_d \omega_w < V_x; \quad -1 < s_x < 0 \quad \text{for braking} \quad (2)$$

---

N. T. Tung (✉) · L. Van Van  
Vinh Long University of Technology Education, 73, Nguyen Hue St, Vinh Long City, Vietnam  
e-mail: [tungnt@vlute.edu.vn](mailto:tungnt@vlute.edu.vn)

**Fig. 1** Graph of longitudinal ratio of grip



When the vehicle is in motion, the longitudinal force  $F_x$  appears between the tire and the road surface,  $F_x = F_z \mu_x$ , and the longitudinal ratio of grip  $\mu_x$  is a function of  $S_x$  in driving and braking as shown in Fig. 1.

The objectives of this paper are to build a dynamics model and simulate the longitudinal ratio of slip of tires in the braking process of the semi-trailer on different kinds of roads.

According to the author’s knowledge, up to now, there have been many studies on the longitudinal ratio of slip in the braking process of the vehicle [1]. However, there have not been many studies on the longitudinal ratio of slip in the braking process of the semi-trailer, especially the studies on the semi-trailer produced and operated in Vietnam. Therefore, the research results of this paper have high scientific and practical significance in Vietnam nowadays.

## 2 The 3D Dynamic Model

The semi-trailer has a complex structure, vehicle with six axles and two bodies linked together by a fifth wheel. The three-dimensional dynamic model of the vehicle is built by the multi-body system method. The Newton–Euler equation was used to build the system of dynamic equations of the vehicle. Equations (3–8) describe the dynamics of the vehicle in the XY plane [2–6]:

$$\begin{aligned}
 (m_{c1} + m_{Ai})\ddot{x}_{c1} &= F_{x1j} \cos \delta_{1j} - F_{y1j} \sin \delta_{1j} \\
 &+ F_{x2j} + F_{x3j} - F_{wx1} - F_{kx1}
 \end{aligned}
 \tag{3}$$

$$\begin{aligned}
 (m_{c1} + m_{Ai})\ddot{y}_{c1} &= F_{x1j} \sin \delta_{1j} + F_{y1j} \cos \delta_{1j} + F_{y2j} \\
 &+ F_{y3j} - F_{ky1} (i = 1 - 3)
 \end{aligned}
 \tag{4}$$



$$\begin{aligned}
J_{zc1}\ddot{\psi}_{c1} = & [F_{x1j} \sin \delta_{1j} + F_{y1j} \cos \delta_{1j}]l_1 \\
& + (F_{xi2} - F_{xi1})b_i - F_{yij}l_i + F_{ky1}l_{k1} \\
& + (F_{x12} \cos \delta_{12} - F_{x11} \cos \delta_{11} + F_{y11} \sin \delta_{11} - F_{y12} \sin \delta_{12})b_1 \quad (i = 1 - 3)
\end{aligned} \tag{5}$$

$$(m_{c2} + m_{Ai})\ddot{x}_{c2} = F_{xij} + F_{kx2} \quad (i = 4 - 6) \tag{6}$$

$$(m_{c2} + m_{Ai})\ddot{y}_{c2} = F_{ky2} + F_{yij} \quad (i = 4 - 6) \tag{7}$$

$$J_{zc2}\ddot{\psi}_{c2} = (F_{xi2} - F_{xi1})b_i - F_{yij}l_i + F_{ky2}l_{k2} \quad (i = 4 - 6) \tag{8}$$

Equations (9–12) describe the dynamics of the vehicle in the XZ plane [2–6] (Fig. 2):

$$m_{c1}\ddot{z}_{c1} = F_{Cij} + F_{Kij} - F_{kz1} \quad (i = 1 - 3) \tag{9}$$

$$J_{yc1}\ddot{\phi}_{c1} = (F_{Cij} + F_{Kij})l_i + F_{kz1}l_{k1} - F_{kx1}(h_{c1} - h_{k1}) + M_{ij} \quad (i = 1 - 3) \tag{10}$$

$$m_{c2}\ddot{z}_{c2} = F_{Cij} + F_{Kij} + F_{kz2} \quad (i = 4 - 6) \tag{11}$$

$$J_{yc2}\ddot{\phi}_{c2} = -(F_{Cij} + F_{Kij})l_i + F_{kx2}(h_{c2} - h_{k2}) + F_{kz2}l_{k2} + M_{ij} \quad (i = 4 - 6) \tag{12}$$

Equations (13–17) describe the dynamics of the vehicle in the YZ plane [2–6] (Fig. 3):

$$J_{xc1}\ddot{\beta}_{c1} = (F_{Ci2} + F_{Ki2} - F_{Ci1} - F_{Ki1})w_i + M_{kx1} \quad (i = 1 - 3) \tag{13}$$

$$J_{xc2}\ddot{\beta}_{c2} = (F_{Ci2} + F_{Ki2} - F_{Ci1} - F_{Ki1})w_i - M_{kx2} \quad (i = 1 - 3) \tag{14}$$

$$\begin{aligned}
J_{Ax1}\ddot{\beta}_{Ai} = & (F_{Ci1} + F_{Ki1} - F_{Ci2} - F_{Ki2})w_i \\
& + (F_{CLi2} - F_{CLi1} - F_{KLi1})b_i - F_{yij}(r_{ij} + \xi_{Aij}) \quad (i = 1 - 6)
\end{aligned} \tag{15}$$

$$m_{Ai}(\ddot{z}_{Ai} + \dot{\beta}_{Ai}\dot{y}_{Ai}) = F_{CLij} + F_{KLi2} - F_{Cij} - F_{Kij} \quad (i = 1 - 6) \tag{16}$$

$$m_{Ai}(\ddot{y}_{Ai} - \dot{\beta}_{Ai}\dot{z}_{Ai}) = F_i + F_{yij} \quad (i = 1 - 6) \tag{17}$$

The dynamics equations of the wheels are as follows [7–9]:

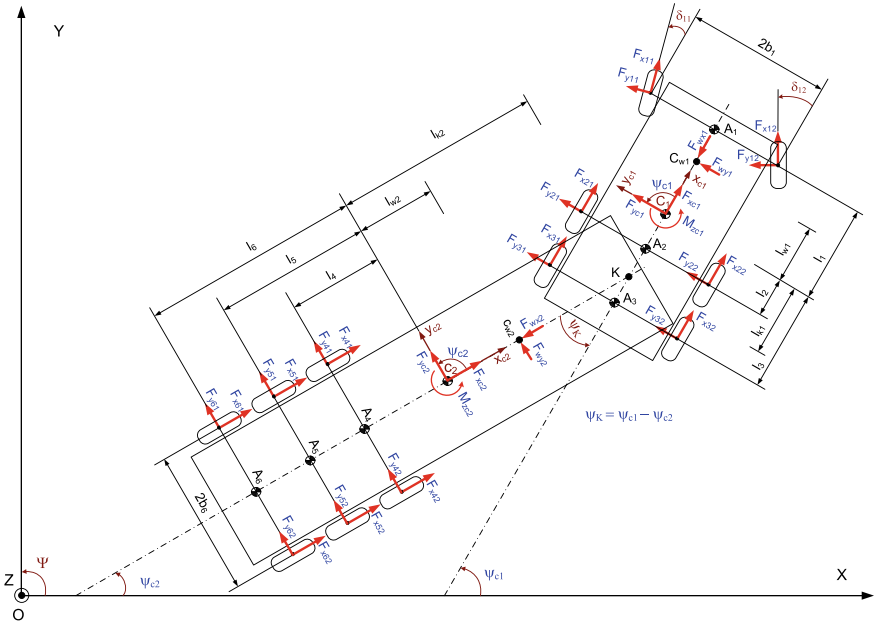


Fig. 2 Diagram of forces and moments acting on the vehicle in the XY plane

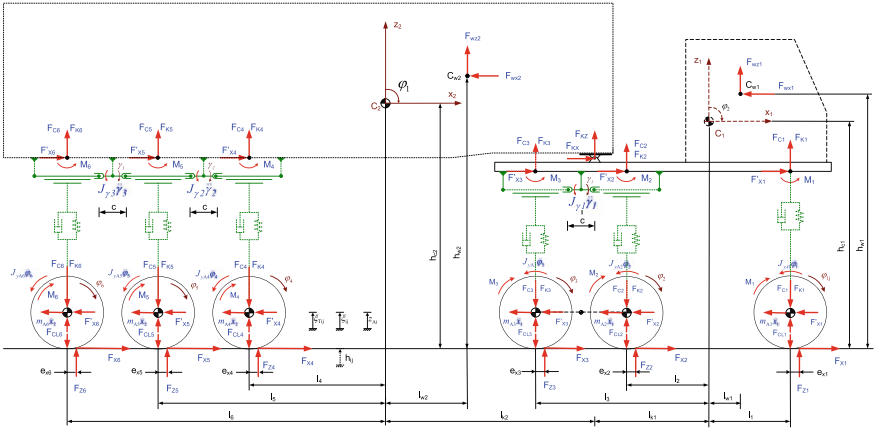


Fig. 3 Diagram of forces and moments acting on the vehicle in the XZ plane

$$J_{Ayij}\ddot{\varphi}_{ij} = M_{Aij} - M_{Bij} - F_{xij}r_{dij} \quad (i = 1, 2, 3, 4, 5, 6; j = 1, 2) \quad (18)$$

### 3 Simulation and Discussion

Simulation of the influence of longitudinal ratio of grip on the vehicle's longitudinal ratio of slip using Matlab software. The vehicle is braked with torque  $M_B = 0.8M_{Bmax}$  when it is running on a straight road at 60 kmph. A vehicle is run on six kinds of roads with six different maximum longitudinal ratio of grip  $\varphi_{xmax} = [0.5:0.1:1.0]$ . Line 1 has  $\varphi_{xmax} = 0.5$ , line 2 has  $\varphi_{xmax} = 0.6$ , line 3 has  $\varphi_{xmax} = 0.7$ , line 4 has  $\varphi_{xmax} = 0.8$ , line 5 has  $\varphi_{xmax} = 0.9$  and line 6 has  $\varphi_{xmax} = 1.0$ . Graphs of active torque and braking torque are shown in Fig. 4.

Graph of the vertical reaction of the road on the tire  $F_{zij}$  of axles 1, 3, and 6 are shown in Fig. 5. Studying Fig. 5, we find that when a vehicle is braked, the vertical reaction of the road on the front tire  $F_{z11}$  has a higher value, whereas the vertical reaction of the road on the middle tire  $F_{z31}$  and the rear tire  $F_{z61}$  have a lower value. On the front axle, the higher the longitudinal friction coefficient is, the greater the vertical force  $F_{zij}$  is. On the rear axle, the higher the longitudinal friction coefficient is, the smaller the vertical reaction of the road on the tire  $F_{zij}$  is.

The graphs of longitudinal force  $F_{Xij}$  of the axles 1, 3, 6 when the vehicle is braked on six kinds of roads with six different maximum longitudinal traction ratio  $\varphi_{xmax} = [0.5:0.1:1.0]$  are shown in Fig. 6. The longitudinal force on the front axle,  $F_{X11} = 19kN$ . For the middle axle, if  $\varphi_{xmax} = 0.5$ , then  $F_{X31} = 16kN$ ; if  $\varphi_{xmax} = 0.6$ , then  $F_{X31} = 20kN$ ; if  $\varphi_{xmax} = [0.7, 0.8, 0.9, 1.0]$ , then  $F_{X31} = 27kN$ . For the rear axle, if  $\varphi_{xmax} = 0.5$ , then  $F_{X61} = 14kN$ ; if  $\varphi_{xmax} = 0.6$ , then  $F_{X61} = 17kN$ ; if  $\varphi_{xmax} = 0.7$ , then  $F_{X61} = 20kN$ ; if  $\varphi_{xmax} = [0.8, 0.9, 1.0]$ , then  $F_{X61} = 25kN$ .

The graphs of longitudinal slip ratios of the axles 1, 3, and 6 when the vehicle is braked on six kinds of roads with six different maximum longitudinal traction ratio  $\varphi_{xmax} = [0.5:0.1:1.0]$  are shown in Fig. 7. The longitudinal slip ratio on the front axle

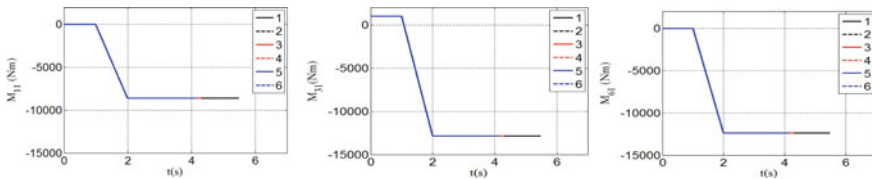


Fig. 4 Graphs of active torque and braking torque on axles 1, 3, 6

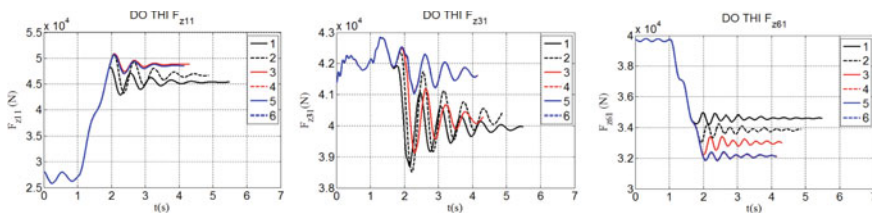


Fig. 5 Graph of the vertical reaction of the road on the front, middle, and rear tire

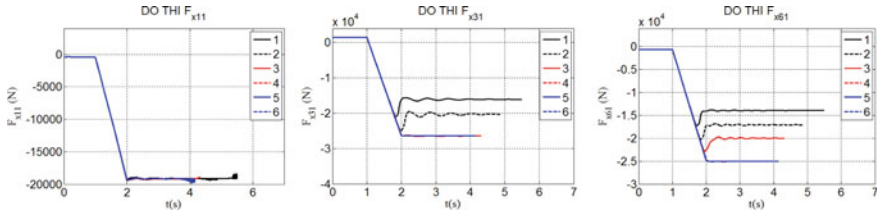


Fig. 6 The longitudinal forces on axles 1, 3, 6

$S_{11}$  is less than 4%, the front wheels operate stably and safely in the linear elastic region. For the middle axle, if  $\varphi_{x\max} = [0.5, 0.6]$ , then  $S = 100\%$ , the middle wheels are locked and full slipped, and the tractor semi-trailer loses its stability; if  $\varphi_{x\max} = [0.7, 0.8, 0.9, 1.0]$ , then  $S = 5\%$ , the middle wheels operate stably and safely in the linear elastic region. For the rear axle, if  $\varphi_{x\max} = [0.5, 0.6, 0.7]$ , then  $S = 100\%$ , the rear wheels are locked and full slipped, and the tractor semi-trailer loses its stability; if  $\varphi_{x\max} = [0.8, 0.9, 1.0]$ , then  $S < 10\%$ , the rear wheels operate stably and safely in the linear elastic region.

The friction use ratio  $f_{ij} = \varphi_{xij\max} / \varphi_{xij}$  of the axles 1, 3, 6 when the vehicle is braked on six kinds of roads with six different maximum longitudinal traction ratio  $\varphi_{x\max} = [0.5:0.1:1.0]$  are shown in Fig. 8. On the front axle, the friction use ratio  $f = 0.4 \div 0.85$ , and the brake force has not used the full friction of the wheel. On the middle axle, if  $\varphi_{x\max} = [0.5, 0.6]$ , then  $f = 1$ , the brake force has used the full friction of the wheel; if  $\varphi_{x\max} = [1.0, 0.9, 0.8, 0.7]$ , then  $f = 0.65 \div 0.95$ , the brake force has not used the full friction of the wheel.

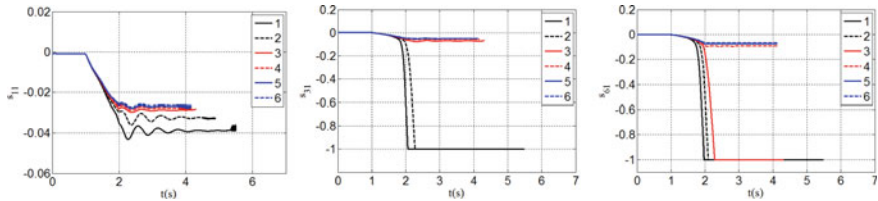


Fig. 7 The longitudinal slip ratios on axles 1, 3, 6

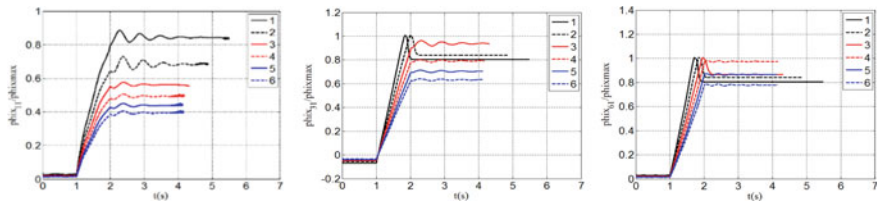


Fig. 8 The friction use ratios on axles 1, 3, 6

## 4 Conclusion

If the vehicle is braked on three kinds of roads with six different maximum longitudinal traction ratio  $\varphi_{x\max} = [0.8:0.1:1.0]$  at 60 kmph, and the vehicle is braked with torque  $M_B = 0.8M_{B\max}$ , the value of the coefficient of longitudinal slip is very small,  $S < 10\%$ ; the brake force reaches the maximum value,  $F_{X11} = 19$  kN,  $F_{X31} = 27$  kN,  $F_{X61} = 25$  kN. If  $\varphi_{x\max} = [0.5, 0.6]$ , the coefficient of longitudinal slip of the middle axle, and rear axle reaches the maximum value,  $S = 100\%$ , the wheel is locked and fully slipped, the brake force reaches min value, and the tractor semi-trailer loses its stability.

## References

1. Jazar RN (2017) Vehicle dynamics theory and application. Springer, Switzerland
2. Tung NT (2021) Setting up the braking force measurement system of the tractor semi-trailer. Eng Solid Mech. <https://doi.org/10.5267/j.esm.2021.6.001>
3. Tung NT, Huong VV (2021) Setting up the 3D dynamic model to study the dynamic wheel load of the tractor semi-trailer. J Phys: Conf Ser (JPCS). IOP Publishing, United Kingdom. <https://doi.org/10.1088/1742-6596/2022/1/012025>
4. Tung NT, Huong VV (2020) The effect of the wheel rotation angle on the braking efficiency of the tractor semi-trailer on the wet roundabout route. Lecture notes in networks and systems. Springer, Switzerland [https://doi.org/10.1007/978-3-030-64719-3\\_87](https://doi.org/10.1007/978-3-030-64719-3_87)
5. Tung NT, Huong VV (2021) Research on the dynamic load of the tractor semi-trailer when braking on the round road. Lecture notes in mechanical engineering, United States Springer, pp 456–461. [https://doi.org/10.1007/978-3-030-69610-8\\_62](https://doi.org/10.1007/978-3-030-69610-8_62)
6. Tung NT, Van Van L (2022) A study on the effects of tire vertical stiffness on dynamic load of DVM 2.5 truck, Lecture notes in mechanical engineering. [https://doi.org/10.1007/978-3-030-92574-1\\_13](https://doi.org/10.1007/978-3-030-92574-1_13)
7. Tung NT, Van Van L (2022) A research on the effects of suspension stiffness on dynamic load on Dongfeng DVM 2.5 truck, Lecture notes in mechanical engineering. [https://doi.org/10.1007/978-3-030-99666-6\\_27](https://doi.org/10.1007/978-3-030-99666-6_27)
8. Tung NT, Van Van L (2022) A study on the effects of braking torque on a dynamic load of tractor semi-trailer on a round road with the maximum longitudinal friction coefficient  $\mu_{x\max}=0.6$ , Lecture notes in mechanical engineering. [https://doi.org/10.1007/978-3-030-99666-6\\_28](https://doi.org/10.1007/978-3-030-99666-6_28)
9. Van Van L, Hung Phi C, Thanh Tung N (2022) Effect of suspension system stiffness on dynamic load action chassis multi-purpose forest fire fighting vehicle. Int J Eng. <https://doi.org/10.5829/ije.2022.35.08b.13>

# Combustion Characteristics of DA465QE Engine Fueled with HHO Enriched Biogas



Anh Vu Vo, Thi Minh Tu Bui, Tan Tien Huynh, and Thong Ngo Tan

**Abstract** This paper presents the results of a numerical simulation of the performance of the DA465QE engine and the impact of adding HHO to biogas on its efficiency and pollutant emissions. The results showed that at a given operating condition, an increase in HHO and CH<sub>4</sub> concentrations, as well as the load regime, led to an increase in the indicative work cycle  $W_i$ . However, this increase decreased as engine speed increased and reached a peak value when the equivalence ratio and advanced ignition timing varied. Additionally, an increase in HHO and CH<sub>4</sub> concentrations, the load regime, and advanced ignition timing was found to result in a rise in the combustion temperature  $T$  and NO<sub>x</sub> content in the exhaust gas. But, when engine speed increased, a decrease was observed, and a peak value was achieved with variations in the equivalence ratio. The rate of increase in NO<sub>x</sub> concentration with the equivalence ratio was found to be higher than that of  $W_i$  and  $T$ . When the HHO concentration in the biogas mixture was below 30%, the improvement in  $W_i$  was observed to be beneficial before the increase in NO<sub>x</sub>. Given that the biogas engine operates with a lean mixture, the addition of HHO is especially intriguing. The optimal ignition timing was found to reduce 6CA as effectively as adding 30% HHO to biogas at a certain engine speed. By properly adjusting the engine's operating parameters when using HHO-enriched biogas as fuel, a balance between performance and NO<sub>x</sub> emissions can be achieved. A compromise between performance and NO<sub>x</sub> emission can be obtained by appropriate adjustment of operating conditions of the engine fueled with HHO enriched biogas.

**Keywords** Renewable energy · Hydrogen · Biogas · HHO · SI engine

---

A. V. Vo (✉) · T. M. T. Bui · T. T. Huynh  
Danang University of Science and Technology, The University of Da Nang, Da Nang, Vietnam  
e-mail: [vavu@dut.udn.vn](mailto:vavu@dut.udn.vn)

T. N. Tan  
University of Technology and Education, The University of Da Nang, Da Nang, Vietnam

## 1 Introduction

Biogas contains  $\text{CH}_4$ , which determines the calorific value of the fuel, while  $\text{CO}_2$  impurities lessen the efficiency of combustion and the release of heat. Biogas has a high octane number, so it can be used on high compression engines allowing for improved thermal efficiency [1, 2]. About pollutant emissions, Verma et al. [3] found that biogas-powered spark-ignition engines have low  $\text{NO}_x$  emissions but higher CO and HC emissions than gasoline engines. This is because the presence of  $\text{CO}_2$  in the fuel mixture lowers the burning temperature, which reduces the reaction to form  $\text{NO}_x$ . To improve the quality of biogas combustion without increasing pollutant emissions, one of the most effective ways is to add hydrogen or HHO into the biogas [4]. Ilbas et al. [5] showed that increasing the hydrogen concentration in the hydrogen-methane mixture accelerates combustion and extends the burning limit. This allows to shorten the time between ignition and the peak of the heat release rate curve, and thus the maximum pressure increases and moves near TDC. The numerical simulation results showed that as the hydrogen content in the fuel increased, the maximum values of pressure and heat release rate increased, and the ignition delay time decreased [6]. The above analysis shows adding hydrogen into biogas has many prospects in energy saving and environmental protection [7, 8]. The challenge of the widespread use of hydrogen concerns the fuel storage, especially in vehicles. In fact, hydrogen has a low volumetric energy, so to provide the same amount of energy as a conventional fuel a larger fuel tank is required. The main storage solution today is to compress hydrogen in a tank up to 700 bar, compared to 200 bar for natural gas. Therefore, using hydrogen in a mixture with oxygen (specifically HHO) produced directly onboard the vehicle or on site for stationary engines with renewable energy, such as solar panels, is more interesting. HHO gas is considered as a clean and promising alternative fuel [9, 10]. In recent years, the automotive industry has developed an interest in HHO [11], attracting the attention of scientists worldwide [12, 13]. Add HHO gas to traditional fuels to enhance combustion, increase the  $\text{Wi}$  and reduce CO and HC emissions. However, the drawback of hydrogen or HHO addition into biogas is the increase in  $\text{NO}_x$  emissions.

The focus of this work was to examine the combustion and emission of an engine fueled with biogas enriched with HHO. The purpose of this study is to determine the harmonized HHO content between  $\text{Wi}$  and  $\text{NO}_x$  emissions under different operating conditions. The study was carried out by numerical simulation on the DA465QE engine.

## 2 Materials and Methods

The DA45QE four-cylinder, four-stroke, multi-point injection was used to simulate biogas-HHO combustion and  $\text{NO}_x$  emissions. The engine features a 9.0 compression ratio, a 65.5 mm cylinder diameter, and a 72 mm piston stroke.

ANSYS Fluent V15.0 (CFD) software was used for the simulations. The basic equations of fluid dynamics are closed by the k-ε model NO<sub>x</sub> formation was modeled using the extended Zeldovich mechanism, which is mostly used in pollutant emission modeling because the combustion temperature of HHO-enriched biogas is usually higher than 1600 K. Calculations are carried out in a theoretically closed system, starting from the point at which the intake valve is closed at 0°CA and ending when the exhaust valve is opened at 360°CA. The initial conditions are taken from the calculation results of the gas exchange process at the end of the intake stroke [14]. The procedure for calculating the influence of fuel composition and operating conditions on engine performance and pollutant emissions has been detailed in [15]. The initial conditions are taken from the calculation results of the gas exchange process at the end of the intake process [14]. In the current research, it is assumed that the biogas mixture containing HHO is homogeneous, and the combustion process is modeled using the partial mixing model. The volume percentages of CH<sub>4</sub> and CO<sub>2</sub> in biogas are represented by the letters M<sub>x</sub> and C<sub>y</sub>, respectively, as fuel. The HHO gas is composed of 2/3 hydrogen (H<sub>2</sub>) and 1/3 oxygen (O<sub>2</sub>) by volume. The HHO content was calculated as the ratio of the HHO volume to the total volume of the mixture of HHO and biogas. Then the composition of each component in the mixture can be determined. For example, the molar compositions in the mixture of a M6C4 biogas enriched with 20% HHO are:

$$\begin{aligned} \%CH_4 &= 80\% * \%V_{CH_4} = 80\% * 60 = 48\%; \\ \%CO_2 &= 80\% * \%V_{CO_2} = 80\% * 40 = 32\% \\ \%H_2 &= 20\% * \%V_{H_2} = 80\% * 2/3 = 16.32\%; \\ \%O_2 &= 20\% * \%V_{O_2} = 80\% * 1/3 = 6.68\% \end{aligned}$$

### 3 Results and Discussion

#### 3.1 The Effect of Equivalence Coefficient

Figure 1a presents the effect of the equivalence coefficient on the contour lines of temperature and NO<sub>x</sub> concentration at TDC on the xy section. The engine runs at 4000 rpm fueled with M6C4 biogas enriched by 40% HHO with a fixed advanced ignition angle at 30°CA before TDC. We see that at the same position of crankshaft angle, when φ = 1, the burned mixture area is much larger than when φ = 0.78 or φ = 1.13. Thus, when the mixture is poor or rich, the burning rate decreases.

Figure 1b and c show the variation of CH<sub>4</sub> and H<sub>2</sub> concentrations during the combustion of biogas enriched by 20% HHO. It can be seen that the consumption rates of CH<sub>4</sub> and H<sub>2</sub> concentrations decrease with poor or rich mixtures. When using a rich mixture, the gas–water reaction CO<sub>2</sub> + H<sub>2</sub> = CO + H<sub>2</sub>O during combustion



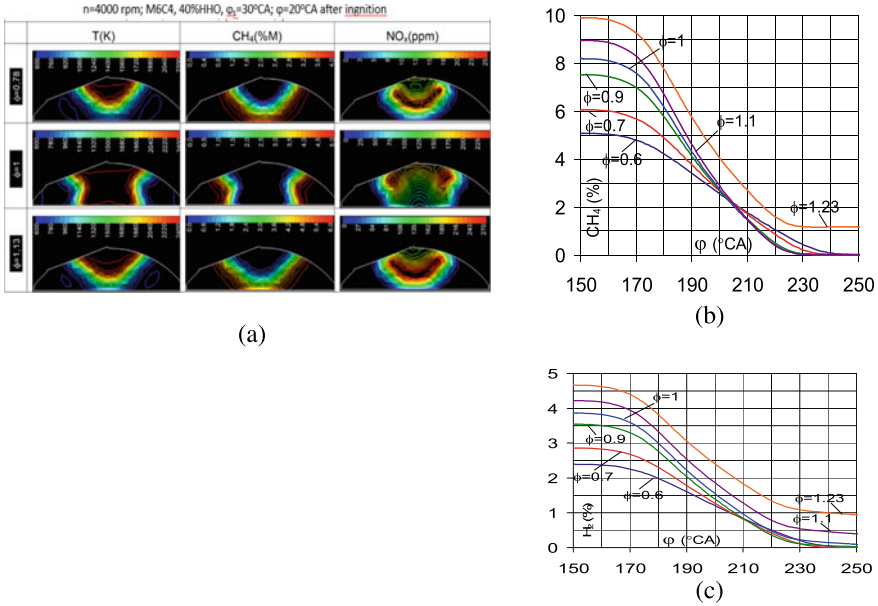


**Fig. 1** Effect of equivalence coefficient on combustion of biogas-HHO mixture: comparison of T,  $\text{CH}_4$ ,  $\text{NO}_x$  at  $20^\circ\text{CA}$  **a**; Effect  $\phi$  of  $\text{CH}_4$  **b**,  $\text{H}_2$  **c** with crankshaft angle (M6C4 Biogas, 40% HHO,  $n = 4500$  rpm,  $\varphi_s = 25^\circ\text{CA}$ )

takes place vigorously, producing hydrogen during expansion. When  $\phi < 1$ ,  $\text{CH}_4$  and  $\text{H}_2$  combustion start immediately after ignition and end almost at the same time. However, when  $\phi > 1$ , the residual  $\text{H}_2/\text{CH}_4$  ratio in the gas mixture increases with  $\phi$ . The above in-cylinder phenomenon study shows that mixed biogas - HHO gas can be burned at a very low equivalence rate and therefore produced low  $\text{NO}_x$  concentration. This is one of the advantages of adding HHO into biogas.

The increase in  $\text{NO}_x$  concentration when blending 10% HHO and 30% HHO to M7C4 biogas is 1.5 times and 2.8 times respectively compared to  $\text{NO}_x$  concentration when the engine runs on biogas only (Fig. 2). Near the burning limit ( $\phi = 0.75$ ), the difference between  $\text{NO}_x$  emissions when running on biogas and on HHO enriched biogas is not significant, while the indicative engine cycle work has a growth rate by 10% and 20%, respectively, when blending 10% HHO and 30% HHO to the biogas. Therefore, HHO blended to biogas is more beneficial when the engine is fueled with a poor mixture.

### 3.2 Effect of HHO Content

The indicative work cycle  $W_i$  of the engine is significantly improved when HHO is blended to the biogas as shown in Fig. 3a.  $W_i$  increased from 233 J/cycle to 282 J/

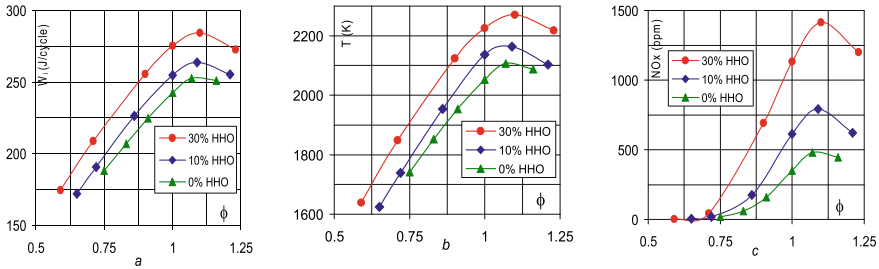


**Fig. 2** Variation of  $W_i$  **a**,  $T$  **b** and  $NO_x$  **c** when the engine runs on biogas M6C4 biogas blended HHO  $n = 4000$  rpm,  $\varphi_s = 25^\circ CA$

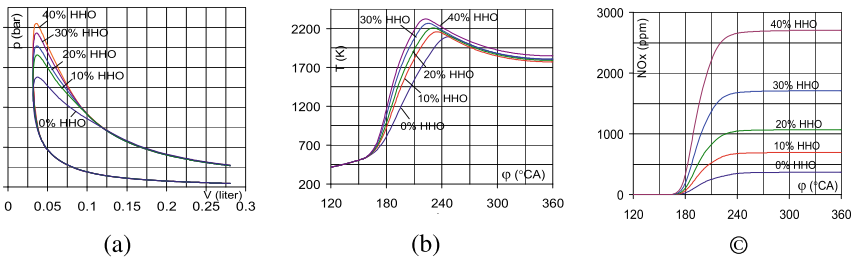


**Fig. 3** Effect of HHO component mixed into biogas M6C4 on cycle indicator work **a**, temperature **b** and  $NO_x$  concentration **c** when the engine runs at  $n = 4000$  rpm,  $\varphi_s = 25^\circ CA$ ,  $\phi = 1$

cycle when switching biogas M6C4 to biogas M6C4 enriched by 40% HHO. This is explained by the increased combustion rate and decreased amount of  $N_2$  inert gas in the mixture when HHO is mixed with biogas. As the combustion rate increases, the temperature and pressure peaks tend to closer to the TDC, thereby increasing the maximum temperature and pressure. When 30% HHO is blended with M6C4 biogas, maximum engine pressure rises from 27 to 41 bar and maximum temperature rises from 2050 to 2325 K (Fig. 2a and b).

The primary causes of the rise in  $NO_x$  concentration in exhaust gas are an increase in heat release rate and combustion temperature. The relationship between the concentration of  $NO_x$  in the combustion products and the amount of HHO in the mixture containing M6C4 biogas is shown in Fig. 3c. The results showed that  $NO_x$  concentration increased significantly when increasing the HHO composition in biogas. When the HHO component in biogas is below 20%, the  $NO_x$  concentration increases slightly. However, when the HHO component was higher than 20%, the  $NO_x$  concentration increased sharply. Specifically, the concentration of  $NO_x$  in the exhaust gas is below 1000 ppm when the HHO component in biogas is lower than 20%, but reaches about 3000 ppm when 40% HHO is added to biogas.

Figure 4a–c introduce the variation of  $W_i$ ,  $T$  and  $NO_x$  emission according to the HHO content in the mixture with biogas M6C4, M7C3 and M8C2 biogas. It can be seen that the  $W_i$ ,  $T$ , and  $NO_x$  concentration increase continuously according to

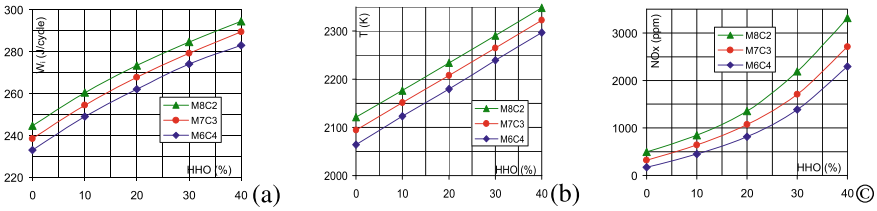


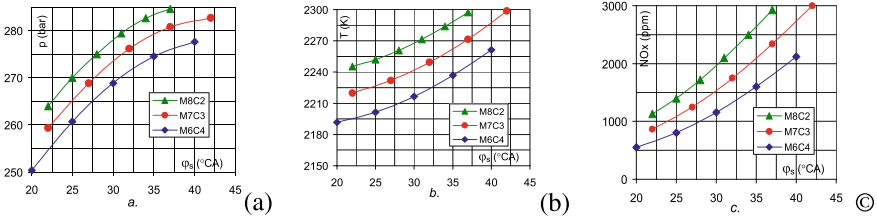
**Fig. 4** Variation of cycle indicator work **a**,  $T$  temperature **b** and  $NO_x$  concentration **c** to HHO content mixed into M6C4, M7C3 and M8C2 biogas; 4000 rpm with  $\varphi_s = 25^\circ CA$ ,  $\phi = 1$

the HHO composition. The rate of increase of  $NO_x$  concentration was higher than the rate of increase of the indicative engine cycle work and temperature. At engine speed of 4000 rpm,  $W_i$  increased on average 11 J/cycle when the  $CH_4$  concentration increased by 20%, but it increased by 29 J/cycle when the HHO content in the biogas increased by 20%. Under that condition, the average increase in  $NO_x$  concentrations was 650 ppm and 2125 ppm for the first and second case, respectively. Therefore, with the same increase in concentration, an increase in HHO concentration results in a higher increase in  $W_i$  and  $NO_x$  than an increase in  $CH_4$  concentration. The above results show that when adding HHO to biogas, the indicative work cycle increases, but at the same time,  $NO_x$  concentration also increases due to the increase in heat release rate and combustion temperature. Because increase of  $W_i$  and  $NO_x$  according to different HHO content (Fig. 4.8), we can choose the operating parameters of the engine and the content of HHO in the mixture with biogas to achieve a high increase in  $W_i$  and moderate increase in  $NO_x$ , in other words to achieve the best  $W_i/NO_x$  ratio. This necessitates research into how the operating parameters of an engine running on biogas that has been blended with HHO affect the indicated work cycle  $W_i$  and  $NO_x$  emission.

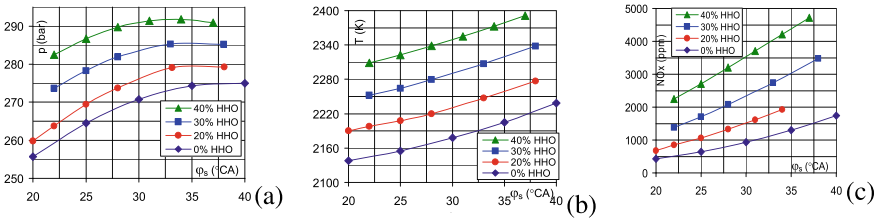
### 3.3 Effect of Advanced Ignition Angle

Figure 5a–c show the variation of  $W_i$ ,  $T$  and  $NO_x$  concentration with increasing ignition angle when the engine is running at 5000 rpm and is fueled by The M6C4, M7C3 and M8C2 biogas were enriched with 30% HHO. Regardless of the biogas composition, the  $T$  and  $NO_x$  concentration increased with the advanced ignition angle. However,  $W_i$  increases slowly after  $\varphi = 35^\circ CA$  and tends to decrease due to pump loss during compression.

With a given biogas, the effect of HHO composition on the variation of  $W_i$ ,  $T$  and  $NO_x$  according to the advanced ignition angle  $\varphi_s$  is shown in Fig. 6a–c. The results show that for a given advanced ignition angle, the increase in HHO composition leads to an increase in  $W_i$ ,  $T$  and  $NO_x$  concentration. Figure 5a shows that the optimal value of  $\varphi_s$  tends to decrease with increasing HHO concentration due to improved burning rate.



**Fig. 5** Effect of biogas composition to variation of cycle indicator work **a**, temperature **b** and  $NO_x$  concentration **c** to early ignition angle (30% HHO,  $n = 5000$  rpm,  $\phi = 1$ , full load)



**Fig. 6** Effect of HHO content mixed into biogas on variation of cycle indicator work **a**, temperature **b** and  $NO_x$  concentration **c** to early ignition angle (M7C3,  $n = 4000$  rpm,  $\phi = 1$ , full load)

The correlation between  $W_i$  and  $NO_x$  concentrations when the engine was fueled with M7C3 biogas enriched with different contents of HHO at 4000 rpm is shown in Fig. 7. The results show that, if the engine runs at 4000 rpm, M7C3 biogas enriched with HHO with different contents, the advanced ignition angle in the range  $25^{\circ}$ CA– $30^{\circ}$ CA will achieve the appropriate balance between  $W_i$  and  $NO_x$  emission.

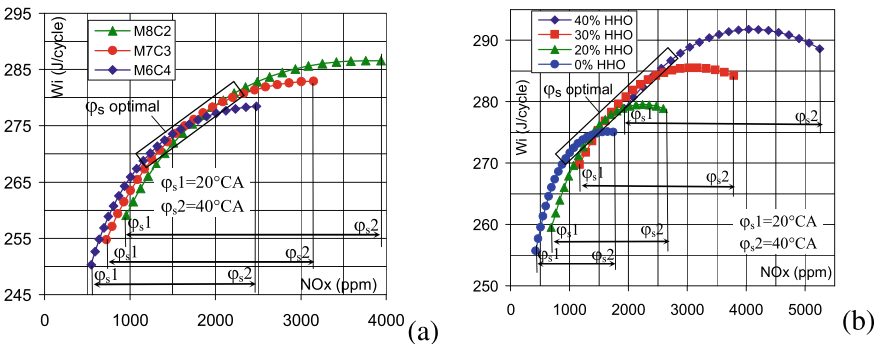


**Fig. 7** Effect of biogas composition **a** and HHO content **b** on the relationship between  $W_i$  and  $NO_x$  concentration when the early ignition angle from  $20^{\circ}$ CA to  $40^{\circ}$ CA ( $n = 4000$  rpm,  $\phi = 1$ )

## 4 Conclusion

The results of this study allow us to draw the following conclusions:

- At a given operating condition, when the engine runs on biogas rich in HHO,  $W_i$  increases with increase in HHO content,  $CH_4$  concentration, loading regime but it lowers as engine speed increase and reaches the peak value according to variation of  $\phi$  and  $\varphi_s$ .  $NO_x$  concentration increases with increasing HHO content,  $CH_4$  concentration, loading regime,  $\varphi_s$ , but it decreases with increasing engine speed and reaches the peak value when  $\phi$  varies.
- Harmonizing engine performance and  $NO_x$  emissions can be obtained by adjusting fuel composition and/or engine operating conditions.
- With a given HHO content, the  $W_i$ ,  $T$ ,  $NO_x$  curves have maximum value when  $\phi \approx 1.1$ . The rate of increase of  $NO_x$  concentration by  $\phi$  was much higher than that of  $W_i$  and  $T$ . When blending 10% and 30% of HHO to biogas M6C4,  $W_i$  increased by 4% and 12% respectively and  $NO_x$  concentration increased respectively 1.5 and 2.8 times respectively compared to when the engine runs on biogas.

**Acknowledgement** This work was supported by The University of Da Nang, University of Science and Technology, code number of Project: T2022-02-05.

## References

1. Ga BV, Tran VN, Truong LBT, Le MT, Le XT (Oct 15–19, 2013) Determination of optimal operational parameters of SI biogas engines converted from diesel engines by modelling and experimental studies. The 14th Asian congress of fluid mechanics-14ACFM, Hanoi and Halong, Vietnam, pp 819–824
2. Ga BV, Tran VN (2015) Appropriate structural parameters of biogas SI engine converted from diesel engine. *IET Renew Power Gener* 9(3):255–261. <https://doi.org/10.1049/iet-rpg.2013.0329>
3. Chen SC, Kao YL, Yeh GT et al (2017) An onboard hydrogen generator for hydrogen enhanced combustion with internal combustion engine. *Int J Hydrogen Energy* 42(33):21334–21342. <https://doi.org/10.1016/j.ijhydene.2017.03.013>
4. Ilbas M, Crayford AP, Yilmaz I, Bowen PJ, Syred N (2006) Laminar-burning velocities of hydrogen-air and hydrogen-methane-air mixture: an experimental study. *Int J Hydrogen Energy* 31(12):1768–1779. <https://doi.org/10.1016/j.ijhydene.2005.12.007>
5. Chung K, Chun KMC (2013) Combustion characteristics and generating efficiency using biogas with added hydrogen. SA E Technical Paper 2013-01-2506. <https://doi.org/10.4271/2013-01-2506>
6. Boretti A (2010) Comparison of fuel economies of high efficiency diesel and hydrogen engines powering a compact car with a flywheel based kinetic energy recovery systems. *Int J Hydrogen Energy* 35(16):8417–8424. <https://doi.org/10.1016/j.ijhydene.2010.05.031>
7. Van Ga B, Van Nam T, Xuan NTT (23–25 March 2010) Utilization of biogas engines in rural area: a contribution to climate change mitigation. Colloque international RUNSUD 2010. Universite Nice-Sophia Antipolis, France, pp 19–31

8. Subramanian B, Ismail S (2018) Production and use of HHO gas in IC engines. *Int J Hydrogen Energy* 43(14):7140–7154. <https://doi.org/10.1016/j.ijhydene.2018.02.120>
9. Musmar SA, Al-Rousan AA (Oct 2011) Effect of HHO gas on combustion emissions in gasoline engines. *Fuel* 90(10):3066–3070. <https://doi.org/10.1016/j.fuel.2011.05.013>
10. Al-Rousan AA (2010) Reduction of fuel consumption in gasoline engines by introducing HHO gas into intake manifold. *Int J Hydrogen Energy* 35(23):12930–12935. <https://doi.org/10.1016/j.ijhydene.2010.08.144>
11. Al-Rousan AA, Musmar SA (2018) Effect of anodes-cathodes inter-distances of HHO fuel cell on gasoline engine performance operating by a blend of HHO. *Int J Hydrogen Energy* 43(41):19213–19221
12. Ma F, Wang Y (2008) Study on the extension of lean operation limit through hydrogen enrichment in a natural gas spark-ignition engine. *Int J Hydrogen Energy* 33(4):1416–1424. <https://doi.org/10.1016/j.ijhydene.2007.12.040>
13. Ga BV, Tram TLB, Tu BTM (2019) Combustion improvement of engine fueled with poor biogas by blending hydroxyl (HHO). *J Sci Technol—The Univ Danang* 1(234). Paper No JST-UD2018-330 36
14. Ga BV, Tu BTM, Vu VA (2019) Air/fuel ratio control of an SI-engine fueled with poor biogas-HHO. *J Sci Technol—The Univ Danang* 2(235). Paper No JST-UD2019-020
15. Verma S, Das LM, Kaushik SC (2017) Effects of varying composition of biogas on performance and emission characteristics of compression ignition engine using exergy analysis. *Energy Convers Manag* 138:346–359. <https://doi.org/10.1016/j.enconman.2017.01.066>

# Electromagnetic Induction Generator by Harvesting Vibration Energy



Hoa Thi Truong and Dung Hoang

**Abstract** Our work aims to develop a vibration generator that generates electrical energy from surrounding mechanical vibrations. This generator represents an alternative to powering wireless sensors without using primary batteries. The generator is an electromagnetic induction generator. When the generator is excited by ambient vibration, the resonant mechanism induces the relative motion of the magnetic circuit relative to the copper coil. This relative motion generates voltage across the coil due to Faraday's laws. This energy harvesting technology has advantages over conventional types concerning size and efficiency, and it is incredibly robust and has low electrical impedance. The generator model can be excited by sine, random, or actual vibration data, and can be easily scaled up to increase the output power in order to generate an expected output power.

**Keywords** Energy harvester · Ambient vibration · Electromagnetic induction

## 1 Introduction

Recently, research and application of smart vibration systems attracts many researchers such as vibration isolator, vibration absorber, and vibration energy harvesting [1–5]. The vibration energy harvesting is the conversion of kinetic energy of vibrations into electricity. The vibrations caused by wind, water, ocean waves, even mechanical vibration from vehicles or civil infrastructures are great sources of energy that need to be harvested. Electromagnetic induction generator is a particularly promising means of energy harvesting, as it is cheap, requiring only coils

---

H. T. Truong (✉) · D. Hoang

The University of Danang, University of Technology and Education, 48 Cao Thang, Danang, Vietnam

e-mail: [tthoa@ute.udn.vn](mailto:tthoa@ute.udn.vn)

and magnets. The energy harvesting system accompanied with an electromagnetic induction generator is designed to convert vibration energy into electrical energy.

The system could be a solution for replacing batteries in wireless low power modules embedded in infrastructures, i.e. skyscrapers, bridges, and railways. Therefore, these structures can be periodic inspected without regular conventional maintenance such as battery replacement. The generator is also suitable for powering battery-free low power modules because of its simply, robustness, and high efficiency [6–8].

The parameters of the generator can be designed according to the frequency and amplitude of the vibration with the aim to maximize the efficiency of energy harvesting.

## 2 Configuration and Principle

### 2.1 Configuration

The generator configuration is shown in Fig. 1. The generator is a rectangular-shaped cantilever consisting of a ferromagnetic core, coil, magnets, and weight. It has dimensions of 225 mm × 30 mm × 37 mm. The core is made from a multi-layer of 30 mm × 5 mm × 180 mm ferromagnetic laminate beams and incorporated a solid part of iron. The magnet is attached to the bottom of the iron core to provide the appropriate magnetic flux for the operation of the system. The coil is wound around the multi-layer of ferromagnetic laminate beams. The weight is also made of iron and is a part of the core placed at the tip of the cantilever. The resonant frequency can be adjusted by changing the mass, the number of layers of ferromagnetic laminate beams, or by the position of the coil along the core. There is an air gap between the iron weight and another part of the iron core. The magnetic circuit is the whole iron-based parts and the air gap. The output power can be maximized when the natural frequency of the generator coincides with the frequency of the vibration object.

### 2.2 Principle

The Fig. 2 depicts the principle of the power generator. The operation is based on the principle of electromagnetic induction. Generators convert vibrations into electrical energy based on the laws of electromagnetic induction when the magnetic flux sent through a closed loop circuit change, it will induce an electromotive force at both ends of the coil. This is a 1-DOF vibration system. The displacement of the weight is calculated [9]. Thus, the gap is determined and the magnetic field strength change in the iron core is also determined.



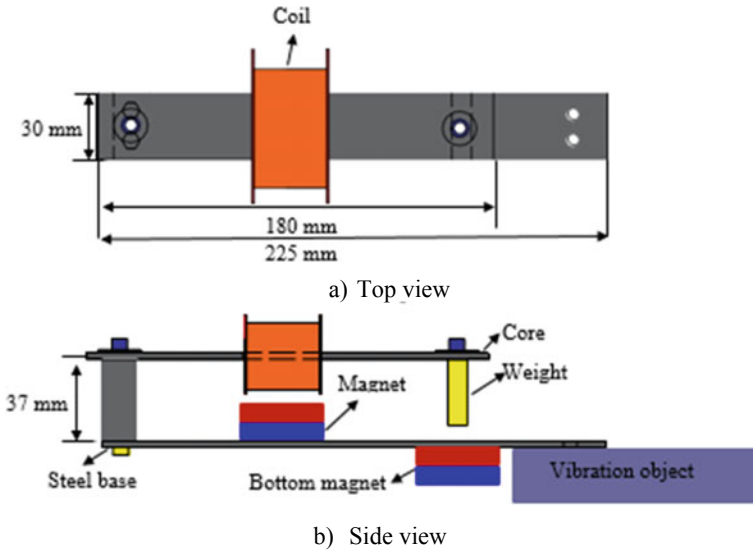


Fig. 1 Configuration of electromagnetic induction generator by harvesting vibration energy

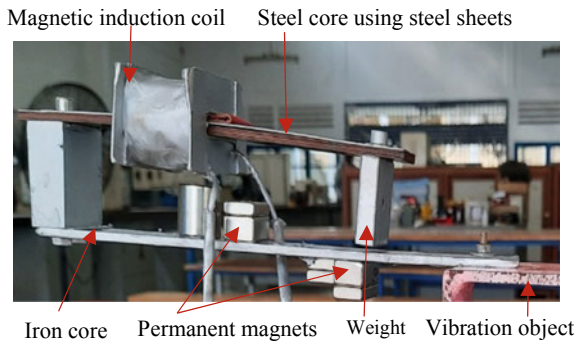
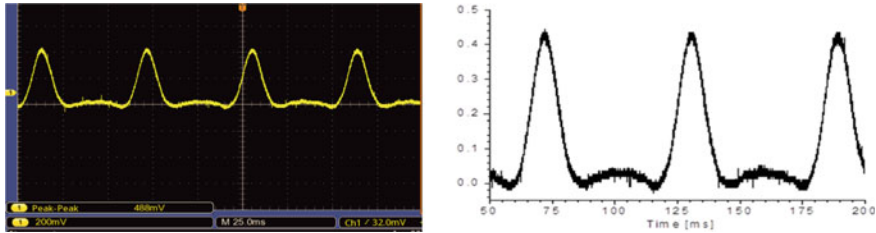


Fig. 2 Photo of experiment system

When the system is excited, the vibration changes the wide of air gap. When there is a downward inertia force due to the acceleration of vibrating acting on the weight, the air gap is pulled to be narrower, consequently, magnetic flux in the magnetic



**Fig. 3** Output voltage of the generator under vibration

circuit increases. Then, the tensile stress occurring inside the ferromagnetic laminate sheet causes an elastic force, which, together with the upward inertia force of the vibration, will pull the weight moved upward, the air gap is then widen and the flux decreases. Because the magnetic conductivity of the air is much lower than that of the steel core, when the distance of the air gap changes, the magnetic flux through the steel core and coil will change. This flux changes induce an electromotive force on the coil due to the laws of induction. The generator converts this energy efficiently because the small inertia force is magnified into a large axial force due to the length of the cantilever. In addition, a generator made of iron material is very strong and can withstand high frequency vibration, high acceleration and high kinetic energy.

### 2.3 *Experimental Results*

Figure 3 shows output voltage of the generator under vibration of a DC motor when the generator was open-circuit. As show in Fig. 3, the output voltage is quasi-triangle shape with a peak of around 450 mV. The voltage pulses were generated with frequency of about 14.6 Hz that is corresponding to the speed of the DC motor. From this result, it is confirmed that the system has successes in converting the vibration into electrical energy. The system can provide sufficient energy for powering functionality of the battery free wireless sensor based on vibrations.

When the vibration frequency changed a little, the resonant happed, and the voltage pulses were generated with a peak of around 936 mV and frequency of about 15.4 Hz as shown in Fig. 4. The voltage peak in this case is nearly double the peak value of the output voltage in the case of without resonant phenomena.

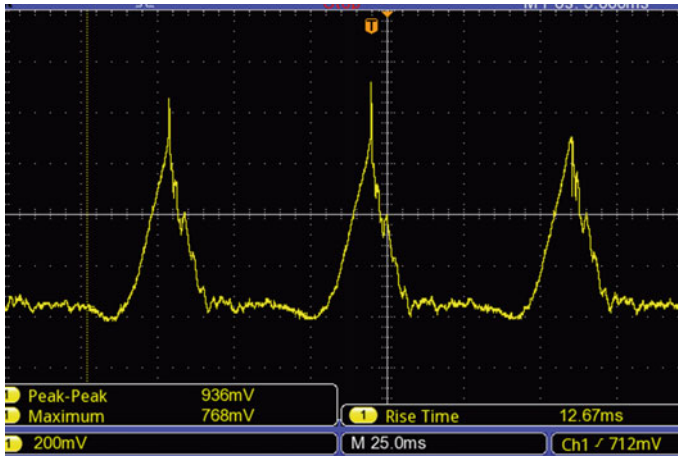


Fig. 4 Output voltage of the generator under vibration when resonant phenomena occur

### 3 Conclusion

In this study, a vibration generator that generates electrical energy from surrounding mechanical vibrations has been developed. The generator is an electromagnetic induction generator. When the system is excited, the vibration changes the wide of air gap, and then change magnetic flux through the steel core and the coil. This flux changes induce an electromotive force on the coil due to the laws of induction. This energy harvesting technology has advantages over conventional types concerning size and efficiency, and it is incredibly robust and has low electrical impedance, can be easily scaled up to increase the output power in order to generate an expected output power. It is confirmed that the system has successes in converting the vibration into electrical energy. The system can provide sufficient energy for powering functionality of the battery free wireless sensor based on vibrations.

### References

1. Nguyen XB, Komatsuzaki T, Truong HT (2020) Novel semiactive suspension using a magnetorheological elastomer (MRE)-based absorber and adaptive neural network controller for systems with input constraints. *Mech Sci* 11:465–479. <https://doi.org/10.5194/ms-11-465-2020>
2. Truong HT, Nguyen XB, Bui CM (2022) Singularity-free adaptive controller for uncertain hysteresis suspension using magnetorheological elastomer-based absorber. *Shock Vibration* 2022:17, Article ID 2007022. <https://doi.org/10.1155/2022/2007022>
3. Zhiwei Z, Xiang H, Shi Z, Zhan J (2018) Experimental investigation on piezoelectric energy harvesting from vehicle-bridge coupling vibration. *Energy Convers Manag* 163:169–179
4. Galchev TV, McCullagh J, Peterson RL, Najaf K (2011) Harvesting traffic-induced vibrations for structural health monitoring of bridges. *JMM* 21. <https://doi.org/10.1088/0960-1317/21/10/104005>

5. Nguyen XB, Komatsuzaki T, Zhang N (2020) A nonlinear magnetorheological elastomer model based on fractional viscoelasticity, magnetic dipole interactions, and adaptive smooth Coulomb friction. *Mech Syst Signal Process* 141
6. Raffinal RS, Aoyama T, Fukagawa N (2018) Development of titanium wire sensor for corrosion monitoring in the concrete structures. P.S Mitsubishi Tech Rep 18:28–29
7. Ueno T (2019) Magnetostrictive vibrational power generator for battery-free IoT application. *AIP Adv* 9(3):035018. <https://doi.org/10.1063/1.5079882>
8. Clark AE, Wun-Fogle M, Restorff JB (2000) Magnetostrictive properties of body-centered cubic Fe-Ga and Fe-Ga-Al Alloy. *IEEE Trans Mag* 37:3238–3240
9. Nguyen XB, Komatsuzaki T, Iwata Y, Asanuma H (2017) Fuzzy semiactive vibration control of structures using magnetorheological elastomer. *Shock Vibration Hindawi* 2017:15

# Reaction Kinetics of the Extraction of Magnesium from Dolomite via the Silicothermic Reduction Process



Vu Viet Quyen, Vu Thi Thu Trang, and Nguyen Duong Nam

**Abstract** The silicothermic reduction process under vacuum is currently the main method for the production of metallic magnesium from calcined dolomite ore. In this paper, the experimental data from ThanhHoa dolomite ore reduction investigations are used to analyze the kinetics of the reduction process of calcined dolomite. Several kinetic models have been investigated to evaluate the rate control step of the reduction reaction. The results show that solid-state diffusion is the controlling stage of the reduction reaction. The activation energy of the reduction reaction under vacuum is 203.2 kJ/mol. Experimental factors affecting the reaction rate are studied, including temperature, ferrosilicon ratio, briquetting pressure. From the analysis results, it can be determined that silicon diffusion is the main factor controlling the diffusion phase.

**Keywords** Magnesium · Silicothermic reduction · Reaction kinetics · Diffusion

## 1 Introduction

Magnesium metal and its alloys have the advantages of particular strength, superior thermal and electrical conductivity, damping and shock absorption, external electromagnetic shielding, ease of processing and recycling. They are widely used after steel and aluminum [1, 2]. The United States Geological Survey (USGS) conveyed that the global production of metallic magnesium in 2020 has reached 1 million tons of which 90% will be produced in China. Currently, silicothermic process is the chief method for Mg production in in China's magnesium plants [3, 4]. This approach uses calcined dolomite and powdered ferrosilicon as reducing agents while  $\text{CaF}_2$

---

V. V. Quyen · V. T. T. Trang · N. D. Nam (✉)  
Vietnam Maritime University, Haiphong, Vietnam  
e-mail: [namnd.khcs@vamaru.edu.vn](mailto:namnd.khcs@vamaru.edu.vn)

V. V. Quyen  
e-mail: [quyenvv.cndt@vamaru.edu.vn](mailto:quyenvv.cndt@vamaru.edu.vn)

contributes as a catalyst, which is combined and briquetted before being placed in a vacuum tube [5]. The mechanism and kinetics of this whole process are complex [6, 7]. In this reaction mechanism, three kind of solid elements (CaO, MgO, Si) react to each other in order to give a gas and another solid with the formation of intermediate compounds. The kinetics of the process include the reduction stage's kinetics and mass transfer from the magnesium vapor step. The solid-state diffusion takes main responsibility in controlling the kinetics of the silicothermal process under the condition of vacuum as well as in Ar atmosphere [8, 9].

The aim of this paper is to research kinetic analysis of silicon thermal reduction of calcined dolomite under vacuum in order to find experimental or semi-empirical equations to make comparison with the results from experiment and prove diffusing which element controls the diffusion process to get a better view of the reaction kinetics of the silicon dolomite thermal process.

## 2 Experimental

### 2.1 Raw Materials

Dolomite used in the study was collected at Long mountain mine, Vietnam with the primary element being  $\text{CaMg}(\text{CO}_3)_2$ . Dolomite is mashed in a jaw crusher to 2–3 cm before being calcined at 1100 °C for 1 h to decompose  $\text{CO}_2$  and get dolomite after calcination with the main components being MgO and CaO. Dolomite after calcination and ferrosilicon are pulverized to 74  $\mu\text{m}$  by ball mill NQM-4 of Yangzhou Nuoya Machinery. The chemical elements of dolomite are shown in Table 1.

Ferrosilicon alloy is used as the reducing agent with the chemical composition includes in weight percentage: 72.2 Si, 0.1 C, 0.03 P, 0.02 S, 1.2 Al, 26.1 Fe. Calcium fluoride 98.5% is used as the catalyst. The mixture is mixed with the rate of 83% calcined dolomite, 17% ferro-silicon alloy, added 3%  $\text{CaF}_2$  and briquetted at 60 MPa using a plunger press.

**Table 1** Chemical elements of dolomite and calcined dolomite

Elements	Dolomite, wt. %	Calcined dolomite, wt. %
MgO	20.30	38.90
CaO	30.10	58.70
$\text{Al}_2\text{O}_3$	0.18	0.45
$\text{SiO}_2$	0.56	0.83
$\text{Fe}_2\text{O}_3$	0.63	0.96
L.O.I*	46.60	–

\*Loss of ignition

## 2.2 Method

The main equipment of kinetic experiments includes a vacuum retort made from 310S stainless steel tube. The experimental process are divided into three fundamental steps. In the first step, the crucible boat is placed into the retort heating zone at ambient temperature. Then, pure argon is continuously charged into the retort to clear residual air. In the second step, the heating part of the retort and the crucible boat are heated from the ambient temperature to the reduction temperature. In the third step, when the temperature in the retort reaches the reduction temperature, the crucible boat is relocated from the heating zone to the tip of the retort. The briquetted pellets are placed in the firing boat and immediately returned to the heating zone. During this process, argon gas is continuously passed through the whole retort to create an inert atmosphere that protects the briquettes from oxidation. As a final step, the retort is closed and the vacuum pump is operated to vacuum up to 100 Pa within 20 s to initiate the experiments.

Eventually, Ar gas is applied into the retort to equalize the pressure, the crucible boat is taken out and cooled to ambient temperature. Residue slag was collected and weighed to calculate the reduction ratio according to the formula:

$$X = \frac{x_1 - x_2}{x_1 \cdot a}$$

where  $X$  is the reduction rate,  $x_1$  the initial mass of the briquettes,  $x_2$  is the post-reaction mass of the briquettes, and  $a$  is the theoretical ratio of Mg in the unreacted briquettes.

## 3 Results and Discussion

### 3.1 Kinetic Analysis Results

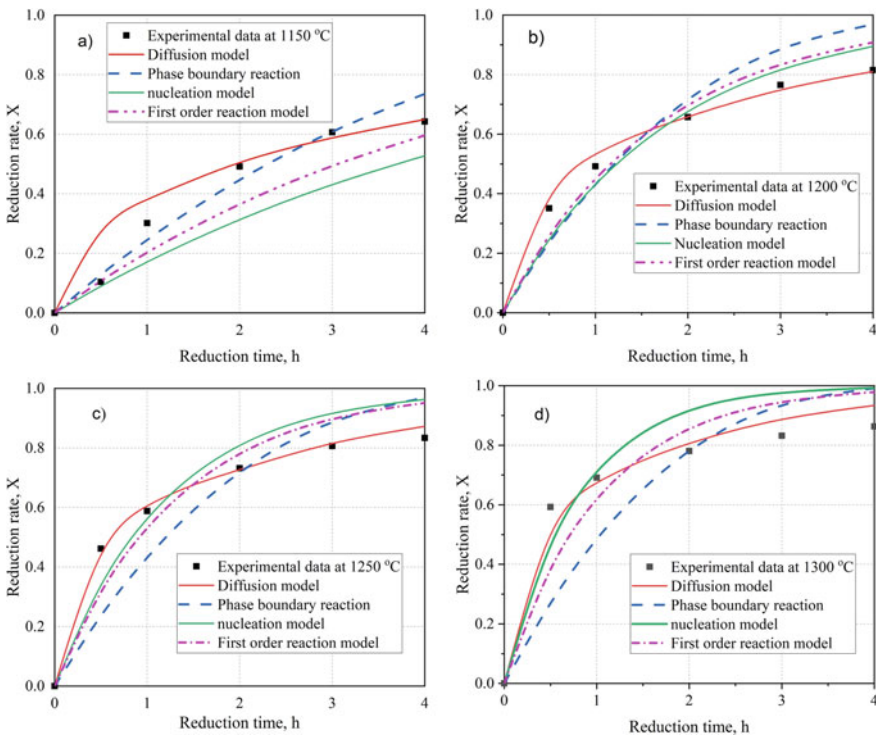
Some experimental kinetic models based on the probability of reaction rate control factors are listed in Table 2. These models are used to compare kinetic experimental data for powder reactions. The rate constants  $k$  are determined experimentally and depend on the particle size, thermochemical properties and temperature through the Arrhenius equation.

Research results from different kinetic models compared with experimental data are presented in Fig. 1. It can be observed from experimental data that the proportion of silicothermic reduction reaction decreases with time, especially from 1 to 4 h at all four temperature zones studied. This result is consistent with the diffusion model while the phase boundary reaction and the first order chemical reaction shows that the reaction rate does not change with time. Especially at the temperature of 1250 °C, the nucleation model and the first order reaction chemical kinetics give much larger

**Table 2** Kinetic models of the powder reaction

Symbol	Reaction model	Kinetic equation
F1	First order reaction	$\ln(1-X) = -kt$
P1	Phase boundary reaction (spherical)	$1-(1-X)^{1/3} = kt$
D1	Diffusion ( <i>Jander</i> )	$[1-(1-X)^{1/3}]^2 = kt$
N1	Nucleation (Avrami)	$[-\ln(1-X)]^{1/2} = kt$

results than the experimental data at 4 h. The correlation coefficient ( $R^2$ ) is used and shown in Table 3 to evaluate the degree of data description between the model and the experiment. The results show that the diffusion model is suitable to describe the rate of the reduction reaction, so the reduction process belongs to the form of diffusion kinetics. According to this mechanism, when two solids are placed next to each other and heated, the atoms of each solid will shift positions leading to the formation of a product layer. This product layer grows over time due to continuous diffusion. The silicon ions must then diffuse through this increasingly large layer of products to continue to react with the dolomite. Therefore, the rate of the reduction reaction will decrease with time.

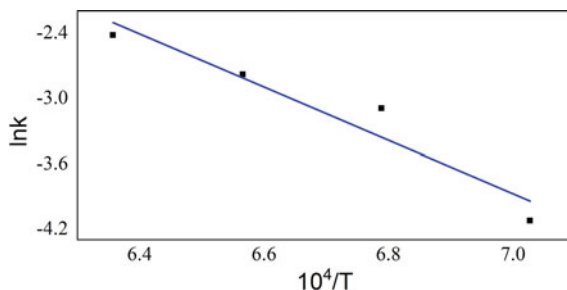


**Fig. 1** Comparison of the calculated results of the models with experimental data



**Table 3** Values of correlation coefficient ( $R^2$ ) of kinetic models

Temperature, °C	Kinetic models			
	F1	P1	D1	N1
1150	0.968	0.966	0.934	0.961
1200	0.975	0.957	0.996	0.972
1250	0.945	0.885	0.996	0.955
1300	0.900	0.801	0.975	0.941

**Fig. 2** Arrhenius plot of relationship between  $\ln k$  and  $1/T$ 

The Jander's diffusion model was used to determine the reduction reaction percentage and the activation energy of the reaction by using the relationship graph of  $\ln k$  and  $1/T$  based on the Arrhenius equation shown in Fig. 2. The resultants indicate that the activation energy of the silicothermic reduction reaction under vacuum is 203.2 kJ/mol. The results show that the activation energy is significantly lower than the activation energy of the reduction reaction in the atmosphere with an Ar gas stream of 306 kJ/mol [8]. It is also slightly lower with the result in a vacuum environment which is between 226 and 232 kJ/mol [9]. This could be due to various sizes of the pellets. The diameter of the briquettes employed in this paper was 15 mm, smaller than the 25 mm diameter used in the study by Toguri et al. or 47 mm by Yusi Che. In addition, the compression force in this study is also higher and the kinetic equations used are different.

### 3.2 Effect of Temperature and Ferrosilicon Ratio on the Reduction Rate

In term of the kinetic analysis, it can be clearly seen that the silicothermic reduction reaction rate is directed by the diffusion stage. The reduction reaction involving three solids consisting of five elements and the diffusion of which element controls the rate of the reaction should be investigated. Therefore, the effects of temperature, ferrosilicon ratio and time on reduction rate were analyzed. The reduction proportion

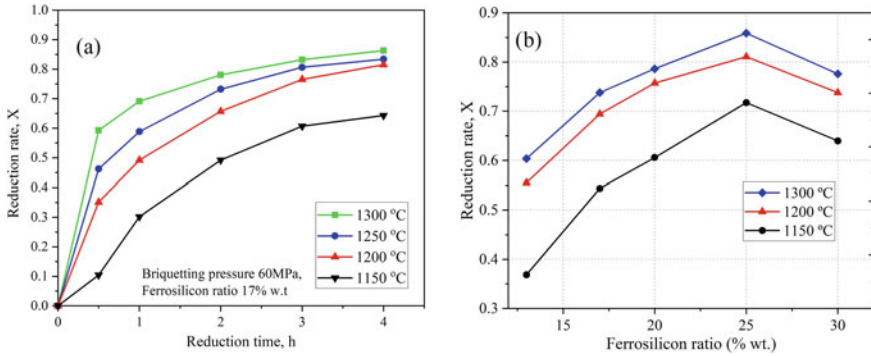


**Fig. 4** Impact of **a** temperature and **b** ferrosilicon ratio on the reduction rate

has improved rapidly in the first 0.5 h at all temperatures with 17% ferrosilicon shown that in Fig. 4a.

The reduction proportion has improved rapidly in the first 0.5 h at all temperatures. After that, the reduction rate gradually has decreased at subsequent time. At the temperature of 1300 °C, the reduction rate has come to 59.3% after only 0.5 h and 83.2% after 3 h. At the end of the experiment, the final reduction rate has reached 86.3% after 4 h. The degree of increase of reduction rate has decreased with increasing reduction temperature. At different temperatures from 1150 to 1300 °C, the reduction proportion rose by 49.2%, 16.2%, 7.5%, 4.9% at 2 h, respectively. The reason is that the silicon reducing agent concentration in the briquettes has decreased and a layer of  $\text{Ca}_2\text{SiO}_4$  product forms around the silicon particles shown in Fig. 5. In order to the reduction reaction to continue, Si must diffuse through the  $\text{Ca}_2\text{SiO}_4$  product layer leading to a decrease in the reduction rate. In addition, two phases Si and  $\text{FeSi}_2$  have existed in ferrosilicon. The  $\text{FeSi}_2$  phase requires a temperature higher than 1150 °C to participate in the reduction reaction from a thermodynamic point of view [10]. The transparent Si atom in the  $\text{FeSi}_2$  phase has a lower activity than the Si phase, so the diffusivity is significantly reduced. Therefore, at higher temperatures, the degree of increase of reduction rate decreases.

Figure 4b shows the results of the reduction experiment from 1150 °C to 1300 °C with the ratio of ferrosilicon varying in the range of 13–30% for 3 h. As the percentage of ferrosilicon increased from 13 to 25%, the reduction rate increased at all temperatures. The results show that with the increase of the ferrosilicon content in this range is in proportion to the reduction rate. The explanation for this phenomenon is that because higher concentration of Si will lead to an increase in the number of Si atoms per unit volume in the briquettes, more Si effects in a given time period. Therefore, the reduction rate of magnesium increases per unit time. However, when increasing the ferrosilicon content from 25 to 30%, the reduction rate decreased quite quickly. Phase analysis of the reduced slag by XRD technique is shown in Fig. 6. The results show that the residue slag of the samples containing 30% ferrosilicon appears  $\text{CaMgSi}_2\text{O}_6$  complex oxide phases with high intensity diffraction peaks. In this case,

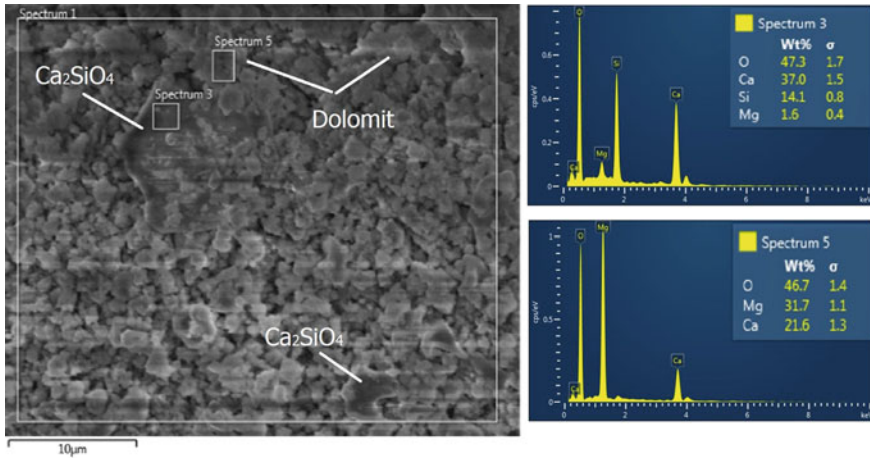
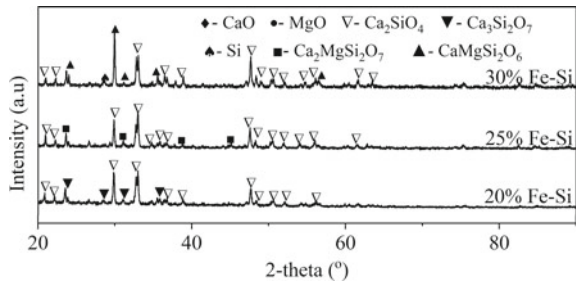


Fig. 5 SEM and EDS of the reduced slag residue after 1 h at 1300 °C

Fig. 6 XRD of the residue slag of the samples containing 20–30% ferrosilicon



MgO participated in the solid dissolution process in  $\text{Ca}_2\text{SiO}_4$  slag to form complex oxide. This leads to a reduction in the reduction rate. The above analysis shows that the main reaction controlling step is the diffusion of Si.

## 4 Conclusion

The kinetics of silicothemic reduction process was examined by isothermal kinetics approach. The analysis results indicate that the production of Mg by ferrosilicon in a vacuum condition can be explained by the Jander diffusion model. The reaction rate decreases over time. It is managed by the Si diffusion stage via the  $\text{Ca}_2\text{SiO}_4$  product layer. The activation energy produced in the reduction reaction is 203.2 kJ/mol.

## References

1. Chen L, Guo Z, Zhang C, Li Y, Wu C, Liu G (2021) Effects of welding current on the microstructure and mechanical behavior of resistance-welded WC-Co/B318 steel joints. *Ceram Int* 47:17400–17410. <https://doi.org/10.1016/j.ceramint.2021.03.056>
2. Liu M, Guo Y, Wang J, Yergin M (2018) Corrosion avoidance in lightweight materials for automotive applications, *Npj Mater Degrad* 2. <https://doi.org/10.1038/s41529-018-0045-2>
3. Liu F, Yang B, Liu BY, Li J, Chang ZM, Shan ZW (2020) Producing pure magnesium through silicothermic under the atmospheric pressure. *Miner Met Mater Ser.* [https://doi.org/10.1007/978-3-030-36647-6\\_46](https://doi.org/10.1007/978-3-030-36647-6_46)
4. Zang JC, Ding W (2016) The pidgeon process in china and its future. In: *Essent readings magnesium technology*. Springer International Publishing, Cham, 113–116. [https://doi.org/10.1007/978-3-319-48099-2\\_18](https://doi.org/10.1007/978-3-319-48099-2_18)
5. Aghion E, Golub G (n.d.) Production technologies of magnesium. In: *Magnesium technology*. Springer, Berlin/Heidelberg, 29–62. [https://doi.org/10.1007/3-540-30812-1\\_2](https://doi.org/10.1007/3-540-30812-1_2)
6. You J, Wang Y (2019) Reduction mechanism of Pidgeon process of magnesium metal, *Guocheng Gongcheng Xuebao/The Chinese J Process Eng* 19:560–566. <https://doi.org/10.12034/j.issn.1009-606X.218236>
7. Chen M, Zhao BJ, Chen YH, Han FL, Wu LE (2017) Reaction mechanisms in the silicothermic production of magnesium. In: T.P, Wang S, Free M, Alam S, Zhang M (eds) *Mater Process Energy Environ Technol Miner Met Mater Ser.* Springer, Cham, 239–249. [https://doi.org/10.1007/978-3-319-51091-0\\_22](https://doi.org/10.1007/978-3-319-51091-0_22)
8. Morsi IM, El Barawy KA, Morsi MB, Abdel-Gawad SR (2002) Silicothermic reduction of dolomite ore under inert atmosphere. *Can Metall Q* 41:15–28. <https://doi.org/10.1179/cmq.2002.41.1.15>
9. Si Che Y, Peng Mai G, Long Li S, Lin He J, Xun Song J, Hong Yi J (2020) Kinetic mechanism of magnesium production by silicothermic reduction of CaO-MgO in vacuum. *Trans Nonferrous Met Soc China (English ed)* 30:2812–2822. [https://doi.org/10.1016/S1003-6326\(20\)65423-1](https://doi.org/10.1016/S1003-6326(20)65423-1)
10. Vu QV, Vu TTT, Doan CM, Duong BN, Tran HD (2021) Silicothermic reduction of thanh hoa dolomite: thermodynamic and experimental. *Acta Metall Slovaca* 27. <https://doi.org/10.36547/AMS.27.3.948>

# Optimizing the Structure of the Axle Housing Multi-purpose Forest Fire Fighting Vehicle by Finite Element Method



Luong Van Van, Nguyen Thanh Tung, Nguyen Thai Van,  
and Mai Phuoc Trai

**Abstract** The drive axle consists of the last elements in the transmission of power from the engine to the driving wheels. The drive axle has three main components: the main transmission, the differential, and the half-shaft mounted in one housing. In there, the axle housing is the part containing all the power transmission components, at the same time it acts as a beam to support the weight of the vehicle body and is subjected to loads from the wheel-road interaction. During operation, the axle housing direct load from self-weight and indirect load from moments of torsion and bending moments. Due to the above loads, the axle housing will be deformed, cracked, and even broken. This paper presents the research results on the evaluation of the fatigue strength of the drive axle housing on the multi-purpose forest fire fighting vehicle, according to the research results, the author has determined the working life of the axle housing when the vehicle moving on the road according to ISO 8608:1995, at the same time, the axle housing structure is proposed to ensure durability.

**Keywords** Rear axle housing · Multi-purpose forest fire fighting vehicle · Fatigue analysis · Finite element analysis

---

L. Van Van (✉) · N. T. Tung · N. T. Van · M. P. Trai  
Vinh Long University of Technology Education, 73, Nguyen Hue Street, Vinh Long City, Vietnam  
e-mail: [vanlv@vlute.edu.vn](mailto:vanlv@vlute.edu.vn)

N. T. Tung  
e-mail: [tungnt@vlute.edu.vn](mailto:tungnt@vlute.edu.vn)

N. T. Van  
e-mail: [vannt@vlute.edu.vn](mailto:vannt@vlute.edu.vn)

M. P. Trai  
e-mail: [traimp@vlute.edu.vn](mailto:traimp@vlute.edu.vn)

## 1 Introduction

Multi-purpose forest fire fighting vehicle built based on Ural 4320, after manufacturing, the volume of the vehicle increases due to the installation of additional fire fighting equipment, thus affecting the structure and durability of the vehicle's components, including the drive axle housing [1–5]. The axle housing has the function of supporting the rear weight of the vehicle and bearing loads from wheel interaction with the road. Therefore, the structure of the axle housing must ensure durability and especially rigidity so as not to affect the working conditions of the internal components. If the axle housing is deformed excessively, the mounting position of the bearings is misaligned, and the axle shaft is bent, increasing the noise level of the drive axle housing and reducing the life of related components. During the working process, the axle housing is subjected to the forces and moments from the drive wheels along with the forces acting on the suspension system. Force components in the direction of impact, including longitudinal force (traction and braking force), lateral force, and vertical force. These forces form the loads acting on the axle housing in the form of forces or moments. During the movement of the vehicle, the axle housing is also under the influence of the forces from the suspended mass transmitted through the positions of the springs and shock absorbers. Therefore, studying the durability and optimizing the axle housing structure to optimize the multi-purpose forest fire fighting vehicle structure is the purpose of this study. In the world, the relevant research on axle housing durability is as follows: According to [6, 7], the method of static strength of the axle housing is only suitable for vehicles moving at low speed and low mass. When the vehicle moves at high speed, the dynamic load has a significant effect on the durability of the axle housing. The research results [8–10] evaluated the fatigue strength of the drive axle housings of trucks subjected to dynamic loads due to random excitation from the road surface bump by using a dynamic model of the vehicle.

## 2 Fatigue Life Prediction

The assessment of the fatigue strength of the part is carried out based on the S–N fatigue curve. If the part is under stress lower than  $S_e'$ , fatigue failure will not occur even if  $N \rightarrow \infty$ . The stress value  $S_e'$  is called the standard fatigue limit of the material. The number of load cycles acting on the part corresponding to the  $S_e'$  value according to the results in Fig. 1 (A517) steel is in the range  $10^6$ – $10^7$  [11].

Fatigue strength can also be calculated according to the ultimate tensile strength of the material  $S_u$  [11].  $S_e' = 0.5S_u$ , with  $S_u \leq 1400$  MPa;  $S_e' = 700$ , with  $S_u > 1400$  Mpa, for cast iron material:  $S_e' = 0.4S_u$  [11]. The experimental results [11–13] show that, for cast iron and steel, the number of load cycles corresponding to the  $S_e'$  value on the S–N graph is usually in the range of  $10^6$ – $10^8$ .

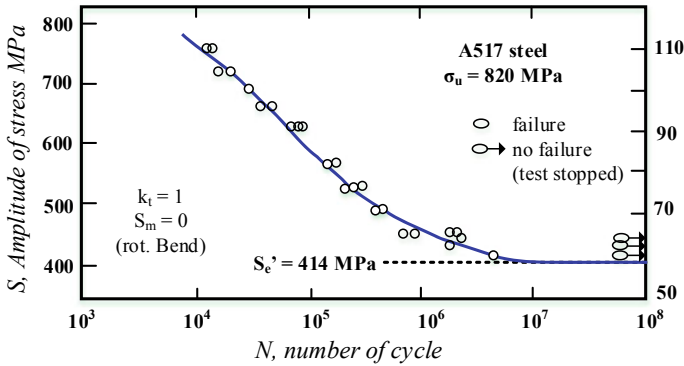


**Fig. 1** Experimental fatigue curve determined from steel sample A157

The part is normally subjected to stress which is not the same as the fatigue curve construction test conditions, therefore determining the actual fatigue limit value  $S_e$  is very complicated. Therefore, the actual fatigue limit is calculated through the correction factors:

$$S_e = k_a \cdot k_b \cdot k_c \cdot k_d \cdot k_e \cdot S_e' \tag{1}$$

In the above formula:  $k_a$  is the coefficient taking into account the effect of surface roughness:  $k_a = a S_u^b$ . It is possible to choose a, b, and other coefficients according to [13]. However, several studies have shown that residual stress produces a strengthening effect. Therefore, when calculating fatigue strength, people usually take:  $k_a = 0.959$  [13].

$k_b$  is the factor taking into account the size:  $k_b = 0.75$ ;  $k_c$  is the load distribution coefficient:  $k_c = 1$  when subjected to bending;  $k_d$  is the coefficient taking into account the effect of temperature:  $k_d = 1$  in the temperature range from 0 to 250 °C;  $k_e$  is the effective coefficient of stress concentration:  $k_e = 1/k_f$ , where k is calculated by the influence factor of the static stress concentration  $K_t$ :

$$K_t = \frac{\sigma_{max}}{\sigma_{no\ min\ al}}$$

where  $\sigma_{max}$  is the limiting stress, and  $\sigma_{nominal}$  is the nominal stress.

### 3 Calculation Model of Drive Axle Housing Strength

In this study, the 3D model of the drive axle housing cover of the multi-purpose forest fire fighting vehicle was built using Solidworks software, the finite element model was built in Ansys software (Fig. 2).

**Fig. 2** 3D model of the rear axle housing

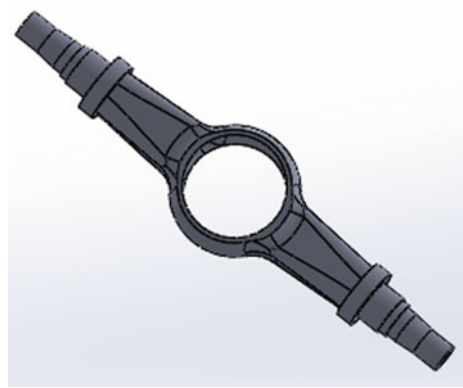


Figure 3 the meshing detailed views, in the analysis, the rear axle housing is meshed with tetrahedral. The element size is 20 mm. The number of elements is 62881 and the number of nodes is 122746. Ansys offers a large stock of proven materials. For the active axle housing of the forest fire truck, the commonly used material is spherical cast iron with the parameters as shown in Table 1 [1, 4].

**Fig. 3** Meshed model



**Table 1** Material parameter of the axle housing

Material type	Steel 40CR
Poisson's ratio ( $\mu$ )	0.3
Young's modulus (E)	205 GPa
Density ( $\rho$ )	7850 kg/m <sup>3</sup>
Yield strength ( $\sigma_y$ )	785 MPa
Ultimate strength ( $\sigma_{ut}$ )	980 MPa



### 4 Evaluation of the Fatigue Strength of the Axle Housing and Structural Improvement

Fatigue assessment of both the original and modified rear axle housings was performed under high dynamic loads with frequent vehicle operation. The survey road surface bump modes are type D-E and E-F according to ISO 8606:1995. The dynamic loads acting on the axle housing when the vehicle is moving on the road are determined from the dynamic model [3, 5]. Due to the characteristics of working with low travel speed, the durability of the axle housing is evaluated when the vehicle is moving at a speed of 20 km/h.

The results of the fatigue strength study for the axle housing when the vehicle is running on the D-E and E-F roads are shown in Figs. 5 and 6. When the vehicle is running on the D-E road, the fatigue point is also the point of greatest stress concentration, element number 444690, located inside the axle housing, at the corners, and several of fatigue cycles of  $93,103 \times 10^4$ . On the E-F road, the main fatigue point is element number 444690, located inside the axle housing, at the corners, with the number of fatigue cycles is  $73475 \times 10^4$ , so the axle housing does not guarantee the fatigue strength when traveling on the road.

To ensure the fatigue strength of the axle housing, the author improved, the area around the fatigue point 444,690 is increased by increasing the radius of the corner. The angle of curvature at the position of stress concentration is adjusted in increments from 25 to 30 mm to increase the material thickness at this position, and increase the number of fatigue cycles of the model beyond the fatigue cycle limit of  $10^6$  times. With dynamic load parameters determined from the dynamics model, the fatigue strength of the axle housing is recalculated (Table 2).

The results of fatigue analysis after improvement show that when the vehicle is running on road D-E, the fatigue cycle is  $61441 \times 10^5$ , on E-F road the fatigue cycle is  $35492.10^5$ . Compared with the unimproved axle housing, the fatigue cycle after improvement is larger. However, the fatigue cycle limit of  $10^6$  times has not been exceeded. Therefore, the axle housing doesn't have enough fatigue strength when traveling on the road. After improvement, the weight of the axle housing is 33 kg (10.7%) heavier than the original. To ensure fatigue strength, the author improved the axle housing for the second time by increasing the thickness of the axle housing by 0.5 mm. The results of the second improved fatigue analysis are shown in Figs. 4 and 5.

**Table 2** Comparison of the fatigue cycles on the original axle housing model, 1st improvement with 2 types of random pavement D-E và E-F

Model	Original axle housing		1st improvement axle housing	
Mass (kg)	273		306	
Type of road	D-E	E-F	D-E	E-F
Fatigue cycles minimum	$9.3103.10^4$	$7.3475.10^4$	$6.1441.10^5$	$3.5492.10^5$

**Fig. 4** Fatigue cycles on axle housing develop, D-E road

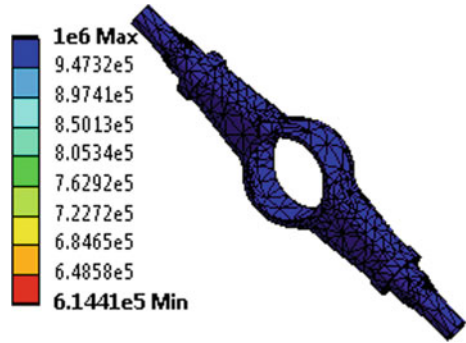


**Fig. 5** Fatigue cycles on axle housing develop, E-F road

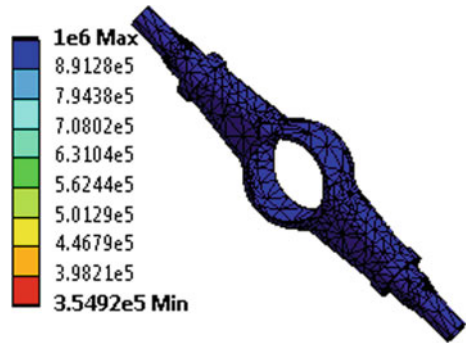
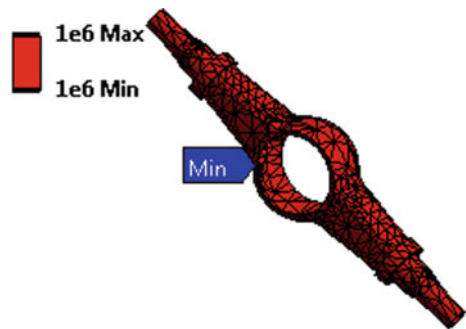


**Fig. 6** Deformation



Figures 6, and 7 show the fatigue cycles on the 2nd improved model and Table 3 shows the comparison results of the fatigue cycles on the original, first improved, and second improved models when driving with road types D-E and E-F according to ISO 8608: 1995. After the 2nd improvement, the fatigue cycle reached  $10^6$ . This fatigue cycle has met the requirements set forth initially, so the axle housing ensures fatigue strength. Through the first improvement, the axle housing has increased the radius of the bevel at the position of stress concentration from 25 to 30 mm, and the

Fig. 7 Equivalent stress

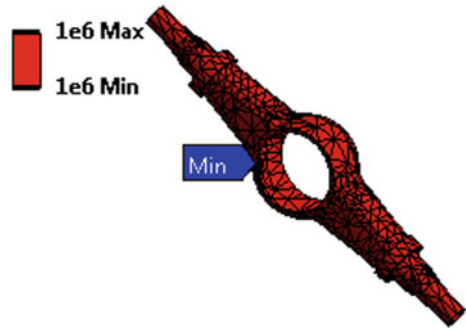


Table 3 Comparison of the fatigue cycles on the original axle housing model, 1st and 2nd improvement with 2 types of random pavement D-E và E-F

Model	Original		1st improvement		2nd improvement	
Mass (kg)	273		306		357.16	
Type of road	D-E	E-F	D-E	E-F	D-E	E-F
Fatigue cycles minimum	$9.310.10^4$	$7.347.10^4$	$6.144.10^5$	$3.549.10^5$	$10^6$	$10^6$

weight of the axle housing is increased to 33 kg. For the second improvement, the axle housing is increased by 0.5 mm in thickness, and the weight is increased by 51.16 kg compared to the first improvement.

## 5 Conclusion

Evaluation of the fatigue strength of the multi-purpose forest fire fighting vehicle when the vehicle is running on bad and very bad roads according to ISO standards. The results show that, after the first improvement, the axle housing has not yet ensured fatigue strength when the vehicle is moving on the road. Therefore, in the 2nd structure improvement, the structure area around the fatigue point has been increased in the material. As a result, the minimum of fatigue cycles on the axle housing has been met (greater than  $10^6$  cycles). The studies were carried out with two software with Solidworks and Ansys. When building the model, it has been done according to the standards and has been evaluated by the software, therefore the survey results are reliable in the calculation.

## References

1. Hoi XN, Van LV, Nguyen TQ, Tuong TV (2020) Assessment on effect of load frequency to durability of chassis of the multi-purpose forest fire fighting vehicle. IOP Conf Series: Mater Sci Eng 886
2. Van VL, Nguyen TQ, Le HQ, Le VA, Tran PH, Nguyen XH, Tuong TV (2020) Determination of dynamic loads from the road surface acting on the chassis by experimental methods. IOP Conf Series: Mater Sci Eng 886
3. Tung NT, Van LV, Quang NT (2020) Survey on the effects of bumpy road to oscillate of multi-purpose forest fire fighting vehicle. Eng Solid Mech 9(2021):291–298
4. Nguyen TT, Luong VV, Nguyen TV (2021) Assessment breaking strength the chassis of Multi-purpose forest fire fighting vehicle. IOP Conf Series: Mater Sci Eng
5. Luong VV, Nguyen TT (2021) Determine the dynamic load acting on the chassis of multipurpose forest fire fighting vehicle. IOP Conf Series: Mater Sci Eng 1173
6. Li K-A (2007) Finite element analysis on the rear axle housing of vehicle. Hunan Vocational College for Nationalities
7. Qinghua M, Huifeng Z, Fengjun L (2011) Fatigue failure fault prediction of truck rear axle housing excited by random road roughness. Int J Phys Sci
8. Gao J, Song J (2008) Fatigue life prediction of vehicle's driving axle house under random loading. J Mech Strength
9. Joshi OP, Jadhav TA, Pawar PR, Saraf MR (2015) Investigating effect of road roughness and vehicle speed on the dynamic response of the seven degrees-of-freedom vehicle model by using artificial road profile. Int J Curr Eng Technol
10. Zheng YP, Ni X (2009) Probability fatigue strength calculation of auto drive axle housing based on the random loading. J Nanjing Forestry Univ
11. Ashby MF, RH Jones D (2012) Engineering materials 1. Fourth edition
12. Budynas R, Nisbett KJ (2013) Shigley's mechanical engineering design, 9th edn. McGraw-Hill, New York
13. Juvinall RC, Marshek KM (2012) Fundamentals of machine component design. 5th edn, Wiley

# Design and Experimental Test of Magneto-Rheological Seal



Le Hai Zy Zy, Diep Bao Tri, Do Qui Duyen, Vo Van Cuong,  
and Quoc Hung Nguyen

**Abstract** This research focuses on design and experimentally testing of a sealing component featuring magneto-rheological fluid for rotary shafts. The working fluid is a lubricant. From review of previous researches on application of MR fluid in sealing, a configuration of a rotary MRF seal for a working lubricant is proposed. Optimal design and modeling of the MRF seal are then realized based on finite element analysis. From optimal results, MRF seal prototypes are manufactured and experimentally tested. The results are then compared with counterpart conventional lip-seals.

**Keywords** Magneto-rheological fluid (MRF) · MRF seal · Finite element analysis · Rotary seal

## 1 Introduction

Nowadays, magnetorheological fluid (MRF) and its applications have attracted significant attention from domestic and foreign scientific researchers. Thanks to its unique properties (like change in viscosity when a magnetic field passes via it). In this study, we will focus on developing mechanisms for devices to prevent leakage on the rotating shaft using MRF to be applied to machines and operating by MRF devices to enhance their performance, such as MRF brakes, MRF clutch, MRF damper, etc.

---

L. H. Zy Zy · D. B. Tri · V. Van Cuong (✉)  
Faculty of Mechanical Engineering, Industrial University of Ho Chi Minh City, Ho Chi Minh City, Vietnam  
e-mail: [vovancuong@iuh.edu.vn](mailto:vovancuong@iuh.edu.vn)

D. Q. Duyen · Q. H. Nguyen (✉)  
Faculty of Engineering, Vietnamese–German University, Thu Dau Mot City, Binh Duong, Vietnam  
e-mail: [hung.nq@vgu.edu.vn](mailto:hung.nq@vgu.edu.vn)

Therefore, there have been a number of studies on the self-sealing component for rotary shafts, and the results show that MRF is one of potential candidates for leak prevention in mechanical equipment. However, these researches are insufficient and highly constrained, with most of the solutions being given and applied to a specific circumstance. Furthermore, there have been no studies focused on optimal configuration design and testing for durability, temperature created during operation, the cycle of life, as well as a comparison between MRF seal and conventional seal. The effectiveness of seals in preventing air leakage via the shaft gap in the compression chamber was tested by Kordonsky et al. [1]. With different currents and MR fluids, the maximum working pressure of the experimental model does not cause leakage in the shaft gap. Additionally, a benefit of sealing applications using MR fluids is low friction torque. Several self-sealing configurations employing MRF for the undersea machinery have been presented by Matuszewski et al. [2]. Nonetheless, this study did not conduct modeling, computations, and experiments. Urreta et al. [3] have studied seals based on magnetic fluids for high-precision spindles of machine tools. The result demonstrated the negligibly low frictional torque. Moreover, when using different MR fluids, the frictional torque is also different. By utilizing a smart seal configuration, Hegger et al. [4] have suggested a method to inhibit the MRF of an MRF actuator from leaking. According to experimental tests, the MRF seal generates extremely little frictional torque, and the system can operate continuously for six months. To fill the shortcomings of previous studies, this study concentrates on the design, optimization, and experimental testing of the basic parameters of the sealing devices using MRF (which is abbreviated to MRF seal) as well as the comparison with conventional seal.

## 2 Configuration and Working Principles

The configuration of the MRF seal with the tooth-shaped pole head is depicted in Fig. 1, as well as its geometry dimensions. Structurally, a permanent magnet that is a crucial component of the MRF seal configuration generates a magnetic field that passes through the MR fluid at the tooth-shaped pole head in order to inhibit MRF leaking. In terms of working principle, a magnet creates a magnetic field through the poles to help prevent leakage of MR fluid. The magnetic separator aims to prohibit the magnetic field moving from one pole to the other without going via the MRF gap. The nonmagnetic envelope used in this proposed MRF seal helps reduce the loss from the outside. The magnetic particles are drawn to one another and subsequently aligned along the magnetic field lines when a magnetic field is applied to the MRF gap. The result is that the MR fluid changes from a liquid state to a solid form. The aforementioned phenomena will assist in stopping the leaking of MRF into the external environment.

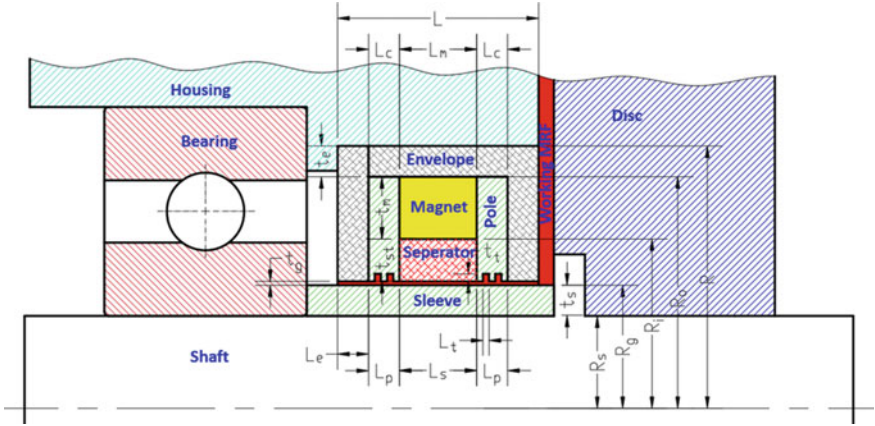


**Fig. 1** Configuration of the proposed MRF seal with tooth-shaped pole head

### 3 Modeling and Optimization

Figure 2 shows the simulated magnetic results of the MRF seal using ANSYS at arbitrary values of design variables (DVs). To simulate the permanent axial magnet in ANSYS software, the Y-axis in ANSYS software is set as the magnetization direction. Besides, the commercial permanent magnet specifications are as follows: NdFeB is component to made of magnet; Nickel plating; axial magnetization direction; suction forces  $F = 34.4N$ ; gauss surface flux density:  $2100 \div 2300G$ ; magnetic field density:  $B_r = 1.26 T$ ; magnetic field strength:  $H_c = 859 KA/m$ . The MR fluid used is the MRF-132-DG produced by Lord Corp. The magnetic property of MR fluid is described by B-H curve.

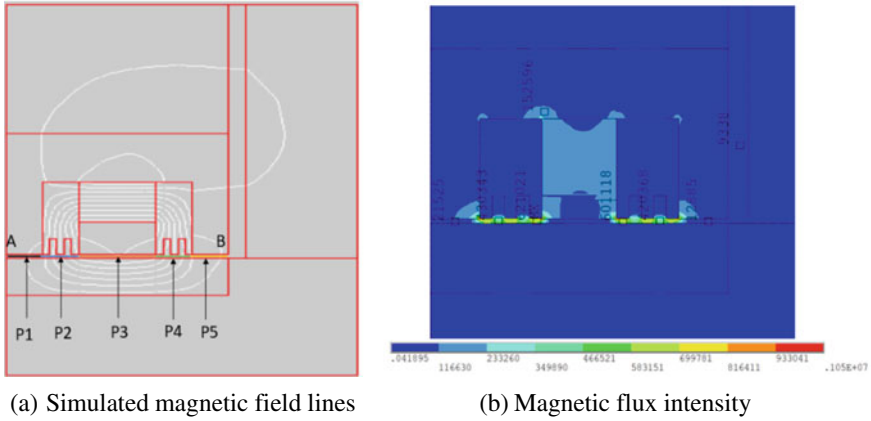


**Fig. 2** Simulated magnetic field of the MRF seal at arbitrary values of DVs

From Fig. 2, it can be seen that by using the above pole head, magnetic flux lines are focused at the poles. A mean value of magnetic flux intensity across the MRF gap is determined, from which performance characteristic of MRF seal is predicted. In order to determine the mean value of the magnetic intensity, the integral of magnetic intensity along the paths P1, P2, P3, P4 and P5, which are depicted in Fig. 2a, is employed.

The maximum working pressure can be determined by [5]:

$$P_{\max} = \Delta P = 2 \cdot c_e \frac{L_e}{t_g} \tau_{y1} + 2 \cdot c_p \frac{L_p}{t_g} \tau_{y2} + c_s \frac{L_s}{t_g} \tau_{y3} \quad (1)$$

where, the coefficients ( $c_e$ ,  $c_p$ ,  $c_s$ ) hinged on the velocity profile of the MRF flow in the gap. Because of the low MRF flow velocity in the gap, these coefficients are equal to 2.0.

The frictional torque produced by MR fluid in the MRF gap is determined by [6]:

$$T_f = 2.T_{f1} + 2.T_{f2} + T_{f3} \quad (2)$$

where  $T_{f1}$ ,  $T_{f2}$ ,  $T_{f3}$  are respectively the frictional torque of MRF in the gap at the envelope, the pole and the separator, which are determined by [6]:

$$\begin{aligned} T_{f1} &= 2\pi R_g^2 L_e \left( \tau_{y1} + \eta \frac{\Omega R_g}{t_g} \right); T_{f2} = 2\pi R_g^2 L_p \left( \tau_{y2} + \eta \frac{\Omega R_g}{t_g} \right); \\ T_{f3} &= 2\pi R_g^2 L_s \left( \tau_{y3} + \eta \frac{\Omega R_g}{t_g} \right) \end{aligned} \quad (3)$$

where  $\Omega$  is the shaft's rotational speed (rad/s).

## 4 Optimal Design of the MRF Seal

In this section, the multi-objective optimization problem (MOOP) of the MRF seal with tooth-shaped pole head is conducted based on the following significant factors: Maximum working pressure and the maximum magnetic flux intensity at the poles head. Therefore, the goal of the multi-objective optimization problem given in this research is to find the maximum working pressure ( $P_{\max}$ ) determined in the Eq. (1) and the maximum magnetic flux intensity ( $H_{\max}$ ) at pole heads (P2 and P4). The reason why we selected  $H_{\max}$  as the second objective function is because large magnetic flux intensity affects the strong connection between iron particles in the MR fluid at the pole heads position and the particles will bond more strongly when high pressure is applied. The multi-objective optimization problem can be stated as follows:

$$\text{Maximum : } Obj_1 = P_{\max}, Obj_2 = H_{\max}; \quad \text{Subjected to } LL_{sl}; DD_{sl}$$



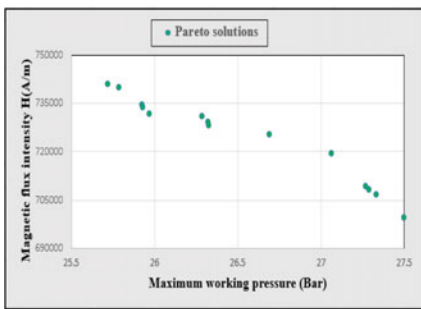
where, the proposed MRF seal’s overall size are  $L$  and  $D$ ;  $L_{sl}$  and  $D_{sl}$  are respectively the corresponding overall size of lip-seal.

Besides, the value of significant dimensions of the MRF seal such as pole length ( $L_p$ ), the core length ( $L_c$ ), the envelope thickness ( $L_e$ ), the sleeve thickness ( $t_s$ ), the separator thickness ( $t_{st}$ ), the teeth length ( $L_t$ ), the teeth height ( $t_t$ ), and the geometry of magnet ( $R_i$ ,  $R_o$ ,  $L_m$ ,  $t_m$ ) are selected as design variables. The MRF gap ( $t_g$ ) is empirically set by 0.2 mm and  $L_m = L_s$ ;  $L_c = L_p$  in order to facilitate the design and fabrication.

To handle the multi-objective optimization problem, many metaheuristic MOOAs (multi-objective optimization algorithms), such as the NSGA-II, SPEA2, SMS-EMOA, MOPSO, MOEA/D, etc., have been proposed and used recently [7]. One of the most effective MOOAs among them is MOPSO, which can help find the global optimal value with simple initialization conditions. It is noted that, in this research, the MOPSO is conducted in MATLAB interfacing with ANSYS Mechanical APDL.

In this research work, the commercial MRF (MRF132-DG) made by LORD Cooperation is employed and the S45C steel is used for magnetic parts including the housing, the sleeve, the poles, and the disc while the shaft is made of nonmagnetic stainless steel (SS304). Additionally, 1350-Aluminum alloy made use of the envelope and the separator. The Parker-62576 commercial lip seal was employed as the object of comparison with the proposed MRF seal, which the following parameters can be obtained  $D_{sl} = 30$  mm,  $L_{sl} = 10$  mm,  $R_s = 5$  mm. The magnet is sized at  $R_i = 18$  mm,  $R_o = 25$  mm,  $L_m = 3$  mm.

Figure 3a shows the optimal results of MOOP of the MRF seal using MOPSO. The magnetic flux intensity of MRF seal at the optimum is shown in Fig. 3b, at which  $P_{max} = 26.287$  bar and  $H_{max} = 730,749$  A/m. The optimal result is summarized in Table 1.



(a) Pareto solutions



(b) Magnetic flux intensity of

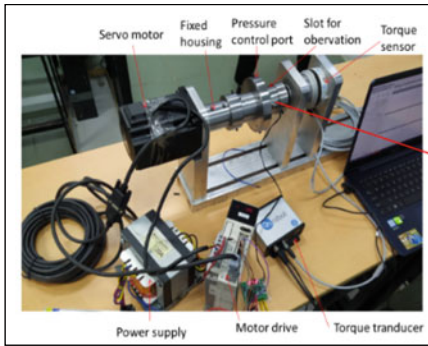
Fig. 3 Optimal result of MRF seal with tooth-shaped pole head

**Table 1** MOOP results of the MRF seal with tooth-shaped pole head

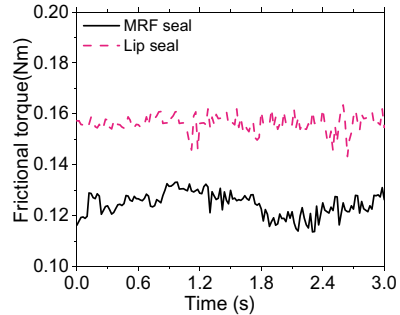
Design parameters	Performance
Overall Length: $L = 9.74$ mm	Max. Pressure: $P_{\max} = 26.287$ bar Max. Magnetic flux density at pole head: $H_{\max} = 730,749$ A/m Frictional torque: $T_f = 0.077$ Nm
Overall diameter: $D = 29.97$ mm	
Sleeve annular thickness: $t_s = 2.705$ mm	
Pole annular length: $L_p = 1.85$ mm	
Teeth length: $L_t = 0.37$ mm	
Teeth thickness: $t_t = 0.5$ mm	
Separator annular thickness: $t_{st} = 1.1$ mm	
Separator annular length: $L_s = 3$ mm	
Enveloped annular thickness: $L_e = 1.52$ mm	
Magnet annular thickness: $t_e = 2.48$ mm	

## 5 Experimental Results

Figure 4a depicts the experimental setup of the MRF seal. The first experiment measures frictional torque of lip seal and MRF seal. In this case, the shaft is rotated at 300 rpm, and the results are shown in Fig. 4b. It can be seen that the frictional torque of the MRF seal is relatively 0.121 Nm, which is significantly lower than that of the conventional seal (lip-seal is about 0.155 Nm). Therefore, from the comparison between both seals above, it can be observed that the MRF seal is greater than the lip-seal. In the second experiment, the maximum working pressure of the MRF seal is measured. In this case, the motor is stopped and pressure is supplied via a pressurized system. During the experiment, the pressure is incrementally increased 1 bar and kept for 2 min. Leakage of MRF is observed from the observation slot. Additionally, sudden pressure drop due to MRF leaking is observed from the pressure gage. The results shows that the maximum working pressure is 24 bar. This result is slightly smaller than the calculated results from the simulation (26.287 bar). The above discrepancy is most likely caused by magnetic losses and fabricating process inputs that do not match the material properties. It is noted that the conventional seal (lip-seal) is often restricted to about 3 bar because of high frictional torque, heat issues, wear, and cycle life of this seal.



(a) Experimental setup



(b) Measured Friction torque

Fig. 4 Experimental test of the MRF seal

## 6 Conclusion

In this research, a MRF-based seal for rotary shafts is proposed in order to replace conventional lip-seal. Firstly, a configuration for the MRF seal was proposed. Afterward, finite element analysis, ANSYS APDL, was employed to predict the performance of the MRF seal. Optimal design of the MRF seal by interacting MATLAB and ANSYS APDL using the multi-objective optimization algorithm, MOPSO, was performed. From optimal results, MRF seal prototypes are manufactured and experimentally tested. Experimental results showed that the frictional torque of the MRF seal (0.121 Nm) is significantly smaller than that of the lip-seal (0.155 Nm). Simultaneously, the maximum working pressure result of MRF seal is 24 bar which is relatively smaller than simulated result (26.287 bar), and significantly greater than the working pressure of the counterpart lip seal (3 bar).

**Acknowledgements** This work was supported by research fund from Ministry of Education and Training (MOET) of Vietnam, Grand no. B2002-VGU-03.

## References

1. Kordonski WL, Gorodkin SR (1996) Magnetorheological fluid-based seal. *J Intell Mater Syst Struct* 7:569–572
2. Matuszewski L, Szydlo Z (2008) The application of magnetic fluids in sealing nodes designed for operation in difficult conditions and in machines used in sea environment. *Polish maritime research* 15:49–58
3. Urreta H, Aguirre G, Pavel K, Luis NL (2018) Seals based on magnetic fluids for high precision, spindles of machine tools. *Int J Precis Eng Manuf* 19:495–503
4. Hegger C, Maas J (2019) Smart sealing for magnetorheological fluid actuators. *J Intell Mater Syst Struct* 30:689–700

5. Nguyen QH, Han YM, Choi SB, Wereley NM (2007) Geometry optimization of MR valves constrained in a specific volume using the finite element method. *Smart Mater Struct* 16:2242–2252. <https://doi.org/10.1088/0964-1726/16/6/027>
6. Nguyen QH, Choi SB (2021) Optimal design of a novel hybrid MR brake for motorcycles considering axial and radial magnetic flux. *Smart Mater Struct* 21. <https://doi.org/10.1088/0964-1726/21/5/055003>
7. Britto A, Pozo A (2002) MOPSO: a proposal for multiple objective particle swarm optimization. *Proceedings of the 2002 congress on evolutionary computation*. <https://doi.org/10.1109/CEC.2002.1004388>

# Study the Effects of Geometry and Materials on Modal Characteristics of Honeycomb Composite



Le Thi Tuyet Nhung, Tran Minh Duy Dat, and Vu Dinh Quy

**Abstract** The honeycomb panels are complex structures whose modal characteristics depend on several factors such as geometry and materials. Therefore, this study aims to investigate the impact of geometrical and material variation on natural frequencies and the mode shape of the honeycomb structure. The research approach is based on the analysis and simulation of a honeycomb plate model by the finite element method in ANSYS 2022R1. All the honeycomb models in the simulation are applied to the same clamped-free boundary condition and their covers are made of carbon fiber-reinforced epoxy composite. A validating model which is equivalent to the previous research is carried out to evaluate the reliability of the paper, the difference between four natural frequencies between the two research is less than 9%. With the same geometry conditions of honeycomb structure, the natural frequencies the aluminum and Nomex cores produce are considerably more than the values of polypropylene. The increase in the core thickness leads to the growth of the natural frequency values in longitudinal bending modes, but the decrease in lateral bending modes. In terms of the cell size, there is a rise in the first six eigenfrequencies of honeycomb structure when expanding the size of the unit cell from 2 to 6 mm.

**Keywords** Modal characteristics · Natural frequency · Mode shape · Honeycomb sandwich composite

---

L. T. T. Nhung · V. D. Quy (✉)

Ha Noi University of Science and Technology, No. 1 Dai Co Viet Road, Ha Noi, Vietnam

e-mail: [quy.vudinh@hust.edu.vn](mailto:quy.vudinh@hust.edu.vn)

T. M. D. Dat

Phenikaa-X JSC, Nguyen Van Trac Str, Ha Dong District, Vietnam

## 1 Introduction

Due to outstanding chemical, physical and mechanical properties, composite materials are applied in a wide range of industries such as aerospace, automotive, construction, manufacturing household or sports equipment, and so on. In each application, different constituent materials are combined to produce a specific type of composite materials for given needs and requirements. For instance, many aircraft components such as leading edges, fairing, engine nacelles, control surfaces, walls, or flooring panels are constructed by honeycomb sandwich composite [1, 2].

In general, sandwich structures including thick cores and two thin high-strength skins possess high stiffness-to-weight and strength-to-weight ratios. Moreover, the great energy-absorbing capacity from crashes and radiation is one of the most beneficial characteristics of the honeycomb sandwich composites, which leads to its applications widely in the aerospace industry [3].

Over nearly two decades, there are a lot of research applying numerical methods to predict the dynamic characteristics of honeycomb composite. Besides, analytical methods based on the equivalent theory have also been developed and applied to validate and compare the numerical results. The dynamic behavior of sandwich plates in which the skin–core interface is partially delaminated is investigated by Vyacheslav and Tomasz. The study indicated that the factors (size, location, and types) of the debonding zones in sandwich plates have an impact on the modal characteristics. The researchers used the commercial software ABAQUS to determine natural frequencies and mode shapes of partially debonded sandwich plates with several boundary conditions [4]. Zhi-jia Zhang et al. concentrated on analyzing the vibration performance of sandwich structures with the honeycomb-corrugation hybrid core. The results were predicted by the equivalent homogenization model (2D model), validated, and compared by the experimental and the 3D finite element models [5].

In this paper, the study focuses on considering and evaluating the influence of design parameters of honeycomb core on modal characteristics of the whole sandwich structure. A 3D honeycomb composite model was simulated to validate the results of natural frequencies with previous literature. The direct finite element method was used to construct a honeycomb sandwich panel in ANSYS 2022R1 where two face sheets were erected by ANSYS Composite PrePost (ACP) to create the detailed designs of carbon fiber-reinforced polymers (CFRP) material before the free vibration analysis.

## 2 Validating Model

In this paper, a honeycomb panel is developed in ANSYS 2022R1 software to compare the natural frequencies and mode shapes of the structure. The 3D solid model is built from dimension inputs of A. Boudjemai et al. [6] and then simplified it into shells. The shell models of the core and two faces are meshed with quad (4-node)

**Table 1** Result comparison

Mode	Natural frequency (Hz)			Error (%)*
	FEM (Ansys)	FEM (Patran) by A. Boudjemai [6]	Experiment by A. Boudjemai [6]	
1	124.07	130.66	134.5	5.04
2	285.17	304.67	311	6.4
3	748.26	790.34	711	5.32
4	1167.4	1278	–	8.65

\*Comparing two FEM models

elements. Aluminum material used for both the cover sheets and the core owns the following mechanical properties: 2800 kg/m<sup>3</sup> density, 72 GPa elastic modulus, and 0.33 Poisson ratio. For the boundary condition, one edge of the short side is fixed at all six degrees of freedom.

The values of the four first natural frequencies shown in Table 1 are compared with the results which A. Boudjemai et al. obtained in FEM models and experimental testing. The difference in natural frequencies between two finite element models is also less than 9%. There is only a remarkable difference with 8.65% in the fourth frequency. Therefore, modeling the honeycomb panels by the finite element method in ANSYS is acceptable for accuracy and reliability.

The difference in the natural frequencies between two finite element methods could be explained by two reasons. Firstly, although the elements of the honeycomb sandwich model in this paper are quad (four nodes), the total elements and nodes in the validating model, 60,415 and 54,704 respectively, are more than the Boudjemai's model with 23,221 elements and 40,426 nodes. Secondly, the model in the present study is ignored two adhesive layers bonding the core and the skins. Besides, Boudjemai's paper also pointed out that the error between the experimental and simulated results is caused by the clamping system at the end of the cantilevered honeycomb plate in experiments.

### 3 Finite Element Model for Honeycomb Beams

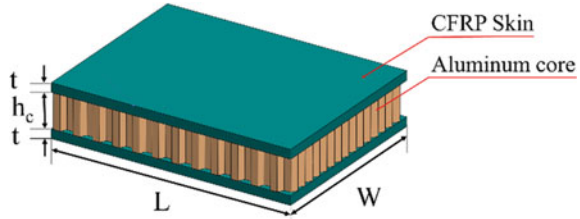
#### 3.1 Geometrical and Meshing Model

Depending on the specific application, the honeycomb sandwich structure could include one or more cores (multi-layer), the core may be a regular or randomly irregular honeycomb. The object of this study concentrates on a sandwich structure with a hexagon-cell core and two face skins, while the purpose is to investigate the effect of design parameters on modal characteristics of the structure. A series of honeycomb sandwich panel models are built with a variation of a specific parameter

**Table 2** Common geometrical parameters for all honeycomb sandwich models

Length ( $L$ )	Width ( $W$ )	Skin thickness ( $t_s$ )	Cell wall thickness ( $t_c$ )
400 mm	40 mm	1 mm	0.2 mm

**Fig. 1** Typical dimensional parameters of a honeycomb panel



and unchanged others. The simulation approach is utilized to determine the natural frequencies and mode shapes of all models which are compared and evaluated the trend of these results while varying the given design factor.

It is difficult to simulate the 3D solid model of the honeycomb sandwich panel so using the shell model is time-saving and suitable for computational capability. The adhesive layers connecting the core and the skins are negligible, instead bonded contact is applied in the interface between the skins and the core. Four unchanged design parameters of all honeycomb models are shown in Table 2 and Fig. 1. The core thickness and height are two factors changed for simulation models and presented in 3.4 and 3.5 sections respectively.

The meshing model with four-node elements is performed by the finite element method in ANSYS 2022R1 software, shown in Fig. 2. There is no difference in the element size between honeycomb models, as a result, the total number of elements depends on the model dimensions.

### 3.2 Materials and Boundary Conditions

Three types of material for the core are aluminum, Nomex, and polypropylene, which is the most popular cores for manufacturing honeycomb sandwich structure. Modal analysis is a linear problem, hence three basic quantities of each material namely density, Young modulus, and Poisson ratio are given in Table 3.

In terms of face skins, they used carbon fiber-reinforced polymer, thus ANSYS Composite PrePost (ACP) was selected to process this composite material. Epoxy carbon woven (230 GPa) wet in ANSYS material library with detailed mechanical properties described in Table 3 was assigned for the new fabric. The modeling group for the skin consists of five plies where the thickness of each ply is 0.2 mm and the ply angle is assigned as the order of  $[0^\circ/90^\circ/0^\circ/90^\circ/0^\circ]$ .



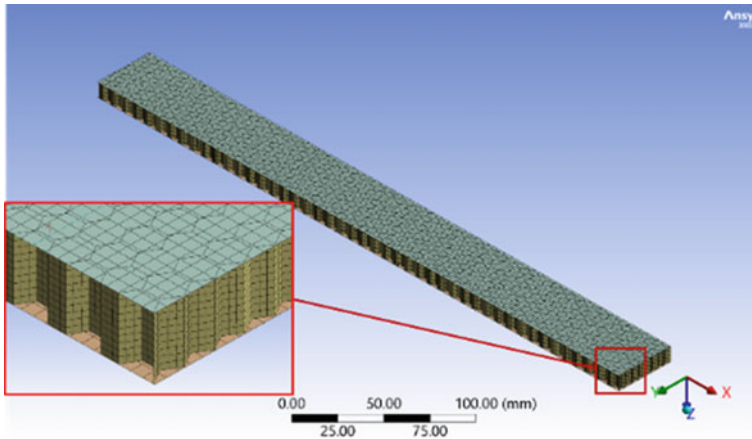


**Fig. 2** Meshing model of honeycomb sandwich beam

**Table 3** Material properties

Property		Aluminum	Nomex paper [7]	Polypro-pylene	Epoxy carbon woven wet
Density (kg/m <sup>3</sup> )		2770	720	44.79	1451
Young modulus (MPa)	X direction	72,000	1300	0.27	59,160
	Y direction	72,000	1300	0.27	59,160
	Z direction	72,000	2500	0.27	7500
Poisson ratio	XY	0.33	0.3	0.46	0.04
	YZ	0.33	0.2	0.46	0.3
	XZ	0.33	0.2	0.46	0.3

Much previous research concluded that boundary conditions have a significant impact on the dynamic response of sandwich structures [6]. This study focuses on the influence of core design factors on the modal performance, thus all honeycomb beam models would only utilize the clamp-free boundary condition, i.e., one end of beams is fixed (Fig. 3).

The composite beam models are simulated to determine the response to free vibration in which there is no external force or vibration acting. In each circumstance, the response is six first frequencies and their mode shape in each frequency.

### 3.3 Effect of Core Materials

In this section, the core of the honeycomb models has the following dimension: the thickness  $h_c = 10$  mm and the cell size  $l_c = 5$  mm. Figure 4 describes the

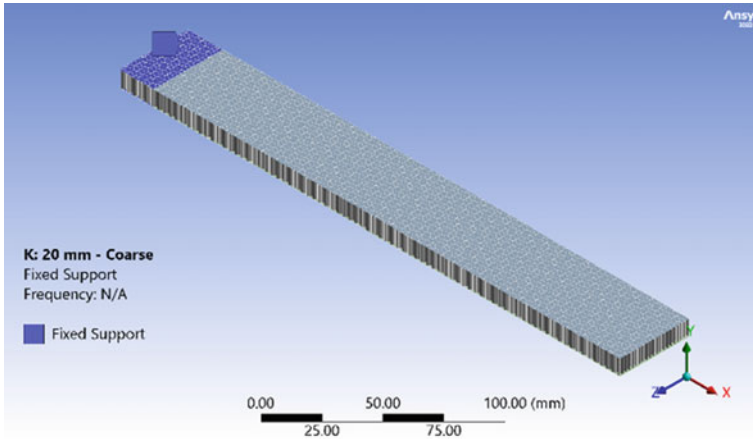


Fig. 3 The clamp location in the composite beam

difference between the four first frequencies of three core materials, and Fig. 5 indicates the mode shapes corresponding to each natural frequency. It is clear that the natural frequencies of honeycomb models with Nomex and aluminum core are significantly higher than polypropylene. The consequence is explained by the reason that the elastic and shear modulus of Nomex and aluminum are dramatically more than polypropylene, these mechanical properties play an essential role in the modal performance of honeycomb sandwich panels.

Considering the mode shapes, in the first frequency, the vibration of all honeycomb models is the first bending mode. Nevertheless, in the higher values of natural

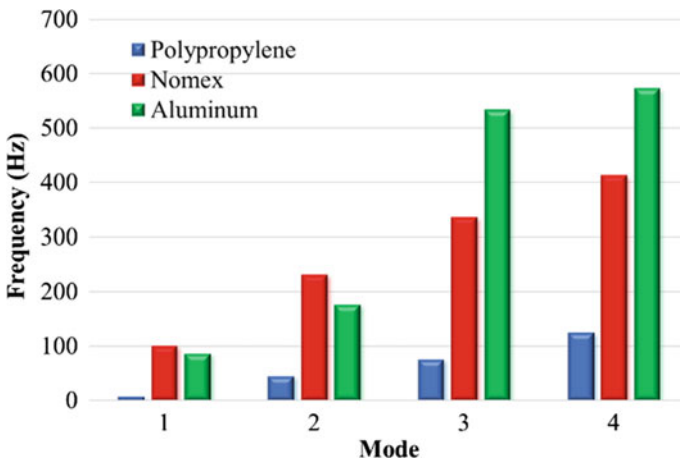


Fig. 4 Comparison of four first frequencies of sandwich structure with the honeycomb core made of polypropylene, Nomex, and aluminum

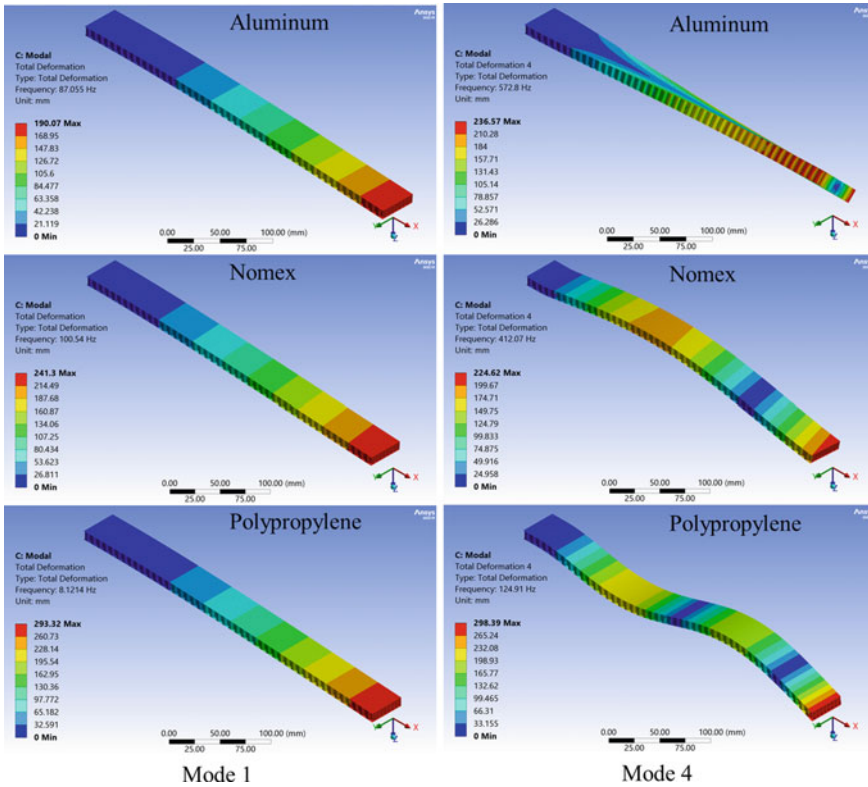


Fig. 5 Mode shapes in the 1st and 4th eigenfrequencies according to three material cores

frequencies, the vibration types of each core material are different. For instance, the first lateral bending mode is in the second natural frequency of the panels with Nomex and aluminum core, in contrast, this vibration kind does not occur in the four first frequencies of the polypropylene-core honeycomb beam. In terms of torsion modes, it occurs at the fourth frequency of the aluminum core and the third eigenfrequency of the Nomex and polypropylene panels. Therefore, selecting core material for honeycomb composite need to consider carefully to have appropriate modal performance.

### 3.4 Effect of the Core Thickness

The impact of core thickness is investigated in this sub-section. The dimensions of the honeycomb beam are described in Table 2, the core applied by aluminum material includes the size of the unit cell  $l_c = 2$  mm, and the core's height  $h_c$  in the range from 5 to 25 mm.

**Table 4** Effect of the core thickness on natural frequencies of sandwich panels

	Mode 1 (Hz)	Mode 2 (Hz)	Mode 3 (Hz)	Mode 4 (Hz)	Mode 5 (Hz)	Mode 6 (Hz)
$h_c = 5$ mm	44.994	169.04	280.36	352.2	777.92	904.58
$h_c = 10$ mm	64.106	131.5	392.79	462.12	703.24	1062.9
$h_c = 15$ mm	78.528	111.33	463.46	488.68	595.39	1195.2
$h_c = 20$ mm	89.929	98.285	466.68	499.35	525.58	1211.7
$h_c = 25$ mm	88.959	98.851	424.94	475.66	506.82	1122

The results of the first six eigenfrequencies are shown in Table 4. It is clear that increasing the core height leads to the growth of the first natural frequencies (first bending modes) but the decline in the second one (first lateral bending mode). Nevertheless, there are fluctuations in the larger natural frequencies between the core thickness due to the difference in the vibration type corresponding to each eigenfrequency. For example, the second bending mode is detected at the third natural frequency of the core thickness of 5 mm, 10 mm and 15 mm, while in cases of 20 mm and 25 mm thickness, it happens at the fourth and fifth frequencies respectively. Hence, comparing the natural frequencies based on the mode shapes of honeycomb panels is convenient for identifying the effect of the core thickness.

Figure 6 illustrates the variation in the eigenfrequencies of the vibration modes according to the core thickness. Two longitudinal bending modes represented by red and orange lines increase gradually due to the increase of the core thickness. In contrast, there is a considerable decline in the natural frequency of lateral bending modes. In the torsion mode, the trend is not clearly determined, the eigenfrequency of 15 mm core height is the highest with 488 Hz.

### 3.5 Effect of the Cell Size

The sub-section refers to the simulation results involving the variation of the cell size in the honeycomb core. Similar to the previous sub-sections, honeycomb sandwich beam models also possess four dimensions shown in Table 2, in addition, the core height  $h_c = 10$  mm, and the range of the cell size is between 2 and 6 mm.

Table 5 depict the results of natural frequencies obtained, it is observed obviously that honeycomb sandwich beam models experience a growth in the natural frequencies at all of the first six modes as a result of the unit cell size. When evaluating the percent difference between the frequency values of the 2 mm and 6 mm cell size, the highest and smallest percentage is respectively 43.86% in mode 1 and 27.80% in mode 4.

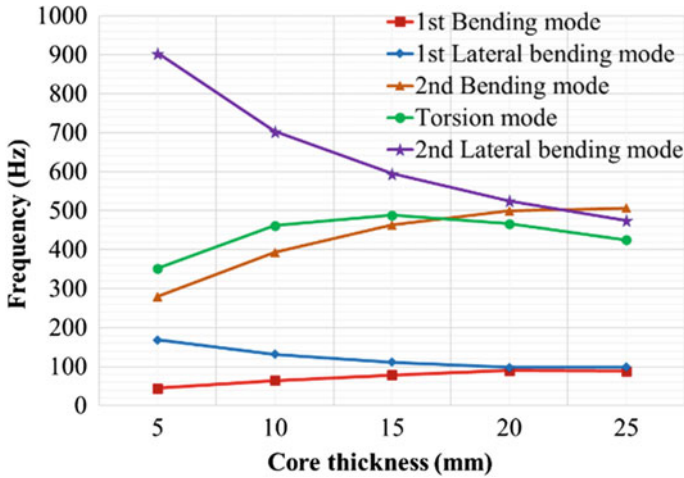


Fig. 6 Impact of the core height on frequencies of five modes of honeycomb panels

Table 5 Natural frequencies depend on the cell size of the aluminum core

	Mode 1 (Hz)	Mode 2 (Hz)	Mode 3 (Hz)	Mode 4 (Hz)	Mode 5 (Hz)	Mode 6 (Hz)
$l_c = 2 \text{ mm}$	64.106	131.5	392.79	462.12	703.24	1062.9
$l_c = 3 \text{ mm}$	74.418	151.92	456.66	516.79	804.12	1238.5
$l_c = 4 \text{ mm}$	81.375	165.46	499.05	541.74	862.8	1352.3
$l_c = 5 \text{ mm}$	87.055	176.86	532.96	572.8	920.1	1440.7
$l_c = 6 \text{ mm}$	92.225	187.13	562.83	590.58	970.32	1514.8

In addition, the five honeycomb sandwich models above witness the same type of vibration in each mode: (1) first longitudinal bending mode, (2) first lateral bending mode, (3) second longitudinal bending mode, (4) torsion mode; (5) second lateral bending mode, (6) third longitudinal bending mode. Therefore, changing the cell size only affects the values of the natural frequencies.

## 4 Conclusion

Several FEM models of the honeycomb sandwich beams consisting of a core and two CFRP skins are established to investigate the change of modal behaviors causing geometrical and material parameters. Mechanical properties of aluminum and Nomex core namely density, elastic modulus, and shear modulus are larger than these of polypropylene, which makes the eigenfrequencies of honeycomb beam with aluminum and Nomex higher. The strength and stiffness play a key role in the

modal performance of any structure. The variation of the core thickness in honeycomb beams influences both the natural frequencies and mode shapes. There is a slight increase in the frequencies in longitudinal bending modes, to the contrary, a dramatic fall occurs in lateral bending modes. The fluctuation in the frequencies of the torsion mode would need to be further studied. Increasing the size of the unit cell from 2 to 6 mm is the reduction of the honeycomb core weight, which consequently leads to the noticeable growth in the natural frequencies of the first six modes.

## References

1. Federal Aviation Administration (2018) Aviation maintenance technician handbook-airframe, vol I, Washington DC
2. DuPont de Nemours, Inc, Honeycomb composite made lighter and stronger. DuPont, [Online]. Available: [www.dupont.com](http://www.dupont.com). [Accessed 30 Jun 2022]
3. Mazumdar SK (2002) Composites manufacturing: materials, product, and process engineering, CRC Press
4. Burlayenko VN, Sadowski T (2010) Influence of skin/core debonding on free vibration behavior of foam and honeycomb cored sandwich plates. *Int J Non-Linear Mech* 45:959–968
5. Zhang Z-J, Han B, Zhang Q-C, Jin F (2017) Free vibration analysis of sandwich beams with honeycomb-corrugation hybrid cores. *Compos Struct* 171:335–344
6. Boudjemai A, Amri R, Mankour A, Salem H, Bouanane MH, Boutchicha D (2012) Modal analysis and testing of hexagonal honeycomb plates used for satellite structural design. *Mater Des* 35:266–275
7. Xie S, Wang H, Yang C, Zhou H, Feng Z (2020) Mechanical properties of combined structures of stacked multilayer Nomex® honeycombs. *Thin-Walled Struct* 151:106729

# An Active Seismic Isolation Two-Layer Floor Based on Hedge Algebra Control



Thanh-Lam Bui and Xuan-Thuan Nguyen

**Abstract** The paper proposes an anti-vibration system to protect equipment and people under the impact of earthquakes. The seismic isolation design consists of 2 floors system that reduces the acceleration and vibration of the object on the top floor. A hedge algebras-based controller (HAC) is applied to increase the system's stability under earthquake excitations. Earthquakes with different properties are also given as input to verify the system's performance. A conventional fuzzy set is designed based on HAC analog parameters. Numerical results indicate the effectiveness of the proposed method with previous method. Moreover, the experiment results also confirm the performance of the controller.

**Keywords** Hedging algebra-based controller (HAC) · Fuzzy controller (FC) · Damping · Seismic isolation

## 1 Introduction

Structural protection of structures and equipment in buildings has been the focus of research in recent decades. Structural vibration control can be considered an optimal solution to reduce the impact of vibrations on structures. Fuzzy control is a control method that has received much attention in recent years, especially in structural vibration reduction [1–4]. Nguyen et al. [1] proposed a semi-active fuzzy controller to improve the performance of the seismic isolation system. Simulation

---

T.-L. Bui

Faculty of Mechanical Engineering, Hanoi University of Industry, Hanoi, Vietnam

X.-T. Nguyen (✉)

School of Mechanical Engineering, Hanoi University of Science and Technology, No. 1, Dai Co Viet, Hanoi, Vietnam

e-mail: [thuan.nguyenxuan@hust.edu.vn](mailto:thuan.nguyenxuan@hust.edu.vn)

results confirmed that FC significantly reduced the relative displacement and absolute acceleration of high-rise buildings. Martin et al. studied the proposed optimal fuzzy controller based on magnetic rheological (MR), and FC dampers to minimize vibration for a 5-storey building. The results shown that both absolute acceleration and relative displacement of buildings were significantly reduced.

The fuzzy controller optimization methods have been proposed in many studies [5–8]. Whale Optimization algorithm was proposed by Mahdi et al. [5] to optimize for FC in structural vibration reduction. The main objective function and performance criteria are considered based on the nonlinear responses of the structure. The Hedge Algebra (HA) theory introduced in 1990s [9–12]. The Hedge Algebra Controller (HAC) has some improvements compared to the Fuzzy algorithms such as: faster response time, easy to establish the linguistic values as an algebraic structure, compatibility with different structures. Bui et al. [9] proposed a controller based on HAC to represent relationships between the state variables. The HAC performance has been verified by numerical simulations in controlling the building equipment vibrations under several types of earthquakes.

It can be remarkable that the studies on the safety systems for small and medium-sized devices under the impact of vibrations have not received much attention. In this paper, a two-stage seismic isolation system based on HAC is presented. This is a new approach with a key property that the semantic order of language values is always guaranteed. HAC is applied to improve the anti-vibration performance of the device. The designed system is simulated on MATLAB with two earthquakes of different amplitudes and frequencies. To evaluate the performance of the proposed system, the simulation results are compared with those in FC. The final results show the superior effectiveness of the proposed device under the earthquake vibrations.

## 2 The Detailed Structure System

### 2.1 Motion Equations of the Structure System

In Fig. 1, the damping system is located on both floors. The first floor is subjected to direct earthquakes. The control force  $u_t$  is set up at the 2nd layer. The motion equation of the two-layer seismic system is presented as follows:

$$M \begin{bmatrix} x_b \\ x_t \end{bmatrix} + C \begin{bmatrix} \dot{x}_b \\ \dot{x}_t \end{bmatrix} + K \begin{bmatrix} x_b \\ x_t \end{bmatrix} = -M \begin{bmatrix} 1 \\ 1 \end{bmatrix} \ddot{x}_w + F \begin{bmatrix} 0 \\ u_t \end{bmatrix} \quad (1)$$

$$M = \begin{bmatrix} m_b & 0 \\ 0 & m_t + m_e \end{bmatrix} \quad (2)$$

$$C = \begin{bmatrix} c_b + c_t & -c_t \\ -c_t & c_t \end{bmatrix} \quad (3)$$



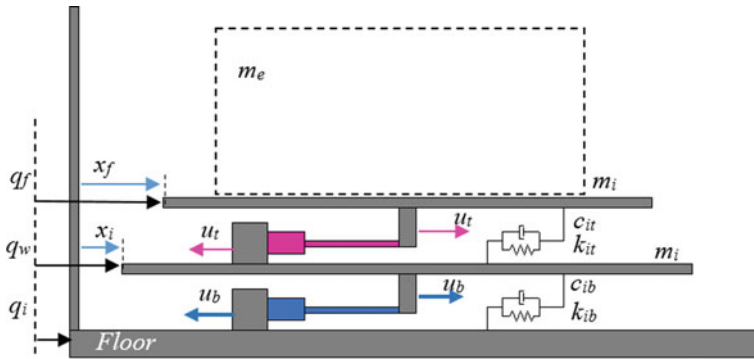


Fig. 1 Schematic drawing of a two-layer seismic system

$$K = \begin{bmatrix} k_b + k_t & -k_t \\ -k_t & k_t \end{bmatrix} \tag{4}$$

$$F = \begin{bmatrix} 0 & -1 \\ 0 & 1 \end{bmatrix} \tag{5}$$

whereas:  $m_e$  is the movable load mass (kg);  $x_f, x_i$  are the layer displacements (m);  $m_i$  is the layer mass (kg);  $q_f, q_i, q_w$  are the positions (m);  $k_{it}, k_{ib}$  are the spring stiffnesses (N/m);  $u_t$  is the control force (N);  $c_{it}, c_{ib}$  are the damping coefficients (Ns/m).

### 3 Theory and Controller Algebraic Hexadecimal

#### 3.1 Controller Algebra

In this section, the HAC controller is established based on [6]. The operating principal diagram of the proportional-differential (displacement–velocity) HAC given by the control force  $u_t$  is shown in Fig. 2. The controller consists of 2 inputs  $x_t$  and  $\dot{x}_t$  (displacement–speed) and 1 output  $u_t$ .

#### 3.2 Normalization and De-Standardization

The assumption that the reference domain of the state and control variables is given by  $x_i \in [-a_i, a_i], u \in [-c_i, c_i]$  is clearly indicated in Fig. 3.

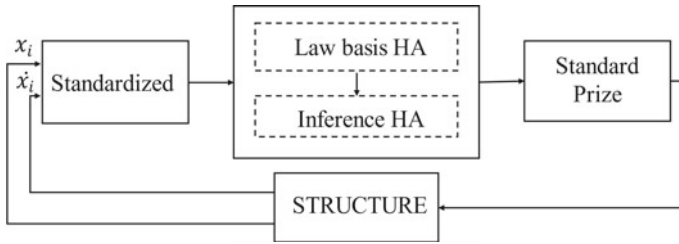


Fig. 2 Control diagram of a proportional-derivative HAC

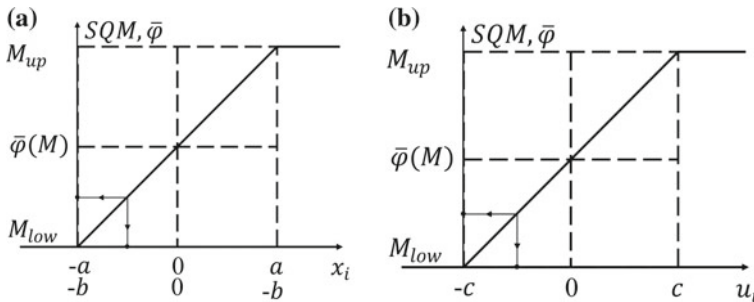


Fig. 3 Linear normalization (a) and denormalization (b) diagram in HAC

Assuming that the language variable  $X$  belongs to the real interval  $[x_0, x_1]$  and its linguistic labels receive quantitative values in the corresponding semantic quantitative interval  $[s_0, s_1]$ , then the real value  $x \in [x_0, x_1]$  is quantified by:

$$\text{Normalization}(x) = s_0 + \frac{s_1 - s_0}{x_1 - x_0}(x - x_0) \tag{6}$$

The problem of quantitative solving is carried out in reverse according to:

$$\text{Denormalization}(s) = x_0 + \frac{x_1 - x_0}{s_1 - s_0}(s - s_0) \tag{7}$$

In FC, after combining inferences, the output fuzzy set is normally complex. The defuzzification step would convert the output fuzzy set to the actual value of the control variable. However, it requires many rather complicated methods such as center of gravity, maximum, minimum, average, and so on. In HAC, to convert from SQM values into the actual values of the control variables, the denormalization step can simply reuse the diagram of the normalization step as shown in Fig. 3.

**Table 1** Law basis with SQM of HAC

$x_t$	$\dot{x}_t$				
	S = 0.25	LS = 0.375	W = 0.5	LL = 0.625	I. = 0.75
S = 0.25	VS = 0.125	VS = 0.125	S = 0.25	LS = 0.375	W = 0.5
LS = 0.375	VS = 0.125	S-0.25	LS-0.375	W-0.5	LL = 0.625
W = 0.5	S = 0.25	LS = 0.375	W = 0.5	LL = 0.625	L = 0.75
LL = 0.625	LS = 0.375	W-0.5	LL-0.625	L-0.75	VL = 0.875
L = 0.75	W = 0.5	LL = 0.625	L = 0.75	VL = 0.875	VL = 0.875

### 3.3 Law Base HA with SQM

The rule base with SQM of the language values in the HAC controller is illustrated in Table 1 with  $f_m(-c) = 0.5$  and  $\mu(h-) = 0.5$ .

### 3.4 Inference HA

The SQM values in the HAC rule system allow the representation of this rule system in geometric form to represent the relationship between the input state variables and the output control variables. These representations can be considered as inference methods of HAC instead of having to use three inference steps as in FC including: evaluating the influence of each rule, determining the conclusion of each rule, combining the conclusions to get the output fuzzy set. Here, the HA inference using the quantitative semantic curve using the multiplication (a) with the weights  $w_1, w_2$  and the quantitative semantic surface (b) for the HAC is clearly shown in Fig. 4.

## 4 Numerical Simulation

The detailed parameters of the system are as follows:

$$m_0 = 30 \text{ kg}; m_e = 725 \text{ kg}; C_1 = 4.9 \text{ Ns/m}; C_2 = 5.2 \text{ Ns/m}; K_1 = 1.9 \times 10^3 \text{ N/m}; K_2 = 2 \times 10^3 \text{ N/m}; c_1 = 3; c_2 = 1; k = 3.5; \eta = 5.$$

The two earthquakes used are Chalfant, Kokuji. The earthquake inputs are shown in Figs. 5a and 8a, respectively, with different properties. Figures 5b and 8b show the control force of the system when using the HAC controller. The driving force is proportional to the amplitude of the vibration of the earthquake.

The responses of the lower layer (unit B) shown in Figs. 6 and 9 are similar to those of the upper layer (unit T) shown in Figs. 7 and 10. It can be seen that when using the proposed controller, the displacement and acceleration of the lower and upper

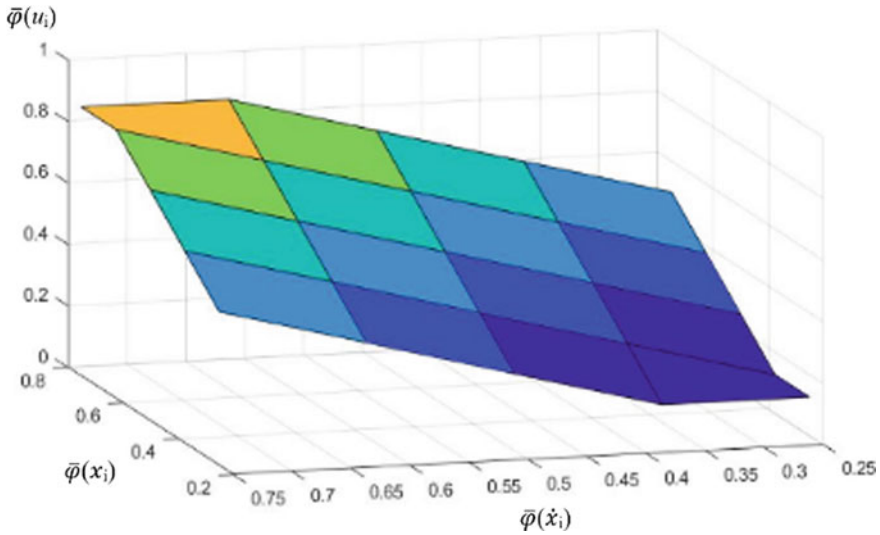


Fig. 4 Inference in HA

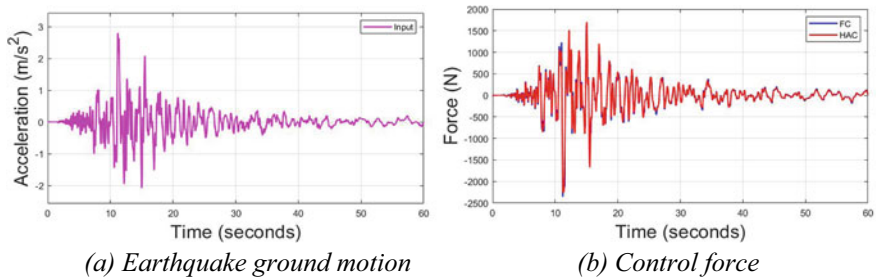


Fig. 5 Chalfant earthquake and control force

decks have been markedly reduced compared with No control. The effect is clearly seen from different earthquakes. Besides, HAC provides better results in terms of position and acceleration than FC. In the Chalfant earthquake, from Figs. 6 and 7, it can be asserted that even in the case where the acceleration response during free oscillation is greatest, the acceleration and displacement when using the controller for is still significantly reduced.

The amplitude of displacement of the upper stage is slightly larger than that of the lower layer. Acceleration is significantly reduced when vibrations are transmitted from lower to upper floors. This is important to ensure that the device is not destroyed. Shows the effectiveness of using a 2-stage isolation system.

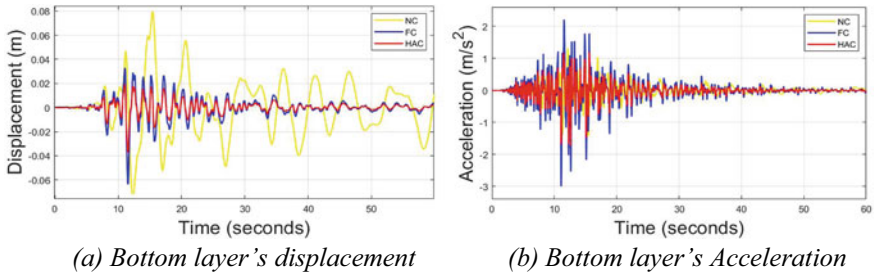


Fig. 6 Bottom layer's responses (Chalfant earthquake)

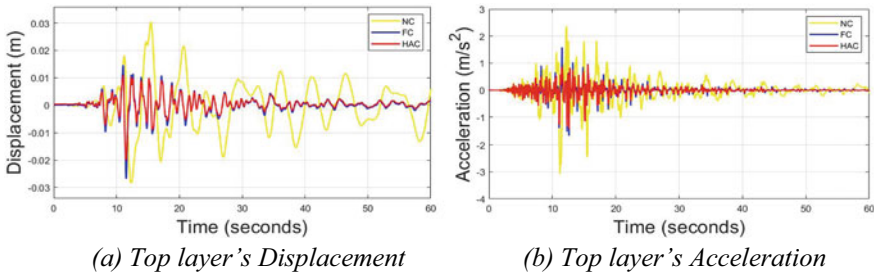


Fig. 7 Top layer's responses (Chalfant earthquake)

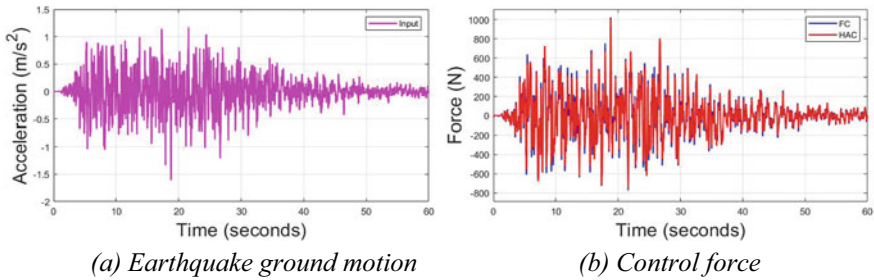


Fig. 8 Kokuji earthquake and Control force

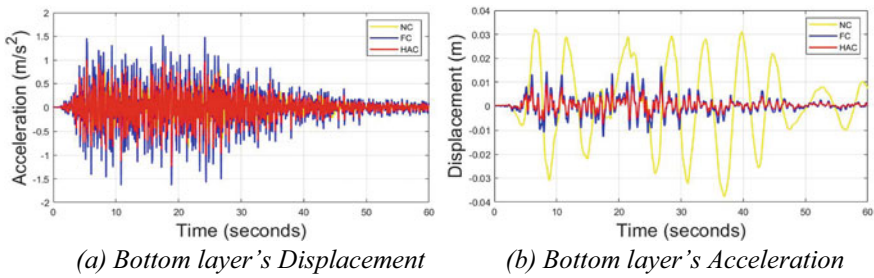
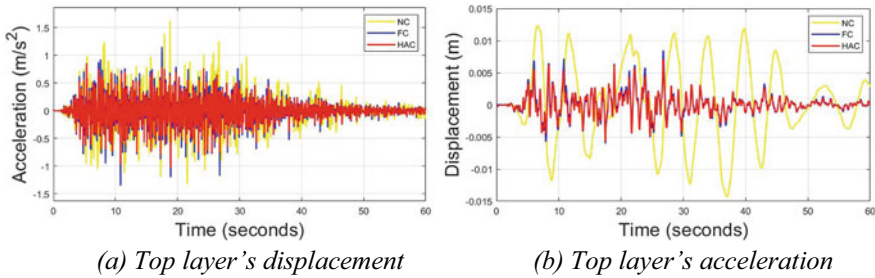


Fig. 9 Bottom layer's responses (Kokuji earthquake)



**Fig. 10** Top layer's responses (Kokuji earthquake)

## 5 Conclusion

The design of the 2-stage anti-vibration device and the HAC controller is shown in the article. The system has good performance when it significantly reduces both absolute displacement and relative acceleration. The numerical and experimental simulation results demonstrate the stability and practical applicability of the 2-stage seismic isolation system. HAC controllers achieve better performance than FC when subjected to different earthquakes. The system can continue to improve the control algorithm to improve control quality, as well as deploy the actual model in the future.

## References

1. Nguyen XB et al (2018) Modeling and semi-active fuzzy control of magnetorheological elastomer-based isolator for seismic response reduction. *Mech Syst Signal Process* 101:449–466
2. Munteanu RI et al (2021) Structural damage mitigation using a fuzzy controller. In: 2021 23rd international conference on control systems and computer science (CSCS), 393–400.
3. Bharath Kumar KR et al (2021) Particle swarm optimization tuned fuzzy controller for vibration control of active suspension system. *Springer Proc Mater* 5:115–125
4. Marji M, Harly, Mindarta ES (2020) Design and investigation of fuzzy control for independent full car suspension model in random road and braking excitation. *Int J Adv Sci Technol* 29:20–33
5. Azizi M, Ghasemi SAM, Ejlali RG, Talatahari S (2020) Optimization of fuzzy controller for nonlinear buildings with improved charged system search. *Struct Eng Mech* 76:781–797
6. Hu G et al (2017) Vibration control of semi-active suspension system with magnetorheological damper based on hyperbolic tangent model. *Adv Mech Eng* 9
7. Mohammadikia R, Aliasghary M (2019) Design of an interval type-2 fractional order fuzzy controller for a tractor active suspension system. *Comput Electron Agricult* 167
8. Kasemi B, Muthalif AG, Rashid MM, Fathima S (2012) Fuzzy-PID controller for semi-active vibration control using magnetorheological fluid damper. *Proc Eng* 41:1221–1227
9. Nguyen CH et al (1999) Hedge Algebras, linguistic-value logic and their application to fuzzy reasoning. *Int J Uncertain Fuzziness Knowl-Based Syst* 7:347–361
10. Nguyen Cat Ho (2007) A topological completion of refined hedge algebras and a model of fuzziness of linguistic terms and hedges. *Fuzzy Sets Syst* 158:436–451

11. Ho NC, Nam HV (2002) An algebraic approach to linguistic hedges in Zadeh's fuzzy logic. *Fuzzy Sets Syst* 129:229–254
12. Bui H-L, Tran N-A, Cao HQ (2023) Active control based on hedge-algebras theory of seismic-excited buildings with upgraded tuned liquid column damper. *J Eng Mech* 149(1):04022091

# Optimization of High Temperature Technology Parameters for 42CrMo Steel



Le Hong Ky

**Abstract** This paper presents research results on the influence of high annealing technology parameters on turbine shaft mechanical properties in turbocharger turbine structure made of 42CrMo steel. The study has established a regression equation showing the relationship between mechanical output factors according to high annealing technology parameters. The research has also determined the optimal value of the technological parameters when highly tempering the turbine shaft.

**Keywords** Hardness · Strength · Relative elongation · Yield strength · High tempering

## 1 Introduction

Turbocharger works with very high temperature, and the working speed is usually 100,000 rpm. The turbine shaft is an important part connecting the two turbine blades [1]. The manufacture of turbine blades is mainly by casting in metal molds [2, 3]. Casting process has been developed and progressively refined to provide a casting profile that requires minimal machining. In practice, the only turbine wheel machining undertaken in-house by Cummins Turbo Technologies is to ‘mass centre’ the hole in the nose of the wheel [4]. Friction welding was developed in the 1980s as a relatively low cost and reliable welding process, which proved ideal for attaching a turbocharger’s comparatively soft steel shaft to the much harder turbine wheel investment casting [4, 5]. EMAG Corporation [6] introduces the automatic production of turbine shafts. Specifically, in the heat treatment part, a robot picks it up from there and transfers it for heat treatment in a MIND-L 1000 from EMAG eldec, which very quickly and precisely heats the component to a specific temperature to relieve

---

L. H. Ky (✉)

Vinh Long University of Technology Education, Vinh Long City, Vietnam

e-mail: [kylh@vlute.edu.vn](mailto:kylh@vlute.edu.vn)



any possible stresses. Previously published studies [7, 8] mentioned the design and manufacture of turbine blades and [9] published the research results on the effects of temperature and heat retention time at high tempering of steam turbine. The material requires high tensile properties along with good impact strength for proper application. However, these two properties are inversely related to each other, i.e., the efforts to increase the tensile strength of materials result in a decrease in impact strength and vice versa. Therefore, one has to select the heat treatment parameters to maintain a good combination of these properties [10]. The most common and very useful test of mechanical properties of materials is a tension (a.k.a. tensile) test. Tension tests provide information on the strength and ductility of materials under uniaxial tensile stresses [11]. The author and his colleagues have had some of studies to design and manufacture important details of the turbocharger, including the turbine shaft [7, 8, 16].

To achieve the fine sorbite organization, the part must go through the high tempering and hardening stages [12]. The study focuses on the high tempering part. Selecting high tempering temperature of Temp\_R, according to [7, 8, 14, 15] with axial parts, because of working in continuous rotating condition at high speed, high pressure, high strength, as well as part material with microstructure of sorbite, in the experiment, the selected temperature range for planning is the two edges of the high tempering mode of 550 °C (the high temperature edge of low tempering) and 670 °C (the high temperature edge of high tempering). Selecting tempering time of time\_R, according to [7, 8, 14, 15] the minimum effective time when high tempering is 120 min, herein selected as the lower limit. The mechanical properties of the turbine shaft part to be achieved are the tensile strength and hardness. With 42CrMo steel, the heat retention time is up to 240 min to ensure that the Martensite and Austenite organizations residual after hardening is transformed into the desired Sorbite organization [9]. This study it is necessary to find the optimal mechanical properties of 42CrMo steel, so the temperature range is from 550 to 670 °C, and high tempering time is 120–240 min.

Among the types of quadratic planning, in the study, the quadratic symmetric mixture planning form of type B is selected. In particular, the output parameters that need to be studied are hardness (*HRC*) and tensile strength ( $\sigma_b$ ), respectively. The center experiment was chosen as 2 to keep the number of experiments to a minimum.

The Wilson Hardness, DX300 devices are used to measure the hardness, the ultimate strength, the yield limit and calculate the relative elongation [6–11] to obtain the results as in Table 1.

**Table 1** Results of the experiment

No	Temp_R	Time_R	$\overline{\sigma}_{0.2}$	$s_{\sigma_{0.2}}$	$\overline{\sigma}_b$	$s_{\sigma_b}$	$\overline{HRC}$	$s_{HRC}$	$\overline{\delta}$	$s_{\delta}$
1	550	120	1091	3	1111	4	38.95	0.18	71.5	0.3
2	670	120	908	12	928	12	23.85	0.48	75	0.2
3	550	240	1080	8	1093	7	37.75	1.24	72.1	0.1
4	670	240	868	12	888	14	22.5	0.52	75.6	0.2
5	550	180	1083	6	1100	4	38.38	0.85	72.3	0.1
6	670	180	893	12	913	13	23.25	0.4	75.9	0.3
7	610	120	958	13	973	7	31.7	0.51	72.5	0.2
8	610	240	930	12	947	13	30.9	0.36	73.1	0.1
9	610	180	945	13	964	13	31.72	0.6	73	0.2
10	610	180	939	13	959	13	31.62	0.24	73.2	0.1

## 2 Results and Discussion

### 2.1 The Output Parameter is HRC Hardness

Use Minitab software to analyze samples by experiment, remove unaffected coefficients, then recalculate the coefficients of the regression equation. The results of analysis of variance for the regression equation showing the influence of input parameters on the hardness of the test specimen have the following natural form [7]:

$$\begin{aligned}
 HRC = & -162.3 + 0.7390 * Temp\_R - 0.01144 * time\_R \\
 & - 0.000685 * Temp\_R * Temp\_R
 \end{aligned}
 \tag{1}$$

The graphs show that the higher the temperature (*Temp\_R*) is, the lower the hardness becomes, and it discussed a lot when the temperature is higher. When the time (*time\_R*) increases, the hardness of the part decreases, but it decreases slightly, Fig. 1.

### 2.2 The Output Parameter is the Ultimate Strength $\sigma_b$

By doing the above, the regression equation is determined as follows:

$$\begin{aligned}
 \sigma_b = & 6568 - 16.65 * Temp\_R - 0.2333 * time\_R \\
 & + 0.01234 * Temp\_R * Temp\_R
 \end{aligned}
 \tag{2}$$

The analysis shows that (Fig. 2), the higher the temperature (*Temp\_R*) is, the lower the ultimate strength gets, and it decreases a lot when the temperature is higher. The time (*time\_R*) increases, the ultimate strength of the part decreases.

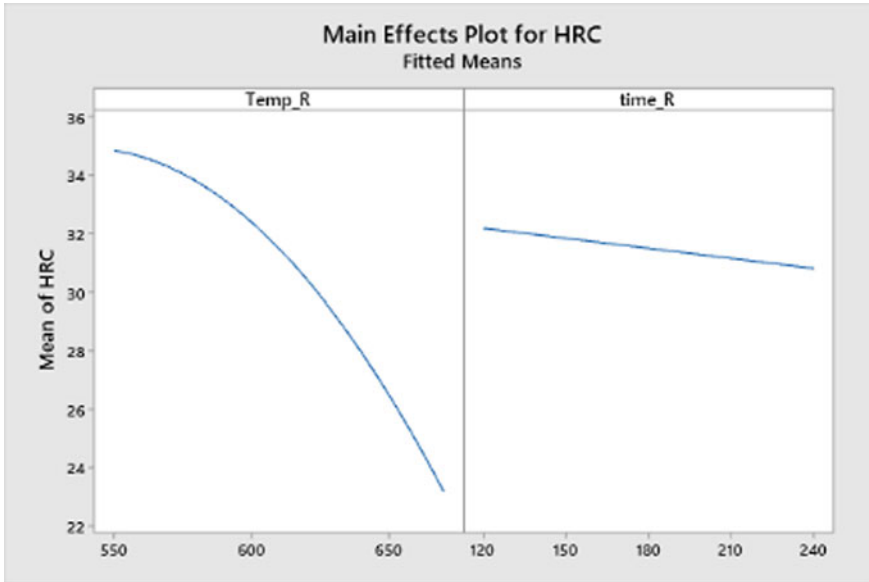


Fig. 1 The effect of parameters on HRC hardness

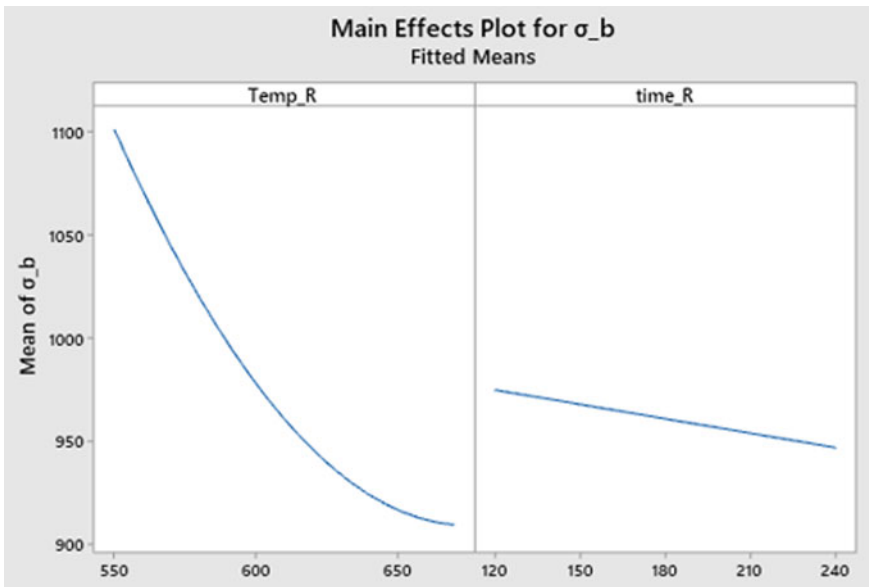


Fig. 2 The effect of parameters on the ultimate strength

### 2.3 The Output Parameter is the Relative Elongation $\delta$ and the Yield Limit $\sigma_{0.2}$

By doing the same, the regression equation characterizing the effect of the input parameters on the relative elongation of the test specimen has the natural form as Eq. (3). The regression equation characterizing the effect of the input parameters on the yield limit of the test specimen has the natural form as Eq. (4) [7] (Figs. 3 and 4).

$$\begin{aligned} \delta = & 121.4 - 0.4199 * Temp\_R + 0.0725 * time\_R \\ & + 0.000383 * Temp\_R * Temp\_R \\ & - 0.000180 * time\_R * time\_R \end{aligned} \tag{3}$$

$$\begin{aligned} \sigma_{0.2} = & 6339 - 16.30 * Temp\_R + 1.008 * time\_R \\ & + 0.01232 * Temp\_R * Temp\_R \\ & - 0.002014 * Temp\_R * time\_R \end{aligned} \tag{4}$$

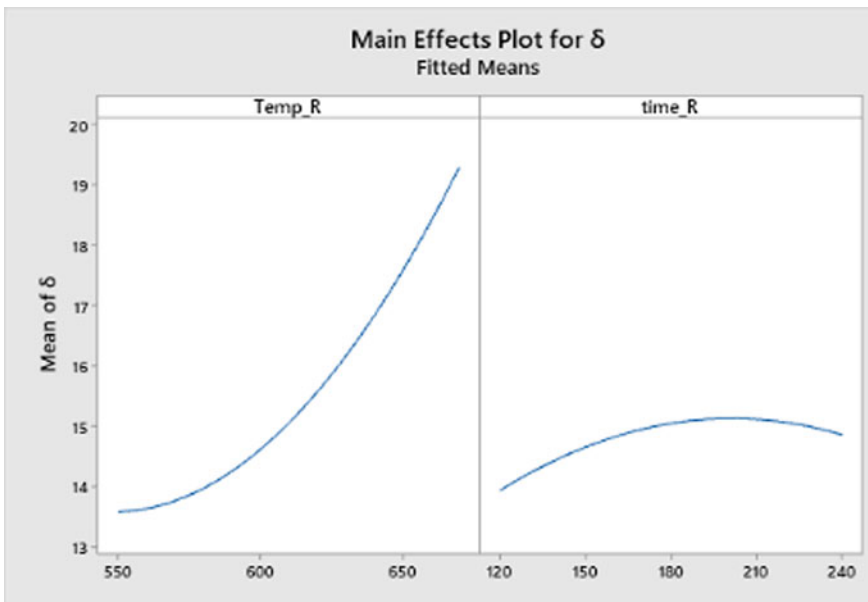


Fig. 3 The effect of parameters on the relative elongation

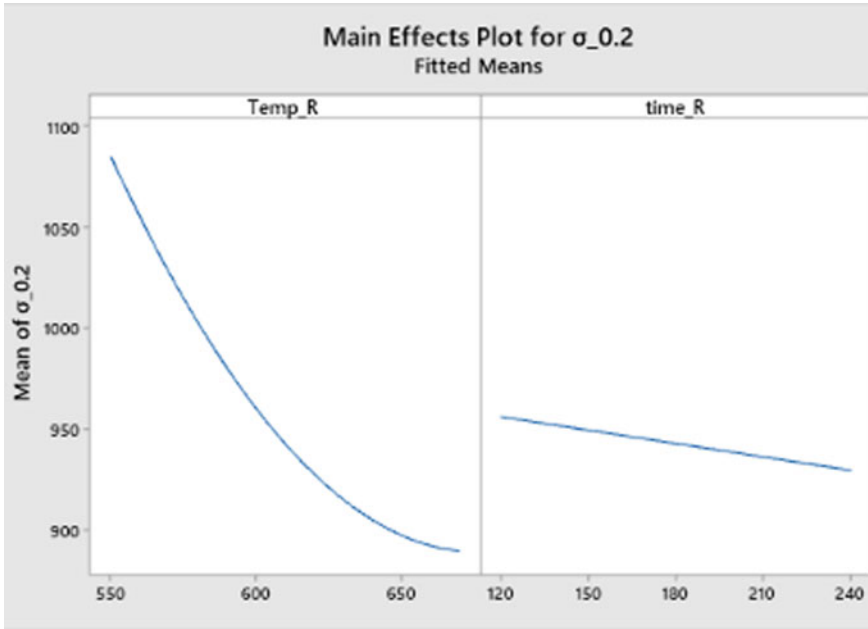


Fig. 4 The effect of parameters on the yield limit

Table 2 Table of permissible values of the results

Response	Goal	Lower	Target	Upper	Weight	Importance
$\sigma_b$	Target	877	1044	1115	0.1	1
$\sigma_{0.2}$	Target	857	1011	1095	0.1	1

### 2.4 Optimization of High Tempering Technology Parameters

Because the ultimate strength and yield limit are two important factors that determine the quality of turbine shaft during working, optimization of these two parameters has been carried out (Table 2).

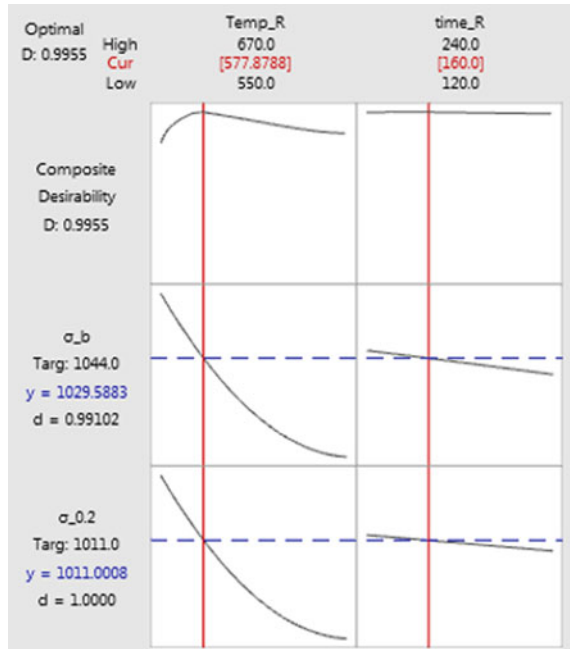
Boundary conditions for input variables are set:

$$550 \leq \text{Temp\_R} \leq 670$$

$$120 \leq \text{time\_R} \leq 240$$

Minitab software is used to calculate the optimal value (Fig. 5):

**Fig. 5** Compatibility function diagram



Solution	Temp_R	Time_R	$\sigma_b$ Fit	$\sigma_{0.2}$ Fit	Composite desirability
1	577,879	160	1029,59	1011,00	0,995,497

The item “Composite Desirability” has a value of 0,995,497. According to the optimization theory [6], it can be concluded that this optimal result is appropriate.

The optimal value to choose for retesting is:

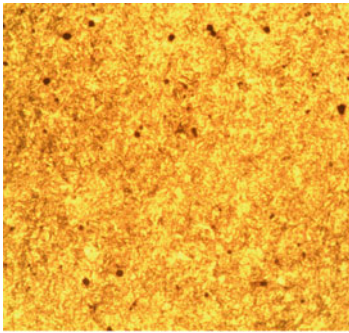
<i>Temp_R</i>	578
<i>time_R</i>	160

The suitability is checked by substituting the above optimized tempering temperature and time with the regression equation to test the hardness (2) and the relative elongation (4), which shows that these values correspond to the original base of the sample shaft. High tempering, tensile test, hardness measurement and microscopic organization review were carried out with the results:

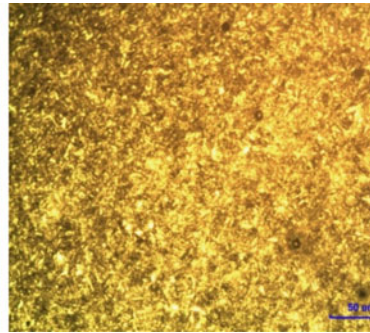
$$\begin{aligned} \sigma_{0.2} &= 985 \text{ N/mm}^2 \\ \sigma_b &= 1027 \text{ N/mm}^2 \\ \text{HRC} &= 30.35 \\ \delta &= 15.8\% \end{aligned}$$

**Table 3** Table comparing the results of sample and optimally calculated parts

Sample parts	Parts with optimal parameters
$\sigma_b = 1044 \text{ N/mm}^2$	$\sigma_b = 1027 \text{ N/mm}^2$
$\sigma_{0.2} = 1011 \text{ N/mm}^2$	$\sigma_{0.2} = 985 \text{ N/mm}^2$
$\delta = 14,3\%$	$\delta = 15,8\%$
$HRC = 28 -32$	$HRC = 30,35$



(a) The research turbine shaft



(b) The sample turbine shaft

**Fig. 6** The microscopic organization

The values of the yield strength, the ultimate strength, the relative elongation and the hardness are compared with the matched sample parts of the HX40W turbo set as shown in Table 3.

The comparison results show that the high tempered turbine shaft with the optimal set of parameters with the mechanical properties is equivalent to the sample turbine shaft of the HX40W turbo set. In order to increase the reliability, the microscopic organization review of the study sample was conducted with the optimal pair of temperature and time parameters, Fig. 6.

### 3 Conclusion

This paper presents the research results on the effects of high tempering technology parameters on the mechanical properties of turbine shafts made of 42CrMo steel. The study has established the regression equations showing the relationship of the yield limit ( $\sigma_{0.2}$ ), the ultimate strength ( $\sigma_b$ ), the hardness ( $HRC$ ) and the relative elongation ( $\delta$ ) according to the tempering temperature ( $Temp\_R$ ) and the tempering time ( $time\_R$ ).

The optimal technology parameters when high tempering are determined: the tempering temperature is 578 oC and the tempering time is 160 min. These are the optimal values to ensure the mechanical properties of the turbine shaft in terms of

the yield limit, the ultimate strength, the hardness and the relative elongation. The optimal parameters were tested again with the test specimen to compare with the turbine shaft model of the HX40W turbocharger.

After high tempering, the hardness decreases very sharply; the steel becomes relatively soft, and the strength decreases but achieves the best combination of the mechanical properties of strength, ductility, and toughness.

## References

1. Sajjad Seifoori, Ahmad Mahdian Parrany, Mojtaba Khodayari, *A high-cycle fatigue failure analysis for the turbocharger shaft of BELAZ 75131 mining dump truck*, Mechanical Engineering Dept, Faculty of Engineering, Vali-e-Asr University of Rafsanjan, Iran.
2. Takeuchi Y, Watanabe T (1992) Generation of 5-Axis Control Collision-Free Tool Path and Post-Processing for NC Data. *CIRP Ann* 41:539–542
3. QingZhen Bi, Hua Chen, Xueqi Zou, LiMin Zhu, Han Ding, *Five-Axis Flank Milling for design and Manufacture of Turbocharger Compressor Impeller*, Proceedings of ASME Turbo Expo, Turbine Technical Conference and Exposition (2014) 1–11.
4. Information on <https://teamafw.com/dissimilar-metal-shape-welding/turbine-to-shaft-welding.html>.
5. Information on [https://dieselnet.com/tech/air\\_turbocharger.php#turbine](https://dieselnet.com/tech/air_turbocharger.php#turbine).
6. Information on <https://www.emag.com/blog/en/finish-machining-turbocharger-shafts/>
7. Nga TTV (2022) Le Hong Ky, Nguyen Ngoc Nhan, and Tran Vinh Hung, *A Study on the Effects of Temperature and Heat Retention Time at High Tempering on the Hardness and Strength Limit of the Turbine Shaft Made of 42CrMo Steel*, ICERA 2021. LNNS 366:117–127. [https://doi.org/10.1007/978-3-030-92574-1\\_12](https://doi.org/10.1007/978-3-030-92574-1_12)
8. Nguyen Ngoc Nhan (2022) Nguyen Chi Thong, Nguyen Hoang Thien, and Le Hong Ky, *Optimization of Grinding Technology Parameters to Surface Roughness and Material Extracting Productivity of Turbine Shaft Parts*, ICERA 2021. LNNS 366:721–730. [https://doi.org/10.1007/978-3-030-92574-1\\_74](https://doi.org/10.1007/978-3-030-92574-1_74)
9. Wei-ZeWang, Fu-ZhenXuanKui, LongZhuShan, TungTu, *Failure analysis of the final stage blade in steam turbine*, School of Mechanical and Power Engineering, East China University of Science and Technology, P.O. Box 402, Shanghai 200237, PR China.
10. Kindo, Ajit Kumar and Goel, Rajesh, *Optimization of heat treatment of steel developed for turbine shafts*. BTech thesis 2012.
11. J.Paulo Davim, *Introduction to Mechanical Engineering*, Springer, ISSN 2195–0911 ISSN 2195–092X (electronic) Materials Forming, Machining and Tribology ISBN 978–3–319–78487–8 ISBN 978–3–319–78488–5 (eBook) <https://doi.org/10.1007/978-3-319-78488-5>.
12. William E Bryson, *Heat treatment, selection, and application of tool steels*, 2nd Edition, Hanser Publishers, Cincinnati, 2013
13. Manual Rockwell 574, Regular, Superficial, and Twin Scale Testing, Wilson Hardness is an Instron ITW Company.
14. Antony Jiju, *Design of Experiments for Engineers and Scientists*, Edition 2nd, Publisher 2014.
15. Nguyen Ngoc Ha, *Building heat treatment mode*, HCMUT-VNU-HCM, 2018.
16. Tran Vinh Hung (2022) Ta Van Ranh, Tran Thi Van Nga, and Le Hong Ky, *Research and Test of the Self-designed and Manufactured Rotary Friction Welding Machine with CT3 Steel Samp*, ICERA 2021. LNNS 366:799–812. [https://doi.org/10.1007/978-3-030-92574-1\\_82](https://doi.org/10.1007/978-3-030-92574-1_82)



# Study on Recycling of Chrome-Tanned Leather and Agriculture Waste for Insole Towards Sustainable Development



Vu Dinh Giap

**Abstract** Currently, the world towards the use of recycled materials from industrial agricultural waste not only contributes to economic development but also contributes to environmental protection—sustainable development. Use of agricultural wastes such as rice straw, rice husk, wood fibers, etc. as additives are increasing. In this study, the potential use of industrial from leather tanning (chrome tanning shavings, CTS) and agricultural wastes (rice husks, RH) as a additive materials for insole for shoe. Thermoplastic rubber (TPR) is selected as the substrate polymer for the synthesis of new materials. CTS released from leather tanning and rice husks from agricultural activities were used in powder form with various percentage to synthesize different composites. These composites were tested for various mechanical properties as hardness, specific gravity, tensile strength, abrasion and tear strength. The addition of any filler improves the mechanical properties of the material. The results showed, rice husk powder (5%, w/w) and chrome tanning shavings (20%, w/w) were the appropriate concentrations studied. The mechanical properties have been determined in insole such as specific gravity ( $0.895 \text{ g/cm}^3$ ); hardness (69 shore A); tensile strength ( $58 \text{ kg/cm}^2$ ); abrasion ( $189 \text{ mm}^3$ ) and tear strength ( $33 \text{ kg/cm}$ ). Rice husk make the material properties better than no filler composite. This contributes to promoting the development of recycled materials towards sustainability in the future.

**Keywords** Chrome tanning shavings · Rice hurk · Chrome-tanned leather waste · Agricultural wastes · Shoe insole · Composite materials

---

V. D. Giap (✉)

HaUI Institute of Technology, Hanoi University of Industry (HaUI), Hanoi, Vietnam

e-mail: [gjapvd@hau.edu.vn](mailto:gjapvd@hau.edu.vn)

## 1 Introduction

The leather tanning industry has generated many negative impacts to the ecological environment. During the production process, an enormous amount of solid waste is emitted from these activities. According to the estimates, one ton of raw leather (includes salted skin, fresh skin, etc.) can only produce 250 kg (25%) of leather products [1]. In which, 75% of that waste, includes wastes emitted in the process and production (chromium tanning shavings, splits, trimmings, finished leather wastes) and the used leather wastes (used bags, jackets, purses, etc.). Chromium tanning shavings (CTS) approximately 9–15%. The composition of the CTS includes (dry weight): moisture (46%), ash content (7.5%), total nitrogen (14.65%),  $\text{Cr}_2\text{O}_3$  (2.1%), protein (91.6%) and pH 3.4 [2]. Among the solid wastes generated in the leather tanning process, CTS waste is the greatest threat to the environment. Presently, the above waste source is recycled into various useful products with economic value such as: gelatin glue, biological fertilizer, animal feed, hydrolyzed collagen, composite materials, etc. [4]. Therefore, the treatment of these wastes becomes an urgent problem for the domestic and foreign leather tanning industry. Besides leather tanning waste, agricultural waste is discharged with a huge amount of waste. Their main component is lignocellulose. The polymers in the structure of lignocellulose are cellulose, hemicellulose and lignin. In addition, other components are also found in this structure such as ash, pectin and protein. It is considered as a rich source of raw materials in the world. In plant cell wall structure, the average amount of cellulose is from 40 to 65%, hemicellulose from 20 to 30% and lignin from 15 to 20% with different percentages depending on the plant species [5]. Annual domestic agro-industry production of hundreds of millions of tons of lignocellulose-rich by-products is an extremely abundant source of materials. On the other hand, it solves the problem of environmental pollution caused by not being treated or exclusion by traditional methods. Millions of tons of lignocellulose are produced in the world mostly as a non-commercialized waste product per year [6]. In Vietnam, this annual rice production leaves estimated 50 million tons of dry rice straw per year, so the biomass obtained from the rice husks is very large, which has attracted research ideas to make use of it as renewable resource for the production of composite materials. However, at the moment still a major part of this raw material is getting lost through burning directly on the fields or composting material. Therefore, shoe insole production from as rice husk is a good solution especially for countries with agriculture like Vietnam. Hence, possible conversion of both forms of wastes into value added products will not only help to save the environment, but also prove to be income generating [7]. The goal was to studies the use of a hot compression moulding process to prepare the composites based on chrome-tanned leather waste (chrome tanning shavings, CTS), thermoplastic rubber and agricultural wastes (rice husks, RH) into a useful product (insole), thereby reducing environmental pollution. The main problems of this composites are related to the hydrophilic properties of the cellulose fiber structure from rice husk. To overcome these problems, it is necessary to modify the fiber surface to reduce the hydrophilic nature of the rice husks. The performance and stability of composite

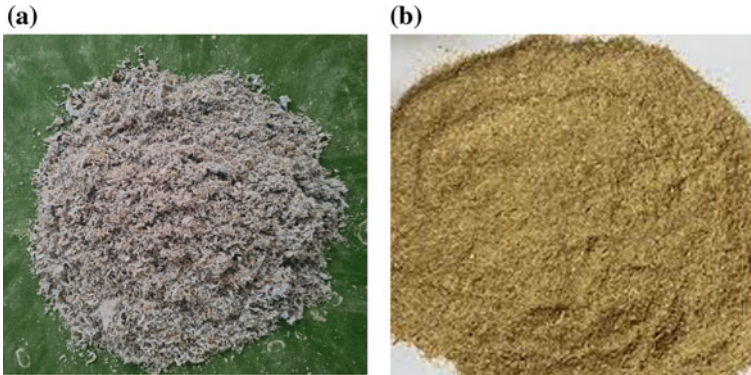


**Fig. 1** Chromium tanning shavings waste from chrome-tanned leather (A, 0.5–1 mm) and rice husk powder from agricultural waste (B, 0.7–1.5 mm)

materials for insole depends on the degree of coherent interfacial bonding between rice husks, CTS and thermoplastic rubber [8]. The product was characterized for mechanical properties such as tensile strength, abrasion, tearing strength, specific gravity and hardness.

## 2 Materials and Methods

### 2.1 Materials

Thermoplastic rubber (TPR) was purchased from LCY chemical CORP (Taiwan). Chromium tanning shavings (CTS) were collected from leather tanning technology center, Leather and Shoe Research Institute, Hanoi, Vietnam. It is milled to size ranged approximately 0.5–1 mm in diameter.

Rice husks (RH) were collected from Dong Anh district, Hanoi, Vietnam (Fig. 1). RH is dried then ground powder (0.7–1.5 mm). RH contains 23–30% lignin, 10–15% moisture, 34–44% cellulose and 13–39% ash [9].

### 2.2 Testing Methods

#### 2.2.1 Specific Gravity

Specific gravity is defined as the ratio of material's density to the density of water at 23 °C. Specific gravity is a measurement of the ratio of the mass of a material to the mass of an equivalent volume of water [10]. It is common to use the density of

water as a reference point as water at this point has the highest density of 0.99576 g/cm<sup>3</sup>. Specific gravity of a material can be calculated by following equation:

$$\text{Specific gravity (g/cm}^3\text{)} = \text{Density (at 23 }^\circ\text{C)} / 0.99576$$

### 2.3 *Hardness*

The hardness is determined by resistance to indentation under a specified load. Shore A is used to measure the hardness of soft elastomers (10–80 shore A) and shore D is used to measure the hardness of hard elastomers (> 80 shore A) [11].

### 2.4 *Tensile Strength*

Tensile strength can be defined as the maximum stress that a material can bear before breaking when it is allowed to be stretched [12].

$$\text{Tensile strength (kg/cm}^2\text{)} = \frac{FP}{T * W}$$

FP Maximum load of the test sample.

T Thickness of the test sample.

W Width of the test sample.

### 2.5 *Abrasion*

Abrasion is the process of rubbing [13].

$$\text{Abrasion (mm}^3\text{)} = \frac{(W1 - W2) * 200}{219 * \text{Specific Gravity}} * 1000$$

W1 The initial weight of the specimen is measured.

W2 The final weight of the specimen is measured.

## 2.6 Tear Strength

Tear strength is the ability to resist the tearing force of a cut on a specimen when tension is applied. This force is determined by dividing by the thickness of the sample [14].

$$\text{Tear strength(kg/cm)} = \frac{FP}{T}$$

FP Maximum load during test sample.

T Thickness of the test sample.

## 2.7 Experimental Model

Fabrication of shoe insole was done by CTS, RH and TPR. CTS and RH powder were used 10%, 20%, 30% and 5%, 10%, 15%, respectively. Thermoplastic rubber approx. 60% was used as binder. Moreover, the composition of mixing additives includes: (1)—vulcanizers and vulcanization accelerators are zinc oxide (ZnO, 2%), mercaptobenzothiazole (MBT, 0.5%), dibenzothiazole disulfide (DM, 0.8%) and sulfur (S, 1%); (2)—anti-aging agent (butylated hydroxytoluene, BHT, 0.6%) and (3)—fatty acids (stearic acid, 0.6%) are used as zinc salts to enhance the dispersion of zinc oxide. The mixing process is carried out on a heat press machines at 70°C (No 09001, KS, Taiwan). Raw material for the test production of shoe soles is cut into small pieces of size 4 × 7 cm, a weight of 100 g. Then, it is put into a hot stamping machine to vulcanize at 140 °C, for 5 min. All experiments were repeated three times.

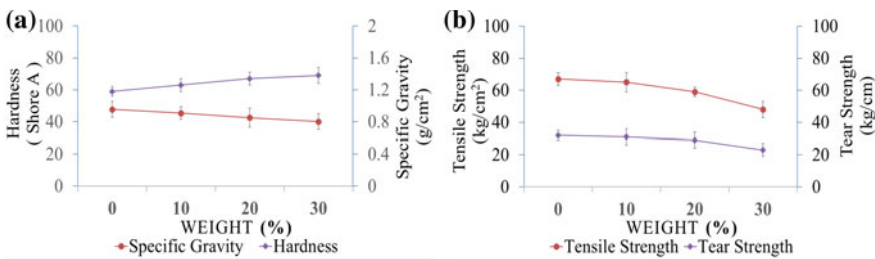
## 3 Results and Discussion

### 3.1 Chromium Tanning Shavings for Shoe Insole

This study evaluates various mechanical tests on composite materials. It was made of thermoplastic rubber (TPR) as the polymeric substrate and chromium tanning shavings (CTS) as the filling material for insole. In which, CTS is adjusted from 10 to 30%, the data showing the results is shown in Figs. 2 and 3.

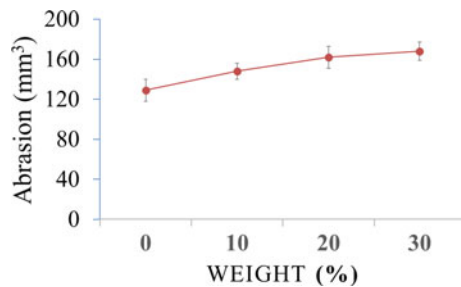
Figure 2a showed, test results of composite materials of TPR as the substrate polymer with different concentrations of CTS for the synthesis of new materials. Specific gravity of 30% weight (0.802%) is lower than control sample of 0% (0.954) when the loading of CTS is increased from 10 to 30%. Meanwhile, hardness increased from 10% (63 shore) to 30% (69 shore), so the fillers CTS harden the material. Due

to the non polar CTS, increase from its concentration has led to decrease from tensile strength and tear strength. They decreased the most at 30% weight (48 and 23 kg/cm), but both are better when CTS are added to 20% (59 and 29 kg/cm), respectively (Fig. 2b). However, the abrasion increases when CTS increases from 10 to 30%, the highest value is 168 mm<sup>3</sup> at 30% weight (Fig. 3). Thus, based on tensile strength and tear strength, it has been determined that the suitable concentration of CTS to make insole is 20% weight. Considering the properties of composites for shoe insole, it can explain that chromium tanning shavings and thermoplastic rubber contributes to the elastic properties of materials. When it was added to the composites, it tends to increase the abrasion. However, when the CTS content exceeds 20% by dry weight of the material, it will inhibit the coagulation process and reduce the adhesion of the rubber to other ingredients and lead to a decrease in the tensile strength of the material. In addition, CTS reduces the water absorption value, which is highly recommended for footwear, as it helps to maintain a dry product surface [15]. So, CTS weight (20%) was used. CTS is proven to improve the required parameters and properties of insole materials. Thus, chromium tanning shavings is evaluated as a potential material for applications to produce leather and footwear.



**Fig. 2** Specific gravity, hardness (a) and tensile strength, tear strength (b) for insole with CTS (10–30%)

**Fig. 3** Abrasion for insole with CTS (10–30%)



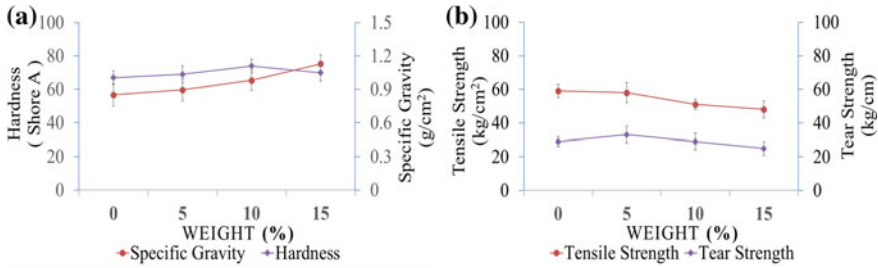


**Fig. 4** Specific gravity, hardness gravity (a) and tensile strength, tear strength (b) for insole with CTS (20%) and RH (0–15%)

### 3.2 Insole Composite from a Mixture of Rice Husk and Chromium Tanning Shavings

In this content, CTS was kept fixed 20% of weight from previous study, three different concentrations of RH (5%, 10% and 15%) were used as an additive for material. The results of this study are showed in Figs. 4 and 5.

Figure 4 showed, the various mechanical tests sample on composites of RH combines with CTS and TPR. Concentration of RH is adjusted from 0 to 15%. The results of this study are showed that, specific gravity increased from 5% of weight RH (0.896 g/cm<sup>2</sup>) to 15% (1.130 g/cm<sup>2</sup>), hardness increases slightly when increasing husk from 5 to 10% and then decreases when RH is higher than 10% (Fig. 4a). Especially, tear strength increases until 10% loading and decreases to 15%. Tensile strength decreases slightly to 5% loading with rice husk and decreasing steeply to increased loading into 15% or even higher concentration (Fig. 4b). Abrasion increases when RH is higher than 10% (Fig. 5a). Therefore, concentrations of RH higher than 5% are not appropriate in the TPR matrix. In addition, the product has a smooth surface and uniform color (Fig. 5b). Rice husks are used suitable for shoe insole (footwear) applications that increase product durability. All materials used to gave positive results in terms of parameters are checked. In general, the addition of additive materials leads to an increase in terms of tear strength, hardness, abrasion and decrease in tensile strength. Thus, 5% of rice hurk and 20% of chromium tanning shavings have shown positive results.

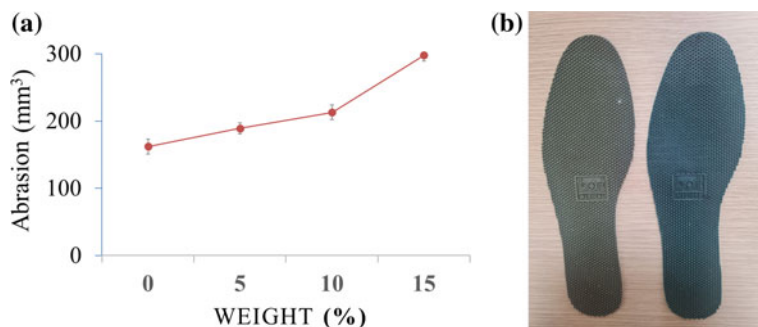


**Fig. 5** Abrasion for insole (a) with CTS (20%), RH (0–15%) and Insole products (b) with CTS (20%), RH (5%)

## 4 Conclusion

This study investigates that the potentials for chromium tanning shavings from leather tanning and rice husk from agricultural wastes were prepared to use thermoplastic rubber as a binder, fabricated insole using cellulose fiber from rice husk (5%) without pretreatment. These material mixture is made by mixing with chromium leather shavings (20%), thermoplastic rubber (approx. 60%) and other additive materials. In addition, additives are also added to the raw material mix and then pressed to shape the material. The thickness of the insole from 8 to 15 mm. Raw materials about 85% by weight of the product. The remaining material consists of sulfur, vulcanization accelerator and other compounds (approx. 15%). The mechanical properties have been determined in shoe insole such as specific gravity ( $0.895 \text{ g/cm}^3$ ); hardness (69 shore A); tensile strength ( $58 \text{ kg/cm}^2$ ); abrasion ( $189 \text{ mm}^3$ ) and tear strength ( $33 \text{ kg/cm}$ ). Recycling raw materials as industrial waste contributes to promoting the development of recycled materials towards sustainability in the future.

## References

1. Getahun H (2017) Value added protein products from chrome shavings
2. Cabeza LF, Taylor MM, Carrio R, DiMaio GL, Brown EM, Celma PJ, Cot J, Marmer WN (1998) Processing of leather waste: pilot scale studies on chrome shavings. Isolation of potentially valuable protein products and chromium. *Waste Manage* 18:211–218
3. Ferreira MJ, Almeida MF (2011) Recycling of leather waste containing chromium—a review. *J Mater Sci Res* 5:327–381
4. Dixit S, Yadav A, Dwivedi PD, Das M (2015) Toxic hazards of leather industry and technologies to combat threat: a review. *J Clean Prod* 87:39–49
5. Shirosaka (1993) Structure and chemical composition of wood as a natural composite material. *Curr. Japanese Mater Res* 1–20
6. Girio FM, Fonseca C, Carvalheiro F, Duarte LC, Marques S, Bogel R (2010) Hemicelluloses for fuel ethanol: a review. *Biores Technol* 101:4775–4800



7. Abba HA, Nur IZ, Salit SM (2013) Review of agro waste plastic composites production. *J Minerals Mater Character Eng* 01:271–279
8. Rajaram J, Rajnikanth B, Gnanamani A (2009) Preparation, characterization and application of leather particulate-polymer composites (LPPCs). *J Polym Environ* 17:181–186
9. Sarkawi SS, Aziz Y (2003) Ground rice husk as filler in rubber compounding 39:135–148
10. ASTM International (2013) ASTM D792–13 standard test methods for density and specific gravity (relative density) of plastics by displacement
11. ASTM International (2010) ASTM D2240–05 standard test method for rubber property-durometer hardness 09.01
12. ASTM International (2013) ASTM D412–06a Standard test methods for vulcanized rubber and thermoplastic elastomers—tensile strength
13. ASTM International (2010) ASTM D5963–04 standard test method for rubber property-abrasion resistance
14. ASTM International (2012) ASTM D624–00 standard test method for tear strength of conventional vulcanized rubber and thermoplastic elastomers
15. Senthil R, Hemalatha T, Kumar BS, Uma TS, Das BN, Sastry TP (2014) Recycling of finished leather wastes: a novel approach. *Clean Technol Environ Policy*

# Influence of Recrystallization Annealing on the Microstructure and Ductility of Al–Zn–Mg–Cu Alloy Added La, Ce



Bùi Thi Ngoc Mai

**Abstract** This article presents about the influence of recrystallization annealing temperature on the microstructure and ductility of Al–Zn–Mg–Cu alloy. This alloy was modified by La and Ce, uniformly annealed and cold rolled with 275%. After the cold rolling process; the structure of the alloy has a grain size of less than 10  $\mu\text{m}$ . The alloy is heated at the other recrystallization annealing temperature for 2 h. Research results show that with recrystallization annealing temperature at 450 °C for 02 h; the microstructure of this alloy is  $\alpha$  phase which has a grain size of less than 10  $\mu\text{m}$ ; the structure of the alloy is uniform. In addition, the intermetallic phase  $\text{Al}_{11}\text{Ce}_3$  and  $\text{Al}_3\text{La}$  are finely dispersed in the matrix. With the structure of this alloy, the ductility of the alloy reaches 667% when tensile is performed at 400 °C. The mechanism of high ductility has also been determined for Al–Zn–Mg–Cu alloy as the grain fine mechanism; uniform and dispersed high hardness particles which increased ductility of the studying alloy.

**Keywords** Recrystallization annealing · Grain size · Intermetallic · Ductility

## 1 Introduction

Recrystallization is a process in that deformed grains are replaced by strain-free and equiaxed grains; these grains will be nucleated and grow until the initial grain is completely lost.

Studies on thermo-mechanical effects [1, 2] on high ductility with different tensile speeds were presented. The studying alloy system is Al–Zn–Mg–Cu which are divided into 2 groups: group A has 0.15% Sc and group B has 2.8%Ni. The samples were molded in sheets and homogenized at 450 °C (for both samples A and B) and

---

B. T. N. Mai (✉)

School of Mechanical Engineering, Vietnam Maritime University, Hai Phong, Vietnam  
e-mail: [maibtn@vmaru.edu.vn](mailto:maibtn@vmaru.edu.vn)

then at 500 °C (for sample B) then rolled at  $410 \pm 10$  °C. The plate thickness up to 1 mm. With the alloy has Ni, the elongation is 450–480% at a constant strain rate between  $10^{-2}$  and  $10^{-1}$  s<sup>-1</sup>, but the alloy with Sc the elongation has from 300 to 600% at much smaller strain rates  $10^{-3}$ – $10^{-2}$  s<sup>-1</sup>. The study uses an alloy sheet of 7075–T651 with a thickness of 4 mm that is treated with friction welding [3]. The microscopic structure of the sample in the weld region showed fine recrystallization with the grain size of 4.65 μm. The maximum elongation to failure reaches 900%.

Studies on ductile behavior [4–6] of 7055 aluminum alloy. Casting and pouring directly through metal molds and homogenizing annealing at 470 °C for 24 h then going through 2 steps: Rolling down 70% at 410 °C then annealing to recrystallize in salt bath for 1 h, then quenching in water. Next, aging at 410 °C for 4 h and cooling at room temperature, then cold rolling to reduce 80%, finally annealing to recrystallize at 410 °C in a salt bath for 1 h. After recrystallization, the particle size is 11 μm and a coaxial shape. The other region consists of small surrounding particles with a size of 2 μm. Below is the development of the microorganism during the 450 °C deformation and the strain rate  $10^{-2}$  s<sup>-1</sup>. The recrystallization process continuously occurs in rolling process and create the superparticle grain.

The research group of R. Kaibyshev and colleagues at the Russian Academy of Sciences studied “High ductility behavior of 7055 aluminum alloy” [7]. The test was performed using alloy 7055 which was homogenized at 470 °C for 24 h and then subjected to a two-step heat treatment: Alloy 7055 was rolled to a 70% thickness reduction at 410 °C, then annealed, recrystallized at 450 °C in a salt bath for 1 h, then quenched in water. Over-aging was performed at 410 °C for 4 h, cooled slowly at room temperature, and then cold rolled to a 70% reduction in thickness. Final recrystallization incubation was performed at 450 °C in a salt bath for 1 h. The authors concluded that a partial recrystallization consists of fully recrystallized particles with an average size of 11 μm interspersed with recovered superparticles with an average size of 2 μm after 2 steps of Thermo-mechanical treatment. The maximum total elongation reaches 960% in the temperature range 400–490 °C, exponent  $m = 0.6$  at 450 °C and  $\dot{\epsilon} = 3.3 \times 10^{-4}$  s<sup>-1</sup>. At this temperature, the optimum range for high ductility to occur is  $8.3 \times 10^{-5}$ – $8.3 \times 10^{-3}$  s<sup>-1</sup>.

In this paper, the effects of recrystallization annealing process on microstructure and ductility of this alloy when adding La and Ce are presented in this paper.

## 2 Material and Method

### 2.1 Material

The Al–Zn–Mg–Cu modified by La, Ce alloys is studied in the current work. The compositions are given in below table.

Elements	Zn	Mg	Cu	Si	Fe	La	Ce	Al
%wt	5.6	2.1	1.56	≤ 0.34	≤ 0.24	0.21	0.16	–

### 2.2 Method

The alloy was deformed by warm rolling, the width reduces from about 6–2 mm. After that, the samples cutting off from this alloy were heated to recrystallization annealing at respectively 350 °C, 400 °C, and 450 °C for 2 h. With these temperature values are guaranteed for the new grains which have fine. These temperatures satisfy the theories for calculating recrystallization annealing temperatures. After the recrystallization annealing process, the sample with the size shown in Fig. 1 was tested tensile.

Tensile tests were performed at temperatures 400 °C and strain rates are at  $\dot{\epsilon} = 1.67 \cdot 10^{-4} s^{-1}$ . The equipment is a Devontrans testing machine shown in Fig. 2.

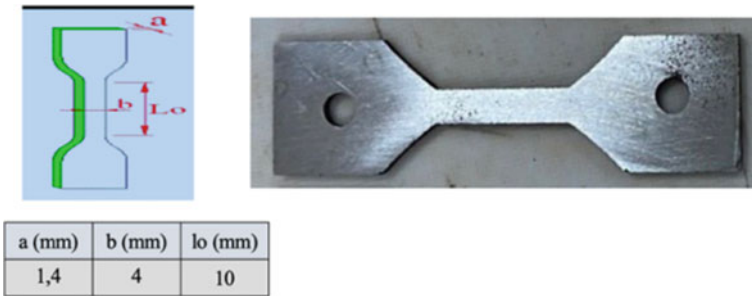


Fig. 1 The size of the tensile test sample

Fig. 2 The testing machine



### 3 Results and Discussion

In this work, La and Ce were compositely added into the Al–Zn–Mg–Cu alloy. The research focused on the influence of recrystallization on the microstructure and ductility of Al–Zn–Mg–Cu added La, Ce alloy. The addition of La, Ce with the optimal condition of recrystallization significantly reduces the grain size of Al–Zn–Mg–Cu—alloys because the  $\text{Al}_{11}\text{Ce}_3$  and  $\text{Al}_3\text{La}$  intermetallic phases have formed. Intermetallic, shown in Fig. 3. The  $\text{Al}_{11}\text{Ce}_3$  intermetallic phase, which is structurally similar to the  $\alpha$ -Al base phase, should act as the nucleation for the solidification. The  $\text{Al}_3\text{La}$  intermetallic phase plays a role in preventing the growth of matrix phases.

From the structural features of  $\text{Al}_{11}\text{Ce}_3$ , the bottom and side faces have the same structure as the bottom and side faces of phase  $\alpha$ -Al. Furthermore, the difference in crystal structure parameters of these is 8.3%. The lattice parameter value of  $\text{Al}_{11}\text{Ce}_3$  is 4.377 Å and the lattice parameter of  $\alpha$ -Al solid solution is 4.04 Å. Thus, it can be concluded that the  $\text{Al}_{11}\text{Ce}_3$  intermetallic phase plays the role of the nucleation for the solidification process of the studied alloy. Rare earth elements combine with aluminum to form the nucleation for the crystallization process, the more nucleation will make the grain finer because at this time, at the same volume, these nucleations grow more and faster. then the primary crystals of the zinc-aluminum substrate will be inhibited, leaving no room to grow.

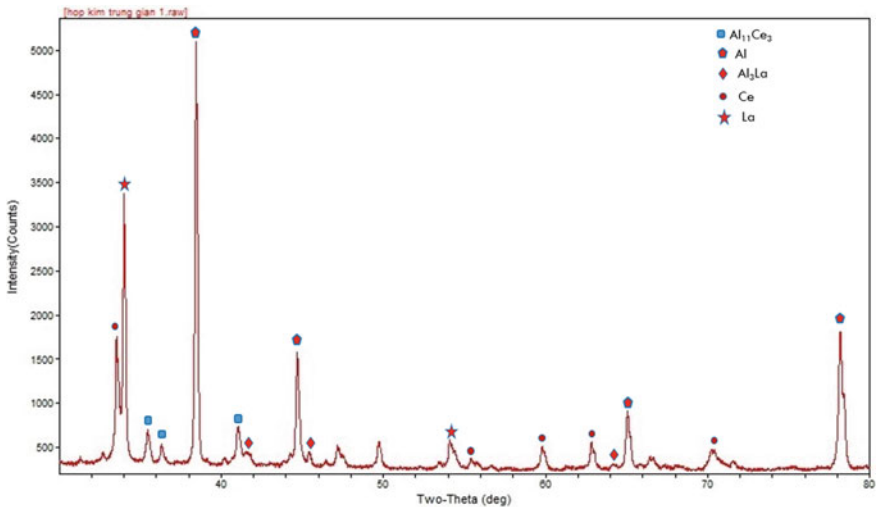


**Fig. 3** The X-ray results of intermetallic phases of the alloy Al–Zn–Mg–Cu–(La + Ce). Microstructure after crystallization

Compare with the grain structure at 350 °C, 400 °C, the average grain size of the alloy after annealing at 450 °C is the smallest. The number of crystallized grains at 350 °C is the fewest and at 450 °C is the most. In Fig. 4b, the coarse grains disappear, the microstructure includes fined and evenly grain, and the average size is about 10  $\mu\text{m}$  (Fig. 5).

The recrystallization has an influence on the ductility of the investigated alloy. The alloy before recrystallization has low ductility. After deformation process, the ductility of this alloy is 14%. Increasing the recrystallization temperature from 400 and 450 °C, the elongation sharply rises from 430 to 667%. At 450 °C, the elongation is at 667%. The values of the elongation are shown in Fig. 6.

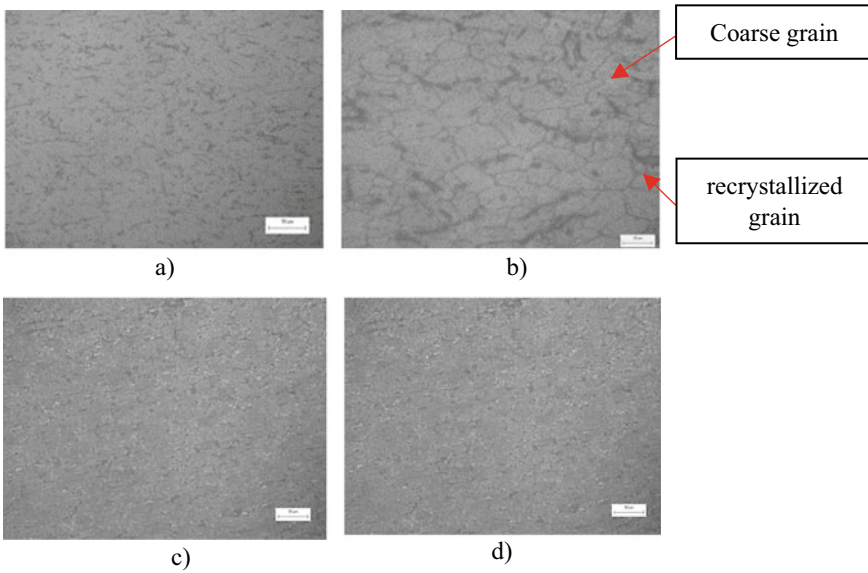


**Fig. 4** Microstructure of the alloy Al-Zn-Mg-Cu-(La + Ce). **a** After warm rolling **b** after recrystallization at 350 °C for 2 h **c** after recrystallization at 400 °C for 2 h. **d** after recrystallization at 450 °C for 2 h

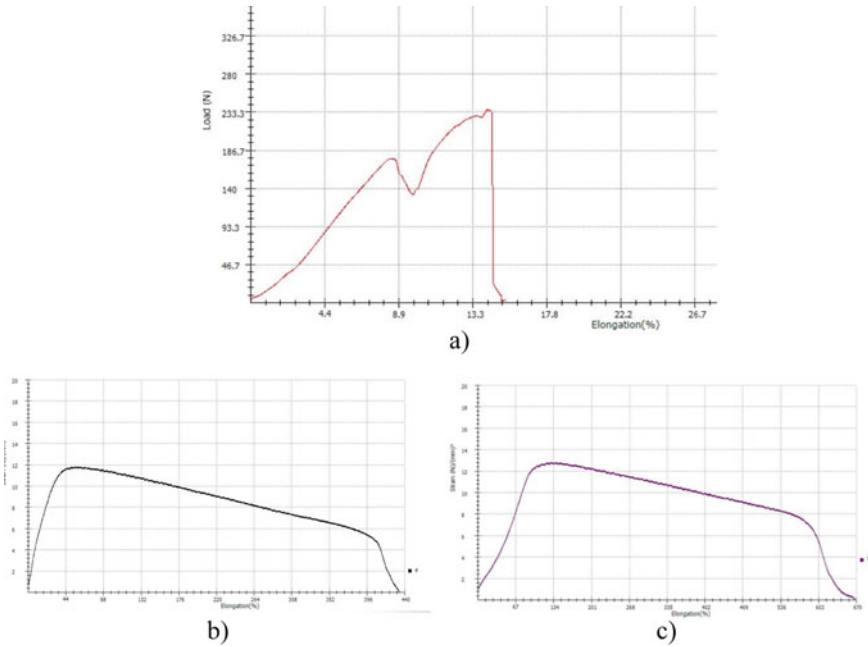


**Fig. 5** The tensile diagram of the sample with the strain rate of  $\dot{\epsilon} = 1.67 \cdot 10^{-4} \text{ s}^{-1}$  at tensile test temperature of 400 °C. **a** deformed sample, **b** sample crystallized at 400 °C, **c** sample crystallized at 450 °C

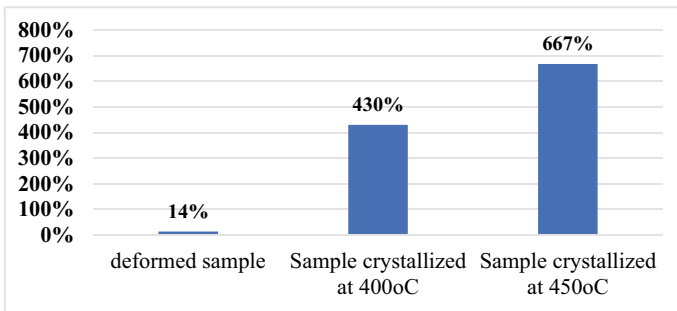


**Fig. 6** Effect of recrystallization on the ductility of the alloy

### 4 Conclusion

The present experimental results can be summarized as follows. A partially recrystallization structure consisting of coarse grains and recovered grains with a mean size of about 10–15  $\mu\text{m}$ . At 450 °C occurred completely recrystallized structure consisting

of fined and evenly grains with a size of about 10  $\mu\text{m}$ . At this temperature, the ductility of the alloy is the best with the elongation reaching the maximum at 667%.

## References

1. Bryukhovetsky VV, Myla DE, Poyda VP, Poyda AV (2020) Effect of homogenization on the superplasticity and microsuperplasticity of the Al–Zn–Mg–Cu aluminum alloy. *J Nano Electron Phys* 12(6):06025–1–06025–8. [https://doi.org/10.21272/jnep.12\(6\).06025](https://doi.org/10.21272/jnep.12(6).06025)
2. Mahidhara RK (1995) Superplastic flow and failure in a fine-grained 7475 al alloy. *Mater Lett* 25(3–4):111–116. [https://doi.org/10.1016/0167-577X\(95\)00142-5](https://doi.org/10.1016/0167-577X(95)00142-5)
3. Ma ZY, Liu FC, Mishra RS (2010) Superplastic deformation mechanism of an ultrafine-grained aluminum alloy produced by friction stir processing. *Acta Mater* 58(14):4693–4704. <https://doi.org/10.1016/j.actamat.2010.05.003>
4. Zhao H et al (2018) Segregation assisted grain boundary precipitation in a model Al–Zn–Mg–Cu alloy. *Acta Mater* 156:318–329. <https://doi.org/10.1016/j.actamat.2018.07.003>
5. Carreño F, Ruano OA (2018) Superplasticity of aerospace 7075 (Al–Zn–Mg–Cu) aluminium alloy obtained by severe plastic deformation. *Defect Diffus Forum* 385:39–44. <https://doi.org/10.4028/www.scientific.net/DDF.385.39>
6. Lin YC, Jiang YQ, Chen XM, Wen DX, Zhou HM (2013) Effect of creep-aging on precipitates of 7075 aluminum alloy. *Mater Sci Eng A* 588:347–356. <https://doi.org/10.1016/j.msea.2013.09.045>
7. Kaibyshev R, Sakai T, Musin F, Nikulin I, Miura H (2001) Superplastic behavior of a 7055 aluminum alloy. *Scripta Mater* 45(12):1373–1380. [https://doi.org/10.1016/S1359-6462\(01\)01172-1](https://doi.org/10.1016/S1359-6462(01)01172-1)



# A New Design of a Three-Speed Gearbox Provides Continuously Variable Torque During Gear Shifting in Electric Cars



Nguyen Hoang Viet, Nguyen Thanh Trung, and Nguyen Hong Thai

**Abstract** In electric car transmissions, multi-speed transmissions provide operating modes to suit different travel needs and thus contribute to the vehicle's desired performance with minimum energy consumption. However, multi-speed gearboxes are not widely used in the electric car manufacturing industry because the car jerks during gear changes, causing energy loss and making passengers uncomfortable, which is incredibly annoying for people with motion sickness. To solve the above problem of the multi-speed gearbox, in this paper, the authors present an alternative to design a gearbox using non-circular gears to provide continuously variable torque during gear shifting. A control strategy is also proposed to provide the same shifting flexibility as an internal combustion engine transmission. On that basis, a calculation and design program was written on Matlab software to verify the theory. The results show that the new design solution has overcome the disadvantages of the traditional multi-speed gearbox in electric cars.

**Keywords** Multi-speed gearboxes · Non-circular gear · Centrode · Variable torque

---

N. H. Viet

School of Mechanical Engineering, Vietnam Maritime University (VIMARU), Haiphong, Vietnam

N. T. Trung

National Research Institute of Mechanical Engineering (NARIME), Hanoi, Vietnam

N. H. Thai (✉)

School of Mechanical Engineering, Hanoi University of Science and Technology (HUST), Hanoi, Vietnam

e-mail: [thai.nguyenhong@hust.edu.vn](mailto:thai.nguyenhong@hust.edu.vn)

## 1 Introduction

On the electric vehicle market today, most models are equipped with motors that come with single-speed gearboxes (SSG), such as VW e-Golf, Nissan Leaf, BYD e6, Tesla Model S, or VF e34. SSG has many advantages but can only be optimized for a single operating mode and cannot provide the same high performance in all different speed ranges and load modes. A 2-speed or even a 3- or 4-speed gearbox can be installed to increase torque, reduce acceleration time and maintain speed, and promote the engine to operate in the high-performance zone in drive cycles, thereby extending the vehicle's operating range [1–3]. This is a solution that has been introduced previously. It was applied by Tesla on the first version of the Tesla Roadster in 2006. However, this option was quickly superseded by SSG, mainly due to torque disruptions—Torque during gearshift causes energy loss and jerks. This is the biggest problem of AMT that, so far, research in the world has not been completely overcome, causing the multiple-speed gearbox (MSG) to be limited in research and application for some EV models. Gao [4] suggested using a dry clutch at the transmission's rear to suppress the traction disruption of traditional MSG. However, the loss caused by clutch friction during gear shifting significantly affects the vehicle's energy efficiency. Liang [5] combines the clutchless automatic transmission (CLAMT) with an assist motor that provides the necessary torque during gear changes. The experimental results demonstrate that this solution significantly improves the shifting quality when changing gears compared to conventional AMT. Another idea is to provide independent power to all wheels, thus allowing increased drivability and a small turning radius without needing a larger engine and transmission. Each motor is coupled to a 2-speed AMT gearbox leads, requiring complex control logic. If not optimized properly, it will cause discomfort to drive and increase transmission losses [6, 7]. In 1975 Kerr [8] applied for a patent for a CVT transmission that used a combination of non-circular gears (NCGs) with a bevel gear and clutch mechanism to overcome the disadvantages point of a CVT gearbox using the pulley-belt mechanism. This idea was further developed in the works of Ferguson [9] and Dooner [10, 11] and perfected by the research group of Hebbale [12]. Meanwhile, Kang [13] uses only a pair of NCGs with specially designed centrodes to provide the desired gear ratio. Both Hebbale and Kang's methods are only suitable for designing two-speed gearboxes. In the case of multi-speed gearboxes, synthesizing the NCGs mechanism centrodes in these two directions is complicated, and the transmission ratio magnitude is also limited. Regarding the curve using the tooth profile design of NCGs, there are four common forms so far: (1) The involute profile of the circle [14] and the ellipse [15, 16]; (2) The Novikov arc profile [17]; (3) The cycloid profile [18]; (4) The improved cycloid curve of the ellipse [19–22]. However, the cycloid and cycloid profile gear pairs improve with the number of tooth pairs involved in meshing, usually leading to large tooth and gear sizes. The tooth Novikov profile has a complicated structure. In contrast, the involute profiles have a contact ratio that can be adjusted to increase the number of tooth pairs participating in the matching. Therefore, to overcome the limitation of torque interruption during gearshifting and continue to develop and

perfect the idea of applying NCGs in MSG, in this study, we propose a new gearbox using NCGs with designing the centrodes of the NCGs to meet the requirement of providing continuous torque during gear shifting.

## 2 Design of Non-circular Gears Providing Continuous Torque

### 2.1 Analysis and Determination of Gear Ratio Function of Non-circular Gears

In this research, the authors chose four operating modes of the Chevrolet Bolt EV [23], corresponding to three levels of gear ratios that have been optimized, including the passing ability (gear ratio 6.0:1.0), the operating range (gear ratio 7.0:1.0), the launching and grade ability (all achieved at gear ratio 9.0:1.0) to illustrate the design of a three-speed gearbox to provide the highest performance in different operating modes of the EV. For the transmission to be smooth, without a jerk, a prerequisite is that the gearbox's transmission ratio must be maintained continuously. On the other hand, to ensure the size and weight of the gearbox, the gear ratio of a pair of gears is usually less than 8.0. Thus, The Chevrolet Bolt EV transmission must be including (a) an auxiliary gear ratio of 2.0:1.0 and (b) three main gear ratios of 3.0:1.0, 3.5:1.0, and 4.5:1.0. To realize this idea, the paper proposes a three-speed gearbox with the scheme described in Fig. 1, in which gear pairs 1–2, 3–4, 5–6, and 13–14 located in the structure on the left are circular gear pairs, while gear pair 7–8 are NCGs; clutches from C1 to C6 have the function of connecting the movement of gear pairs to the output shaft.

This study uses trigonometric functions to establish the gear ratio for the transition period, and the gear ratio equation is presented in Table 1, with  $\varphi_7$  being the rotation angle of the NCG. The general form of gear ratios at stages a, b, and c are  $i_{78} = m_1 + m_2(1 + \cos(n_1\varphi_7 + n_2))$ , where  $m_1$  is the average gear ratio value, component  $m_2(1 + \cos(n_1\varphi_7 + n_2))$  is the amplitude value of the gear ratio change with  $m_2$ ,  $n_1$ ,  $n_2$  is the parameters determining the rate of change of the gear ratio. The results are presented in Fig. 2. Specifically, from level two, EV can switch to level three or level one; meanwhile, if the EV is operating in third gear, it can shift to second gear before returning to first gear so that the shifting process is smoother and smoother. Figure 3 shows how the clutches operate to accommodate a complex shifting process: from the initial state at the first level to the second level, then to the third level, then again turn to the second level and first level, finally shifting up and maintaining the gear ratio at the second level.

Thus, with the proposed shift cycle above, when encountering different gearshift cycle requirements, the EV only needs to select the appropriate clutch control mode without changing NCGs or the entire gearbox. This feature is suitable for EVs operating in complex urban roads or uneven terrain environments.

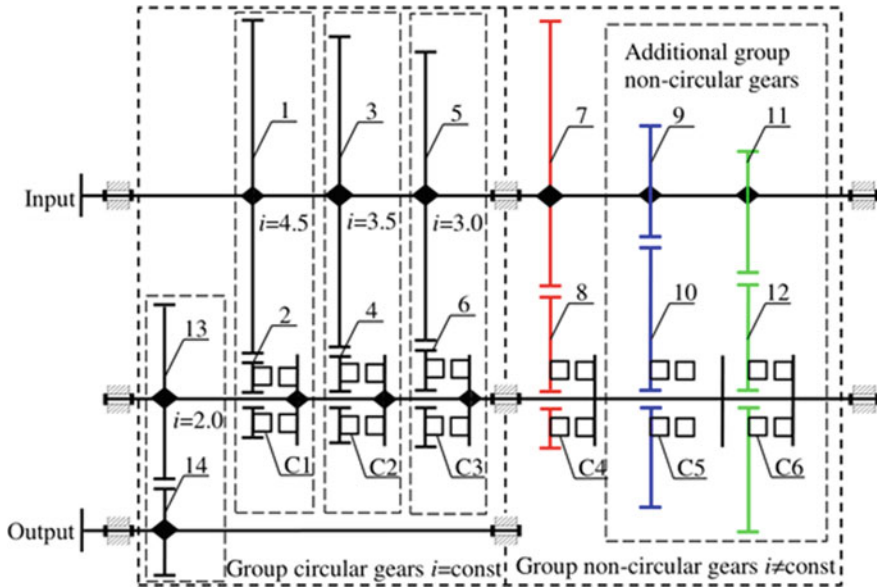


Fig. 1 Diagram of gearbox

Table 1 Equation of gear ratio of the sections

Section	Rotation angle $\varphi_7$	Gear ratio function $i_{78}$
1	$[0, \frac{227}{600}\pi], [\frac{281}{150}, 2\pi]$	$i_{78} = 3$
a	$[0, \frac{227}{600}\pi], [\frac{281}{150}, 2\pi]$	$i_{78} = 3 + 0.25(1 + \cos(4\varphi_7 - \frac{\pi}{2}))$
2	$[0, \frac{227}{600}\pi], [\frac{281}{150}, 2\pi]$	$i_{78} = 3.5$
b	$[0, \frac{227}{600}\pi], [\frac{281}{150}, 2\pi]$	$i_{78} = 3.5 + 0.5(1 + \cos(4\varphi_7 + \frac{\pi}{2}))$
3	$[0, \frac{227}{600}\pi], [\frac{281}{150}, 2\pi]$	$i_{78} = 4.5$
b'	$[0, \frac{227}{600}\pi], [\frac{281}{150}, 2\pi]$	$i_{78} = 3.75 + 0.75(1 + \cos(4\varphi_7 - \frac{\pi}{2}))$

### 2.2 The Equation for Determining the Centroides of the Non-circular Gears

Equation of the centroide of the non-circular gears is determined according to [24]:

$$r_7(\varphi_7) = a_{78}(i_{78} + 1)^{-1}; r_8(\varphi_8) = i_{78}a_{78}(i_{78} + 1)^{-1} \text{ and}$$

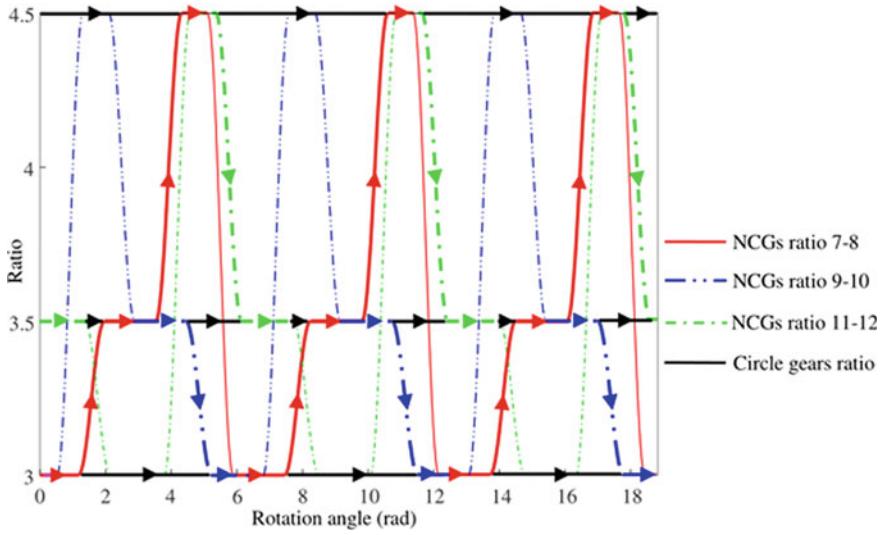


Fig. 2 The transmission ratio

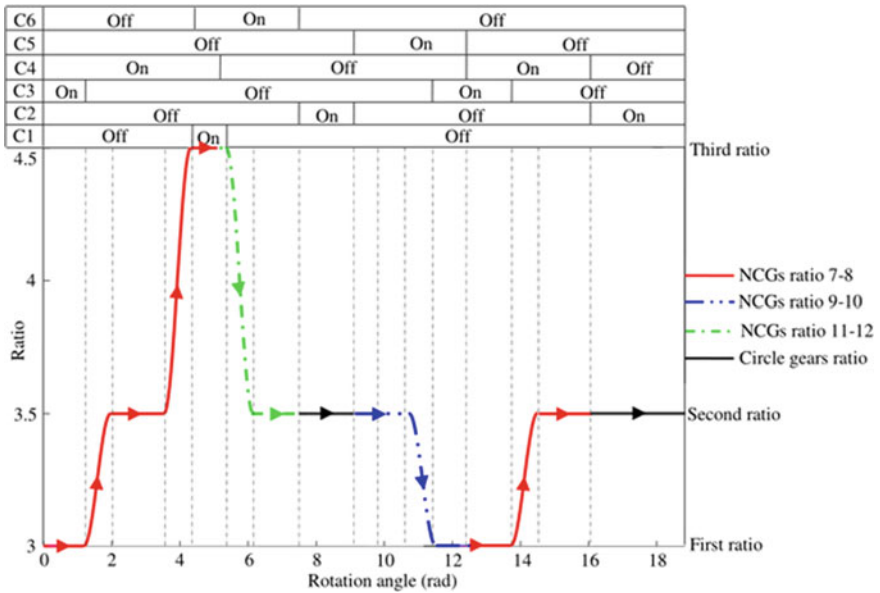


Fig. 3 Clutch operating state in response to a gear shift procedure

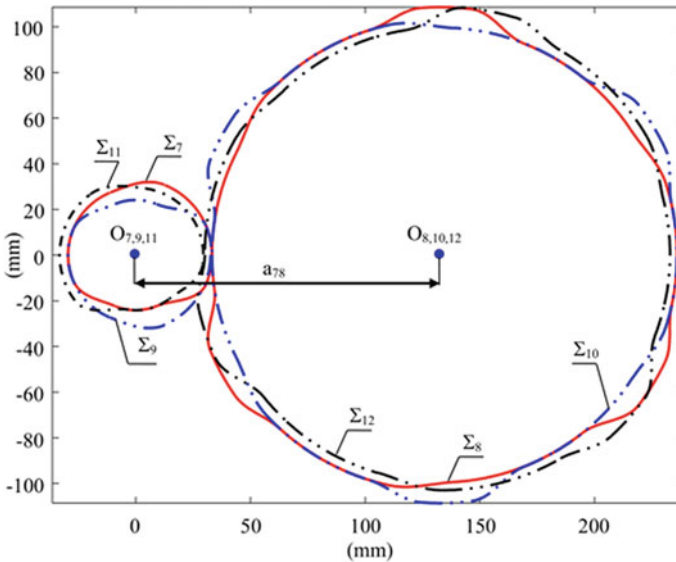


Fig. 4 The centres of non-circular gears

$$\varphi_8(\varphi_7) = \int_0^{\varphi_7} i_{78}^{-1} d\varphi_7 \tag{1}$$

where  $a_{78}$  is the axial distance of the NCG pair;  $r_7(\varphi_7)$ ,  $r_8(\varphi_8)$  are pole radius of  $\Sigma_7$ ,  $\Sigma_8$  with  $\varphi_7$ ,  $\varphi_8$  being the rotation angles of two non-circular gears 7, 8 respectively. Perform calculations and simulations using Matlab software on the basis of the system of Eq. (1) and the data in Table 1, with shaft distance  $a_{78} = 132.75$  mm, the results of centres of gear pairs 7–8, 9–10, 11–12 are summarized in Fig. 4.

The centres of the non-circular gear train in Fig. 4 show that the addition of new pairs of non-circular gears besides the non-circular gear pairs 7–8 does not change the radial size of the transmission, which is the advantage of this alternative when compared with other methods uses pairs of non-circular gears that differ in centres.

### 3 Conclusion

This paper proposes a new three-speed gearbox in which the NCS and cylindrical gear mechanisms are combined with the clutch mechanism to provide a continuously variable torque during the gear shift operation for electric cars. The study’s preliminary results are summarized and summarized as follows: (i) Continuous supply of torque during gearshifts using gear ratios in the form of trigonometric equations that mediate transitions between gear ratios that are constants optimized for each operating mode

of vehicle motion and (ii) Provides flexible gear shifting without increasing the radial size of the gearbox by combining the movement of pairs of non-circular gears with the same centrodes and phase difference through clutch mechanisms.

## References

1. Ahssan EG (2018) Electric vehicle with multi-speed transmission: a review on performances and complexities, *SAE. Int J Alt Power* 7(2):169–181
2. Machado FA, Kollmeyer PJ, Barroso DG, Emadi A (2021) Multi-speed gearboxes for battery electric vehicles: current status and future trends, *IEEE Open J Vehic Technol* 2:419–435
3. Mazali II, Daud ZHC, Hamid MKA, Tan V, Samin P, Jubair A, Ibrahim KA, Kob MSC, Xinrui W, Talib MHA (2022) Review of the methods to optimize power flow in electric vehicle powertrains for efficiency and driving performance. *Appl Sci* 12(3):1735
4. Gao B, Qiong Liang Y, Xiang LG, Chen H (2015) Gear ratio optimization and shift control of 2-speed I-AMT in electric vehicle. *Mech Syst Signal Process* 50–51:615–631
5. Liang J, Yang H, Jinglai W, Zhang N, Walker PD (2018) Power-on shifting in dual input clutchless power-shifting transmission for electric vehicles. *Mech Mach Theory* 121:487–501
6. Meng D, Tian M, Miao L, Wang Y, Hu J, Gao B (2021) Design and modeling of an in-wheel two-speed AMT for electric vehicles. *Mech Mach Theory* 163:104383
7. Meng D, Wang F, Wang Y, Gao B (2021) In-wheel two-speed AMT with selectable one-way clutch for electric vehicles. *Actuators* 10(9):220
8. Kerr (1975) Variable output transmission, US Pat. 3919895
9. Ferguson RJ, Daws LF, Kerr JH (1975) The design of a stepless transmission using non-circular gears. *Mech Mach Theory* 10:467–478
10. Dooner S (1996) Synthesis of non-circular gears for a continuously variable transmission. In: *Proceedings of international congress on gear transmission*, pp 38–45
11. Dooner YS (1998) Kinematic considerations for reducing the circulating power effects in gear-type continuously variable transmission. *Proc Inst Mech Eng Part D J Autom Eng* 212(6):463–478
12. Hebbale K, Li D, Zhou J, Duan C, Kao C-K, Samie F, Lee C, Gonzales R (2014) Study of a non-circular gear infinitely variable transmission. In: *Proceedings of the ASME 2014 dynamic systems and control conference*
13. Kang J, Komori M, Zhang S, Sugiyama K (2012) Control method for output speed during velocity ratio change under high rotational speed using an uninterrupted transmission system. *J Adv Mech Des Syst Manuf* 6(7):1281–1297
14. Thai NH, Thom PV (2021) Research on the characteristics of tooth shape and size of the oval gear drive with an involute profile. In: *The AUN/SEED-Net joint regional conference in transportation, energy, and mechanical manufacturing engineering*, pp 167–184
15. Thai NH, Thom PV, Lam DB (2021) Effects of pressure angle on uneven wear of a tooth profile of an elliptical gear generated by ellipse involute. *Sci Technol Develop J* 24(3):2031–2043
16. Thai NH (2021) Shaping the tooth profile of elliptical gear with the involute ellipse curve. *Sci Technol Develop J Eng Technol* 4(3):1048–1056
17. Thai NH, Trung NT, Duong NT, Viet N (2020) H, Tooth profile of common non-circular gears using Rack and Novikov tooth profile. *J Sci Technol Tech Univ* 140:011–017
18. Thai NH, Giang TC (2018) Influence of geometrical dimensions on the profile slippage in the hypogenerator pump. *Vietnam J Sci Technol* 56(4):482–491
19. Thai NH, Long ND (2021) A new design of the Lobe pump is based on the meshing principle of elliptical gear pairs. *Sci Technol Develop J Eng Technol* 4(2):861–871
20. Thai NH, Trung NT (2022) A novel curve for the generation of the non-circular gear tooth profile. *Int J Eng Trans B Appl* 3(5):1024–1036

21. Trung NT, Viet NH, Thai NH (2021) Research and manufacture of external non-circular gear-pair with improved cycloid profile of the ellipse. *Sci Technol Develop J Eng Technol* 4(2):835–845
22. Thai NH, Tien TN (2018) Influence of the designing parameters on the profile slippage and flow of the Roots blower. *Sci Technol Develop J Eng Technol* 1:13–19
23. Liu J (2016) Design of the Chevrolet bolt EV propulsion system, SAE. *Int J Altern Powertrains* 5(1):79–86
24. Litvin FL, Gonzalez-Perez I, Yukishima K, Fuentes A, Hayasaka K (2007) Generation of planar and helical elliptical gears by application of rack-cutter, hob and shaper, *Comp. Meth Appl Mech Eng* 196:432–4336



# Research Design and Manufacture Eccentric Elliptical Gear Pair with an Improved Cycloid Profile



Nguyen Hong Thai, Nguyen Thanh Trung, and Phung Van Thom

**Abstract** Eccentric elliptical gears are a special case of non-circular gears used in generating gear drives with variable gear ratios. This type of gear can create a speed increase and reducer of the output shaft relative to the input shaft in one working cycle. In this study, the authors present a method to establish computational expressions for the geometrical design of a pair of improved cycloid profile eccentric elliptical gears taking into account avoiding undercutting. First, a mathematical model of the centrode of an eccentric ellipse gear pair is established. After, the mathematical equation describing the tooth profile of the eccentric ellipse gear is established based on the theory of the enveloping by rack cutter with an improved cycloid profile. Based on research theory, this research wrote a numerical calculation program for the survey and design purposes on Matlab software. Since then, a pair of eccentric elliptical gears has been manufactured on a 3-axis CNC milling machine to demonstrate the practicality of the research theory. Experimentally manufactured gear drives the output shaft has a variable speed and torque range from 0.33 to 3 times versus input shaft, which makes it different from traditional circular gear drives and conventional non-circular gear pairs.

**Keywords** Eccentric elliptical gears · Improved cycloid tooth profile · Rack cutter · Undercutting

---

N. H. Thai (✉) · P. V. Thom

School of Mechanical Engineering, Hanoi University of Science and Technology (HUST), Hanoi, Vietnam

e-mail: [thai.nguyenhong@hust.edu.vn](mailto:thai.nguyenhong@hust.edu.vn)

N. T. Trung

National Research Institute of Mechanical Engineering (NARIME), Hanoi, Vietnam

## 1 Introduction

Elliptical gear is a non-circular gear (NCG) with the advantage of creating a gear drive that changes speed and torque according to a particular rule with a simple mechanical structure. In recent years, many scientists have studied the application of NCG in practice, including using the NCG to replace the crank-slider mechanism of a nail machine [1], using NCG for reciprocating high-pressure compressors [2], silk reeling machines [3], applications in the design of gear driver for the Roots blowers [4, 5]; Research on building a method for designing and manufacturing elliptical gears with the ellipse involute profile of the ellipse [5, 6] and Novikov-type circular arc [7, 8]. Besides, the NCG there are the following studies: Study on the application of NCG pairs in blood pumps for cardiac surgery [9]; Application of the EG train in the transplanting structure of the automatic rice transplanter [10]; Application of the EG train in combination with cylindrical gears to create a drive system for the water pumps of the mining system [11]; Application of NCG in continuously variable transmission gearbox of automobiles [12], or research, design and manufacture pairs of NCGs with improved cycloid profiles [13]. From the above analysis, it is found that most studies focus on the tooth profile as the involute of the circle. The literature [14] has shown that when using tooth profiles such as the involute of the circle, or the involute of an elliptical, and the circular arc then disadvantageous that the minimum number of teeth is often large to satisfy the condition to avoid undercutting. Furthermore, the teeth are arranged in different positions on the EEG unequal and often have pointed teeth at the elliptical centrede's semi-major axis [15–17].

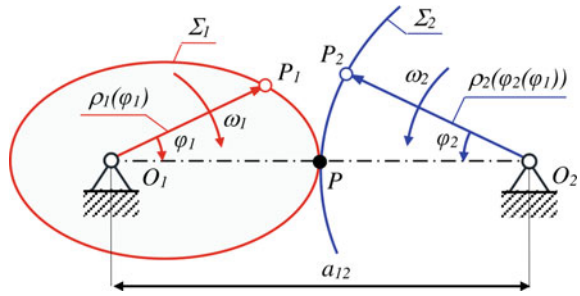
To overcome the above disadvantages, our previous studies have proposed to novel curve by replacing the generating circle [18–20] with a generating ellipse rolling without slipping on the line or curve to design the tooth profile of the rack cutter and the shaper cutter [20–23] is called the novel profile. For that purpose, this study focuses on establishing the analytic expressions relating the shaping parameters of the cutting tool (rack cutter) with the design parameters of the EEGs when considering avoiding undercutting. The content of the paper includes (1) Synthesis of the centrede of EEGs; (2) Establishment of analytic equations describing the relationship between the design parameters of the rack cutter with improved cycloid profile and pinion with a design parameter for EEG pair; (3) Design, prototype manufactured of an EEG pair.

## 2 Synthesis of the Centroides for the Eccentric Elliptical Gear Pair

If  $\Sigma_1$  is called the centrede of the EEG driving, then the mathematical equation describing  $\Sigma_1$  is determined by [24]:

$$\rho_1(\varphi_1) = a_1(1 - E_1^2)(1 - E_1 \cos \varphi_1)^{-1} \quad (1)$$

**Fig. 1** Geometric relationship of the eccentric elliptical centrode pair



wherein  $\rho_1(\varphi_1)$  is the pole radius,  $\varphi_1 \in [0 \div 2\pi]$  is the pole angle,  $E_1 = \sqrt{1 - (b_1 \cdot a_1^{-1})^2}$  with  $a_1, b_1$  are the major and minor axis of  $\Sigma_1$ , respectively.

From Fig. 1, the mathematical equation of the centrode  $\Sigma_2$  is described by [3, 25–27]:

$$\begin{cases} \rho_2(\varphi_2(\varphi_1)) = a_{12} - a_1(1 - E_1^2)(1 - E_1 \cos \varphi_1)^{-1} \\ \varphi_2(\varphi_1) = \int_0^{\varphi_1} (a_1(1 - E_1^2)(a_{12}(1 - E_1 \cos \varphi) - a_1(1 - E_1^2))^{-1}) d\varphi_1 \end{cases} \quad (2)$$

Thus, the gear ratio function of the EEG pair is defined:

$$i_{21}(\varphi_1) = a_1(1 - E_1^2)(a_{12}(1 - E_1 \cos \varphi_1) - a_1(1 - E_1^2))^{-1} \quad (3)$$

The shaft distance of gear drive  $a_{12}$  is given by:

$$f(n_1, a_1, b_1) = 2\pi - n_1 \int_0^{2\pi} (a_1(1 - E_1^2)(a_{12}(1 - E_1 \cos \varphi) - a_1(1 - E_1^2))^{-1}) d\varphi_1 = 0 \quad (4)$$

Here  $n_1$  is circumference coefficient of EEG 1 relative to EEG 2.

### 3 Shaping the Tooth Profile for the Eccentric Elliptical Gears by the Rack Cutter with an Improved Cycloid Profile

#### 3.1 Mathematical Model of the Rack Cutter Profile

According to the literature [13, 23], the novel rack cutter with an improved cycloid profile is described in Fig. 2 has the profile equation  $\Gamma_R$  expressed as below [13]:

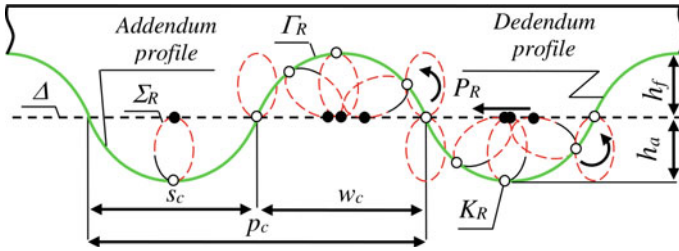


Fig. 2 The novel rack cutter with an improved cycloid curve [13]

$$\mathbf{r}_{K_R} = \begin{bmatrix} x_{K_R} \\ y_{K_R} \end{bmatrix} = \begin{bmatrix} v_2(\varphi) - a_R \sin(\psi) \\ (-1)^g v_3(\varphi) - a_R \cos(\psi) \end{bmatrix} \tag{5}$$

In Eq. (5)  $g = 0$ , then  $\Gamma_R$  is the tooth tip profile;  $g = 1$ ,  $\Gamma_R$  is the tooth root profile, with  $a_R$  being the semi-major axis of  $\Sigma_R$ .

Thus, the design parameters of the rack cutter:

$$\text{Tooth pitch: } p_c = s_c + w_c = 2C_R \tag{6}$$

$s_c = w_c$ ,  $C_R = \int_0^{2\pi} \sqrt{r_{K_R}^2(\varphi) + (dr_{K_R}(\varphi)/d\varphi)^2} d\varphi$  is the circumference of the ellipse generating  $\Sigma_R$ .

$$\text{Whole depth: } h = h_a + h_f = 4a_R \tag{7}$$

Here  $h_a, h_f$  are the addendum and dedendum tooth,  $h_a = h_f$

$$\text{Modules are defined: } m_c = p_c \pi^{-1} \tag{8}$$

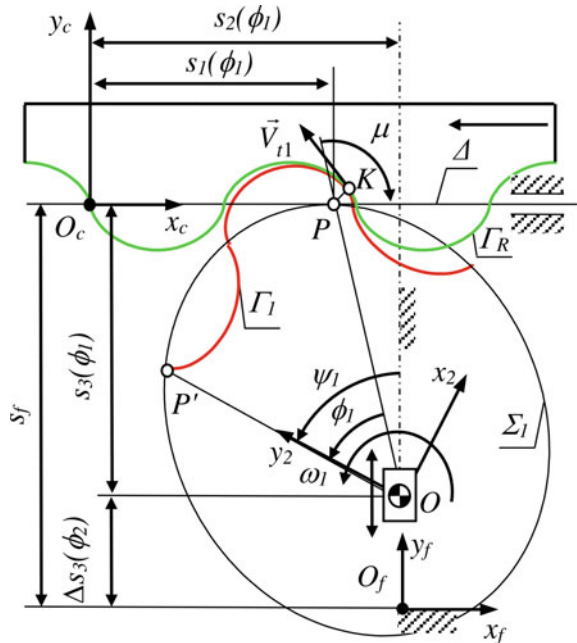
### 3.2 Mathematical Model of Eccentric Elliptical Gear

The mathematical model of the tooth profile of the eccentric EEG was shaped by the rack cutter as described in Fig. 3, is expressed by:

$$\mathbf{r}_{K_1} = \begin{bmatrix} x_{K_1} \\ y_{K_1} \end{bmatrix} = \begin{bmatrix} (s_2(\varphi_1) - x_{K_R}(\varphi)) \sin \psi_1(\varphi_1) + (s_3(\varphi_1) + y_{K_R}(\varphi)) \cos \psi_1(\varphi_1) \\ (s_2(\varphi_1) + y_{K_R}(\varphi)) \sin \psi_1(\varphi_1) - (s_3(\varphi_1) - x_{K_R}(\varphi)) \cos \psi_1(\varphi_1) \end{bmatrix} \tag{9}$$

In Eq. (9), the relationship between the parameter  $\phi$  of the rack and kinematic parameter  $\phi_1$  of the EEG is determined through the meshing condition [28].

**Fig. 3** Relative motion between the rack cutter and the EEGs



### 3.3 Conditions for Avoiding Undercutting

In the process of shaping the tooth profile of EEGs so that the rack cutter does not cut into the root of the EEG, the following conditions must be satisfied [29]:

$$\Delta_1 = \left| \begin{matrix} \frac{dx_{K_R}(\varphi)}{d\varphi} & -V_{t1x} \\ \frac{\partial f(\varphi)}{\partial \varphi} & \frac{\partial f(\varphi_1)}{\partial \varphi_1} \frac{d\varphi_1}{dt} \end{matrix} \right| \neq 0 \text{ and } \Delta_2 = \left| \begin{matrix} \frac{dy_{K_R}(\varphi)}{d\varphi} & -V_{t1y} \\ \frac{\partial f(\varphi)}{\partial \varphi} & \frac{\partial f(\varphi_1)}{\partial \varphi_1} \frac{d\varphi_1}{dt} \end{matrix} \right| \neq 0 \quad (10)$$

with  $V_{t1x}$ ,  $V_{t1y}$  are the components of the sliding velocity on the rack profile  $\Gamma_R$  at the meshing point  $K_R$ .

## 4 Experimental Manufactured

Based on research theory, a numerical design calculation program has been programmed on Matlab. After surveying the design parameters to satisfy the condition of avoiding undercutting, Table 1 are the EEG pair manufacturing parameters. Figure 4a has demonstrated that the design data of the EEG pair selected through the investigatory in Table 1 is not undercutting. Figure 4b is the gear ratio of the designed EEG pair. Figure 4b shows that the gear ratio of the gear drive varies from

**Table 1** Eccentric EEG pair design parameters

Parameter	Notation	Values
Semi-major axis (mm)	$a$	41
Eccentricity (mm)	$E$	0.50
Module (mm)	$m$	3.83
Circumference coefficient	$n$	1
Shaft distance (mm)	$a_{12}$	82
Number of teeth	$z$	20
Tooth pitch (mm)	$p$	12.04
Tooth thickness (mm)	$s$	6.02
Width of space (mm)	$w$	6.02
Whole depth (mm)	$h$	4.40
Tooth addendum (mm)	$h_a$	2.20
Tooth dedendum (mm)	$h_f$	2.20

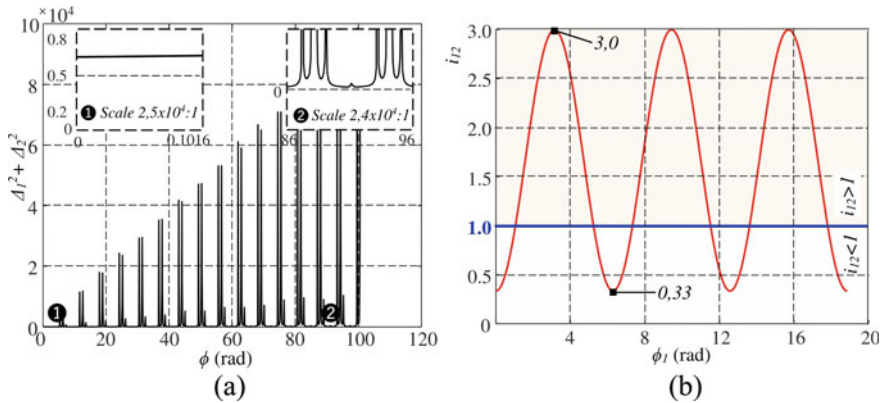


**Fig. 4** Characteristics of the designed EEG pair

0.33 to 3.0, which means that in one duty cycle, the gear drive is designed to have two working modes: acceleration and deceleration.

Figure 5 are the results of the EEG pair design and manufacturing with the data set in Table 1. Figure 5 shows that the designed EEG pair is equal to the teeth' geometric shape and dimension. The number of teeth is less than the involute profile of the circle [15, 17], or the involute profile of the ellipse [6, 30] and Novikov circle arcs [7, 16], resulting in increased gear load capacity.

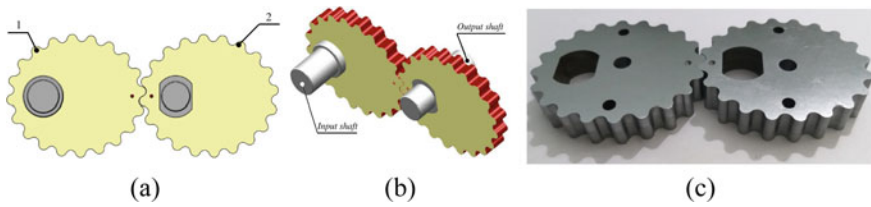


Fig. 5 EEG pair with **a** the vertical view, **b** 3D description and **c** after manufacturing

## 5 Conclusion

From the results of theoretical research, experimental fabrication, discussion and evaluation above, this study has achieved the following results: (i) A relationship has been established between the machining of the cutting tool (rack cutter) and the design parameters of the EEG to ensure to avoid undercutting; (ii) A numerical calculation program module allows the investigation, calculation, and selection of EEG design parameters with an improved cycloid profile; (iii) Manufactured EEG pair with a speed variation range: deceleration from 1 to 0.33 and acceleration from 1 to 3 in one working cycle to verify the correctness of the research theory and practical applicability.

It then shows that the results of this study have practical significance in the design of EEG speed converters with two working modes: acceleration and deceleration, to meet the particular requirements of practices such as the implants of agricultural machines or the steering systems of autonomous mobile robots AGV, UGV, etc.

However, the limitation of this study is that it has not the coefficient of coincidence and the unverified ability to perform the gear ratio function of the EEG pair after manufacturing. As such, it will be considered part of our future research goals.

## References

1. Niculescu DM, Andrei L, Cristescu A (2016) Generation of noncircular gears for variable motion of the crank-slider mechanism. In: 7th international conference on advanced concepts in mechanical engineering, IOP conf. series: materials science and engineering, vol 147
2. Mundo D, Danieli GA (2004) Use of non-circular gears in pressing machine driving systems. In: Proceedings of IASME international conference on mechanics and mechatronics, pp 483–172
3. Chen JN, Yan JJ, Sun L, Zhou M (2014) Analysis of a novel traverse mechanism driven by non-circular gears with Fourier pitch-line applied on silk reeling machine. *Appl Mech Mater* 536–537:1295–1300
4. Trung NT, Viet NH, Thai NH (2021) Research and manufacturing of oval gear pair applied in rotor of a roots type compressor. *Eng Technol Sustain Dev* 31(5):031–038
5. Thai NH, Trung NT, Viet NH (2021) Research and manufacture of external non-circular gear-pair with improved cycloid profile of the ellipse. *Sci Technol Dev J-Eng Technol* 4(2):835–845
6. Thai NH, Thom PV, Lam D (2021) B, Effects of pressure angle on uneven wear of a tooth profile of an elliptical gear generated by ellipse involute. *Sci Technol Dev J* 24(3):2031–2043

7. Korotkin VI, Onishkov NP, Kharitonov YD, Gearing N (2011) Achievements and developments. Nova Science Pub Inc
8. Thai NH, Trung NT, Duong NT, Viet NH (2020) Shaping tooth profile of common non-circular gears using rack and Novikov tooth profile. *J Sci Technol Tech Univ* 40:011–017
9. Ottaviano E, Mundo D, Danieli GA, Ceccarelli M (2008) Numerical and experimental analysis of non-circular gears and cam-follower systems as function generators. *Mech Mach Theory* 43:996–1008
10. Guo LS, Zhang WJ (2001) Kinematic analysis of a rice transplanting mechanism with eccentric planetary gear trains. *Mech Mach Theory* 36:1175–1188
11. Xu G, Hua D, Dai W, Zhang X (2017) Design and performance analysis of a coal bed gas drainage machine based on incomplete non-circular gears. *Energies* 10:2–19
12. Kang J et al (2012) Control method for output speed during velocity ratio change under high rotational speed using an uninterrupted transmission system. *J Adv Mech Des Syst Manuf* 6(7):1281–1297
13. Thai NH, Trung NT (2022) A novel curve for the generation of the non-circular gear tooth profile. *Int J Eng Trans B Appl* 35(5):1024–1036. <https://doi.org/10.5829/ije.2022.35.05b.18>
14. Thai NH, Thom PV (2021) Research on the characteristics of tooth shape and size of the oval gear drive with an involute profile. In: The AUN/SEED-Net joint regional conference in transportation, energy, and mechanical manufacturing engineering, pp 167–184. [https://doi.org/10.1007/978-981-19-1968-8\\_14](https://doi.org/10.1007/978-981-19-1968-8_14)
15. Bair BW (2001) Computer aided design of non-standard elliptical gear drives. *Proc Inst Mech Eng C J Mech Eng Sci* 216:473–482
16. Bair BW, Sung M-H, Wang J-S, Chen C-F (2009) Tooth profile generation and analysis of oval gears with circular-arc teeth. *Mech Mach Theory* 4:1306–1317
17. Prikhodko AA (2021) Force analysis of the two-satellite planetary mechanism with elliptical gears. *Mech Mech Eng* 25(1):39–46
18. Thai NH, Trung NT, Nghia LX, Duong NT (2021) Profile sliding phenomenon in the external non-circular gear-train with cycloidal profile. *Eng Technol Sustain Dev* 31(2):053–057
19. Thai NH, Trung NT, Nghia LX, Duong NT (2020) Synthesis of the external non-circular gear-train with cycloid profile. *J Sci Technol Tech Univ* 145:033–039
20. Viet NH, Thai NH (2021) Geometric design and kinematics analysis of non-circular planetary gear train with cycloid profile. *Eng Technol Sustain Dev* 31(3):105–112
21. Thai NH, Thom PV, Trung NT (2021) Influence of centrodes coefficient on the characteristic of gear ratio function of the compound non-circular gear train with improved cycloid tooth profile. In: IFToMM Asian conference on mechanism and machine science, pp 204–214. [https://doi.org/10.1007/978-3-030-91892-7\\_19](https://doi.org/10.1007/978-3-030-91892-7_19)
22. Thai NH, Thom PV, Trung NT (2021) Experimental design and manufacture a pair of the internal non-circular gears with an improved cycloid profile. In: The AUN/SEED-Net joint regional conference in transportation, energy, and mechanical manufacturing engineering, pp 118–134. [https://doi.org/10.1007/978-981-19-1968-8\\_11](https://doi.org/10.1007/978-981-19-1968-8_11)
23. Thai NH, Ly TTK, Trung NT (2021) Research design and experimental manufacturing of compound non-circular gear train with an improved cycloid profile of the ellipse. In: International conference on engineering research and applications, pp 813–825
24. Litvin FL, Alfonso F-A, Ignacio G-P, Kenichi H (2009) Noncircular gears design and generation. Cambridge University Press, New York
25. Thai NH, Trung NT (2020) Pitch line synthesis of noncircular planetary gears. *J Sci Technol Tech Univ* 140:05–010
26. Jung SY, Han SM, Cho HY, Kim C (2009) Automated design system for a rotor with an ellipse lobe profile. *J Mech Sci Technol* 23:2928–2937
27. Litvin FL, Fuentes F (2004) Gear geometry and applied theory. Cambridge University Press, New York
28. Litvin FL et al (2008) Design and investigation of gear drives with non-circular gears applied for speed variation and generation of functions. *Comput Methods Appl Mech Eng* 197(45–48):3783–3802



29. Litvin FL et al (2007) Generation of planar and helical elliptical gears by application of rack-cutter, hob, and shaper. *Comput Methods Appl Mech Eng* 196(41–44):4321–4336
30. Thai NH (2021) Shaping the tooth profile of elliptical gear with the involute ellipse curve. *Sci Technol Dev J* 4(3):1048–1056

# Studying the Influence of Geometric Design Coefficient on Flow and Pressure of Lobe Blower by Numerical Method



Nguyen Hong Thai, Trinh Dong Tinh, and Nguyen Thanh Trung

**Abstract** Unlike traditional designs, the novel Lobe blower proposed recently by the authors has two completely different rotors, which are developed based on the meshing principle of the oval gear pair. Each rotor has two tooth pairs that are symmetrical according to the two semi-axes of the base oval. The paper presents the influence of the base oval's geometric design coefficient  $\lambda$  (equalled to the ratio of the semi-minor axis and semi-major axis) on this novel blower's flow rate and pressure. The CFX module of Ansys software calculates six blower designs with different coefficients numerically  $\lambda$ . The k- $\epsilon$  turbulence model also considers the kinematics and dynamics of the airflow through the blower. The numerical calculation results show that the design coefficient  $\lambda$  is a factor affecting the dimension, flow rate, pressure, and airflow quality at the blower outlet. Specifically, for blowers designed with a small coefficient  $\lambda$ , the average flow rate can increase from 0 to 32% compared to  $\lambda = 1$ , and the dimension of the blower can decrease from 1 to 21.43%.

**Keywords** Lobe blower · Flow fluctuations · Pressure fluctuations · Rotor profile · Ansys software

## 1 Introduction

Since the first design in the world by George [1] in 1843 in England, and through nearly 180 years of development, the Roots blowers have had many different improvements mainly based on two principles rotor drive. Which is: (i) Driven by an external

---

N. H. Thai (✉) · T. D. Tinh  
School of Mechanical Engineering, Hanoi University of Science and Technology (HUST), Hanoi, Vietnam

e-mail: [thai.nguyenhong@hust.edu.vn](mailto:thai.nguyenhong@hust.edu.vn)

N. T. Trung  
National Research Institute of Mechanical Engineering (NARIME), Hanoi, Vietnam

cylindrical gears pair with the gear ratio of 1:1 [2, 3] and (ii) Driven by a non-circular gears pair with the various gear ratio [4, 5]. Roots blowers are widely used in many industrial fields such as the papermaking industry, mining industry, pharmaceutical industry, and sewage treatment because of their high reliability, low cost, easy maintenance, etc. And they are classified to: (i) The Roots blower has the rotor with only two lobes [2, 6] and (ii) The Lobe blower has the rotor with three or more lobes [5]. The development of Roots blowers primarily involves designing the rotor profile; Including the following original studies: Litvin et al. [7] developed the rotor profile using conjugate arcs and curves; Palmer and Knox [8] used cycloid (hypocycloid and epicycloid) curves in the rotor profile design; Hsieh [9] used an improved cycloid which is the locus of a fixed point on the generate ellipse for the rotor profile design; Thai et al. [10, 11] developed a new curve according to the meshing principle of oval gear pairs to design the rotor profile of the Roots blower. In addition, some studies continue to improve these original profiles to enhance the flow and efficiency of blowers such as [6, 12]. Regarding the research method of Roots blower, there are three main directions: (1) Using the analytic model to calculate flow and pressure [2, 4, 13]. This method has the advantage of global optimization, but it has not considered the kinematic and dynamics of the airflow in the blower; (2) Using numerical simulation in the blower design research [3, 6, 9, 12]. This method has already considered the kinematics and dynamics of the airflow through the blower. Still, it has the disadvantage that it is not general and only suitable for local problems; (3) Combining two previous methods with experimental control to study [6, 14, 15] to achieve more accurate results.

In this study, we continue to develop a novel type of Lobe blower that we recently proposed [5], which is entirely different from most published research since it has two completely different rotors. Each rotor has two completely different pairs of teeth. Numerical methods are used to study by considering the kinematics and dynamics of airflow through the blower. On that basis, an evaluation of the influence of the blower design coefficient  $\lambda$  on the airflow flow rate and pressure instantaneous at the blower outlet.

## 2 The Geometric Design of the Lobe Blower

**Structure of the lobe blower:** According to [5], the blower generates from two rotors that differ in shape and dimensions. The two rotors of the blower are driven by the external oval gear pair with a variable gear ratio.

The drive gear pair and the rotor pair have the same centred, as shown in Fig. 1. Thus, the two rotors move relative to each other according to the principle meshing and they combine with the casing to generating the working chambers as follows: ① is the suction chamber which gradually increases in volume to create suction pressure at the inlet blower; ② is a chamber that has a constant volume. It is a function of displacing air from the suction chamber to the discharge chamber; ③ is the discharge chamber which lowers the volume to create high pressure to push the airflow out of

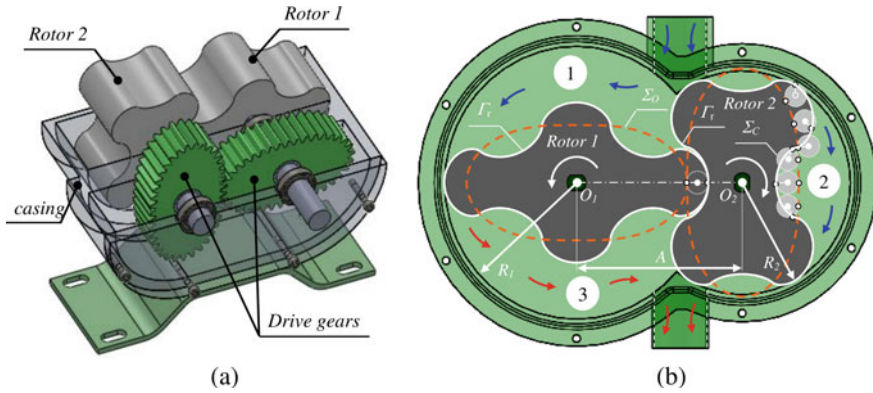


**Fig. 1** The lobe blower with the rotor has four lobes with **a** blower structure and **b** cross-section of the working chamber of the blower

the blower. From Fig. 1b, if set:  $A$  is the axis distance,  $R_1$  is a radial dimension of the left blower chamber with center at  $O_1$ ,  $R_2$  is a radial dimension of the right blower chamber with center at  $O_2$ ,  $B$  is an axial dimension of the blower. The geometrical design parameters of the blower are determined by:

$$A = a_o + b_o, R_1 = a_o + 2r_c \text{ and } R_2 = \rho_{\max} = \sqrt{x_{\Gamma_2}^2 + y_{\Gamma_2}^2} \quad (1)$$

where  $a_o, b_o$  is the semi-major and semi-minor axes of the oval centre  $\Sigma_O$ , respectively;  $r_c$  is the radius of the generating circle  $\Sigma_C$  and  $x_{\Gamma_2}, y_{\Gamma_2}$  are the coordinates of the rotor profile 2.

**Mathematical model of rotor profile design:** The rotor profile  $\Gamma_r$  is the locus of a fixed point on generating circle  $\Sigma_C$  when  $\Sigma_C$  circle rolls without slipping on the oval centre  $\Sigma_O$  of the rotor. The rotor tip profile formed when  $\Sigma_C$  rolls without slipping outside  $\Sigma_O$ , while the rotor root profile formed when  $\Sigma_C$  rolls without slipping inside  $\Sigma_O$  as described in Fig. 1b. With the principle of generating rotor profile as above, according to [4, 5] the rotor profile equation is given by:

$$\begin{cases} x_{\Gamma} = r_c \cos(\psi(\theta) + \xi(\theta)) + r_c \cos(\xi(\theta)) + r_o(\theta) \cos(\theta) \\ y_{\Gamma} = (-1)^j r_c \sin(\psi(\theta) + \xi(\theta)) + r_c \sin(\xi(\theta)) + r_o(\theta) \sin(\theta) \end{cases} \quad (2)$$

wherein:  $\xi(\theta) = \tan^{-1}\left(\frac{\partial x_o(\theta)/\partial \theta}{\partial y_o(\theta)/\partial \theta}\right)$ ,  $\gamma(\theta) = \frac{1}{r} \int_0^\theta \left(\frac{\partial x_o(\theta)}{\partial \theta}\right)^2 + \left(\frac{\partial y_o(\theta)}{\partial \theta}\right)^2$  with  $x_o(\theta) = r_o(\theta) \cos \theta$ ,  $y_o(\theta) = r_o(\theta) \sin \theta$ ,  $r_o(\theta) = 2a_o b_o ((a_o + b_o) - (a_o - b_o) \cos(2\theta))^{-1}$  [16–18].

**Conditions for generating the rotor surface:** According to [19, 20], to generate the rotor profile of the lobe blower, the relationship between  $r_c$  and  $r_o$  must be satisfied:

**Table 1** Design parameters of Lobe blower according to coefficient  $\lambda$

No.	$\lambda$	$a_O$ (mm)	$b_O$ (mm)	$r_C$ (mm)	No.	$\lambda$	$a_O$ (mm)	$b_O$ (mm)	$r_C$ (mm)
1	0.5	58.4498	29.5502	5.7751	4	0.8	57.0508	45.9492	6.4746
2	0.6	58.0328	34.9672	5.9836	5	0.9	56.6026	50.3974	6.6987
3	0.7	57.5670	40.4330	6.2165	6	1.0	56.0000	56.0000	7.0000

$$r_C = (16\pi)^{-1} \int_0^{2\pi} \sqrt{(r_O^2(\theta) + (\partial r_O(\theta)/\partial \theta)^2)} d\theta \tag{3}$$

### 3 Design and CFX Model for Lobe Blower

#### 3.1 Design of the Lobe Blower According to the Coefficient $\lambda$

To evaluate the influence of the coefficient  $\lambda$  on the flow rate, pressure and air quality at the outlet of the Lobe blower, the design parameters  $a_O$ ,  $b_O$ ,  $r_C$  of the Lobe blower are calculated according to coefficient  $\lambda$  so that the radial radius  $R_1$  of the casing is constant. According to [8], radial and axial dimensions of the Lobe blower fixed are  $R_1 = 70$  mm,  $B = 40$  mm. With the coefficient  $\lambda$  is chosen from 0.5 to 1 to avoid undercutting the rotor [4] and  $R_1$ , the parameters  $a_O$ ,  $b_O$ ,  $r_C$  numerically calculated on Matlab according to the formulas from (1) to (3) and statistics in Table 1.

In Table 1, when  $\lambda = 1.0$ , the oval degenerates into a circle and becomes the design traditional of Palmer [2, 8]. On the other hand, tip gap  $\Delta R$ , Lobe gap  $\Delta K$ , and axial gap  $\Delta B$ , according to [14], chose for all design with  $\Delta R = 0.07$  mm,  $\Delta K = 0.07$  mm,  $\Delta B = 0.11$  mm, so that the leakage flow is minimal.

#### 3.2 The Numerical Calculation Parameters in the CFX Module of Software Ansys

**Computational model:** An Embedded boundary model used in this study assumes the two rotors are solid bodies moving in the gas mass inside the casing.

**Grid generation:** The ICEM was used to generate a quadrangular structure grid to improve accuracy and reduce grid elements. The number of boundary elements is divided with a high density, while the number of interior elements is divided with a lower density, as shown in Fig. 2.

**Parameter setting of airflow through a blower:** The inlet and outlet pressures are  $P_1 = 1$  atm,  $P_2 = 1$  atm; Airflow through the blower is assumed to be the standard, and

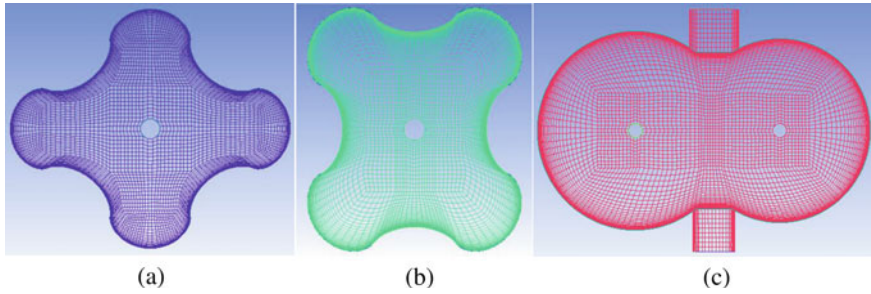


**Fig. 2** Generation grid of computational model with **a** grid of the rotor 1, **b** grid of the rotor 2, and **c** grid of the casing

have following parameters: specific weight  $d = 1.185 \text{ (kg/m}^3\text{)}$ , dynamic viscosity  $\mu = 0.00001831 \text{ (kg/ms)}$ , specific heat  $c = 1004.4 \text{ (J/kgK)}$  at  $25 \text{ }^\circ\text{C}$  and pressure 1 atm.

**Kinematic parameter setting:** The rotational speed of rotor 1 is  $n_1 = 1500 \text{ (rpm)}$ , while the rotational speed of rotor 2 is determined by [21]:

$$n_2 = n_1 (f(i_{12}(\varphi_1)))^{-1} \tag{4}$$

wherein  $f(i_{12}(\varphi_1)) = (A - r_O(\varphi_1))/r_O(\varphi_1)$  is the gear ratio function of the driving oval gears pair. The setting time for each revolution of the drive shaft of 0.04 s corresponds to 180 sampling points.

### 4 Analysis of Calculation Results and Discussion

After calculation and numerical simulation with the design database in Table 1 and the numerical calculation settings above, Figs. 3 and 4 are the instantaneous graphs of flow rate and pressure at the blower outlet, respectively. Consider the steady cycle (cycle 4 and later) then from Figs. 3 and 4 easy to see: (1) When the design coefficient  $\lambda$  increases from 0.5 to 1.0, then the instantaneous value of the flow and the pressure at the blower outlet decreases in both amplitude and period; (2) At  $\lambda = 1$ , the novel design of the blower degenerates to the traditional design, and then the instantaneous values of flow rate and pressure at the outlet are minimum.

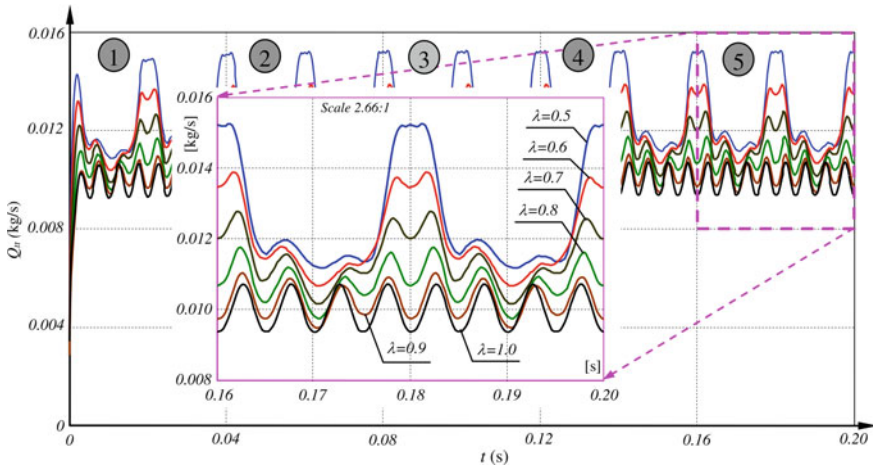


Fig. 3 Instantaneous flow rate

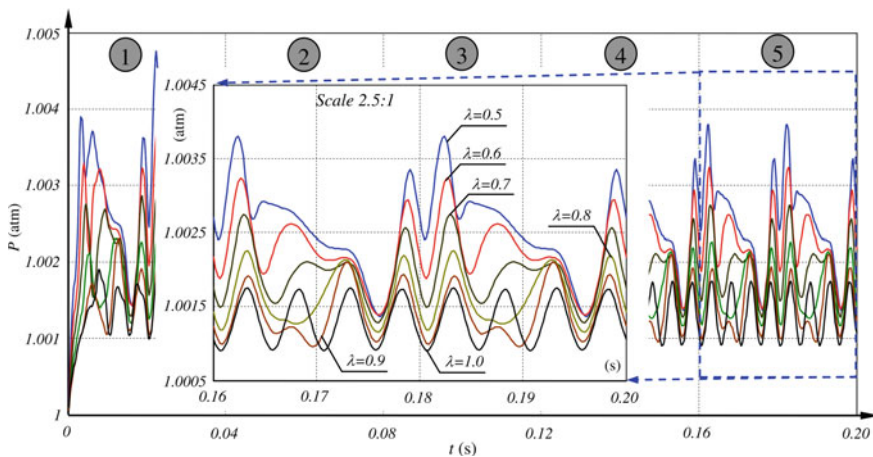


Fig. 4 Instantaneous pressure

### 5 Conclusion

From the numerical simulation and calculation results, combined with the evaluation and discussion above, the main results of this work are the design coefficient  $\lambda$  is the factor that affects the flow and size of the blower. A small design coefficient  $\lambda$  gives a more significant blower flow and a smaller fan size. Specifically, when the design coefficient  $\lambda$  is reduced from 1.0 to 0.5, the average blower flow increases to 32%, while the blower size decreases to 21.43% compared to the traditional design

at  $l = 1$  [2, 8]. The above-obtained results have important implications in applying and developing the proposed novel lobe blower into practice.

**Acknowledgements** This work was supported by Hanoi University of Science and Technology, under grant Number: T2018-PC-020.

## References

1. Jones G (1843) Jones's gas and air exhauster or blower. *Mech Mag* 39:305–306
2. Thai NH, Tien TN (2018) Influence of the designing parameters on the profile slippage and flow of the Roots blower. *Sci Technol Dev J Eng Technol* 1(1):13–19
3. Kang Y-H, Vu H-H (2014) A newly develop rotor profile for lobe pump: generation and numerical performance assessment. *J Mech Sci Technol* 28(3):915–926
4. Tien TN, Thai NH, Long ND (2019) Effects of head gaps and rotor gap on flow rate and hydraulic leakage of a novel non-contact rotor blower. *Vietnam J Sci Technol* 57(6A):125–140
5. Thai NH, Long ND (2021) A new design of the Lobe pump is based on the meshing principle of elliptical gear pairs. *Sci Technol Dev J Eng Technol* 4(2):861–871
6. Guo Q, Qin K, Li D, Huang C, Luo K (2020) Numerical investigation and performance enhancement of Roots pumps operating with gas-liquid mixtures. *Vacuum* 176:109303
7. Litvin FL, Feng PH (1996) Computerized design and generation of cycloidal gearings. *Mech Mach Theory* 31(7):891–911
8. Palmer L, Knox W (1875) Improvement in rotary pressure-blowers. US166295A Patent
9. Hsieh C-F (2015) A new curve for application to the rotor profile of rotary lobe pumps. *Mech Mach Theory* 87:70–81
10. Thai NH, Trung NT (2022) A novel curve for the generation of the non-circular gear tooth profile. *Int J Eng Trans B Appl* 35(5):1024–1036. <https://doi.org/10.5829/ije.2022.35.05b.18>
11. Thai NH, Thom PV, Trung NT (2021) Influence of centrodes coefficient on the characteristic of gear ratio function of the compound non-circular gear train with improved cycloid tooth profile. In: IFToMM Asian conference on mechanism and machine science, pp 204–214. [https://doi.org/10.1007/978-3-030-91892-7\\_19](https://doi.org/10.1007/978-3-030-91892-7_19)
12. Zhou S, Jia X, Yan H, Peng X (2021) A novel profile with high efficiency for hydrogen-circulating Roots pumps used in FCVs. *Int J Hydrogen Energy* 46:22122–22133
13. Tong S-H, Yang DCH (2000) On the generation of new lobe pumps for higher pumping flow rate. *Mech Mach Theory* 35:997–1012
14. Sun S, Singh G, Kovacevic A, Bruecker C (2020) Experimental and numerical investigation of tip leakage flows in a Roots blower. *Designs* 4(1):3. <https://doi.org/10.3390/designs4010003>
15. Xing L, Feng J, Tang H, Peng X (2021) Performance improvement of a large capacity Roots blower based on profile modification. *Proc IMechE Part C: J Mech Eng Sci* 235(13):1–9. <https://doi.org/10.1177/0954406220953175>
16. Thai NH (2021) Shaping the tooth profile of elliptical gear with the involute ellipse curve. *Sci Technol Dev J Eng Technol* 4(3):1048–1056
17. Thai NH, Trung NT, Viet NH (2021) Research and manufacture of external non-circular gear-pair with improved cycloid profile of the ellipse. *Sci Technol Dev J Eng Technol* 4(2):835–845
18. Thai NH, Trung NT, Nghia LX, Duong NT (2020) Synthesis of the external non-circular gear-train with cycloid profile. *J Sci Technol Tech Univ* 145:033–039
19. Thai NH, Thom PV, Trung NT (2021) Experimental design and manufacture a pair of the internal non-circular gears with an improved cycloid profile. In: The AUN/SEED-Net joint regional conference in transportation, energy, and mechanical manufacturing engineering, pp 118–134. [https://doi.org/10.1007/978-981-19-1968-8\\_11](https://doi.org/10.1007/978-981-19-1968-8_11)



20. Thai NH, Ly TTK, Trung NT (2021) Research design and experimental manufacturing of compound non-circular gear train with an improved cycloid profile of the ellipse. In: International conference on engineering research and applications, pp 813–825. [https://doi.org/10.1007/978-3-030-92574-1\\_83](https://doi.org/10.1007/978-3-030-92574-1_83)
21. Thai NH, Thom PV (2021) Research on the Characteristics of tooth shape and size of the oval gear drive with an involute profile. In: The AUN/SEED-Net joint regional conference in transportation, energy, and mechanical manufacturing engineering, pp 167–184. [https://doi.org/10.1007/978-981-19-1968-8\\_14](https://doi.org/10.1007/978-981-19-1968-8_14)

# Dynamic Simulation of Differential-Driven Mobile Robot Taking into Account the Friction Between the Wheel and the Road Surface



Trinh Thi Khanh Ly, Hoang Thien, Dam Khac Nhan,  
and Nguyen Hong Thai

**Abstract** The dynamics problem is essential in designing dynamic control laws for tracking autonomous mobile robots (AMR). Differential-driven mobile robots (DDMR) among AMR are commonly researched and applied. Thus, this article focuses on modelling and simulating the dynamics of a DDMR when moving on an arbitrary trajectory. The reverse dynamics model of a DDMR is established, taking into account the sliding phenomenon between the wheel and the road surface. The coefficient of friction is determined experimentally based on a platform DDMR and an S-type load cell. NURBS interpolation is used to design the motion trajectory of the DDMR in the general case. The research results have important implications for designing kinematics and dynamics controllers for the DDMR to follow a complex trajectory without slipping at a certain speed.

**Keywords** Differential-drive mobile robot · Dynamic modeling · Simulation · NURBS curve · Friction

## 1 Introduction

Mobile robots (MBs) are being widely applied in many different fields, such as in industrial logistics [1], medical logistics [2], tunnelling robots in mining [3], or service restaurant service [4]. MBs were one of the important elements in the industrial production system 4.0 [4–7]. Modeling dynamics is a significant problem when

---

T. T. K. Ly · D. K. Nhan

Faculty of Automation Technology, Electric Power University (EPU), Hanoi, Vietnam

H. Thien · N. H. Thai (✉)

School of Mechanical Engineering, Hanoi University of Science and Technology (HUST), Hanoi, Vietnam

e-mail: [thai.nguyenhong@hust.edu.vn](mailto:thai.nguyenhong@hust.edu.vn)

designing, manufacturing, and controlling MBs. There have been many studies on the dynamics of different types of MBs [8–10]. Ren et al. [11] modelled and simulated an open-loop dynamics controller of an omnidirectional MB with three wheels, ignoring wheel slip and friction between the wheels with the working environment. Sarkar et al. [12] proposed a feedback nonlinear dynamics controller that follows the trajectory according to the Dubins method with the assumption of ignoring slip and friction. Several other studies have tried to design different controllers to improve the position and posture accuracy of MBs during movement with the assumption that there is no friction between the wheel and road surface [13–16]. Zamanian et al. [17] modelled the dynamics problem of a 4-wheel MB taking into account the longitudinal and transverse sliding when moving on arbitrary sloped surfaces, Sidek et al. [18] proposed a nonlinear dynamics controller to improve the lateral slip of a DDMR when navigating an MB. Cerkala et al. [19] modelled the frictional states in the newton dynamics model to design a PI controller that follows the trajectory is a second-order curve similar are some other studies [20, 21], etc. In the above studies, in which friction between wheel and road surface is assumed, have the disadvantage of not being close to practice.

In this work, a dynamic model for a DDMR was established considering the friction between the wheel and road surface with variable load. In addition, a complex curve was applied when the coefficient of friction was determined experimentally based on a platform robot manufactured as input data for the simulation problem.

## 2 Mathematical Models of Dynamics

### 2.1 Kinematic Model

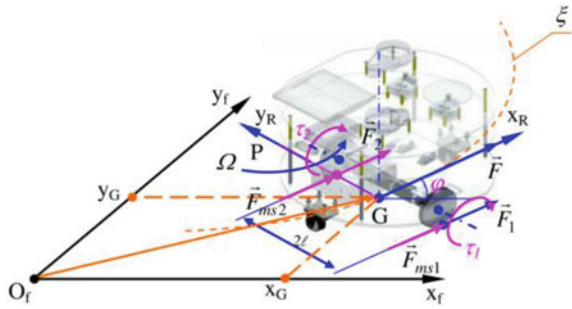
Consider a DDMR moving along the trajectory  $\xi$  with no longitudinal slip in the global coordinate  $\vartheta_f\{O_f, x_f, y_f, z_f\}$  as described in Fig. 1. According to [22], the kinematic of the DDMR is defined by:

$$\begin{cases} V_G = (V_2 + V_1)/2 = r(\dot{\varphi}_2 + \dot{\varphi}_1)/2 \\ \Omega = (V_2 - V_1)(2\ell)^{-1} = r(\dot{\varphi}_2 - \dot{\varphi}_1)(2\ell)^{-1} \end{cases} \quad (1)$$

The linear velocity of the robot in the global coordinate is determined by:

$$\mathbf{q}_f = [x_G \ y_G \ \theta]^T = \begin{bmatrix} \cos \theta & \sin \theta & 0 \\ 0 & 0 & 1 \end{bmatrix}^T \begin{bmatrix} V_G \\ \Omega \end{bmatrix} \quad (2)$$

**Fig. 1** Illustrate the kinematic relationship of DDMR in the global coordinate



### 2.2 The Dynamic Model of DDMR

If \$\tau\_1, \tau\_2\$ are the torque of the left and right driving wheels; \$F\_{ms1}, F\_{ms2}\$ are the friction force between the two wheels and the road surface; \$m\_p\$ is the mass of the robot; \$m\_w\$ is the wheel's mass; \$I\_p, I\_w, I\_m\$ are the moment of inertia of the robot, the wheel about its axis and the wheel around its diameter, respectively. Applying Lagrange dynamics equation we have the dynamic equation of the DDMR is given by:

$$\begin{cases} m\ddot{x}_G - \lambda_1 \sin \theta + (\lambda_2 + \lambda_3) \cos \theta = 0 \\ m\ddot{y}_G + \lambda_1 \cos \theta + (\lambda_2 + \lambda_3) \sin \theta = 0 \\ I\ddot{\theta} + \ell(\lambda_3 - \lambda_2) = 0 \\ I_w\ddot{\varphi}_1 - \lambda_2 r = \tau_1 - r F_{ms1} \\ I_w\ddot{\varphi}_2 - \lambda_3 r = \tau_2 - r F_{ms2} \end{cases} \quad (3)$$

wherein \$m = m\_p + 2m\_w\$; \$I = I\_p + 2m\_w\ell^2 + 2I\_m\$; \$\lambda\_1, \lambda\_2\$ and \$\lambda\_3\$ are Lagrange multipliers.

Writing Eq. (3) in the form of an algebraic matrix, we have [23]:

$$\mathbf{D}(\mathbf{q})\ddot{\mathbf{q}} + \mathbf{M}^T(\mathbf{q})\boldsymbol{\lambda} = \mathbf{E}(\boldsymbol{\tau} - \mathbf{F}), \quad \mathbf{q} = [x_G, y_G, \theta, \varphi_1, \varphi_2]^T \quad (4)$$

Transform Eq. (4) using the matrix \$\mathbf{B}(\mathbf{q})\$ with \$\mathbf{v}(t) = [V\_G \ \Omega]^T\$, we have the dynamics of DDMR when considering the frictional force:

$$\bar{\mathbf{D}}(\mathbf{q})\dot{\mathbf{v}}(t) + \bar{\mathbf{C}}(\mathbf{q})\mathbf{v}(t) = \bar{\mathbf{E}}(\boldsymbol{\tau} - \mathbf{F}), \quad \mathbf{B}(\mathbf{q}) = \begin{bmatrix} \cos \theta & \sin \theta & 0 & r^{-1} & r^{-1} \\ 0 & 0 & 1 & -\ell r^{-1} & \ell r^{-1} \end{bmatrix}^T \quad (5)$$

### 3 Simulation Results and Discussion

#### 3.1 Setting Simulation Parameters

**Step 1.** Determine the inertia parameters of DDMR

Inertia parameters matrix of the DDMR, the frames, and the wheel are determined from the design by the Mass Properties tool of Solidworks software, given by:

$$\begin{aligned}
 \mathbf{I}_r &= \begin{bmatrix} 0.128 & -0.001 & -0.004 \\ -0.001 & 0.130 & 0.007 \\ -0.004 & 0.007 & 0.142 \end{bmatrix}, \quad \mathbf{I}_t = \begin{bmatrix} 0.114 & -0.001 & -0.004 \\ -0.001 & 0.126 & 0.007 \\ -0.004 & 0.007 & 0.131 \end{bmatrix}, \\
 \mathbf{I}_b &= \begin{bmatrix} 0.153 \times 10^{-3} & 0 & 0 \\ 0 & 0.299 \times 10^{-3} & 0 \\ 0 & 0 & 0.153 \times 10^{-3} \end{bmatrix} \tag{6}
 \end{aligned}$$

**Step 2.** Experimental determination of the coefficient of friction of the driving wheel with the road surface

Experimental determination of the coefficient is carried out according to the diagram Fig. 3, with the platform as described in Fig. 2, has the parameters: DDMR mass  $m = 10.4$  (kg), driving wheel radius  $r = 0.0475$  (m), the distance between two driving wheels  $2\ell = 0.3$  (m).

Experimental process is carried out with 3 cases: (1) No load, (2) Test load with  $m_{L1} = 1$  kg and (3) Test load with  $m_{L2} = 2$  kg. For each test case 10 times. The experimental data is described in Table 1.

With the experimental values in Table 1, the coefficient of friction between the wheel and the road surface is calculated by the formula below:

**Fig. 2** A photo of the platform DDMR



**Fig. 3** Determine the coefficient of friction

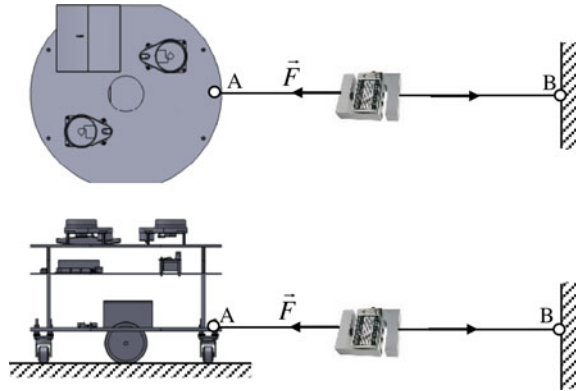


**Table 1** Experimental data determine the coefficient of friction

No.	Case 1	Case 2	Case 3	No.	Case 1	Case 2	Case 3
	$F_1$ (kgf)	$F_2$ (kgf)	$F_3$ (kgf)		$F_1$ (kgf)	$F_2$ (kgf)	$F_3$ (kgf)
1	3.535	4.060	4.490	6	3.560	4.020	4.570
2	3.570	4.130	4.520	7	3.565	4.035	4.550
3	3.550	4.160	4.485	8	3.570	4.015	4.525
4	3.535	4.150	4.520	9	3.565	4.035	4.520
5	3.570	4.075	4.545	10	3.550	4.120	4.525

The average value: **Case 1:** 3.557, **Case 2:** 4.080, **Case 3:** 4.525

$$\mu_i = F_{tb}(m_{\Sigma}g)^{-1}, \mu_c = \mu_{tb} = (\mu_{kt} + \mu_{i1} + \mu_{i2})3^{-1} \tag{7}$$

where  $F_{tb}$  is the mean force value,  $m_{\Sigma} = m + m_{Li}$  ( $i = 1, 2$ );  $g = 9.81 \text{ m/s}^2$ .

Thus, the coefficient of friction between the wheel and the road surface is  $\mu_c = 0.355$ .

**Step 3. Simulated trajectory settings**

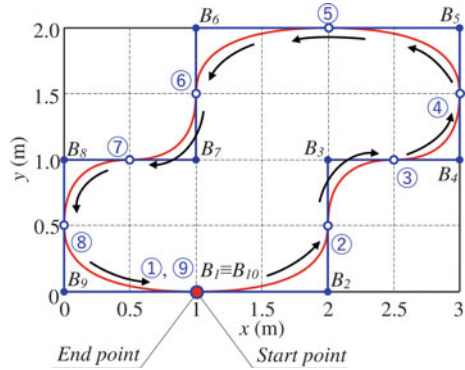
To simulate DDMR dynamics in the general case, we use the NURBS curve [23, 24] to design the motion trajectory of the DDMR, as shown in Fig. 4,  $B_i$  points ( $i = 1-10$ ) are NURBS interpolation points. The red curve is the motion trajectory of DDMR after performing NURBS interpolation on Matlab software.

**Step 4. Set the kinematics and dynamics parameters**

From the motion trajectory  $\xi$  is defined in Fig. 4, the radius of curvature of the trajectory is obtained as follows:

$$\rho(t) = \left| (\dot{x}(t)^2 + \dot{y}(t)^2)^{3/2} (\dot{x}(t)\ddot{y}(t) - \dot{y}(t)\ddot{x}(t))^{-1} \right| \tag{8}$$

**Fig. 4** Motion trajectory of DDMR



Here  $(x(t), y(t))$  is the coordinates of trajectory  $\xi$ .

Set the linear velocity  $V_G$  of the DDMR  $V_G = 0.2$  (m/s). Thus, the angular velocity and angular acceleration of the DDMR is determined by:

$$\Omega(t) = 2V_G\rho^{-1}(t), \quad \varepsilon(t_i) = \dot{\Omega}(t_i) = \Delta\Omega(t_i)(\Delta t_i)^{-1} = (\Omega(t_{i+1}) - \Omega(t_i))(t_{i+1} - t_i)^{-1} \tag{9}$$

### 3.2 Simulation Results and Discussion

From the kinematics and dynamics equations established in Sect. 2 and the setting parameters are presented in Sect. 3.1. Figure 5 is a calculation diagram simulating the dynamics problem of DDMR set up on Simulink of Matlab software. Figure 6 is a graph describing the angular velocity and acceleration of the DDMR with the markers corresponding to those in Fig. 4.

The simulation results in Fig. 6 shown at inflexion points 2, 3, 6, and 7 in Fig. 4 have curvature radii 0.954 m, 0.988 m, 0.988 m, and 0.978 m, respectively, angular velocity of DDMR has a sudden jump from positive to negative or vice versa. That leads to an abrupt change of moment  $\tau_1, \tau_2$  as described in Fig. 7. While at inflexion points 1, 5 with corresponding curvature radii of 4.0 m, 3.950 m, and no change of direction  $\tau_1, \tau_2$  at that time is a point on the smooth curve. At inflexion points 4, 8 have curvature radii of 0.628 m and 0.499 m and no change of direction. From the simulation results and discussion above, it can be seen that at inflexion points with the change of direction of DDMR, the angular velocity has jumped, causing the driving torque of the driving wheels to change suddenly, causing the slip phenomenon.

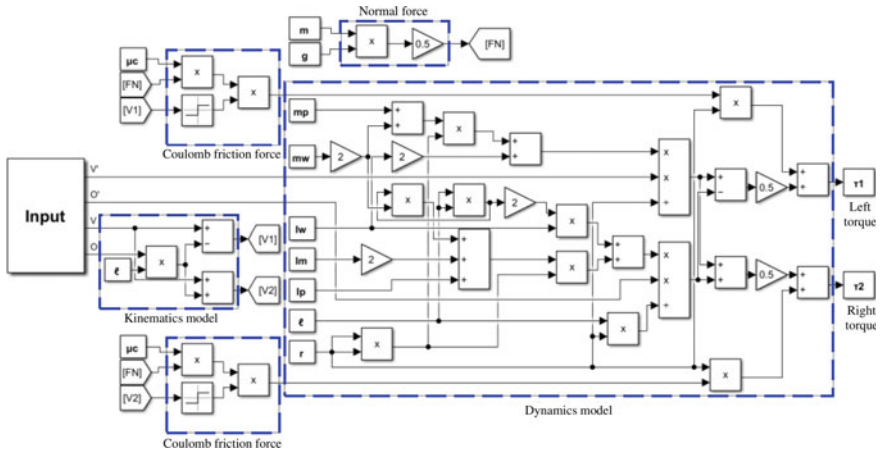


**Fig. 5** Simulink diagram calculates dynamic simulation for DDMR

**Fig. 6** The velocity and acceleration angular of DDMR

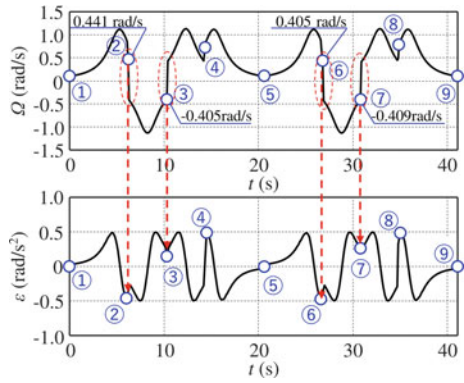
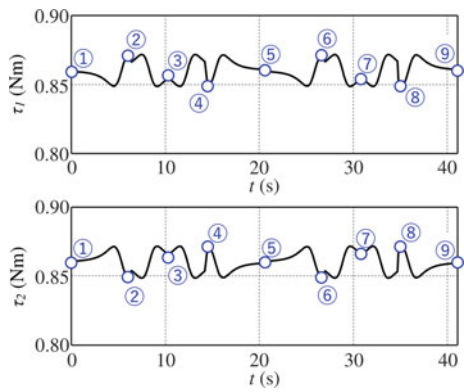


**Fig. 7** Torque value of two driving wheels for DDMR





## 4 Conclusion

From simulation results, experimental, discussion above, this research has achieved the following results: (i) The dynamics problem with a simple friction model is considered in the case of DDMR moving along a general trajectory; (ii) At inflexion points with a small radius of curvature and DDMR, there is a change of direction, resulting in a sudden change in torque. At that time, there is a slippage between the wheel and the road surface, causing the position and posture error of the DDMR. These results have scientific significance in designing trajectory tracking dynamics controllers for practical DDMRs such as AGVs serving logistics in industry or hospitals. However, the limitation of this research is that it has not considered the influence of rough and material homogeneity of the road surface in practice on the coefficient of friction. These factors affect the ability to grip the road and the motion accuracy of DDMR. As such, it will be considered part of our future research goals.

**Acknowledgements** Hoang Thien was funded by the Master Scholarship Programme of Vingroup Innovation Foundation (VINIF), code VINIF.2022.ThS.128.

## References

1. Cardarelli E, Digani V, Sabattini L, Secchi C, Fantuzzi C (2017) Cooperative cloud robotics architecture for the coordination of multi-AGV systems in industrial warehouses. *Mechatronics* 45:1–13
2. Sjøraa RA, Fostervold ME (2021) Social domestication of service robots: the secret lives of automated guided vehicles (AGVs) at a Norwegian hospital. *Int J Hum Comput Stud* 152:102627
3. Nguyen TH, Nguyen TQ (2017) A kinematic control algorithm for blasthole drilling robotic arm in tunneling. *Sci Technol Dev J* 20(K5):13–22
4. Shimmura T, Ichikari R, Okuma T, Ito H, Okada K, Nonaka T (2020) Service robot introduction to a restaurant enhances both labor productivity and service quality. *Procedia CIRP* 88:589–594
5. Thai NH, Trinh LTK, Dzung LQ (2021) Roadmap, routing and obstacle avoidance of AGV robot in the static environment of the flexible manufacturing system with matrix devices layout. *Sci Technol Dev J* 24(3):2091–2099
6. Ahmadi SM, Taghadosi MB, AmirReza Haqshenas M (2021) A state augmented adaptive backstepping control of wheeled mobile robots. *Trans Inst Meas Control* 43(2):434–445
7. Ly TTK, Thai NH, Dzung LQ, Thanh NT (2020) Determination of kinematic control parameters of omnidirectional AGV robot with mecanum wheels track the reference trajectory and velocity. In: Sattler KU, Nguyen DC, Vu NP, Long BT, Puta H (eds) *Advances in engineering research and application. ICERA 2020. Lecture notes in networks and systems*, vol 178, pp 319–328
8. Yu R, Ding S, Tian H, Chen Y-H (2021) A hierarchical constraint approach for dynamic modeling and trajectory tracking control of a mobile robot. *J Vib Control*, 1–13
9. Andaluz VH, Roberti F, Carelli R, Toibero JM, Wagner B (2011) Adaptive dynamic path following control of an unicycle-like mobile robot. In: *International conference on intelligent robotics and applications*, pp 563–574
10. Vázquez JA, Villa MV (2008) Path-tracking dynamic model based control of an omnidirectional mobile robot. *IFAC Proc* 41(2):5365–5370

11. Ren C, Ma S (2013) Dynamic modeling and analysis of an omnidirectional mobile robot. In: IEEE/RSJ international conference on intelligent robots and systems, pp 4860–4865
12. Sarkar N, Yun X, Kumar V (1994) Control of mechanical systems with rolling constraints: application to dynamic control of mobile robots. *Int J Robot Res* 13(1):55–69
13. Thai NH, Ly TTK, Long NT, Dzung LQ (2021) Trajectory tracking using linear state feedback controller for a mecanum wheel omnidirectional. In: Khang NV, Hoang NQ, Ceccarelli M (eds) *Advances in Asian mechanism and machine science. ASIAN MMS 2021. Mechanisms and machine science*, vol 113, pp 411–421
14. Thai NH, Ly TTK (2022) Trajectory tracking control for mecanum wheel mobile robot by time-varying parameter PID controller. *Bull Electr Eng Inf* 11(4):1902–1910
15. Thai NH, Ly TTK (2022) Path tracking control for car-like robots by PID controller with time-varying parameters. *Sci Technol Dev J* 5(2)
16. Ly TTK, Thien H (2022) Bézier trajectory tracking control of the omnidirectional mobile robot based on a linear time-varying state feedback controller. *Sci Technol Dev J* 25(2):2444–2452
17. Zamanian H, Javidpour F (2016) Dynamic modeling, and simulation of 4-wheel skid-steering mobile robot with considering tires longitudinal and lateral slips. *Int J Sci Res Knowl* 4(2):040–055
18. Sidek N, Sarkar N (2008) Dynamic modeling and control of nonholonomic mobile robot with lateral slip. In: *Third international conference on systems*, pp 35–40
19. Čerkala J, Jadlovska A (2014) Mobile robot dynamics with friction in Simulink. In: *Proceedings of the 22th annual conference proceedings of the international scientific conference—technical computing*, Bratislava, pp 1–10
20. Xie Y, Zhang X, Meng W, Zheng S, Jiang L, Meng J, Wang S (2021) Coupled fractional-order sliding mode control and obstacle avoidance of a four-wheeled steerable mobile robot. *ISA Trans*, 282–294
21. Sun Z, Xie H, Zheng J, Man Z, He D (2021) Path-following control of mecanum-wheels omnidirectional mobile robots using nonsingular terminal sliding mode. *Mech Syst Signal Process* 147:107–128
22. Thai NH, Ly TTK, Thien H, Dzung LQ (2022) Trajectory tracking control for differential-drive mobile robot by a variable parameter PID controller. *Int J Mech Eng Robot Res* 11(8):614–621
23. Thai NH, Thien H, Ly TTK (2022) NURBS curve trajectory tracking control for differential-drive mobile robot by a linear state feedback dynamic controller. In: Le AT, Pham VS, Le MQ, Pham HL (eds) *The AUN/SEED-Net joint regional conference in transportation, energy, and mechanical manufacturing engineering. RCTEMME 2021*, pp 610–623
24. Thai NH, Ly TTK (2022) NURBS curve trajectory tracking control for differential-drive mobile robot by a linear state feedback controller. In: Nguyen DC, Vu NP, Long BT, Puta H, Sattler KU (eds) *Advances in engineering research and application. ICERA 2021. Lecture notes in networks and systems*, vol 366, pp 685–696

# Research on the Vibration of Passenger Car Using Magnetorheological Fluid Damper



Nguyen Anh Ngoc, Le Hong Quan, Vu Hai Quan, Nguyen Minh Tien,  
and Nguyen Ngoc Anh

**Abstract** Vehicle vibration is a problem that is currently in need of research attention to improve the quality of automobile exploitation. The suspension system directly affects vibration as well as safety and performance. It helps control and suppresses the vibration of the road acting on the chassis, helping the vehicle to move stably and the passengers on the vehicle to feel smooth. The design to optimize the suspension, more specifically the damping is being interested in and developed, one of the ideas is to add shock absorbers using magnetorheological fluid, which can change the viscosity by electricity. This study will simulate the traditional suspension system and the suspension system with the addition of using magnetorheological fluid dampers (MR dampers) when the vehicle moves into different profiles on the road. MR dampers are activated and supplement the damping force for a certain period to quickly reduce the amplitude of the vibration, test with different values of the force from the MR damper to evaluate and select the most reasonable value. The results show that the body vibration amplitude is improved, the ability to suppress vibration increases, the shake angle of the vehicle body decrease, respond the smoothness, and increase the convenience of the car.

**Keywords** Vehicle vibration · MR dampers · Suspension system · Passenger vehicle

---

N. A. Ngoc (✉) · L. H. Quan · V. H. Quan (✉) · N. M. Tien · N. N. Anh  
Faculty of Automotive Technology, Hanoi University of Industry, Hanoi, Vietnam  
e-mail: [ngocnguyencnoto@hau.edu.vn](mailto:ngocnguyencnoto@hau.edu.vn)

V. H. Quan  
e-mail: [quanvh@hau.edu.vn](mailto:quanvh@hau.edu.vn)

## 1 Introduction

In the process of economic development and serving social life, the demand for transportation of passengers and goods is increasing daily. With its advantages, car transportation is better than other means of transport. Many modern cars were born to meet the needs and purposes of human use. Research aimed at improving the quality of automobiles is needed. Research on oscillation and its effect on transport service quality, durability of automobile parts and structures is increasingly interesting.

When a car moves on the road and encounters bumps on the road, the car will experience a loss of smoothness. This force tends to cause the coordinates of the center of gravity of the suspended mass to change, causing the vehicle to become unstable, causing discomfort to people in the vehicle. Therefore, limiting this phenomenon in the vehicle is necessary. The solution is to increase the value of the damping force, one of the methods of adding a damping element [1].

The problem of longitudinal instability of the vehicle has been studied by domestic and foreign scientists as well as many solutions, one of the solutions given is the use of additional dampers [2]. However, previous studies have often focused on passive damping. To increase the value of resistance against the force from the road surface feedback to the vehicle, it is necessary to increase the stiffness of the suspension. Today, vehicles are often equipped with dampers to minimize the reaction from the road surface to the vehicle. The stiffness and size of the shock absorbers are proportional to the mass of the vehicle, larger vehicles require larger diameter and stiffer shock absorbers. Therefore, it will greatly affect the smoothness of the car when moving on the road.

Given the above problems, instead of using conventional mechanical dampers, some midsize and high-end vehicles have been equipped with electrically or hydraulically controlled dampers. Active damping has the advantage of reducing body movement when entering bumpy areas, thereby increasing the smoothness of the vehicle when in motion.

This paper focuses on simulating the working efficiency of dampers to propose a design option for active dampers equipped with MRF to provide additional force value against pavement reaction when entering uneven roads.

## 2 Building a Simulation Model of the Suspension System with MR Damper

Research, orientation to build diagrams studied in the document [3, 4]. From the literature [5], 1/2 and 1/4 suspension models are built, we have constructed and formulated a mathematical differential equation for the whole vehicle vibration. For example, we have a left-front suspension diagram (Fig. 1).

The damping force of the left wheel:

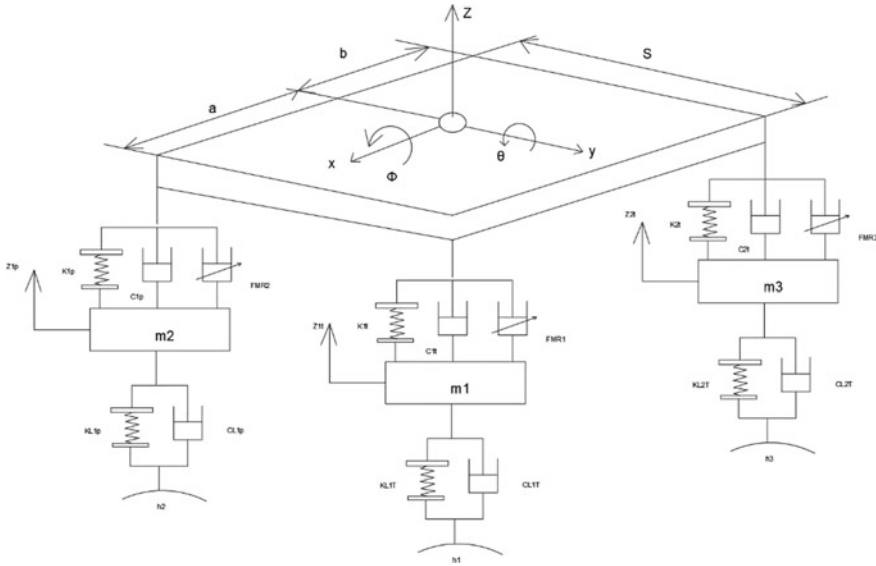


Fig. 1 Overall spatial model to survey the vibrations of passenger cars

$$F_{CLIT} = (\dot{h}_1 - \dot{Z}_{IT}) \cdot C_{LIT} \tag{1}$$

The elastic force of the left wheel:

$$F_{KLIT} = (h_1 - Z_{IT}) \cdot K_{LIT} \tag{2}$$

Call  $Z_{IT}$  the point on the left of the front axle connected to the body through the left front suspension.

The damping force of the left front suspension:

$$F_{C1t} = \left( \frac{s}{2} \dot{\varphi} - a\dot{\theta} - \dot{z} - \dot{Z}_{IT} \right) \cdot C_{1T} \tag{3}$$

The elastic force of left front suspension:

$$F_{K1t} = \left( \frac{s}{2} \dot{\varphi} - a\dot{\theta} - \dot{z} - \dot{Z}_{IT} \right) \cdot K_{1T} \tag{4}$$

From this we can get the equilibrium equations.

The force balance equation of the vehicle body in the Z direction:

$$F_{C1t} + F_{K1t} + F_{C1p} + F_{K1p} + F_{C2t} + F_{K2t} + F_{C2p} + F_{K2p} + F_{MR1} + F_{MR2} + F_{MR3} + F_{MR4} = F_{qt}(m) \tag{5}$$

**The equation of moment balance in the X direction:**

$$I_x \cdot \ddot{\varphi} = (-F_{C1t} - F_{K1t} + F_{C1p} + F_{K1p} - F_{C2t} - F_{K2t} + F_{C2p} + F_{K2p}) \cdot \frac{S}{2} + S/2 \cdot F_{MR1} - S/2 \cdot F_{MR2} - S/2 \cdot F_{MR3} + S/2 \cdot F_{MR4} \quad (6)$$

**The Y-direction moment balance equation:**

$$I_y \cdot \ddot{\theta} = (F_{C1t} + F_{K1t} + F_{C1p} + F_{K1p}) \cdot a - (F_{C2t} + F_{K2t} + F_{C2p} + F_{K2p}) \cdot b - aF_{MR1} - aF_{MR2} + bF_{MR3} + bF_{MR4} \quad (7)$$

### 3 Vehicle Vibration Simulation

Based on the differential equations describing the vibration of the whole vehicle to simulate the vibration of the full body vehicle. Then proceed to solve the vibration equation.

Vehicle parameters

The parameters are referenced from the passenger car line with the following specific parameters:

- Load of the whole vehicle at no load:  $M = 4000$  (kg)
- Moment of inertia along X axis:  $J_x = 10,000$  (kg m<sup>2</sup>)
- Moment of inertia along Y axis:  $J_y = 5760$  (kg m<sup>2</sup>)
- Tire hardness:  $K_{L1} = 200,000$  (N/m);  $K_{L2} = 240,000$  (N/m)
- Tire damping coefficient:  $C_L = 2000$  (Ns/m)
- Front damping drag coefficient:  $C_t = 10,000$  (Ns/m)
- Rear damping drag coefficient:  $C_s = 10,000$  (Ns/m)
- Front suspension stiffness:  $K_t = 100,000$  (N/m)
- Rear suspension stiffness:  $K_s = 120,000$  (N/m)
- Distance from center of gravity to front axle:  $a = 2.1$  (m)
- Distance from center of gravity to rear axle:  $b = 1.9$  (m)
- Vehicle speed:  $v = 60$  km/h.

Road surface agitation function

$$h1 = \frac{0.1}{2} \times (1 - \cos(8\pi t)) \text{ and } h2 = \frac{0.05}{2} \times (1 - \cos(8\pi t)) \quad (8)$$

### 4 Simulation Results

The simulation is performed with a suspended mass of 4000 kg when moving on an amplitude of the road of 5 cm and 10 cm.

- (a) Simulation and comparison of the results of the center of gravity amplitude of the vehicle with and without the use of MR dampers.

Survey with  $h = 5$  cm and  $h = 10$  cm (Fig. 2).

- For  $h = 5$  cm with the value  $F_{MR} = 7000$  N, the maximum amplitude of fluctuation reaches the minimum value of  $1.142 \times 10^{-2}$  (m).
- For  $h = 10$  cm with the value of  $F_{MR} = 14,000$  N, the maximum amplitude of fluctuation reaches the minimum value of  $2.011 \times 10^{-2}$  (m) (Fig. 3).

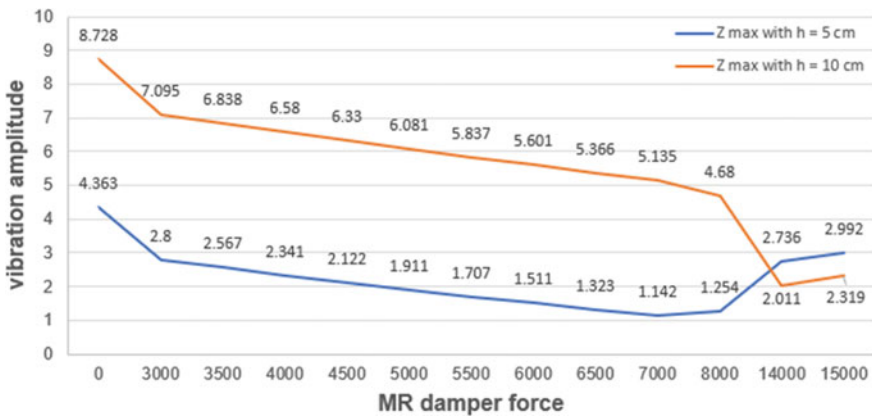


Fig. 2 The graph of the maximum value of the body vehicle vibration amplitude with MR damper force

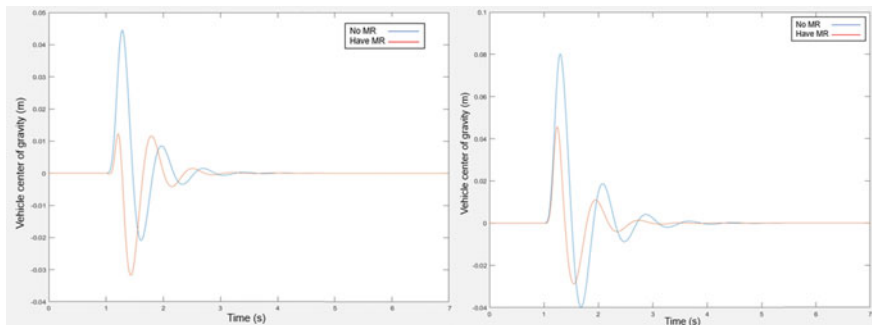
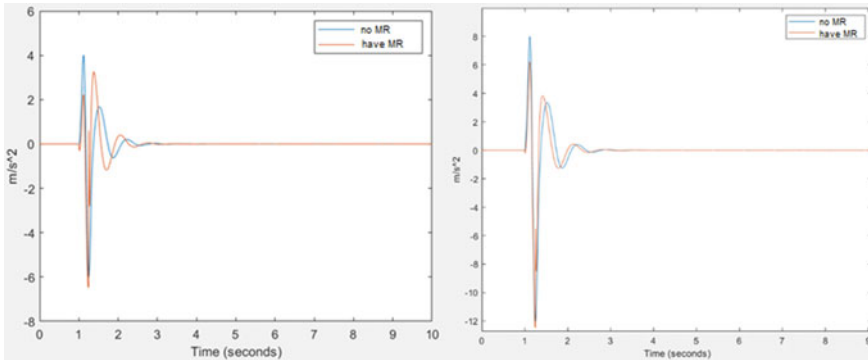


Fig. 3 Graph comparing the vehicle’s center of gravity with  $F_{MR} = 7000$  N,  $h = 5$  cm (left) and  $h = 10$  cm (right)



**Fig. 4** Vehicle acceleration graph with pavement amplitudes 5 cm and 10 cm

The vibration of the vehicle's center of gravity has been reduced:

- 72.5% from  $4.449 \times 10^{-2}$  to  $1.224 \times 10^{-2}$  m for pavement amplitude  $h = 5$  cm
- 41.166% from  $8.728 \times 10^{-2}$  to  $5.135 \times 10^{-2}$  m with pavement amplitude  $h = 10$  cm.

With the addition of an MR damper, the body vehicle displacement is less, which proves that there is an optimum in terms of comfort when adding an MR damper.

- (b) Simulation comparison of acceleration results between vehicles with and without magnetic damper MR (Fig. 4).

The vibration acceleration has decreased:

- 18.71% from  $4.013 \text{ m/s}^2$  to  $3.262 \text{ m/s}^2$  for pavement amplitude  $h = 5$  cm
- 21.94% from  $8.001 \text{ m/s}^2$  to  $6.245 \text{ m/s}^2$  with pavement amplitude  $h = 10$  cm.

Due to the change in body vehicle vibration amplitude, the acceleration also changes, this change is appropriate when adding an MR damper. Although there has been a change in amplitude, there is not much change in vibration quenching time, This is a limitation as well as can become the next research direction to be able to further optimize the results.

## 5 Conclusion

With simulation results, it has been shown that the damper using magnetorheological fluid (MR damper) affects the displacement of the body's center of gravity. When an additional force of 7000 N is applied, the MR damper works more effectively reduced by 41.166% compared to when no MR force is added. Theoretically, the more force applied to the damper, the lower the body displacement decreases, which makes the vehicle move more smoothly, but in practice, the design of the MR damper must



ensure the main geometric dimensions of the components. Details in the suspension such as volumetric length and width, orifice diameters, as well as the thicknesses of the main components, so that the production of larger force values is possible but in practice is affected by the size, so in this research, the survey team with MR force is 7000 N. With the obtained simulation results, it can be seen that after adding the MR damper with force  $F = 7000$  N, the vehicle has moved more smoothly when the vibration amplitude is reduced in both cases of the test road, despite the time vibration quenching time does not change much, this may be the next research direction to improve the efficiency of the design.

## References

1. Jang J, Dong M (2018) Research on vibration of automobile suspension design
2. Oh J-S, Choi S-B (2019) Suspension system featuring magnetorheological dampers with multiple orifice holes
3. [Online]. Available: <http://www.timtailieu.vn/tai-lieu/luan-van-tot-nghiep-tim-hieu-simulink-trong-matlab-2812/>
4. Mohammadzadeh A, Haidar S (2006) Analysis and design of vehicle suspension system using MATLAB and Simulink. Grand Valley State University, p 11.213.1
5. Trai NK, Hoan NT, Huong PH, Chuong NV (2010) Automobile structure

# Design and Durability Test of the Main Assemblies of Active Anti-roll bar



Nguyen Anh Ngoc, Tran Phuc Hoa, Vu Hai Quan, Nguyen Minh Tien,  
and Kieu Huu Bang

**Abstract** The anti-roll bar has the effect of increasing the stable motion of the vehicle. It has the role of receiving, transmitting force and torque between the wheel and the chassis, reducing the vibration frequency of the car, ensuring the smoothness and stick on the road of the vehicle. Therefore, this paper conducts research on “*design and durability test of the main assemblies of active anti-roll bar*”. The active anti-roll bar uses MR fluid, the design of the magnetic brake assembly replaces two rubber bearings on the conventional anti-roll bar, this is also the position to increase the torque for the bar. The article conducts research and simulation with different materials, in different working modes to evaluate the durability of the bar, and gives the most suitable results for the design, ensuring the durability detail. At the same time, evaluate and give suitable materials for the MR brake assembly.

**Keywords** Durability test · Design and simulation anti-roll bar · Active anti-roll bar · MR brake · MR fluid

## 1 Introduction

The suspension system on modern vehicles must ensure two basic criteria: smoothness to the driver and firmness when the vehicle is in motion (such as when turning around or braking sharply). To meet the above two basic requirements, one of the methods is to use an active anti-roll bar. The body vehicle tilt angle  $\psi$  has a great influence on the stability of the motion. To improve the lateral stability of the car, solutions can be applied such as: changing the size of the passive anti-roll bar, using control

---

N. A. Ngoc (✉) · T. P. Hoa · V. H. Quan (✉) · N. M. Tien · K. H. Bang  
Automobile Technology Department, Hanoi University of Industry, Hanoi, Vietnam  
e-mail: [ngocnguyencnoto@hau.edu.vn](mailto:ngocnguyencnoto@hau.edu.vn)

V. H. Quan  
e-mail: [quanvh@hau.edu.vn](mailto:quanvh@hau.edu.vn)

systems such as suspension, steering and brake system... But in the above research cases, the smoothness and safety of movement and vice versa are not guaranteed. In order to satisfy both of the above criteria in accordance with the characteristics of the road and the stability and structure of the vehicle, the research team this time designed a passive anti-roll bar using MR fluid. With this passive anti-roll bar, in addition to the torsional values of the normal passive rod, it can be changed to increase the torque value for the rod to match the vehicle's stability with the road profile [1].

The research will approach the active anti-roll bar from the design, then evaluate and test the durability, select the right material for the active anti-roll bar and the component assemblies to serve the purpose of long-term use, avoiding damage that affects the movement as well as endangers the occupants of the vehicle.

## 2 Design Active Anti-roll bar

Bar design: In the active anti-roll bar model using MR magnetic oil with the design of the MRF magnetic brake assembly so that there is not much change in the rod structure and chassis structure on the vehicle to optimize, the research team has The design of the MRF brake assembly is the point to replace the two rubber bearings on the conventional anti-roll bar (passive bar) and at the same time, it is also the point to increase the torque for the rod [2]. The parameters selected in the study include size and shape according to the actual car model. After referencing documents, the research team has designed 01 stabilizer bar model created on Solidworks software with the standards and parameters shown in Table 1 (Table 2).

The research team selected 3 types of spring steel materials used to manufacture tweezers, springs, ... for testing, which are AISI 1065, SAE 5160, SAE 9262 with the following characteristics [3] (Table 3).

**Table 1** Steel parameters and values

Parameter	Value
Length	1100 mm
Type of section	Hollow section
Bearing position	440 mm
Swing arm length	150 mm
Inner-outer diameter	15-Ø20

**Table 2** Characteristics of steel grade AISI 1018

Parameter	Value
Gradual recovery module (Pa), E	2.05e11
Poisson's ratio	0.29
Density ( $\text{kg/m}^3$ ), $\rho$	7870
Tensile strength (MPa), Sy	370

**Table 3** Characteristics of steel grades

Characteristic	AISI 1065	SAE 5160	SAE 9262
Elastic modulus (MPa)	207	207	207
Poisson’s ratio	0.3	0.3	0.3
Tensile strength (MPa)	280	1487	455
Max tensile strength (MPa)	420	1584	923

MR Brake design and assembly: MR brake assembly is designed to replace and install in place of two rubber bearing assemblies being used on current vehicles. The design requirement is that the magnetic oil brake assembly has the same shape and size as the rubber bearing assembly. The purpose of placing in the position of the bearing helps to keep the chassis design unchanged from the original size. With the design close to the position of the swingarm, it also helps to make the most of the generated torque to make the vehicle’s stabilization time faster [4] (Figs. 1 and 2).

In order to come up with the optimal design in terms of the number of poles and the length of the brake, the authors have simulated and tested the design with different sizes and different numbers of poles on Ansoft Maxwell software and selected the 4-pole magnetic design. After selecting the number of poles, we continue to run the test of lengths of 45 mm, 50 mm, 60 mm, 70 mm, 80 mm respectively to evaluate the change in torque when the length size changes. The author chooses AISI 1018 magnetic steel as shown in Table 4 to evaluate and test two important main details, rotor and stator. The rotor is a very important detail in the MRF brake assembly, which is considered a core part (bone part) to assemble other details on it such as wire wrapping, magnetic shield, bolt holes (Fig. 3).

**Fig. 1** MR brake assembly

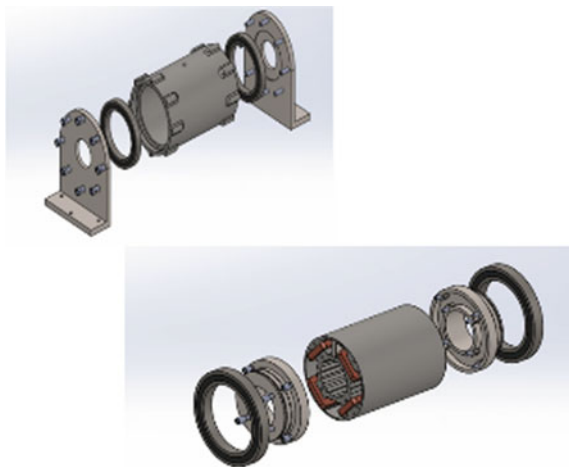


**Fig. 2** The brake assembly is installed on the anti-roll bar

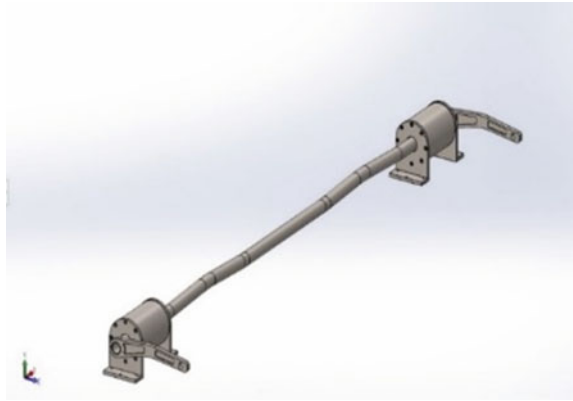


**Table 4** Nodes and elements of details after meshing

Steel marks	AISI 1065	SAE 5160	SAE 9262
Maximum stress (MPa)	420	1584	923

The material chosen for the shield is aluminum because aluminum is a non-magnetic material, has high corrosion resistance and is easy to process and manufacture. The detail assembly cover is responsible for keeping the force and sealing with the internal components to form the MRF brake assembly. In order to ensure long-term use conditions, the material used for the detailed lid is stainless steel. And are fastened together with bolts. In the MRF brake assembly, the stator is an external fixed element that is hung on the iron cylinder through the brackets on both sides (Figs. 4 and 5).

The two ends of the stator have been designed to install oil-shielded ball bearings, to avoid the leakage of MR oil during use, and moreover, it also limits the swing angle of the rod to help the MRF brake assembly operate in the most stable way [5]. After the MRF brake assembly is fully assembled and sealed, the MR magnetic oil is poured into the MRF brake assembly through the threaded hole in the stator body.

### 3 Simulation

Link Settings: The stabilizer bar works based on the support of the ball bearing, so the condition of face-to-face contact is set, swing conditions for the swing arm. Then, setup bar boundary condition, rotor boundary conditions, stator boundary condition (Fig. 6).

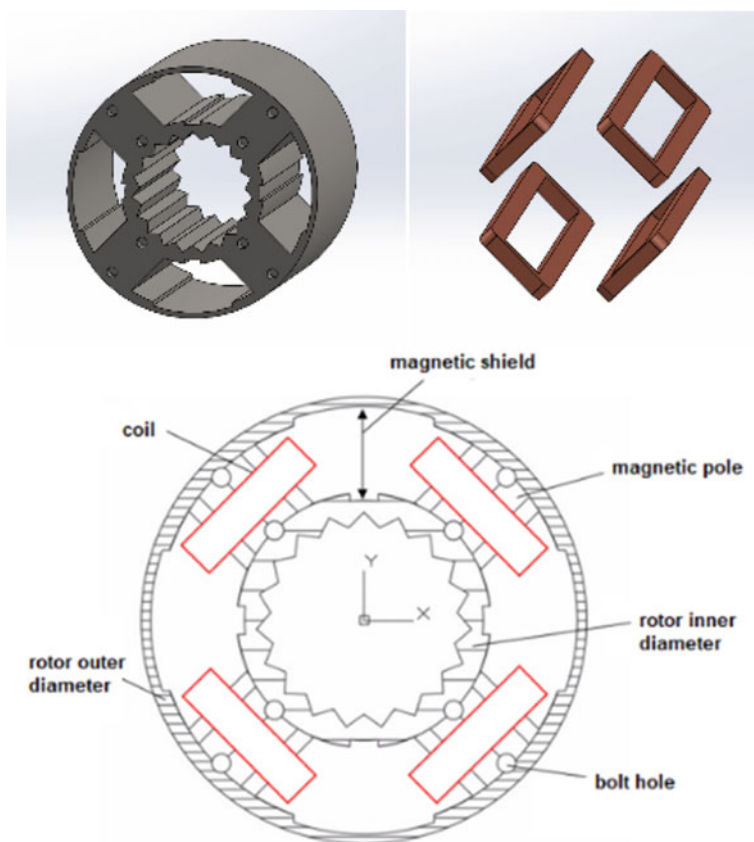


**Fig. 3** Definition of parameters and rotor—winding

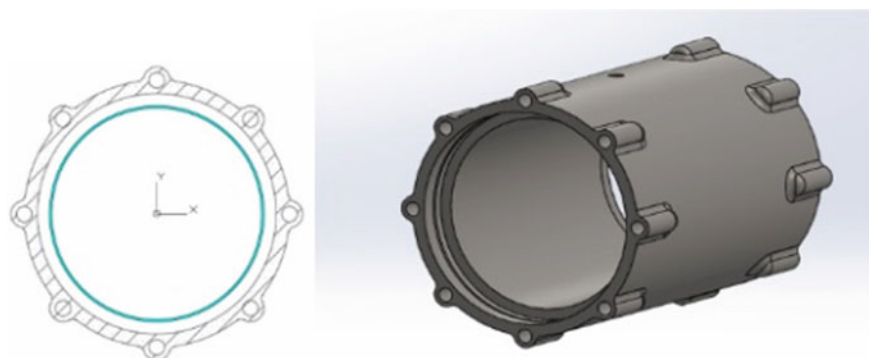


**Fig. 4** Stator design model

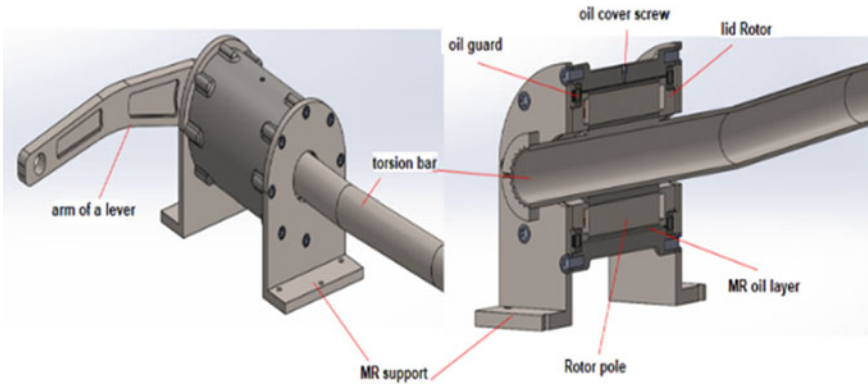


Fig. 5 Assembly model

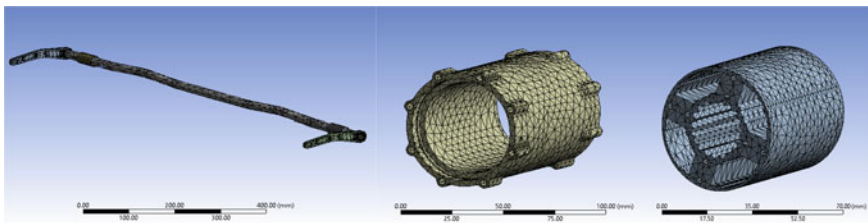


Fig. 6 Meshing the stator-rotor simulation model

### 4 Results and Discussion

**Result:** We run with each material in turn with the inner and outer diameters of ( $\varnothing 14$ – $\varnothing 20$ ), ( $\varnothing 15$ – $\varnothing 20$ ) (Fig. 7).

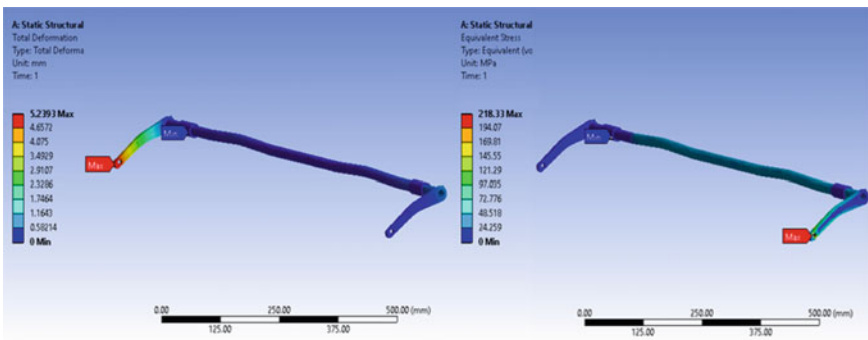


Fig. 7 Displacement and stress of steel grade SAE 5160

When changing rotation angle increases, the stress also increases gradually and reaches the maximum value for diameter 14 is 1423.1 MPa, for diameter 15 is 1337.5 MPa. The bar is durable enough, not destroyed even when reaching the largest rotation angle.

In Fig. 8, when the rotation angle increases, the stress also increases gradually and reaches the maximum value for diameter 14 is 1419.4 MPa, for diameter 15 is 1334.1 MPa. The bar can only be rotated to 40 rotations angle, check with 60 rotations angle, the maximum stress on the bar exceeds the allowable stress.

In Fig. 9, as the rotation angle increases, the stress also increases gradually and reaches the maximum value of 1432 MPa for diameter 14, 1345.8 MPa for diameter 15. The bar can only be rotated to a rotation angle of 80, check with a rotation angle of 100, the maximum stress on the bar exceeds the allowable stress (Figs. 10, 11 and 12).

Stress on Rotor and Stator is very small (<1 MPa), displacement on Rotor and Stator is very small (<1 mm). Rotor and Stator is durable enough under operating conditions.

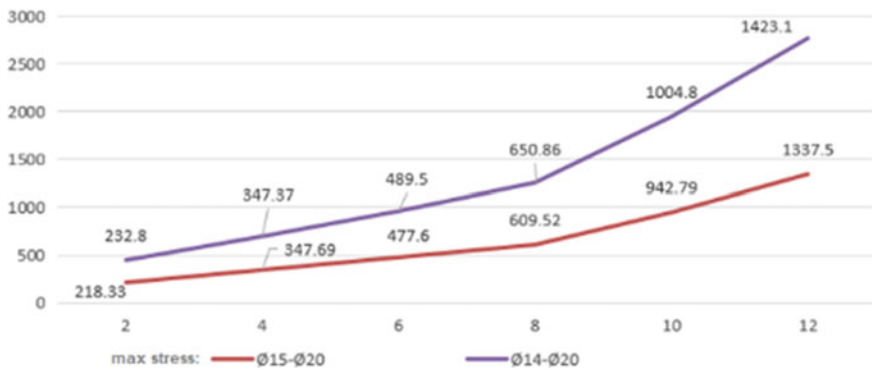


Fig. 8 Comparing the effect of diameter with steel SAE 5160 with each rotation angle

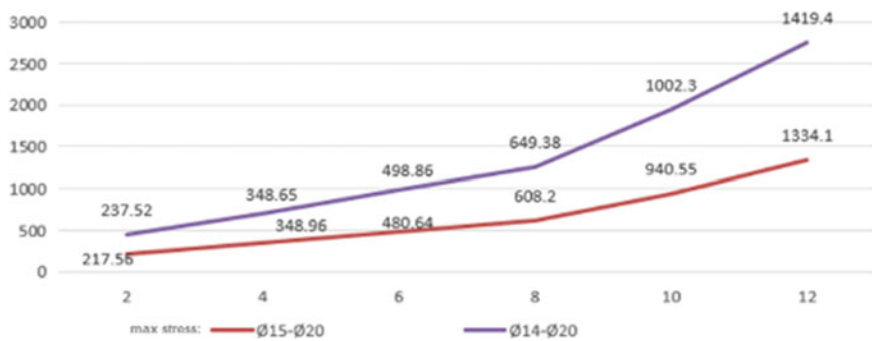


Fig. 9 Comparing the effect of diameter with steel AISI 1065 with each rotation angle



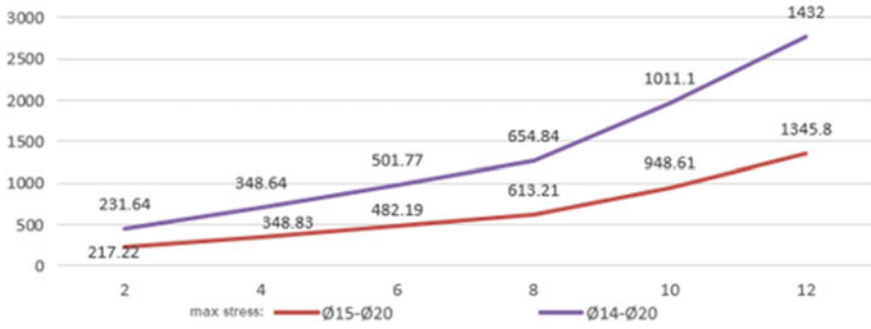


Fig. 10 Graph comparing the effect of diameter with steel SAE 9262 with each rotation angle

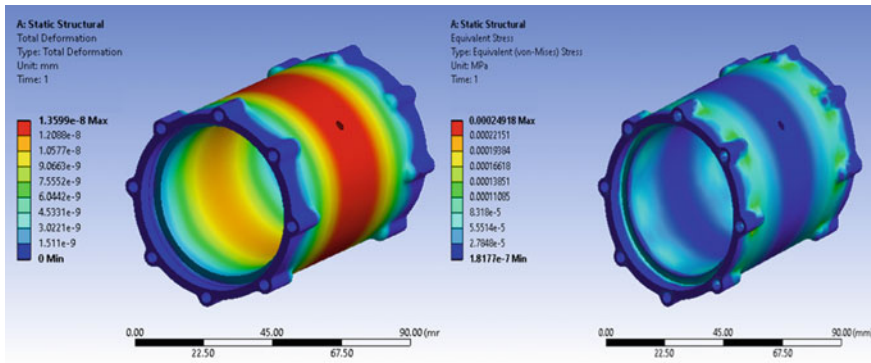


Fig. 11 Displacement and stress of rotor of MR brake

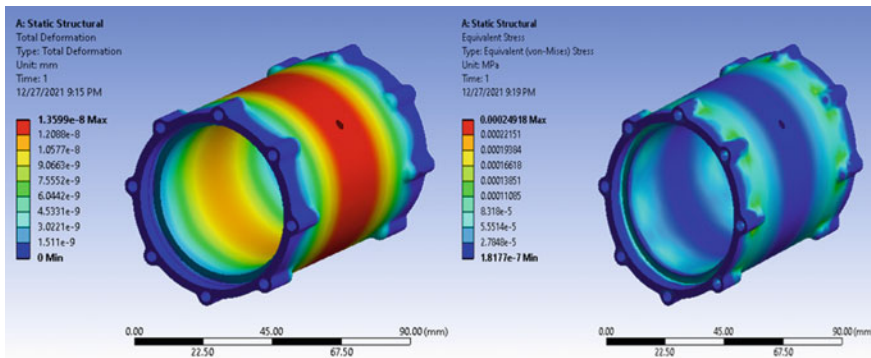


Fig. 12 Displacement and stress of stator of MR brake

**Table 5** Max stress with diameter 14 and 15

Steel marks		AISI 1065	SAE 5160	SAE 9262
Max stress (MPa) with diameter	14	1222.9	1200.3	1195
	15	1091.5	1070.4	1065.3

**Evaluation:** The time required to construct, simulate and determine the reaction and stress of the rod is also not too long. It is possible to repeatedly seal the balance bars with different materials as well as bars with different sizes and materials used. To find the optimal solution designed balance bar.

*Anti-roll bar:* We have the maximum allowable tensile strength of steel grade.

After simulation we get the following results (Table 5).

*Inference:* Only one SAE 5160 material is qualified for durability.

*MR brake assembly:* According to simulation, the highest stress and displacement of the Rotor are  $1.9147e-8$  MPa and  $2.0093e-004$  mm, respectively, of the Stator is  $1.3599e-008$  MPa and  $2.4918e-004$ . The stress and displacement of the MR brake assembly are satisfactory under the operating conditions, making it suitable for long-term use.

## 5 Conclusion

The study has produced a detailed design for the active anti-roll bar using MR brake, from that design, a simulation of testing and durability assessment was conducted, choosing the optimal diameter from two values of 14 and 15, and select materials with high strength and stress tolerance in AISI 1065, SAE 560, SAE 9262 materials for the anti-roll bar and test with AISI 1018 material for rotor and stator. The simulation results show that the rod size with diameter  $\varnothing 15$  and SAE 5160 material is the optimal material to ensure the conditions during operation, this is a reliable material for designing and manufacturing for the bar, max stress of each rotor and stator part is lower than the allowable stress value of AISI 1018 steel of 370 MPa and the displacement of the assembly is very small. With the design size and simulation conditions as above, it is completely reasonable. From the above results, it can be seen that the details are super durable, which can be extended to a number of further research directions: fatigue strength, dynamic durability, ... in the case of moving vehicles, building optimization problems to improve detail quality.

## References

1. Quan VH, Ngoc NA (2023) Design and optimizing analysis of front lower control arm by using Hyperwork and Matlab Simulink. J Biomech Sci Eng Jpn Soc Mech Eng. ISSN: 1880-9863. <https://doi.org/10.17605/OSF.IO/2V897>

2. Ngoc NA, Tao NQ, Kien NT, Quan VH (2023) Design and calculations of fomular car chassis. J Biomech Sci Eng Jpn Soc Mech Eng. ISSN: 1880-9863. <https://doi.org/10.17605/OSF.IO/9GNH7>
3. Bhanage A, Krishna P (2015) Static and fatigue simulation of automotive anti roll bar before DBTT 2015
4. Shiao YJ, Nguyen QA, Zhang ZY (2015) Design and experiment of a new magnetorheological brake
5. Shiao Y, Ngoc NA, Lai CH (2016) Optimal design of a novel multi-pole bi-layer magnetorheological brake. Smart Mater

# Determination of Magnetorheological Brake Characteristics by Experiment on the Test Rig



Tuan-Hoang Quang, Hoang-Trinh Minh, Ngoc-Nguyen Anh,  
and Tung-Tran Thanh

**Abstract** In this study, braking torque characteristics of a disc-shaped Magnetorheological brake (MRB) structure are determined on the test platform. The primary purpose of this study is to determine the relationship between the generated braking torque depending on the current supplied to the coil on the MRB device. The process of determining the brake torque characteristics on the test platform consists of three steps. In the first step, the study deals with the magnetorheological fluid (MRF) characteristics and the MRB structure. In the second step, a brake test platform is built to measure the torque generated on the MRB. In the third step, the measurement procedure on the platform is introduced, and experiment results are analyzed. These results show that the relationship between the generated braking torque depends on the input amperage. The study's results confirm the effectiveness of magnetorheological fluid in highly appropriate scientific and technical fields.

**Keywords** Magneto-Rheological Fluid (MRF) · MR brake · Test rig

## 1 Introduction

In scientific research, the research on the test platform is one of the commonly used methods. The results of the measurements on the test platform can be used as input parameters for simulation problems or to evaluate the model's reliability or the system's efficiency and performance. Also, for these purposes, in the world, there

---

T.-H. Quang · H.-T. Minh (✉) · N.-N. Anh  
Hanoi University of Science and Technology, Hanoi, Vietnam  
e-mail: [hoang.trinhminh@hust.edu.vn](mailto:hoang.trinhminh@hust.edu.vn)

T.-H. Quang · N.-N. Anh  
Hanoi University of Industry, Hanoi, Vietnam

T.-T. Thanh  
Vietnam Maritime University, Hai Phong, Vietnam

have been many experimental studies on the MR brake system in order to determine the braking torque characteristics when changing the current, speed, or changing brake system structure.

Research by Mousavi et al. [1] with a new configuration of the MR hybrid brake consisting of a T-shaped drum with an arc surface. The author has experimentally determined the braking torque when changing the amperage, through which the maximum braking torque is 38.5 Nm when the maximum current in each coil is 1.2 A. Another study by Sukhwani and Hirani [2] determined the torque characteristics of the MRB when changing the current from 0 to 1.2 A and the number of revolutions of the motor from 200 to 1200 rpm. Another synthetic study was carried out with the analysis on the test bench of the moments generated with different structures of MR brakes such as drum, multilayer magnetic, and disc type [3] and showed some Braking torque characteristics with current and structure. Research by Dr. Ngoc Nguyen Anh [4] has proposed a new type of MR brake with the features of modeling, structure optimization, testing, and prototype analysis. The main contribution of this work is the optimal design of the new configuration of the MR brake to improve the braking torque. However, for magnetic brakes, to evaluate the application effectiveness for specific objects, the output braking torque characteristics need to consider the structure's mass and volume. Therefore, with the specific MRB structure chosen by the authors, the goal is to use the experimental method on the brake test platform with high stability and accuracy to determine the characteristics of the braking torque generated on the MRB when changing the input current value is necessary.

The structure of the paper is that after the overview, the second part introduces the basic operating principle of the brake using MR fluid. The third part presents the structure and operating principle of the brake test platform, including the method, equipment, and measurement parameters. The final part presents the results and comments.

## 2 Theory

### 2.1 *Magneto-Rheological Fluid*

Magnetorheological Fluid is an oil containing ferromagnetic particles. It is an innovative material that can quickly change phase state (liquid-semi-solid) and whose reversible properties are controlled by an applied electric current. When applying a current to the coil, a magnetic field will appear, and that magnetic field directly affects the properties of the oil. Usually, soft ferromagnetic or paramagnetic particles (0.03–10  $\mu\text{m}$ ) are dispersed in the oil layer. Without a magnetic field, ferromagnetic particles are distributed mainly in the liquid. However, under the action of the applied magnetic field, the ferromagnetic particles acquire a dipole moment by the external magnetic field and form chains. In addition, the yield stress of the magnetic oil can be adjusted continuously and rapidly as it responds to the applied magnetic field

strength [5]. The properties of MR fluids used in brake equipment are often expressed as Bingham models with varying yield strength ( $\tau_y$ ), depending on the magnetic field ( $H$ ), [4, 6].

## 2.2 Working Principle of MR Brake

To apply MRF technology to the automotive auxiliary brake system, the structure of the MRB consists of a fixed part and a rotating part (Fig. 1). The fixing includes the mounting parts on the brake support, including details such as the outer stop plate, the outer stop plate, the outer stop disc, and the bolts, nuts, and screws on the fixing assembly. On the fixed assembly, two conductive coils are placed between the inner stop and the outer stop, each winding 1000 turns, with a wire diameter of 0.5 mm. Fixing elements are bolted together by standard bolts. The rotating cluster has the main detail as the rotating disc. In addition, to ensure smooth movement between the rotating part and the fixed part, in the design, there are two more assemblies of ball bearings and an oil seal. Outside there is a stop disc to prevent the oil seal from slipping out of the installation position. The space between the rotating disc and the two inner plates is filled with magnetic oil.

With the above structure, the torque transmitted from the active part (the motor through the gearbox) will make the passive part (the rotating disc) rotate at a certain speed. In the state where no current is supplied to the coil arranged in the cavity of the MRB, there exists a resistance between the MRF layer itself and the rotating disc part. When applying current to the coil, the magnetic field generated by the

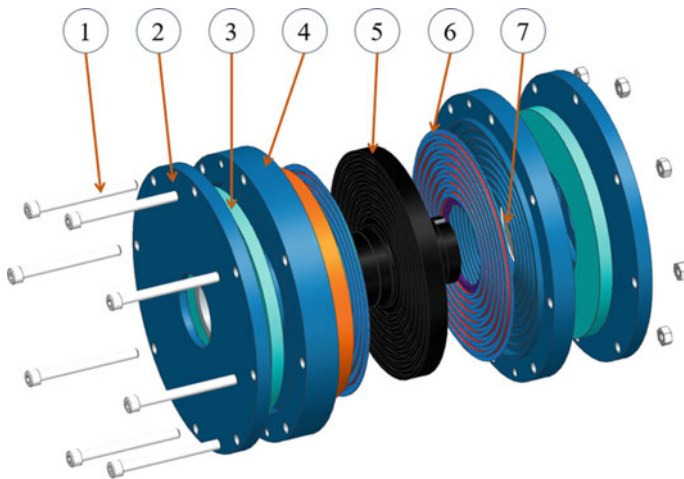


**Fig. 1** MRB construction. 1—Bolt; 2—Outer stopper cover; 3—Coil; 4—Inner stopper; 5—Rotary disc; 6—Magneto-Rheological Fluid; 7—Bearing assembly and oil seal

coil will act on the oil areas in different positions on the brake disc, changing the shear stress of the oil. Doing so will change the state of the MRF and create some of the MR oil's frictional resistance when the oil layer's structure hardens. From there, generate the motor's shaft braking torque. An engine cover is arranged to hang on the pedestal through the bracket. The braking torque will act, tending to rotate the motor's housing. Therefore, to determine this torque, a lever is arranged with one end attached to the motor housing, the other end resting on the spring of the rheostat torque sensor.

### 3 Determination of MR Brake Characteristics on the Test Platform

The MR brake test stand should meet the following objectives and requirements:

- Determination of brake torque-current characteristics; Braking torque -revolution speed in different modes.
- Ensure that there is no strong vibration or fluctuation during the measurement, affecting the measurement results;
- Compact manufacturing, easy to transport and install;

When applying current, the shear stress of the changing magnetic oil will create resistance to the rotor shaft of the electric motor, creating a torque that tends to rotate the motor housing, through the lever mechanism will exert a force on the electric motor. A brake force sensor will convert to a voltage signal, send this signal to the processor, and display the measured brake torque value on the screen.

#### 3.1 Structure of Brake Test Rig

The test pedestal consists of  $40 \times 40$  shaped aluminum frame bars supporting the entire load and  $20 \times 20$  aluminum frames as the outer cover. We divide the test platform into two main parts:

- The lower part of the test platform is located in the control system: control circuit, transformer, driver, and laptop, and the circuit are separated from the inverter by POM plastic.
- The upper part of the test platform includes mechanical mechanisms: hybrid servo motor, gearbox, coupling, magnetic brake, and accompanying mounting plates (Fig. 2).

The 110J12190EC-1000 stepper motor provides a maximum torque of 20 Nm at 1000 rpm. Included with the 110J12190EC-1000 stepper motor is a 3HSS2208H driver. The 3HSS2208H stepper servo drive system integrates perfect motor control

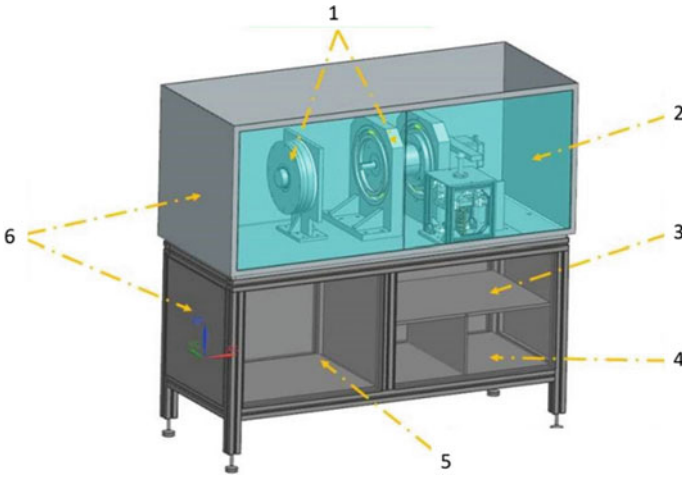


**Fig. 2** Model of MR brake test rig. 1—Mechanical part; 2—Front door; 3—Control Circuit location; 4—Transformer location; 5—Laptop location; 6—Test rig frame part

and is suitable for three-phase stepper motors. Compared with traditional stepper drive, this hybrid servo motor driver can avoid the problem of the stepper motor losing a step and effectively limit the motor’s temperature rise, reducing the motor’s vibration and greatly enhancing the performance of high-speed motors. A lever is captured from the engine. It will cause a load on the sensor when the MRB is engaged. In addition, bearings and couplings are used in the mechanical system to provide a smooth movement from the engine to the MRB.

### 3.2 Measurement Process

The investigation of the braking torque characteristics of the MRB on the pedestal is carried out in two modes:

- Mode 1: Investigate the relationship between braking torque and amperage (brake). In this study, fixed motor speed investigated the change of MRB brake torque generated when changing current.
- Mode 2: Investigate the relationship between braking torque and engine speed. In this mode, fix the current value, and investigate the change of MRB brake torque generated when changing motor speed (Table 1).



**Table 1** Two test modes on the test rig

Run test	Engine speed (rpm)	Current (A)	Step	Number of runs	Output
1	1000	1	100 mA	3	Excel + Chart
2	0–2500	1	250 rpm	3	Excel + Chart

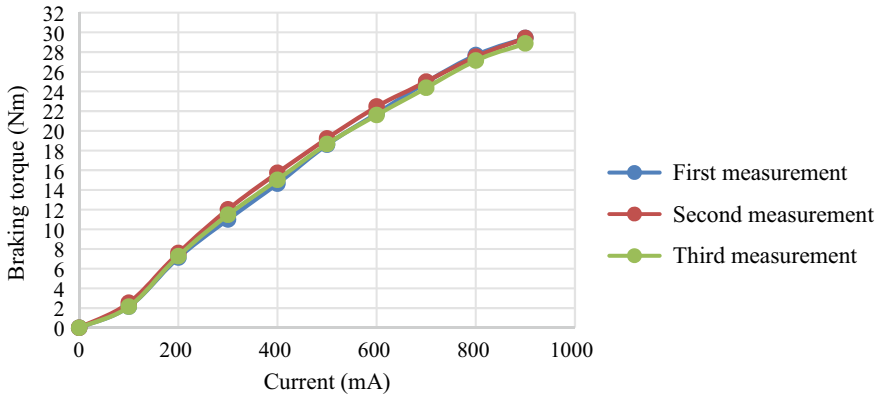


**Fig. 3** Braking torques are measured when changing the current in 100 mA increments

### 4 Results and Comments

Figure 3 shows the result of amperage-dependent braking torque in three measurements when keeping the engine speed at 1000 rpm. The amperage varies from 0 to 900 mA, 100 mA steps. The results show that the braking torque increases with increasing current, and the braking torque characteristic is almost linear. When the current increases from 0 A to 900 mA, the measured braking torque value on the platform increases from 0 to the maximum value of 29.42 Nm respectively.

Figure 4 shows the braking torque in three measurements depending on engine speed. In this study, the current was kept constant at 500 mA, and variable motor speed from 0 to 2000 rpm, step 250 rpm. The results show that when fixing the supply current to the MRB brake device and changing the number of engine revolutions, the value of the braking torque produced is almost unchanged. Reach a steady value of about 18 Nm at 250 rpm. The results confirm that the braking torque of the MRB is mainly influenced by the value of the amperage supplied to the coil.

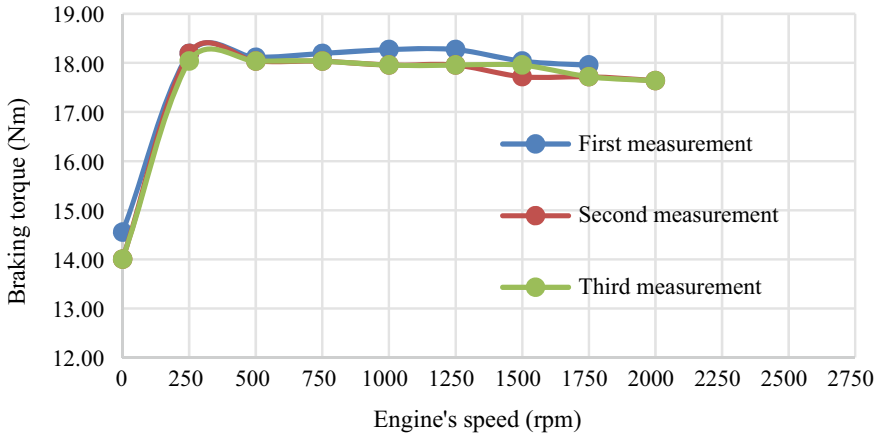


Fig. 4 Braking torques are measured when changing the motor speed

## 5 Conclusion

The research results of this paper are the basis for intensive application studies on brake systems using magnetic oil technology in the field of science and technology in general, as well as the automobile industry in particular. Braking torque characteristics can be used as input for the research and development of automobile brake assist systems. In addition, the research results can also be used as a basis for the problems of optimizing the MRB structure to increase the braking torque or determine the safe working area of the MRB.

## References

1. Mousavi SH, Sayyaadi H (2018) Optimization and testing of a new prototype hybrid MR brake with arc form surface as a prosthetic knee. *IEEE*, pp 1204–1214
2. Sukhwani VK, Hirani H (2007) Design, development, and performance evaluation of high-speed magnetorheological brakes. <https://doi.org/10.1243/14644207JMDA120>
3. Avraam T (2009) MR-fluid brake design and its application to a portable muscular rehabilitation device. Active Structures Laboratory Department of Mechanical Engineering and Robotics
4. Ngoc NA (2016) Development and analysis of new multipole magnetorheological brake. College of Mechanical and Electrical Engineering, College of Mechanical and Electrical Engineering
5. Kciuk M, Turczyn R (2006) Properties and application of magnetorheological fluids, vol 18, issue 1–2, September–October 2006
6. Edminister A (1993) *Schaum's outline of theory and problems of electromagnetics*, 2nd ed. McGraw-Hill

# A Short Review of Renewable Energy Generation: Sustainable Development, Successful Lessons from Leading Countries



V. L. Trinh, C. K. Chung, X. C. Nguyen, Q. T. Nguyen, and T. S. Nguyen

**Abstract** Renewable energy (RE) is the most priority issue to keep global sustainable development with a non-pollution environment, non-gas emissions, and no global warming. Renewable energy is generated from renewable sources that immensely exist in nature such as wind, solar, ocean, bioenergy, and geothermal energies instead of fossil energy sources with many harmful problems for human health and environment. This paper reviews recently RE technologies and successful lessons from applying modern science and technology in developing renewable energy for a sustainable economy, society, and industrial development in leading countries of sustainable energy development. The results hope that renewable energy will be bloomed in research and practical application all over the world.

**Keywords** Energy · Renewable energy · Sustainable energy · Sustainable development

## 1 Introduction

Most countries need a huge amount of energy for social and economic development demand. Traditional energy that comes from fossil energy resources by using technologies with toxic wasted pollutions of carbon dioxide or sulfur gases through

---

V. L. Trinh (✉) · Q. T. Nguyen · T. S. Nguyen  
Faculty of Mechanical Engineering, Hanoi University of Industry, 298 Caudien Street,  
Hanoi 10000, Vietnam  
e-mail: [longtv@hau.edu.vn](mailto:longtv@hau.edu.vn)

C. K. Chung (✉)  
Department of Mechanical Engineering, National Cheng Kung University, Tainan 701, Taiwan  
e-mail: [ckchung@mail.ncku.edu.tw](mailto:ckchung@mail.ncku.edu.tw)

X. C. Nguyen  
Vietnam-Japan Centre, Hanoi University of Industry, Hanoi, Vietnam

burning or power plant techniques, has been still numerous used in over the world. The use of traditional energy is parallel with a long time negative consequences of environmental pollution, gas emission, climate change, and human health effects. Renewable energy, which comes from renewable energy resources of solar energy and nature energies with non-toxic pollution and human health protection, is quick development based on sustainable energy sciences and technologies for converting renewable energy sources into useful energy recently. These methods include renewable energy conversion techniques of wind power, solar photovoltaic, biofuels, hydropower, and geothermal energy technique [1–7]. With outstanding advantages, the renewable energy is rapidly exploiting and applying for sustainable development in all fields of economy, society, health care, transportation, and industry. Many countries show strong movements in the development and application of renewable energy in replacement of traditional energy by renewable energy such as China with the planning of the electricity of renewable energy of 139,450 GWh in 2050 [8], developing policy and technology related to renewable energy with solar home systems in Sub-Saharan Africa [9], developing advanced technologies in renewable generations for island power grids [10], building a smart energy city with one hundred percent renewable energy for Denmark and Europe in 2050 [11], building the renewable energy policy with regional allocation in China to get carbon neutralization in 2060 [12], and providing a roadmap for sustainable development in South Korea with transition scenarios toward the renewable energy by 2050 [13]. This paper reviews recently renewable energy technologies and successful lessons from the strategy of applying modern science and technology in developing and exploiting renewable energy for sustainable energy development. The results hope that renewable energy will be strongly developed and exploited in countries all over the world.

## 2 Renewable Energy Generation

Renewable energy generation (REG) changes renewable energy sources into valuable energy like electricity. Table 1 shows the renewable energy production from the top 5 countries in the years of 2019, 2020, and 2021. China goes the first position with REG of  $742 \times 10^3$  gigawatt-hours (GWh) in 2019,  $863.2 \times 10^3$  GWh in 2020, and  $1152.5 \times 10^3$  GWh in 2021, respectively. The United States stands the second place with REG of  $483.7 \times 10^3$  GWh  $547.7 \times 10^3$  GWh, and  $624.5 \times 10^3$  GWh in the years of 2019, 2020, 2021, respectively. Germany comes the third place with REG of  $220.6 \times 10^3$  GWh in 2019,  $231.8 \times 10^3$  GWh in 2020, and  $217.6 \times 10^3$  GWh in 2021, respectively [14].

**Table 1** The renewable energy generation from the top 5 countries (Gigawatt-hours)

Country	Year		
	2019	2020	2021
China	$742 \times 10^3$	$863.2 \times 10^3$	$1152.5 \times 10^3$
US	$483.7 \times 10^3$	$547.7 \times 10^3$	$624.5 \times 10^3$
Germany	$220.6 \times 10^3$	$231.8 \times 10^3$	$217.6 \times 10^3$
India	$141.1 \times 10^3$	$152 \times 10^3$	$171.9 \times 10^3$
Brazil	$117.6 \times 10^3$	$126.5 \times 10^3$	$144 \times 10^3$

### 3 Sustainable Energy Development

Sustainable development is one of the first criteria of social development. Most of the fields need the energy to develop. Some areas have also contributed to sustainable energy development such as information technology, environment technology, power grid. That, renewable energy technology has a vitally important role in sustainable energy development strategies in over the world. Some research groups have developed new models or indexes to enlarge services of sustainable energy development such as using multi-dimensional indicators to measure sustainable energy development [15], using tools of internet of thing in sustainable energy systems [16], using hybrid harvesters to get sustainable energy [17], and applying blockchain to the sustainable energy systems [18]. To get sustainable development related to renewable energy, some dimensions need to use to estimate the satisfaction levels of society, economy, environment, energy, and technology. Some criteria also need to use to measure the application ability of renewable energy such as resource potential, energy efficiency, energy grid, energy variability, cost, carbon dioxide emission, energy conversion efficiency, employment, and environmental impact. Figure 1 shows the relationship between renewable energy, dimensions, and criteria in the sustainable development strategy.

### 4 Some Successful Lessons from Leading Countries

Some countries show outstanding abilities in developing and applying renewable energy in living, economy, and society. For examples: developing a framework of the service-oriented operation system for a power system in China with new technologies of communication technology, internet of things, cloud computing, and smart grid [19], transiting to renewable energy in Azerbaijan [20], using biofuels to reduce urban air pollution and CO<sub>2</sub> in Brazil [21], using optimization method of biogas production in Zimbabwe with anaerobic digestion [22], using the energy security and sustainable energy policy for sustainable development in Bangladesh [23], constructing a one hundred percent renewable electricity supply scenario with about 10.6 GW of solar power, 4.5 GW of wind power, and 25 GW of photovoltaic up to 2050 [24]. The

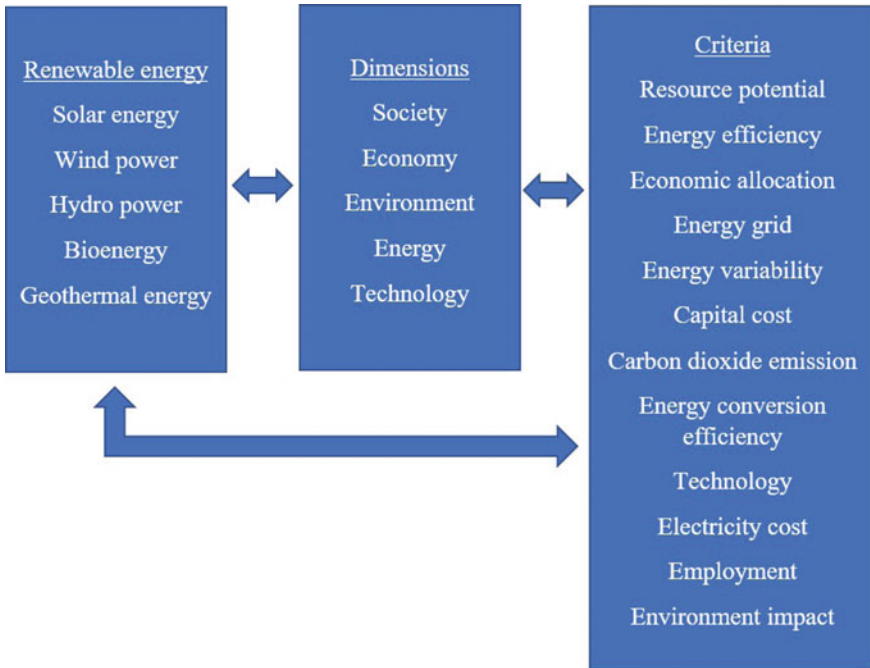


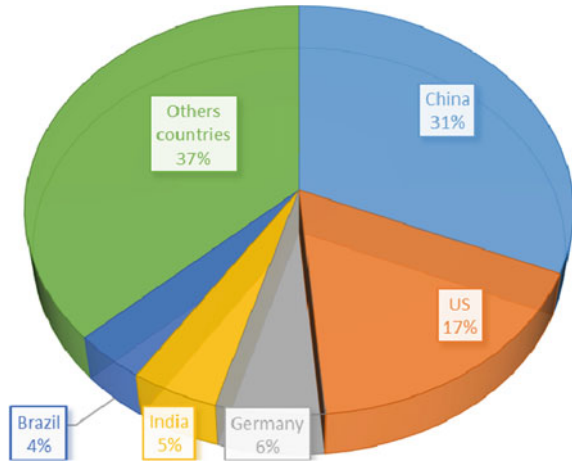
**Fig. 1** The relationship between renewable energy, dimensions, and criteria in the sustainable development strategy

United States projects that renewable energy generation will increase up to 44% in 2050 from 21% in 2021 [25]. Table 2 shows the top 5 countries with the total renewable energy generation in the world in 5 years from 2017 with the first place of China with  $502 \times 10^3$  GWh in 2017 and up to  $1152.5 \times 10^3$  GWh in 2021 [14]. The global renewable energy generation increases from  $2182.3 \times 10^3$  GWh in 2017 to  $3657.2 \times 10^3$  GWh in 2021. Figure 2 shows the share of renewable energy generation from the 5 leading countries in the world in 2021 with the biggest place of China with 31.5%, followed by the US 17.1%, Germany 5.9%, India 4.7%, and Brazil 3.9% [14].

**Table 2** The top 5 countries with the total renewable energy generation in the world in 5 years from 2017 to 2021 (Gigawatt-hours)

	2017	2018	2019	2020	2021
China	$502 \times 10^3$	$636.4 \times 10^3$	$742 \times 10^3$	$863.2 \times 10^3$	$1152.5 \times 10^3$
US	$417.7 \times 10^3$	$451.6 \times 10^3$	$483.7 \times 10^3$	$547.7 \times 10^3$	$624.5 \times 10^3$
Germany	$194.7 \times 10^3$	$204.4 \times 10^3$	$220.6 \times 10^3$	$231.8 \times 10^3$	$217.6 \times 10^3$
India	$99.1 \times 10^3$	$123.9 \times 10^3$	$141.1 \times 10^3$	$152 \times 10^3$	$171.9 \times 10^3$
Brazil	$96.1 \times 10^3$	$106.3 \times 10^3$	$117.6 \times 10^3$	$126.5 \times 10^3$	$144 \times 10^3$
Total world	$2182.3 \times 10^3$	$2489.2 \times 10^3$	$2799.2 \times 10^3$	$3146.6 \times 10^3$	$3657.2 \times 10^3$

**Fig. 2** The share of renewable energy generation from the 5 leading countries in the world in 2021



## 5 Conclusion

Renewable energy has a critically important role in the energy development strategy. Renewable energy brings long-term sustainable development with non-gas emissions, a non-pollution environment, no global warming, and saving environment. This paper reviews recent renewable energy technologies and successful lessons of renewable energy development from leading countries. The results hope that renewable energy will be strongly developed and exploited in countries all over the world.

**Acknowledgements** This work was partially sponsored by Department of Mechanical Engineering and Core Facility Center, National Cheng Kung University, Taiwan. It was also supported in part by Hanoi University of Industry, Vietnam. The work was also supported in part by Faculty of Mechanical Engineering, Hanoi University of Industry, Hanoi 10000, Vietnam.

## References

1. Singh GK (2013) Solar power generation by PV (photovoltaic) technology: a review. *Energy* 53:1–13
2. Parida B, Iniyani S, Goic R (2011) A review of solar photovoltaic technologies. *Renew Sustain Energy Rev* 15:1625–1636
3. Singh VK, Singal SK (2017) Operation of hydro power plants—a review. *Renew Sustain Energy Rev* 69:610–619
4. Ofualagba G, Ubeku EU (2008) Wind energy conversion system—wind turbine modeling. 2008 IEEE power and energy society general meeting—conversion and delivery of electrical energy in the 21st century, pp 1–8
5. Østergaard PA, Duic N, Noorollahi Y, Mikulcic H, Kalogirou S (2020) Sustainable development using renewable energy technology. *Renew Energy* 146:2430–2437



6. Faaij A (2006) Modern biomass conversion technologies. *Mitig Adapt Strat Glob Change* 11:343–375
7. Zhou Y, Li S, Sun L, Zhao S, Ashraf Talesh SS (2020) Optimization and thermodynamic performance analysis of a power generation system based on geothermal flash and dual-pressure evaporation organic Rankine cycles using zeotropic mixtures. *Energy* 194:116785
8. He Y, Xu Y, Pang Y, Tian H, Wu R (2016) A regulatory policy to promote renewable energy consumption in China: review and future evolutionary path. *Renew Energy* 89:695–705
9. Kizilcec V, Parikh P (2020) Solar home systems: a comprehensive literature review for sub-Saharan Africa. *Energy Sustain Dev* 58:78–89
10. Kuang Y, Zhang Y, Zhou B, Li C, Cao Y, Li L et al (2016) A review of renewable energy utilization in islands. *Renew Sustain Energy Rev* 59:504–513
11. Thellufsen JZ, Lund H, Sorknæs P, Østergaard PA, Chang M, Drysdale D et al (2020) Smart energy cities in a 100% renewable energy context. *Renew Sustain Energy Rev* 129:109922
12. Zhou D, Hu F, Zhu Q, Wang Q (2022) Regional allocation of renewable energy quota in China under the policy of renewable portfolio standards. *Resour Conserv Recycl* 176:105904
13. Hong JH, Kim J, Son W, Shin H, Kim N, Lee WK et al (2019) Long-term energy strategy scenarios for South Korea: transition to a sustainable energy system. *Energy Policy* 127:425–437
14. BP (2022) BP statistical review of world energy 2022. <https://www.bp.com/statisticalreview>
15. Iddrisu I, Bhattacharyya SC (2015) Sustainable energy development index: a multi-dimensional indicator for measuring sustainable energy development. *Renew Sustain Energy Rev* 50:513–530
16. Salam A (2020) Internet of things in sustainable energy systems. In: Salam A (ed) *Internet of things for sustainable community development: wireless communications, sensing, and systems*. Springer International Publishing, Cham, pp 183–216
17. Ryu H, Yoon H-J, Kim S-W (2019) Hybrid energy harvesters: toward sustainable energy harvesting. *Adv Mater* 31:1802898
18. Wu J, Tran NK (2018) Application of blockchain technology in sustainable energy systems: an overview. *Sustainability* 10:3067
19. Zhou K, Yang S (2015) A framework of service-oriented operation model of China's power system. *Renew Sustain Energy Rev* 50:719–725
20. Vidadili N, Suleymanov E, Bulut C, Mahmudlu C (2017) Transition to renewable energy and sustainable energy development in Azerbaijan. *Renew Sustain Energy Rev* 80:1153–1161
21. La Rovere EL, Pereira AS, Simões AF (2011) Biofuels and sustainable energy development in Brazil. *World Dev* 39:1026–1036
22. Jingura RM, Matengaifa R (2009) Optimization of biogas production by anaerobic digestion for sustainable energy development in Zimbabwe. *Renew Sustain Energy Rev* 13:1116–1120
23. Amin SB, Chang Y, Khan F, Taghizadeh-Hesary F (2022) Energy security and sustainable energy policy in Bangladesh: from the lens of 4As framework. *Energy Policy* 161:112719
24. Kiwan S, Al-Gharibeh E (2020) Jordan toward a 100% renewable electricity system. *Renew Energy* 147:423–436
25. EIA (2022) Annual energy outlook 2022 (AEO2022). <https://www.eia.gov/>

# Research Automotive Line Performance Increasing by Using Modular Assembly



Nguyen Thanh Quang

**Abstract** There are three types of automotive assembly on the line: conventional assembly, automatic assembly and modular assembly. Modular assembly is the use of an integrated model of modules in the design and manufacture of cars and its parts on the basis of applicable standards. The article analyzes the key elements of the application of the modular assembly for automotive manufacture in order to increasing the performance of the assembly line. The results show the high performance and performance of the automobile assembly. They also show two key factors: the level of modularization of the assemblies and the use of standards in assembly.

**Keywords** Automotive line · Modular · Performance

## 1 Introduction

Modularity is a strategy applied by many industries, in product development or in production configuration. Modular assembly reduces production costs as a result of reducing assembly time, labor and material savings. A product is considered to be a modular assembly when it is assembled from at least two structures (or components) or more. Determining the interaction between such structures does not need to be clearly identified in advance because it is difficult to determine since there is also a change in one of them according to new product design requirements [1]. To identify a module from the design, it is necessary to separate the product into parts or assemblies. Since the structure of the product (vehicle) is basically fixed (except for the different requirements of each design or company), the product characteristics can only change within the functional limits of the elements that constitute the module. Therefore, the replacement of modules needs to be identified in advance and requires

---

N. T. Quang (✉)  
Hanoi University of Industry, Hanoi, Vietnam  
e-mail: [nguyenthanhquang@hau.edu.vn](mailto:nguyenthanhquang@hau.edu.vn)

the following modules to have the same function as the previous modules and ensure the interchangeability of the modules [2].

Based on the level of production, all elements are classified in module design and in module production according to the model of “module level classification matrix”. In manufacturing, four factors are given and chosen to apply: module manufacturing and integrated design; Conventional manufacturing and integrated design; Module production and module design; Conventional manufacturing and modular design.

The modules have interaction that is difficult to identify, depending on the requirements of the product, for example, the characteristics of the exploitation and use, the technology level of the assembly facility, the cost of the product. Factors depending on the conditions of each unit’s product development strategy will be considered individually in specific projects. There are normally two methods of product development: The first, it is under the responsibility of a manager who implements the system internally and keep technological know-how. The second, it depends on an organization and a chain of external suppliers and vulnerable to technological secrets. Derived from these methods, module standards are formed, those are standards of details, assemblies, and standards of relationships between modules. Some standards are implemented internally, others are sent to external suppliers to form and develop a chain of suppliers.

## 2 Basis of the Modular Assembly

Some basic assembly lines include: Rudimentary assembly line, flow assembly line (traditional assembly) and automatic assembly line (Conveyor belt installed on it). The assembly line’s performance is calculated the rudimentary OEE (Overall Equipment Effectiveness) indicators determined by formula (1) [3, 4].

$$OEE = (A) \times (P) \times (Q) \quad (1)$$

In the module assembly line made by the smallest number of professional workers. The prepared modules will be supplied to the line as planned. Once the assembly is complete, there will be one thing to do to adjust the order of the modules. The indicators in the module assembly line are calculated below.

The performance of a module assembly line is calculated by formula (2) [5].

$$LE = \frac{\sum_{i=1}^k TW_i}{K \times TC} \times 100\% \quad (2)$$

In which:  $LE$  is the performance of the line,  $TW_i$  is the total working time at the position  $i$ ,  $K$  is the number of working positions on the line,  $TC$  is the operating time cycle of the line. Thus, when time is reduced, the cycle will have a greater value for the performance of the line, which means that the assembly line can produce more products.

### 3 Analysis of Results

On the basis of a body in white (BIW), there is a total of 463 details classified into 10 different assemblies. Basically, the BIW mounted on the car has the same structure, including the front assembly, rear assembly, two side, floor assemblies and other auxiliary components including canvas assemblies and support frames [6, 7]. The figure of the BIW is shown in Fig. 1.

Calculating the performance of the model BIW assembly line in case of modular assembly on automatic lines and traditional lines. The detailed assemblies of the BIW are given in Table 1.

The calculated parameters that are selected for the BIW assembly output are 70 body per day (equivalent to 12 units per working hour), as shown in Table 2.

The performance calculation results of the line depend on the type of supplying spare parts, the number of container modules. The calculation results are shown in Table 3.

On rudimentary assembly lines, the performance is calculated by formula (1). Comparing the two module assembly lines on the graph as in Fig. 2, we get the result that when assembling the module, the use of the automatic line will bring a higher performance up to 35% than that on the traditional line.

The reason for this discrepancy is that on the traditional chain there are more processes, it takes more time ( $t_s$ ) due to the workers' moving ( $v_w$ ) to bring modules and components to the assembly location. In the traditional assembly line, more stations will be required to accommodate modules, components and equipment,

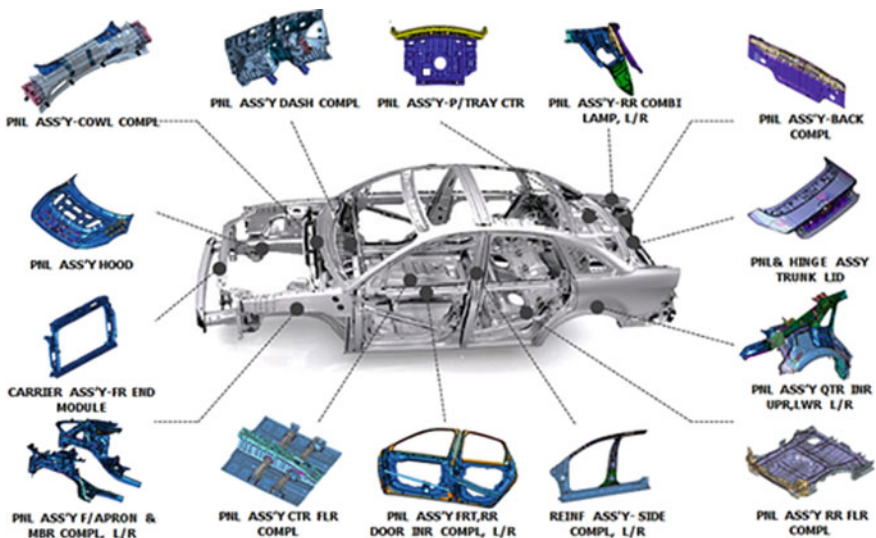


Fig. 1 The parts of BIW car

**Table 1** Dividing detailed assemblies

No.	Name of detailed assembly	Number of components assembly	Number of parts in the assembly
1	Front panel	1	27
2	Left front side panel	1	32
3	Right front side panel	1	32
4	Middle column, right and left	2	16 * 2
5	Right rear side panel	1	39
6	Left rear side panel	1	39
7	Floor panel	1	22
8	Rear side panel	1	28
9	Rear corner column, right and left	2	19 * 2
10	Other parts	54	174
	Total		463

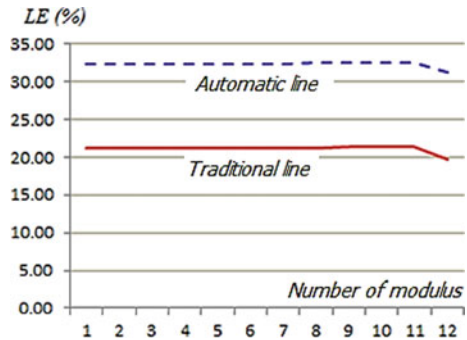
**Table 2** Calculated parameters for the BIW shipping container assembly lines

Symbols	Parameter	Value		
		Rudimentary line	Automatic line	Traditional line
I	Number of working positions on the line ( $i = 1, 2, \dots, n$ )	36	12	16
M	Number of modules ( $m = 1, 2, \dots, s$ )	289	11	21
J	Number of remaining components (components) ( $j = 1, 2, \dots, k$ )	174	2	10
$w_{ij}$	Assembly time of component j at position i (minutes)	35	10	16
$P_{ij}$	Operating arm time to assemble component j at position i (minutes)	7	2	4
$u_{ij}$	Component using factor j (for module m)	N/A	0.18	0.48
$R_{ij}$	The ratio of the number of modules and the number of components	N/A	11	21
L	The length of the line (meters) – (assumed)	100	45	60
$v_c$	The average speed of the line (m/min)	N/A	30	N/A
d	Average distance from the point of taking details to the assembly location (meters)	N/A	2	6
$v_w$	Movement speed of workers (m/min)	N/A	N/A	50
$t_s$	Time for each module	N/A	0.2	2

**Table 3** Performance calculation results of the BIW module assembly line

No.	Module name	Performance of the line (%)	
		Automatic line	Traditional line
1	Front panel	32.31	21.1
2	Left front side panel	32.32	21.2
3	Right front side panel	32.36	21.1
4	Middle column, right side	32.38	21.2
5	Middle column, left side	32.4	21.2
6	Right rear side panel	32.45	21.23
7	Left rear side panel	32.45	21.23
8	Floor panel	32.48	21.27
9	Rear side panel	32.48	21.29
10	Right ear corner column	32.49	21.3
11	Left rear corner column	32.49	21.3
12	Other separate details	31.3	19.7

**Fig. 2** Efficiency comparison results of the two assembly line

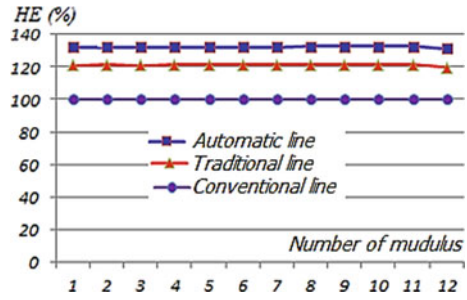


which will affect the “smoothness” of the line. The third reason is because the BIW modules are supplied and received by two different ways.

Assembly Effectiveness (HE%) of the lines used a comparison between the achieved result and the set goal (can be quantity, time targets or financial costs) we can see that the module assembly brings a higher effectiveness.

In Fig. 3, the specific calculation result on the traditional assembly line increases by 20% and on the automatic assembly line, it increases by 30% in comparison with

**Fig. 3** Efficiency comparison results of the assembly line



conventional assembly, this is a minimum increase level because in the calculation process, some calculations are taken for all three assembly lines. The fact that the module assembly on automated lines can increase performance up to 100% when using standardized modules.

### 4 Conclusion

Automotive assembly lines need a high customization. Modular assembly is developed in lieu of conventional assembly lines due to the following characteristics: (1) Can be arranged as independent module assembly stations. Independent stations are only affected by assembled products, regardless of the fixed transport system or the general time of the line. (2) Use automated guided vehicles (AGV) in the module transport. Reduce shipping labor and increase assembly productivity. (3) Modular assembly lines can be moved by assembly stations.

A published study on alternatives to assembly production lines in the automotive industry, proposed the following nine principles: (1) Identify the assembly order, (2) Smart assignment of assembly stations, (3) Identify the assembly time and assembly cycle, (4) Flexible responses to mutations from suppliers, (5) Flexible responses to mutations from product, (6) Adaptation to changes, (7) Integrated transportation of vehicles and components with AGV, (8) Flexible integration of quality control circles, (9) Adaptable to many assembly workers. Therefore, the above nine principles need to be flexibly applied in practice.

## References

1. McAlinden SP, Smith BC, Swiecki BF (1999) The future of modular automotive systems: where are the economic efficiencies in the modular-assembly concept. UMTRI Report No. 2000-24-1, Michigan Automotive Partnership Research Memorandum No. 1
2. Henriques FE, Migue PAC (2017) Use of product and production modularity in the automotive industry: a comparative analysis of vehicles developed with the involvement of Brazilian engineering centers. *Gest Prod, São Carlos* 24(1):161–177. <https://doi.org/10.1590/0104-530X341-15>
3. Aman Z, Ezzine L, Fattah J, Lachhab A (2017) Improving performance of a production line by using overall equipment effectiveness: a case study. In: Proceedings of the international conference on industrial engineering and operations management, Rabat, Morocco, April 11–13
4. Subramaniam SK, Husin SH, Yusop Y, Hamidon AH, Moussami HE (2009) Machine performance and man power utilization on production lines. In: Proceedings of the 8th WSEAS international conference on electronics, hardware, wireless and optical communications
5. Kurniadi KA, Islamoglu E, Ryu K (2012) Performance comparison of two assembly line concepts: conveyor line and box assembly line. *Int J Ind Manuf Eng* 6(2)
6. Kuys B, Gutowski M, Li S (2016) modular design and assembly of automotive and architectural structures: product integration through adhesive bonding. *Adv Manuf Sci Technol* 40(3):2016. <https://doi.org/10.2478/amst-2016-0013>
7. Al-Zaher A, ElMaraghya W (2014) Design method of under-body platform automotive framing systems. *Procedia CIRP*. <https://doi.org/10.1016/j.procir.2014.03.116>



# Aerodynamic Characteristics of Multi-door Thrust Reverser Using Fan Flow in High Bypass-Ratio Turbofan Engine



Anh-Tuan Nguyen, Van-Hiep Nguyen, Van-Hoang Nguyen, Tuong-Linh Nha, Van-Thuc Tran, The-Mich Nguyen, Cong-Thanh Nguyen, Cong-Truong Dinh, and Xuan-Truong Le

**Abstract** Aircraft landing speed is usually high, and the effect of the braking system is important. Besides, the braking system will work more efficiently when combined with a thrust reverser. Nowadays, research, design, and building of thrust reverser on aircraft engines is a particularly challenging problem due to the inherent complexity. This study presented the aerodynamics characteristic, performance, efficiency, and stability of a Turbofan Engine with multi-door crocodile thrust reverser system by using 3D RANS equations with scalable wall function  $k-\epsilon$  turbulence model. The design of multi-door crocodile thrust reverser system changes correspondingly to the variation of the opening angle of the outer doors, combined with the inlet Mach number. The results indicate a stable progress operation of the thrust reverser, safety, and the best performance. The results of reverse thrust efficiency reach maximal values at the opening angle of outer doors  $\alpha = 50^\circ$ .

**Keywords** Turbofan engine · Thrust reverser · Multi-door crocodile · Navier Stokes equations · Aerodynamic characteristics

## 1 Introduction

Currently, many modern aircraft are equipped with thrust reversers to reduce the damage to the brake system and shorten the landing distance. A typical brake system is not safe for aircraft in conditions of wet and slippery runways. According to a

---

A.-T. Nguyen · V.-H. Nguyen · V.-H. Nguyen · T.-L. Nha · V.-T. Tran · T.-M. Nguyen ·

C.-T. Nguyen · C.-T. Dinh · X.-T. Le (✉)

School of Mechanical Engineering, Hanoi University of Science and Technology, Hanoi 11615, Vietnam

e-mail: [truong.lexuan@hust.edu.vn](mailto:truong.lexuan@hust.edu.vn)

numerical study by Qian et al. [1], the number of wind tunnels that can undertake this experiment is minimal nowadays. Furthermore, these tests are usually performed in the final stages of the design process. Therefore, it is crucial to develop tools to shorten this period by Aurélio et al. [2]. In recent years, computational fluid dynamics (CFD) has made significant progress in simulating complex field cases. Computational fluid dynamics has become a new and effective method of thrust reverser design.

Gissen et al. [3] presented the flow control effectiveness down to 47% of the nominal bullnose length with four bullnose geometries. The established scaling laws indicate that the mass flow rate recovery is directly proportional to the actuation flow rate for a given flow configuration and condition, and it is strongly nonlinear with the flow pressure ratio for a given flow control rate. Bi et al. [4, 5] presented that aircraft fuselage surface noise of engine nacelle forward extension 11% is higher than that of forward extension 17%, and the noise value of moving downward is obviously smaller than that of moving upward, because of the combination of engine nacelle installation position and the reverser airflow.

## 2 Numerical Analysis

### 2.1 Description of Geometry

Details of the multi-door crocodile thrust reverser model are demonstrated in Fig. 1. The fan of the engine in this study is a design based on NASA rotor 67 with 22 blades at angular velocity of 16,043 rpm (100% designed velocity). For the convenience of tracking, there are three parameters, i.e.,  $\alpha$  ( $^\circ$ ),  $\beta$  ( $^\circ$ ), and Ma (Mach number), which are the focused variables of this study. Where  $\alpha$  ( $^\circ$ ) is the opening angles of outer doors,  $\beta$  ( $^\circ$ ) is the inner door angle, and Ma is the velocity at the inlet as Mach number (Tables 1 and 2).

### 2.2 Numerical Method

The model multi-door thrust reverser is simulated with commercial software ANSYS 19.1 [6] with the hexahedral grids type. The nacelle meshing was generated by ANSYS ICEM. With NASA Rotor 67 blades, the mesh model was created by the module Ansys TurboGrid. This O-type grids was used to mesh the computational domain around the blade surfaces. The other regions of the rotor are meshed with the H/J/C/L-type grids as shown in Fig. 2. CFX-Pre, CFX-Solver, and CFD-Post were employed to set up the simulation, solve the 3D RANS equations, and visualize the numerical results, respectively.

The performance parameters in this research were the fan nozzle pressure ratio (FNPR), and reverse thrust efficiency ( $\eta_{rev}$ ), which were presented by the research

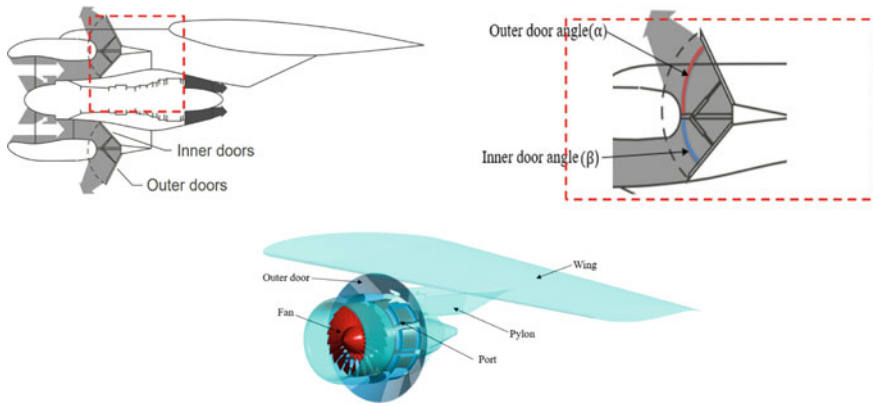


**Fig. 1** Multi-door crocodile thrust reverser system

**Table 1** Reference value of the multi-door crocodile thrust reverser

Parameter	$\alpha$ (°)	$\beta$ (°)	FNPR	Fan
Ref. value	50	36	$1 \div 2$	No

**Table 2** The range for parametric studies

Parameter	$\alpha$ (°)	$\beta$ (°)	Ma	Fan
Min. value	20	36	0.1	Yes
Max. value	60	36	0.3	Yes
Step	10	Constant	0.1	Yes

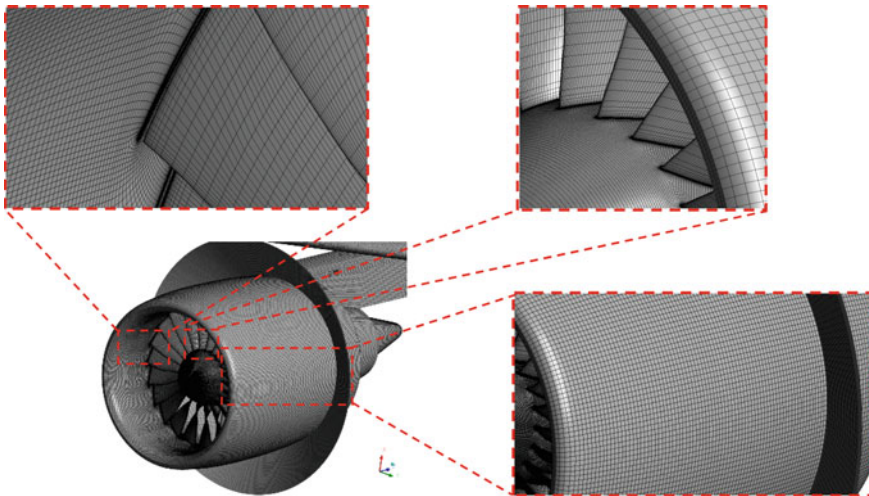


**Fig. 2** Mesh of the computational domains

group of Scott et al. [3]:

$$FNPR = \frac{p_{t, fan}}{p_0}; \quad \eta_{rev} = \frac{F_{rev}}{F_{fan}}$$

where  $p_{t, fan}$  is total pressure fan flow,  $p_0$  is engine ambient pressure,  $F_{rev}$  is gross reverse thrust (corrected balance axial force),  $F_{fan}$  is fan flow forward thrust.

### 3 Results and Discussion

#### 3.1 Validation of Numerical Method

To validate the applicability of CFD methodology in this study, the multi-door crocodile thrust reverser was simulated in the condition that FNPR varies from 1 to 2 and the fan has not been installed. The predicted reverse thrust ratio  $\eta_{rev}$  is compared with the experimental data [3], as shown in Fig. 3.

Under different FNPRs, the predicted  $\eta_{rev}$  is slightly higher than the experimental results, and the agreement is achieved in the distribution trends with the value relative error of relatively small. The approximate treatment of the calculation model and the leakage in the experiment may be the main reason to cause the error. Overall, the calculated results agree with the experimental data, especially for the case under large FNPR, so it shows that the predicted flow field is reasonable. Besides, the present calculation method can simulate the flow field in the multi-door crocodile thrust reverser in the following sections.

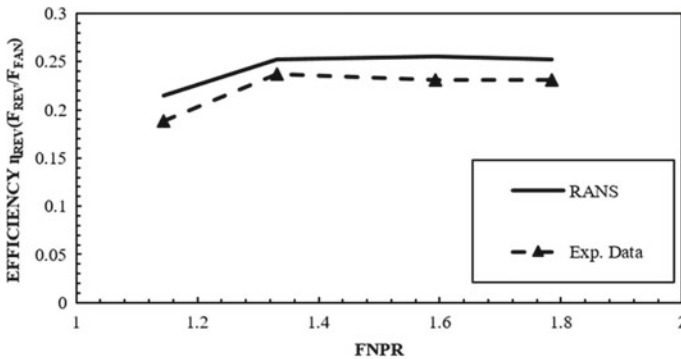


Fig. 3 Comparison of  $\eta_{rev}$  between calculation and experiment under different FNPR

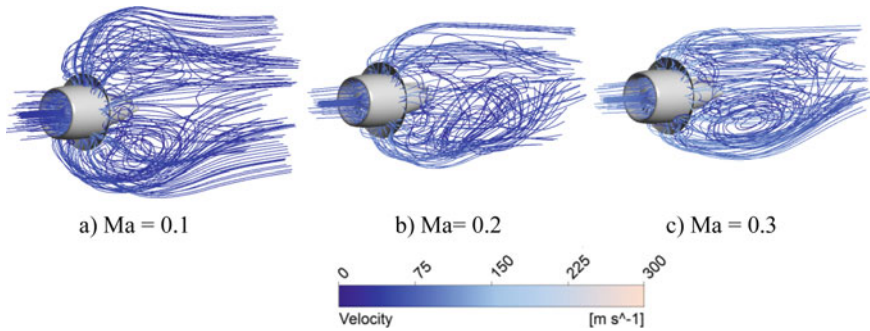


Fig. 4 Streamlines in 3D-view through the thrust reverser at different Mach numbers

### 3.2 Simulation Results

Figure 4 shows the efflux streamline released from the thrust reverser exit section at different inlet Mach numbers. Because of the aircraft's forward movement, the efflux eventually turns back by the effect of the relative wind. With the decrease of the Mach number, the stream influenced by the reverse flows expanded forward and outward. Specifically, with the Mach number at 0.1, the reverse flows are expanded outward and forward more than the more prominent Mach number cases (0.2 and 0.3). When the relative wind speed is small enough, it doesn't affect the reverse flows much, so it is easy to create reverse thrust.

Figure 5 illustrates relative Mach number contour through the effects of different opening angles outer doors. Apparently, with the increase of the opening angles outer door, especially with the opening angle of  $50^\circ$ , the thrust reverser will achieve the best performance. This is because the reverse flows in this case extend outward and forward the most, which means this case is easy to create a reverse thrust. Besides, in addition to being less effective, small opening angle cases can also cause impacts on the wings as shown in Fig. 5, and it can cause loss of control of various control surfaces such as spoilers.

Moreover, Fig. 6 shows the most important parameter of a thrust reverser: reverse thrust efficiency. From Fig. 6, the efficiency will be improved with large opening angles for outer doors than with small opening angles. In which, the case the opening angle of  $50^\circ$  has the best performance value, and the case of the opening angle of  $20^\circ$  has the most negligible efficiency (including a negative efficiency value at Mach number 0.3. This happens because the opening angle case of  $20^\circ$  made the range reverser flow very small and directed it to the relative wind. When increasing relative wind speed, the reverser flow, in this case, will lose its reverse value completely). Besides, reverse thrust efficiency is better when the relative wind speed is negligible. This is entirely true compared to the operation of aircraft. The results obtained are completely reasonable with the above explanations.

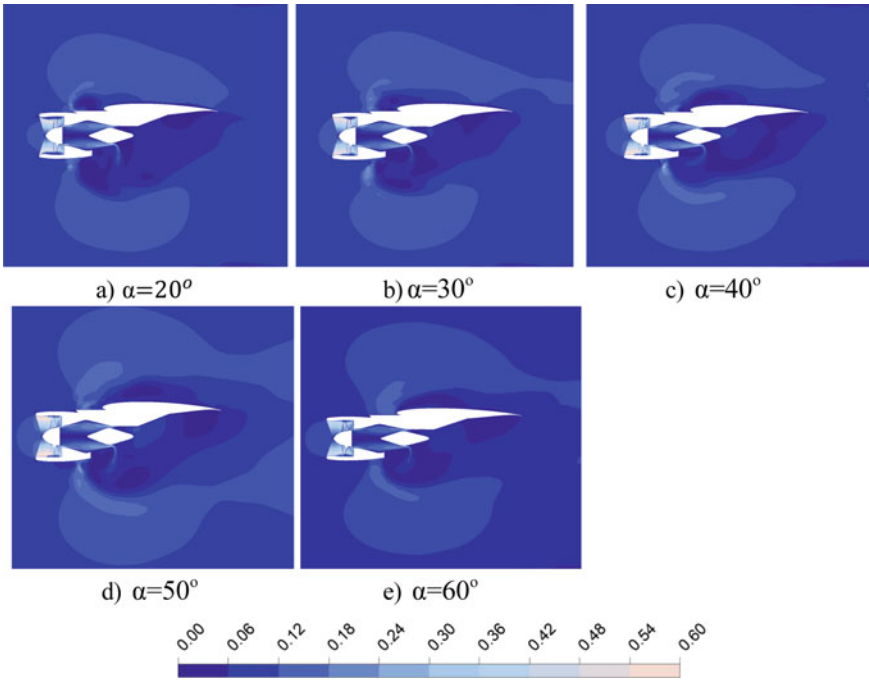


Fig. 5 Relative Mach number contour with different opening angles outer doors

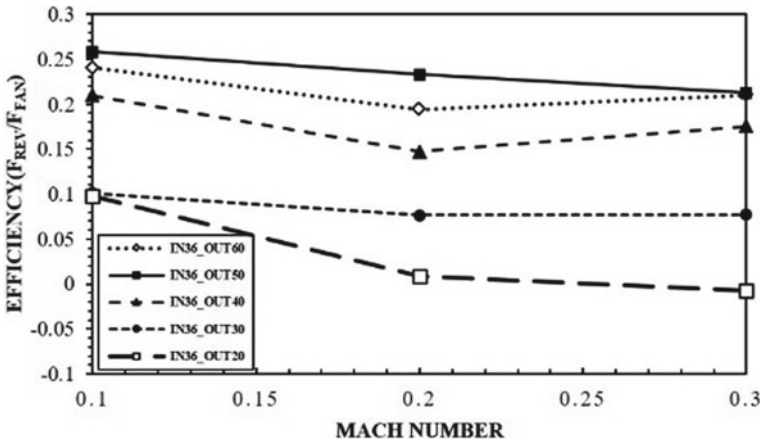


Fig. 6 Effect of parametric studies on reverse thrust efficiency

## 4 Conclusion

In this study, multi-door crocodile thrust reverser studies have been simulated using the  $k-\epsilon$  turbulence model to solve Reynolds-averaged Navier Stokes equations. Two study parameters of the thrust reverser, i.e., opening angles outer doors and Mach number, are changed to investigate their effects on the thrust reverser aerodynamic performances. The results of reverse thrust efficiency reach maximal values at the opening angle of outer doors  $\alpha = 50^\circ$ . Besides, with the small opening angle is  $20^\circ$ , reverse thrust efficiency is very low and reached a negative value (reverse thrust no more effect). Moreover, the small opening angle can cause problems with losing control of the control surface or wings.

**Acknowledgements** This study is funded by Hanoi University of Science and Technology (HUST) under grant number T2022-PC-032.

## References

1. Ruizhan Q, Ziqiang Z, Zhuoyi D (2011) Thrust reverser optimization for safety with CFD. *Procedia Eng* 17:595–602. <https://doi.org/10.1016/j.proeng.2011.10.075>
2. Santin MA, Barbosa JR, Bontempo LP, dos S Silva FJ, Jesus AB, Trapp LG, Oliveira GL (2005) Overview on thrust reverser design. In: 18th international congress of mechanical engineering, pp 1–8
3. Gissen AN, Vukasinovic B, Packard NO, Brzozowski DP, Glezer A (2017) Flow control of a cascade thrust reverser. *J Propul Power* 33(4):1020–1030. <https://doi.org/10.2514/1.B36064>
4. Bi S, Mao J, Han X (2019) Study on aerodynamic and noise characteristics of thrust reverser in aircraft propulsion system integration design. In: AIAA Propulsion and energy forum and exposition, 2019. American Institute of Aeronautics and Astronautics Inc., AIAA. <https://doi.org/10.2514/6.2019-3823>
5. Bi S, Mao J, Han X, Cai K, Wang F (2021) Study of the aerodynamic characteristics on the computed flowfield during thrust reversers operation. *J Appl Fluid Mech* 14(5):1497–1509. <https://doi.org/10.47176/JAFM.14.05.32297>
6. ANSYS CFX-19.1 (2018) ANSYS Inc

# Study on Selecting the Appropriate Process Parameters When CNC Cylindrical Grinding Heat-Treated Alloy Steel



Ngoc Tuyen Bui and Trong Nghia Hoang

**Abstract** The grinding method is often used for finishing parts made of materials with high mechanical strength and hardness. When manufacturing parts with high hardness such as heat-treated steel, grinding methods are often used to ensure dimensional accuracy, surface roughness. This paper presents experimental research results on the process of cylindrical grinding tempered alloy steel on CNC cylindrical grinding machines. The effects of process parameters such as workpiece speed, feed rate and depth of cut on the surface roughness and dimensional precision of parts are studied. Experimental setup and investigation of the contribution of process parameters to the characteristics of the part have been carried out on the basis of the application of Taguchi technique and analysis of variance (ANOVA). Besides, the optimal sets of parameters to achieve the smallest roughness and the highest machining accuracy have also been determined in turn. The multi-object optimization problem to achieve the minimum roughness and the highest machining accuracy at the same time has been solved on the basis of a combination of Taguchi technique and grey relation analysis (GRA).

**Keywords** CNC cylindrical grinding machine · Workpiece speed · Feed rate · Depth of cut · Taguchi technique · Grey relational analysis (GRA)

---

N. T. Bui (✉) · T. N. Hoang

Hanoi University of Science and Technology, Hanoi, Vietnam

e-mail: [tuyen.buingoc@hust.edu.vn](mailto:tuyen.buingoc@hust.edu.vn)

T. N. Hoang

29 Mechanical One Member Limited Liability Company, Tuyenquang, Vietnam



## 1 Introduction

Machine parts with high precision, surface quality and durability are the basis for the introduction of modern, high-quality machines and equipment (accuracy, reliability, long life). Grinding has an important place in modern mechanical engineering because of its ability to outperform other cutting methods when it comes to machining materials with high mechanical strength and hardness. Because grinding is often chosen as the final finishing process, the surface quality of the grinding surface directly affects the durability and working quality of the machine part. Surface roughness after machining greatly affects chemical corrosion and fatigue strength of the part. Because at the bottom of the undulations is the place where the stress is concentrated with a very large value, where microcracks appear, which is the cause of part failure [1].

The following are some publications related to the cylindrical grinding process as well as the optimization method based on the Taguchi approach combined with gray relation analysis. The study of the effects of EN24 steel cylindrical grinding process parameters based on the Taguchi method is introduced in [2]. The impact of grinding process parameters on surface roughness of ENS steel has also been published in [3]. From there, the optimization for improved surface roughness is done. The multi-objective optimization of the cylindrical grinding parameters to achieve three objectives simultaneously as contact temperature, material removal rate (MRR), and machining cost are presented in [4]. In the study [5], the authors presented a study on the influence of process parameters on roughness and machining accuracy when drilling heat-treated steel. The multi-objective optimization process based on Taguchi method combined with gray analysis is also presented here.

This paper presents a study on round grinding of hardened X12M alloy steel on a CNC universal grinder. Taguchi technique and analysis of variance (ANOVA) combined with gray relation analysis (GRA) were used here. The contribution of each process parameter on the roughness and dimensional precision were defined. Besides, the optimal combination of parameters for both the roughness and dimensional accuracy objectives was obtained.

## 2 Theoretical Basis

### 2.1 Taguchi Technique and ANOVA [6]

Taguchi technique combined with ANOVA is widely used in process optimization. One of the essential tools of the technique is the Signal to Noise (S/N) ratio.

S/N (Sign-to-Noise) represents quality characteristics of the observed data and is determined by using equation

$$S/N = -10 \lg(\text{MSD}) \quad (1)$$

MSD is mean squared deviation and is determined on a case-by-case basis. If the required response value is smaller, it is better:

$$MSD = \frac{1}{n} \sum_{i=1}^n y_i^2 \quad (2)$$

If the required response value is larger, it is better:

$$MSD = \frac{1}{n} \sum_{i=1}^n \frac{1}{y_i^2} \quad (3)$$

where

$y_1, y_2 \dots y_n$  are results of the experiments or output responses  
 $n$  is the number of iterations of an experimental run.

By applying ANOVA, the contribution of an input variable to the output objective function is determined.

## 2.2 Grey Relation Analysis Method [7, 8]

Grey relation analysis method is often applied to solve multi-objective optimization problems. The GRA process consists of two steps:

First step is normalizing the output responses. Data values of the output responses are normalized to values from 0 to 1.

Second step is calculating Grey Relational Coefficient and Grey Relational Grade.

Based on Gray Relation grade, which process is optimal for multiple objectives can be determined.

## 3 Experiments, Results and Discussion

### 3.1 Experimental Setup

#### 3.1.1 Experimental Conditions

The test part is a push pin of the plastic mold with the design drawing as shown in Fig. 1. The parts are made of alloy steel X12M and tempered to a hardness of 58-62 HRC. The experiment was conducted on Universal Grinder Supertec (Fig. 2). Main specifications of the grinder are presented in Table 1. Measurement equipments are

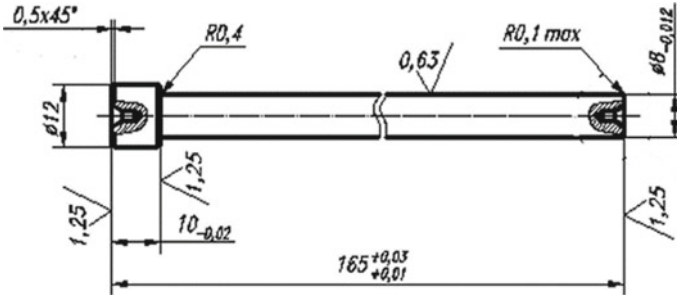


Fig. 1 The test part

device for measuring roughness HOMMEL TESTER T1000 and digimatic outside micrometer MITUTOYO with resolution of 0.001 mm.

Fig. 2 CNC Universal Grinder SUPERTEC



Table 1 Specification of SUPERTEC 32P-100CNC

Grinding wheel (Dia. × Width × Bore)	500 × 50–100 × 152.4 mm
Max grinding diameter	Φ360 mm
Wheel spindle speed	1735 rpm
Work head spindle speed	30–350 rpm
Feed rate	1–10,000 mm/min
X-axes ServoMotor	0.6 kW
Z-axes ServoMotor	0.6 kW
Wheel spindle motor	3.75 kW
Work head spindle motor	1 kW
Controller	FANUC

### 3.1.2 Experimental Design

The experiment is carried out based on the orthogonal array  $L_9$ . Three input variables are workpiece speed ( $n$ ), feed rate ( $f$ ), depth of cut ( $t$ ). Each variable has three levels as shown in Table 2. The speed of the grinding wheel remains unchanged at 1735 rpm. The cylindrical part of the test part ( $\Phi 8 \times 150$ ) is ground in the condition of flushing cutting fluid with different sets of process parameters. According to orthogonal array  $L_9$ , there are 9 runs of experiments with 9 input data sets is presented in Table 3. However, to ensure accuracy, 3 samples are machined for each test run. Thus, there are 27 test samples. The average value of the measurement results of roughness and diameter deviation of 3 samples will be recorded. The average value of the roughness measurements ( $R_a$ ) and the average value of the diameter deviations ( $\Delta D$ ) are recorded in column 6 of the table, in turn. The ratios  $S/N_{R_a}$  for  $R_a$  and  $S/N_{\Delta D}$  for  $\Delta D$  are determined according to Eqs. (1) and (2) and are presented in this table, too.

**Table 2** Process parameters and their levels

$N^0$ TT	Parameters	Low level	Average level	High level
1	Work speed $n$ , rpm	100	150	200
2	Feed rate $f$ , mm/min	30	40	50
3	Depth of cut $t$ , mm	0.005	0.025	0.045

**Table 3** Orthogonal array  $L_9$  of the experimental runs and results

$N^0$	$n$ (rpm)	$f$ (mm/min)	$t$ (mm)	$R_a$ ( $\mu\text{m}$ )	$\Delta D$ ( $\mu\text{m}$ )	$S/N_{R_a}$	$S/N_{\Delta D}$
1	100	30	0.005	0.216	5.5	13.3109	-14.8073
2	100	40	0.025	0.329	6.3	9.6561	-15.9868
3	100	50	0.045	0.631	14	3.9994	-22.9226
4	150	30	0.025	0.340	6.7	9.3704	-16.5215
5	150	40	0.045	0.630	9.3	4.0132	-19.3697
6	150	50	0.005	0.151	4	16.4205	-12.0412
7	200	30	0.045	0.590	9.3	4.5830	-19.3697
8	200	40	0.005	0.134	3.5	17.4579	-10.8814
9	200	50	0.025	0.246	6	12.1813	-15.5630

### 3.2 Determining the Influence of Process Parameters on the Roughness

The effects of workpiece speed (n), feed rate (f), depth of cut (t) on the surface roughness (Ra) are shown in Fig. 3. The average S/N values of these influence levels are presented in Table 4. When S/N is larger then Ra is smaller. By using ANOVA we have determined the influence of the process parameters on the surface roughness as shown in Table 5.

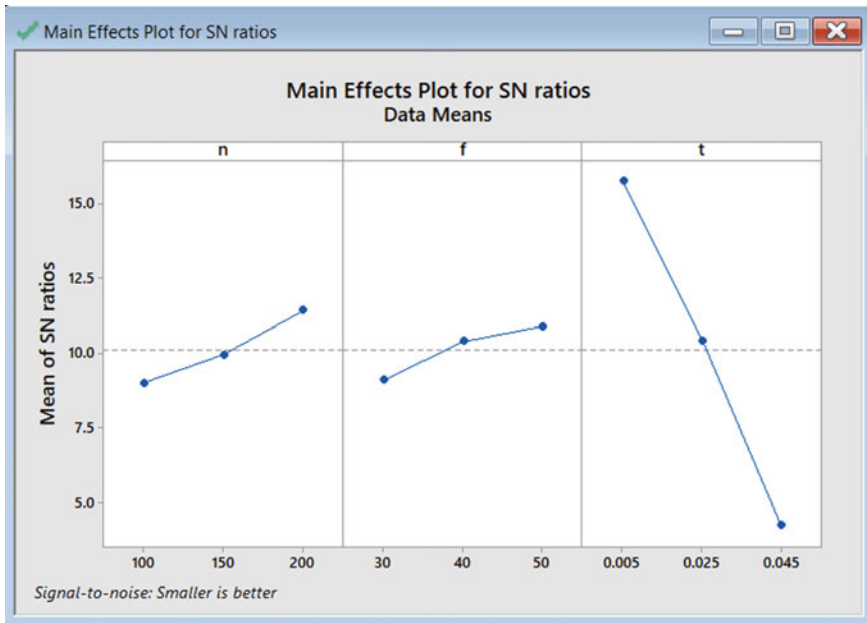


Fig. 3 The effects of n, f, t on Ra

Table 4 The average S/N values of influence levels of n, f, t to Ra

S/N			
Level	n	f	t
1	8.989	9.088	17.702*
2	9.935	10.376	10.403
3	11.407*	10.867*	15.730

The symbol ‘\*’ shows that the S/N value of the parameter (n or f or t) at the corresponding level is the largest compared to the other two levels of that parameter. From that, it can be seen that the optimal parameter set is the parameter set at the levels with the largest S/N values

**Table 5** The contribution of factors to Ra

N <sup>0</sup>	Parameter	Percentage contributions, %
1	Workpiece speed (n)	4.16
2	Feed rate (f)	2.37
3	Depth of cut (t)	93.3
4	Error	0.17

Depth of cut (t) has the greatest impact (93.3%). workpiece speed (n) and Feed rate (f) have little effect on the surface roughness. Their influence levels are 4.16% and 2.37%, respectively. The effect of noise factors is not significant (0.17%). Analysis of the influence of factors by Taguchi method (Fig. 3) shows that the optimal set of process parameters for the smallest roughness is (n3f3t1). That means the optimal parameter set for the smallest roughness is the workpiece speed of 200 rev/min, the feed rate of 50 mm/min and the depth of cut of 0.005 mm.

### 3.3 Determining the Influence of Process Parameters on the Dimension Accuracy

The effects of workpiece speed (n), feed rate (f), depth of cut (t) on the diameter deviation ( $\Delta D$ ) are shown in Fig. 4. The average S/N values of these influence levels are presented in Table 6. When S/N is larger then  $\Delta D$  is smaller. By using ANOVA we have determined the influence of process parameters on diameter deviation as shown in Table 7.

The rule of the effect of process parameters on diameter deviation is the same as for surface roughness. Depth of cut (t) has the greatest impact (84.95%). The influence levels of feed rate (f) and depth of cut (t) are 9.87% and 3.77%, respectively. The effect of noise factors is 1.41%. Analysis of the influence of factors by Taguchi method (Fig. 4) shows that the optimal set of process parameters for the smallest diameter deviation ( $\Delta D$ ) is (n<sub>3</sub>f<sub>2</sub>t<sub>1</sub>). That means the optimal parameter set for the smallest diameter deviation is the workpiece speed of 200 rev/min, the feed rate of 40 mm/min and the depth of cut of 0.005 mm.

### 3.4 Multi-object Optimization for the Lowest Roughness and the Highest Dimensional Precision

Firstly, the data of two target functions Ra and  $\Delta D$  is normalized. Normalized data are recorded in columns 1 and 2 of Table 8. The deviation sequences between reference sequences and comparable sequences are calculated. The results are shown in column 3 and column 4. The gray coefficients for each experiment are determined and are

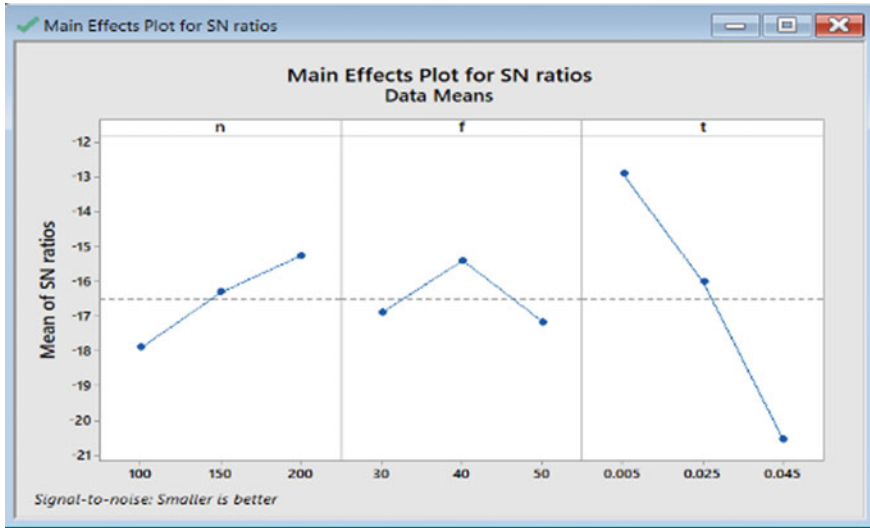


Fig. 4 The effects of n, f, t on  $\Delta D$

Table 6 The average S / N values of influence levels of n, f, t to  $\Delta D$

S/N			
Level	n	f	t
1	-17.906	-16.899	-12.577*
2	-15.977	-15.413*	-16.024
3	-15.271*	-16.842	-20.554

The symbol ‘\*’ shows that the S/N value of the parameter (n or f or t) at the corresponding level is the largest compared to the other two levels of that parameter. From that, it can be seen that the optimal parameter set is the parameter set at the levels with the largest S/N values

Table 7 The contribution of factors to  $\Delta D$

$N^0$	Parameter	Percentage contributions, %
1	Workpiece speed (n)	9.87
2	Feed rate (f)	3.77
3	Depth of cut (t)	84.95
4	Error	1.41

shown in column 5, column 6. Finally, the grey relational grade for each run is calculated and is shown in the last column.

All individual performance characteristics can be expressed by a single criterion such as the grade. So, grade is considered as a common criterion for both surface

**Table 8** Results of grey relational analysis

Runs	Normalization		Deviation sequence		Grey relational coefficient		Grade
	Roughness Ra	Diameter error ΔD	Roughness Ra	Diameter error ΔD	Roughness Ra	Diameter error ΔD	
1	0.835	0.8095	0.165	0.1905	0.7519	0.7241	0.738
2	0.6076	0.7333	0.3924	0.2667	0.5603	0.6521	0.6062
3	0	0	1	1	0.3333	0.3333	0.3333
4	0.5855	0.6952	0.4145	0.3048	0.5467	0.6213	0.584
5	0.002	0.4476	0.998	0.5524	0.3338	0.4751	0.4045
6	0.9658	0.9048	0.0342	0.0952	0.9360	0.84	0.888
7	0.0825	0.6952	0.9175	0.3048	0.3527	0.6213	0.487
8	1	1	0	0	1	1	1
9	0.7746	0.7619	0.2254	0.2381	0.6893	0.6774	0.6834

roughness and dimensional accuracy. Therefore, it is possible to convert the multi-objective optimization problem to the one-objective grade optimization problem. Solve this problem using Taguchi method with the choice “the larger, the better” we have S/N ratio for each run by using (1) and (3). Main effects of workpiece speed (n), feed rate (f), depth of cut (t) to the grade are shown in Fig. 5. From that, the optimal parameter set for the highest grade is defined as  $n_3f_1t_1$ . So, with the workpiece speed of 200 rev/min, the feed rate of 30 mm/min and the depth of cut of 0.005 mm we will have the lowest roughness and the highest dimensional precision.

## 4 Conclusions

A study about the CNC cylindrical grinding process of heat-treated alloy steel has been introduced in the paper. Taguchi method and gray relation analysis have been applied in this study. The effect of the three process parameters of workpiece speed, feed rate and depth of cut on surface roughness is similar to their effect on machining accuracy. The effect of depth of cut on roughness and machining accuracy is very large. Meanwhile, the influence of workpiece speed and feed rate on roughness as well as machining accuracy is very small. In which, the effect of workpiece speed is slightly larger than the effect of feed rate. Single-objective and multi-objective optimal parameter sets in the experimental domain are also found. These research results help the machine operator to select the machining parameters suitable for the desired goal.



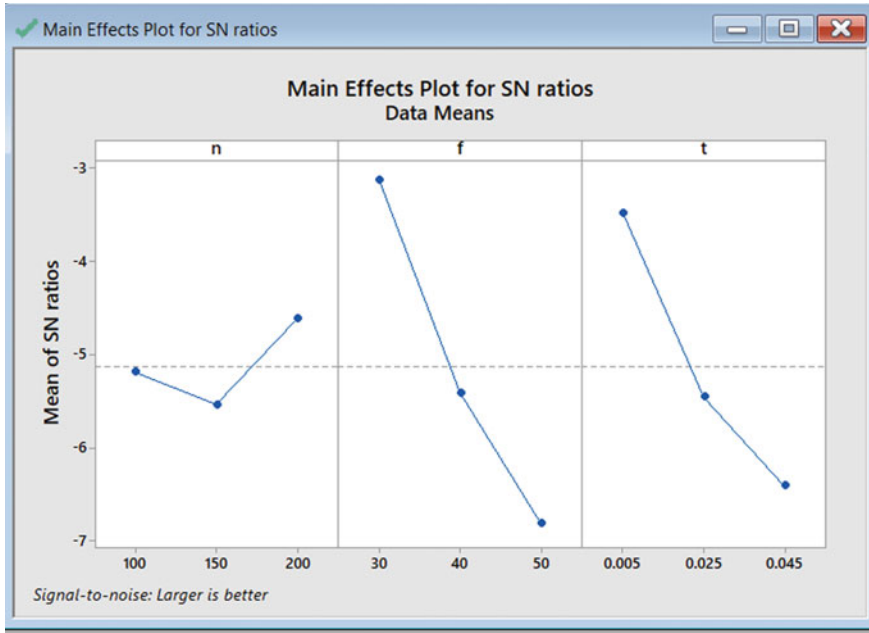


Fig. 5 The effects of n, f, t on the grade

## References

- Stephenson DA, Agapiou JS (2006) Metal cutting theory and practice. CRC Taylor and Francis Group
- Shanmuganathan R, Sudhakar M, Kannan TTM, Vijayakumar P, Sukumar S (2021) Optimization of cylindrical grinding process parameters on EN24 steel. *Int Res J Eng Technol (IRJET)*
- Patel DK, Goyal D, Pabla BS (2018) Optimization of parameters in cylindrical and surface grinding for improved surface finish, vol 5. The Royal Society
- Roy R, Ghosh SK, Kaisar TI, Ahmed T, Hossain S, Aslam M, Kaseem M, Rahman MM (2022) Multi-response optimization of surface grinding process parameters of AISI 4140 alloy steel using response surface methodology and desirability function under dry and wet conditions. *Coatings*
- Bui NT, Phan TH (2022) A study on selecting cutting regime to attain suitable roughness and dimensional precision in both when drilling tempered steel 20XHM. In: The AUN/SEED-Net joint regional conference in transportation. *Proceeding of RCTEMME2021*, pp 286–300
- Taguchi G (1990) A primer on the Taguchi method—Joyce Cary, TS156.R69
- Julong D (1989) Introduction to grey system theory. *J Grey Syst*
- Lin JL, Tarn YS (1998) Optimization of the multi-response process by the Taguchi method with grey relational analysis. *J Grey Syst* 4:355–370

# Analysis of Vehicle Structural Performance During Side Impact Using Computer Model



Van Hieu Phan and Luu Phu Thuong Nguyen

**Abstract** This paper examines the structure of a vehicle when it collides with a Moving Deformable Barrier (MDB) using a computer simulation model. The model was created to simulate actual test conditions created with Hyper Mesh and LS-DYNA software. The crash simulation results were then compared to the rating guidelines of the Insurance Institute for Highway Safety (IIHS) to evaluate the overall vehicle structure and measure intrusion. This study utilized a full vehicle finite element model to construct a crash analysis model in accordance with the IIHS side impact test regulations and conducted a crash analysis. The results were then compared to the actual vehicle crash test results to validate the analysis model, and a side body member that had a significant impact on the side impact performance was identified using the verified analysis model. The crash analysis using finite element models revealed that the most severe damage to the vehicle frontal structure occurred when the vehicle model collided with the Moving Deformable Barrier on the left side of the vehicle model. This study concluded that the B pillar and roof need to be improved to achieve a higher rating from the IIHS.

**Keywords** Vehicle structure · Analysis · Moving deformable barrier (MDB) · Side impact · Simulation

---

V. H. Phan

School of Mechanical Engineering, Hanoi University of Science and Technology (HUST), No.1 Dai Co Viet Street, Ha Noi 100000, Vietnam

L. P. T. Nguyen (✉)

Faculty of Automotive Engineering, School of Technology, Van Lang University, Ho Chi Minh City, Vietnam

e-mail: [luu.npt@vlu.edu.vn](mailto:luu.npt@vlu.edu.vn)

Department of Automotive Engineering, Faculty of Engineering and Technology, Binh Duong Economics and Technology University, Binh Duong City, Vietnam

## 1 Introduction

In car accidents, the passengers are always at risk of injury, with the crash forces being applied outside of the vehicle's longitudinal structure [1]. Furthermore, these forces are attached to the front suspension with wheels, the firewall, and the base of the A-pillar, which are not typically designed to absorb and disperse crash forces [2–6].

Researchers are working towards improving the frontal crashworthiness of vehicle structures. Halloway et al. have introduced classifiers to determine the number of longitudinal members required for the structure [7]. Jakobsson et al. have documented the significance and advancements in car design over the past two decades, specifically when it comes to partial overlap in severe frontal collisions [8]. Chittepu has explored the advantages of robustness analysis in virtual product development, using a crash load case from the insurance industry as an example [9]. Despite these efforts, most studies only consider a single barrier scenario. The challenge is finding a balance between reducing weight and fulfilling the demands of various load cases.

No studies have been published yet on the recent research topic. The IIHS has improved its small-overlap research program with updated barrier designs, which are used in crash experiments [9–13]. The aim of this study was to assess the overall structural safety ratings of vehicles during a side impact crash, based on the IIHS test. The research focused on analyzing truck accidents involving heavy trucks and sedans, particularly in terms of under-ride crashworthiness [15], which can result in significant vehicle damage and put occupants of smaller vehicles at risk [10]. The study used a computer model of a sedan and applied it to a real IIHS crash test [14], simulating the side impact scenario with LS-DYNA software [7].

The introduction sets the stage for the paper. Section 2 covers standard crash tests. Section 3 showcases the finite element model used for simulation. Section 4 details the model experiments for side impact scenario evaluation. Results are analyzed for full vehicle structural safety. The paper concludes with potential future research avenues.

## 2 Side Impact Modeling

### 2.1 Moving Deformable Barrier Model Designs

This study involved the design of a moving deformable barrier, as shown in Fig. 1, based on the specifications outlined in [14]. The barrier setup is illustrated in Fig. 2. The CATIA software was utilized to construct the barrier, and Hyper Mesh was then used to develop its finite element model. Figure 3 presents the evaluations used in the side impact simulation crash test.

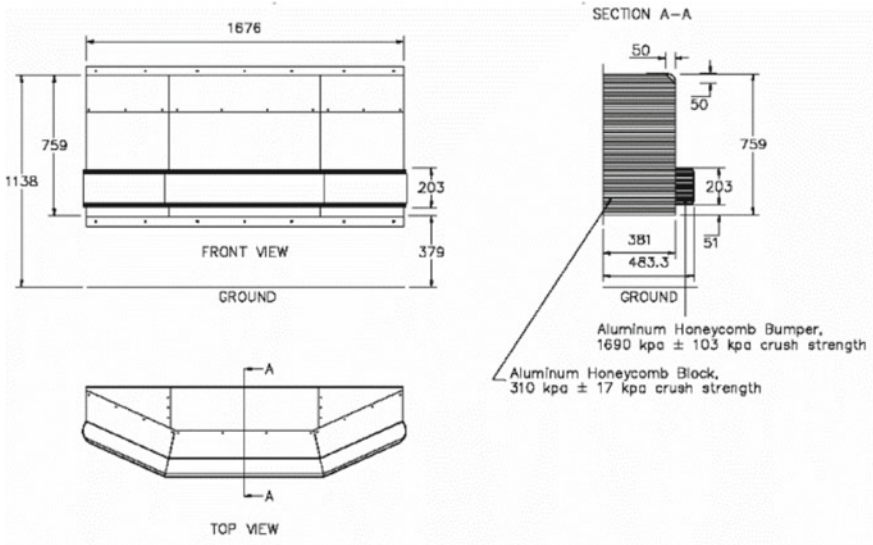


Fig. 1 Moving deformable barrier elements and dimensions in 2D drawing

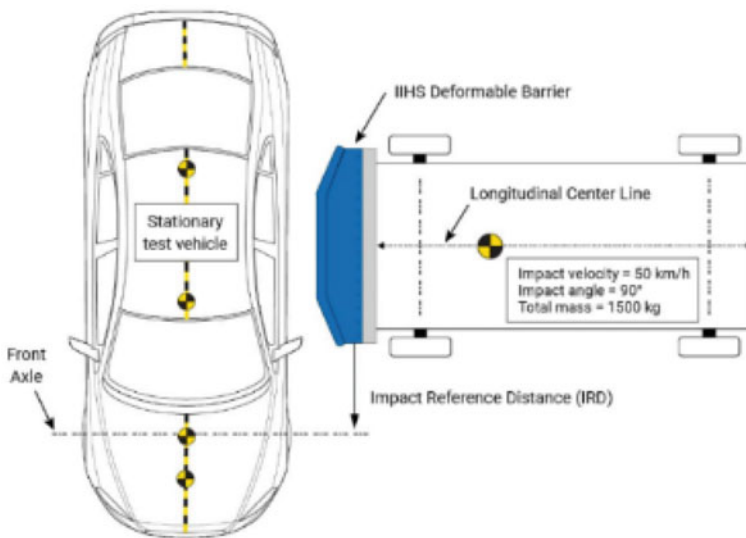
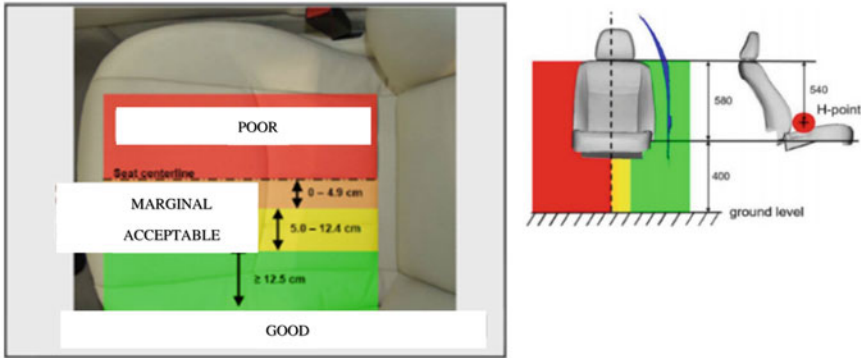


Fig. 2 Moving deformable barrier setting for side impact



**Fig. 3** The IIHS structural performance criteria, measured at the B-pillar at top, front and side views

### 2.2 Side Impact Test Model

The side impact crash test model was based on the real-life IIHS crash test. It involved a stationary vehicle hit on the driver side by a crash cart with an IIHS deformable barrier. The 1500 kg barrier impacted the vehicle at 50 km/h and a 90-degree angle. The longitudinal impact point of the barrier depends on the vehicle’s wheelbase. The impact reference distance (IRD) is the distance from the front axle to the center of the barrier at first contact (Fig. 2).

## 3 Side Impact Test Simulation

### 3.1 Full Vehicle Model with Side Impact Simulation

In a side impact collision, the affected area covers half of the vehicle’s side compared to its full length, causing significant damage to the car’s body. Figures 4, 5, 6, 7 and 8 illustrate the setup of the vehicle model in a side impact test simulation, the results of a real crash test conducted by the IIHS (Insurance Institute for Highway Safety), and a comparison of these results with the simulation. The results indicate that the majority of the load was absorbed by the side structures of the vehicle, including the floor, roof, rocker arm, and B pillar, leading to significant intrusion into both the upper and lower parts of the occupant compartment. The comparison of the IIHS test and simulation results is shown in Table 1, which reveals an error of 2% in the side impact intrusion of the vehicle structure. Figure 8 shows the positions of the A, B, and C pillars.

**Fig. 4** Top view of the side crash test simulation model

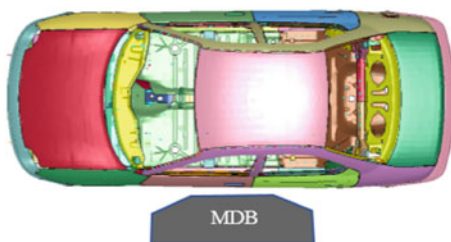


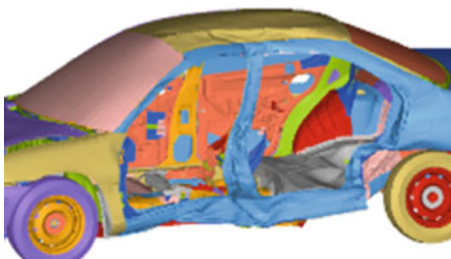
**Fig. 5** IIHS side crash test



**Fig. 6** The side impact test result by IIHS



**Fig. 7** The side impact test result by simulation



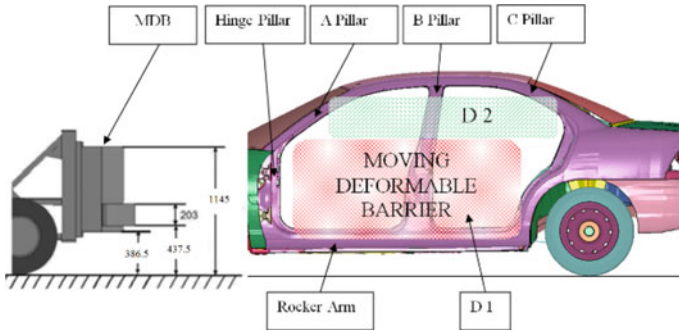


**Fig. 8** Pre-crash of vehicle body frame structure in side impact

**Table 1** Comparison of physical test and simulation

	Test	Simulation	Error (%)
Intrusion (mm)	-25	-24.5	2
Mass (kg)	1203	1218	1.2
Rating	Poor	Poor	

### 3.2 Vehicle Structure Side Impact Analysis

In the side crash, the energy absorption area is the passenger and driver side areas with the highest intrusions into the occupant compartment: the barrier primarily loads the B pillar and doors, mostly missing contact with the A and C pillar. The positions of A, B, C pillars and rocker arm are shown in Fig. 8. This concentrates energy absorption on the B pillar and lower rocker arm structures and for most Sedan, the moving deformable barrier impacts above the vehicle rocker arm, requiring all energy to be absorbed by the B pillar and door structures.

The area D1 of the vehicle structure include lower B pillar and rocker arm as shown in Figs. 9 and 10, and the area D2 contain the upper B pillar and the roof, A pillar and C pillar as show in Fig. 8. The left side body of the vehicle include the frame outside and the structure inside the frame as shown in Fig. 9.

D1 region: In this stage, the moving deformation barrier attached to the B pillar and rocker arm. It causes the B pillar bent and the energy absorb was missing. The rocker arm was serious damaged with the broken at the middle point. The B pillar and the rocker arm are divided into 9 parts as shown in Figs. 11 and 12 to analysis the vehicle structure.

D2 area: the energy absorbing is totally missing due to the MDB size. In this case only the roof was attached by the B pillar bent. The energy absorbing of B pillar and the roof as shown in Fig. 13. Base on the results in the Table 1 the rating from IIHS is POOR so that the B pillar is needed to improve for side impact. So that the sensitive part analysis was used to optimal design the vehicle structure. In Fig. 14, the components are the parts causing the deformation for side impact test simulation.

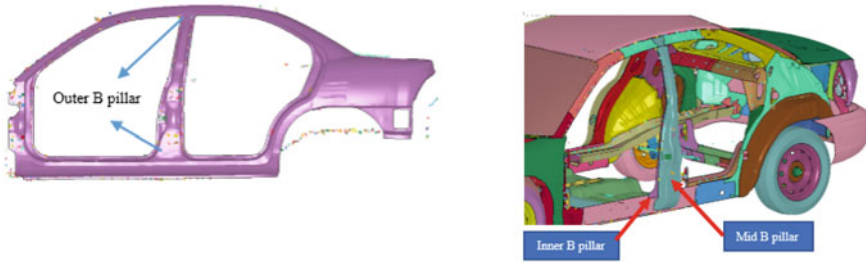


**Fig. 9** Right view outside of body structure pre-crash on the left hand side

**Fig. 10** Left view inside of body structure pre-crash on the left hand side

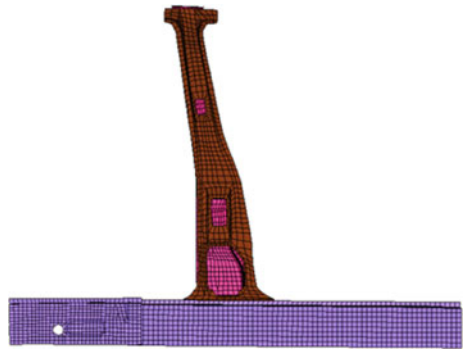


**Fig. 11** B pillar and rocker arm parts analysis on the outside

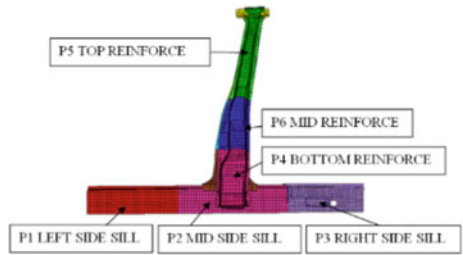


**Fig. 12** B pillar and rocker arm parts analysis on the inside

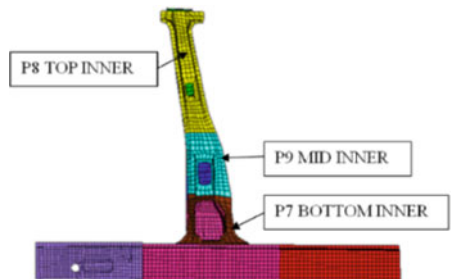




**Fig. 13** B pillar vertical profiles

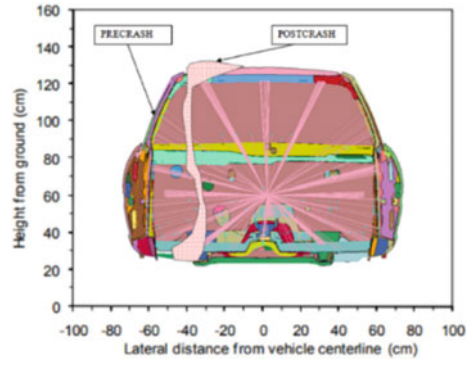
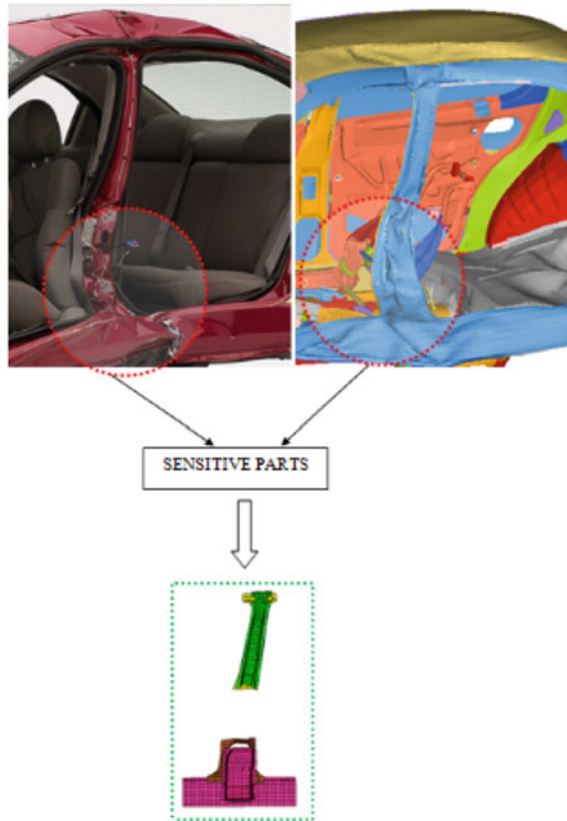


**Fig. 14** Sensitive parts analysis



## 4 Conclusion

In this research, a finite element model was utilized to simulate the impact of a side collision on a vehicle. The simulation outcomes indicated substantial intrusion into the passenger compartment, resulting in a bent B-pillar, damage to the A-pillar and C-pillar of the vehicle structure, and widespread damage to the side of the vehicle. Currently, most vehicles are designed to absorb impact through the front end, but this simulation showed that the side collision caused the B-pillar to buckle, preventing proper energy absorption and causing serious harm to passengers, especially the driver. To rectify this issue, future research will focus on enhancing the design of the B-pillar and the body frame structure to optimize their cross-sectional design for better performance during side impact tests.

**Acknowledgements** The authors express their gratitude to Van Lang University in Vietnam for their invaluable contribution in financing this study.

## References

1. Luu NPT, Anh LH (2021) A study on optimal design of longitudinal shape for improving small-overlap performance. In: Abdel Wahab M (eds) Proceedings of the 8th international conference on fracture, Fatigue and Wear
2. Bois PD, Chou CC, Fileta BB, Khalil TB, King AL, Mahmood HF, Mertz HJ, Wisnans J (2004) Vehicle crashworthiness and occupant protection. Michigan, pp 11–176
3. Brumbelow ML, Zuby DS (2012) Impact and injury patterns in frontal crashes of vehicles with good ratings for frontal crash protection. IIHS paper No 09-0257. USA
4. Halloway DE, Pintar F, Saunders J, Anelli AB (2012) Classifiers to augment the CDC system to distinguish the role of structure in a frontal impact taxonomy. SAE paper, NO 2012-01-0575
5. Jakobsson L, Mcinally G, Axelson A, Lindman M, Kling A, Broberg T, Fermer M, Wagstrom L (2013) Severe frontal collisions with partial overlap-two decades of car safety development. SAE paper, NO 2013-01-0759
6. Chittepu K (2011) Significance of robustness evaluation in crash analysis. SAE paper, NO 2011-26-0017
7. Hallquist JO (2007) LS-DYNA keyword user manual, Livermore software technology corporation
8. Murri R, Caviezel S, Gerster B (2013) Relevance of the IIHS small-overlap crash test in Europe. Internal study DTC Dynamic Test Center AG, Report number pSi-13-0130
9. Luu NPT (2019) Analysis of bus structural performance during full frontal impact. In: IEEE proceeding on system science and engineering, pp 635–638. <https://doi.org/10.1109/ICSSE.2019.8823416>
10. Luu NPT (2018) Vehicle frontal impact to Pole Barrier simulation using computer finite element model. In: IEEE proceeding on green technology and sustainable development, 2018, pp 273–277. <https://doi.org/10.1109/GTSD.2018.8595702>
11. Luu NPT (2017) An optimisation approach to choose thickness of three members to improve IIHS small-overlap structural rating. Int J Crashworthiness 22(5):518–526. <https://doi.org/10.1080/13588265.2017.1281203>
12. Nguyen PTL, Lee JY, Yim HJ, Lee SB, Heo SJ (2015) Analysis of vehicle structural performance during small-overlap frontal impact. Int J Autom Technol 16(5):799–805

13. Nguyen PTL, Lee JY, Yim HJ, Lee SB, Kim HK, Heo SJ (2015) A study on optimal design of vehicles structure for improving small overlap rating. *Int J Autom Technol* 16(6):959–965
14. Insurance Institute for Highway Safety, Side Impact Crashworthiness Evaluation Test Protocol, Version VII, 2014
15. Anh TT, Luu NPT (2021) A study on car-to-truck rear underride with and without protection device. In: Long BT, Kim YH, Ishizaki K, Toan ND, Parinov IA, Vu NP (eds) *Proceedings of the 2nd annual international conference on material, machines and methods for sustainable development (MMMS2020)*

# Investigation on TiAgN Thin Film Formation Employing Co-Sputtering Method Toward Applying for Medical Instruments



Dinh Quang Nguyen, Luan Duc Nguyen, Viet Quoc Dang,  
and Cuong Duc Pham

**Abstract** Titanium nitride (TiN) thin film has been used widely in surgical instruments, and dental and medical implants providing an inert surface barrier that protects the products from corrosion and improves the wear resistance. By adding silver (Ag) to TiN, titanium silver nitride (TiAgN) is predicted to be able to perform the antibacterial effect. In this work, a co-sputtering technique was employed for TiAgN fabrication. Pure titanium and silver targets were sputtered by DC (direct current) and pDC (pulse direct current) powers, respectively. The pulse frequency of pDC power was varied to examine the coating's constituent, microstructure, and formation velocity. The chemical composition of the coating was investigated by the Energy Dispersive Spectroscopy (EDS), whereas the morphology and thickness of the coating were observed by Field Emission Scanning Electron Microscope (FESEM). The experimental results showed that TiAgN coating was well formed on Si wafers. The pulse frequency strongly affected composition and morphology, and the Ti/Ag ratio of the coating as well. At 70 kHz, the TiAgN coating has the highest dense structure and fastest formation velocity. After that, TiAgN was coated onto prosthetic eyeballs made of PEEK (Poly-ether-ether-ketone)—a popular material used in biomedical. Preliminary examination indicated that there is no dispersion of TiAgN coating to tissue that is directly in contact with the implant coated ball.

**Keywords** Co-sputtering · PVD · TiAgN · PEEK · Medical implant

---

D. Q. Nguyen · L. D. Nguyen · V. Q. Dang · C. D. Pham (✉)  
Institute of Technology, Ha Noi University Industry, No. 298, Cau Dien Street, Bac Tu Liem  
District, Hanoi, Vietnam  
e-mail: [phamcuong@hau.edu.vn](mailto:phamcuong@hau.edu.vn)

## 1 Introduction

Titanium alloys are widely used due to their low-density high hardness, wear resistance, and oxidation resistance, hard coatings have been used in a wide range of applications such as aerospace, automotive, dies, mold, cutting tools, and decoration purposes as well. In all kinds of Ti-base hard coatings, titanium nitride (TiN) hard coating is commonly used in industry [1–3]. Titanium nitride coating is also utilized to provide improved performance on surgical instruments and dental and medical implants providing an inert surface barrier that protects the products from corrosion and improves the wear resistance maintaining the integrity of the cutting edge longer. TiN, however, does not contain antibacterial properties. Silver (Ag) has been demonstrated to possess an effective antibacterial effect and has been widely used in medicine. Moreover, Ag can be manufactured into silver nanoparticles through nanotechnology to have improved physical, chemical, and biological properties. The introduction of Ag into TiN created a new antibacterial biomaterial [4–6].

With regard to PVD (Physical Vapor Deposition) method, poly-metallic thin films which are constructed from nanoparticles can be fabricated by two methods including using poly-metallic targets and co-technique. The former use targets that are composed of desired metals with desired percentages. While the latter use pure metal targets and metal will be deposited at the same time onto a substrate. With a poly-metallic target, the constituent of fabricated thin coating is dependent on the constituent of a poly-metallic target. As a result, the method is not suitable for research but for industrial purposes. By controlling some factors such as power source, inlet gas, and constituent of thin coatings, that are fabricated by co-technique, are able to be controlled. Kang et al. [4, 5] used a titanium-silver alloy target with wt% silver content varying from three to twelve to form TiAgN by arc ion plating. Biocompatibility and antibacterial testing indicated that the existence of silver not only does not create cytotoxic effects but also increases the effectiveness of antibacterial. Meanwhile, Moseke et al. [6] used electric arc and RF (Radio Frequency) magnetron sputtering sources to vapor pure Ti and Ag, respectively. Hardness testing results showed an increase in hardness since introducing silver at suitable weight content. At a concentration of 1.4% the coating reached the highest hardness and the value decreased correspondingly to the increase in silver content. Nonetheless, this deposition technique created many droplets on the coating surface coming from the use of an arc source.

In this research, we proposed a novel fabrication method that can control the percentage of silver in a TiAgN coating. Two separated DC (Direct Current) sources will be employed to sputter two pure targets. The fabrication of TiAgN coatings was preliminarily investigated to find out suitable fabricating parameters. The TiAgN coating, then, was applied on prosthetic eyes which were made by PEEK (Polyetheretherketone) for biomedical investigations.

## 2 Experimental Details

Before coating onto the sphere surface, TiAgN firstly is deposited on flat samples (Silicon wafers). Secondly, we investigate the properties of the TiAgN coating and determine the fabrication parameters. Finally, TiAgN will be coated onto spheres which will be utilized as an artificial eyeball. The co-sputtering technique will be employed to form the coating with the constitution of each element Ti, Ag, and N controllable. In the sputtering technique, there are five parameters that strongly affect thin film formation capability and its quality including power supply, pulse frequency, substrate temperature, substrate—target distance, working pressure, and gas flow rate.

### 2.1 Equipment and Materials

UNIVEX400 vacuum system (Leybold, Germany) is used for the coating's fabrication. Ti target (99.95%, Angstronscience, USA) and Ag target (99.99%, Angstronscience, USA) of  $\text{Ø}54 \times 10$  mm in dimension were used; Ar 99.999% and N<sub>2</sub> 99.999% (Cryotech, Vietnam) were used as processing and precursor gasses, respectively. Airflow was controlled by Mass Flow Control MKS MF1. Two sputtering sources with two kinds of power supply were utilized. The first one is DC power supply GS20, ADL with fast and automatic arc handling having output power, voltage, and current maximum 2000 W, 800 V, and 3.5 A, respectively. The second one is pulse DC power supply having a maximum value of output power 2000 W, output voltage 800 V, output current 12.5 A, and pulse frequency can be changed in the range of 2–100 kHz.

Before coating, all samples were cleaned with acetone (99.8%, Merck, Germany), and DI water (Merck, Germany). Cleaning processes were performed in an ultrasonic bath (S30H,  $W \times D \times H = 301 \times 189 \times 218$  mm, Elma, Germany). Sample materials that were used in this research include silicon wafers and PEEK (Polyetheretherketone). The former was cut into pieces of around  $8 \times 8$  mm, while the latter was examined with two different kinds of surfaces including flat (sample pieces in a dimension of  $20 \times 8 \times 5$  mm in length, width, and depth, respectively) and sphere (with a diameter of 12 mm) as shown in Fig. 1.

### 2.2 Fabrication TiAgN Onto Si Wafers and Prosthetic Eye Balls

Silver target was assembled on sputtering source supplied by DC power, while titanium target was put on pulse DC power source. Before fabricating, target surfaces

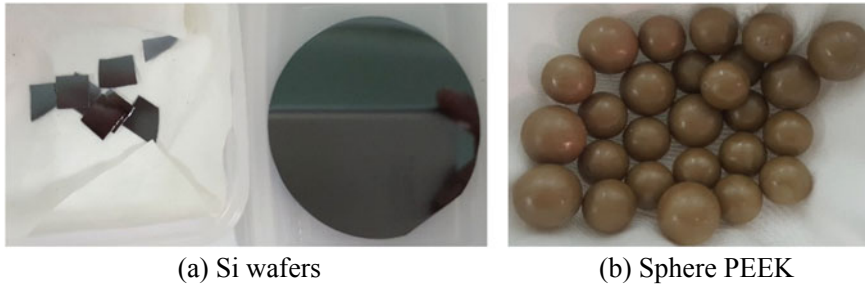


**Fig. 1** Samples used in the research. **a** Si wafer. **b** sphere PEEK

**Table 1** Fabrication parameters

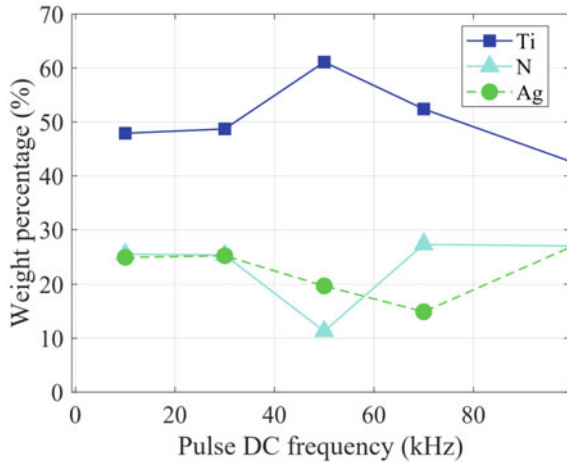
Fabrication parameters	Value
Base pressure	$1.5 \times 10^{-6}$ mbar
Working pressure	$3.7 \times 10^{-3}$ mbar
Substrate temperature	Room temperature
Substrate—target distance	100 mm
Fabrication time	60 min
Argon flow rate	20 sccm
Nitrogen flow rate	1.1 sccm
DC power (Ag target)	5 W
Pulse DC power (Ti target)	180 W
Pulse DC frequency	10, 30, 50, 70, 100 kHz

were clean by plasma to remove the surface oxide layer. Table 1 shows the fabricating parameters for TiAgN thin film fabrication. Regarding prosthetic eye balls, after 60 min, PEEK balls were taken out and turned over to coating onto the back sides. The coating process was performed as same as for the upper sides. In this work, after finishing the coating process, PEEK balls stayed in the vacuum chamber for two hours before venting and taking out. This will help reduce the thermal stress of the TiAgN coatings.

### 3 Results and Discussion

Figure 2 shows the variation of elements percentage of TiAgN thin film depending on the variation of fabricating frequency. In the range of pDC frequency from 10 to 30 kHz, the percentage of the elements is almost unchanged. The values witnessed a significant variation when pDC frequency increases from 30 to 100 kHz. The TiAgN fabricated at 100 kHz has a constituent roughly similar to that at 10 kHz. Because silver might effect on mechanical properties of the thin coating, we desire

**Fig. 2** The variation of element percentage in TiAgN thin film



to obtain the weight percentage of silver in the coating below 20%. Additionally, the microstructure of the coatings fabricated at different frequencies was also investigated.

SEM images of coatings' cross-section (see Fig. 3) indicated that all fabricated coatings have a columnar structure. However, the dense level and deposition rate are different. It can be seen that thin coatings fabricated at 10 kHz and 50 kHz have a low dense structure, while these at 70 kHz and 100 kHz were formed with a higher dense structure. Regarding deposition rate (see Fig. 3), this value increases corresponding to the increase of pDC frequency from 10 to 70 kHz (reaching a peak of approximately 21.6 nm/s) and then going down significantly to 14.7 nm/s at 100 kHz. Based on information of elements constituent, coating's microstructure and deposition rate, a pulse frequency of 70 kHz is chosen.

The coated balls were implanted in dog and rabbit eyeballs. After implanting, animals were monitored for 4 and 8 weeks. Prosthetic intraocular, then, were taken out and investigated on tissue at surrounding implanted TiAgN coated ball. Preliminary estimation indicated that there is no dispersion of TiAgN coating to tissue that directly contact to implant coated ball. Additionally, the coated prosthetic surface has no discolored phenomenon and no pitted marks. There is no change in the surface's morphology in the comparison with originally coated balls (as shown in Fig. 4).



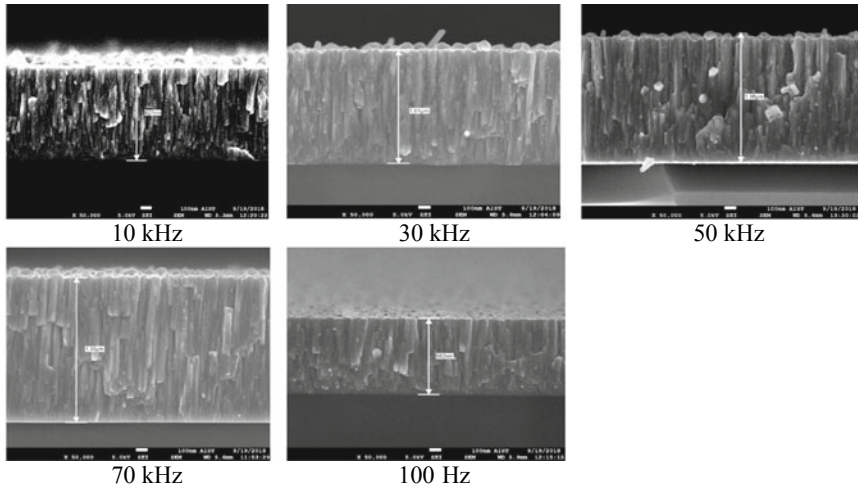


Fig. 3 SEM images of TiAgN coatings onto Si wafers at different pDC frequencies

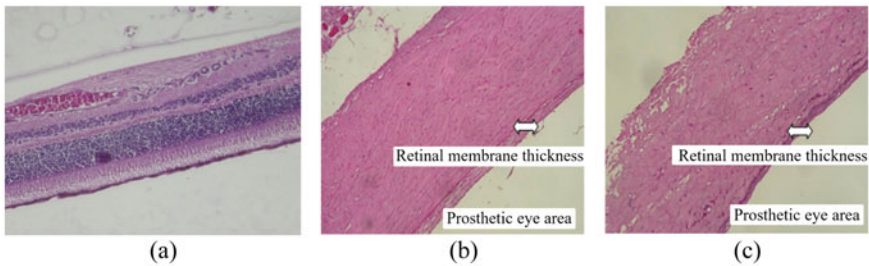


Fig. 4 Microscopic retinal after implanting prosthetic PEEK eye coated by TiAgN

## 4 Conclusion

This paper proposed the novel method to fabricate TiAgN film. Co-sputtering technique, in which each pure target was sputtered dependently, was employed for the film formation resulting in controllability of the coating component (Ti, Ag, and N). Pulse frequency was varied to examine the coating formation process and the variation of silver in the coating. At 70 kHz, the process achieves the highest deposition rate with high dense coating. Additionally, at this frequency, the content of silver is nearly the lowest which might result in nearly the highest hardness TiAgN coating. The coated balls were implanted in dog and rabbit's eyeballs. Preliminary estimations showed the biocompatibility of the coating. These pave the way for the applications of TiAgN in medical implants.

In future works, we intend to investigate not only the mechanical properties of the TiAgN coating such as wear resistant capability, and hardness but also the antimicrobial properties. The formation process will be carefully investigated for the best constituent of each element that is suitable for medical applications.

## References

1. Chuan SP et al (2012) Analysis of Ti-based hard coating performance in machining process: a review. *J Appl Sci* 12:1882–1890
2. Dowson D (Gt.Britain) (2003) Coatings tribology—properties, techniques and applications in surface engineering. *Tribol Ser* 41
3. Alfonso E, Olaya J, Cubillos G (2012) Thin film growth through sputtering technique and its application. *Crystalliz Sci Technol* 397–423
4. Kang B-M et al (2014) Antibacterial properties of TiAgN and ZrAgN thin film coated by physical vapor deposition for medical applications. *Trans Electr Electron Mater* 15(5):275–278
5. Kang B-M et al (2015) The characteristics of an antibacterial TiAgN thin film coated by physical vapor deposition technique. *J Nanosci Nanotechnol* 15:6020–6023
6. Moseke C et al (2011) Hard implant coating with antimicrobial properties. *J Mater Sci Mater Med* 22:2711–2720

# Estimating the Uncertainty of the Torque Standard Machine at Vietnam Metrology Institute



Vu Van Duy, Pham Thanh Ha, Ta Thi Thuy Huong, and Vu Toan Thang

**Abstract** This paper presents the estimation of the uncertainty of the torque standard machine manufactured and integrated at the Vietnam Metrology Institute. The uncertainty is composed of the uncertainty of component quantities such as arm length, weight, frictional moment, shaft tilt, and load oscillation... From that, an estimate of the uncertainty of the primary torque standard was made. The machine with dead weight is designed in the torque range of 2 kNm, horizontal shaft, integrated with rotary air bearing to minimize the coefficient of friction. The standard arm of the machine is made from Invar material, has a low coefficient of thermal expansion, has an adjustment to compensate for manufacturing errors, and ensures the standard length. This research is one of the national projects aimed at creating the primary torque standard machine in Vietnam of 2 kNm with measurement uncertainty  $5 \times 10^{-4}$ .

**Keywords** Uncertainty · Standard torque machine · Arm length · Rotary air-bearing · Dead weight

---

V. Van Duy  
Hanoi University of Industry, Hanoi, Vietnam

P. T. Ha  
Vietnam Metrology Institute, Hanoi, Vietnam

T. T. T. Huong  
Hai Phong University, Hai Phong, Vietnam

V. T. Thang (✉)  
Hanoi University of Science and Technology, Hanoi, Vietnam  
e-mail: [thang.vutoan@hust.edu.vn](mailto:thang.vutoan@hust.edu.vn)

## 1 Introduction

Torque standard machines are used to generate standard torque values and ensure accuracy in torque measurement equipment. Each country has its own primary torque standard machine, and differences in measurement uncertainty between countries are a concern. Many countries, particularly those with developed industries, have shown interest in manufacturing torque standard machines with standard torque values in different ranges and varying levels of uncertainty. These machines are built on the principle of generating standard torque using a dead weight suspended on the arm, with the torque value transmitted through a torque sensor. The standard torque values are compared through key comparisons.

Several countries, including Spain, Korea, Mexico, and Turkey, have developed their own torque standard machines with varying levels of uncertainty. The Spanish machine uses an air bearing and has a relative uncertainty of  $2 \times 10^{-5}$  for torque values ranging from 1 Nm to 1 kNm [1]. The Korean machine uses an air bearing and has an extended uncertainty of  $5 \times 10^{-5}$  for standard torque values of 100 Nm [2]. The Mexican machine uses a radial-loaded air bearing and has a frictional moment value of 20–25  $\mu\text{Nm}$  [3], while the Turkish machine has symmetrical arms made of Invar alloy and an uncertainty of less than 1  $\mu\text{m}$  [4].

There are also studies on the influence of humans performing operations to obtain data, such as the torque standard machine at the National Metrology Institute of Brazil, which is manually operated and has torque reference values up to 3 kNm [5]. The study presented a comparison of results achieved by operators with varying levels of experience but did not provide information on the economic benefits of using a low-cost manual-torque reference machine.

In Vietnam, the Metrology Institute has developed a high-precision torque standard machine up to 2 kNm with a measurement uncertainty of  $5 \times 10^{-4}$ . This machine integrates components such as rotary air bearings, deadweight, balance measurement sensors, and domestically designed levers using Invar materials. The machine will be experimentally evaluated to assess its uncertainty and find solutions to improve its accuracy.

Overall, the measurement uncertainty of torque standard machines varies between countries due to differences in machine construction, material used for the arm, measuring ambient temperature, and ability to balance the lever arm in the direction of acceleration due to gravity.

## 2 Principle of Torque Standard Machine

The principle of a torque standard machine can be designed as shown in Fig. 1.

The distance probe (7) determines the balance position of the lever. Hanging a load of mass  $m$  with the gravity force and the length of the lever will produce a torque  $T$ , which will cause the lever to rotate. To regain the equilibrium position, the stepper

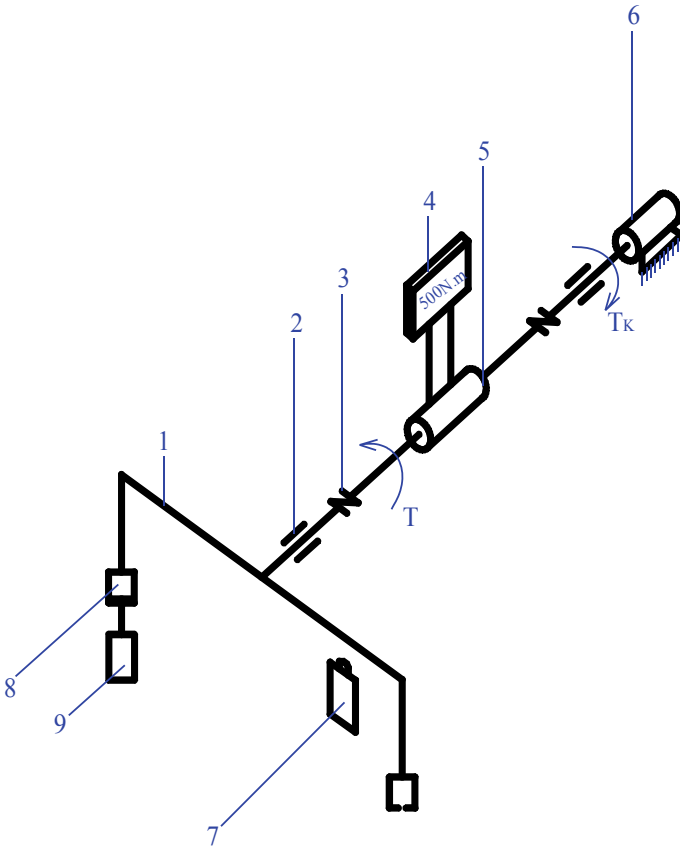


**Fig. 1** Principle of torque standard machine. 1—lever arm; 2—air bearing; 3—elastic coupling; 4—display panel; 5—torque sensor; 6—step motor; 7—distance probe; 8—load hook; 9—dead weight

motor will generate a torque against the torque  $T$ , causing the lever to return to its original state. With standard quantities according to SI system, the generated torque value is the standard torque, now the torque sensor (5) will take this standard torque signal and transmit it to the secondary standard, or work standards.

Torque standard machine from all over the world use deadweight and lever lengths. Static loads are created by the deadweight, which is the base unit of the International System of Measurements (SI). Currently, some countries have equipment and methods to determine the gravitational acceleration at specific locations, for example, VMI has cooperated with the Korea National Institute of Metrology and Science (KRISS) to determine the acceleration due to gravity in Hanoi is  $g = 9.78668787 \text{ m/s}^2$  [6].

Determining the working length of the lever arm is difficult because the center of rotation is the imaginary center. Moreover, in order to increase the magnitude of the

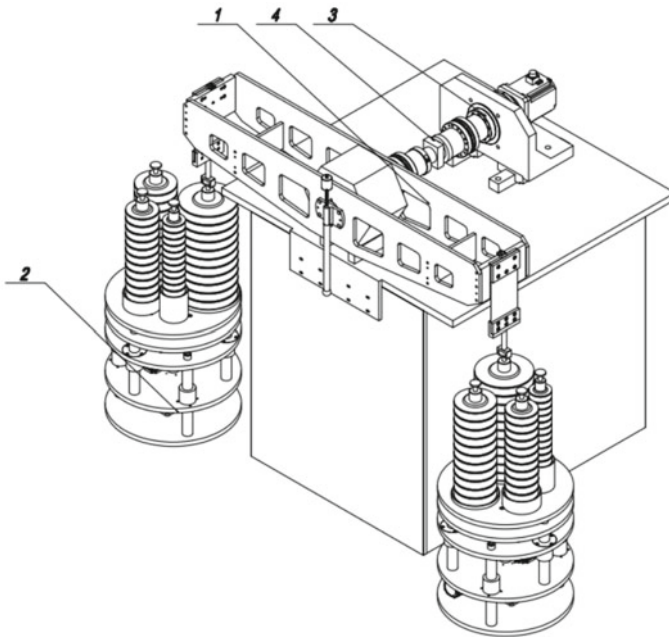


**Fig. 2** Design of deadweight torque standard machine. 1—lever arm; 2—deadweight; 3—position return cluster; 4—torque transfer

torque value, the lever arm must have a large length. To determining the exact large length of the lever arm is not easy to do. The lever dimension is also changed due to the impact of the ambient temperature, due to the deformation of the arm when subjected to force during the generation of torque.

The direct load torque standard machine at VMI is selected and designed according to the model of deadweight torque standard machine with horizontal axis, loading on both sides of the lever arm, has the overall design as shown in Fig. 2.

The standard torque value  $T$  is calculated according to the following formula [2]:

$$T = m \times g_{loc} \times L \times \left(1 - \frac{\rho_a}{\rho_w}\right) - T_f \quad (1)$$

In there:

$m$ : is the standard mass;  $g_{loc}$ : acceleration due to gravity at the location of the machine;  $L$ : lever arm length;  $\rho_a$ : density of air;  $\rho_w$ : Density of the mass material;  $T_f$ : frictional moment of the air bearing.

### 3 The Component Uncertainties Affect the Uncertainty of the Torque Standard Machine

Based on the mathematical model of the deadweight torque standard machine, the combined uncertainty of the machine is influenced by the following components:

- Overall uncertainty of the mass ( $u_w$ ); Uncertainty of acceleration due to gravity ( $u_g$ ); Total uncertainty of lever arm ( $u_L$ ); Uncertainty of air density ( $u_{\rho a}$ ); Uncertainty of the mass density ( $u_{\rho w}$ ); Uncertainty due to mass fluctuations ( $u_{ws}$ ); Uncertainty due to air bearing friction ( $u_{Tf}$ ). Thus, we have the formula to determine the measurement uncertainty of the deadweight torque standard machine as follows:

$$u_c = \sqrt{u_w^2 + u_g^2 + u_L^2 + (u_{\rho a}^2 + u_{\rho w}^2) \times \left(\frac{\rho_a}{\rho_w - \rho_a}\right)^2 + u_{Tf}^2 + u_{ws}^2} \quad (2)$$

where  $u_c$  is the total uncertainty of the machine.

#### 3.1 Estimation of the Combined Uncertainty of the Mass

The combined uncertainty of the mass depends on the following factors: Maximum allowable tolerance of the mass; Extended uncertainty of the mass measurement; The stability of the mass during use. We have the formula for determining the expanded uncertainty of the mass as follows:

$$U_w = \delta m + Umm + Ums = 5 \times \delta m / 3 \quad (3)$$

In there:

$U_w$ : expanded uncertainty of the mass;  $\delta m$ : Maximum tolerance of the mass;  $Umm$ : Extended uncertainty of mass measurement ( $Umm \leq \delta m / 3$ );  $Ums$ : Stability of the load during use ( $Ums = \delta m / 3$ ).

The combined uncertainty of the mass is determined as follows:

$$u_m = \frac{U_w}{m} = \frac{5 \times \delta m}{3 \times m} \quad (4)$$

where:  $m$  is the nominal mass.

### 3.2 Estimate the Uncertainty of the Acceleration Due to Gravity

$G_{loc}$  is the gravitational acceleration at the place where the standard machine is located,  $\Delta g_{loc}$  is the largest error due to time difference, altitude, measurement, etc. Then the uncertainty of the gravitational acceleration is calculated as follows:

$$u_g = \frac{1}{\sqrt{3}} \times \frac{\Delta g_{loc}}{g_{loc}} \quad (5)$$

### 3.3 Estimate the Uncertainty of Lever Arm

The uncertainty of the lever arm is determined by the following formula:

$$u_L = \sqrt{\left(\frac{1}{\sqrt{3}} \times \alpha \times \Delta T\right)^2 + \left(\frac{U_{Lm} + mpe_L}{2L}\right)^2 + \left(\frac{1}{\sqrt{3}} \times \frac{L - \sqrt{L^2 - y^2}}{L}\right)^2 + \left(\frac{1}{\sqrt{3}} \times (1 - \cos(\delta))\right)^2} \quad (6)$$

Here are:

$\alpha$ : Coefficient of thermal expansion of the arm material ( $1/^\circ\text{C}$ );  $\Delta T$ : Temperature difference ( $^\circ\text{C}$ );  $L$ : lever arm length;  $U_{Lm}$ : Extended uncertainty due to measurement of arm length;  $mpe_L$ : Deviation from nominal dimension;  $\delta$ : deflection angle of the level arm from the horizontal;  $y$ : bending of the lever arm under load.

### 3.4 Uncertainty Due to Bearing Friction

Let  $\Delta Tf$  be the frictional moment of the rotating bearing,  $T_{\min}$  is the minimum torque produced by the torque standard machine [7]. The uncertainty due to bearing friction is calculated by the formula:

$$u_{Tf} = \frac{1}{\sqrt{3}} \times \frac{\Delta Tf}{T_{\min}} \quad (7)$$

### 3.5 Uncertainty Due to Mass Oscillation

During operation, it is impossible to avoid external influences that cause the mas to be unstable and oscillate around a position. The mass is affecting the accuracy of the



standard machine. By many methods, we can measure the amplitude of vibration of the mass, so it is possible to determine the vibration angle of the mass according to the formula:

$$\theta = \arctan\left(\frac{d}{l}\right) \tag{8}$$

In there:

$\theta$ : maximum oscillation angle of the mass (°);  $d$ : maximum vibration amplitude of the mass (mm);  $l$ : distance from mass hanging position and oscillating measuring plane (mm).

The uncertainty of the influence due to vibration of the mass is determined by the formula:

$$u_{ws} = \frac{1 - \cos(\theta)}{2 \times \sqrt{3}} \tag{9}$$

### 3.6 Uncertainty of the Density of the Mass

Let  $\Delta_{\rho_w}$  be the maximum error in the measurement of the density of the mass, the uncertainty of the density of the mass is determined by the formula:

$$u = \frac{1}{\sqrt{3}} \times \frac{\Delta_{\rho_w}}{\rho_w} \tag{10}$$

### 3.7 Uncertainty of Air Density

The density of air is approximated by the formula:

$$\rho_a = \frac{0.34848 - 0.009 \times hr \times \exp(0.061 \times t)}{273.15 + t} \tag{11}$$

where:

$p_a$ : is the atmospheric pressure (hPa);  $hr$ : humidity of the environment (%RH);  $t$ : ambient temperature (°C).

In fact, the environmental conditions are always changing, we only keep the environment control in one domain. Let  $p_{\min}$  be the minimum atmospheric pressure,  $p_{\max}$  is the maximum atmospheric pressure,  $\Delta T$  is the temperature difference,  $hr_{\min}$  is the smallest ambient humidity,  $hr_{\max}$  is the maximum ambient humidity.

The uncertainty of air density is calculated by the formula:

$$u_{\rho a} = \frac{1}{\sqrt{3}} \times \frac{\Delta \rho a}{\rho a} = \frac{1}{\sqrt{3}} \times \frac{\rho_{a \max} - \rho_{a \min}}{\rho_{a \max} + \rho_{a \min}} \tag{12}$$

With controlled environment at temperature  $T = (23 \pm 5)^\circ\text{C}$  humidity  $H = (60 \pm 20) \%RH$ , pressure around  $(99 \div 110)$  kPa, lever arm is used INVAR steel has a length of 1 m, the mass is made of stainless steel SUS304 and the mass oscillates up to 1 mm at a position 1000 mm from the hanging position, the acceleration due to gravity with a combined uncertainty of  $1.10^{-6}$  thus:

$$u_c^2 = \left( \frac{5 \times \delta_m}{3 \times m} \right)^2 + \frac{1}{4} \times (U_{Lm} + mpe_L)^2 + \left( \frac{1}{\sqrt{3}} \times (1 - \cos(\delta)) \right)^2 + 9.504582 \times 10^{-11} \tag{13}$$

Figure 4 shows the variation of the extension uncertainty of lever arm when the arm deflection angle from the horizontal with 3 level of accuracy of the mass E2, F1, F2. We can see that with the accuracy level of the mass E2 and F1, the extended uncertainty of the lever arm needs to be achieved is higher than the accuracy level of the F2 and is almost the same. So, we can choose the accuracy class of the mass as E2 or F1 for the design of the deadweight torque standard machine. However, in Vietnam, it will be more difficult and expensive to manufacture the mass with precision level E2 than F1 level, both of which have similar effects with uncertainty of the standard machine. Therefore, choosing the correct F1 level for the design of the deadweight torque standard machine is the most optimal solution.

Based on the graph of the angle of deviation  $< 0.1^\circ$  has little effect on the measurement uncertainty of the reference machine with a deviation angle  $> 0.1^\circ$ , and the extended uncertainty of the lever arm needs to be achieved to ensure the uncertainty. The measurement guarantee of the machine decreases gradually, the larger

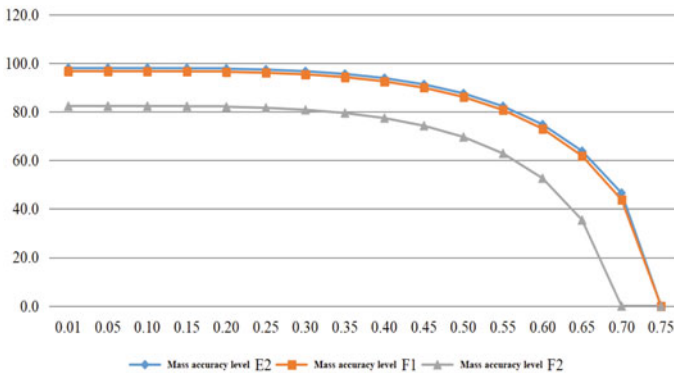


**Fig. 4** The variation of the extension uncertainty of lever arm when the arm deflection angle from the horizontal with 3 level of accuracy of the mass E2, F1, F2

the deflection angle, the lower the uncertainty in the extension of the lever arm. Due to measurement, it is necessary to ensure that the deflection angle of the lever arm relative to the horizontal is  $< 0.1^\circ$ .

## 4 Conclusion

In this study, to ensure the uncertainty of the deadweight torque standard machine is  $U = 5 \times 10^{-4}$ , the machine should be designed with the following parameters and conditions: Ambient Temperature  $23 \pm 5^\circ\text{C}$ ; Ambient Humidity  $60 \pm 20\% \text{RH}$ ; Minimum barometric pressure 990 hPa; Maximum barometric pressure 1100 hPa; Maximum rotary frictional torque  $20 \mu\text{Nm}$ ; The coefficient of thermal expansion of the arm material  $1.2 \times 10^{-6}/^\circ\text{C}$ ; Lever arm length on each side 1 m; Maximum deformation at the tip of the lever arm under maximum load 3 mm; The maximum deflection angle of the lever arm from the horizontal  $0.1^\circ$ ; Vibration of the mass at 1000 mm position from the mass hanging point 1 mm; Accuracy level of mass F1; Extended uncertainty due to arm length measurement and tolerance to nominal dimension  $96.6 \mu\text{m}$ .

**Acknowledgements** This research is funded by Vietnamese Government under the project number DTĐLCN.49/15. The authors would like to thank Associate Professor Vu Khanh Xuan for his serving as scientific advisor.

## References

1. Carbonell JAR, Verdecia JLR, Robledo AL (2006) Torque standard machines at CEM. In: XVIII IMEKO world congress, metrology for sustainable development, September 17–22, 2006 Rio de Janeiro, Brazil
2. Yon-Kyu P, Min-Seok K, Jong-Ho K, Jae-Hyuk C, Dae-Im K (2007) Establishment of torque standards in Kriss of Korea. In: IMEKO 20th TC3. 3rd TC16 and 1st TC22 international conference
3. Ramirez-Ahedo D, Torres-Guzman JC, Martinez-Juarez F (2007) Hybrid torque standard machine for 1 kNm developed in CENAM. In: IMEKO 20th TC3, 3rd TC16 and 1st TC22 international conference, cultivating metrological knowledge, 27th to 30th November. Merida, Mexico
4. Doğan C, Akkoyunlu O, Kuzu C (2002) National metrology institute of Turkey (UME) development of the 1 kNm static torque standard machine at UME. In: 18th IMEKO TC3 conference on Force, mass and torque 2002, Proceedings of a meeting held 24–26 September 2002, Celle, Germany
5. Oliveira RS, Guilherme RF, Cabral LC (2012) Influence of operational parameters on a hand-operated torque standard machine. *Measurement* 45(10)
6. Test Report Certificate No.: 1501-00281-002 (2015) KRISS (Korea Research Institute of Standard and Science)
7. Van Duy V, Thang VT, Van Hung P (2017) Evaluation of measurement uncertainty for torque standard machine using air rotary bearing. *Appl Mech Mat (AMM)* 870:215–222. ISSN 1662-7482. <https://doi.org/10.4028/www.scientific.net/AMM.870.215>

# Using of Composite Materials for the Rear Axle Housing



Nguyen Thanh Quang, Nguyen Quang Thai, Pham Viet Thanh, and Le Dinh Manh

**Abstract** The rear axle housing of the truck receives the load directly from the weight of the cargo and the vehicle's mass and causes an indirect load of torque, bending leading to deformation, cracking, and possibly breakage. Truck's rear axle housing are usually made from main materials such as cast steel, welded steel or cast iron. In the general case, stress and strain analysis when is subjected to bending will predict the failure modes for design and manufacturing. Finite element method (FEM) and simulation in Ansys Workbench 2022R1 software were used in this study. Some composite materials are selected to replace the original material to casting and welding technology replace and reduce the overall mass of trucks. The results of stress and strain analysis on 3 types of materials (steel, cast iron, composite) shown that the maximum value of equivalent stress (von-misses), maximum principal stress, and the maximum shear stress. The crack analysis results shown that the maximum value of J-Integral. When replacing composite material compared with the original material, the mass of the rear axle housing was reduced by 54%, and reliability and durability were also improved.

**Keywords** Steel carbon · Cast iron · Composite · Stress and strain · Mass reduce

## 1 Introduction

Truck's rear axle is one of the main components bearing weight of cargo and of itself, torques, bending moments and dynamic loads during movement on bumpy roads. The rear axle housing of axle (hereinafter called the rear axle housing) is used

---

N. T. Quang (✉) · P. V. Thanh · L. D. Manh  
Hanoi University of Industry, Hanoi, Vietnam  
e-mail: [nguyenthanhquang@hau.edu.vn](mailto:nguyenthanhquang@hau.edu.vn)

N. Q. Thai  
Kettering University, Flint, MI, USA

to support the vehicle's body and to protect components inside such as differential assembly, half shafts, at the same time, to transmit forces and moments from vehicle's wheels to body. The rear axle housing's common damage is warp due to breaking or cracking. Truck's rear axle housing is usually made of steel or cast iron. It is an independent component with big dimensions and mass. Its manufacturing technology continuously combines main casting fabrication and mechanical manufacturing in working machines. The current trend is to reduce mass and manufacturing cost of car's components.

There are different design solutions to reduce mass. The main solution is to reduce the rear axle housing's thickness, but it raises the cost of main casting fabrication and manufacturing. Another solution is lightweight material instead of traditional steel or cast iron. Composite is a popular lightweight material.

The advantage of lightweight material is low cost and less weight [1, 2]. Composite, plastic and polyme are good alternatives for reducing vehicle's weight thanks to high durability, easy to improve aesthetics [3]. An experiment shows that if the vehicle's weight reduces by 10%, then fuel consumption decreases by 5–7%, and greenhouse gas (GHG) emissions decreases [4]. In 1970 the average share of composite was 6% of vehicle's weight. The share increased to 16% in 2010. It is forecasted to 18% in 2020, [5]. The use of composite should meet following environmental and safety requirements: Light weight to reduce fuel consumption, increase environmental friendliness; Increasing vehicle's safety by absorbing energy from impacts outside; Reducing manufacturing and running cost to increase economic efficiency; Possibility of reusing, recycling, prolonging working time of components. Therefore, in designing the rear axle housing, it is necessary to calculate suitable technical criteria, such as stress and deformation due to bending or torsion. Since the rear axle housing has complex structure, the common tools can hardly help to calculate. Modern calculating methods can give accurate results and save time. Finite Element Analysis (FE) is a popular method today to calculate 2 states of strength: fatigue strength and breaking strength by static load multiplied by dynamic load coefficient. There are typical works of FE analyzing stress values and equivalent deformation which help determine static strength parameters of rear axle housing [6]. The local stress—deformation analyzing method is a good tool to forecast parts' fatigue life. In a study of fatigue strength, the rear axle housing, made of high resistance alloy, is cyclically bent at 4 points. The simulation uses Smith—Watson—Topper and Fatemi—Socie parameters to investigate fatigue cycle and starting point of fatigue cracks [8].

## 2 Simulating Rear Axle Housing of Trucks

This study uses Ansys Workbench 2022R1 to analyze the rear axle housing's strength under bending by static load.

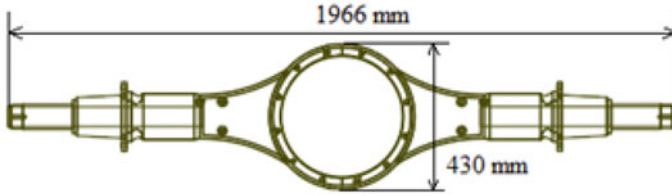


**Fig. 1** A truck rear axle housing

### 2.1 Modeling the Rear Axle Housing

The rear axle housing has complex box shape with average thickness of 10 mm. A 3-D model has been designed according to actual dimensions of a rear axle housing. The dimensions are given in Fig. 1.

### 2.2 The Rear Axle Housing’s Material

The rear axle housing materials are cast steel or cast iron. Some alternatives are composites. The main material parameters are: strength criteria  $\sigma$ , elasticity modulus E and specific mass  $\rho$ . The main specifications and strength limits of materials according to SI unit system are given in Table 1, [3, 9].

**Table 1** Material properties

Properties	Carbon steel, cast	Cast iron (BS grade Si 10)	Composite PA6/glass fiber
Density (kg/m <sup>3</sup> )	7825	7000	1800
Young modulus (Gpa)	203.4	123.9	21.95
Tensile U, Strength (Mpa)	447.9	164.3	396.9
Tensile Y, strength (Mpa)	234.3	164.3	396.9
E/ $\rho$ (GPa—m <sup>3</sup> /kg), shear stiffness	0.02652	—	0.034
E1/2/ $\rho$ (Pa1/2—m <sup>3</sup> /kg)—buckling stiffness	58.3	—	116.6
E1/3/ $\rho$ (Pa1/3—m <sup>3</sup> /kg)—bending stiffness	0.7582	—	1.759



Fig. 2 Rear axle housing’s meshing model

### 2.3 3-D Meshing

The finite meshing model uses quadratic 4-node elements. Finer meshing needed in bending corners, where would be more stress. The element’s size is 6 mm. Free meshing method assures meshing flexibility in bending areas or complex shapes. The degrees of freedom are determined by the nodes. There are 3 degrees of freedom per node, i.e. there could be movement to x, y, z direction. Use quality checking function to optimize the mesh. There are 139,122 elements and 245,084 nodes. The meshing model is shown in Fig. 2.

### 2.4 Load Conditions and Boundary

The load impacts to rear axle housing at 4 points A, B, C, D. Load from cargo and vehicle’s body impacts to 2 points C and D and at dampers. Reaction forces impact to wheels and axle at 2 point A and B, Fig. 3.

Forces acting to the rear axle housing at any area are determined by formula (1)

$$P_{cr} = \frac{\pi^2 EI}{L^2} \tag{1}$$

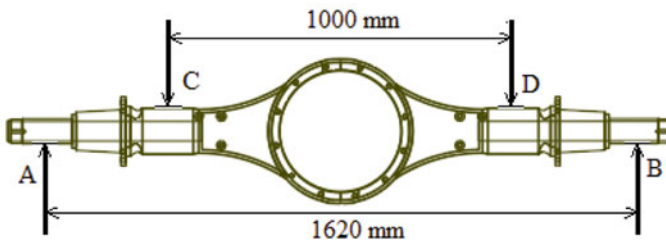
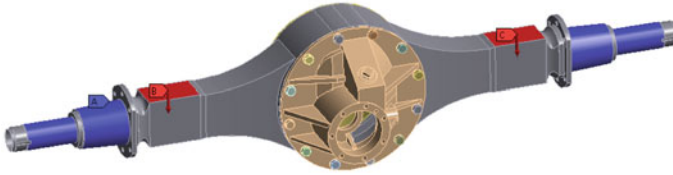


Fig. 3 Drawing of forces placed to rear axle housing



**Fig. 4** Model of load placing and boundary conditions

Here:  $P_{cr}$  is the force acting to vertical direction (kG).  $E$  is elastic modulus (Young’s modulus—GPa).  $I$  is the 2nd moment of inertia at area of force placing ( $m^4$ ).  $L$  is the length of the rear axle housing—distance of force placing (m).

The rear axle housing’s mass according to load  $P_{cr}$  is calculated by formula (2)

$$M = \frac{2L^2\sqrt{P_{cr}}}{\sqrt{\pi}} = \frac{1}{\sqrt{E/\rho}} \tag{2}$$

$M$  is the rear axle housing’s mass (kg).  $\rho$  is the specific mass (density) of the rear axle housing’s material ( $kg/m^3$ ).

Parameter  $E/\rho$  is a strength criteria shown in Table 1. In designing, criterias should be checked in following order: (1)  $E/\rho$ ; (2)  $(R_{0.2})/2/\rho$ ; (3)  $(E)/3/\rho$ ; (4)  $R_{0.2}/\rho$ ; (5)  $E/2/\rho$ ; (6)  $R_{0.2}/3/\rho$ .

Parameter  $R_{0.2}$  is the minimum yield strength [10].

Considering the symmetrical full load of 7200 kg evenly distributed on positions C and D. Positions A and B are boundary surfaces of the model. Force placing and boundary are shown in Fig. 4.

### 3 Simulating and Analyzing Results

#### 3.1 In Case of Static Load

Under static load, the 2 reducing positions, connected with hubs, are subjected to the greatest stress. Here, the dangerous cross section has maximum stress of 21.81 Mpa. Figure 5 illustrates simulating the rear axle housing’s stress in case of symmetrical static load. Figure 5a–c illustrate maximum stress in dangerous cross sections.

Results of simulating stress on the rear axle housing according to different materials are shown in Table 2.



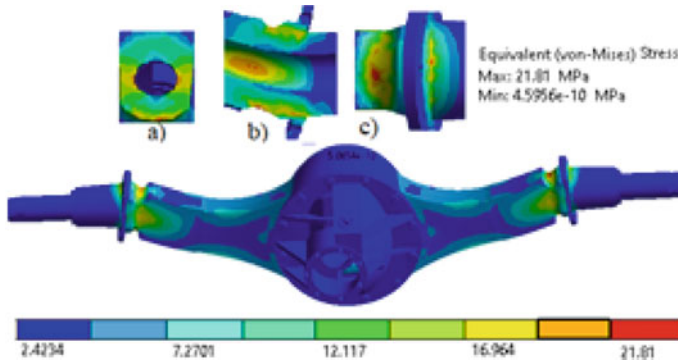


**Fig. 5** Distribution of maximum stress in dangerous cross sections

**Table 2** Results of simulating maximum stress on the rear axle housing

No.	Parameters	Carbon steel	Cast iron	Composite PA6	Difference (%)
1	Max. stress (MPa)	21.81	22.319	25.602	(+) ~ 15
2	Mass (kg)	144.16	133.54	66.813	(-) ~ 54

### 3.2 In Case of Load Changes

During running, load acting to the rear axle housing can change according to bumpy level of road surface. We consider sinusoidal road surface. Acting force frequency of 130 Hz is divided into 10 survey intervals. Dephasing between left and right load causes rear axle housing’s bending and torsion. Load magnitudes and phase angle are shown in Fig. 6.

The simulation gives equivalent stress values in the rear axle housing using cast steel and composite materials. Stress values according to different frequencies of acting loads are shown in Table 3 and Fig. 7. In cast steel rear axle housing, the

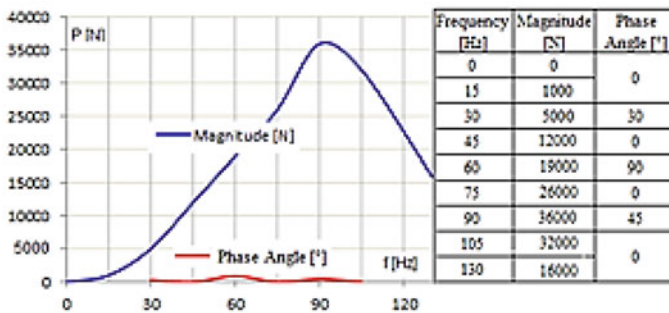


**Fig. 6** Load acting to the rear axle housing

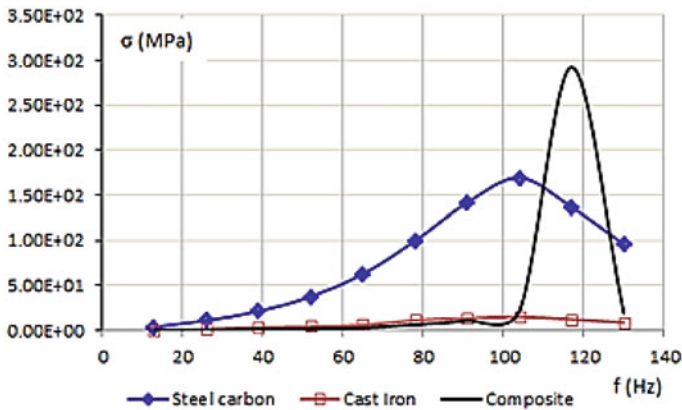
maximum stress is 169 Mpa. In composite rear axle housing, the maximum stress is 292.34 Mpa. As the results, the composite rear axle housing has greater maximum stress than that in cast steel rear axle housing.

Figure 9 shows the distribution of rear axle housing’s stress in case of load changes.

Table 4 compares maximum stress in case of load changes and that of static load. During running in bumpy road with asymmetrical load, the maximum stress is many times bigger.

**Table 3** Stress in the rear axle housing according to acting load frequencies

f (Hz)	26	39	52	65	78
Steel carbon	1.10E+01	2.12E+01	3.77E+01	6.28E+01	9.95E+01
Cast iron	1.3857	3.4605	4.2666	6.0981	11.318
Composite	0.53902	1.3696	1.7292	2.8286	6.4627



**Fig. 7** Rear axle housing’s stress

**Table 4** Comparing maximum stress in 2 cases

		Carbon cast steel	Cast iron	Composite PA6/Glass fiber
1	Static load	21.81	22.319	25.602
2	Changing load	169	14.96	292
	Difference	129%	67%	<b>87</b>

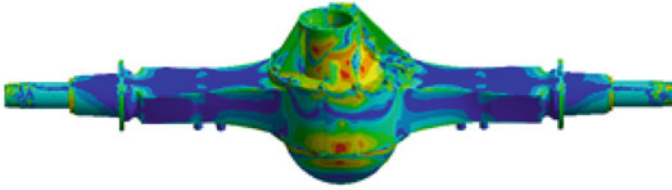


Fig. 8 Model of rear axle housing's fatigue analysis

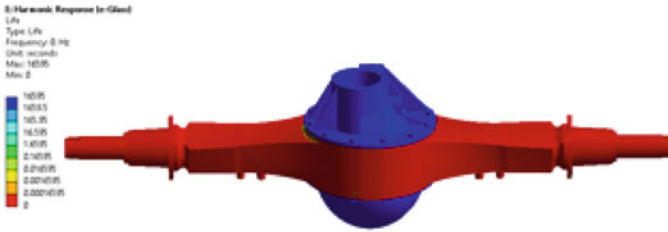


Fig. 9 Distribution of fatigue cycles in the rear axle housing

### 4 Analyzing Fatigue Cycle

Fatigue analysis uses fatigue tool in the software. Marginal and load conditions are used in case of load changes. Goodman theory, which analyzes equivalent stress, is used to determine cycle life. Figure 8 shows image of simulating fatigue analysis.

The number of fatigue cycles in maximum stress areas is different in rear axle housings using the 2 materials. In steel rear axle housing, there are 7692 cycles. In cast iron rear axle housing, there are 7898 cycles. In composite rear axle housing, there are 16,595 cycles. Green area shows infinite number of cycles.

### 5 Conclusion

The research analyzes the use of composite material, instead of cast steel and cast iron, for rear axle housing. In the results, the mass can reduce by 54% (144.16/133.54/66.813 kg). The rear axle housing's maximum stress increases by 15% (21.81/22.319/25.602 MPa). Using composite, the rear axle housing's hardness reduces but the number of fatigue cycles increases: 7692 cycles in cast steel rear axle housing, 7898 cycles in cast iron rear axle housing, 16,595 cycles in composite rear axle housing. Therefore, composite material creates double strength, compared with cast steel and cast iron.

Finite element method (FEM) and simulating in Ansys Workbench 2022R1 help to analyze equivalent stress (von-Mises) and determine the rear axle housing's flexural rigidity. Using composite, it is necessary to improve both axle's side, where is concentrated stress, to increase the rear axle housing's reliability and durability.

Material with core of Epoxy E-Glass, which is used popularly thanks to its simple technology, is suitable for experiments and low cost manufacturing.

## References

1. Nunes R, et al (1990) SM handbook, volume 2 properties and selection: nonferrous alloys and special—purpose materials, ASM international, handbook committee. United States of America. ISBN 0-87170-378-5 (v.2)
2. Njuguna J (2016) Lightweight composite structures in transport: design, manufacturing, analysis and performance. ISBN: 978-1-78242-325-6 (print), ISBN: 978-1-78242-343-0 (online), Woodhead Publishing Series in Composites Science and Engineering: Number 67, 2016, Elsevier
3. Jones RM (1999) Mechanics of composite materials, 2nd edn. Taylor & Francis, Inc. ISBN-1-56032-712-1
4. Mayyas AT, Omar M (2019) Eco-material selection for lightweight vehicle design. <https://doi.org/10.5772/intechopen.88372>
5. Todor M-P, Kiss I (2016) Systematic approach on materials selection in the automotive industry for making vehicles lighter, safer and more fuel-efficient. *Appl Eng Lett* 1(4):91–97
6. Monica P, Babu KJM (2018) Analysis on the rear axle housing of heavy truck using Ansys. *Int Res J Eng Technol (IRJET)* 05(07)
7. Socie DF (1993) Critical plane approaches for multiaxial fatigue damage assessment. In: McDowell DL, Ellis R (eds) *Advances in multiaxial fatigue*, ASTM STP 1191. American Society for Testing and Materials
8. Firat M (2011) A computer simulation of four-point bending fatigue of a rear axle assembly. *Eng Failure Anal Elsevier* 18(8):2137–2148. <https://doi.org/10.1016/j.engfailanal.2011.07.005>
9. Kaw AK (2006) *Mechanical of composite materials*, 2nd edn. Taylor & Francis, Inc. ISBN 978-0-8493-1343-1
10. Lüdke B, Pfestorf M (2006) Functional design of a “lightweight body in white”—how to determine body in white materials according to structural requirements. In: *International symposium on niobium microalloyed sheet steel for automotive application*. TMS (The Minerals, Metals & Materials Society)
11. <https://www.ansys.com/academic/students>

# FEM Simulation and Experimental Study on Improving the Forming Ability in Stamping SS400 Sheet Material with a Variable Blank Profile



The-Thanh Luyen, Duc-Toan Nguyen, Van-Nam Nguyen, and Thi-Hoa Pham

**Abstract** A study on the stamping process of a chair surface with complex profiles made from SS400 material sheets, this part is welded to the mounting bracket used for transporting mining workers in the mines. During the stamping process, the seat surface often appears tearing at the front position of the seat. This position has non-uniform deformation, a large degree of deformation is easy to tear, and the surface after deformation will be uneven, affecting the quality and aesthetics of the product. Defects occur when stamping the seat surface due to many reasons such as the calculation of the initial profile of the workpiece, selection of geometrical parameters, and inappropriate technology. Therefore, this study has conducted a simulation of the stamping process with different types of billet profiles, after being simulated stamping, the deformation and thickness will be determined at many locations. From there, select the appropriate billet profile so that the part after stamping does not appear to be torn, ensuring the size requirements and no need to add rim cutting operations. The suitable workpiece profile will be simulated and verified with the corresponding experiment.

**Keywords** Chair surface · Complex profiles · Finite element method (FEM) · Blank profile · Stamping process · SS400 steel sheet

---

T.-T. Luyen · T.-H. Pham (✉)

Faculty of Mechanical Engineering, Khoai Chau, Hungyen University of Technology and Education, Dan Tien, Hung Yen, Vietnam

e-mail: [hoapt2108@gmail.com](mailto:hoapt2108@gmail.com)

D.-T. Nguyen

School of Mechanical Engineering, Hanoi University of Science and Technology, Hai Ba Trung District, 1A-Dai Co Viet Street, Hanoi City, Vietnam

V.-N. Nguyen

Faculty of Mechanical Engineering, Hai Phong Industrial Vocational College, An Dong, An Duong, Hai Phong, Vietnam

## 1 Introduction

In the stamping process, tearing often occurs on the part, the tearing position is mainly the position subject to the most deformation. In previous studies [1, 2], the influence of parameters such as the blank holder force, the nose radius of the punch, the shoulder radius of the die, the clearance between the punch and the die to the forming height, and the thinness of the cylindrical cup. Some researchers on the optimization of the shape of the blank to the forming process of the product such as Wang et al. [3] researched to determine the optimal level of the design of the workpiece for deep stamping, a new method for generating optimally designed workpieces using finite element analysis is proposed, this method is divided into several steps. During optimization, the shape error is calculated by comparing the deformation contour of the blank and the desired target contour. Based on the material flow characteristics, the blank geometry is modified several times until the shape error is within a predetermined tolerance. Starman et al. [4] present a numerical method for simultaneous optimization of blank geometry and forming tool geometry during three-dimensional sheet metal forming, applied to automotive products with complex shapes. Nguyen et al. [5] optimized the geometry and process parameters for deep stamping of cylindrical cups, using FEM simulations combined with Taguchi's orthogonal arrays, then study using the Hill48 stress function, it is possible to simulate the appearance of the excess ear during deep stamping of cylindrical cups by improving the original shape of the workpiece.

This study simulated the stamping process of the seat surface with different types of blank profiles, the part after being simulated for stamping will be determined for deformation and thickness at many locations. From there, select the appropriate billet profile so that the part after stamping does not appear to be torn, ensuring the size requirements and no need to add rim-cutting operations.

## 2 Geometric Model and Stamping Detail Material

### 2.1 Geometric Model of Stamping Detail

Sheet billets are calculated and shaped by deformation formulas and accurately redefined from numerical simulation software, then verified by forming experiments on presses. Details, as shown in Fig. 1a, have a flat bottom structure and an equal wall height of 17 mm with no rims, so determining the correct billet profile will reduce the work of cutting the edge of the product after stamping.

On the contour of the part, there are convex and concave arcs of different sizes, so the deformation in these areas is also different. The metal in this section is both in compression and in tension and the strain stress also varies over the arc length and at the center of the arc will be the most deformed part. The curvature radii R16, R2, R1.5 are the points with the most complex deformation due to their small size and opposite

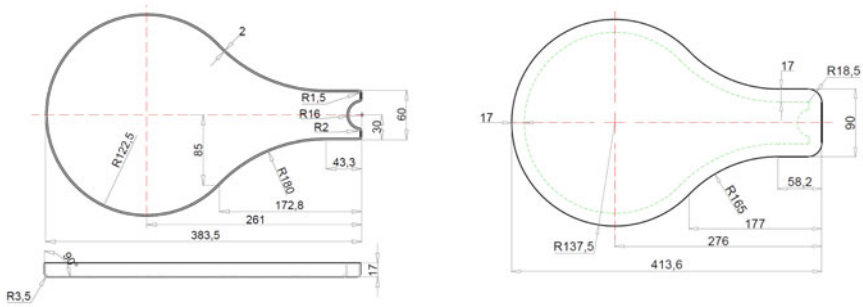


**Fig. 1** Geometric parameters. **a** Stamping details; **b** Initial billet profile

direction of deformation, so this is also the place with the most deformation and the easiest to tear. From the dimensions of the part being analyzed, the initial blank for stamping is determined by the method of equalizing the area with the dimensions as shown in Fig. 1b.

### 2.2 Stamping Material for Seat Details

The material used in this study is an SS400 steel plate [6]. The stress–strain curve for the SS400 steel plate was obtained using Voce’s model [7] as Eq. (1). The SS400 sheet material properties are also described in Table 1.

$$\bar{\sigma} = \sigma_Y + A(1 - \exp(-B\varepsilon_{eq}^{pl})) \tag{1}$$

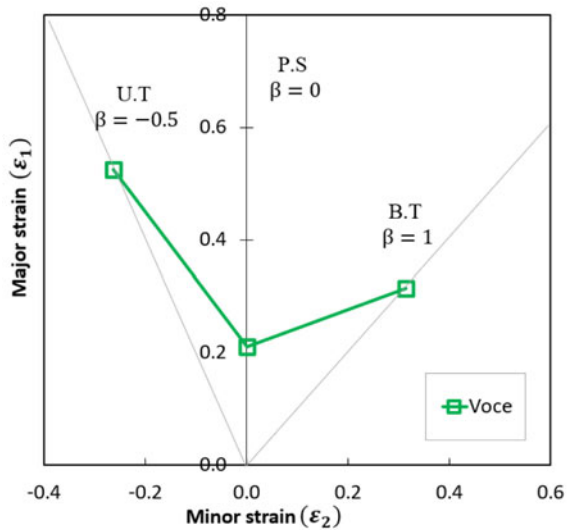
where A and B are plastic coefficients;  $\bar{\sigma}$ ,  $\sigma_Y$  and  $\varepsilon_{eq}^{pl}$  are equivalent stress, equivalent strain and tensile strength of the material, respectively.

The forming limit curve of SS400 is constructed by graphical method [1, 8]. The method is calculated for special deformation modes such as planar strain (PS) ( $\beta = 0$ ), uniaxial tensile strain (UT) ( $\beta = -1/2$ ) and uniform tensile strain in both directions (BT) ( $\beta = 1$ ) as shown in Fig. 2.

**Table 1** Material properties of SS400 steel [6]

Young’s modulus (GPa)	Possion’s ratio	Density ( $\rho$ , kg m <sup>-3</sup> )	Yield stress ( $\sigma_Y$ , MPa)	A (MPa)	B
213	0.3	7850	348	188.86	28.3293

**Fig. 2** FLC of SS400 plate material



### 3 Simulation and Experimental Model of Stamping Process

#### 3.1 Experimental Model

The stamping process is described based on the constitution of the die set as shown in Fig. 3. The die part is installed with the fixed lower table, the punch part (3) is installed with the punch base plate (1) through the strut (2), and the punch base is mounted with the upper table moving up and down creating a stamping motion. The die (5) is installed with the die plate (7) through the spacers (6), and the die plate is fixed to the lower table of the hydraulic press. The blank is positioned on the die and the blank holder (4), which is pushed by the springs (8). This part has the effect of pressing the blank to the underside of the punch to keep the bottom surface of the blank flat and not displaced horizontally during deformation. At the end of the down stroke, the punching press moves up with the upper table back to the original position. The force of the springs will lift the support plate and the part out of the die and end the stamping process.

The stamping process is machined on a hydraulic press with a maximum capacity of 150 tons. Lubricants used in stamping are commercially available oils. In this study, the friction between the punch, the blank, and the blank holder during the stamping process was referred to [2]. The experimental set of molds with the main parts are shown in Fig. 4, the model of deformation state and the structure of the stamping die set are shown in Fig. 3. The blank holder force of the stamping process is calculated to be 12.8 tons. Parameters such as the nose radius of punch is 3.5 mm, the shoulder radius of die is 5 mm, the clearance between the punch and the die is 2.5 mm, the stamping speed is 10 mm/s, the coefficient of friction between the punch



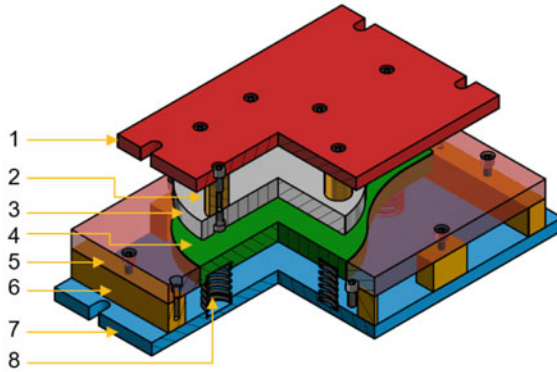


**Fig. 3** Structure of the chair surface stamping die set

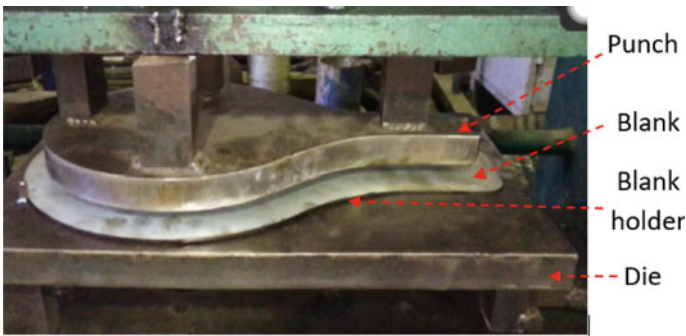


**Fig. 4** Main parts of the experimental set

and the blank is  $\mu_p = 0.25$ ; coefficient of friction between blank holder and blank is  $\mu_h = 0.15$ ; The coefficient of friction between the die and the blank is  $\mu_d = 0.15$  [1].

### 3.2 Finite Element Model

In this study, the stamping process to forming the part is simulated using ABAQUS software [1]. In which the die is fixed, the punch, blank and blank holder are moved vertically to achieve the depth dimension of the detail. The absolute hard model is used for punch, blank holder, and die. The blank is modeled as flat and mesh surface deformation and is subdivided according to the integrated reduced S4R element type.

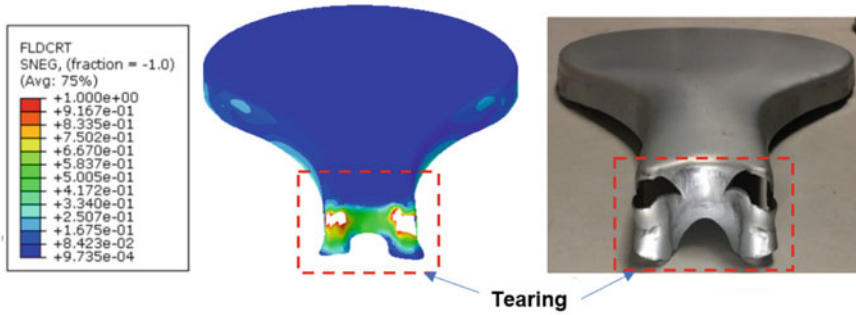


Fig. 5 The tearing phenomenon of the part when simulating and experimenting

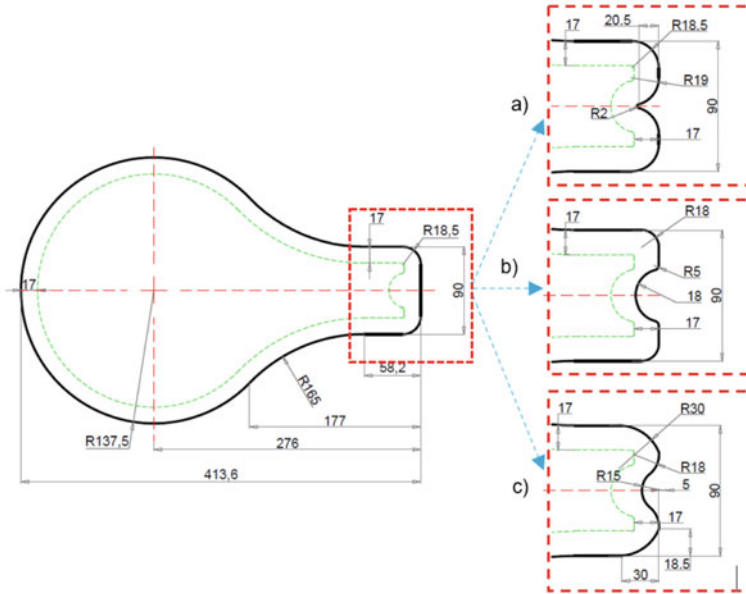
### 3.3 Change the Contour of the Blank

In the stamping process, tearing often occurs on the part, the tearing position is mainly at the position subject to the most deformation, which is usually the edges as shown in Fig. 5. The main reason for the tearing process is because this deformation is too large to exceed the tensile limit of the material, it also causes tearing. Therefore, the research focuses on the change of the blank profile, especially the head position of the blank with the changed profile as shown in Fig. 6. For Fig. 6a, the blank profile is constructed by moving 17 mm parallel to the stamping part, followed by Fig. 6b, creating a radius of curvature of 18 mm in the middle and 17 mm from the detail and bevelled on the sides 18.5 mm, and finally, the third type of profile as shown in Fig. 6c is a combination of different semi-curvatures. These blanks were in turn used in numerical simulation to determine strain and thickness was measured at 12 locations as shown in Fig. 7, in which position from 1 to 5 is on the top of the part, and position from 6 to 12 is on the middle position of the wall of the stamping part.

## 4 Results and Discussion

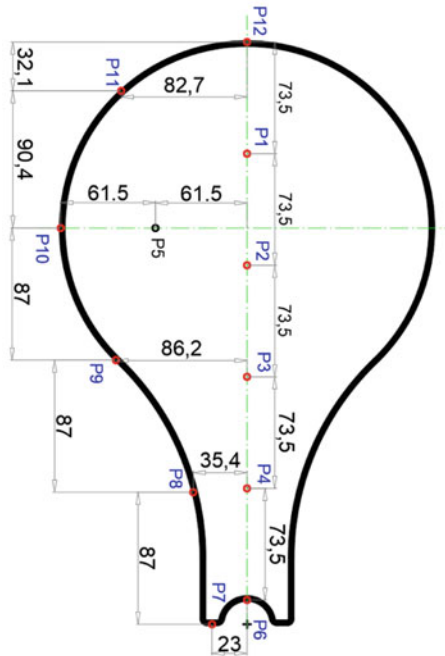
In order to determine the deformation of the part after the stamping simulation, the study conducts the deformation test at special locations on the part as shown in Fig. 7. When the profile of the blank changes in three cases as shown in Fig. 8, all positions P1-P5 are shown on the right side of the graph and show small deformation in both directions, while positions P8-P12 are shown on the left side of the graph and has tensile and compressive deformation. Especially, positions P6, P7 have large deformation in the main direction and compression in the secondary direction.

As detailed in Fig. 8a, after simulating stamping for two major deformation positions, P6 and P7, position P6 occurs a lot of thinning with a thickness of 1.465 mm, followed by position P7 for thinnest variable with the thickness achieved is 1.138 mm. The detailed profile according to this first option gives a large deviation in shape from



**Fig. 6** Changing the blank profile. **a** Blank profile 1; **b** blank profile 2; **c** blank profile 3

**Fig. 7** Deformation and thickness measurement positions on the detail



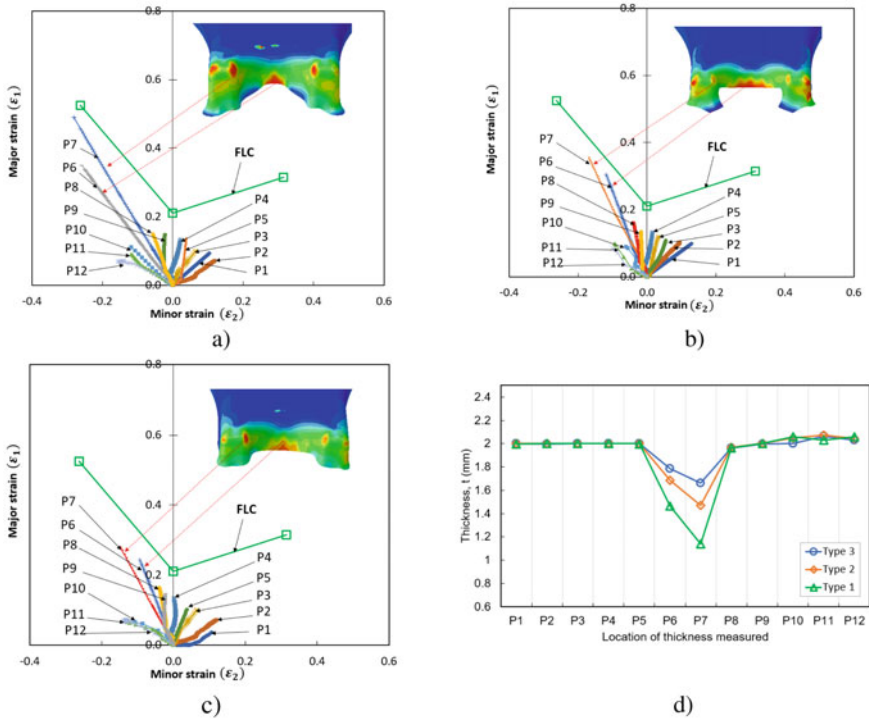


**Fig. 8** Strain and thickness at the positions of the detail. **a** Blank profile 1; **b** blank profile 2; **c** blank profile 3; **d** thickness

the original detailed model, the position of the concave arc has not reached the height, and the position of the convex arc exceeds the required height. Next is the result as shown in Fig. 8b is that for the blank with the profile changed according to the 2nd variant, the position P6 occurs thinning phenomenon with the achieved thickness is 1.685 mm and the position P7 has a thickness of 1.469 mm. The blank profile in this second case has the concave arc position achieved, but the convex arc position has a larger size than the original part's model. Finally, the result as shown in Fig. 8c is that for the workpiece with variable profile according to option 3, the position P6 has a slight thinning phenomenon with a thickness of 1.784 mm and the position P7 with a thickness of 1.662 mm. This degree of thinning is not large compared to the thickness of the original blank. The detail profile in this third case has concave and convex arc positions, both reaching the size of the part height after stamping. The suitable blank profile is simulated and tested for good agreement as shown in Fig. 9, the detail after stamping is not wrinkled, tearing and reaches the size of the wall height without having to go through the rim cutting operation.

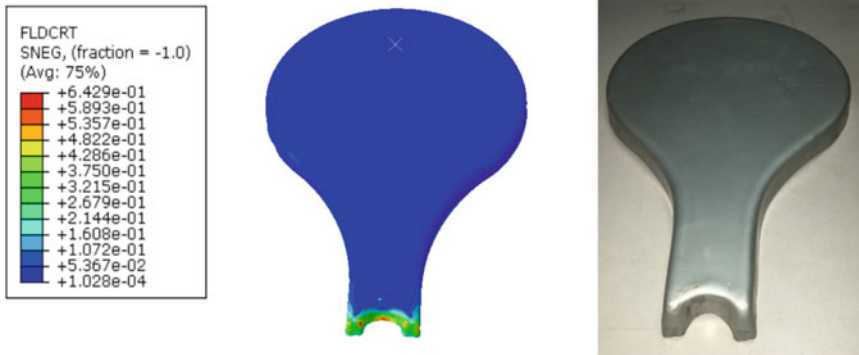


Fig. 9 Simulation and experimentation with reasonable blank profile

### 5 Conclusions

Simulation study and experiment on the process of stamping chair surface details with the geometrical parameters of the mold set being fixed. The blank profile is changed, with the blank determined by the area balance method, and the part after stamping appears tearing. When the blank profile changes according to the first option, the detail after simulation gives a large deviation from the original detailed model and the thickness at the thinnest position is 1.138 mm. Next, for the blank with the profile changed according to the second option, the profile after the simulation is close to the original detailed model and the thickness at the thinnest position is 1.469 mm. Finally, for the blank with the profile changed according to option 3, the position with the thinnest thickness is 1.662 mm, this degree of thinning is not large compared to the thickness of the original blank. The detailed profile in this third case has concave and convex arc positions, both reaching the size of the part height after stamping. The appropriate blank profile is simulated and experimentally verified for good agreement, the part after stamping is not wrinkled, tearing, and the size of the wall height is achieved without having to go through the rim cutting operation.

### References

1. Luyen TT, Tong VC, Nguyen DT (2021) A simulation and experimental study on the deep drawing process of SPCC sheet using the graphical method. Alexandria Eng J 61(3):2472–2483. <https://doi.org/10.1016/j.aej.2021.07.009>
2. The-Thanh L, Tien-Long B, The-Van T, Duc-Toan N (2019) A study on a deep-drawing process with two shaping states for a fuel-filter cup using combined simulation and experiment. Adv Mech Eng 11(8):1–11. <https://doi.org/10.1177/1687814019872674>
3. Wang J, Goel A, Yang F, Gau JT (2009) Blank optimization for sheet metal forming using multi-step finite element simulations. Int J Adv Manuf Technol 40(7–8):709–720. <https://doi.org/10.1007/s00170-008-1383-y>

4. Starman B, Cafuta G, Mole N (2021) A method for simultaneous optimization of blank shape and forming tool geometry in sheet metal forming simulations. *Metals (Basel)* 11(4):1–19. <https://doi.org/10.3390/met11040544>
5. Nguyen D et al (2014) Formability improvement and blank shape definition for deep drawing of cylindrical cup with complex curve profile from SPCC sheets using FEM. *J Cent South Univ* 21:27–34
6. Hai VG, Minh NTH, Nguyen DT (2020) A study on experiment and simulation to predict the spring-back of SS400 steel sheet in large radius of V-bending process. *Mater Res Express* 7. <https://doi.org/10.1088/2053-1591/ab67f5>
7. Voce E (1978) The relationship between stress and strain for homogeneous deformation. *J Inst Metals* 74:537–562
8. Luyen T-T, Pham Q-T, Kim Y-S, Nguyen D-T (2019) Application/comparison study of a graphical method of forming limit curve estimation for DP590 steel sheets. *J Korean Soc Precis Eng* 36(9):883–890. <https://doi.org/10.7736/kspe.2019.36.9.883>

# Researching the Effect of High-Velocity Oxygen Fuel Spraying Parameters on Porosity of WC-12Co Coating on Inner Cylinder



Thanh-Phu Nguyen, Van-Chien Dinh, Van-Thoai Le, Khac-Khanh Bui, and Thanh-Hoa Doan

**Abstract** This study optimizes and determines effect of HVOF (High-velocity oxygen fuel) spraying parameters to porosity of the WC-12Co coatings sprayed on inner cylindrical surface of S40C steel pipe. The studied spraying parameters include: Spray distance (L); Powder feed rate (P); Surface velocity of substrate (V). Experimental parameters using Taguchi L9 orthogonal design. The results determined optimal spraying parameters  $L_3 = 0.3$  m;  $P_2 = 26$  g.min<sup>-1</sup>;  $V_2 = 0.15$  m.s<sup>-1</sup>) for the minimum coating porosity with 1.19%. Effect of spraying parameters on porosity is L (46%) > V (34.1%) > P (14.2%). An experimental function for the relationships of porosity with spraying parameters was built to evaluate of influence of research spraying parameters on porosity.

**Keywords** High-velocity oxygen fuel · WC-12Co · Porosity

## 1 Introduction

Steel pipes are widely used in industry to transport raw materials and fuel for production. However, wearing and corrosion are difficult for protection, replacement and also increase production costs. Special materials are one solution to produce steel pipes, however, the it can affect mechanical properties or the cost is very expensive. Therefore, thermal spray coatings with a variety of materials are very suitable for different work surface requirements, providing necessary and effective solutions.

---

T.-P. Nguyen (✉) · V.-T. Le · K.-K. Bui · T.-H. Doan

Faculty of Mechanical Engineering, Hung Yen University of Technology and Education, Hung Yen, Vietnam

e-mail: [thanhpnhk3@gmail.com](mailto:thanhpnhk3@gmail.com)

V.-C. Dinh

Hanoi University of Mining and Geology, Hanoi, Vietnam

Tungsten carbide material is quite perfect solution, with very high temperature and wear resistance. This is proven by the fact that WC is an important component of hard alloys for metal cutting tools. HVOF method reduces decomposition and composition changing of carbide materials by spraying particles with high speed, medium temperature compared to other spraying heating sources in which flame temperature impact is in a short time [1–4]. Coating properties are influenced by spraying parameters. The coating properties is improved through improving hardness, adhesion strength and coating porosity reducing [3–6]. The precise influencing parameters are spray distance, powder feed rate, combustible gas-flow ratio, spray gun displacement speed, spray pitch and other parameters. In most published studies, the coating is sprayed on the surface of the plate or the outer cylindrical surface. For inner cylindrical surfaces, coating formation is more difficult that is not only with HVOF spraying but also with other spray methods. Therefore, this study investigates the influence of HVOF thermal spraying parameters on the porosity of the WC-12Co coating on the inner cylindrical surface of steel pipes from S40C [7]. Taguchi experimental design with L9 orthogonal array is used to arrange experimental parameters [8]. ANOVA analysis determines the influence of spraying parameters. Experimental relationship of spraying parameters on coating porosity is determined by a mathematical function based on experimental results. Hence, the trend of influence of spraying parameters on porosity of coatings was determined.

## 2 Experimental Procedure

### 2.1 *Materials and Experimental Parameters*

WC-12Co spraying powder supplied by Eutectic Corp. (USA) with particle shape and size in the range of 15–45 ( $\mu\text{m}$ ) (Fig. 1) was used in this study. The coating is deposited by HVOF spraying on the inner cylindrical surface of DN 400 steel pipe from material S40C (JIS G-4051) (OD = 406.4 mm, ID = 390.54 mm). The substrate is roughened with  $R_a = 10 \mu\text{m}$ . The thickness of coating after the spraying process was 400–550 ( $\mu\text{m}$ ). The range of values of spraying parameters in this study is presented in Table 1. The experimental parameters are arranged according to the L9 orthogonal array of the Taguchi method as shown in Table 2. The values of other spraying parameters are constants as shown in Table 3. The principle of spraying process on the inner cylinder surface is as shown in Fig. 2.



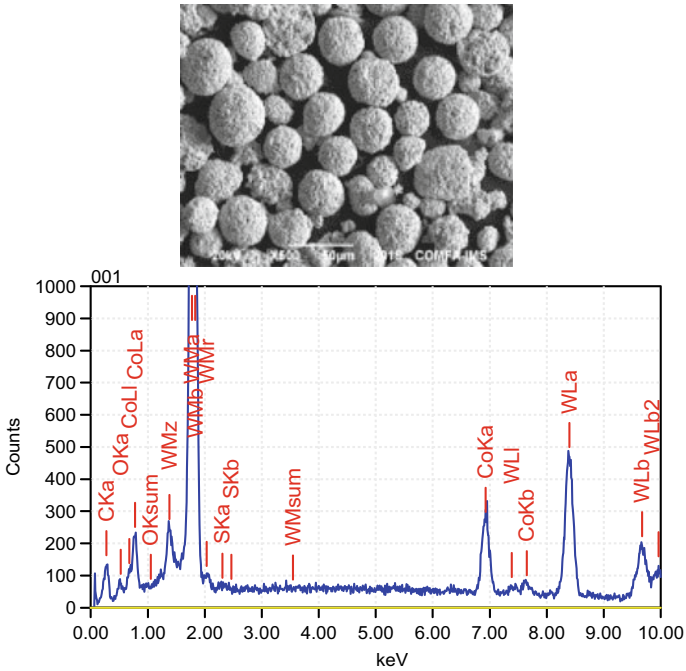


**Fig. 1** SEM micrographs and EDX scanning results of the WC-12Co powder

**Table 1** Spray parameter for three levels of Taguchi method

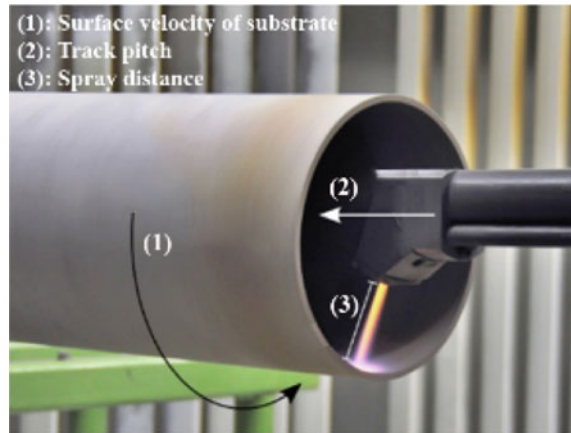
Parameter	Symbol	Range of values	Level		
			1	2	3
Spray distance (m)	L	0.2–0.3	0.2	0.25	0.3
Powder feed rate (g.min <sup>-1</sup> )	P	20–32	20	26	32
Surface velocity of substrate (m.s <sup>-1</sup> )	V	0.1–0.2	0.1	0.15	0.2

**Table 2** Experiment plan according to the L9 orthogonal array

Expt. no.	L (m)	P (g.min <sup>-1</sup> )	V (m.s <sup>-1</sup> )
1	0.20	20	0.10
2	0.20	26	0.15
3	0.20	32	0.20
4	0.25	20	0.15
5	0.25	26	0.20
6	0.25	32	0.10
7	0.30	20	0.20
8	0.30	26	0.10
9	0.30	32	0.15

**Table 3** Other spraying parameters used in this study

Parameter	Oxygen pressure (MPa)	Propane pressure (MPa)	Propan flow ( $\text{l}\cdot\text{min}^{-1}$ )	Air pressure (MPa)	Air flow ( $\text{l}\cdot\text{min}^{-1}$ )	Nitrogen pressure (MPa)	Nitrogen flow ( $\text{l}\cdot\text{min}^{-1}$ )
Value	0.98	0.686	40	0.686	550	0.4	20

**Fig. 2** Principle of spraying process on the inner cylinder surface by HVOF

### 3 Results and Discussion

#### 3.1 Experimental Results

The coatings' porosity is determined by metallographic techniques according to ASTM B 276 [9]. Porosity is determined as a percentage of the total area of the pores (dark color) to the total area of the micrograph. The calculated average porosity percentage results on 4 micrographs with 400x magnification at four different locations will be used. Axiovert 25 CA optical microscope from Carl Zeiss (Germany) is used for this study. The calculation is done on KS 300 3.0 software. The porosity results of the samples are presented in Table 4.

The results from Table 4 show that: the porosity of the coating changes in the range of 1.48–3.06%, the 7th sample with spraying parameters  $L_3P_1V_3$  ( $L = 0.3 \text{ m}$ ,  $P = 20 \text{ g}\cdot\text{min}^{-1}$ ,  $V = 0.2 \text{ m}\cdot\text{s}^{-1}$ ) has the lowest porosity with 1.48%. The change of spraying parameters affects the coating porosity which proves that their selection for this study is appropriate. The optimization method according to Taguchi, ANOVA analysis and mathematical function will be performed to determine optimal spraying parameters, influence and trend of the spraying parameters on the coating following porosity.

**Table 4** Experiment results for porosity of coating and corresponding S/N values

Expt. no.	L	P	V	Porosity (%)	$S/N = -10\log(\frac{1}{n} \sum y_i^2)$
1	0.20	20	0.10	3.06	-9.714
2	0.20	26	0.15	1.92	-6.319
3	0.20	32	0.20	2.62	-8.366
4	0.25	20	0.15	1.78	-5.008
5	0.25	26	0.20	1.61	-4.137
6	0.25	32	0.10	2.62	-8.366
7	0.30	20	0.20	1.48	-3.405
8	0.30	26	0.10	1.90	-5.977
9	0.30	32	0.15	1.63	-3.750

### 3.2 Optimizing Spraying Parameters for Porosity of Coatings

According to the Taguchi method, smaller quality characteristic gives better S/N ratio (smaller is better) that is used to optimize the coating porosity. The S/N results have been determined to correspond to the experimental results. From there, the average impact of each parameter are also determined (Table 4). The aforementioned values are shown on the scale chart in Fig. 3. The results of determining the optimal spray parameter  $L_3P_2V_2$  which have the highest average S/N values. At the same, the predicted optimal value with 1.19% is smaller than measured values from experimental results which have demonstrated highly efficient optimal results.

The optimal results with parameters for the smallest porosity with  $L_3 = 0.3 \text{ m}$ ;  $P_2 = 26 \text{ g}\cdot\text{min}^{-1}$ ;  $V_2 = 0.15 \text{ m}\cdot\text{s}^{-1}$  were used to conduct experiments to verify the reliability of the results predicted by the Taguchi method. Hence, porosity is determined to be 1.23%, which is similar to the value predicted by Taguchi method (1.19%) and demonstrated the reliability of this study. Thus, the predicted results are in good agreement with measured data.



Level	L	P	V
1	-7.915	-6.043	-7.885
2	-5.837	-5.126	-4.973
3	-4.408	-6.992	-5.303
Delta	3.507	1.866	2.912
Rank	1	3	2
Prediction: S/N ratio = -2.64941; Mean = 1.1855			

**Fig. 3** Optimal level of L, P, V parameters to porosity based on S/N

### 3.3 Effect of Spraying Parameters on Porosity of Coatings

The influences of spraying parameters on porosity was determined by ANOVA analysis of variance (Table 5), showing that: the spraying distance has a great influence on the porosity with 46.0%; surface velocity of substrate is 39.1%; powder feed rate is 14.2%; the effect of error is 0.7%, proving that the studied parameters are main parameters. The reliability based on the P-value index is all less than 0.05, showing the reliability of statistical results.

The relationship between spraying parameters and porosity was determined by Eq. (1).

$$Por = 17.8437 - 28.3.L - 0.545648.P - 58.8333.V + 39.3333.L^2 + 0.010787.P^2 + 175.333.V^2 \tag{1}$$

The value of  $R = 0.99$ ;  $R_{adj} = 0.98$  shows that, the goodness of fit test results for regression function (1).

From function (1), 3D graph describes influence of spraying parameters on coating porosity built on matlab R2015a software. Figure 4b, c shows that, when L increases from 0.1 to 0.3 (m), the porosity tends to decrease because of small distance and spraying particles do not have an optimal state when impacting (particle temperature, particle molten state, kinetic energy). The large overlay of the spray particles then also causes the increase in porosity. Therefore, the spray distance (L) needs to ensure that particles are heated to the optimum temperature and that they have enough time to accelerate to maximum speed due to the pressure of the gas flame. Figure 4a, c shows: when powder feed rate (P) increases from 20 to 26 g.min<sup>-1</sup>, porosity tends to decrease and increase when P increases from 26 to 32 g.min<sup>-1</sup>. The reason is that P has the right value at which the powder flow rate matches the heat of the spray flame and the spray particles will have right particle temperature for impact to form the best coating and reduce porosity. The best value of the P range studied in this case is 26 g.min<sup>-1</sup>. When V changes: if the value of V is large, spraying particles creates larger oblique-angled when impact. The impact state then is not good for coating deposition, the adhesion strength and porosity then tend to decrease (coating deposition is best when the spray particles fly in a direction perpendicular to the surface of the part). If V is small, the spray density of one location increases, the

**Table 5** Analysis of variance results

Source	DF	Adj SS	Adj MS	F-value	P-value	Effect (%)
L	2	1.13736	0.568678	65.28	0.015	46.0
P	2	0.35202	0.176011	20.21	0.047	14.2
V	2	0.96709	0.483544	55.51	0.018	39.1
Error	2	0.01742	0.008711			0.7
Total	8	2.47389				100.0

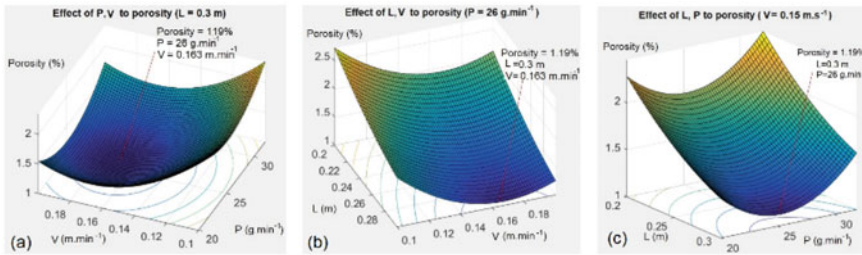


**Fig. 4** Response graphs for coating hardness. **a** Effect of V and P; **b** effect of L and V; **c** effect of L and P

spraying layer thickness increases, the larger to heap up spray particles will increase the porosity. The optimal process is determined with  $V = 0.15 \text{ m.s}^{-1}$  for minimum coating porosity (Fig. 4a, c).

The simultaneous impaction of two spraying parameters creates the range of values of the layer porosity simulated by the 3D surface on the graph of Fig. 4 based on the function (2). The above graphs allow to evaluate the influence trend of the parameters spray and select the appropriate porosity value.

### 4 Conclusion

This study optimize and determines influence of HVOF spraying parameters on the porosity of the WC-12CO coating on the inner cylinder surface of S40C steel pipes. Following conclusions can be obtained from this study:

1. Taguchi optimization method determines the optimal parameter with few experiments but high reliability. Optimal results were determined: Spray distance = 0.3 m, Powder feed rate =  $26 \text{ g.min}^{-1}$ , Surface velocity of substrate =  $0.15 \text{ m.s}^{-1}$  for the minimum coating porosity of 1.19%. Experimental validation with a porosity of 1.23% confirms the reliability of the method.
2. The influence of spraying parameters determined based on ANOVA analysis of variance showed that: Spraying distance had the greatest influence with 46.0% > Surface velocity of substrate with 39.1% > Powder feed rate with 14.2%. The determined results allow the spraying parameters to be adjusted to achieve the coating with suitable porosity.
3. The relationship function of spraying parameters to porosity determines the influence trend of spraying parameters. Porosity plots can be used to determine the range of porosity values of WC-12Co coatings by HVOF spray for the specific applications required without complicated calculations.

**Funding** The author(s) disclosed receipt of the following financial support for the research, authorship, and/or publication of this article: This work was supported by the Ministry of Education and Training, Vietnam (Grant No. B2021-SKH-02).

## References

1. Pawlowski L (2008) The science and engineering of thermal spray coatings. Wiley
2. Ilavsky J, Písacka J, Chraska P, Margandant N, Siegmann S, Wagner W, Barbezat G et al (2000) Microstructure-wear and-corrosion relationships for thermally sprayed metallic deposits. In: ITSC 2000. ASM International, pp 449–454
3. Karimi A, Verdon C, Barbezat G (1993) Microstructure and hydroabrasive wear behaviour of high velocity oxy-fuel thermally sprayed WC-Co (Cr) coatings. *Surf Coat Technol* 57(1):81–89
4. Wang LJ, Chen H, Liu Y, Gou GQ, Li D (2011) Effects of Cr on microstructure and hardness of HVOF-sprayed WC-Co coating. In: *Advanced materials research*, vol 317. Trans Tech Publications Ltd., pp 301–306
5. Schwetzke R, Kreye H (1999) Microstructure and properties of tungsten carbide coatings sprayed with various high-velocity oxygen fuel spray systems. *J Therm Spray Technol* 8(3):433–439
6. Wang Q, Xiang J, Chen G, Cheng Y, Zhao X, Zhang S (2013) Propylene flow, microstructure and performance of WC–12Co coatings using a gas-fuel HVOF spray process. *J Mater Process Technol* 213(10):1653–1660
7. JIS G-4051 (2016) Carbon steels for machine structural use. <https://kikakurui.com/g4/G4051-2016-01.html>
8. Taguchi G, Konishi S (1987) *Taguchi Methods, orthogonal arrays and linear graphs, tools for quality* American supplier institute, American Supplier Institute, Dearborn, Michigan.
9. ASTM B276-05 (2015) Standard Test Method for Apparent Porosity in Cement-ed Carbides, ASTM International, West Conshohocken, [www.astm.org](http://www.astm.org)

# Research on Effects of Welding Amperage, Velocity and Voltage on Tensile Strength of Joint Welding Metal on Narrow Gap Welding SAW



Khac-Khanh Bui, Van-Thoai Le, Thanh-Phu Nguyen, and Van-Nhat Nguyen

**Abstract** This paper presents the optimization results of automatically welding technological parameters of joint welding for narrow gap welding SAW, including: Welding amperage ( $I_h$ ), velocity ( $V_h$ ) and voltage ( $U_h$ ) to ensure the maximum weld tensile strength. After determining model, the welding is carried out according to Taguchi experimental design with L9 array together with analysis of ANOVA variance to optimize technological parameters and evaluate their effect on tensile strengths of welding metal. The results give an optimal technological parameter that improve the tensile strength and their influence. Reliability of the optimal results has been confirmed through control experiments.

**Keywords** Narrow gap welding · Tensile strength · Optimization · Experiments · Weld metal

## 1 Introduction

Automatic welding technology connected with narrow gap welding plays a very important role in welding large-dimensional parts from carbon steel and low metal. It is very necessary to study and define main technologies parameter ( $I_h$ ,  $V_h$ ,  $U_h$ ) to ensure tensile for weld metal of narrow gap. Welding productivity can be improved by increasing the fill metal yield through increasing the number of electrodes during welding or by using the addition of filler metal powder during welding [1, 2]. In addition, the application of narrow gap bonding is an effective solution in increasing productivity and quality of the weld; Narrow gap connection is applied in many different welding methods such as: TIG, MIG, MAG, SAW... [3]. Narrow gap

---

K.-K. Bui (✉) · V.-T. Le · T.-P. Nguyen · V.-N. Nguyen  
Faculty of Mechanical Engineering, Hung Yen University of Technology and Education, Hung Yen, Vietnam  
e-mail: [khanhutehy@gmail.com](mailto:khanhutehy@gmail.com)

welding technology SAW has many outstanding advantages compared to conventional SAW technology [2, 4, 5]. Therefore, it is necessary to study Effect of technological parameters on mechanical properties of the weld. Through experimental results according to Taguchi L9 method, the optimization process is performed in combination with ANOVA analysis of variance to determine the optimal set of welding parameters and their Effect on tensile strength. From there, we can determine the Effect trend of parameters on studied value domain.

## 2 Experimental Procedure

### 2.1 Testing Material and Equipment

**\*Base material:** SS400 carbon steel plate (JIS G3101–2004 Japan) [6] used to weld the experimental joints of this study with thickness  $S = 20$  mm, chemical composition and mechanical properties determined as in Table 1.

**Welding material:** AWS.17.EL12 welding wire have diameter  $d = 3.2$  mm that is used for joint welding in the study. Chemical composition and mechanical properties are suitable for SS400 steel determined in Table 2. HJ431-GB/T5293-1999 welding solder has the same chemical composition as Table 3.

**Welding equipment:** Automatic welding machine “DC Dragon 1000SAW” that welding power can reach 1000 (A).

**Table 1** Chemical composition and mechanical properties of SS400 steel (%)

Chemical composition (%)					Mechanical properties		
C	Si	Mn	Ni	Cr	Tensile strength (N/mm <sup>2</sup> )	Yield strength (N/mm <sup>2</sup> )	Elongation in 100–150 mm (%)
0.1946	0.868	0.8107	0.030	0.0276			
V	Cu	W	S	P	496	343	50
0.0025	0.0374	0.0035	0.0043	0.028			

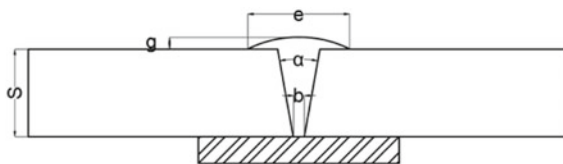
**Table 2** Chemical composition and mechanical properties of welding wire EL12 (%)

Chemical composition (%)			Mechanical properties			
C	Si	Mn	Tensile strength (N/mm <sup>2</sup> )	Yield strength (N/mm <sup>2</sup> )	Elongation in 100–150 mm (%)	Ak <sub>v</sub> (J) -400c (KJ/cm <sup>2</sup> )
0.04–0.14	≤ 0.1	0.25–0.60				
Cu	P	S	≥ 450	≥ 360	1 ≥ 29	2 ≥ 80
≤ 0.35	≤ 0.03	≤ 0.03				



**Table 3** Chemical composition of welding solder HJ431

SiO <sub>2</sub>	Ai <sub>2</sub> O <sub>3</sub> + MnO	CaO + MgO	CaF <sub>2</sub>	FeO	S	P
40-44	35-42	7-14	3-7	≤1.8	≤0.06	≤0.08

**Fig. 1** Welding joint next to narrow gap**Fig. 2** Welding joint for testing sample

## 2.2 Welding Joint

In the welding joint of narrow gap, the chamfer angle of selected in the range of  $1^{\circ}$ – $3^{\circ}$  [7, 8], the width of weld groove depends on thickness of welding material and tip. SS400 steel plate has dimensions of  $20 \times 140 \times 300$  mm and is chamfered on one side with a chamfer angle of  $2^{\circ}$ . To evaluate penetration of the weld, a  $20 \times 140 \times 300$  mm steel plate from SS400 [2, 9] is used to make the bottom lining. Weld clearance  $b = 12$  mm at the bottom of the connection (Fig. 1). The connection is mounted on the bottom plate, the weld size parameters are calculated according to the theory (weld width  $e = 22$  mm, weld height  $g = 2.0$  mm) and cleaned and guaranteed not have rust before welding (Fig. 2).

## 2.3 Conduct Experimental Welding

Technological parameters selected during the survey include:  $I_h$  (450, 500, 550) (A);  $V_h$  (16, 18, 20) (cm.min<sup>-1</sup>);  $U_h$  (30, 32, 34) (V) [4, 7]. The number of welding layers is calculated to perform in the experiment with  $n = 3$  (layers).

**Table 4** Welding parameters of samples

Test	Denominator	$I_h$ (A)	$V_h$ (cm/ph)	$U_h$ (V)	Welding layers no.
1	1	450	16	30	3
2	2	450	18	32	3
3	3	450	20	34	3
4	4	500	16	32	3
5	5	500	18	34	3
6	6	500	20	30	3
7	7	550	16	34	3
8	8	550	18	30	3
9	9	550	20	32	3

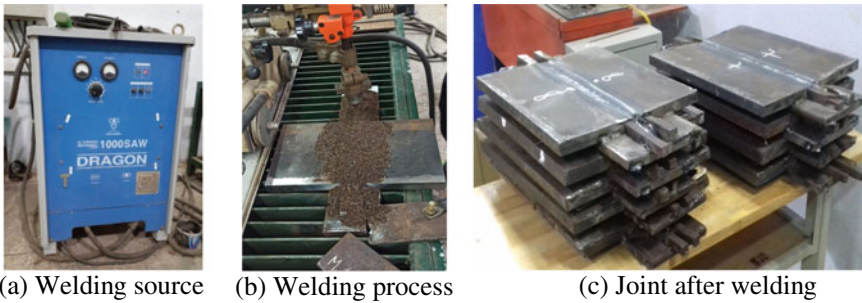


**Fig. 3** Sample welding test

The experimental process is conducted based on the value levels of welding parameters ( $I_h$ ,  $V_h$ ,  $U_h$ ). These parameters consist of 3 levels and are arranged according to Taguchi’s L9 orthogonal array as shown in Table 4 [8].

The welding process is carried out on the equipment (Fig. 3a) and took place as shown in Fig. 3b. After being welded, the welding sample is cleaned to cool in the air as shown in Fig. 3c.

### 3 Results and Discussion

#### 3.1 Weld Metal Tensile Test

The joint after welding is processed for tensile test pieces with dimensions as shown in Fig. 4 [9]. After being machined and cut (Fig. 5), the samples are tested for tensile strength on a Super L device. 120/TO.

**Fig. 4** Drawing of tensile test

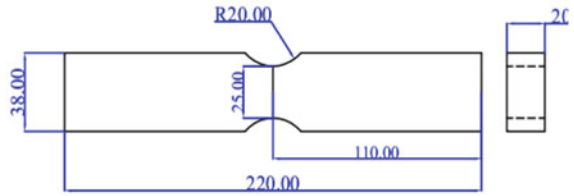


**Fig. 5** Tensile test of welding joint metal



After conducting to check the respective samples, sum up the pulling results and the S/N ratio. S/N values with larger quality characteristics are better calculated and presented in Table 5.

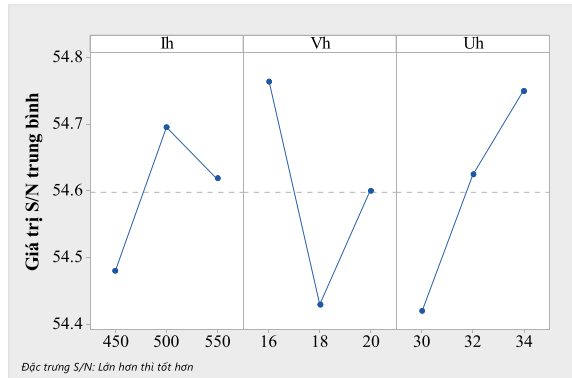
**Table 5** Tensile strength measurement results and corresponding S/N ratio

STT	I <sub>h</sub> (A)	V <sub>h</sub> (cm.min <sup>-1</sup> )	U <sub>h</sub> (V)	σ <sub>b</sub> (Mpa)	S/N
1	450	16	30	526	54.4197
2	450	18	32	518	54.2866
3	450	20	34	535	54.5671
4	500	16	32	558	54.9327
5	500	18	34	542	54.6800
6	500	20	30	534	54.5508
7	550	16	34	555	54.8859
8	550	18	30	525	54.4032
9	550	20	32	545	54.7279

**Table 6** Analysis of effect of  $I_h$ ,  $V_h$ ,  $U_h$  parameters on strength of welding joint

Level	Welding parameters		
	A	B	C
1	54.38	54.73	54.49
2	54.77	54.51	54.61
3	54.65	54.56	54.7
Effectuated no.	1	2	3

**Fig. 6** Optimal scale chart of parameters on tensile strength of welding joint



### 3.2 Optimizing Information Mode Welding on Welding Tensile Strength

The average Effect of welding parameters on tensile strength is based on the S/N ratios of experimental results. Results of determination and classification of the effect of parameters on tensile strength are presented in Table 6 and illustrated in detail on the chart in Fig. 6.

Based on classification chart of the factors, we find that: With the requirement of higher quality characteristics, the better, the appropriate level of the elements to have the maximum tensile strength is  $I_{h2} = 500$  (A),  $V_{h1} = 16$  (cm.min<sup>-1</sup>),  $U_{h3} = 34$  (V). The optimum tensile value predicted by the Taguchi method is 559.9 Mpa.

### 3.3 Determine the Effect Ratio of Technological Parameters on the Tensile Strength of the Weld

To determine the Effect of each welding parameter, ANOVA analysis is used to evaluate. The results of ANOVA analysis presented in (Table 7) show that studied welding parameters are main parameters because of their large effect of 27–38.9% while the Effect of the error is small with 1.4%. Welding current ( $I_h$ ) has the greatest

**Table 7** ANOVA analysis results of samples in tensile strength testing

Parameters	Degree of freedom	Sum of squares	Average squared	Value P	Affection level (%)
$I_h$	2	580.22	290.11	0.034	38.9
$V_h$	2	486.89	243.44	0.04	32.7
$U_h$	2	402.89	201.44	0.048	27.0
Error	2	20.22	10.11	–	1.4
Total	8	1490.22	–	–	100

effect with 38.9%; followed by welding speed ( $V_h$ ) (32.7%) and welding voltage ( $U_h$ ) with 27%. The P-index of the parameters with high confidence (95.2% 96.6%) proves reliability of analysis results and affected parameters are studied with values reaching the highest accuracy and reliability.

## 4 Experimental Verification

Experimentally verify the welding parameters with the level of  $I_{h2} = 500$  (A),  $V_{h1} = 16$  (cm.min<sup>-1</sup>),  $U_{h3} = 34$  (V) and conduct a tensile test for 557.5 Mpa. The above results are completely consistent with the tensile strength value predicted by the Taguchi method (result error is 0.43%), In addition to the tensile test, the control sample is also tested for impact toughness and durability. resulting hardness: impact toughness results in 114.6 (J/cm<sup>2</sup>); hardness gives the result 151.5 (HV), which proves the reliability of the calculation result.

## 5 Conclusion

This study optimize and define Effect of welding parameters on the tesible strength of base metal S/N in automatic welding with narrow gap. Following conclusions can be obtained from this study:

- From optimal results, values of technological parameters to ensure the maximum weld tensile strength are defined as follows: Current strength  $I_{h2} = 500$  (A); Welding speed  $V_{h1} = 16$  (cm.min<sup>-1</sup>); Welding voltage  $U_{h3} = 34$  (V).
- Defining the Effect of technological parameters on tensile strength of welding joint as follows: The effect of current ( $I_h$ ) is: ( $I_h$ ) 38.9%; Welding speed ( $V_h$ ) 32.7%; ( $V_h$ ) 32.7%; Welding voltage ( $U_h$ ) is 27%; error 1.4%.
- Results of tensile strength verification test are consistent with results predicted by the Taguchi method (error of 0.43%). It proves that the optimal result is accurate with a high reliability.

## References

1. Layus P, Kah P, Martikainen J, Gezha VV, Bishokov RV (2014) Multi-wire SAW of 640 MPa arctic shipbuilding steel plates. *Int J Adv Manuf Technol* 2014(75):771–782. <https://doi.org/10.1007/s00170-014-6147-2>
2. Thomas PD (1986) Automatic submerged arc welding with metal power additions to increase productivity and maintain quality. Newport news Shipbuiding 4101 Washington avenue Newport news, va 23607
3. Loehberg R, Pellkofer D, Schmidt J (1986) Advantages and successful use of TIG narrow-gap welding. In: International conference on welding in nuclear engineering, 63–68
4. Yohei ABE, Takahiro FUJIMOTO, Mitsuyoshi NAKATANI, Masaya SHIGETA, Manabu TANAKA (2020) Development of a welding condition optimization program for narrow gap SAW. *Proc Japan Welding Assoc* 38(2):98–102
5. International Welding Engineer (IWE).
6. <https://zh.scribd.com/doc/219973528/Jis-g3101-Ss-400-Steel>.
7. Ngo Le Thong (2004) Electric fusion welding technology. Column I, II. Science and Technology Publisher, Hanoi
8. Taguchi G, Chowdhury S, Wu Y (2005) Taguchi's quality engineering handbook. Wiley, Hoboken, NJ
9. Nguyen, Duc, Thang (2009) Welding quality insurance. Science and Technology Publisher, Hanoi

# Study the Design Automation of Two-Plate Plastic Injection Molds



Truong Duc Phuc and Pham Vu Hung

**Abstract** In this paper, the authors present the design automation of three-dimensional (3-D) models of moldbase for two-plate plastic injection molds. Design automation of moldbase is an important stage in the mold design process, because it helps to reduce errors and time spent on tedious, repetitive modeling tasks. VBA programming language was used to build an automation tool for quickly designing of a moldbase with various input geometrical parameters. The input geometrical parameters of the moldbase can be customized by the user or defined according to the moldbase supplier's catalogues. The VBA design automation tool was implemented in Catia software and Microsoft Excel in order to rapidly create moldbase for two-plate injection mold design. The results show that the various moldbase can be rapidly created using the tool developed in this study. This demonstrates that the tool can be further developed for design automation of subsequent stages in the mold design process as well as enormous potential application in designing products in plenty of other areas.

**Keywords** Design automation · Parametric design · Injection molding · VBA

## 1 Introduction

The development of computer aided design (CAD) from 2-D design to 3-D design and Virtual Reality (VR) has led to the appearance of various rapid, effective, and high-productivity design tools, which inevitably require programming technique and other

---

T. D. Phuc (✉) · P. V. Hung  
School of Mechanical Engineering, Hanoi University of Science and Technology, No.1 Dai Co  
Viet Road, Hai Ba Trung, Hanoi, Vietnam  
e-mail: [phuc.truongduc@hust.edu.vn](mailto:phuc.truongduc@hust.edu.vn)

P. V. Hung  
e-mail: [hung.PV212639M@sis.hust.edu.vn](mailto:hung.PV212639M@sis.hust.edu.vn)

automatic design tools. Recently, automatic designing tool for a wide variety of gears has been created [1–5]. These tools are based on parameterization design principle, in which the tools can be incorporated with engineers' knowledge, experience in order to quickly generate the design products and components. The parametric design and design automation is play an important role in the engineering design process. This is because it does not only help to reduce errors and time spent on tedious, repetitive designing and modeling tasks, but it can also be scaled to streamline downstream development processes.

Injection molds play a key role in manufacturing components by molding and non-cutting shaping technology, as well as has a wide application in many industries in both military and civil sectors such as automotive, telecommunication, smart devices, electric equipment [6–10]. Injection mold design process is normally time consuming process. This is because every product has its own shape and structure which requires a specific mold design to form that product. Since, the product is normally different from other products. Therefore, the molds to form every product are different from each other. This requires people to design each mold for each product correspondingly. However, the mold design process is normally conducted manually by engineers. Particularly, mold design process nowadays is often implemented manually in 3D CAD design software like Catia, NX, Creo, etc. [11, 12]. The process starts with parting surface definition, then a moldbase will be called out (from available libraries in the softwares) and inserted with the part already separated by the parting surface to make boolean operations for core and cavity creation. After that, engineers will create other systems of the mold manually like ejector system, runner system, cooling system, sliders, etc. The disadvantages using the integrated moldbase provided from the 3D CAD design software is due to the fact that the designer difficult to customize the dimension or input parameters of the moldbase components. Instead, the designers have to select the predefined moldbase provided by the software. This sometimes cause the moldbase is not suitable or to big for the mold to form a product. In addition, the predefined moldbase library provided by the 3D CAD design software is normally limited in types, size, or standard, etc. Therefore, creating a design automation tool which enables us to automatically and rapidly create customizable moldbase according to any standard is highly demand. In order to address this problem, this research focuses on method to create design automation of moldbase incorporated with cooling system, runner systems, and other mold components to make the mold design process more effective and productive. In this paper, the authors present method to create design automation of moldbase for two-plate injection molds.



## 2 Design Automation Process

### 2.1 Methodology

Figure 1 shows the general process of designing a plastic injection mold proposed in this study. The process consists of the following main steps: (1) study product requirement; (2) Product design; (3) Determine number of cavities; (4) Define mold type; (5) Design mold layout; (6) Create moldbase and split core and cavity; (7) Design runner system; (8) Design cooling system; (9) Design ejection system; (10) Calculate mold strength; (11) Molding CAE simulation; (12) Design air venting system; (13) Design guiding and positioning system; (14) Mold material selection; (15) Technical drawing creation. The highlighted stages in the process are supposed to be utilized design automation in this study.

The design automation of the moldbase studied in this paper is utilized for two-plate injection mold. Figure 2 shows the flow chart to design a mold using the moldbase which is created by using the design automation tool developed in this paper.

In order to create design automation tool of moldbase by the method proposed in this paper. First of all, all necessary input parameters are defined in an Excel file. This file can consist of user defined parameters for a moldbase or consist the predefined parameters of moldbases standard of some moldbase suppliers in the market such as FUTABA, DME, Hasco, etc. The design automation tool is developed to create any moldbase for two-plate injection mold with arbitrary valid input parameters. However, for demonstration, in this paper, FUTABA moldbase type was chosen to be created using the developed tool in this paper (Fig. 3).

There is a total of 6 types of two-plate-type moldbase provided by FUTABA supplier with the standardized parameters are described in the Table 1. These input parameters are assigned value according to the moldbase part number as described in the Excel file as in the Fig. 4.

### 2.2 VBA Programming

To make it more convenient for designers to choose parameters available in the catalog, which is displayed in Excel, a VBA program will be written in the same software, functioning as a button for opening Catia and creating components and products automatically. VBA (Visual Basic for Applications) is a programming language hosted in applications such as CATIA, Microsoft Word, Excel, etc. VBA provides a complete programming environment with an editor, debugger, and help object reviewer. Declaring the object library used is allowed. In CATIA, VBA has the full Visual Basic syntax and IDE, which is like VBA in Excel. It is event-driven, GUI-oriented, and has full IDE yet cannot run a program without the host application running. Its advantages are using the GUI, building forms, and the debugging ability

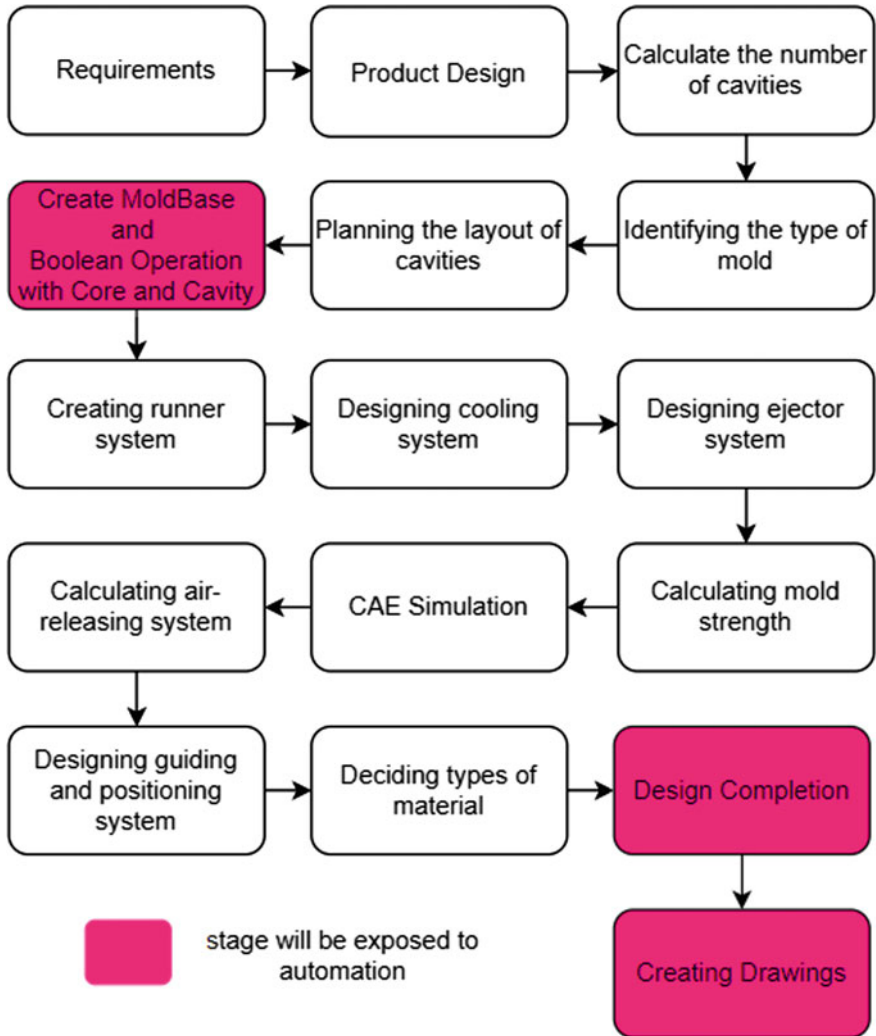


Fig. 1 General process of injection mold designing process

of the macro editor, while the disadvantage of it is that VBA programs cannot be compiled into executables or DLLs and they do not run in their own memory space. The extension is **.catvba**. [13].

Figure 5a shows the flow chart to create VBA for the design automation tool to generate a MoldBase automatically. First of all, a parametric mold of moldbase is created in Catia. Then an excel form is created to assign the value for the parameters in the parametric model of the moldbase. Then a VBA program is created to create the moldbase with the parameters matched with parameters in the Excel form. This process is repeated until the creating moldbase meets the requirements.

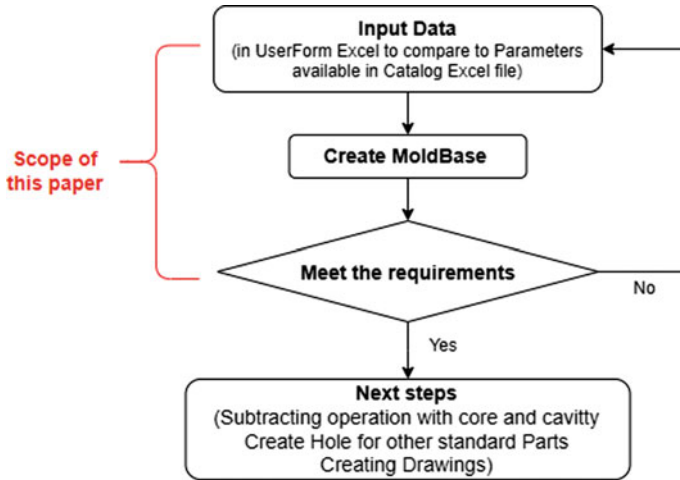


Fig. 2 Flow chart to design a mold using moldbase

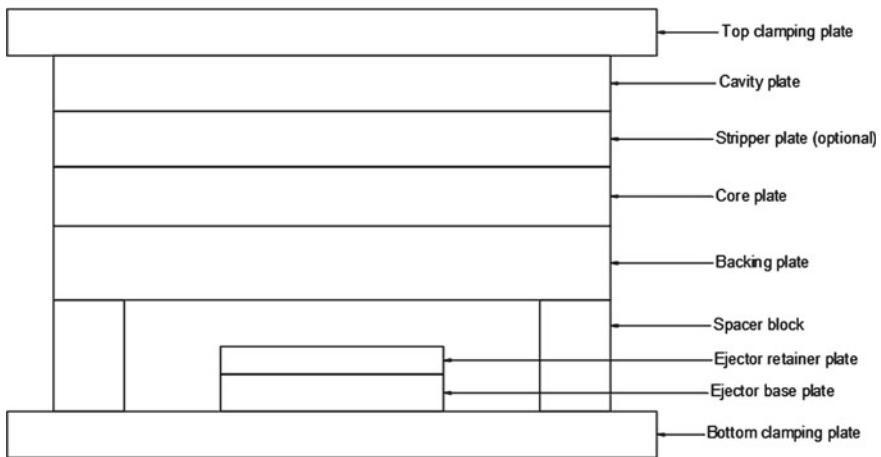


Fig. 3 Structure of a moldbase for two-plate injection mold

To be able to work with Catia from Excel without unexpected problems, the environment setting for the VBA program is shown as in the Fig. 5b.

Each reference is a type library (.tlb) found in CATIA “bin” directory, which are necessary for exposing functions to Windows by acting as maps pointing to the function inside of the dll files that make CATIA V5 work.

Firstly, a piece of code is written to call Catia environment from Excel no matter whether Catia is open already or not.

**Table 1** List of input parameters

Denotes	Description
Mold W	The width of moldbase
Mold L	The length of moldbase
TCP_h	The height of top clamping plate
BCP_h	The height of bottom clamping plate
C_w	The width of spacer block
EF_w	The width of ejector plates
EJA_h	The height of ejector retainer plate
EJB_h	The height of ejector base plate
AP_h	The height of cavity plate
BP_h	The height of core plate
CP_h	The height of spacer block
T_w	The width of top clamping plate
U_h	The height of supporting plate
S_h	The height of stripper plate

PartNumber	mold_w (mm)	mold_l (mm)	TCP_h (mm)	BCP_h (mm)	C_w (mm)	EF_w (mm)	EJA_h (mm)	EJB_h (mm)	S_h (mm)
1515	150	150	20	20	28	90	13	15	15
1518	150	180	20	20	28	90	13	15	15
1520	150	200	20	20	28	90	13	15	15
1523	150	230	20	20	28	90	13	15	15
1525	150	250	20	20	28	90	13	15	15

**Fig. 4** Some input parameters for FUTABA moldbase catalogue

```

'Get CATIA or Launch it if necessary
Dim CATIA As Object

On Error Resume Next
Set CATIA = GetObject(, "CATIA.Application")

If CATIA Is Nothing Then
    Set CATIA = CreateObject("CATIA.Application")
    CATIA.Visible = True
End If
On Error GoTo 0
    
```

To cover all the available parameters in the catalog, a UserForm is designed along with the corresponding codes as shown in Fig. 6.

After choosing the proper type of mold base as well as other parameters in the UserForm, the click “CREATE MOLDBASE” button to assign all the values to the parameter of the 3-D model needing to be called as shown in the Fig. 7. It will be opened if it is not called in the Catia environment yet and it will be updated its parameter if it is called already. As a result, the 3D model of moldbase will be automatically created rapidly.

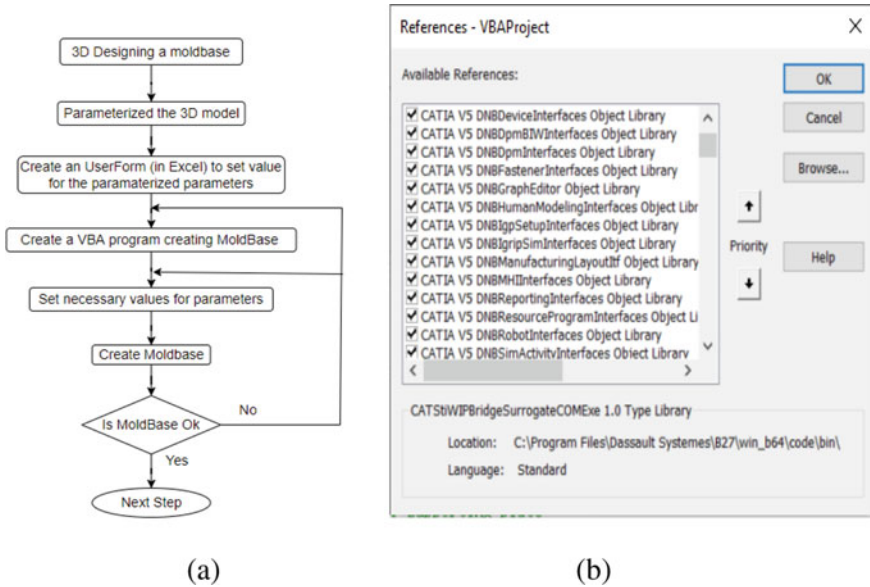


Fig. 5 a Flow chart to create moldbase automatically, b setting environment in CATIA for VBA program running

### 3 Results and Discussions

Application of design automation tool developed in this study, any type of moldbase for two plate injection mold can be created rapidly. As demonstration 4 set of FUTABA moldbases with various geometrical parameters are tested to create using the tool developed in this paper. Set 1 is SA-type Moldbase; Set 2 is SB-and-SE-type Moldbase; Set 3 is SC-type Moldbase; and Set 4 is SD-and-SF-type Moldbase. The four set of moldbase with the input parameters and information are as in the Table 2.

The result of the moldbases created by the design automation tool developed in this paper are shown as in Fig. 8.

The design automation is effective to automatically create moldbase for two-plate injection mold rapidly. This tool helps the mold designer save a lot of time during the mold design process. In addition, it also enhance the accuracy of the designing process. The design automation tool for subsequence systems in the injection mold are under research process and will be represented in near future.

CHƯƠNG TRÌNH TẠO MOLDBASE - FUTABA-5

INPUT Parameters

Type:

Mold\_w (The width of mold):

Mold\_l (The length of mold):

AP\_h (The height of cavity):

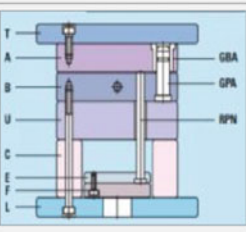
BP\_h (The height of core):

CP\_h (The height of rising bar):

TW (The width of top clamping plate):

U\_h (The height of supporting plate):

NEXT



The value of TW:

The value of U\_h:

CREATE MOLDBASE

Fix Parameters

INDEX:

TOP\_h (The height of Top plate):

BOP\_h (The height of Bottom Plate):

C\_w (Dimension X of riser bar):

EF\_w (Dimension X of 2 ejecting plates):

EAA\_h (The height of keeping plate):

EEL\_h (The height of ejecting plate):

S\_h (The height of stripper plate):

CANCEL

```

Private Sub MoldLengthComboBox_Change ()
    f = f + 1

    If e >= 1 Then
        Select Case MoldWidthComboBox.Value
            Case Is = 150
                If MoldLengthComboBox.Value < 150 Or MoldLengthComboBox.Value > 300 Then
                    MsgBox "There is no value in standard"
                    MoldLengthComboBox.Value = ""
                End If
            Case Is = 180
                If MoldLengthComboBox.Value < 180 Or MoldLengthComboBox.Value > 350 Then
                    MsgBox "There is no value in standard"
                    MoldLengthComboBox.Value = ""
                End If
            Case Is = 200
                If MoldLengthComboBox.Value < 200 Or MoldLengthComboBox.Value > 450 Then
                    MsgBox "There is no value in standard"
                    MoldLengthComboBox.Value = ""
                End If
            Case Is = 230
                If MoldLengthComboBox.Value < 230 Or MoldLengthComboBox.Value > 400 Then
                    MsgBox "There is no value in standard"
                    MoldLengthComboBox.Value = ""
                End If
            Case Is = 250
                If MoldLengthComboBox.Value < 250 Or MoldLengthComboBox.Value > 500 Then
                    MsgBox "There is no value in standard"
                    MoldLengthComboBox.Value = ""
                End If
            Case Is = 270
                If MoldLengthComboBox.Value < 300 Or MoldLengthComboBox.Value > 500 Then
                    MsgBox "There is no value in standard"
                    MoldLengthComboBox.Value = ""
                End If
            Case Is = 290
                If MoldLengthComboBox.Value < 300 Or MoldLengthComboBox.Value > 400 Then
                    MsgBox "There is no value in standard"
                    MoldLengthComboBox.Value = ""
                End If
            Case Is = 300
                If MoldLengthComboBox.Value < 300 Or MoldLengthComboBox.Value > 600 Then
                    MsgBox "There is no value in standard"
                End If
        End Select
    End If

```

Fig. 6 User form and code to define input parameters for the moldbase

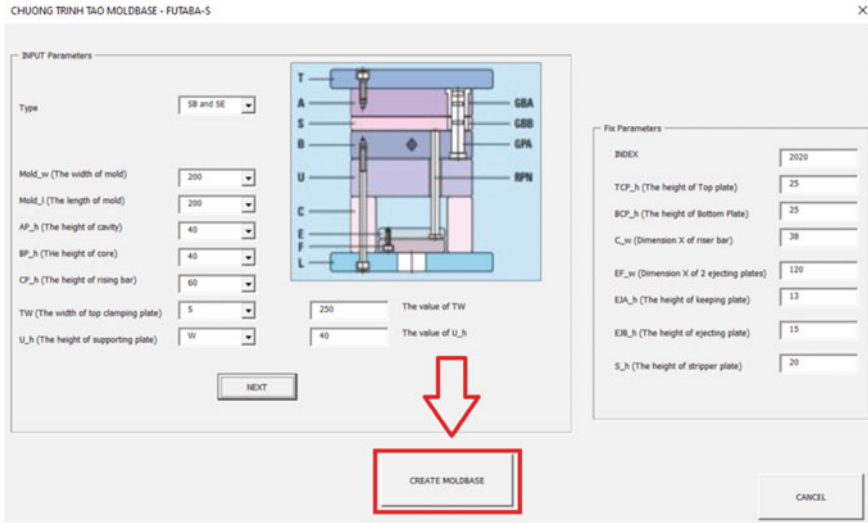
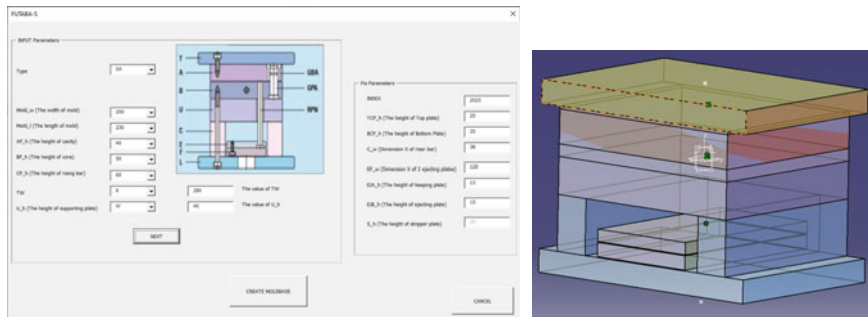


Fig. 7 Input parameters for creating of the moldbase

Table 2 Input parameters for the various moldbase types (unit is mm)

Input parameters	Mold_W	Mold_L	AP_h	BP_h	CP_h	TW	U_h
Set 1	200	230	40	50	60	280	40
Set 2	500	500	60	80	70	600	80
Set 3	400	450	90	90	90	550	50
Set 4	330	350	100	108	80	400	60



(a) Moldbase Set 1, (SA-type, Mold\_w=200, Mold\_l=200, AP\_h=40, BP\_h=50, CP\_h=60, TW=280, U\_h=40)

Fig. 8 Moldbases created automatically by developed VBA program

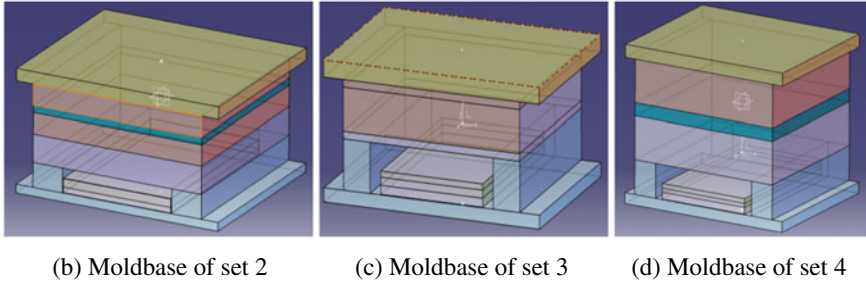


Fig. 8 (continued)

## 4 Conclusion

In this paper, the authors have successfully developed a design automation tool to automatically creation of 3D models of moldbase for two-plate plastic injection molds by using VBA programming in Catia software and Microsoft Excel software. This tool enables the designers to create any type of moldbases for two-plate injection mold in which input geometrical parameters of the moldbase can be customized by the user or defined according to the moldbase supplier's catalogues. The results show that various moldbase types can be quickly generated using the tool developed in this study. This demonstrates that the tool can be further developed for design automation of subsequent stages in the mold design process as well as other product design process.

## References

1. Ai-Qin L, Kai H (2004) 3D parametric modeling of spiral bevel gears under Pro/E. *J Liaoning Instit of Tech* 24(5)
2. Drecun VM, Dean TA (1991) A parametric CAD program for die sets for precision forging spur gears. *Int J Mach Tools Manufact* 31(2):183–191
3. Phuc TD (2016) Parametric design of 3-D models for shifted spur gears. In: *Proceedings of National Conference on Mechanical & Transportation Engineering, Vol 2*, pp 491–496, 13th October. HUST (Hanoi University of Science and Technology), Hanoi, Vietnam, ISBN: 978-604-95-0041-1
4. Phuc TD (2017) Automated designs of shifted spiral bevel gears with parameterized three dimensional. In: *Proceeding of National Conference on Mechanical & Transportation Engineering*. ISBN 978-604-73-5602-7, pp 84–92
5. Phuc TD (2018) Study on the parameterized three-dimensional models of different shifted helical gear pairs. In: *International Conference of Fluid Machinery and Automation Systems—ICFMAS2018*. Hanoi, 27–28 October, ISBN: 978-604-95-0609-3, pp 614–621
6. Mohammad Reza Khosravani & Sara Nasiri (2020) Injection molding manufacturing process: review of case-based reasoning applications. *J Intell Manuf* 31:847–864
7. Kale PD, Darade PD, Sahu AR (2021) A literature review on injection moulding process based on runner system and process variables. In: *IOP Conference Series: Materials Science and Engineering* 1017, 012031



8. Phúc TD, Kiên HT, Phúc PH (2021) Nghiên cứu tối ưu hóa thông số đúc phun vỏ thiết bị máy tính bảng. Kỳ yếu Hội nghị Khoa học toàn quốc Cơ học Vật rắn lần thứ XV 2021, 769–768, ISBN 978-604-9987-74-8
9. Kamal MR, Isayev A, Liu SJ (2009) Injection molding: technology and fundamentals. Hanser Publications
10. Phuc TD, Dung AN (2022) Study optimization of process parameters in overmolding of multi plastic materials. In: Le AT, Pham VS, Le MQ, Pham HL (eds) The AUN/SEED-Net Joint Regional Conference in Transportation, Energy, and Mechanical Manufacturing Engineering. RCTEMME 2021. Lecture Notes in Mechanical Engineering. Springer, Singapore. [https://doi.org/10.1007/978-981-19-1968-8\\_59](https://doi.org/10.1007/978-981-19-1968-8_59)
11. <https://www.plm.automation.siemens.com/global/en/products/nx/>
12. <https://www.3ds.com/products-services/catia/>
13. Ross E, VB scripting for CATIA V5, 4th edn

# Study Effects of Cutting Parameters on Surface Quality in High Speed Milling of CuZn40Pb1 Brass Alloy



Truong Duc Phuc, Pham Hong Phuc, Nguyen Thanh Trung,  
Hoang Tien Dung, and Hoang Trung Kien

**Abstract** In this paper, the authors developed a 4 axis high precision milling machine and using the machine to study the effect of cutting parameters on the surface roughness during high speed milling of CuZn40Pb1 brass alloy material. During machining process, the cutting forces and spindle vibration were measured to investigate the cutting forces and vibration for all the cutting conditions. Moreover, an equation of surface roughness as a function of spindle speed, feed rate, and depth of cut was established based on linear regression with least squares method. It is found that the regression equation of surface roughness shows good accuracy and agrees well with the experimental results. Moreover, the validation experiments were also conducted to evaluate the accuracy of the regression mathematical function of surface roughness. It is found that the maximum errors of the surface between validation experiments and the regression function is less than 15% which is relative small and acceptable.

---

T. D. Phuc (✉) · P. H. Phuc · N. T. Trung  
School of Mechanical Engineering, Hanoi University of Science and Technology (HUST), No.1  
Dai Co Viet Road, Hai Ba Trung, Hanoi, Vietnam  
e-mail: [phuc.truongduc@hust.edu.vn](mailto:phuc.truongduc@hust.edu.vn)

P. H. Phuc  
e-mail: [phuc.phamhong@hust.edu.vn](mailto:phuc.phamhong@hust.edu.vn)

N. T. Trung  
e-mail: [trung.nguyenthanh2@hust.edu.vn](mailto:trung.nguyenthanh2@hust.edu.vn)

H. T. Dung  
Department of Mechanical Engineering, Hanoi University of Industry (HaUI), No.298 Cau Dien  
Road, Bac Tu Liem, Hanoi, Vietnam  
e-mail: [tiendung@hau.edu.vn](mailto:tiendung@hau.edu.vn)

H. T. Kien  
Department of Mechanical Engineering, Le Quy Don Technical University, No.236 Hoang Quoc  
Viet Road, Bac Tu Liem, Hanoi, Vietnam  
e-mail: [kienht@lqdtu.edu.vn](mailto:kienht@lqdtu.edu.vn)

**Keywords** High speed milling · Surface roughness · Regression equation · Cutting force · Spindle vibration

## 1 Introduction

Brass alloys are widely used for valves, pipes, connectors and fittings in water and/or hydraulics systems because of their outstanding corrosion resistance [1, 2]. Machinability of brass alloys will be improved if they are added with several different elements during the material processing. Lead is one of the most well known alloying element for improving machinability of brass alloys. Normally, lead is added to traditional brasses alloys at levels of 2–5% mass in order to enhance their machinability [3–6]. However, adding of lead element to these brass alloys causes severe hazard not only to the environment and but also to the human health [7, 8]. Therefore, it is desirable to reduce the percentage of lead element in brass alloys. Unfortunately, lower content of lead element causes brass alloys more difficult to machine.

On the other hand, machining is one of the most popular processes using for manufacturing parts made of brass alloys. More and more competition of the manufacturers in providing higher quality products produced by sustainable ways. High speed machining is important for manufacturing of mechanicals parts since it can product high quality parts effectively. Therefore, studying the machinability of brass alloys in high speed machining is highly desired in order to produce high quality parts made of these materials at effective cost and time.

There have been many reports on studying the machinability of various metal materials [9–14]. Sai et al. [9] studied on the residual stresses, microstructure, surface roughness and hardness of carbon steels and stainless steels during milling operations. It was reported that the machining surface quality is improved when cutting at high speed and low feed rate. Selvaraj et al. [10] studied the effects of cutting speed, feed rate on surface roughness of ASTM A 995 stainless steels in dry turning operation using carbide cutting tools. It is also reported that better surface roughness was achieved at high cutting speed and lower feed rate. Wang et al. [11] investigated the effects of cutting parameters and cutting tool geometry on surface roughness during end milling process of Al 2014-T6 material. They established the mathematical function of surface roughness with the input parameters for both dry and wet cutting conditions. Palanikumar [12] studied machinability of glass fiber reinforced plastics composites in turning operation. They established equation of surface roughness as a function of cutting speed, feed rate, and depth of cut. Premnath et al. [13] investigated the influences of cutting parameters in face milling operation of hybrid aluminum composites. They found that cutting speed was the major factor which affects the surface roughness. Ramesh et al. [14] investigated the effects of cutting conditions on surface roughness in turning operation of titanium alloys. It was presented that feed rate affects the most on the surface roughness. However, reports on machinability of brass alloys such as CuZn40Pb1 is limited. Therefore, in this research, the authors study the machinability of this material during high speed milling operation. The

effects of cutting parameters such as spindle speed, feed rate, and depth of cut on the surface roughness of machining surface will be presented.

## 2 Experiment Method

In this research, the authors developed a high precision and high speed milling machine in order to conduct machining experiment of various materials. Figure 1 shows the design and the real machine developed in this study. The machine has three translation axes X, Y, Z, and one rotation axis A. the stroke of the X, Y, and Z axes is 200 mm, 150 mm, and 110 mm, respectively. The rotation angle of the A axis is  $\pm 360^\circ$ . The spindle speed can be up to 20,000 RPM. The control system of the milling machine is built based on Mach3 CNC controller of Artsoft USA.

In this paper, the authors study the effect of cutting parameters on the surface roughness during high speed machining of CuZu40Pb1 brass alloy material. The chemical condition of the workpiece material was analyzed by using the Ametek spectrum materials analysis machine as shown in the Fig. 2, and the chemical compositions of the CuZu40Pb1 brass alloy material consists of approximately 55.33% copper, 40.69% zinc, 1.43% lead, 0.65% iron, tin 0.48%, nickel 0.22%, aluminum 0.92%, and some other elements with relative small percentages.

The cutting tool used in the milling experiments was solid carbide end mill tool with the diameter of 1 mm as shown in the Fig. 3, and the surface hardness of the cutting tool is HRC55.

The cutting parameters such as the spindle speed, feed rate, and depth of cut were chosen to study its effect on the surface roughness. Each cutting parameters have two levels of value which are shown in Table 1.

An L8 orthogonal array design of experiment was utilized in order to investigate the effects of spindle speed, feed rate, and depth of cut on the surface roughness. The experiment conditions are arrange as in Table 2.

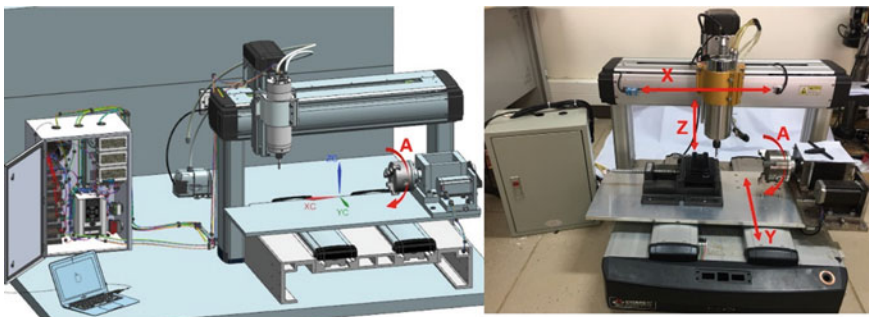


Fig. 1 The design and manufactured of 4 axis CNC milling machine

**Fig. 2** Analysis of chemical composition of the workpiece material



**Fig. 3** Carbide end mill tool using in the machining experiments



**Table 1** Cutting parameters using for experiments

Cutting parameters	Level 1	Level 2
Spindle speed ( <i>S</i> ) (rpm)	11,000	13,000
Feed rate ( <i>f</i> ) (mm/min)	100	200
Depth of cut ( <i>t</i> ) (mm)	0.1	0.3

**Table 2** Design of experiment for machining

Run	Spindle speed ( <i>S</i> ) (rpm)	Feed rate ( <i>f</i> ) (mm/min)	Depth of cut ( <i>t</i> ) (mm)
1	13,000	100	0.1
2	11,000	200	0.3
3	13,000	200	0.3
4	11,000	200	0.1
5	11,000	100	0.3
6	13,000	200	0.1
7	13,000	100	0.3
8	11,000	100	0.1

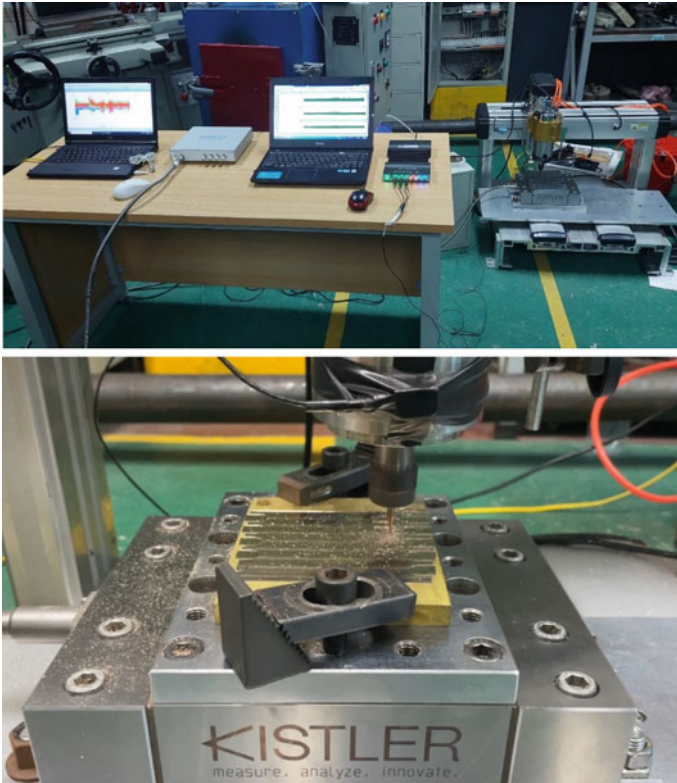


**Fig. 4** Milling machine and machining experiment setups

The cutting forces during milling were measured by using Kistler 9139AA dynamometer, and the spindle vibration was measured by using a Bruel and Kjaer triaxial accelerometer type 4524-B-001. The surface roughness of the machining surface was measured by using Mitutoyo SJ-301 portable surface roughness tester. Figure 4 shows the setup of milling machine and measurement system for cutting experiments.

### 3 Results and Discussions

#### 3.1 Machining Results

For each run of experiment of cutting, the cutting forces and the vibration of the spindle are measured. Figure 5 shows the result of cutting forces and vibration of the spindle in the form of acceleration in  $x$ ,  $y$ , and  $z$  direction when cutting with parameters

as spindle speed  $S = 11,000$  rpm, feed rate  $f = 100$  mm/min, and depth of cut  $t = 0.1$  mm. It is found that the cutting forces are relative small. The maximum cutting forces in  $x$  and  $y$  direction are about 10 N, while the maximum cutting force in  $z$  direction is about 5–6 N. It is also found that the vibration of the spindle is relative small. The maximum accelerates of the spindle vibration are about  $3 \text{ m/s}^2$  in  $x$  and  $y$  direction, while the maximum accelerate of the spindle vibration in  $z$  direction is about  $1.3 \text{ m/s}^2$ . From the measurement analysis software (Bruel and Kjaer—PULSE Labshop version 17.0.0), it is determined that the frequency of the vibration of the spindle is about 500 Hz. Therefore, the displacement of vibration of the spindle can be calculated based on the vibration theory [15, 16]. The calculation results show that the maximum displacement of the spindle vibration are about  $0.3 \text{ }\mu\text{m}$  in  $x$  and  $y$  direction, while the maximum displacement of the spindle vibration in  $z$  direction is about  $0.13 \text{ }\mu\text{m}$ . Similarly, for other run of experiments, the cutting forces and the vibration of the spindle can be measured with the same procedures.

For each run of experiment of cutting, the surface roughness of machining surface is measured by using a portable surface roughness tester (Mitutoyo SJ-301). Figure 6 shows the surface roughness measurement device and the measurement result of surface roughness of the machining surface when cutting with parameters as spindle speed  $S = 11,000$  rpm, feed rate  $f = 100$  mm/min, and depth of cut  $t = 0.1$  mm. In this paper, the average surface roughness  $R_a$  is selected as output analysis parameter. It is found that the surface roughness of the machining surface is  $R_a = 0.3 \text{ }\mu\text{m}$ . Similarly, for other run of experiments, the surface roughness of the machining surface were measured and recorded by the same procedures. The surface roughness measured for each run of experiments are summarized in Table 3.

### 3.2 Regression of Surface Roughness Function with Input Cutting Parameters

Response surface methodology (RSM) is a combination of statistical and mathematical methods that are useful to establish a mathematical function to express the relationship between the input process parameters and the output response [17]. From experimental results, it is important to establish the relationship between surface roughness of machining surface and the cutting parameters. Since, knowing of this relationship helps to predict the output surface roughness of a machining surface with a specific cutting conditions. This is very helpful in selection of suitable cutting parameters. The regression function of surface roughness can be expressed as in Eq. 1.

$$Ra = C.S^m.f^n.t^q \quad (1)$$

where,

$R_a$ : is surface roughness of machining surface ( $\mu\text{m}$ ).

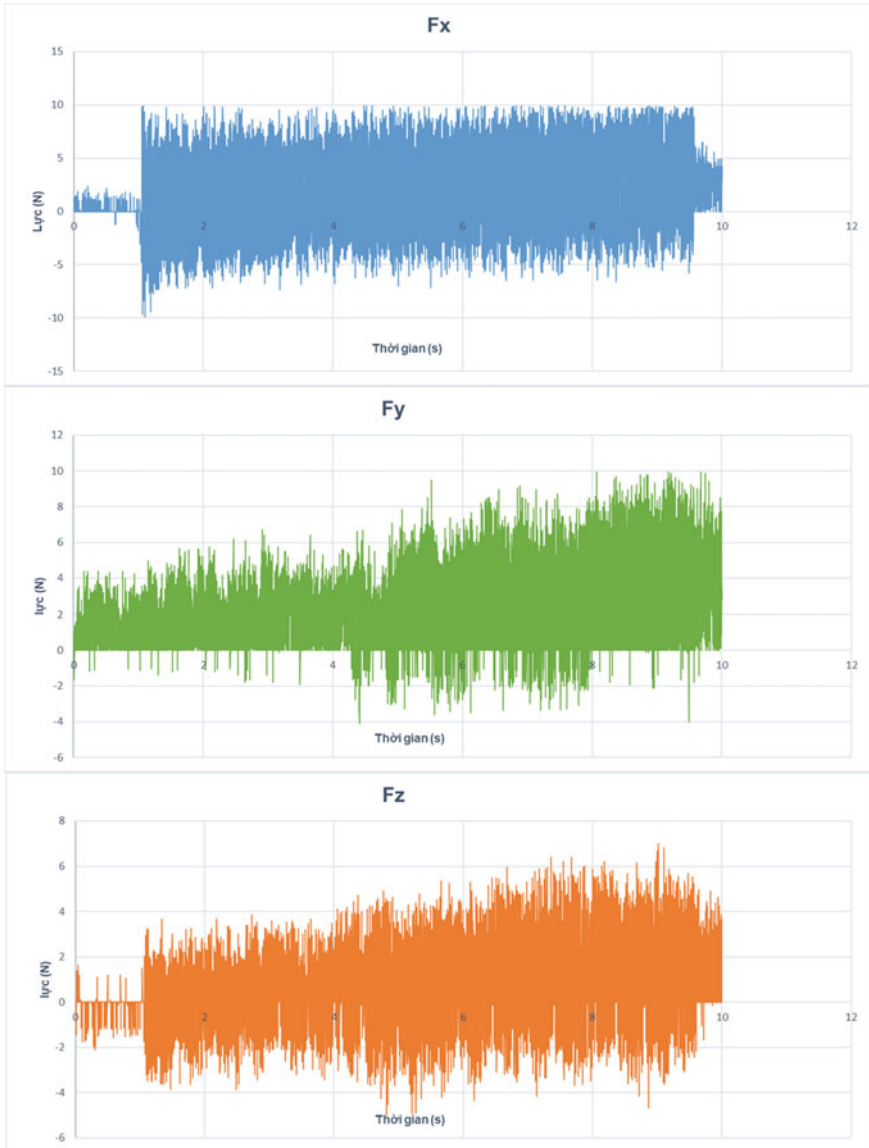


**Fig. 5** Cutting forces and vibration of spindle during cutting ( $S = 11,000$  rpm,  $f = 100$  mm/min,  $t = 0.1$  mm)



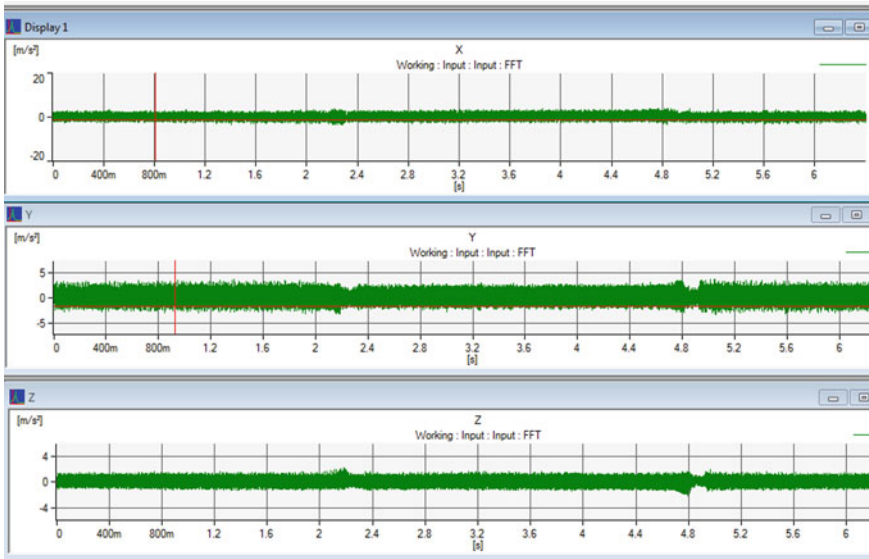
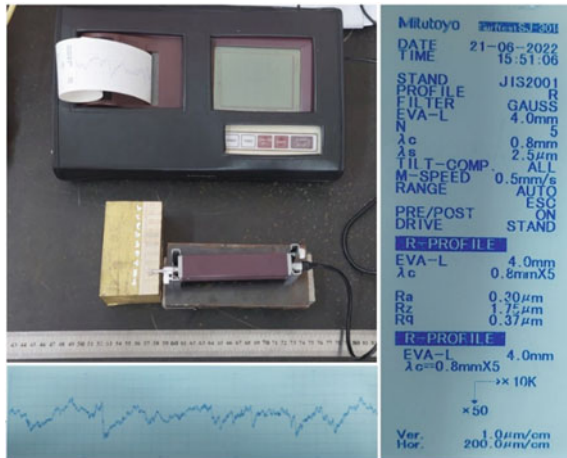


Fig. 5 (continued)

Fig. 6 Measurement of surface roughness of machining surface after cutting ( $S = 11,000$  rpm,  $f = 100$  mm/min,  $t = 0.1$  mm)



- $S$ : is spindle speed (rpm).
- $f$ : is feed rate (mm/min.)
- $t$ : is depth of cut (mm).
- $C$ : is a constant.
- $m, n, q$ : are the are exponents.

In order to determine constants and exponents, the Eq. (1) was linearized by performing a logarithmic transformation as follows:

**Table 3** Experimental surface roughness of machining surface

Run	Spindle speed (rpm)	Feed rate (mm/min)	Depth of cut (mm)	Surface roughness (μm)
	<i>S</i>	<i>f</i>	<i>t</i>	<i>Ra</i>
1	13,000	100	0.1	0.29
2	11,000	200	0.3	0.53
3	13,000	200	0.3	0.56
4	11,000	200	0.1	0.54
5	11,000	100	0.3	0.58
6	13,000	200	0.1	0.44
7	13,000	100	0.3	0.33
8	11,000	100	0.1	0.3

$$\ln Ra = \ln C + m \ln S + n \ln f + q \ln t \tag{2}$$

The constants and exponents *C*, *m*, *n*, and *q* are determined by the method of least squares. From Eq. (2), by using least squares method, the first order linear equation is expressed as follows:

$$Y = b_0 + b_1.X_1 + b_2.X_2 + b_3.X_3 \tag{3}$$

By using least squares method, the natural logarithm of variables and constants in Eq. (3) and Table 3 are calculated as in Table 4 as follows:

By using matrix expression form, the Eq. (3) can be rewritten in the matrix form as follows:

$$X \times b = Y \tag{4}$$

where,

**Table 4** Natural logarithm value calculated for variables in Eq. (3)

Run	<i>X1 (S)</i>	<i>X2 (f)</i>	<i>X3 (t)</i>	<i>Y (Ra)</i>
1	9.472704636	4.605170186	-2.302585093	-1.237874356
2	9.305650552	5.298317367	-1.203972804	-0.634878272
3	9.472704636	5.298317367	-1.203972804	-0.579818495
4	9.305650552	5.298317367	-2.302585093	-0.616186139
5	9.305650552	4.605170186	-1.203972804	-0.544727175
6	9.472704636	5.298317367	-2.302585093	-0.820980552
7	9.472704636	4.605170186	-1.203972804	-1.108662625
8	9.305650552	4.605170186	-2.302585093	-1.203972804

$$X = \begin{pmatrix} 1 & 9.472704636 & 4.605170186 & -2.302585093 \\ 1 & 9.305650552 & 5.298317367 & 1.203972804 \\ 1 & 9.472704636 & 5.298317367 & -1.203972804 \\ 1 & 9.305650552 & 5.298317367 & -2.302585093 \\ 1 & 9.305650552 & 4.605170186 & -1.203972804 \\ 1 & 9.472704636 & 5.298317367 & -2.302585093 \\ 1 & 9.472704636 & 4.605170186 & -1.203972804 \\ 1 & 9.305650552 & 4.605170186 & -2.302585093 \end{pmatrix}$$

$$Y = \begin{pmatrix} -1, 237874356 \\ -0, 634878272 \\ -0, 579818495 \\ -0, 616186139 \\ -0, 544727175 \\ -0, 820980552 \\ -1, 108662625 \\ -1, 203972804 \end{pmatrix} \text{ and } \mathbf{b} = \begin{pmatrix} b_0 \\ b_1 \\ b_2 \\ b_3 \end{pmatrix}.$$

Solving Eq. (4) is as follows:

$$X^T \times X \times \mathbf{b} = X^T \times Y \quad (5)$$

Or

$$F \times \mathbf{b} = X^T \times Y \quad (6)$$

where,

$$F = X^T \times X \quad (7)$$

$X^T$  is the transform matrix of  $X$ .

If matrix  $F$  is inversable, the Eq. (6) can be rewritten as follows:

$$\mathbf{b} = F^{-1} \times X^T \times Y \quad (8)$$

where,

$$\mathbf{X}^T = \begin{pmatrix} 1 & 1 & 1 & 1 \\ 9.472705 & 9.472705 & 9.305651 & 9.305651 \\ 4.60517 & 5.298317 & 4.60517 & 5.298317 \\ -2.30259 & -1.20397 & -1.20397 & -1.20397 \\ 1 & 1 & 1 & 1 \\ 9.305651 & 9.472705 & 9.472704636 & 9.305650552 \\ 5.298317 & 5.298317 & 4.605170186 & 4.605170186 \\ -2.30259 & -2.30259 & -1.203972804 & -2.302585093 \end{pmatrix}$$

$$\mathbf{F} = \mathbf{X}^T \times \mathbf{X} = \begin{pmatrix} 8 & 75.11342 & 39.61395 & -14.0262 \\ 75.11342 & 705.3091 & 371.9424 & -131.695 \\ 39.61395 & 371.9424 & 197.119 & -69.4543 \\ -14.0262 & -131.695 & -69.4543 & 27.00579 \end{pmatrix}$$

Since the determinant of matrix  $\mathbf{F}$  is  $\det(\mathbf{F}) \neq 0$ , Therefore,  $\mathbf{F}$  is inversable, and the inverse of matrix  $\mathbf{F}$  is calculated as follows:

$$\mathbf{F}^{-1} = \begin{pmatrix} 1606.384 & -168.222 & -5.1532 & 0.726327 \\ -168.222 & 17.91661 & 1.25E - 12 & -1.3E - 13 \\ -5.1532 & 2.14E - 12 & 1.040684 & 2.28E - 15 \\ 0.726327 & -2.4E - 13 & 7.46E - 16 & 0.414268 \end{pmatrix}$$

By substitution the above values into Eq. (8), we achieve:

$$\mathbf{b} = \mathbf{F}^{-1} \times \mathbf{X}^T \times \mathbf{Y} = \begin{pmatrix} 7.48634198 \\ -1.118756895 \\ 0.520586948 \\ 0.230046417 \end{pmatrix}$$

Therefore, the Eq. (2) can be written as follows:

$$\ln Ra = 7.486364198 - 1.118756895 \ln S + 0.520586948 \ln f + 0.230046417 \ln t \tag{9}$$

Finally, we achieve the surface roughness function is as follows:

$$Ra = 1782.906185 \times S^{-1.118756895} \times f^{0.520586948} \times t^{0.230046417} \tag{10}$$

Recalculating the value surface roughness by using the regression Eq. (10) and compare with the experimental data, the results are shown in Table 5.

The accuracy comparison of the surface roughness calculated from the regression (10) and the experimental data is calculated by the following equation:

**Table 5** Experimental surface roughness and the surface roughness calculated from regression equation

Run	Spindle speed (rpm)	Feed rate (mm/min)	Depth of cut(mm)	Surface roughness Ra (μm)			
				Experimental results	Calculated from Eq. (10)		
	<i>S</i>	<i>f</i>	<i>t</i>	<i>Y (Ra)</i>	$\hat{Y}$	$(\hat{Y} - \bar{Y})^2$	$(Y - \bar{Y})^2$
1	13,000	100	0.1	0.29	0.288	0.025	0.024
2	11,000	200	0.3	0.53	0.643	0.038	0.007
3	13,000	200	0.3	0.56	0.532	0.008	0.013
4	11,000	200	0.1	0.54	0.498	0.003	0.009
5	11,000	100	0.3	0.58	0.447	1.3E-6	0.018
6	13,000	200	0.1	0.44	0.414	0.001	3.9E-5
7	13,000	100	0.3	0.33	0.371	0.006	0.014
8	11,000	100	0.1	0.3	0.348	0.009	0.021
				$\bar{Y} = 0.446$			
Sum						0.0899	0.105

$$R^2 = \frac{\sum_{i=1}^8 (\hat{Y} - \bar{Y})^2}{\sum_{i=1}^8 (Y - \bar{Y})^2} = \frac{0.0899}{0.105} = 0.856 \tag{11}$$

It is found that  $R^2 = 0.856$  which is approximately reach to 1. Therefore, the regression model is accurated.

### 3.3 Validating of the Regression Equation of Surface Roughness

Since the regression equation of surface roughness is established as Eq. (10). For different cutting conditions, it is possible to predict the output surface roughness of the machining surface. In this section, the validating experiments are conducted to compare the experimental surface roughness with the calculated one from the regression equation. The cutting conditions for the validating experiments are shown in the Table 6.

It is found from Table 6 that the calculated surface roughness from the regression equation agrees well with the experimental results. The maximum error between the calculated surface roughness and the experimental results is less than 15% which is acceptable for the regression mathematical model.

**Table 6** Design of experiments for validating machining experiments

Run	Spindle speed (rpm)	Feed rate (mm/min)	Depth of cut (mm)	Surface roughness Ra ( $\mu\text{m}$ )		Errors(%)
				Experimental results	Calculated from Eq. (10)	
	$S$	$f$	$t$	$Y(Ra)$	$\hat{Y}$	
1	12,000	100	0.2	0.33	0.369739	10.75
2	12,000	150	0.3	0.44	0.501273	12.22
3	12,000	200	0.1	0.39	0.452227	13.76

## 4 Conclusion

In this paper, the authors developed a 4 axis milling machine and study the effects of cutting parameters on the surface roughness during high speed machining of CuZn40Pb1 brass alloy material. The cutting forces and vibration of the spindle during machining process were measured by using a dynamometer and a triaxial accelerometer to understand the cutting forces and vibration for all the cutting conditions. It is found that the both cutting forces and the displacement of spindle vibration are relative small. In addition, based on the experimental data, a regression mathematical model of surface roughness as a function of spindle speed, feed rate, and depth of cut was established. It is found that the regression equation of surface roughness provides good accuracy and agrees well with the experimental results. Moreover, the validation experiments were also conducted to evaluated the accuracy of the regression mathematical function of surface roughness. It is found that the maximum error of the surface between validation experiments and the regression function is less than 15% which is relative small and acceptable.

**Acknowledgements** This research was supported by the Asahi Glass Foundation under the Grant *AFG.2022-02*.

The authors express grateful thankfulness to the Vietnam-Japan International Institute for Science of Technology (VJIIST) and the School of Mechanical Engineering (SME) of Hanoi University of Science and Technology (HUST), and the Department of Mechanical Engineering of Hanoi University of Industry (HaUI), Vietnam for providing them with academic facilities and space for the research.

## References

1. Japan Capper and Brass Association (1994) Base and industrial technology of copper and copper alloys
2. Imai H et al (2010) Characteristics and machinability of lead-free P/M Cu60–Zn40 brass alloys dispersed with graphite. *Powder Technol* 198:417–421
3. Thiele EW, Kundig KJA, Murphy DE, Soloway G, Duffin B (1990) CDA's universal machinability index. SAE Technical Paper Series, No. 900365, International Congress and Exposition, Detroit, MI

4. Wu JX, Ji MR, Galeotti M, Giusti AM, Rovida G (1994) *Surf Interface Anal* 22:323–326
5. Vilarinho C et al (2005) Influence of the chemical composition on the machinability of brasses. *J Mater Process Technol* 170:441–447
6. García P, Rivera S, Palacios M, Belzunce J (2010) *Eng Fail Anal* 17:771–776
7. Kuyucak S, Sahoo M (1996) *Can Metall Q* 35(1):1–15
8. Chen X, Hu A, Li M, Mao D (2008) *J Alloys Compd* 460:478–484
9. Sai WB, Salah NB, Lebrun JL (2001) Influence of machining by finishing milling on surface characteristics. *Int J Mach Tools Manuf* 41(3):443–450
10. Selvaraj DP, Chandramohan P (2010) Influence of cutting speed, feed rate and bulk texture on the surface finish of nitrogen alloyed duplex stainless steels during dry turning. *Engineering* 2(6):453–460
11. Wang MY, Chang HY (2004) Experimental study of surface roughness in slot end milling AL2014-T6. *Int J Mach Tools Manuf* 44(1):51–57
12. Palanikumar K (2007) Modelling and analysis for surface roughness in machining glass fiber reinforced plastics using response surface methodology. *Mater Des* 28(10):2611–2618
13. Premnath AA, Alwarsamy T, Abhinav T, Krishnakant CA (2012) Surface roughness prediction by response surface methodology in milling of hybrid Aluminium composites. *Proc Eng* 38(1):745–752
14. Ramesh S, Karunamoorthy L, Palanikumar K (2012) Measurement and analysis of surface roughness in turning of aerospace titanium alloy (gr5). *Measurement* 45(5):1266–1276
15. <https://www.newport.com/t/vibration-control-unit-conversion-charts-and-constants>
16. <https://irdmech.zohodesk.com/portal/en/kb/articles/convert-vibration-amplitude>
17. Montgomery DC (2009) *Design and analysis of experiments*, 7th edn. Wiley, New York

# A Study on Integrated Flexible Manufacturing Systems



Vuong Gia Hai, Le Thi Lan, Do Thi Thu Thuy, Dinh Van Hien,  
and Hoang Van Quy

**Abstract** Nowadays, automatic workpiece feeding lines and CNC machining integrating many operations to process machine parts are used more and more widely. These systems operate with high stability, accuracy and flexibility when changing different product types. In this study, an integrated CNC machining and automatic workpiece feeder system were designed and fabricated. This is a modern system, that increases machining productivity and ensures operator safety. The design system includes a conveyor that transports the workpiece to the machining location and transports the part after the processing is complete to the container, a robotic arm that picks the workpiece from the conveyor to the CNC machining machine and picks the part after processing on the conveyor. The results of the research can be applied in production or training in programming, operating automatic workpiece feeding systems and integrated CNC machining.

**Keywords** Manufacturing · Automatic workpiece feeding system · 3-Axis CNC milling machines · Mach3 · PLC

## 1 Introduction

In the current strong development trend of science and technology, the use of automatic lines and systems to manufacture products is no longer a new thing for countries around the world. For countries with developed industries, these machining systems are invested, designed, fully equipped and extremely modern, with very precise mechanical structures, the robots in the line are very flexible. And especially, the work of controlling the line is very simple, easy, convenient for users and can easily change the program to control the operation of the line to manufacture machine

---

V. G. Hai · L. T. Lan · D. T. T. Thuy · D. Van Hien · H. Van Quy (✉)  
Hai Phong University, Hai Phong, Vietnam  
e-mail: [hoangquyctm@gmail.com](mailto:hoangquyctm@gmail.com)



parts, products other according to the actual requirements of the market. The operation process of the system is a closed continuous cycle, from the work of feeding the billet to the process of packing the product into the warehouse or bringing it to the market, which is automated.

With our Vietnam, it is a country with a developing industry, trying to learn, access and inherit the world's high technologies in CNC machine design and manufacture [1–4]. Currently, in our country, most of the new research focuses on CNC processing machines [5–8] to replace traditional machining machines. Due to low economic conditions, facilities and human qualifications, the technology of high-tech automatic production lines and CIM-integrated processing lines has not been mastered. Therefore, it is urgent to research and manufacture an automatic billet feeding system and integrated CNC machining. In this study, we will introduce the automatic workpiece feeding lines system about conveyor, robot with 2 degrees of freedom, sensor and CNC milling machine.

## **2 Design of Integrated CNC Machining and Automatic Workpiece Feeding System**

### ***2.1 System Diagram***

In the Fig. 1 shows a schematic diagram of the integrated automatic workpiece feeding system and integrated CNC machining.

The workpiece is transported on the conveyor when it encounters an object detection sensor, the robot arm will pick up the workpiece from the conveyor and put it on the table on the CNC milling machine. When the workpiece is placed on the machine table, the workpiece clamping system automatically clamps and then machining takes place. After the processing is complete, the robot will take the product from the CNC milling machine and place it on the conveyor, the conveyor will receive the order to transport the product to the container and put the next workpiece into processing.

### ***2.2 Design of Automatic Workpiece Feeding System***

In the Fig. 2 shows the structure of the automatic workpiece feeding system. When the system starts working, the conveyor motor works to bring the workpiece to move on the conveyor surface, when the workpiece moves to a position with a preset sensor, the sensor receives the signal and sends it back to the PLC and the PLC will stop the motor. Next, the workpiece picker robot arm starts to pick up the workpiece and put it into the processing machine. When the processing is complete, the system will give a signal to the PLC to control the robot arm to pick up the parts from the processing machine and put it on the conveyor. When the position is reached, the part detection

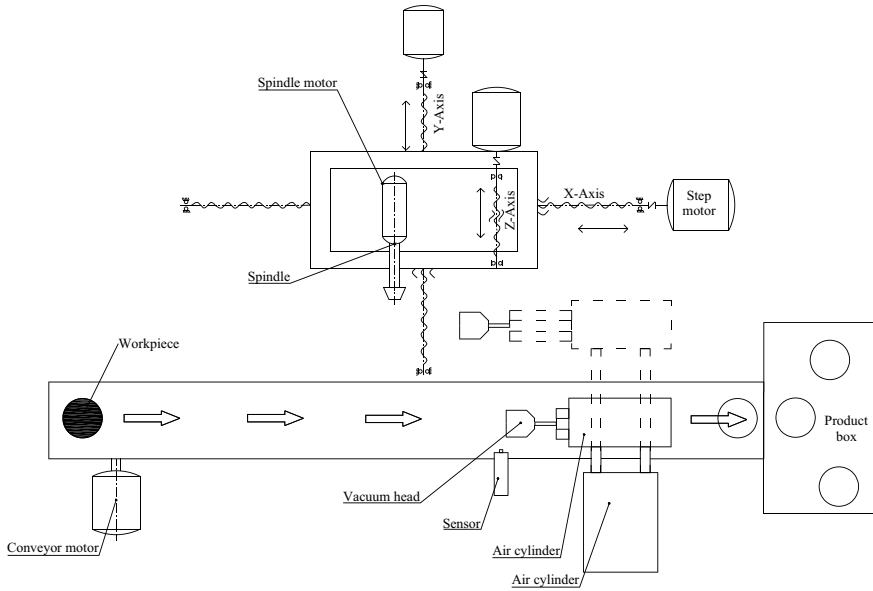


**Fig. 1** Block diagram of the integrated CNC machining and automatic bar feeding system

sensor will give a signal to the PLC and the PLC will give the opposite signal to the conveyor for the conveyor to operate, bringing the part to fall to the place where the production is stored. And then the sensor continues to detect the workpiece and send a signal to the PLC to perform the next part machining processing.

The technical parameters of the workpiece feeding system are presented in Table 1.

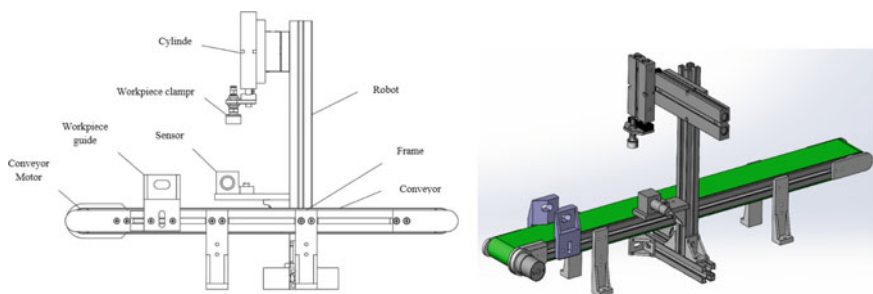


**Fig. 2** Automatic workpiece feeding system for CNC machine

**Table 1** Specifications of workpiece feeding system

Conveyor specifications		Robot specifications	
Conveyor length (mm)	800	Y-axis stroke (mm)	150
Conveyor width (mm)	70	Z-axis stroke(mm)	55
Conveyor speed max (m/ph)	1632	Lift load (kg)	10
Load capacity (kg)	5		
Motor with reducer GB37 3530 24 V	Motor power 6W, spin speed 60 rpm		

### 2.3 CNC Milling Machine Design

The structure design of a 3-axis CNC milling machine is shown in Fig. 3. The structure of the machine consists of a spindle assembly that creates cutting motion, and three assemblies of a tool axis in the X, Y and Z directions. Specifications of the milling machine CNC machine is presented in Table 2.

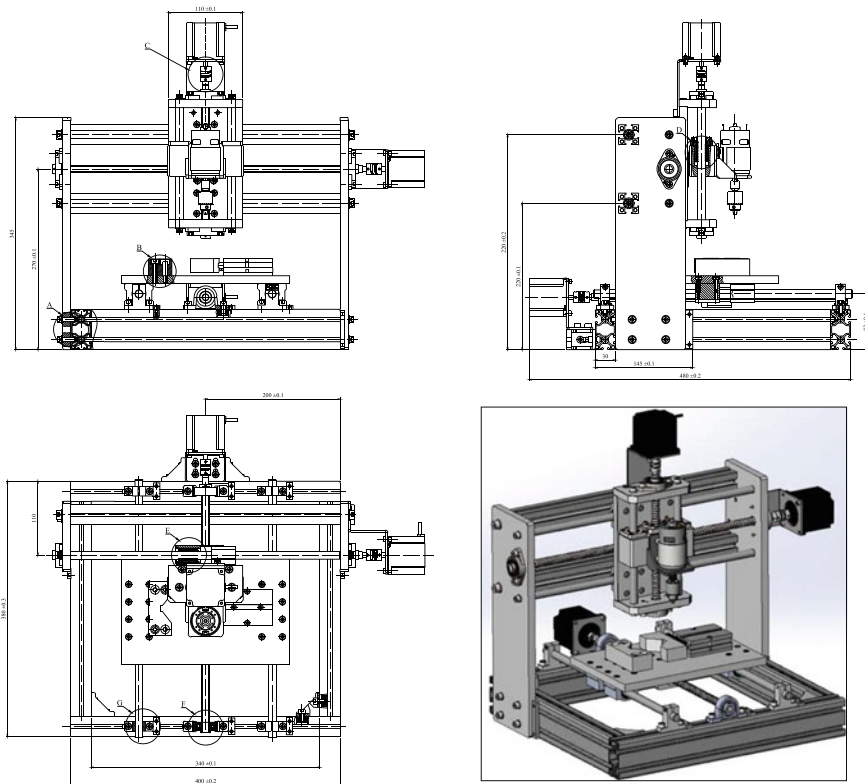


**Fig. 3** A3-axis CNC milling machine design

**Table 2** Specifications of 3 axis CNC milling machine

Table size (length × width) (mm)	250 × 150
Spindle motor power (w)	400
Spindle speed (rpm)	18,000
Stroke of each axis X/Y/Z (mm)	310/230/110
X/Y/Z motor	STEP57
Control system	Mach3
Machining accuracy (mm)	0.01–0.06

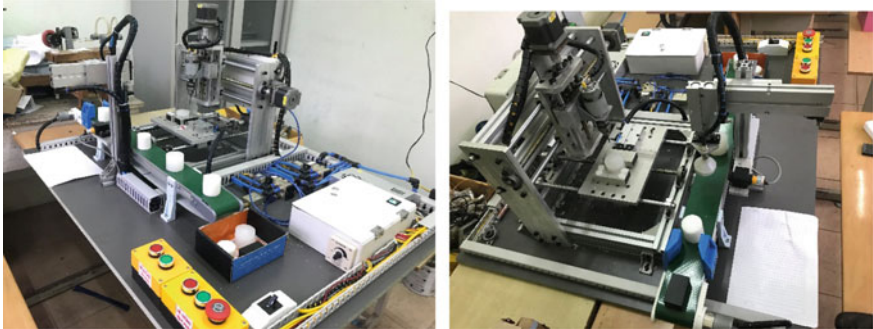


**Fig. 4** Fabrication of automatic workpiece feeding system and integrated CNC machining

### 3 Fabrication of Automatic Workpiece Feeding System and Integrated CNC Machining

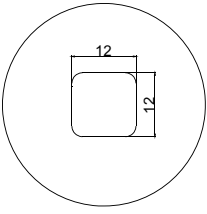
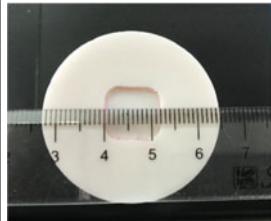
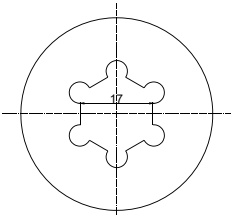
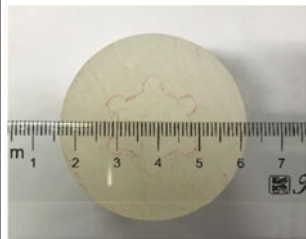
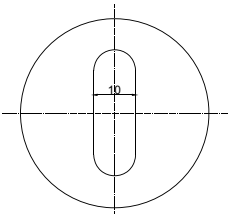
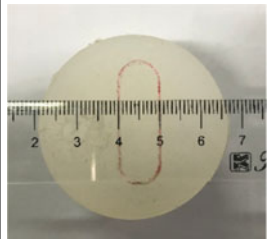
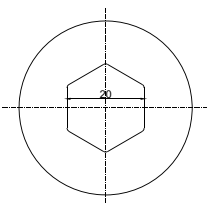
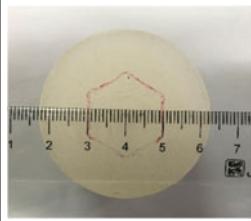
After designing and completing the structure of the automatic billet feeding system in Sects. 2.2 and 2.3, the research team carried out fabrication according to the designed drawings. The system that has been fabricated and assembled is shown in Fig. 4. The main materials for the construction of the system are aluminum and plastic.

### 4 Investigate the Reliability of the System Designed and Manufactured

After the system is fully fabricated, the research team conducts testing activities to investigate the accuracy of the fabrication system compared to the design. First of all, check the working process of the automatic workpiece feeding system, working with two types of cylindrical and rectangular workpiece made from hard plastic Fig. 4. The results show that the bar feeding system works well, in accordance with the design requirements. Next, check the operation of the 3-axis CNC machine, then check the operation of the system including the automatic workpiece feeding process,

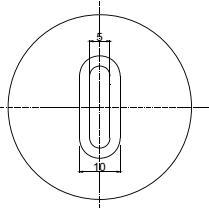
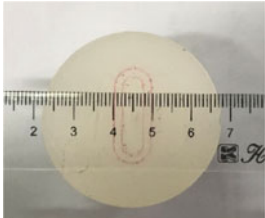
automatic machining, and after processing the product is put on the conveyor and transported to the container. The results of the experimental process that proved the reliability of the designed and fabricated system are presented in Table 3.

**Table 3** Statistical table sample of designs and experiments

Specimen	Design	Experiment
Number 1		
Number 2		
Number 3		
Number 4		

(continued)

**Table 3** (continued)

Specimen	Design	Experiment
Number 5		

## 5 Conclusion

In this study, a integrated CNC machining and automation workpiece feeding system has been designed and engineered with a well-arranged and assembled system of components. The system is quite flexible, easy to disassemble, transport and connect to the computer, easy to operate, very suitable for practice, practice integrated machining system. This system can work with parts made by aluminum, wood or mica plastic, PA. Through product inspection, we see that the system is designed and manufactured to fully meet the requirements set forth. The results of the research can be developed with many other modern machines and control systems such as bottle capping systems, packaging systems, product sorting systems, etc.

## References

1. Hidayanti N, Ambrizala B, Farooqib A, Alsultanc OI, Yusoffd B (2017) Design and development of CNC robotic machine integrate-able with Nd-Yag laser device. *Proc Eng* 184:145–155
2. Srinivasan VP, Arulvalan A, Amarnath J, Dhinesh L, Dhivyan RBF, Rizwan M, Navashanmugam A, Mowyanivesh P (2021) Design and fabrication of dual axis writing machine. *Mat Today: Proc* 45(7):6743–6749
3. Sevic MK (2019) Design of CNC milling machine as a base of industry 4.0 enterprise. *MM Sci J* 12:3555–3560
4. Shivanand HK, Benal MM, Koti V (2006) *Flexible manufacturing system*. New Age Publications
5. Dich TV (2004) *Giao trình công nghệ CNC*. NXB KHKT
6. Dao NN (2004) *CAD-CAM-CNC*. NXB DHSPKT Tp.HCM
7. Luc BQ (2006) *He thong Dieu khien so trong công nghiệp*. NXB KHKT HN
8. Trang NTT, Cuong PT, Tuan TN, Huynh ND, Huong NH (2018) Thiet ke va che tao mo hinh may CNC 3 trục. *Tap chi KHNN Viet Nam* 16(11):1005–1016

# Accuracy Evaluation of Slump and Slump-Flow Test for 3D Concrete Printing with the Kinect v1



Van-Bien Bui, Thi-Loan Pham, Duc An Pham, and Thi Thu Thuy Do

**Abstract** The primary challenge for successful 3D concrete printing is the complicated characteristics the materials should own, especially printability. The result and the slump-flow tests probably determine this parameter. Unfortunately, the traditional slump and slump-flow test methods are basically based on length and time measured by a ruler and a stopwatch then the result may reflect error caused by human. We introduce in this research an efficient method for slump and slump-flow test data receiving with Kinect v1. Our approach is based on the non-contact measurement and data processing. After capturing the dynamically changing 3D surface of concrete using a 3D device during the test, the results are processed into a point cloud. The slump flow diameter and height at any location simultaneously can be indicated from this point cloud. Finally, the experimental results show that the efficiency of the proposed method is significantly improved.

**Keywords** 3D concrete printing · Slump and slump-flow test · 3D scanning · Kinect v1 · Point cloud

## 1 Introduction

In recent years, there has been a fast-developing interest in 3D printing technology, especially in the construction industry in general and civil construction in particular [1, 2]. 3D concrete printing is defined as the continuous extrusion of cementitious materials to build objects in layer-by-layer appearance. This technique can potentially help to remove the use of the formwork, then the material's rheological properties

---

V.-B. Bui (✉) · T.-L. Pham · T. T. T. Do  
Hai Phong University, Hai Phong City, Vietnam  
e-mail: [bienbv80@dhhp.edu.vn](mailto:bienbv80@dhhp.edu.vn)

D. A. Pham  
Hanoi University of Technology and Science, Ha Noi City, Vietnam

are principally crucial for the material to be pumped and able to hold its shape after printing [3].

Pumpability and buildability are the two essential material parameters in 3D concrete printing concerning plastic viscosity and the material's yield stress. Pumpability is the ease of conveying material from storage to the nozzle. However, concrete pumping is a complex process. In addition to the time-dependent properties of the material, changes in concrete properties for pumping conditions such as stratification and water separation can make the pumpability of the material difficult to predict [4]. Meanwhile, separating water from the aggregate can also clog the pump pipe. This reality is generally caused by inadequate particle size distribution or enormous water-to-binder ratio. Therefore, in an accordingly designed mixture, there should be enough excess paste to fill the spaces between the aggregates. This paste content forms a coating that envelops the totals, which acts as a "lubricant" between the aggregates when shear stress is forced onto the mixture [5]. This lubricating layer reduces friction between the aggregates and enhances the workability of the printed material.

Buildability has been newly defined and utilized for 3D concrete printing applications [6], which is associated with the material's yield stress, the fabric, the structural formation of the material, and the shape stability of the cross-section of the layers. The static yield stress of the material causes the initial rigidity of the material. This rigidity, which concerns the material's ability to maintain its original shape after extrusion from the nozzle, is necessitated before the structural build-up of the mixture occurs. In [7], the authors showed that the structural build-up of the mixture is connected with the rate of flocculation and hydration of the binder. If the forming of the next layer is faster than the structural build-up rate of the mixture, the structure will be damaged [6]. Therefore, the balance between the structural build-up of the mixture and the printing process parameters is critical to achieving high buildability. The supplement of admixtures such as accelerators can increase the mixture's structural build-up rate [8].

There is currently no standard test method to measure or quantify pumpability and buildability for 3D concrete printing. During the research on 3D concrete printing at Hai Phong University, to evaluate the pumpability and buildability of concrete mortar, a slump flow-test method was implemented and illustrated in Fig. 1. It is the simplest and most widely used. However, this method always has a significant measurement error and depends on the operator.

With the development of technology and equipment, instead of conventional testing devices, a rheometer has been introduced to determine the working parameters of concrete [9]. For instance, it has been used to evaluate the workability of concrete, thereby monitoring the workability of high-rise buildings [10]. Recently, based on computational fluid dynamics analysis, the concrete flow has been dramatically investigated with a rheometer [11]. However, understanding concrete rheology in the construction field through which to determine pumpability and buildability is still very poor. Furthermore, with the price of a rheometer ranging from \$20,000 to \$180,000, its use in 3D concrete printing is limited by its costliness. Therefore, an



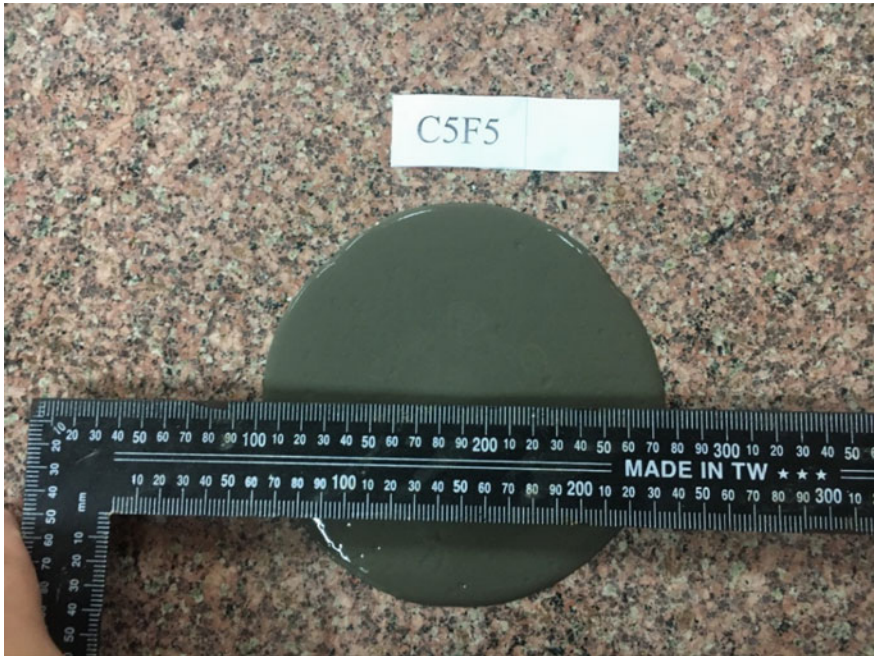


**Fig. 1** The slump-flow test at Hai Phong University

effective and low-cost measurement method in the field of 3D concrete printing and the construction field, in general, is a necessary solution.

This paper introduces a new approach to evaluating the slump and slump-flow test results using a depth sensor. Microsoft Kinect v1, a low-cost depth sensor used to determine the surface of the concrete pattern during slump and slump-flow test, is set up as shown in Fig. 2. According to the original design, Kinect v1, which uses structured light technology to collect depth data, was developed for human motion recognition in role-playing games. However, with good resolution and scanning speed, the application of Kinect v1 is being expanded to areas such as simultaneous localization and mapping [12], 3D modeling of mechanical parts [13], and construction quality monitoring [14]. In addition, visualizing spatial technology data using depth sensors is useful in numerical analysis and simulation of concrete flow during 3D printing.



**Fig. 2** Utilization of the depth sensor during the slump and slump-flow test

## 2 Methodology

### 2.1 Acquisition Data Using Kinect v1 and Skanect

Kinect v1 includes two cameras, an infrared (IR) camera, and an RGB camera. In this device, there is a laser source that emits infrared light. This laser source emits a beam of infrared light, which is then projected onto the object. The object illuminated by infrared light will be captured by the infrared camera and compared with the reference sample to obtain the depth value. Specifications of the device are shown in Table 1.

Skanect, developed by ManCTL, was used to collect the data. This software allows the user to combine the Kinect v1 device into a 3D scanner that can operate up to 30 fps. With a set of predefined scenarios, Skanect makes it easy to 3D scan objects suitable for most use cases. With this software, users can export standard 3D files

**Table 1** The specifications of Kinect v1 [15]

Parameters	Value
RGB camera resolution (pixels)	640 × 480
Infrared camera resolution (pixels)	320 × 240
Framerate (Hz)	Up to 30
RGB camera field of view (degrees)	60 × 50
Infrared camera field of view (degrees)	57 × 43
Range of operation (m)	From 0.4 to 4



**Fig. 3** Acquisition data framework

such as .obj, .ply, and .stl, and automatically correct 3D models of objects, simplify complex geometrical components and perform precise editing.

A data collection process through Kinect v1 and Skanect is shown in Fig. 3. First, in the Prepare step, the operator needs to set up parameters such as scanning object, working area, and aspect ratio to determine the reasonable working process in the following steps. After clicking the “Start” button, the Record step will automatically run to start the scanning process. Before writing data, the operator can change the delay time and the working time. After setting the time options, click the “Record” button on the top left of the screen to perform the data collection. After obtaining enough 3D data on Skanect, the operator will create the complete point cloud of the scanned object using the “Fusion” function in the Reconstruct step. Next, the outliers are removed in the Process step, and the complete 3D model will be completed using the “Mesh” function. Finally, in the Share step, the finished 3D model will be saved and retrieved as a file for other applications.

## 2.2 Data Processing by Geomagic Design X

After data collection, the next step is to process the data to determine the resulting values of the slump and slump-flow test. Because the Skanect does not directly measure, Geomagic Design X is used as an additional solution for processing material slump and slump-flow test data.

The output data of the data collection process can be retrieved in many types. However, the point cloud is the most accurate data collection type, as this type is representative of the actual points to be determined. Use the Mesh Buildup Wizard tool to import data into Geomagic Design X, as shown in Fig. 4. This tool has four stages of implementation: Data Preparation, Noise Reduction, Data Editing, and Data Merging. In some cases, not all stages are carried out. In this paper, data preparation and data editing are performed.

After importing data into Geomagic Design X, some tools will be used to define parameter values of the slump and slump-flow test. First, the Measure tool will determine the dimension and angle. Then, to evaluate the shape and change of the concrete surface during slump testing, the point cloud of the CAD model obtained from 3D scanning with Kinect v1 will be processed by the Alignment tool before determining the measurement parameters in this experiment.

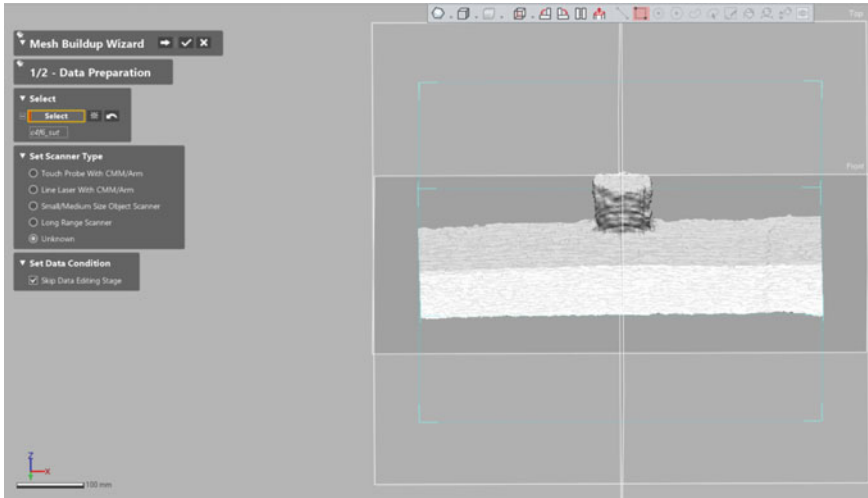


Fig. 4 Geomagic Design X interface

### 3 Results and Discussion

#### 3.1 Experimental Setup

The experiment aims to test the method of evaluating the results of the slump and slump-flow test used in 3D concrete printing. The experiment results will be assessed through two factors: the specimen’s shape and the value of the parameters determined after the experiment.

The experimental process to determine the slump and slump-flow test results using Kinect v1, Skanect, and Geomagic Design X software installed on a computer with configuration as follows: Intel(R) Xeon(R) CPU E3-1505 M v5 @ 2.80 GHz 2.81 GHz; RAM 32 GB; Quadro M1000M. The Kinect v1 is mounted on a tripod, which makes it easy to move around the specimen.

The experiment was conducted with 03 samples mixed using PC40 cement by Chinfon, fly ash by Hai Phong thermal power plant, sand with a nominal maximum aggregate size of 2.5 mm, water, and superplasticizer Sika Visconcrete 3000 M. The mixture proportion is shown in Table 2.

Table 2 The mixture ratio

	Cement (g)	Fly ash (g)	Sand (g)	Water (g)	SP (g)
Mix01	500	500	800	300	4
Mix02	500	500	800	250	6
Mix03	568	568	800	250	8

### 3.2 Result Validation

After obtaining all 15 point clouds of 03 mixtures, each mixture with 03 times for slump-flow test and 02 times for slump test, the point clouds are retrieved as PLY files from Skanect. First, the slump-flow test data is processed using the Measure tool in Geomagic Design X. The slump-flow results are represented by the diameter and are illustrated in Fig. 5. The results of the 03 times slump-flow test are shown in Table 3.

For the slump test, the results are expressed through three parameters, the slump height,  $h_s$ , the height of the biggest cross-section,  $h_b$ , and the diameter of the cross-section  $\Phi_b$ . Before determining the slump results, the point cloud is transformed using the Alignment tool. Then, like the slump-flow test, the dimensions are measured with the Measure tool in Geomagic Design X. The results are presented in Table 4.

Thus, compared with the conventional method of determining slump and slump-flow test results in the construction field, the measurement method using Kinect v1 gives more accurate and detailed results. This is because the parameters in each test

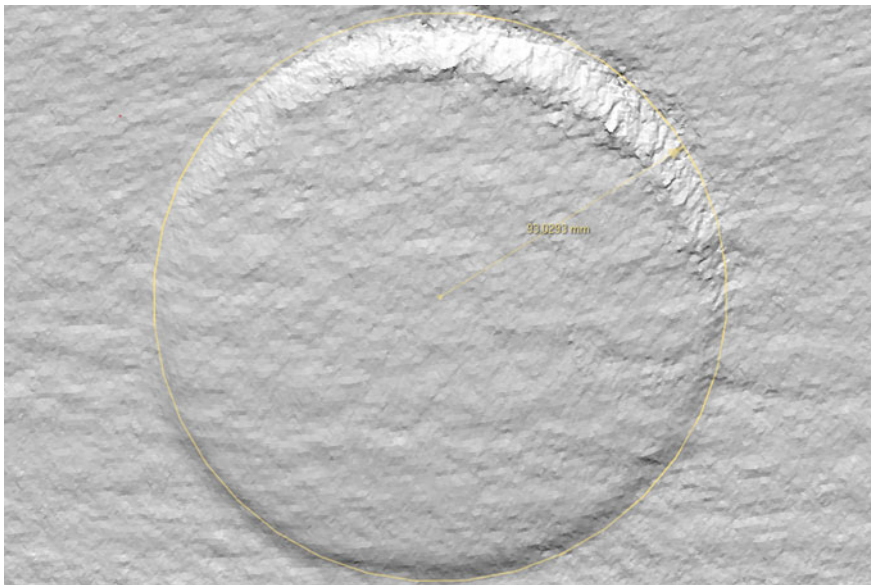


**Fig. 5** The second slump-flow result of Mix02

**Table 3** The slump-flow result

Runs	1 (mm)	2 (mm)	3 (mm)
Mix01	174	152	148
Mix02	206	186	164
Mix03	212	172	166

**Table 4** The slump result

Runs	1			2		
	$h_s$ (mm)	$h_b$ (mm)	$\Phi_b$ (mm)	$h_s$ (mm)	$h_b$ (mm)	$\Phi_b$ (mm)
Mix01	6	14	85	5	12	81
Mix02	15	13	91	17	15	93
Mix03	5	18	85	3	14	85

are accurately determined through direct measurement of the CAD model created by the 3D scanning process. Furthermore, the slump test results determined by the conventional method did not determine the height of the biggest cross-section and the diameter of the cross-section.

## 4 Conclusion

Compared with the traditional method, this study has shown the advantages of evaluating the slump and slump-flow test results by the Kinect v1 device. With the low cost of the Kinect v1 device and Skanect, it is an alternative to expensive 3D scanners for applications that are suitable with mm accuracy. As outlined above, the 3D model obtained during scanning can be further analyzed and measured using other applications. The 3D model of the specimen in the slump and slump-flow test by Kinect v1 and related analysis data can be used to optimize the mixtures used in the 3D concrete printing. In the future study, the 3D model scanned with Kinect v1 will be compared with 3D data scanned with more expensive and precise equipment to assess the accuracy of this method.

## References


1. Daniel TYW, Panda B, Paul SC, Mohamed NAN, Tan MJ, Leong KF (2017) 3D printing trends in building and construction industry: a review. *Virtual Phys Proto* 12:261–276
2. Avinash N, Aditya SD, Adarsh RN, Nandan M, Dharek MS, Sreedhara BM, Prashant SC, Sreekechava KS (2020) Additive Manufacturing of Concrete: Challenges and opportunities. *IOP Conf Series: Mat Sci Eng* 814:12–22
3. Nicolas R (2018) Rheological requirements for printable concretes. *Cem Concr Res* 112:76–85
4. Dimitri F, Khayat KH, Perez-Schell A, Khatib R (2015) Prediction of pumping pressure by means of new tribometer for highly-workable concrete. *Cement Concr Compos* 57:102–115
5. Ghasemi Y, Emborg M, Cwirzen A (2019) Effect of water film thickness on the flow in conventional mortars and concrete. *Mater Struct* 52(62):1–15
6. Perrot A, Rangeard D, Pierre A (2016) Structural built-up of cement-based materials used for 3D-printing extrusion techniques. *Mater Struct* 49:1213–1220
7. Roussel N, Ovarlez G, Garraut S, Brumaud C (2012) The origins of thixotropy of fresh cement pastes. *Cem Concr Res* 42:148–157

8. Delphine M, Kawashima S, Bessaies-Bey H, Mantellato S, Ng S (2018) Hydration and rheology control of concrete for digital fabrication: potential admixtures and cement chemistry. *Cem Concr Res* 112:96–110
9. Eric PK, Fowler DW, Ferraris CF, Amziane S (2006) A new, portable rheometer for fresh self-consolidating concrete. Am Concrete Institute, ACI Special Publication, 97–115
10. Nehdi Moncef L (2013) Only tall things cast shadows: Opportunities, challenges and research needs of self-consolidating concrete in super-tall buildings. *Constr Build Mater* 48:80–90. <https://doi.org/10.1016/j.conbuildmat.2013.06.051>
11. Jinglong G, Fourie A (2015) Spread is better: An investigation of the mini-slump test. *Miner Eng* 71:120–132
12. Kourosh K, Elberink SO (2012) Accuracy and resolution of kinect depth data for indoor mapping applications. *Sensors* 12:1437–1454
13. Bui V-B, Banh T-L, Nguyen D-T (2019) Improving the depth accuracy and assessment of Microsoft Kinect v2 towards a usage for mechanical part modeling. *PJ Korean Soc Precis Eng* 36:691–697
14. Qi X, Licht D, El-Badry M, Chow J, Ang K (2014) Vertical dynamic deflection measurement in concrete beams with the Microsoft Kinect. *Sensors (Switzerland)* 14:3293–3307
15. Tölgyessy M, Dekan M, Chovanec L, Hubinský P (2021) Evaluation of the azure kinect and its comparison to kinect v1 and kinect v2. *Sensors(Switzerland)* 21:1–25. <https://doi.org/10.3390/s21020413>



# Comparative Analysis of Simulated and Experimental Results for SUS-304 Sheet Material in Incremental Sheet Metal Forming Process



Nguyen Duc Toan  and Hoang Trung Kien

**Abstract** In this study, the Incremental Sheet Metal Forming (ISMF) simulation was conducted using Abaqus 6.13 software for SUS 304 sheet material at elevated temperature. The Taguchi experimental method was applied to investigate the impact of three technological parameters, namely part temperature (T) ranging from 100 to 400 °C, the step in the z direction of the tool (z) ranging from 0.2 to 0.5 mm, and tool diameter (D) ranging from 6 to 12 mm, on the forming angle. A regression equation was developed to predict the forming angle based on these input parameters. The results showed that temperature (T) had a significant effect on the forming angle, whereas the influence of tool diameter (D) was the least significant. The simulation predicted the largest forming angle to be 76.08°.

**Keywords** ISMF · SUS 304 · Taguchi experimental method · FEM · The forming angle

## 1 Introduction

The Incremental Sheet Metal Forming (ISMF) technology is a significant advancement in moldless forming. It consists of a sheet metal, clamping part, lower support part, and forming tool [1]. The workpiece is secured in a fixed support frame and the forming tool moves according to a pre-determined geometry, which is controlled by a central CNC machine. This method of machining does not require a mold and the

---

N. D. Toan (✉) · H. T. Kien

School of Mechanical Engineering, Hanoi University of Science and Technology, 1A-Dai Co Viet Street, Hai Ba Trung District, Hanoi City 100000, Vietnam

e-mail: [toan.nguyenduc@hust.edu.vn](mailto:toan.nguyenduc@hust.edu.vn)

H. T. Kien

Faculty of Mechanical Engineering, Thainguyen University of Technology, Thainguyen 100000, Vietnam



**Table 1** Chemical compositions of SUS-304

Elements	C	N	Mn	Cr	P	S	Mo	Ni
wt%	0.05	0.05	1.8	18.3	<0.03	<0.001	0.3	<8.1

material deforms under the force applied by the tool. The toolpaths are programmed into the computer and executed in layers.

ISMF is suitable for single or small-batch production [2]. The parameters of the machining technology can be selected and imported from CAD software to CAM software [3]. The influence of technological parameters on the final shape of the part can be studied through simulations or experiments [4]. Research has shown that the diameter of the tool and the down step have a significant impact on the forming mode of the part at room temperature, while elevated temperature plays a key role in shaping the part at high temperatures [5].

This technology is usually applied to materials with low hardness and high plasticity at room temperature, but heating support or alternative processing technologies may be necessary for materials with high hardness. In this study, the combined effects of elevated temperature and technological/geometrical parameters are analyzed through simulations and experiments, leading to the proposed application of heating in ISMF and its potential for wider use in experiments and production.

## 2 Material Properties

The study was performed on a 1 mm thick SUS-304 stainless steel sheet. The chemical composition of the material is presented in Table 1. The temperature mechanical behavior of the SUS-304 is displayed in Fig. 1 and Table 2.

## 3 Experiment and Simulation Procedure

The experimental setup is shown in Fig. 2a, where the sheet is clamped with six degrees of freedom at the four edges and the bottom is a support plate with a shape that matches the part being formed. To simplify the simulation, the mathematical model eliminates the support plate, which has minimal effect on the simulation results, and retains the six degrees of freedom for the sheet. The forming tool is a rigid body that moves in the x, y, and z directions, as shown in Fig. 2b. Figure 2c depicts the profile of the part, which has a  $200 \times 200 \times 1$  mm square plate size. The initial forming angle is set at  $29.5^\circ$ , reducing the computational time for the experiments and simulations. The forming curve is in the form of a concave curve with a radius of curvature R80, leading to a continuously changing forming angle based on the tool's down step (z). The forming angle reaches its maximum value

**Fig. 1** Stress–strain curve of SUS-304 materials at elevated temperature [6]

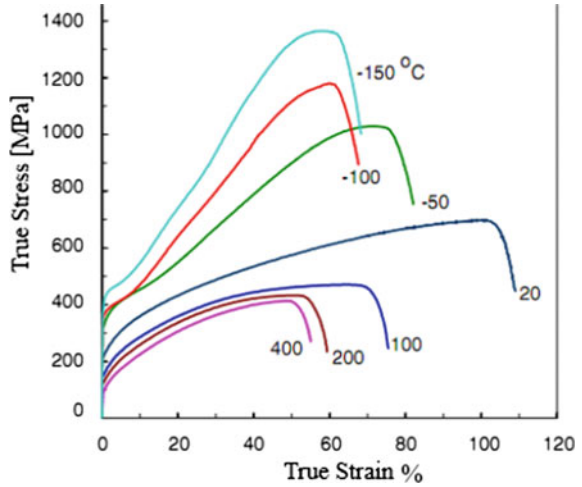


**Table 2** Properties of SUS-304 materials at different temperatures

Materials	SUS 304
Thermal conductivity coefficient (W/m.K)	16.2 (0–100 °C) and 21.5 (<500 °C)
Thermal expansion coefficient (mm/mm.K)	$12.1 \times 10^{-5}$
Specific heat (mmJ/ton.°C)	500
Density ( $\rho$ kg/mm <sup>3</sup> )	7.8e-6
Elastic modulus (E, kN/mm <sup>2</sup> )	200
Poisson ratio ( $\mu$ )	0.29

at the maximum fracture height of the part, which reduces the number of samples needed for testing.

The focus of the study is to examine the effect of three parameters on the forming ability of SUS-304 metal sheet using ISMF method. These parameters are temperature (T), the step in the z-direction (Z), and tool dimension (D). The feed rate (V<sub>xy</sub>) is fixed at 1500 (mm/min) to reduce the time and simulation cases while still obtaining enough experimental data for comparison. The study utilizes Taguchi method, which uses a L4 orthogonal matrix with 4 cases, to perform simulations with three factors, each with two levels. This method reduces the number of cases compared to the normal approach but still provides complete and accurate results. Experiments were conducted with variable parameters as presented in Table 3.

**Fig. 2** Experimental (a), simulation (b) setup and profile of the part (c)

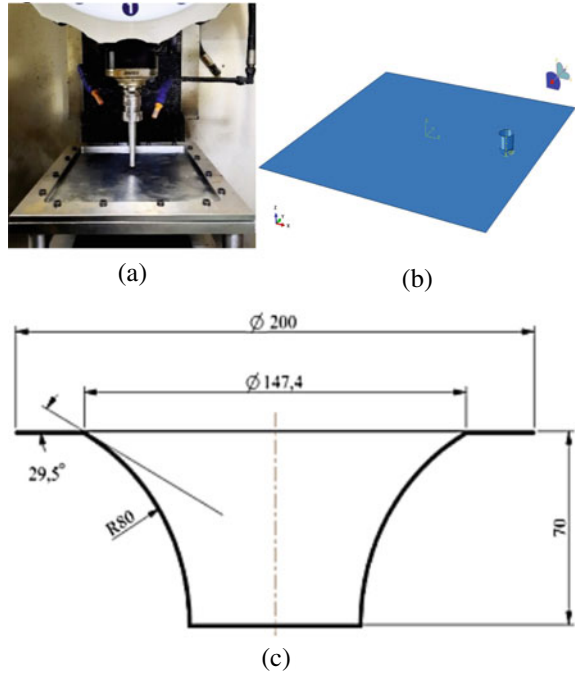


**Table 3** L4 orthogonal matrix by the Taguchi method

No.	T (°C)	Z (mm)	D (mm)
1	0.695	0.688	1.02
2	0.665	0.649	2.34
3	0.612	0.599	2.19
4	0.573	0.579	1.04

## 4 Results and Discussion

In the simulation process, the precision of the model is enhanced with a finer mesh size. The mesh can be divided based on the location to be evaluated or the simulation needs. However, a finer mesh size increases the computation duration. To prevent errors during the simulation and save time, it is suggested to start with a coarser mesh size and verify for any mistakes. Then, if no mistakes are present, the mesh can be refined.

The simulation was performed using Abaqus 6.13 software and experiments were conducted on a CNC machine using the parameters listed in Table 3. The simulation was run until the mesh deviated or failed, and the fracture height of the corresponding

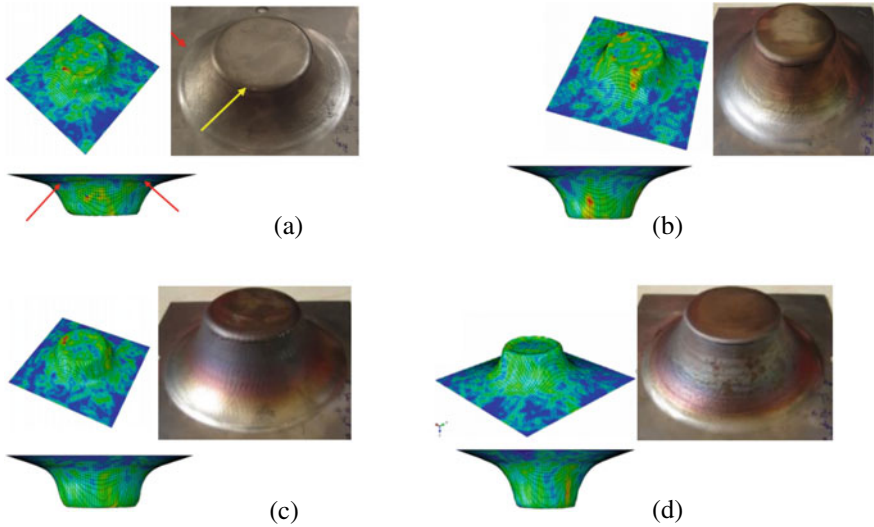


**Fig. 3** Deformed shapes in FEM simulation and corresponding experiment **a** No. 1 **b** No. 2 **c** No. 3 and **d** No. 4

**Table 4** Comparison between experiment and simulation

No.	Fracture height (mm)		Forming angle (°)		Forming angle error (%)
	Sim	Exp	Sim	Exp	
1	31.15	31.50	60.95	61.23	0.46
2	36.50	40.70	65.24	68.52	4.79
3	41.65	43.35	69.24	70.54	1.84
4	44.1	44.80	71.11	71.64	0.47

experimental product was measured. The simulation was used to calculate the deformation angle using the Z value and this was compared to the actual value measured on the CNC machining. The results of the simulation and experiments are shown in Fig. 3 and Table 4. It can be seen that the workpiece has a convex appearance due to the forming tool being pushed up, which can be observed during the simulation. The mesh is initially deformed evenly, and torsion occurs when the detail reaches the maximum deformation limit. The forming tool’s small diameter makes it easier to penetrate the metal sheet. The simulation’s curved profile is smaller than the value measured in CAD, which confirms the simulation’s ability to predict the part’s spring-back phenomenon. The tool diameter and down-step are the main parameters affecting the spring-back phenomenon.

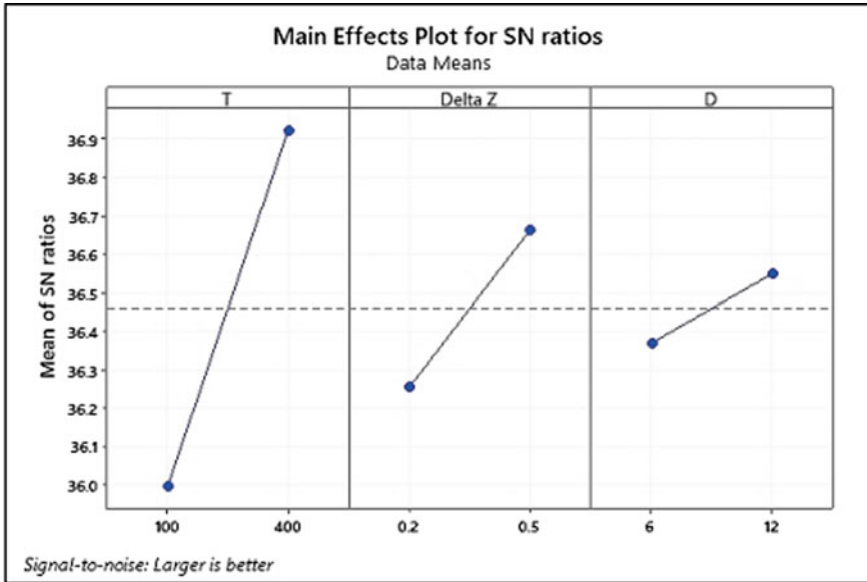


Fig. 4 The effects of input parameters on the forming angle

The capacity of sheet metal deformation is represented by the forming angle, with a larger forming angle indicating better results. The study analyzed the impact of three parameters, temperature (T), tool down-step (Z), and tool diameter (D), on the forming angle by using the S/N value in the Taguchi method. The S/N value was calculated by the formula:  $S/N = -10 \cdot \log_{10}((1/N) \sum (1/y^2))$ . Figure 4 shows the average influence of each parameter on the maximum forming angle. The steeper the line for each factor T, Z, and D, the greater its impact on the maximum forming angle. Figure 5 reveals that temperature (T) has the highest effect, followed by the tool down-step (Z), and then tool diameter (D). The regression equation for the parameters' effect was obtained through Minitab software as Eq. (1). ANOVA analysis was used to determine the optimal set of parameters for maximum forming angle: Z = 0.5 mm, D = 12 mm, and T = 400 °C. The calculation resulted in a forming angle of 76.08° and a fracture height of 50.75 mm.

$$\text{Maximum forming angle} = 66.64 + 3.54T + 1.54Z - 0.61D \quad (1)$$

Factor Information			
Factor	Type	Levels	Values
T	Fixed	2	100, 400
Delta Z	Fixed	2	0.2, 0.5
D	Fixed	2	6, 12

Analysis of Variance							
Source	DF	Seq SS	Contribution	Adj SS	Adj MS	F-Value	P-Value
T	1	50.126	82.07%	50.126	50.126	*	*
Delta Z	1	9.486	15.53%	9.486	9.486	*	*
D	1	1.464	2.40%	1.464	1.464	*	*
Error	0	*	*	*	*		
Total	3	61.077	100.00%				

Fig. 5 ANOVA analysis of the influence of the parameters

## 5 Conclusion

In this study, a comparison was made between simulation and experimental results for fracture height and forming angle. The maximum error observed for forming angle was 4.79%, with the minimum error being 0.46%. The tool down-step (Z) was found to significantly impact surface roughness, with temperature (T) having the largest effect on fracture height and forming angle, followed by Z and then tool diameter (D). To minimize fracture height and forming angle, it was determined that a reduction of Z and an increase in T in combination with a larger D is necessary. However, this reduction in Z would result in decreased forming productivity. Conversely, changes in D and T are beneficial as they do not require a machine with high capacity or low electrical energy consumption. Overall, the close match between experiment and simulation results with regards to geometry suggests that simulation results can be used to accurately predict fracture height and maximum forming angle in industrial applications.

**Acknowledgements** This work was also supported by Vietnam Ministry of Education and Training (MOET) under grant number B2022-BKA-08.

## References

1. Allwood JM, King GPF, Duflou J (2005) A structured search for applications of the incremental sheet-forming process by product segmentation. *Proc Instit Mech Eng, Part B: J Eng Manuf* 219(2):239–244
2. Do V-C, Nguyen D-T, Cho J-H, Kim Y-S (2016) Incremental forming of 3D structured aluminum sheet. *Int J Precis Eng Manuf* 17(2):217–223
3. Nguyen D-T, Park J-G, Lee H-J, Kim Y-S (2010) Finite element method study of incremental sheet forming for complex shape and its improvement. *Proc Instit Mech Eng, Part B: J Eng Manuf* 224(6):913–924
4. Duc-Toan N, Seung-Han Y, Dong-Won J, Tae-Hoon C, Young-Suk K (2011) Incremental sheet metal forming: numerical simulation and rapid prototyping process to make an automobile white-body. *Steel Res Int* 82(7):795–805
5. Nguyen D-T, Park J-G, Kim Y-S (2010) Ductile fracture prediction in rotational incremental forming for magnesium alloy sheets using combined kinematic/isotropic hardening model. *Metall and Mater Trans A* 41(8):1983–1994
6. Chen J, Young B (2006) Stress–strain curves for stainless steel at elevated temperatures. *Eng Struct* 28(2):229–239